

Imperial College
London

**Synthetic Modifications of Metal Organic
Framework Adsorbents for Environmental
Remediation**

By: Luqman Hakim Mohd Azmi

A thesis submitted in fulfilment of the requirements for the degree of Doctor of Philosophy

Imperial College London
Department of Chemical Engineering

November 2021

Statement of Originality

I, Luqman Hakim Mohd Azmi hereby declare that this thesis titled, “Synthetic Modifications of Metal Organic Framework Adsorbents for Environmental Remediation” and the work presented therein are originally from me. I confirm that:

- This work was carried out wholly during my candidature for a PhD research degree since 30th September 2017 at this University.
- This thesis has not previously been submitted in whole or in part for the award of another degree or professional qualification except to my registered University.
- Any published and unpublished work(s) of others has been clearly acknowledged in the text and they have been appropriately cited.
- Where there is a work in the thesis jointly completed between me and other people, I have made a distinction between what I have contributed myself and contributions from the others.

By: Luqman Hakim Mohd Azmi

Date: November 2021

Copyright Declaration

The copyright of this thesis rests with the author. Unless otherwise indicated, its contents are licensed under a Creative Commons Attribution-Non Commercial 4.0 International Licence (CC BY-NC).

Under this licence, you may copy and redistribute the material in any medium or format. You may also create and distribute modified versions of the work. This is on the condition that: you credit the author and do not use it, or any derivative works, for a commercial purpose.

When reusing or sharing this work, ensure you make the licence terms clear to others by naming the licence and linking to the licence text. Where a work has been adapted, you should indicate that the work has been changed and describe those changes.

Please seek permission from the copyright holder for uses of this work that are not included in this licence or permitted under UK Copyright Law.

(Copyright 2021, Luqman Hakim Mohd Azmi)

Acknowledgements

“Whoever has not thanked people, has not thanked God” – Sunan Abi Dawud 4811. The culmination of this thesis is only possible with the support of many individuals behind the scenes. My utmost gratitude goes to Yayasan Khazanah Malaysia for believing in me and invested generously for my postgraduate studies here. This also applies to their ancillary funds that provided me with amazing opportunities to present my work at international conferences and be inspired by the discoveries of prominent scholars and industry practitioners alike.

I wish to offer my humble appreciation to both my supervisors, Daryl Williams and Bradley Ladewig for your dedication, forbearance, and the lifeline financial aid when I was your student. Know that our discourses had left an indelible mark in my scientific and professional developments. I enjoyed my time in both groups. My colleagues were very friendly and cooperative to help me progress with my PhD. Notably, Shanxue and Tingwu who, even after their graduation and now based in far-flung China, relentlessly put their heads together and worked out new ideas with me at all costs. In trying circumstances, speaking to Elwin and Pavani made my research a breeze while fatherly Othman gave me strength. My side consultations with several respected lecturers and research associates were highly valued too. In the lab, Patricia and Kaho were always available to help me with data analysis and collection.

Outside the professional life, my friends are my source of cherishment. To Badrul, Afiq, Fadzli, Nasrul, Muzamir, Taufiq, Irina, Hafiz, and Faris; thank you for letting me speak my heart out. Talking with our mother tongue transcended me beyond all formalities. My brethren, Nacime, Fady, and Tufail soaked my complaints and turned them into good times and foods. My family is always by my side. I am especially euphoric when my beloved wife, Farhana is with me, who is also my solace. The encouraging words by my dearest mother Rohana soothed me when I lamented my woes to her. Your filial love is unmatched. The banter from my siblings, Zainul and Balqis never ceases to lift my mood. For the unsung heroes: cleaners, store managers, admins, and my circle of acquaintances all over the globe, thank you for making my learning environment as conducive as possible. Finally, from this academic sojourn, God has blessed me to travel afar and meet numerous great people; enriching my worldview that would last a lifetime. For these and more to come afterwards, to You alone I would increase my devotion.

Abstract

The widespread usage of organic chemicals has led to an unprecedented level of pollution and associated health risk concerns. Although activated carbon (AC) based adsorption is commonly used in wastewater treatment and air purification processes, now, new metal-organic frameworks (MOFs) adsorbents with superior surface areas, chemically tuneable structures, and excellent reusability are available. This thesis evaluates the application of selected MOFs and their modified variants for removing organic pollutants from aqueous and humid air streams, reporting adsorption capacity and kinetics. For the removal of aqueous phase pollutant 2-chlorophenol, the higher surface area of MIL-101 (Cr) even with improved surface amination, gave inferior adsorption capacity compared to the hydrophobic AC, indicating the importance of MOF's hydrophobicity. A hydrophobic MIL-101 (Cr) was synthesized using a PDMS vapour coating protocol, creating a new material with the same surface area and pore volume as pristine MIL-101 (Cr). For 0.5% toluene P/P₀ vapour co-adsorption at 40% RH, this composite showed a 60% higher uptake capacity and a 34% higher aggregate adsorption rate compared to pristine MIL-101 (Cr), and 360% faster kinetics relative to AC. A solution-based treatment for MIL-100 (Fe) was developed using calixarene, producing super hydrophobic surfaces, which at 40% RH and 0.5% toluene P/P₀, exhibited a 68% higher aggregate uptake rate, despite having lower pore volumes and surface areas. Finally, MIL-96 (Al) was modified using hydrolysed polyacrylamide polymer, which enlarged the 3.2- μm particles by 225% and transformed their crystal morphology. The polymer also contains amide with NH₂ moieties which improved the modified MIL-96 (Al)'s uptake capacity of perfluorooctanoic acid. Overall, this thesis highlights the complexity of co-adsorption when hydrophobic and hydrophilic adsorbates are both present. It also recalls the importance of adsorption kinetics, in contrast with current MOF research emphases, which are on surface area and adsorption capacity. Faster adsorption kinetics may be preferred over a slow-diffusing adsorbate, even if the final uptake capacity is superior, for some industrial applications.

Table of Contents

Statement of Originality.....	2
Copyright Declaration.....	3
Acknowledgements.....	4
Abstract.....	5
Table of Contents.....	6
List of Figures.....	14
List of Tables.....	27
List of Abbreviations.....	30
List of Academic Achievements.....	32
Chapter 1: Introduction.....	33
1.1 Persistent organic water pollutants	33
1.2 Airborne organic pollutants	35
1.3 Porous adsorbents	38
1.3.1 Activated carbon (AC).....	38
1.3.2 Metal-organic frameworks (MOFs).....	40
1.3.3 Comparison between AC and MOFs	42
Chapter 2: Literature Review - A ‘Hole’ New World	48
2.1 Water remediation.....	48
2.1.1 Limitations of existing water treatment technologies	48
2.1.2 Removal of phenols	50
2.1.3 Removal of perfluorinated compounds.....	66
2.1.4 Water stability in MOFs.....	77
2.1.5 Summary of literature gaps and the rational design of MOFs in water decontamination.....	83
2.2 Air purification.....	85

2.2.1	Limitations of current indoor air VOC removal technologies	85
2.2.2	Developing MOFs to remove VOCs from humid air	86
2.2.3	Summary of best approaches to designing adsorbents for humid VOCs capture.	117
2.3	Structural stability in MOFs.....	120
2.3.1	Addition of initiation solvents	121
2.3.2	Addition of coordination modulators.....	122
2.3.3	Addition of surfactants.....	124
2.3.4	Addition of a hard template	125
2.3.5	Denser MOF formation.....	125
2.4	Research objectives.....	128
2.4.1	Research objective 1: Amine functionalised MOF for aqueous phase phenol removal	128
2.4.2	Research objective 2: Improving a MOF's moisture stability via a vapour phase hydrophobic surface treatment.....	128
2.4.3	Research objective 3: Wet-phase hydrophobic treatments for MOFs	129
2.4.4	Research objective 4: Role of surface chemistry, crystal morphology and particle size in MOFs for perfluorochemical removal.....	129
Chapter 3: Experimental Materials and Methods		130
3.1	Powder x-ray diffraction (PXRD).....	130
3.2	Thermogravimetric analysis (TGA).....	133
3.3	Surface area and pore measurement	136
3.3.1	Surface area analysis.....	136
3.3.2	Pore size distribution analysis.....	140
3.4	Fourier-transform infrared (FTIR) spectroscopy	142
3.5	Scanning electron microscopy (SEM)	146
3.6	Water contact angle.....	146
3.7	Static vapor sorption	150
3.8	Dynamic vapor sorption.....	156

3.9 Liquid-phase chlorophenol adsorption experiments (Chapter 4).....	161
3.9.1 Materials	161
3.9.2 Hydrofluoric acid-free synthesis of MIL-101 (Cr) and MIL-101-NH ₂	161
3.9.3 Material characterizations	162
3.9.4 Batch adsorption of 2-chlorophenol (2-CP).....	163
3.9.5 Adsorption isotherm modelling	164
3.9.6 Kinetics study for 2-chlorophenol adsorption.....	168
3.9.7 Influence of pH and zeta potential in 2-chlorophenol batch adsorption.....	171
3.9.8 Adsorbent reusability study	172
3.10 Toluene vapour capture experiments from humid air by PDMS-treated MIL-101 (Cr) (Chapter 5)	172
3.10.1 Materials	172
3.10.2 Synthesis of MIL-101 (Cr).....	173
3.10.3 PDMS coating method.....	173
3.10.4 Material characterizations	174
3.10.5 Hydrophobicity index	174
3.10.6 Single and dual component vapor sorption setup	174
3.10.7 Moisture stability and adsorbent reusability tests.....	175
3.11 Toluene vapour capture experiments from humid air by modified MIL-100 (Fe) (Chapter 6)	175
3.11.1 Materials	175
3.11.2 Synthesis of high temperature MIL-100-HT (Fe).....	175
3.11.3 Preparation of silane-coated MIL-100 (Fe) particles.....	176
3.11.4 Synthesis of room temperature MIL-100 (Fe)	176
3.11.5 Preparation of phosphorous oxyacid-treated MIL-100 (Fe) particles.....	177
3.11.6 Preparation of calixarene-treated MIL-100 (Fe) particles	177
3.11.7 Material characterizations	178
3.11.8 Hydrophobicity index	179

3.11.9 Single and dual component vapor sorption setup	180
3.11.10 Moisture stability and adsorbent reusability tests	180
3.12 Liquid-phase PFOA adsorption experiments (Chapter 7)	181
3.12.1 Materials	181
3.12.2 Synthesis of MIL-96 (Al).....	181
3.12.3 Material characterizations	182
3.12.4 ¹⁹ F NMR analysis	183
3.12.5 PFOA adsorption	183
3.12.6 PFOA desorption	183
3.12.7 PFOA homologue: n-octane vapor adsorption kinetics analysis	184
Chapter 4: Aminated MIL-101 for aqueous-phase phenol removal	185
4.1 Introduction.....	185
4.2 Results and discussion	185
4.2.1 PXRD.....	185
4.2.2 SEM	187
4.2.3 Porosity analysis	187
4.2.4 FTIR.....	189
4.2.5 TGA	189
4.2.6 Water contact angle.....	191
4.2.7 Adsorption isotherm modelling	192
4.2.8 Batch adsorption of 2-chlorophenol.....	194
4.2.9 Kinetics study for 2-chlorophenol adsorption.....	199
4.2.10 Influence of pH and zeta potential on 2-CP adsorption.....	200
4.3 Conclusions.....	203
Chapter 5: Hydrophobic MOFs from vapour phase coating.....	205
5.1 Introduction.....	205
5.2 Results and discussion	206

5.2.1 PXRD and SEM.....	206
5.2.2 FTIR.....	207
5.2.3 XRF.....	208
5.2.4 Porosity analysis	210
5.2.5 Water contact angle.....	214
5.2.6 Water sorption isotherms	215
5.2.7 Toluene sorption isotherms.....	217
5.2.8 Hydrophobicity index	220
5.2.9 Water and toluene co-adsorption experiments.....	221
5.2.10 Uptake capacity at 40% RH and 0% toluene P/P ₀	221
5.2.11 Uptake capacity at 40% RH and 0.5% toluene P/P ₀	223
5.2.12 Adsorption kinetics for 40% RH and 0.5% toluene P/P ₀	224
5.2.13 Uptake capacity at 40% RH and 10% toluene P/P ₀	227
5.2.14 Adsorption kinetics for 40% RH and 10% toluene P/P ₀	228
5.2.15 High humidity test.....	230
5.2.16 Adsorbent reusability study	231
5.2.17 Toluene co-adsorption mechanisms after PDMS treatment	232
5.3 Conclusions.....	233
5.3.1 Future Work.....	234
Chapter 6: Hydrophobic MOFs from wet phase coating.....	235
6.1 Introduction.....	235
6.2 Results and discussion	236
6.2.1 Calixarene structural properties	237
6.2.2 PXRD patterns of calixarene-treated MIL-100 (Fe).....	238
6.2.3 FTIR spectra of calixarene-treated MIL-100 (Fe)	240
6.2.4 TGA data for calixarene and PA-treated MIL-100 (Fe).....	241
6.2.5 Porosity analysis of calixarene-treated MIL-100 (Fe).....	242

6.2.6 Water contact angles of calixarene-treated MIL-100	243
6.2.7 Water sorption isotherms of calixarene-treated MIL-100 (Fe).....	244
6.2.8 Toluene sorption isotherms of calixarene-treated MIL-100 (Fe)	245
6.2.9 Hydrophobicity index of calixarene-treated MIL-100 (Fe)	247
6.2.10 Toluene co-adsorption by calixarene-treated MIL-100 (Fe) at 40% RH.....	248
6.2.11 Toluene co-adsorption by calixarene-treated MIL-100 (Fe) at 40% RH and 0.5% toluene.....	250
6.2.12 Toluene co-adsorption by calixarene-treated MIL-100 (Fe) at 40% RH and 10% toluene.....	253
6.2.13 Adsorption kinetics for calixarene-treated MIL-100 (Fe)	256
6.2.14 Adsorption kinetics for calixarene-treated MIL-100 (Fe) using a nonlinear pseudo first order kinetics model	256
6.2.15 High humidity test for calixarene-treated MIL-100 (Fe).....	258
6.2.16 Adsorbent reusability study on calixarene-treated MIL-100 (Fe)	259
6.2.17 Toluene co-adsorption mechanisms after calixarene surface treatment	260
6.3 Conclusions.....	261
Chapter 7: Modified MIL-96 (Al) particles for perfluorooctanoic acid removal	263
7.1 Introduction.....	263
7.2 Results and discussion	264
7.2.1 SEM	264
7.2.2 PXRD.....	267
7.2.3 FTIR.....	269
7.2.4 Elemental analysis	272
7.2.5 TGA	273
7.2.6 Porosity analysis	275
7.2.7 Particle size analysis	276
7.2.8 Batch adsorption of perfluorooctanoic acid using MOFs	277
7.2.9 Perfluorooctanoic acid adsorption kinetics analysis.....	280

7.2.10 Perfluorooctanoic acid adsorption and desorption processes	284
7.3 Conclusions.....	290
Chapter 8: Conclusions and Outlook	291
8.1 Conclusions.....	291
8.2 Future work ideas.....	295
8.2.1 To perform adsorption experiments based on industrially relevant conditions....	295
8.2.2 To manipulate fine particulate MOF powders into more robust shapes and properties.....	297
8.2.3 Adsorbent reusability experiments using a thermal/pressure swing adsorption ...	298
8.3 Perspectives on MOF advancements	299
8.3.1 Reasonable costs	299
8.3.2 Superior performance.....	299
8.3.3 Facile and safe regeneration.....	300
Chapter 9: References	301
Chapter 10: Appendices	344
10.1 Appendix for Chapter 3	344
10.1.1 Differences between DSC and DTA.....	344
10.1.2 Data from AC's water sorption validation experiment on IGA.....	345
10.1.3 Steps to setting up a competitive adsorption experiment on a DVS machine	346
10.2 Appendix for Chapter 4	348
10.2.1 MIL-101 (Cr) structural integrity using PXRD analysis	348
10.2.2 N ₂ adsorption and desorption isotherms	348
10.2.3 FTIR and elemental analysis.....	349
10.2.4 Linear Langmuir-1 isotherm plots	351
10.3 Appendix for Chapter 5	353
10.3.1 SEM images of MIL-101-PDMS composites.....	353
10.4 Appendix for Chapter 6	356

10.4.1 Hydrophobic chemical agent structural properties	356
10.4.2 Silane surface modification.....	358
10.4.3 PXRD patterns of PA-treated MIL-100 (Fe)	360
10.4.4 Sample colour changes after calixarene coating treatment.....	361
10.4.5 SEM images of calixarene-treated MIL-100 (Fe).....	362
10.4.6 FTIR spectra of PA-treated MIL-100 (Fe).....	366
10.4.7 Porosity analysis for PA-treated MIL-100 (Fe)	367
10.4.8 Porosity analysis for Cx-treated MIL-100 (Fe) samples.....	368
10.4.9 N ₂ adsorption and desorption isotherms	369
10.4.10 Water contact angles of PA-treated MIL-100 (Fe).....	369
10.4.11 Water contact angle images of Cx-treated MIL-100 (Fe).....	370
10.4.12 Water sorption isotherms of PA-treated MIL-100 (Fe)	371
10.4.13 Toluene sorption isotherms of PA-treated MIL-100 (Fe).....	372
10.4.14 Hydrophobicity index of PA-treated MIL-100 (Fe)	373
10.4.15 Uptake capacity of PA-treated MIL-100 at 40% RH and 0% toluene.....	374
10.4.16 Uptake capacity of PA-treated MIL-100 (Fe) at 40% RH and 0.5% toluene ...	375
10.4.17 Uptake capacity of PA-treated MIL-100 (Fe) at 40% RH and 10% toluene	376
10.4.18 Adsorption kinetics of PA-treated MIL-100 (Fe) at 40% RH and 0.5% toluene	377
10.4.19 Adsorption kinetics of PA-treated MIL-100 (Fe) at 40% RH and 10% toluene	378
10.4.20 Overall kinetics analysis of PA-treated MIL-100 (Fe) using a linear initial slope fit.....	379
10.4.21 Overall kinetics analysis of PA-treated MIL-100 (Fe) using a nonlinear pseudo first order kinetics model	380
10.5 Appendix for Chapter 7	382
10.5.1 SEM images of MIL-101-HPAM	382
10.5.2 FTIR analysis of HPAM-treated trimesic acid ligand	384

10.6 Granted permission for copyrighted materials.....	385
--	-----

List of Figures

Figure 1.1: Possible entry pathways for persistent pollutants into the domestic water pipelines. Reproduced with permission from (Barbosa <i>et al.</i> , 2016). Copyright 2016, Elsevier.	35
Figure 1.2: The chart forecasts a century-span greenhouse gas emissions scenarios from year 2000 under multiple assumptions; (a) if no climate policies are implemented, (b) continuing with existing policies, (c) if the countries involved achieved their current future pledges to reduce the emissions and (d) drastic and necessary actions that are compatible to reduce major emissions are taken. Reprinted with permission from (Ritchie & Roser, 2020). Copyright 2020, online.	36
Figure 1.3: The types of surface functional groups that can exist on a pyrolyzed carbon surface: (a) oxygen, (b) nitrogen and (c) sulphur. Basic and acidic functionalities are marked in blue and red respectively. Reproduced with permission from (de Clippel <i>et al.</i> , 2013). Copyright 2013, RSC Publishing.	39
Figure 1.4: A schematic illustration of the elements making up a 3D, porous, crystalline metal-organic framework (MOF). The 3D structure will be the repeating entity, which forms a larger network.	40
Figure 1.5: Formation of open metal sites by thermal activation in MIL-100/101, Cu-BTC and UiO-66 (oxygen = red, metal atom = green/orange/blue, carbon = grey, hydrogen = white). Figure is taken with granted permission from (Hall & Bollini, 2019). Copyright 2019, RSC Publishing.	41
Figure 1.6: Pore size distributions of typical activated carbons. Data is replotted by (Hubbe, Azizian & Douven, 2019) from original source (Perrich, 2018).	43
Figure 2.1: Processes involved in a three-stage WWTP, from the left, primary, secondary, and tertiary stages. The black bold arrows indicate the flow of wastewater (Los Angeles County Sanitation Districts, 2021).	49

- Figure 2.2: Proposed adsorption mechanisms of bisphenol S (left), sulfamethoxazole (centre) and bisphenol A (right) over MIL-101 (Cr)-NH₂ via 6-membered H-bonding configuration for the molecules containing SO₂ moiety. Reproduced with permission from (Park & Jung, 2020). Copyright 2020, Elsevier.54
- Figure 2.3: Adsorption mechanisms of BPA on Al-MOF/sodium alginate-chitosan composite beads. Reprinted with permission from (Luo et al., 2019). Copyright 2019, Elsevier.....58
- Figure 2.4: Possible binding mechanisms of HKUST-1 (Cu) to PNP (a) ionic interaction between the negatively charged oxygen of the PNP and the Cu metal site, (b) development of covalent bonding between the oxygen belonging to the PNP and the Cu metal site and (c) π - π stacking of the benzene rings from the PNP and the ligand of HKUST-1 (Cu). Reprinted with permission from (Lin & Hsieh, 2015). Copyright 2015, Elsevier.62
- Figure 2.5: PFOS uptake rate (at pH 5) over 80 hrs of defective UiO-66 (Zr), powdered AC (PAC) and anion exchange resin IRA-900. Results were fitted with a pseudo-second order kinetics model. Inset image shows the sorption trend in the first 2 hrs. Reprinted with permission from (Clark *et al.*, 2019). Copyright 2019, ACS Publications.....69
- Figure 2.6: Structural topologies of ZIF-7 (Zn), ZIF-8 (Zn), and ZIF-L (Zn). The internal golden spheres represent the pore void. Reprinted with permission from (Chen et al., 2016). Copyright 2016, Elsevier.72
- Figure 2.7: Structures of MIL-100 (Cr) and MIL-101 (Cr) showing their (a) small cages, (b) large cages, and (c) pentagonal and hexagonal windows. The chromium octahedra is in green whereas the carbon atoms are in black. Image is taken with permission from (Trung *et al.*, 2010). Copyright 2010, Elsevier.82
- Figure 2.8: (a) Water adsorption isotherms measured at 298 K for MOF-74 (Co) (red), HKUST-1 (Cu) (blue), UiO-66 (Zr) (grey) and SION-82 (Sr)' (yellow) and (b) recyclability of benzene capture under humid atmosphere for the same adsorbents. Reproduced with permission from (Sudan *et al.*, 2020). Copyright 2020, ACS Publications..99

Figure 2.9: (a) SEM image of the MOF filter, (b) XRD spectra of simulated CAU-3, MOF filter and NWF, (c) N₂ adsorption-desorption plots of the MOF filter and NWF at 77 K, (d) image of NWF and MOF filter, (e) image showing the encapsulation of MOF particles into a face mask, (f) photograph of a household hair dryer (with the inset displaying the relationship between the outlet temperature and the distance), (g) schematic of the bespoke adsorption breakthrough experimental setup, (h) breakthrough curves of 2 ppm hexanal of the filters at 298 K and 50% RH, (i) breakthrough curves of 2 ppm hexanal of the MOF filter under 50% RH and after three regeneration cycles (adsorption and desorption temperatures are 298 K and 358 K respectively) whereas the inset shows the regeneration procedure using a hair dryer. Reproduced with permission from (Zheng *et al.*, 2020a). Copyright 2020, ACS Publications. 100

Figure 2.10: Attachment of calixarene molecules onto UiO-66 (Zr) framework to improve its oleophilicity. Figure from (Jeong *et al.*, 2019) with permission. Copyright 2019, ACS Publications. 101

Figure 2.11: (Left) Measured water contact angle, acidic (AFG) and basic (BFG) functional groups of original AC and after a series of PDMS coating temperatures. (Right) The influence of total micropore volume, water contact angle and AFG towards the adsorbents' water vapour adsorption capacity. Reprinted with permission from (Liu, Yang & Xue, 2016). Copyright 2016, Elsevier..... 102

Figure 2.12: A schematic illustrating the sequential amide reaction and PDMS vapour coating on CAU-1 (Al) Reproduced with permission from (Zheng *et al.*, 2020b). Copyright 2020, Elsevier..... 104

Figure 2.13: Two constructive approaches to build MOFs with constrained pores either (A) by network interpenetration with conventional linear ligands or (B) by substituting the linear types with angular ligands. Reprinted with permission from (Xie *et al.*, 2018). Copyright 2018, Elsevier. 109

Figure 2.14: The removal performance of octane and *p*-xylene by ZIF-412 (Zn) and BPL carbon at 298 K. (a) Static octane vapor adsorption isotherm where ZIF-412 shows 260% higher uptake than BPL carbon, (b) static *p*-xylene vapor adsorption isotherm with 250% higher uptake by ZIF-412 (Zn) than BPL carbon, (c)

breakthrough curves for octane in both dry (0% RH) and wet (65% RH) conditions, (d) breakthrough curves for <i>p</i> -xylene. Solid and empty circles in the breakthrough curves refer to adsorption and desorption points respectively. Reprinted with permission (Yang <i>et al.</i> , 2017a) Copyright 2017, ACS.....	110
Figure 2.15: A schematic illustration showing the influence of reaction times, 2-MI and methanol concentrations on MOF-74 (Co)'s particle size evolution. Reproduced with permission from (Guo <i>et al.</i> , 2018). Copyright 2018, RSC Publishing.....	123
Figure 2.16: Frequently studied MOFs that have been shaped using granulation and pressing methods. Reproduced with permission from (Lee <i>et al.</i> , 2021). Copyright 2021, Springer.....	126
Figure 3.1: A 2-dimensional schematic of XRD principle.	130
Figure 3.2: The three balance designs in a TGA instrument (from left to right): top, bottom-loading, and horizontal arrangement (Gabbott, 2008).	135
Figure 3.3: Six classifications of physisorption isotherms. Image is taken with permission from (Thommes <i>et al.</i> , 2015). Copyright 2015, IUPAC and De Gruyter.....	139
Figure 3.4: A sample image of an ATR sampling method in a modern FTIR spectrometer (Agilent, 2021).	145
Figure 3.5: Contact angle forces.	147
Figure 3.6: Illustrations showing (a) the advancing contact angle measurement technique involving liquid addition to an existing droplet and (b) the receding contact angle measurement technique that removes the liquid from an existing droplet. Image is reproduced with permission from (Jayaramulu <i>et al.</i> , 2019). Copyright 2019, Wiley-VCH.	148
Figure 3.7: Images of (left) a pelletized, green-coloured MIL-101 (Cr) and (right) a uniformly pressed, orange-coloured MIL-100 (Fe) powder on a glass slide.....	149
Figure 3.8: A dissected picture of an Intelligent Gravimetric Analyser (IGA). Image is taken from (Hiden Isochema, 2021).	150

Figure 3.9: A sample image of the user interface on the IGA software when setting a toluene vapour adsorption and desorption isotherm experiment at 25 °C.....	151
Figure 3.10: The main sensor display window of the IGA software.	152
Figure 3.11: IGA measurement validation based on water sorption isotherms by AC at 25 °C. Filled symbols are the adsorption isotherms whereas empty symbols shapes are for desorption.....	154
Figure 3.12: Experimental and model-fitted water sorption data at 25 °C of (a) BPL activated carbon and (b) nitric acid-treated BPL activated carbon. Image is reproduced with permission from (Do, Junpirom & Do, 2009). Copyright 2009, Elsevier.	155
Figure 3.13: A schematic diagram of the working principles inside a DVS Resolution.	157
Figure 3.14: DVS measurement validation involving triplicate competitive adsorption experiments by AC at 25 °C and 40% RH using 0%, 0.5% and 10% toluene P/P ₀	160
Figure 3.15: Calibration plot of 2-CP solutions with a molar absorptivity (ϵ) = 0.0137 L/mol.cm.	164
Figure 3.16: Rate of 2-CP uptake data (left) by AC and (right) by MIL-101 (Cr) fitted with a linear pseudo second order (PSO) kinetics equation.	171
Figure 3.17: An illustration of the sample preparation before it is heated in the oven for PDMS vapor deposition.	173
Figure 4.1: PXRD patterns of (a) simulated MIL-101 (Cr), (b) as-prepared MIL-101 (Cr), (c) as-prepared MIL-101 (Cr)-NH ₂ and (d) AC.	186
Figure 4.2: SEM images for (a) MIL-101 (Cr) and (b) MIL-101 (Cr)-NH ₂ nanocrystals.....	187
Figure 4.3: Pore size distribution plots for MIL-101 (Cr), MIL-101 (Cr)-NH ₂ and AC adsorbents.....	188
Figure 4.4: Thermal weight loss profiles of (a) MIL-101-NH ₂ , (b) MIL-101 and (c) AC....	190

Figure 4.5: Static water contact angle measurement on MIL-101 (Cr) pellet at (left) $t = 0$ second and when the liquid has penetrated the porous pellet (right) at $t = 15$ seconds. .	192
Figure 4.6: 2-CP uptake capacity versus concentration after 24 hrs of adsorption. Dashed lines are the fitted data using a nonlinear Langmuir isotherm model.	195
Figure 4.7: The author's proposed hydrogen bond formation between 2-CP and the coordinated linker of MIL-101 (Cr)-NH ₂ during the adsorption process.	198
Figure 4.8: Amount of adsorbed 2-CP by MIL-101 (Cr) and AC at 25 °C after specific time intervals using [2-CP] = 500 mg/L, [MOF] and [AC] = 1 mg/mL solution.	200
Figure 4.9: Influence of solution pH on the uptake of 2-CP by MIL-101 (Cr) and AC.	201
Figure 4.10: 2-CP speciation as a function of pH. Image from (Chuang <i>et al.</i> , 2008) with permission. Copyrights 2008, ACS Publications.	202
Figure 4.11: Zeta potential distribution for MIL-101 (Cr) and AC.	202
Figure 5.1: PXRD patterns of PDMS-coated MIL-101 (Cr) samples.	206
Figure 5.2: FTIR spectra of the MIL-101 (Cr)-PDMS composites.	208
Figure 5.3: Repeating unit of PDMS polymer.	208
Figure 5.4: Elemental Si wt% quantification of all samples using XRF.	209
Figure 5.5: N ₂ adsorption (full symbols) and desorption (empty symbols) isotherms.	211
Figure 5.6: 0 to 0.1 P/P ₀ of the N ₂ adsorption (full symbols) and desorption (empty symbols) isotherms.	211
Figure 5.7: Pore size distribution analysis for all samples estimated from Tarazona non-local density functional theory model (N ₂) using a cylindrical pore geometry assumption.	213
Figure 5.8: Images of the static water contact angle measurements for (left) MIL-PDMS-Dow-6 and (right) MIL-PDMS-Sigma-6 at ambient temperature.	214

Figure 5.9: Water adsorption-desorption isotherms at 25 °C. Filled symbols and empty symbols are the adsorption and the desorption data points, respectively.....	216
Figure 5.10: Advancing contact angle measurements for PDMS-Sigma-coated microscope slide at 25 °C. (Left) Water contact angle is $92 \pm 3^\circ$. (Right) Toluene contact angle is $22 \pm 3^\circ$	218
Figure 5.11: Dry toluene adsorption-desorption isotherms at 25 °C. Filled symbols and empty symbols are the adsorption and the desorption data points, respectively.	218
Figure 5.12: Dry toluene adsorption kinetics for MIL-101 (Cr), MIL-PDMS-Sigma-0.25 and AC at < 10% toluene P/P ₀ region.....	219
Figure 5.13: Calculated molar hydrophobicity index (HI) for selected adsorbents as a function of % water P/P ₀ at 25°C.....	220
Figure 5.14: Adsorption capacity of all studied adsorbents at 40% RH and 0% toluene P/P ₀	222
Figure 5.15: Toluene uptake quantity by PDMS-coated MIL-101 samples at 0.5% toluene P/P ₀ . All experiments were performed at 40% RH saturation and at 25 °C.....	223
Figure 5.16: (Left) Adsorption kinetics at 40% RH and 0.5% toluene P/P ₀ by MIL-PDMS samples. Solid lines are the experimental data whereas dotted lines are the fitted values derived from pseudo first order (PFO) kinetics model. (Right) The initial adsorption plot.....	224
Figure 5.17: Toluene uptake quantity by PDMS-coated MIL-101 samples at 10% toluene P/P ₀ . All experiments were performed at 40% RH saturation and at 25 °C.....	228
Figure 5.18: (Left) Adsorption kinetics at 40% RH and at 10% toluene P/P ₀ . Solid lines are the experimental data whereas dotted lines are the fitted values derived from pseudo first order (PFO) kinetics model. (Right) The initial adsorption plot.	229
Figure 5.19: Reusability study of MIL-101 (Cr), MIL-PDMS-Sigma-0.25 and AC at 10% toluene P/P ₀ and 40% RH, 25°C for 10 cycles.	232

Figure 5.20: 0.5% toluene P/P ₀ uptake quantity by MIL-101 (Cr) after exposure to varying relative humidity ranging from 0% to 80%.	233
Figure 6.1: Diagrammatic representation of a calix[4]arene supramolecule.	236
Figure 6.2: PXRD patterns of calixarene-treated MIL-100 (Fe).	239
Figure 6.3: FTIR spectra of calixarene-treated MIL-100 (Fe).....	240
Figure 6.4: TGA profiles of PA and calixarene-treated MIL-100 (Fe). Values denoted in the brackets are the final residual masses.	241
Figure 6.5: Water adsorption and desorption isotherms of calixarene-treated MIL-100 (Fe). Filled symbols are for adsorption while empty symbols are for desorption. Multi-coloured texts on the figure's right-hand side refer to the micropore volume of each adsorbent.	245
Figure 6.6: Dry toluene adsorption and desorption isotherms of calixarene-treated MIL-100 (Fe). Filled symbols are for adsorption while empty symbols are for desorption.	246
Figure 6.7: Dry toluene adsorption kinetics of AC and calixarene-treated MIL-100 (Fe) at low P/P ₀	247
Figure 6.8: Molar hydrophobicity index (HI) of calixarene-treated MIL-100 (Fe).....	248
Figure 6.9: 40% RH and 0% toluene P/P ₀ adsorption capacity of calixarene-treated MIL-100 (Fe).....	249
Figure 6.10: 40% RH and 0.5% toluene P/P ₀ adsorption capacity of calixarene-treated MIL-100 (Fe).....	250
Figure 6.11: A sample plot showing the use of nonlinear pseudo first order kinetics model which generates q_m on experimentally measured adsorption data or q_e . Inset shows the linear-fitted kinetics plot during the initial 120 minutes of adsorption time.	252
Figure 6.12: (Left) 40% RH and 0.5% toluene P/P ₀ full range adsorption kinetics of calixarene-treated MIL-100 (Fe) samples. (Right) The first 120-minute adsorption rate is inclusive of the linear-fitted slope values given in the legend brackets.....	253

Figure 6.13: 40% RH and 10% toluene P/P ₀ equilibrium adsorption capacity of calixarene-treated MIL-100 (Fe) samples.....	254
Figure 6.14: (Left) 40% RH and 10% toluene P/P ₀ adsorption kinetics of calixarene-treated MIL-100 (Fe). (Right) Initial 30-minute adsorption data with linear-fitted slope values given in the legend brackets.....	255
Figure 6.15: Quantity of toluene adsorbed at 40% RH and 10% toluene P/P ₀ concentration by MIL-100 (Fe), MIL-Cx6-1 wt% and AC for a duration of 10 adsorption-desorption cycles.....	260
Figure 7.1: Chemical structures of the polymers used: (a) HPAM, (b) PAM and (c) PAA. .	265
Figure 7.2: Modified MIL-96 (Al) crystals with (a) no polymer, (b) 2 mL HPAM (R _{HPAM} = 0.2), (c) 6 mL HPAM (R _{HPAM} = 0.6), (d) 20 mL HPAM (R _{HPAM} = 2), (e) 20 mL PAM (R _{PAM} = 2), and (f) 20 mL PAA (R _{PAA} = 2).	266
Figure 7.3: PXRD patterns of the simulated MIL-96 (Al) compared to the as-synthesized MIL-96 (Al) samples modified with different types and proportions of polymers.....	268
Figure 7.4: The FTIR spectrum for the parent MIL-96 (Al) is in black. The spectra of as-synthesized MIL-96-RHPAM2 is in red. The blue line refers to MIL-96-RHPAM2's spectra after PFOA adsorption whilst the green line is the spectra after PFOA desorption.....	270
Figure 7.5: Elemental analysis for C, H, N and S in modified MIL-96 (Al) samples (n = 3).	272
Figure 7.6: TGA results for MIL-96 (Al) samples containing various HPAM quantities.....	274
Figure 7.7: Compiled TGA-MS %mass loss spectra (left y-axis) as a function of temperature for MIL-96 (Al) (solid red line) and MIL-RHPAM2 (dotted red line). The quantity of H ₂ O desorbed over temperature is represented by the m/z = 18 current intensity on the right y-axis. The quantity of H ₂ O desorbed by MIL-96 (Al) is shown in solid blue line whereas by MIL-96-RHPAM2, it is the dotted blue line.....	274

Figure 7.8: N ₂ adsorption and desorption isotherms performed at 77 K on AC and modified MIL-96 (Al) materials. Filled symbols ■ adsorption whereas unfilled symbols □ desorption.....	275
Figure 7.9: Pore size distribution plots for MIL-96 (Al) samples modified with HPAM, PAM and PAA compared to the unmodified MIL-96 (Al) (inset).	276
Figure 7.10: Hydrodynamic particle size distribution (mean volume equivalent sphere diameter in bracket) of polymer-modified MIL-96 (Al) in water by laser light diffraction (n = 5).	277
Figure 7.11: Batch PFOA adsorption isotherm plots by modified MIL-96 adsorbents after 18 hrs.....	278
Figure 7.12: Solvents tested for desorption of PFOA from used MIL-96-RHPAM2 adsorbent.	279
Figure 7.13: Experimental and kinetics modelling results for the adsorptive PFOA removal by MIL-96-RHPAM2; [PFOA] = 1000 mg/L, [MOF] = 1 mg/mL.	281
Figure 7.14: Kinetics plot of n-octane vapour sorption on MIL-96-RHPAM2.....	282
Figure 7.15: Pseudo second order kinetics model fitting of n-octane vapour adsorption on MIL-96-RHPAM2.	282
Figure 7.16: Percentage of PFOA desorbed from MIL-96-RHPAM2 and AC using NaCl solutions (temperature 25 °C, adsorbent dose = 2 mg/mL, [PFOA] = 1000 mg/L).	285
Figure 7.17: Proposed PFOA adsorption mechanisms by HPAM-treated MIL-96 (Al) used in this study; (a) hydrogen bonding between the -NH ₂ of HPAM and PFOA, (b) hydrogen bonding between COO ⁻ of HPAM and PFOA, (c) weak Van der Waals interaction established between the carbons of PFOA and the repeating HPAM monomer unit and (d) primary electrostatic interactions involving the COO ⁻ groups of PFOA with the protonated amide (NH ₃ ⁺) on MIL-96-RHPAM2.	287
Figure 7.18: Proposed PFOA binding mechanisms with the MIL-96 (Al) original framework detailing (a) simplified PFOA structure, (b) formation of less prevalent 3°	

carbocation stable intermediate metal complex 1 between the PFOA and the Al metal centres (c) primary electrostatic interaction between the oppositely charged Al^{3+} of MIL-96 (Al) and COO^- groups on PFOA and (d) formation of more dominant metal complex 2.....	288
Figure A10.1: DVS method stage. Step 1: sample drying and 40% RH adsorption step.....	346
Figure A10.2: DVS method stage. Step 2: competitive adsorption experiment at 40% RH with 0.5% toluene P/P_0	346
Figure A10.3: DVS method settings for Step 1, pre-drying and 40% RH equilibration.	347
Figure A10.4: DVS method settings for Step 2, at 40% RH with 0.5% toluene P/P_0 adsorption.	347
Figure A10.5: PXRD patterns of (a) simulated MIL-101 (Cr) and after 3-day immersion in (b) pH = 1 and (c) pH = 11 solutions.....	348
Figure A10.6: N_2 adsorption and desorption isotherms of all tested adsorbents where full symbols denote adsorption while empty symbols are for desorption.	349
Figure A10.7: Comparison of the measured FTIR spectra between (a) fresh MIL-101 (Cr), (b) 2-CP loaded MIL-101 (Cr), (c) 2-CP and (d) MIL-101 (Cr)- NH_2	350
Figure A10.8: Linear isotherm plots of Langmuir-1 type for all studied adsorbents.	352
Figure A10.9: SEM images of (A) pristine MIL-101 (Cr), (B) MIL-PDMS-Sigma-0.25, (C) MIL-PDMS-Sigma-6, (D) MIL-PDMS-Dow-0.25 and (E) MIL-PDMS-Dow-6.	355
Figure A10.10: Silanisation reaction on the surface of the MOF MIL-100 (Fe). The silane model shown has R as a fluoroalkyl pendant group.	358
Figure A10.11: Static water contact angle at $t = 0$ s for (left) MIL-NS-7.5 vol% and (right) MIL-TCFTPS-7.5 vol%.	359
Figure A10.12: 95% toluene P/P_0 uptake capacity of MIL-TCTFPS-7.5 vol%.	359
Figure A10.13: PXRD patterns of PA-treated MIL-100 (Fe).....	361

Figure A10.14: Numbered from the left are vials containing the pristine (1) MIL-100 (Fe), (2 – 6) MIL-Cx4-0.3, 0.5, 1, 3, 5 wt%, (7 – 10) MIL-Cx6-0.5, 1, 3, 5 wt% and (11 – 13) MIL-Cx8-1, 3, 5 wt%.	361
Figure A10.15: SEM images of (A) pristine MIL-100 (Fe), (B) MIL-Cx4-1 wt%, (C) MIL-Cx4-5 wt% (D) MIL-Cx6-1 wt%, (E) MIL-Cx6-5 wt%, (F) MIL-Cx8-1 wt% and (G) MIL-Cx8-5 wt%.	365
Figure A10.16: FTIR spectra of PA-treated MIL-100 (Fe).	366
Figure A10.17: Pore size distribution plots for MIL-PA samples.	368
Figure A10.18: Pore size distribution plots for calixarene-treated MIL-100 (Fe) samples.	368
Figure A10.19: N ₂ adsorption and desorption isotherm plots for all studied samples. Filled shapes refer to adsorption while empty shapes are for desorption.	369
Figure A10.20: Images showing formation of a liquid marble when (left) MIL-Cx4-1 wt% and (right) MIL-Cx6-1 wt% powder is in contact with water droplets.	370
Figure A10.21: Water adsorption and desorption isotherms of PA-treated MIL-100 (Fe). Filled symbols denote adsorption while empty symbols refer to desorption.	371
Figure A10.22: Dry toluene adsorption and desorption isotherms of PA-treated MIL-100 (Fe). Full shapes refer to adsorption whereas empty shapes are for desorption.	372
Figure A10.23: Molar hydrophobicity index of PA-treated MIL-100 (Fe).	373
Figure A10.24: 40% RH and 0% toluene P/P ₀ adsorption capacity of PA-treated MIL-100 (Fe).	374
Figure A10.25: 40% RH and 0.5% toluene P/P ₀ adsorption capacity of PA-treated MIL-100 (Fe).	375
Figure A10.26: 40% RH and 10% toluene P/P ₀ adsorption capacity of PA-treated MIL-100 (Fe).	376

Figure A10.27: (Left) 40% RH and 0.5% toluene P/P₀ full range adsorption kinetics of PA-treated MIL-100 (Fe). (Right) The first 120-minute adsorption rate is shown on the right inclusive of the linear-fitted slope values given in the legend brackets.378

Figure A10.28: (Left) 40% RH and 10% toluene P/P₀ full range adsorption kinetics of PA-treated MIL-100 (Fe). (Right) The first 30-minute adsorption rate is shown on the right inclusive of the linear-fitted slope values given in the legend brackets.379

Figure A10.29: SEM images of HPAM-modified MIL-101 (Cr) where (a) MIL-101 (RHPAM = 0), (b) MIL-101 with 1 mL HPAM (RHPAM = 0.2) and (c) MIL-101 with 3mL HPAM (RHPAM = 0.6).383

Figure A10.30: FTIR spectra of the linker trimesic acid (TMA) before and after the hydrothermal heating process with HPAM.384

List of Tables

Table 1.1: Primary properties of granular and powdered AC (Perrich, 2018)	43
Table 1.2: Summary of typical commercial ACs and MOFs used for adsorption. Some BASF MOFs are listed here (Silva <i>et al.</i> , 2015).	47
Table 2.1: POP examples from the Stockholm Convention recognized to have deleterious effects on humans and our ecosystems.	51
Table 2.2: Comparison of phenol removal technologies from wastewater. The information is harmonized from (Ortega-Méndez <i>et al.</i> , 2017; Raza <i>et al.</i> , 2019; Eryılmaz & Genç, 2021; Tufail <i>et al.</i> , 2021; Said <i>et al.</i> , 2021; Saputera <i>et al.</i> , 2021).	55
Table 2.3: Summary of literature on MOFs used in removal of phenolic pollutants from water.	63
Table 2.4: Comparison of MOFs used to adsorb PFCs from water at ambient condition (25 °C).	74
Table 2.5: Performance metrics used to evaluate a packed adsorbent bed performance for air quality monitoring applications. Formulae are taken from (Szulejko & Kim, 2019; Szulejko, Kim & Parise, 2019).	89
Table 2.6: Compilation of VOC capture reports at room temperature and in humid conditions using unmodified MOFs.	93
Table 2.7: Synthetically modified MOFs for the removal of VOCs at room temperature and in humid conditions.....	113
Table 3.1: Specifications of the FTIR spectrometer used in this thesis.....	144
Table 3.2: Classification of the 13 adsorption isotherm models (Wang & Guo, 2020).	165
Table 3.3: The six linearized variations of the nonlinear Langmuir isotherm model.....	167
Table 3.4: Details of the Freundlich adsorption isotherm model used in this study.....	168
Table 3.5: Nonlinear and linear forms of pseudo first and second order kinetics equations.	170

Table 4.1: Surface area and pore volume analysis of all studied adsorbents.....	188
Table 4.2: Detailed descriptions of the adsorbents' TGA profiles.	191
Table 4.3: Isotherm parameters from a linear Langmuir-1 and a nonlinear Langmuir model	193
Table 4.4: Dimensionless separation factor values (R_L) calculated for each adsorbent.	194
Table 5.1: Calculated PDMS wt% content from XRF data.	210
Table 5.2: Surface area, pore volume and water contact angles for MIL-101 samples and AC.	212
Table 5.3: Experimental and estimated kinetics parameters at 40% RH/0.5% toluene P/P ₀	225
Table 5.4: Experimental and estimated kinetics parameters at 40% RH and 10% toluene P/P ₀	230
Table 5.5: Adsorption of 0.5% toluene P/P ₀ following high humidity exposure.	231
Table 6.1: The chemical structures of the supramolecule calixarenes.....	237
Table 6.2: Quantity of coating agent on treated MIL-100 (Fe).	242
Table 6.3: Porosity analysis for selected calixarene-treated MIL-100 (Fe).....	243
Table 6.4: Water contact angles of some calixarene-treated MIL-100 (Fe) samples.	244
Table 6.5: Linear-fitted parameters of all calixarene-treated MIL-100 (Fe) samples.	256
Table 6.6: Fitted values of the calixarene-treated MIL-100 (Fe) samples' adsorption kinetics profiles using a nonlinear pseudo-first order equation.....	257
Table 6.7: Adsorbed 0.5% toluene P/P ₀ amount for MIL-Cx4-1 wt%, MIL-Cx6-1 wt% and AC, before and after 90% RH exposure.	259
Table 7.1: Band assignments for FTIR spectra of MIL-96 samples synthesized with HPAM.	271
Table 7.2: Details about the distinct material decomposition stages up to 800 °C in N ₂	273

Table 7.3: BET surface area and pore volume measurements of all studied samples.	275
Table 7.4: Comparison of the pseudo-second order kinetics parameters for PFOA adsorption by select MOFs and AC.	283
Table A10.1: Comparison between DSC and DTA techniques.	344
Table A10.2: Water adsorption data at 25 °C by AC on IGA.	345
Table A10.3: Water desorption data at 25 °C by AC on IGA.	345
Table A10.4: Elemental analysis of sorbents used in Chapter 4.	351
Table A10.5: Details about the linear Langmuir isotherm plots.	351
Table A10.6: Differences between phosphonic and phosphinic acids.	356
Table A10.7: The chemical structures of the hydrophobic agents.	357
Table A10.8: Pore properties and static water contact angles of MIL-100 (Fe) and its silane- modified variants.	360
Table A10.9: Porosity analysis for select PA-treated MIL-100 (Fe).	367
Table A10.10: Advancing water contact angles of all PA and Cx-treated MIL-100 (Fe) samples.	370
Table A10.11: Linear-fitted parameters of all PA-treated MIL-100 (Fe) samples.	380
Table A10.12: Fitted values of the PA-treated MIL-100 (Fe) samples' adsorption kinetics profiles using nonlinear pseudo-first order equation.	381

List of Abbreviations

AC	activated carbon
BDC	terephthalic acid (TPA) or 1,4-benzenedicarboxylate
BET	Brunauer-Emmett-Teller
BPA	bisphenol A
BTC	trimesic acid (TMA) or 1,3,5-benzenetricarboxylate
BTV	breakthrough volume
CAU	Christian-Albrechts-Universität zu Kiel, Germany
CP	chlorophenol
CPM	crystalline porous material
CUS	coordinatively unsaturated sites
Cx	calixarene
DVS	dynamic vapor sorption
EDC	endocrine disrupting compound
FTIR	Fourier-Transform infrared
HI	hydrophobicity index
HKUST	Hong Kong University of Science and Technology, Hong Kong
HPAM	hydrolysed polyacrylamide
KIT	Karlsruhe Institute of Technology, Germany
MCM-41	Mobil Composition of Matter No. 41 mesoporous material series
MIL	Matériaux de l'Institut Lavoisier or Materials of Institut Lavoisier, France
MOF	metal organic framework
MS	mass spectrometry
NIOSH	United States' National Institute of Occupational Safety and Health
NLDFT	non-local density functional theory
NMR	nuclear magnetic resonance

NP	nitrophenol
OSHA	United States' Occupational Safety and Health Administration
PA	phosphorous oxyacid inclusive of phosphonic and phosphinic acids
PAA	polyacrylic acid
PC	partition coefficient
PDMS	polydimethylsiloxane
PFO	pseudo first order
PFOA	perfluorooctanoic acid
PFOS	perfluorooctanesulfonic acid
POP	persistent organic pollutant
PSM	post-synthetic modification
PSO	pseudo second order
PXRD	powder x-ray diffraction
Q	adsorption capacity
RH	relative humidity
SBU	secondary building unit
SCU	Soochow University, China
SEM	scanning electron microscopy
SION	École Polytechnique Fédérale de Lausanne, Sion, Switzerland
TGA	thermal gravimetric analysis
UiO	Universitetet i Oslo or University of Oslo, Norway
USEPA	United States' Environmental Protection Agency
VOC	volatile organic compound
WWTP	wastewater treatment process/plant
ZIF	zeolitic imidazolate framework
ZSM-5	Zeolite Socony Mobil type with a 5 Å pore diameter and > 5 Si/Al ratio

List of Academic Achievements

Publications

1. **Azmi, L.H.M.**, Cherukupally, P., Hunter-Sellars, E., Ladewig, B.P. and Williams, D.R., 2022. Fabrication of MIL-101-polydimethylsiloxane composites for environmental toluene abatement from humid air. *Chemical Engineering Journal*, 429, p.132304.
2. **Azmi, L.H.M.**, Williams, D.R. and Ladewig, B.P., 2021. Polymer-assisted modification of metal-organic framework MIL-96 (Al): influence of HPAM concentration on particle size, crystal morphology and removal of harmful environmental pollutant PFOA. *Chemosphere*, 262, p.128072.
3. **Azmi, L.H.M.**, Williams, D. and Ladewig, B.P., 2020. Can metal organic frameworks outperform adsorptive removal of harmful phenolic compound 2-chlorophenol by activated carbon? *Chemical Engineering Research and Design*, 158, pp. 102-113.

Conferences

1. **Luqman Hakim Mohd Azmi**, Elwin Hunter-Sellars, Bradley Ladewig and Daryl Williams. *Facile Hydrophobic Modification Strategy on Hydrophilic Metal Organic Frameworks to Improve Volatile Organic Compounds Removal from Air and Aqueous Environments*. AIChE Annual Meeting. San Francisco, USA (held virtually due to COVID-19 restrictions). November 16th – 20th 2020. Virtual oral presentation.
2. **Luqman Hakim Mohd Azmi**, Elwin Hunter-Sellars, Bradley Ladewig and Daryl Williams. *Facile Hydrophobic Modification Strategy on Hydrophilic Metal Organic Frameworks to Improve Volatile Organic Compounds Removal from Air and Aqueous Systems*. The 16th Conference of the International Society of Indoor Air Quality & Climate (Indoor Air 2020). Seoul, South Korea (held virtually due to COVID-19 restrictions). November 1st – 5th 2020. Virtual oral presentation.
3. **Luqman Hakim Mohd Azmi** and Bradley Ladewig. *Facile Surface Modification Strategy for Hydrophilic Metal Organic Frameworks*. 3rd European Conference on Metal Organic Frameworks and Porous Polymers (EuroMof 2019). Paris, France. October 27th – 30th 2019. Poster presentation.

Chapter 1: Introduction

1.1 Persistent organic water pollutants

The need for clean water source is central to everyone's lives. However, with the continuous growth in the global population, water demand is expected to increase by 1% per year (United Nations World Water Assessment Programme, 2018). However, these available global water resources might not be able to supply the necessary rate given the severe climate change currently facing the world. This problem is further exacerbated by significant increases in our water consumption patterns. These increases are partially driven by the commercial needs for more product varieties to fulfil our daily needs in medicine, industry, agriculture, and common household products. The manufacture and utilisation of these products will result in the accidental or intentional release of chemicals, which will be disposed into the sewage systems or enter water catchment systems. To produce our drinking water, or for more general recycling purposes, these contaminated water sources must be treated in wastewater treatment plants prior to safe discharge into the waterbodies. There are however, some chemicals which cannot be efficiently removed by the conventional water treatment processes (The United Kingdom Parliamentary Office of Science and Technology, 2018).

Within the vast literature pertaining to water treatments, there is an ever growing list of pollutants either known by the term emerging pollutants, contaminants of emerging concerns, micropollutants and priority pollutants (Teodosiu *et al.*, 2018). Although emerging pollutants which are newly appeared group of contaminants, and contaminant of emerging concerns, contaminants that have traditionally appeared in the environment, but only recently raised concerns, as spurred by newly found scientific evidences are definitively different, nevertheless, these pollutants assume similar characteristics (Sauvé & Desrosiers, 2014). They can be identified as chemicals that typically exist in low concentrations (ng/L or µg/L) in wastewaters or in contaminated waterbodies yet, even at these trace levels, they pose potential adverse risks to human health and the environment upon their consumption or exposure too (Shah *et al.*, 2020). Their natively high level of chemical resistance towards natural or bio-degradation also means they can accumulate over time, potentially leading to irreversible harms to humans and our ecosystems (Sousa *et al.*, 2017).

Water contaminants can be broadly classified into inorganic, organic, or pathogenic, depending on their chemical compositions and biological forms. Generally, inorganic pollutants such as oxyanions, cations, and metal ions, are more persistent in the environment than the organics. Due to their charged nature, they are highly soluble in water and can easily enter the human bodies from the lower tiers of our food chain via bioaccumulation process. What is more worrying is that the metals, particularly among the heavy and the radioactive types, possess a narrow concentration range between the lowest safely acceptable and the lethal consumable limits (Mon *et al.*, 2018). On the other hand, organic contaminants make up a larger family of species than the inorganic contaminants. Organic contaminants can originate from industrial sources including dyes, phthalates, phenols, nitrobenzene, artificial sweeteners, animal feed additives, domestic sources such as pharmaceuticals and personal care products, as well as agricultural sources including veterinary drugs, herbicides and pesticides (Dias & Petit, 2015).

Additionally, among the organic pollutants, there are 28 persistent organic pollutants (POPs) which have been compiled in a global treaty known as The Stockholm Convention (Stockholm Convention Secretariat United Nations Environment, 2017). The list originally contained 12 chemicals in 2004, but as of 2017, 16 new POPs have been added. The ratified agreement requires signatory parties to take cooperative action in reducing or completely ceasing their POP production as these POPs pose adverse risks to both human health and the environment. Following the enactment of this Convention, larger industrial emissions of POPs have been substantially reduced. However, certain exemptions, such as those given to pesticides, mean they are still being used heavily in the agricultural industry (Wagner *et al.*, 2021). The main route of potential human exposure to POPs has been identified to be through the food chain. Although current POP levels are not yet of significant concerns for human health, but the importance of developing effective means for their removal is duly recognized (UK DEFRA, 2017).

POP compounds can be sporadically or directly discharged into the sewage or other catchment areas. They can diffusely or convectively make their own ways into the soil or water media (Figure 1.1), but inefficient wastewater treatment processes (WWTPs) are considered the primary route of entry into the water supply systems (Rasheed *et al.*, 2020; Yadav *et al.*, 2021). Conventional WWTPs are not designed technologically to remove these persistent and novel classes of contaminants (Krzeminski *et al.*, 2019). Therefore, a tertiary treatment stage is

required, of which adsorption by activated carbon (AC) is the best established removal technology (Sophia A & Lima, 2018; Rout *et al.*, 2021). Even for modern day treatment facilities, aside from the additional costs that need to be incurred by the operator, the lack of state-level regulatory requirements for removal of these pollutants impedes necessary developments. So far, stringent standards relating to water reuse are only practiced in a few developed countries (i.e., select states in Europe, United States) driven mainly by clear economic incentives (Paranychianakis *et al.*, 2015) whereas for low to middle-income countries (i.e., Middle East, Singapore, Maldives), the severe water scarcity drives a different practice (Yoonus & Al-Ghamdi, 2020).

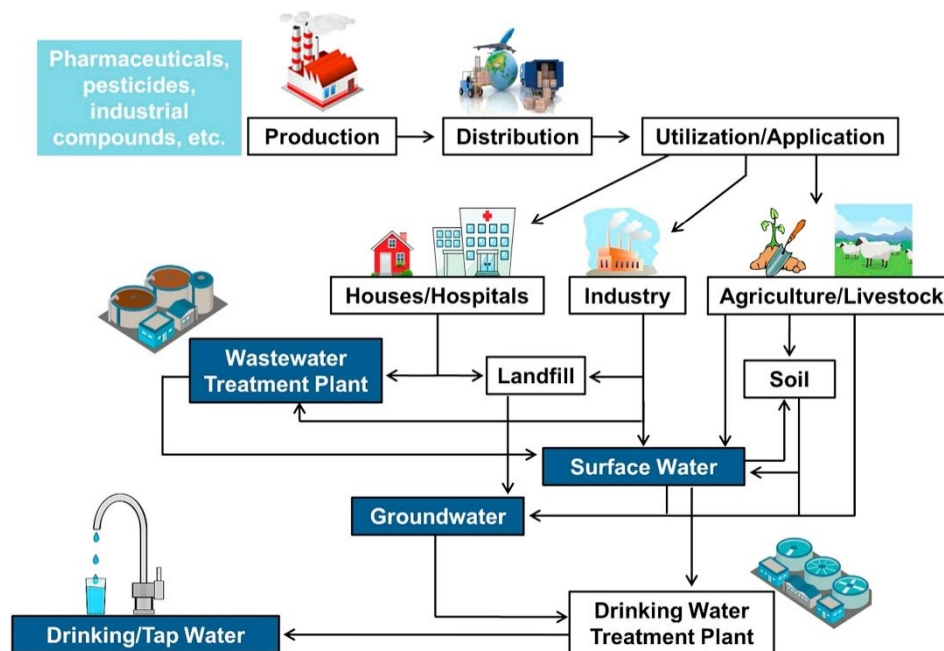


Figure 1.1: Possible entry pathways for persistent pollutants into the domestic water pipelines. Reproduced with permission from (Barbosa *et al.*, 2016). Copyright 2016, Elsevier.

1.2 Airborne organic pollutants

The Paris Climate Agreement in 2015 marked a momentous event that witnessed the convening nations unveiling their strategies to curb greenhouse gas emissions and to limit global temperature increase to between 1.5 and 2 °C (Figure 1.2). Direct greenhouse gases are those that are multilaterally agreed in the 1997 Kyoto Protocol while the 1987 Montreal Protocol encompasses the list of chlorofluorocarbons, hydrochlorofluorocarbons and halons. After CO₂

and CH₄, the tropospheric ozone is the third most important greenhouse gas, which can also be treated as an indicator of the present-day atmospheric burdens.

Some gases are termed as indirect greenhouse gases including the likes of carbon monoxide (CO), non-methane volatile organic compounds (VOCs), sulphur oxides (SO_x), and nitrogen oxides (NO_x = NO + NO₂) because they do not directly influence the atmospheric chemistry, but they play a key role in controlling the abundance of the direct species. Mass emitted VOCs are one of the significant precursors for the ozone formation (Lu *et al.*, 2020). When ozone is oxidized, it can transform into CO₂. Unfortunately, VOCs have short lifetimes and given their geographically varying sources, quantification of the global average emissions is almost impossible. Measurements of VOCs are usually conducted in proximity of their concentrated sources (Ehhalt *et al.*, 2001).

Global greenhouse gas emissions and warming scenarios Our World in Data

- Each pathway comes with uncertainty, marked by the shading from low to high emissions under each scenario.
- Warming refers to the expected global temperature rise by 2100, relative to pre-industrial temperatures.

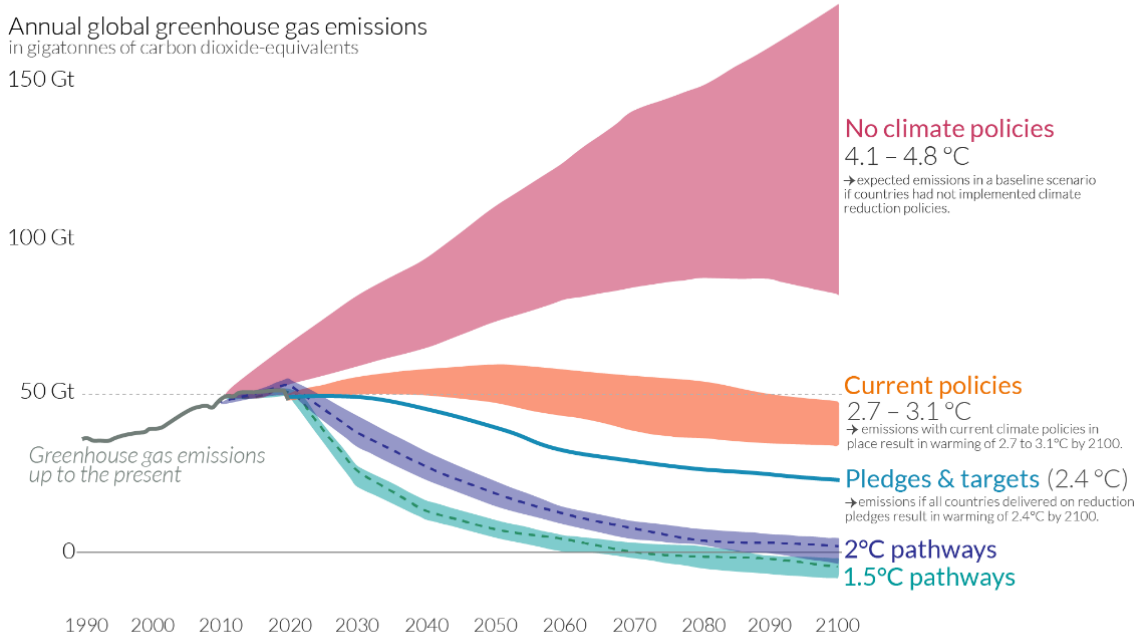


Figure 1.2: The chart forecasts a century-span greenhouse gas emissions scenarios from year 2000 under multiple assumptions; (a) if no climate policies are implemented, (b) continuing with existing policies, (c) if the countries involved achieved their current future pledges to reduce the emissions and (d) drastic and necessary actions that are compatible to reduce major emissions are taken. Reprinted with permission from (Ritchie & Roser, 2020). Copyright 2020, online.

VOCs are volatile because of their low boiling points, usually less than 250 °C at a standard atmospheric pressure of 101.3 kPa (United States Environmental Protection Agency, 2021). Common organic chemical categories include aromatics, alcohols, hydrocarbons, aldehydes, and ketones. Their chemical diversity and their high utility give them extensive presence as ingredients in household products, paints, solvents (Goldstein *et al.*, 2020), as raw materials in the chemical industries (Li *et al.*, 2020e) and in vehicular fuel emissions (McDonald *et al.*, 2018). However, behind their utility, the ubiquitous distribution of VOCs can cause significant damage to human health and environments. In fact, the most concerning reality is the mounting evidences on long term accumulation of VOCs in indoor spaces (Cheng *et al.*, 2019; Norris *et al.*, 2019).

Continuous exposure to VOCs can cause many adverse health effects including impaired foetal development (Montero-Montoya, López-Vargas & Arellano-Aguilar, 2018), increased risks of cancer (Spycher *et al.*, 2017; Montero-Montoya, López-Vargas & Arellano-Aguilar, 2018), diabetes (Di Ciaula & Portincasa, 2021), as well as respiratory and cardiovascular diseases (Shuai *et al.*, 2018). Therefore, given the VOCs' pervasiveness in our daily life and as people spend increasing time indoors, a safe VOC elimination method must be sought since it is difficult to imagine individuals who are not currently exposed to some of these chemicals. Furthermore, VOCs that are released from various outdoor sources can cross transfer and contaminate the indoor air quality level. Activated carbon (AC) is usually installed in air filtration devices to remove VOCs, where such devices are deployed. However, AC has some disadvantages such as low selectivity, poor performance in humid operating conditions and modest regeneration costs. Generally, the total surface areas for AC are relatively low, ranging between 450 and 1800 m²/g (Perrich, 2018) in comparison to metal organic frameworks (MOFs) which have a greater range, between 1000 and 10,000 m²/g (Li, Ye & Chen, 2019). So, there is a serious need to develop novel adsorbent materials such as the highly porous MOFs that can adsorb VOCs in real world conditions, especially to prevent competitive VOCs adsorption with moisture.

In summary, adsorption-based removal methods have been widely used for removal of water and air pollutants on the account of simplicity, lower cost, and energy considerations (Rojas & Horcajada, 2020). While AC is universally hailed as the conventional adsorbent, MOFs are

increasingly being investigated as potential second-generation VOC adsorbents. A brief description of each of these material classes is given in the following Sections.

1.3 Porous adsorbents

Porous materials or adsorbents can be divided into three groups based on their respective pore size ranges; microporous (< 2 nm), mesoporous (from 2 to 50 nm) and macroporous (> 50 nm) (IUPAC, 2014). The specific adsorbent's pore properties like surface area and pore volume can be determined from the analyses of their N₂ (77 K) physical adsorption-desorption isotherms. Knowledge on these properties is critical in the precise design of an effective adsorbent and to identify the governing relationships that link to their uptake rates and affinities of certain adsorbates.

1.3.1 Activated carbon (AC)

Activated carbon or colloquially charcoal (AC) has an amazingly rich history. Although earlier applications might have not been properly recorded, the Egyptians and the Sumerians had been using charcoal since 3750 BC for the reductions of Cu, Zn and Sn ores to make bronze. In 157 AD, charcoal began to be used for treatment of many diseases and for water purification. The adsorptive power of carbon materials was only recognized in the year 1773 by Car Wilhelm, a chemist from Pomerania, a Baltic Coast of Europe. His discovery led to the term “activated carbon” used today which refers to any form of carbon capable of adsorption. Despite the steady use of AC throughout the centuries, marketing of the first industrially manufactured powdered AC sourced from peat and under the trade name Eponit was reported in 1911 by an Austrian company called Fanto Works. Currently, the largest global market for AC lies in the purification of municipal water supplies, with newer forays into the domestic air purification systems (Gupta, 2018). The strong foothold of AC in these areas is the reason to why AC is considered as an important benchmark adsorbent. If an adsorbent cannot outperform AC, it is unlikely to be commercially successful at the industrial scale.

AC is a cost-effective adsorbent as it can be produced at a large scale from a multitude of relatively cheap and easily available materials including biomass or coal. The activation process generally comprises two phases. Initially, the raw materials are heated sequentially

from 170 °C to 400 – 600 °C to form a carbonaceous char. At this point, around 80% of the non-carbon elements in the materials have been removed. This intermediate product is then activated by using CO₂ or steam at a temperature of 750 to 950 °C to completely burn off the decomposition products, leading to the developments of AC's pore and surface area. Depending on the final mode of activation, either through chemical or physical treatments, the activation process can selectively erode the surface to increase the final AC's surface area, porosity and creating surface chemical sites with specific adsorbate affinities (Perrich, 2018). AC is usually microporous and is a hydrophobic material, although any physically or chemically introduced surface functionalities can have a major influence on its adsorption behaviour (Figure 1.3).

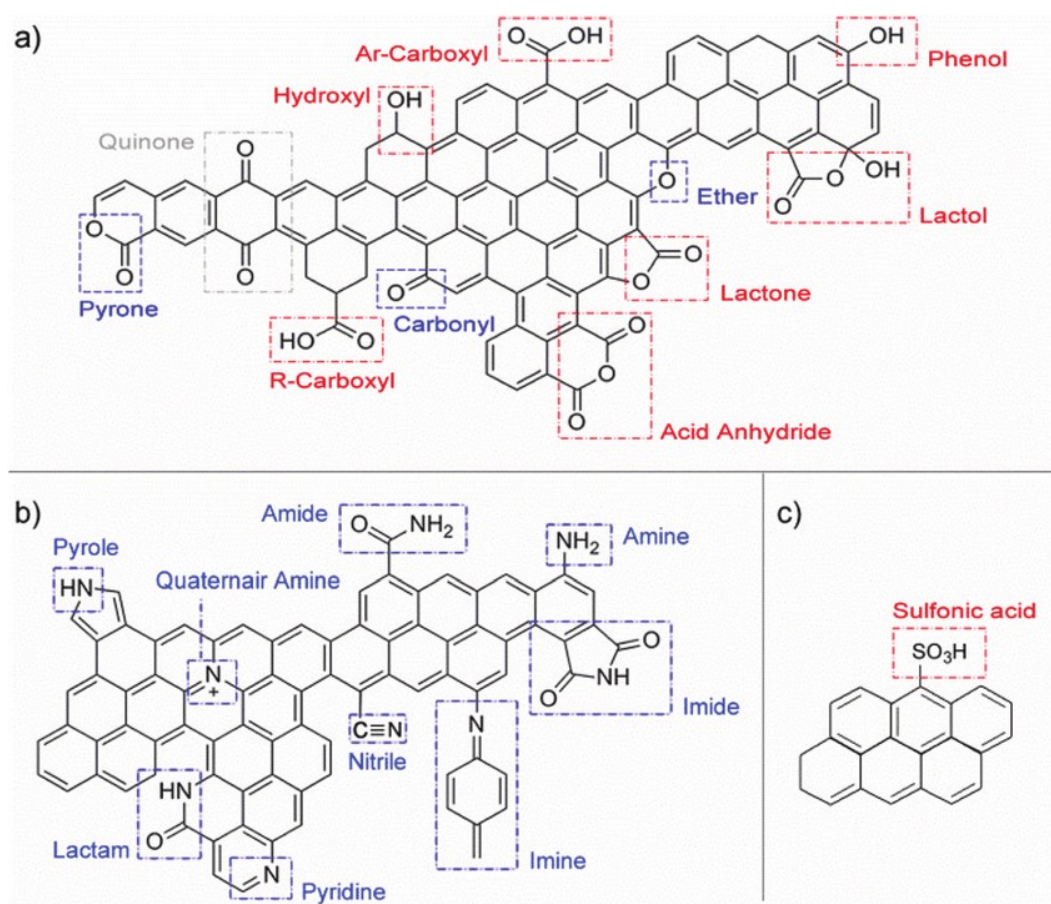


Figure 1.3: The types of surface functional groups that can exist on a pyrolyzed carbon surface: (a) oxygen, (b) nitrogen and (c) sulphur. Basic and acidic functionalities are marked in blue and red respectively. Reproduced with permission from (de Clippel *et al.*, 2013). Copyright 2013, RSC Publishing.

1.3.2 Metal-organic frameworks (MOFs)

Metal organic frameworks (MOFs) are a relatively new class of porous materials formed from the covalent coordination between inorganic metal ions (M) and organic ligand linkers (L), often resulting in the creation of nanometre-scale pore spaces (Figure 1.4). The first mention of MOFs dated back in 1995 when Omar Yaghi and his group (Yaghi, Li & Li, 1995) synthesized a porous network structure using $\text{Co}(\text{NO}_3)_2$ and 1,3,5-benzenetricarboxylate (BTC). It was however not until 1999, that the first two key MOFs were developed, HKUST-1 (Cu) (Chui *et al.*, 1999) and MOF-5 (Zn) (Li *et al.*, 1999). Since then, there have been strong research interest in MOFs as evident from the surge of registered structures in the Cambridge Structural Database. In 2017, there were approximately 70,000 pre-deposited MOFs in the database, but by August 2019, the number had escalated to 96,000, which amounts to an average of 1000 new structures being released every month (Li *et al.*, 2020a).

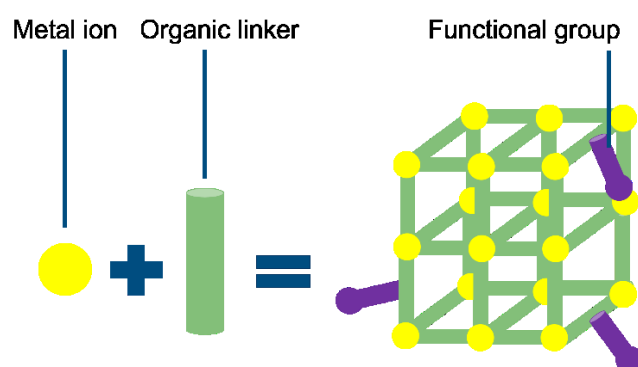


Figure 1.4: A schematic illustration of the elements making up a 3D, porous, crystalline metal-organic framework (MOF). The 3D structure will be the repeating entity, which forms a larger network.

The enormity of the Cambridge Structural datasets can be thought to be the result of the interplay between the two building blocks and the adjustments of the chemical environment, capable of creating virtually infinite possibilities of crystal pore sizes and framework structures. The rational design of MOF structures depends on the reticular synthesis concept, or more simply, the art of using secondary building units (SBUs) to form ordered networks. SBUs are designated as metal ion clusters that are joined to more than one other metal via non-metal (linker) bonds. For example, M-O-M and M-O-C-O-M, or oxo and carboxylate bonds, can form a wide range of 3D periodic networks (Ha, Lee & Moon, 2020). Not only are the metal-ligand (M-L) bonds that are formed between the SBUs, and the organic linkers are very strong,

but they also simultaneously serve as the backbone that provides the MOFs with structural stability as well as directionality that determines the final MOF structure.

These SBUs are also the centre of many post-synthetic modifications (PSMs), like the creation of open or coordinatively unsaturated metal sites (CUS) (by removing the neutral terminal ligands) or functionalization of specific chemical groups like amines (NH_2) through ligand exchange reactions (Kalmutzki, Hanikel & Yaghi, 2018). Figure 1.5 shows the schematic evolution of how the presence of at least one labile ligand in the bridged SBUs can be reversibly removed to establish coordinatively unsaturated metal or Lewis acidic sites.

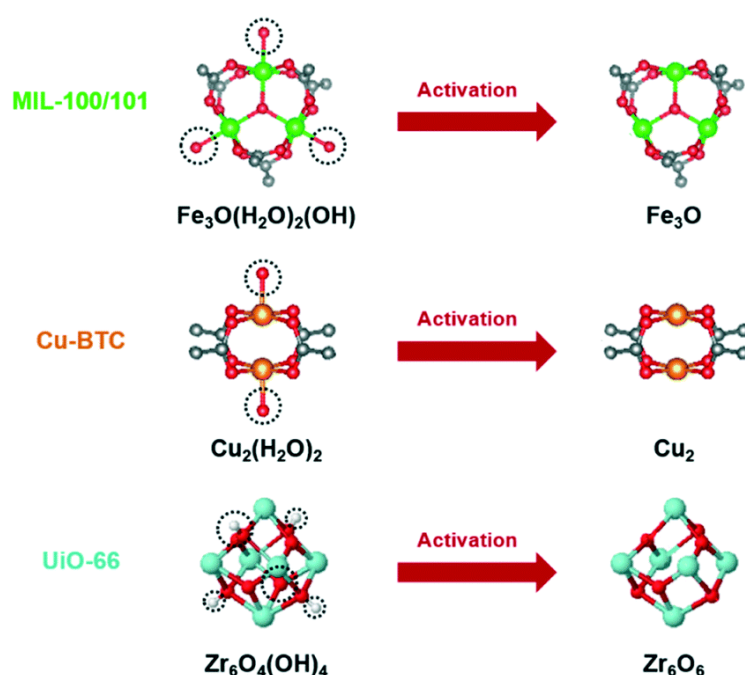


Figure 1.5: Formation of open metal sites by thermal activation in MIL-100/101, Cu-BTC and UiO-66 (oxygen = red, metal atom = green/orange/blue, carbon = grey, hydrogen = white). Figure is taken with granted permission from (Hall & Bollini, 2019). Copyright 2019, RSC Publishing.

Typically, a MOF synthesis takes place as a heated, one-pot, self-assembly reaction. The assigned synthesis type depends on the solvent used, either as hydrothermal (water is used as the solvent), solvothermal (non-water solvents) or ionothermal (with ionic liquids). The mixture is sealed in an autoclave, which is then heated in an oven under autogenous pressure. The solvothermal synthesis can either use amine-based (typically trialkyl amine or pyridine), amide-based (like *N,N*-dimethylformamide and diethyl formamide) or organic solvents (ethanol, methanol) (Clerici & Kholdeeva, 2013; Kaskel, 2016).

In the final stage, after the synthesis ends, any residual solvent or unreacted linker molecules trapped in the MOF's pores are removed by successive solvent exchange, followed by suitable heating and vacuum treatment to obtain dry final MOF products. This whole series of the final steps is termed as activation.

Realizing that some of the reaction solvents used are harmful, there is now a strong paradigm shift moving towards a more environmentally friendly synthesis route. Greener MOF synthesis aims to utilize non-hazardous reactants/solvents/additives, to develop milder reaction conditions (at ambient conditions) and to produce less waste (Chen, Shen & Li, 2017). For example, the use of near-critical water as the reaction solvent is an excellent safer alternative to using polar toxic organic solvents (Ibarra *et al.*, 2012). Sometimes, additives or modulators are used in the synthesis to control the MOF's particle size, phase purity and product morphology. Usually being a group of monodentate ligands, they share similar chemical functionality with the linker. During the synthesis reaction, they will compete with the linker species, thus slowing down the crystal growth process and effectively promotes nucleation processes (Delville & Taubert, 2018). To gain a better understanding between AC and MOFs, the upcoming Section will elucidate their differences in several key aspects.

1.3.3 Comparison between AC and MOFs

1.3.3.1 Surface area, porosity, and pore volume

From the list of AC activation methods, those that are activated chemically have many advantages such as low pyrolysis temperature, short processing time, high carbon yield and high specific surface area as well as controllable pore structure. Pore formation by chemical activating agents can be either from acidic, alkaline, neutral, or self-activating type. For clarity, the three types of self-activating agents that can be found in the literature comprise organic Na/K/Ca-based acid salts (i.e., sodium gluconate, potassium acetate, calcium citrate), natural components in certain carbon precursors (i.e., lignin, cellulose, hemicellulose, or polysaccharide) and by distributing pyrolysis gases throughout the AC interior. However, among all activation methods, alkaline-based activation especially by KOH is generally preferred as it can produce AC with super high specific surface area ($> 3000 \text{ m}^2/\text{g}$) and total pore volume ($\sim 2.5 \text{ cm}^3/\text{g}$) (Gao *et al.*, 2020a). For liquid-phase applications, AC is available in two physical forms: granular and powdered, as compared in Table 1.1.

Table 1.1: Primary properties of granular and powdered AC (Perrich, 2018)

Type of AC	Granular	Powdered
Deployment	Packed in a bed and the liquid is passed through it	Stirred with the liquid, then isolated from the media by filtration/settling
Particle size range	Larger than 20 mesh U.S. Standard Sieve size (0.84 mm)	100% lower than 100 mesh U.S. Standard Sieve size (0.149 mm)
Price	Moderate	Lower than granular AC
Treatment suitability	Highly concentrated effluents	Low concentration effluents
General property	High abrasion resistance, low bed pressure drops	Easy filterability and quick settling time if the AC has a high bulk density

Normally, a commercial AC's application is determined based on its range of pore sizes. If it is intended mainly for gas adsorption, an AC normally consists of micropores. By contrast, if the target application is for adsorption of compounds from liquid media, then an AC has a broader pore size distribution inclusive of meso and macropores. Such pore size diversity is meant to provide a balance between the two different applications. The presence of micropores gives AC a high surface area whereas the meso and the macropores contribute to quicker diffusion into the AC's internal pores. Figure 1.6 shows the pore size distributions of typical liquid and gas-phase ACs.

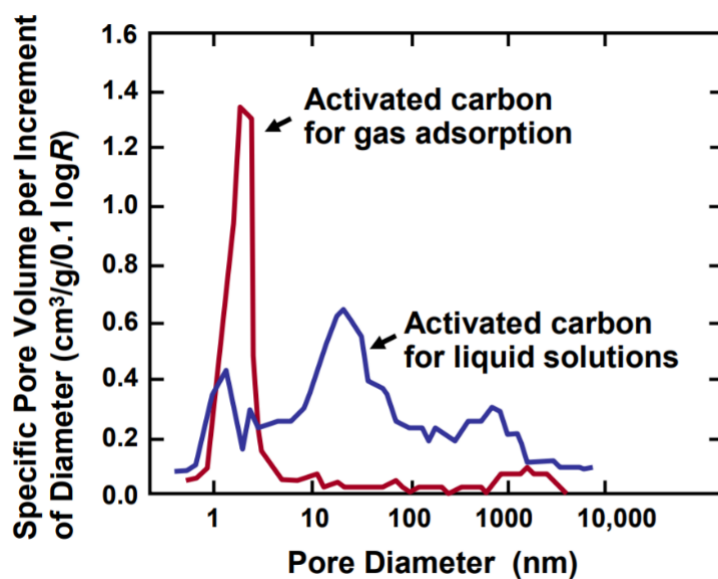


Figure 1.6: Pore size distributions of typical activated carbons. Data is replotted by (Hubbe, Azizian & Douven, 2019) from original source (Perrich, 2018).

In comparison, for MOFs, the manipulation of their reticular chemistry already plays a pivotal role to the development of higher porosity (inclusive of the complete micro, meso and macroscale pore range too) and stability. When this manipulability is combined with the implementation of specific activation methods, it enables exceptional molecular access to their pore networks. Supercritical drying of MOFs by CO₂ (Zhang *et al.*, 2020) is one good example of how to prepare a record-breaking NU-1501 (Al) with surface area close to 10,000 m²/g (Chen *et al.*, 2020) and DUT-60 (Zn)'s pore volume of 5.02 cm³/g (Hönicke *et al.*, 2018). Since high porosity in the adsorbents is the foundation for a high uptake capacity of guest molecules, MOFs are clearly the winner. Moreover, the high MOF porosity will facilitate a broader size range of molecules that can be adsorbed, not only constrained by adsorption of smaller molecules. Some commercial ACs and MOFs used for adsorption are shown in Table 1.2.

1.3.3.2 Post-synthetic modifications

The earlier discussion on AC's chemical activation has briefly touched on the possibility of introducing specific surface functional groups onto the AC surface. Normally, the alkaline activation process will establish high quantity of basic surface groups. However, changes in pore size distribution using certain activating agents are unpredictable and the presence of specific chemical functionalities cannot be controlled precisely.

On the contrary, although MOFs have a much higher production cost, the finer degree of structural control possible on them through in situ reticular chemistry and post-synthetic modifications (surface chemistry, ligand exchange) gives them a significant edge. Moreover, in certain specific applications where only low quantities of material are required, the MOFs' higher costs may be justifiable.

1.3.3.3 Adsorbent reusability

When AC reaches its operational adsorption saturation, the trapped adsorbates need to be removed to reinstitute the AC's adsorption capacity. From a positive economic and safe disposal standpoint, spent AC is usually regenerated for subsequent reuse instead of being disposed. Among the many types of processes, thermal regeneration is the most widely applied in wastewater treatment. The sequential stages of a thermal regeneration involve drying, physical desorption, re-carbonization and finally, gasification. From these steps, the

gasification step is the most critical. Here, the spent AC is heated in a furnace between 1000 and 1800 °F (538 and 982 °C accordingly) under controlled conditions (temperature, residence time, carbon loading) to gasify the adsorbed components while minimizing the gasification of the core carbon structure (Perrich, 2018). Clearly, the high energy investment involved in the regeneration of AC requires other approaches that are more eco-friendly.

The regeneration processes for MOFs are either achieved through the common means of solvent exchange or vacuum, heat, chemical treatments, and other assorted methods like using supercritical CO₂ or photothermal (UV light irradiation) method. Some of these techniques are applicable on AC too, but most AC manufacturers prefer regenerating the used AC via thermal procedures. On top of that, due to the AC's cheap unit costs, the used AC may also be disposed to landfills and replaced with a freshly manufactured batch. Therefore, compared to AC, MOFs could offer several regeneration benefits including:

1. Much lower energy requirements than the conventional regeneration processes of spent AC.
2. Highly reversible and effective procedures to revert to the original MOF performance.
3. Abundance of non-toxic regenerant choices like ethanol or liquid CO₂.
4. Simple procedures with short reaction times.

Although some mass-produced MOFs are already available for industrial purchase, their high costs are still a very significant hurdle to overcome, unlike AC that can be made from very inexpensive biomass sources (Kumar *et al.*, 2019a). On the other hand, one way to reduce the overall expense on MOF synthesis is to use cheaper ligand sources. For example, the commonly used terephthalic acid linker can be derived from the depolymerization of waste polyethylene terephthalate bottles as an alternative (Ren *et al.*, 2016; Lo *et al.*, 2016). Not only this approach is an economically attractive strategy for large-scale MOF synthesis, but this would also save a significant portion of polyethylene terephthalate wastes from going to landfills.

1.3.3.4 Multifunctional applications

While the popularity of AC is common within the applications for pollutant treatment, MOFs are suitable for a wider range of industrial applications, well beyond those for simply environmental remediation. Examples include gas storage and separation which is a popular application (Li *et al.*, 2019a), as well as the adsorption of trace and hazardous gases (Woellner *et al.*, 2018). Wastewater treatment is well studied too (Mon *et al.*, 2018), coupled with photocatalytic degradation of the captured pollutants (Pi *et al.*, 2018). There are nascent prospects in the biomedical and drug delivery applications (Yang & Yang, 2020), as luminescent sensors (Lustig *et al.*, 2017), as heterogeneous catalysts (Bavykina *et al.*, 2020) and as advanced functional electrodes for electrochemical energy storage (Lu *et al.*, 2021).

To a greater extent, the versatility of MOFs has resulted in their feasibility being evaluated for adventurous applications like the removal of industrial chemicals and warfare agents (Bobbitt *et al.*, 2017), niche problems such as cultural heritage preservation (Dedecker *et al.*, 2018) and in food packaging/safety considerations (Sharanyakanth & Mahendran, 2020). Further to that, the MOF's unique functionalities are regularly combined with low-cost polymeric bases to create new classes of composite materials. The intention of such hybridization is to produce advanced functional composite materials with properties that cannot be realized by the individual components, thus extending the application range for these new hybrid materials (Kitao *et al.*, 2017). Finally, flexible MOFs that respond to external stimuli (i.e., guest insertion, temperature, pressure, electric field, and light) are gaining traction over the years compared to rigid MOFs. Due to their finer controlled pore opening and closing mechanisms, this feature opens new dimensions towards the enhancement of MOFs' practical performances (Liu, Zhang & Sun, 2020).

Table 1.2: Summary of typical commercial ACs and MOFs used for adsorption. Some BASF MOFs are listed here (Silva *et al.*, 2015).

Adsorbent	BET surface area (m ² /g)	V _{total} (cm ³ /g)	V _{micro} (cm ³ /g)	Particle size (mm)	Density (kg/m ³)	Cost	Application	Reference
GAC BPL[®] (Calgon Carbon, USA)	1136	0.58	0.37	3.7	440	\$6/kg AC	Gas phase applications	(Li, Lee & Gullett, 2001; Szulejko, Kim & Parise, 2019)
GAC FILTRASORB[®] 400 (Calgon Carbon, USA)	1100	0.70	0.50	0.55 – 0.75	540	\$0.12/m ³ treated water	Removal of organic compounds from aqueous streams	(Al-Degs <i>et al.</i> , 2005; Belkouteb <i>et al.</i> , 2020)
GAC Darco[®] BG 1 (Cabot Norit, USA)	520	0.41	0.13	0.5 – 0.85	432 – 481	\$10.7/kg of H ₂ S removed	Removal of H ₂ S	(Cabot, 2016; Frilund, Hiltunen & Simell, 2021)
PAC HYDRODARCO[®] C (Cabot Norit, USA)	545	0.25	0.25	0.025 (D50)	490	\$1.2 – 1.4/kg AC	Treatment of industrial water effluents	(Miguel, Fowler & Sollars, 1998; Whang <i>et al.</i> , 2004; Zhang, Singh & Stuckey, 2017; Vundala, 2018)
Basolite[®] F300	1300 – 1600	0.42	0.27	0.005 (D50)	160 – 350	\$9000 – 18,000/kg MOF	Lewis acid catalysis, energy storage, CO ₂ adsorption	(Ursueguía, Díaz & Ordóñez, 2020; Sigma-Aldrich, 2021c)
MIL-100 (Fe)								
Fe-BTC								
Basolite[®] C300	1500 – 2100	1.24	0.71	0.016 (D50)	350	\$24,000 – 49,000/kg MOF	Catalysis, gas adsorption and liquid absorption	(Ursueguía, Díaz & Ordóñez, 2020; Sigma-Aldrich, 2021b)
HKUST-1 (Cu)								
Cu-BTC								
Basolite[®] A100	1100 – 1500	1.05	0.28	0.032 (D50)	400	\$14,000 – 49,000/kg MOF	Gas adsorption and separation	(Ursueguía, Díaz & Ordóñez, 2020; Sigma-Aldrich, 2021a)
MIL-53 (Al)								

1

¹ Abbreviations in Table 1.2 explained: GAC = granular AC, PAC = powdered AC, D50 = median value for a volume distribution, BTC = 1,3,5-benzenetricarboxylate.

Chapter 2: Literature Review - A 'Hole' New World

2.1 Water remediation

2.1.1 *Limitations of existing water treatment technologies*

Figure 2.1 below shows the typical treatment processes involved in a wastewater treatment plant (WWTP), starting from primary to secondary, until the tertiary stage. In the primary treatment, the solid materials contained in the influent will settle to the bottom of several large and long concrete settling tanks. Certain low-density solids cannot settle by gravity, thus causing them to remain as suspended materials in the wastewater. There are also dissolved organic materials, total nitrogen and total phosphorus in the wastewater which can mostly be removed using a biological treatment in the secondary stage. Here, the wastewater is flown into aeration tanks filled with active microorganisms (activated sludge) that consume the organics. Air is bubbled in a controlled amount to ensure the organisms can proliferate and deplete greater amounts of organics.

The type of WWTP process is chosen depending on the influent contents as well as the target effluent standards which can differ considerably between municipals. Some of the available process types include: (1) anaerobic-anoxic-oxic, (2) University of Cape Town, (3) Bardenpho and (4) alternating aerobic-anoxic. The process depicted in Figure 2.1 is the Modified Ludzack-Ettinger (MLE) nitrification-denitrification (NDN) type where the nitrified mixed liquor in the aeration zone is recycled to the pre-anoxic zone for denitrification. Nitrification is a biological process that oxidises ammonia to nitrite, then to nitrate. However, because nitrate brings health and environmental dangers, denitrification is needed to reduce it to a benign nitrogen gas that can be discharged safely. Although the secondary biological treatment can remove the bulk of the organics, highly resistant POPs are an exception. Ergo, making it more essential for the wastewater to undergo an additional tertiary stage to eliminate the contaminants.

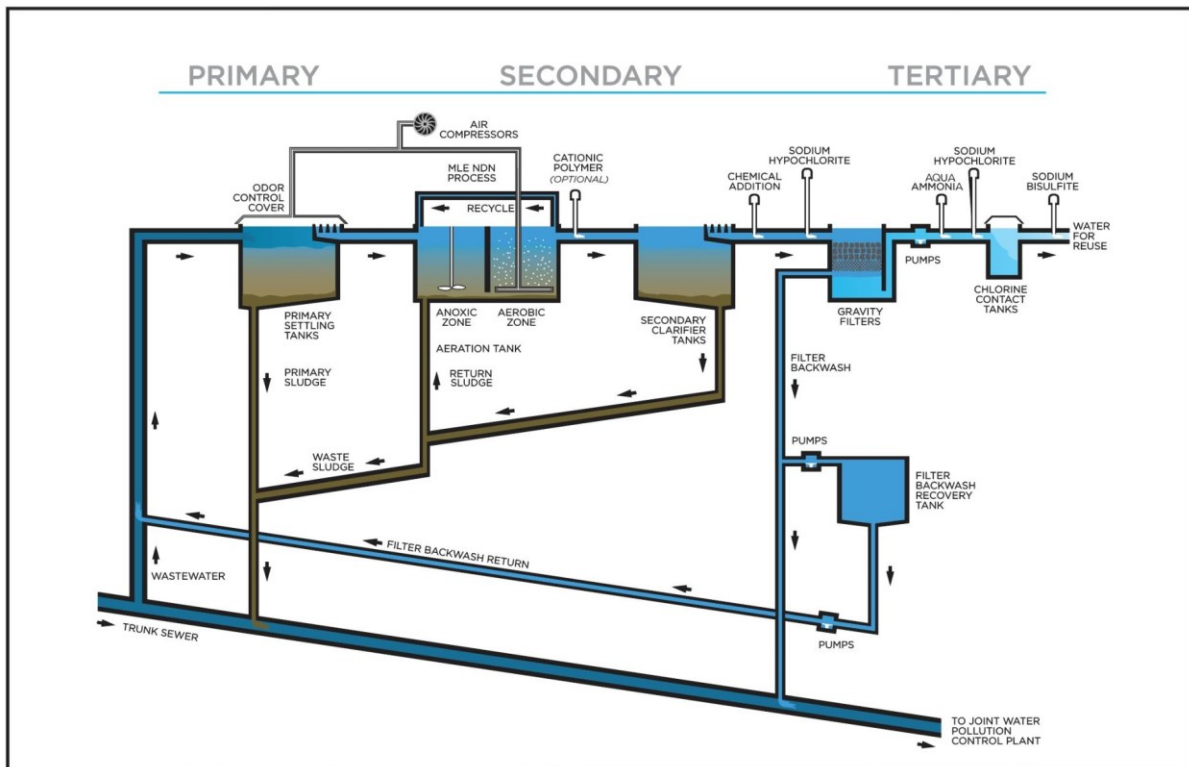


Figure 2.1: Processes involved in a three-stage WWTP, from the left, primary, secondary, and tertiary stages. The black bold arrows indicate the flow of wastewater (Los Angeles County Sanitation Districts, 2021).

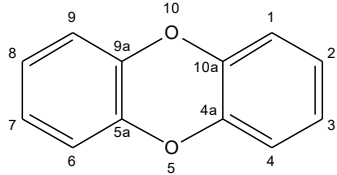
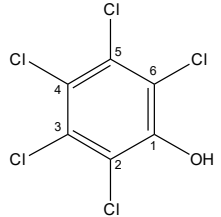
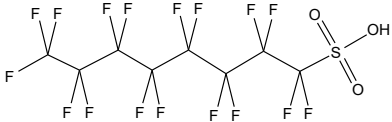
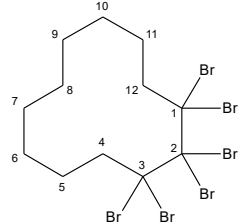
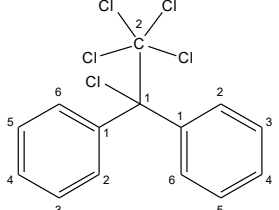
In this final tertiary stage, any remaining organics and suspended materials are removed from the water by passing it through a filter bed of sand and AC. This filtered water is further disinfected either with ultra-violet light or mixed with a chemical disinfectant (oxidant) to kill residual harmful bacteria, viruses, and microorganisms. Once these compounds are eliminated, the excess chemicals and the disinfectants are removed again to produce clean water, now ready for various recycling and reuse applications. It is clear, at the forefront of commercial tertiary technologies, adsorption using porous materials typically by AC is the most commonly used method due to its simple process design, no harmful generation of secondary products, and its cost-effectiveness (Joseph *et al.*, 2019). However, despite AC's good basic adsorption performance to some extent, it has limited porosity and functionality. Should an adsorbent's pore structures/chemistry could be carefully tailored to specific applications, it will enable superior adsorption kinetics, selectivity and capacity (Pi *et al.*, 2018). In this regard, MOFs have potentially the desired features to address these gaps in water remediation.

Therefore, this Section will critically review the published literature on studies that have employed MOFs for adsorptive removal of POPs, with a focus on phenols and perfluorinated compounds (PFCs). However, some reports reviewed here do not investigate the original POPs in the Stockholm Convention lists, but related compounds such as the POPs' precursors, degradation products or other analogous molecules were used in lieu. The reasons for this variation are: (1) some chemicals pose acute toxicity, which makes sample preparation extremely difficult (Wang *et al.*, 2019a) and (2) challenges in existing analytical methods to detect the trace POPs' concentrations (Lorenzo, Campo & Picó, 2018). For example, handling of dioxins is complicated due to their high toxicity and low volatility. So, investigations often use polychlorobenzenes as substitutes because of their similarity in the structural characteristics and the toxicity of dioxins (Bullot *et al.*, 2017). Table 2.1 lists several POPs from the 28 chemicals that are listed in the 2017 amendment of the Stockholm Convention, although at the time of writing, there are additional chemicals under review for possible incorporation.

2.1.2 Removal of phenols

Aromatic compounds such as chloro-phenol (CP), nitro-phenol (NP) and other substituted phenols, have been found to be in relative abundance, persistent and bio-refractory in aqueous environments as well as in the effluent from oil and gas processing industries (Ailijiang *et al.*, 2020). The World Health Organization currently recognises 19 forms of chlorinated phenols. 2-chlorophenol (2-CP), 2,4-dichlorophenol (2,4-DCP) and 2,4,6-trichlorophenol (2,4,6-TCP) are the three most likely CPs to be detected in drinking water whose presence is linked to disinfection by-products (World Health Organization, 2003). Another source of CPs includes the degradation of phenoxy-containing herbicides (Sharma & Lee, 2016) which are a widely used herbicide family found in agricultural activities worldwide since the 1950s due to their effectiveness. CP concentrations vary depending on the kind of water ecosystems being considered (lakes, rivers, oceans), but they typically exist at trace levels of parts per billion (ppb, ng/L) range and their presence can be easily distinguished by their distinct odours (Garba *et al.*, 2019). The permissible phenol concentration in drinking water according to the World Health Organization is 1 µg/L whereas for industrial effluents, the United States' Environmental Protection Agency sets a limit at 1 mg/L (Salari *et al.*, 2019).

Table 2.1: POP examples from the Stockholm Convention recognized to have deleterious effects on humans and our ecosystems.

Name of POP	Annex	Chemical structure	Use	Sources
<p>Polychlorinated dibenzo-<i>p</i>-dioxins (PCDD) and dibenzofurans (PCDF) (structure shown here is unchlorinated DD)</p>	<p>Reduce or prevent the unintentional production</p>		<p>Produced unintentionally from incomplete combustion, and during manufacture of pesticides and other chlorinated chemicals.</p>	<p>Unintentional release</p>
<p>Pentachlorophenol (PCP) and its esters</p>	<p>Eliminate production and use</p>		<p>Herbicide, disinfectant, ingredient in antifouling paint.</p>	<p>Pesticides and industrial sources</p>
<p>Perfluorooctane sulfonic acid (PFOS), its salts and perfluorooctane sulfonyl fluoride (structure shown here is PFOS)</p>	<p>Restrict production and use</p>		<p>Electric and electronic parts, firefighting foam, photo imaging, hydraulic fluids, and textiles.</p>	<p>Industrial sources</p>
<p>Hexabromocyclododecane (HBCD)</p>	<p>Eliminate production and use</p>		<p>Flame retardant additive on polystyrene materials</p>	<p>Industrial sources</p>
<p>Dichloro-diphenyl-trichloroethane (DDT)</p>	<p>Restrict production and use</p>		<p>Agricultural and household pesticide.</p>	<p>Pesticides</p>

Apart from being a potent endocrine disrupting agent, CPs present potential carcinogenicity and toxicity risks towards wildlife and human health alike (Pollack *et al.*, 2018). They are also classified as one of the priority pollutants by the United States' Environmental Protection Agency (United States Environmental Protection Agency, 2014) and listed in the European Parliament Decision No. 2455/2001/EC (European Communities, 2001); highlighting the stringent need of monitoring and regulation required for these chemicals. Moreover, CPs are suspected precursors of very toxic by-product compounds like polychlorodibenzo-p-dioxins (PCDDs), polychlorodibenzofurans (PCDFs) and polychlorophenoxyphenols (PCPPs) (Pan, Fu & Zhang, 2017). These compounds are all part of the Stockholm Convention watch list (Stockholm Convention Secretariat United Nations Environment, 2017).

Generally, treatments for phenol-contaminated wastewaters can be divided into three types: (1) biological, (2) conventional (distillation, adsorption, extraction) and (3) advanced (chemical/electrochemical/photocatalytic oxidation processes, membrane systems) as summarised in Table 2.2. Regarding CP removal specifically, treatment processes that have been investigated include biological methods (Martínez-Jardines *et al.*, 2018; Liang *et al.*, 2018; Sun *et al.*, 2018), adsorption (Gan *et al.*, 2018; Smolin, 2018), photocatalytic degradation (Dobaradaran *et al.*, 2018; Zhang *et al.*, 2018) and advanced oxidation processes (Li *et al.*, 2019b). Nevertheless, selecting the most appropriate treatment method, especially for treatment of industrial influents, surely involves many technical, environmental, and economic considerations. Therefore, to aid the selection, these criteria should be prioritized:

1. Technologies that have low energy requirements. So, distillation is excluded.
2. Targeted for low concentration phenolic wastewater, after it has undergone biological treatment in the secondary WWTP stage. So, membrane processes are excluded.
3. Does not use and produce toxic compounds. So, liquid-liquid extraction and chemical oxidation are respectively excluded.
4. Already employed for industrial applications. So, photocatalytic processes are excluded.

By following this generalised deductive reasoning, adsorption, or electrochemical oxidation are likely to be the best tertiary treatment options. Even though detailed cost analyses are out of the thesis scope, it is worth mentioning the point brought forth by Said *et al.* (Said *et al.*, 2021) in their cost comparison analysis for phenol technologies. Based on the financial data in Table 2.2, adsorption has purportedly higher costs than electrochemical oxidation. However, the final cost of the latter is determined by the location-specific electricity tariff. Plus, the treatment of high industrial wastewater volumes will cause two major repercussions: (1) necessitating parallel operation of the electrochemical oxidation equipment, which will dramatically increase the overall costs and (2) the total surface area of the electrode could reach hundreds of cm², also resulting to the same implication.

It is then a reasonable conclusion, among all of these technologies, adsorption has a number of key advantages including easy handling, high removal efficiency for pollutants at low concentration, no generation of toxic intermediates or secondary products and its comparatively low cost to other treatment processes (Hadjltaief *et al.*, 2018; Jang *et al.*, 2018). Furthermore, because aromatic CP compounds possess intrinsic low biodegradability in water (Sophia A & Lima, 2018), their removal via the standard biological treatment methods has limited success (Vashi, Iorhemen & Tay, 2018). Therefore, a combined system involving pre-treatment of the wastewater with biological method followed by adsorption should yield promising CP removal results.

Although adsorption is the mainstream technology employed in the WWTP's tertiary phase, isolating the adsorbent from the aqueous media can be challenging. Especially for MOF particles, as they generally have particle diameters of < 1 µm. Keshvardoostchokami *et al.* tried solving this issue by synthesizing a recoverable magnetic composite through a multi-stage synthesis procedure (Keshvardoostchokami *et al.*, 2021). Firstly, magnetic Fe₃O₄ nanoparticles were chelated with chitosan. Then, individual additions of zinc acetate followed by imidazole linker ensured the ZIF-8 (Zn) particles grow on the chitosan template to form a nano bio-composite. Their scheme for the materials' fabrication used a response surface methodology model. Response surface methodology is a statistical technique that seeks to optimize the number of experiments, costs and materials based on several variables within the umbrella and proper design of experiments methodology.

The variables studied by Keshvardoostchokami et al. were initial phenol concentration, pH, contact time, adsorbent dosage, and quantities of Fe_3O_4 . They found that increasing the Fe_3O_4 content decreased the phenol removal uptake, leading to a conclusion that the main adsorption mechanism is the π - π stacking between the phenol and the imidazole aromatic rings of the ZIF-8 (Zn). The H-bond that developed between the nitrogen-containing functional groups in ZIF-8 (Zn) and the hydroxyl group of the phenol also plays an important role.

Bisphenol S (BPS) is a structurally analogous chemical that is increasingly used to replace the more potentially toxic pollutant bisphenol A (BPA) in the manufacturing of polycarbonates as well as epoxy resins. In the first ever report to remove BPS, Park and Jung compared the effect of introducing basic NH_2 groups onto MIL-101 (Cr) (Park & Jung, 2020). Surprisingly, the MIL-101 (Cr)- NH_2 showed higher adsorption capacity than the pristine MIL-101 (Cr) even though it has lower porosity. In this case, the authors concluded that the superior adsorption performance of MIL-101 (Cr)- NH_2 is due to the strong interaction between its amino group and the sulfonyl groups on BPS (Figure 2.2).

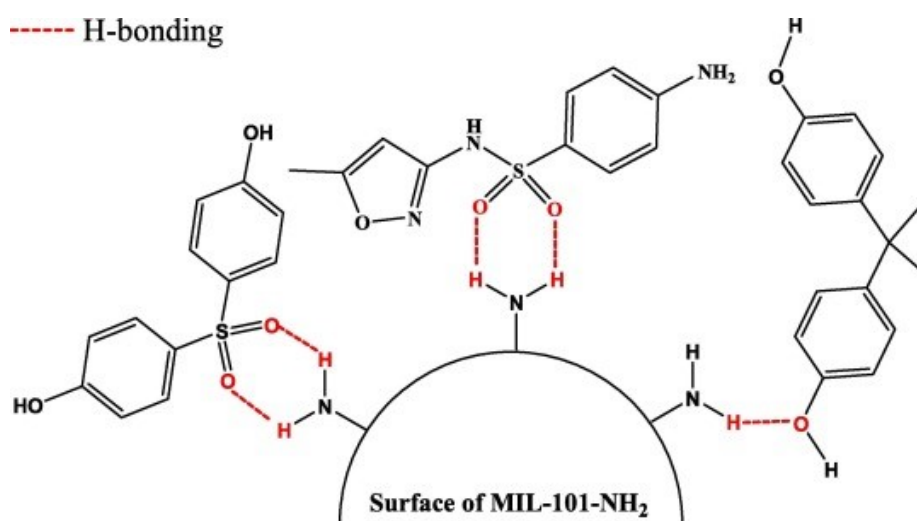


Figure 2.2: Proposed adsorption mechanisms of bisphenol S (left), sulfamethoxazole (centre) and bisphenol A (right) over MIL-101 (Cr)- NH_2 via 6-membered H-bonding configuration for the molecules containing SO_2 moiety. Reproduced with permission from (Park & Jung, 2020). Copyright 2020, Elsevier.

Table 2.2: Comparison of phenol removal technologies from wastewater. The information is harmonized from (Ortega-Méndez *et al.*, 2017; Raza *et al.*, 2019; Eryılmaz & Genç, 2021; Tufail *et al.*, 2021; Said *et al.*, 2021; Saputera *et al.*, 2021).

Technology	Description	Advantages	Disadvantages	Cost
Distillation	Separation of two immiscible liquids (phenol-water) by using steam distillation.	Rapid process. 100% separation is possible.	High-energy capital, hence, not suitable for treatment of low phenol concentration solutions (< 3000 mg/L). Needs large spaces to erect distillation towers	$\frac{\$798 \times 10^3}{1 \text{ m}^3 \text{ phenol year}}$
Biological degradation	Using microbial or enzymatic actions to break down phenols.	Simple design and maintenance. Transforms highly toxic phenol to less toxic products. A baseline treatment method for comparison.	Requires large land plots to install the tanks. Inefficient in treating high phenol concentration, aromatic and halogenated compounds. Highly dependent on reaction conditions, possible enzyme deactivation.	$\frac{\$81 \times 10^3}{174 \frac{\text{GJ}}{\text{h}} \text{ algae feed}}$
Adsorption	Separation of phenols from an aqueous stream onto a solid porous material.	Simple design. Highly efficient for a wide range of phenol concentration (50 – 2200 mg/L).	High adsorbent quantity is needed, raising the total costs. Extra treatment is needed for safe disposal of the spent adsorbents.	$\frac{\$107}{1 \text{ kg AC year}}$
Extraction	Separation of phenols from a liquid-liquid mixture based on their relative solubility.	The saturated adsorbent/solvent can be regenerated for reuse. No generation of harmful by-products.	Usage of harmful solvents. Extra treatment is needed for safe disposal of the spent liquids.	$\frac{\$47 \times 10^3}{1 \text{ m}^3 \text{ phenol year}}$

Chemical oxidation	Destroys phenols by using strong oxidants like H ₂ O ₂ and O ₃ .	Applicable for high phenol concentration. Improved efficiency when paired with UV light.	Can create recalcitrant by-products during the process, which are harder to degrade than the phenols. High energy and chemical requirements.	$\frac{\$115 \times 10^3}{\text{year}}$
Electro chemical oxidation	Electricity-powered oxidation of phenols on an anode surface.	No chemical reagents are involved. Easy operation and maintenance.	Can be costly due to continuous dependence on electricity supply. Prone to electrode fouling, needing regular replacement.	$\frac{\$15}{\frac{m^3 \text{ phenol}}{80 \text{ mA}} \text{ cm}^2 \text{ electrode}}$
Photo catalytic oxidation	Usage of light-responsive semiconductors/catalysts, typically TiO ₂ to degrade phenols into CO ₂ and H ₂ O.	Cost-effective. Low toxicity. Catalysts have high photochemical stability.	Not yet used in industrial applications. Limited catalysts' performance. Separation of catalysts post-usage is crucial as they can contribute to the toxicity of the treated effluents.	$\frac{\$869}{m^3 \text{ phenol}}$
Membranes	Separation of phenol-water mixture through a porous membrane driven by either concentration, pressure, or thermal differential forces.	High-quality effluent. Produces almost zero carbon emissions. Small footprint. Easily integrated with other treatments.	High operational and maintenance costs. Membrane fouling is common. Only suitable for treating highly concentrated phenol solutions.	$\frac{\$2.81}{m^3 \text{ chlorophenol}}$

Meanwhile, in a separate attempt to remove BPA from water, Ahsan, and his co-workers incorporated graphene oxide and carbon nanotubes into a Cu-BDC MOF to form a range of composites (Ahsan *et al.*, 2019). In their time-dependent experiments, the original Cu-BTC only adsorbed a maximum of about 20%, whereas both hybrid nanocomposites adsorbed 100% from the initial 20 ppm BPA solution. The composites' adsorption capacity also increased by a factor of three as well as showing faster BPA uptake rate than the original Cu-BTC. The authors proposed that the improvements are because of the synergistic effects between the parent MOF and the added nanomaterials. The dispersion of both the graphene oxide and the carbon nanotube additives simultaneously created a new pore morphology, and these new smaller pores are favourable for adsorption of small molecules like BPA.

Luo *et al.* tried to remove the BPA pollutant too, but using beads made from Al-MOF (MIL-68) which were firstly modified with sodium alginate (SA), then by chitosan (CS) (Luo *et al.*, 2019). Through the introduction of different CS wt%, new micropores were formed, thus, giving the Al-MOF/SA-CS composite a higher surface area than pristine Al-MOF. Apart from the π - π interactions between the composite's linker and the BPA, the N atoms from the newly added CS could form H-bonds with the OH groups in the BPA. The protonated amino (NH_3^+) group in the CS also participated in the cation- π interaction with the π -rich BPA aromatic structures. These adsorption mechanisms are shown in Figure 2.3. The presence of CS and SA both remarkably increased the maximum BPA uptake rate by approximately 2-fold compared to the original Al-MOF. Moreover, the formation of Al-MOF/SA-CS beads made it easier to isolate these materials in regeneration experiments. These adsorbents were stable over five adsorption-desorption cycles, only decreasing by 2.4% in capacity following the final cycle.

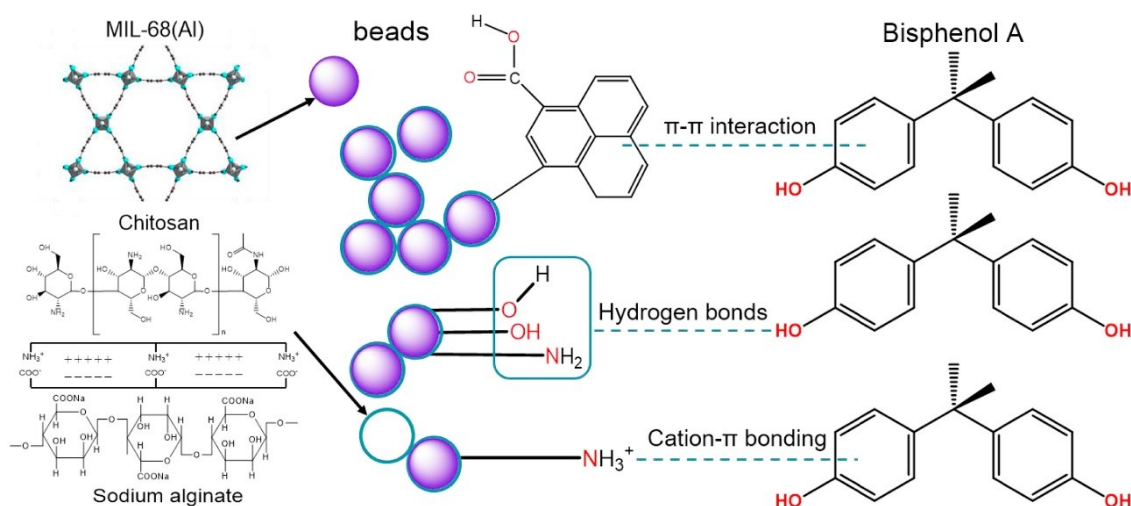


Figure 2.3: Adsorption mechanisms of BPA on Al-MOF/sodium alginate-chitosan composite beads. Reprinted with permission from (Luo et al., 2019). Copyright 2019, Elsevier.

Guo et al. have assessed the suitability of MIL-88B (Fe)-NH₂ to remove a trinitrophenol (TNP) derivative, specifically, 2,4,6-TNP (Guo *et al.*, 2019). The MOF showed very high adsorption capacity (164 mg/g), more than the nonpolar Amberlite™ XAD16 resin (61 mg/g) and bagasse fly ash (74 mg/g). However, AC, the industrial adsorbent reference, was not part of the comparison. So, even though the MOF exhibited high adsorption capacity, it cannot reasonably be claimed as the best adsorbent for TNP removal if it has not been compared with a commercial AC. In terms of the adsorption mechanism, the authors ascribed the high TNP uptake due to the existence of NH₂ groups on the MIL-88B (Fe). The NH₂ can form a stable six-membered structure via hydrogen bond with the acidic nitro group on the TNP.

So far, it has been understood that a MOF's performance can be improved by enhancing its chemical interactions like NH₂-H-bonding and π - π stacking. A physical modification technique like ultrasound has been investigated for the same purpose too. For instance, Abazari et al. initially prepared 1-2 μ m single crystals of [Zn(ATA)(BPD)]_∞ where ATA = 2-aminoterephthalic acid and BPD = 1,4-bis(4-pyridyl)-2,3-diaza-1,3-butadiene, via a slow diffusion reaction (Abazari, Salehi & Mahjoub, 2018). A similar reaction was then used with an ultrasonication reaction technique.

After Abazari et al. manipulated the reaction times and the reagent (ATA and BPD) concentrations, the single MOF crystals were transformed into un-aggregated nano-sized plates. These nanoplates have slightly increased BET surface area arising from the creation of structural defects. Some of the nanoplates were also modulated with triethanolamine (TEA) to expedite the nucleation rate and to reduce the plate size. Among the nanoplate samples, MOF-VII has the highest surface area (675 m²/g) due to the highest TEA addition (3 mL) and exposure to the longest ultrasonication time (120 mins). The synthesized samples were then tested to remove 2,4-dichlorophenol (DCP). MOF-VII achieved a maximum of 91% removal and faster removal kinetics compared to the bulk [Zn(ATA)(BPD)]_∞ (170 m²/g) which only attained 68% removal. The authors simply linked the difference in surface area as the sole reason for a higher and a faster uptake by the MOF-VII. It is believed that by performing more detailed solid characterizations, like measuring the FTIR spectra and acquiring the SEM images of the adsorbents before and after adsorbing 2,4-DCP, then a clearer understanding of the adsorption/binding mechanism could be determined. For example, NH₂ groups within the ATA/BPD linkers and from the grafted TEA might have participated in the adsorption mechanism, but the authors did not address this possibility.

The same group, Abazari and Mahjoub also utilized the same ultrasonication technique on another MOF, [Zn(TDC)(4-BPMH)]_{n.n}(H₂O) where TDC = 2,5-thiophene dicarboxylic acid and 4-BPMH = N,N-bis-pyridin-4-ylmethylene-hydrazine (Abazari & Mahjoub, 2018). Their objective was to transform the MOF single crystals (0.47 mm × 0.38 mm × 0.23 mm) into nanoparticles. In this study, pyridine was chosen as the modulator. The adsorption challenge species were the antibiotic amoxicillin (AMX) and 2,4-DCP. Sample 6, which was modulator-free was taken as the reference sample given its optimal results: with a low ultrasonication temperature, power, and time, it produced a good particle size distribution. When pyridine was added, it successfully changed the disordered nanoparticles of Sample 6 into more orderly nanoplates (Sample 13). The authors again inferred the higher adsorption capacity and the faster removal rate by both Sample 6 and 13 were as a result of their higher surface area, pore diameter and volume than the original [Zn(TDC)(4-BPMH)]_{n.n}(H₂O).

Besides chlorophenol, nitrophenol is also listed as one of the priority pollutants by the United States' Environmental Protection Agency. Given its high toxicity, an effective nitrophenol decontamination from wastewater is equally paramount. Using nitroresorcinol (NRC) as a model, Yang et al. devised a MSU-Zr core-shell composite structure, formed from a combination of magnetic Fe₃O₄ (M), silica (S) and UiO-66 (Zr) or U (Yang *et al.*, 2017b). They studied the influence of pH on the composite's performance for removing NRC. Best performance was found in acidic conditions (243 mg/g, pH 2) where they postulated that the Zr₆-(OH)₄ clusters acted as the base for the acidic NRC. In contrast, a basic condition inhibits the adsorption performance as the OH⁻ competes with the Zr₆-(OH)₄ to bind the NRC. To explain the composite's lower NRC uptake in basic conditions, additional zeta potential measurements were performed. The composite has an isoelectric point at pH = 5, showing a negatively charged surface above pH 5. On the other hand, NRC has a pK_a of 4.9, so at pH < 4.9, it dissociates mainly into -OH groups while at pH > 4.9, the O⁻ species dominates the solution. Therefore, when the solution becomes basic (pH > 5), there will be an electrostatic repulsion between the NRC (O⁻) and the negatively charged MSU (Zr) surface, hence, the reason to the composite's lower uptake in basic solutions.

Contrary to most studies that reported their data based on batch adsorption experiments, Pan et al. packed ZIF-67 (Co) into a glass column and conducted a breakthrough analysis of phenol solutions on this MOF (Pan *et al.*, 2016). However, their tested solution pH range was quite narrow; between 6 to 11. ZIF-67 (Co) has a positive surface charge below pH 10, close to the pK_a of phenol at 9.8. The ZIF-67 (Co)'s adsorption capacity reduced when the pH is above 10 since when the pH > pK_a, phenol will dissociate into OH⁻ ions. Therefore, these phenolic OH⁻ ions will repel the negatively charged ZIF-67 (Co) surface. When the ZIF-67 (Co) was studied for a 2-cycle regeneration test, negligible capacity loss was observed, indicating that this MOF is very stable for phenol adsorption.

In 2015, Zhang et al. highlighted the potential of using graphene oxide as an adsorbent to remove *p*-nitrophenol (PNP), with a reported uptake capacity of 269 mg/g (Zhang *et al.*, 2015). However, graphene oxide is hydrophilic, which makes it difficult to be separated from the aqueous solution after being used for adsorption. Reducing the surface functional groups of the

graphene oxide can help reduce its hydrophilicity, but at the expense of a much lower PNP uptake (16 mg/g).

Since MOFs generally have high surface area, Wu et al. attempted to form a hybrid material between MIL-68 (Al) (MA) and a reduced graphene oxide (RG) (Wu *et al.*, 2016). The composite containing 15% RG/MA ratio gave the highest surface area, micro and mesoporous volumes. Given its higher surface area, the composite was able to achieve a maximum PNP adsorption capacity of 307 mg/g, which is 64% and 123% higher compared to using MA and RG alone. The π electron-rich regions from the incorporated graphene layers also increased the π - π dispersion interaction between the composite and the PNP. To further investigate the composite's selectivity, it was immersed in a mixture of various phenols. It turns out that the nitro-substituted phenols (PNP, *o*-nitrophenol and *m*-nitrophenol) were adsorbed more favourably than the unsubstituted phenol. Because the nitro group in the nitrophenols function as an electron withdrawing group, it reduces the overall electron density in the aromatic ring of the MOF composite, creating a stronger phenol acidic site for surface adsorption.

The same PNP selectivity over phenol was also observed for HKUST-1 (Cu) for a mixture of *p*-nitrophenol (PNP) and phenol by Lin and Hsieh (Lin & Hsieh, 2015). The co-presence of phenol (up to 400 mg/L) gave a minimal 2% capacity decrease than the single-PNP uptake and only 5% when the co-phenol concentration is higher (800 mg/L). They believed the high PNP selectivity, and the high adsorption capacity of HKUST-1 (Cu) are due to the affinity of NO₂ from the PNP towards the Cu metal sites as well as the π - π interaction between the aromatic rings of the phenol and the MOF's BDC (1,4-benzene dicarboxylic acid) linker's benzene rings. Additionally, PNP was proposed to chemically bond to the HKUST-1 (Cu) (Figure 2.4). To prove their hypothesis, they tried to wash the PNP-saturated MOF with methanol and ethanol, followed by vacuum drying at 100 °C for 12 hrs. However, the adsorption capacity of both washed and dried MOFs was only 1/3 of the pristine capacity, implying the pores were still occupied. When they analysed the TGA data of these MOFs, they found that the PNP started decomposing at 150 °C. So, the then activation temperature at 100 °C was insufficient to fully decompose the adsorbed PNP.

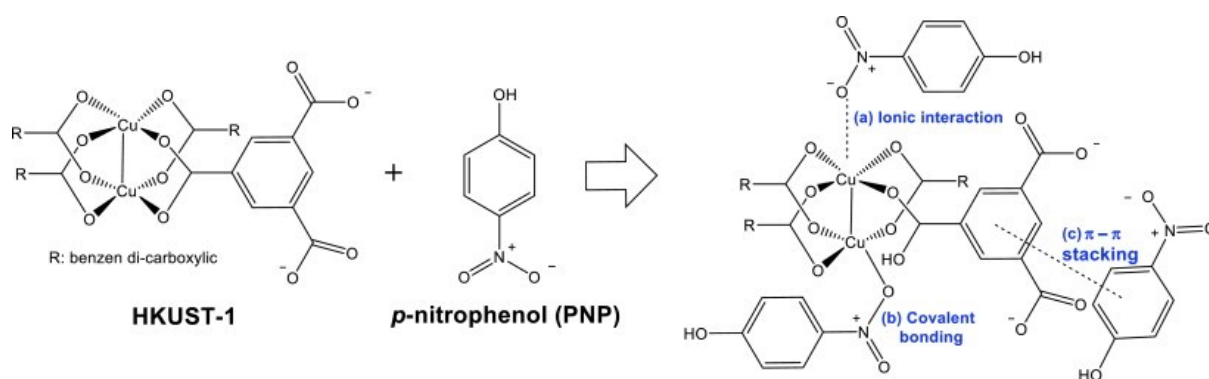


Figure 2.4: Possible binding mechanisms of HKUST-1 (Cu) to PNP (a) ionic interaction between the negatively charged oxygen of the PNP and the Cu metal site, (b) development of covalent bonding between the oxygen belonging to the PNP and the Cu metal site and (c) π - π stacking of the benzene rings from the PNP and the ligand of HKUST-1 (Cu). Reprinted with permission from (Lin & Hsieh, 2015). Copyright 2015, Elsevier.

Liu et al. evaluated phenol and PNP removal performance by MOFs made from Fe, Cr, Al metal ions including AC as a benchmark (Liu *et al.*, 2014). The adsorption capacity for phenol follows the order of AC > MIL-100 (Fe) \approx MIL-100 (Cr) \approx MIL-101 (Al)-NH₂. The equal capacity shared among these MOFs suggests that different metal ions did not affect the adsorption interactions and performance. The strong water interaction with the CUS on the MIL-100 (Fe, Cr) also hindered phenol adsorption. Whereas, for the removal of PNP, NH₂-MIL-101 (Al) significantly exceeded AC and MIL-100 (Fe, Cr). Using a modified ideal adsorbed solution theory model, Liu et al. could predict the multi solute adsorption equilibrium selectivity by using only their single solute isotherm data. Their calculations indicate that the NH₂ analogue has considerably higher PNP selectivity (4 – 6 times) than AC. They said this strong adsorption affinity came from the NH₂ (proton donor) and the nitro group of the PNP (proton acceptor) as well as the H-bonding formed between the NH₂ and the PNP's nitro groups.

Further details on the previously discussed studies can be found in Table 2.3, which summarises the list of MOFs used to remove phenols from water.

Table 2.3: Summary of literature on MOFs used in removal of phenolic pollutants from water.

Pollutant	Adsorbent	Analyte pH concentration and instrument method	Adsorbent concentration (mg/mL)	Results				Adsorption mechanism proposed	Reference
				q_e (mg/g)	t_e (hr)	BET (m^2/g)	Pore volume (cm^3/g)		
Phenol	Fe ₃ O ₄ /chitosan/ZIF-8	20 mg/L pH 9.91 UV-Vis	0.1	6.4	0.7	144	N/S	π - π stacking and H-bonding.	(Keshvardoostchokami <i>et al.</i> , 2021)
BPS	MIL-101 (Cr)	200 mg/L pH 7	0.1	196	12	3234	1.68	H-bonding between the OH and SO ₂ of BPS with the NH ₂ group on MIL-101.	(Park & Jung, 2020)
	MIL-101 (Cr)-NH ₂			513		2304	1.38		
	AC	UV-Vis		123		N/S	N/S	Other mechanism includes π - π stacking between the aromatics.	
BPA	Cu-BDC	20 mg/L pH 4 UV-Vis	0.5	60	24	N/S	N/S	The π - π stacking between the BPA and the hybrid nanomaterials.	(Ahsan <i>et al.</i> , 2019)
	Cu-BDC@GrO			182		N/S	N/S		
	Cu-BDC@CNT			164		N/S	N/S	The dispersed GrO and CNT increased quantity of active sites and formed new small pores. H-bonding between the OH, COOH of the composites and the H-receptors in the BPA.	
BPA	Al-MOF/SA-CS-0	50 mg/L pH 7 Using HPLC	0.2	101	18	249	0.27	Via π - π stacking, H-bonding, and cation- π interaction.	(Luo <i>et al.</i> , 2019)
	Al-MOF/SA-CS-3			137		688	0.61		
2,4,6-TNP	MIL-88B (Fe)-NH ₂	10 – 35 mg/L. pH 1 – 9 UV-Vis	0.5	164	1.5	414	0.12	H-bonding between TNP and the NH ₂ of the MOF. Complexation between OH in TNP and unsaturated Fe (III) on the MOF surface.	(Guo <i>et al.</i> , 2019)
2,4-DCP	[Zn(ATA)(BPD)] _∞	60 mg/L	0.3	136	1.5	170	N/S		

	MOF-VII	UV-Vis		182		675	N/S	The best performing nano MOF-VII has higher surface area.	(Abazari, Salehi & Mahjoub, 2018)		
2,4-DCP	[Zn(TDC)(4-BPMH)] _n .n(H ₂ O)	60 mg/L	0.4	125	3	39	0.245	The higher capacities and faster removal rate shown by Sample 6 and 13 are due to their relatively higher surface area than the original MOF.	(Abazari & Mahjoub, 2018)		
	Sample 6 (without PRD)			131		165	0.267				
	Sample 13 (with PRD)			142		235	0.302				
AMX	[Zn(TDC)(4-BPMH)] _n .n(H ₂ O)	UV-Vis	0.4	134	3	39	0.245			The higher capacities and faster removal rate shown by Sample 6 and 13 are due to their relatively higher surface area than the original MOF.	(Abazari & Mahjoub, 2018)
	Sample 6 (without PRD)			139		165	0.267				
	Sample 13 (with PRD)			143		235	0.302				
NRC	MSU-Zr	400 mg/L UV-Vis	1	221	10	653	0.3982	Electrostatic and acid-base interaction.	(Yang <i>et al.</i> , 2017b)		
Phenol	ZIF-67 (Co)	10 mg/L pH = 9 UV-Vis	0.1	379	10	1267	0.548	Electrostatic interaction.	(Pan <i>et al.</i> , 2016)		
PNP	MA/RG-15%	200 mg/L pH 3 – 11 UV-Vis	0.4	307	25	762	0.266	H-bond and π - π dispersion force	(Wu <i>et al.</i> , 2016)		
PNP	HKUST-1 (Cu)	20 mg/L UV-Vis	0.5	372	1	1140	0.42	Electrostatic interaction, π - π stacking, ionic/covalent bonding	(Lin & Hsieh, 2015)		
Phenol	MIL-101 (Al)-NH ₂	174 mg/L UV-Vis	4.5	38	24	1942	N/S	Proton donor-acceptor and H-bonding.	(Liu <i>et al.</i> , 2014)		
PNP		550 mg/L UV-Vis		167							

² Abbreviations used in Table 2.3: q_e = equilibrium adsorption capacity, t_e = equilibrium time, BPS = bisphenol S, BPA = bisphenol A, SMZ = sulfamethoxazole, GrO = graphene oxide, CNT = carbon nanotubes, BDC = benzene dicarboxylic acid, SA = sodium alginate, CS = chitosan, TNP = trinitrophenol, DCP = dichlorophenol, ATA = 2-aminoterephthalic acid, BPD = 1,4-bis(4-pyridyl)-2,3-diaza-1,3-butadiene, ∞ = single-crystals made from slow diffusion reaction technique, AMX = amoxicillin, TDC = 2,5-thiophene dicarboxylic acid linker, 4-BPMH = N,N-bis-pyridin-4-ylmethylene-hydrazine, PRD = modulated with pyridine, vDW = van Der Waals interaction, MSU-Zr = magnetic Fe₃O₄, silica, UiO-66 composite, NRC = nitro resorcinol, RG = reduced graphene oxide.

2.1.3 Removal of perfluorinated compounds

In 2017, the toxic and persistent perfluorinated compounds (PFCs) were added to the Convention list (Stockholm Convention Secretariat United Nations Environment, 2017). These PFCs have recently received much attention because not only they are ubiquitous contaminants in the aquatic environment, their high toxicity can cause detrimental health consequences when exposed to wildlife and humans (Piekarski, Diaz & McNerney, 2020). The most commonly found PFCs in surface waters are perfluorooctanoic acid (PFOA) and perfluorooctane sulfonate (PFOS) (Rivera-Utrilla *et al.*, 2013). Surprisingly, thus far, there is no mutually agreed international drinking water standard for acceptable concentrations of PFOA and PFOS, but the United States' Environmental Protection Agency have recommended a strict combined concentration limit of 70 ng/L (Cordner *et al.*, 2019). Recent analysis of global water samples even revealed concentrations exceeding this provisional threshold (Valsecchi *et al.*, 2017; Li *et al.*, 2018b; Scher *et al.*, 2018; Andersson *et al.*, 2019; Lorenzo *et al.*, 2019; Feng *et al.*, 2020).

Although most fluorochemical manufacturers have ceased their production of PFOA and PFOS in the early 2000s, this measure does not address the legacy pollution caused by these compounds (Wang *et al.*, 2017). The ubiquitous presence and the long-range mobility of PFCs is attributed to the high chemical stability of their C-F bonds (bond dissociation energy, $D^{\circ}_{298K} = 485 \text{ kJ/mol}$) (Richardson, 2008), rendering them suitable as ingredients to make fluoropolymers (McNamara *et al.*, 2018), fire-fighting foams (Cordner *et al.*, 2019), and stain-repellent products (Richardson, 2008). Typical contamination PFC hot spots can include vicinity of select industrial areas, military training sites, airports and wastewater treatment plants (Hu *et al.*, 2016). Moreover, exposures to PFCs can adversely affect body immunity (Sunderland *et al.*, 2019), neurological functions (Piekarski, Diaz & McNerney, 2020), reproductive systems (Rashtian, Chavkin & Merhi, 2019), as well as giving strong correlations to coronary heart disease (Huang *et al.*, 2018), and cancer (Mancini *et al.*, 2020) among many others. As a result, there is an urgent need to investigate efficient materials for PFCs remediation from contaminated water.

Among the treatments available for PFCs removal from water (Ateia *et al.*, 2019), adsorption is extensively used given its simplicity, relatively lower cost and high selectivity (Du *et al.*, 2014). Studied adsorbents range from AC (Du *et al.*, 2015; Xu *et al.*, 2020), alumina (Wang & Shih, 2011; Shih & Wang, 2013), magnetic nanoparticles (Badruddoza, Bhattarai & Suri, 2017), β -cyclodextrin polymers (Xiao *et al.*, 2017), ion exchange resins (Yang *et al.*, 2018), functionalized cellulose (Ateia *et al.*, 2018), graphene oxide-silica hybrid (Ali *et al.*, 2020), and metal-organic frameworks (MOFs) (Sini *et al.*, 2018; Liu *et al.*, 2015b; Jun *et al.*, 2019; Chen *et al.*, 2016; Sini *et al.*, 2019). However, except for MOFs, most adsorbents only exhibit between low and moderate PFOA uptake compared to the industrial AC standard (> 90% removal, 3M Company, USA) (Vecitis *et al.*, 2009).

It is important for an adsorbent to have a high uptake capacity, but an ideal industrial adsorbent must also display fast adsorption kinetics. Generally, the adsorption kinetics can be influenced by two key factors namely the adsorbent's particle and pore sizes. In a review article by Du *et al.*, finely powdered and mesoporous activated carbons were found to exhibit faster adsorption rate than their granular and microporous counterparts, speculatively due to the former's greater degree of intraparticle diffusion (Du *et al.*, 2014).

Additionally, if the adsorbates are ionic compounds like phenols and PFCs, then an adsorbent's surface functional groups and the solution pH are some of the factors that can affect the adsorbent's adsorption capacity. Unlike AC, a MOF's surface chemistry is easily tuneable through various parameters, as exemplified in the meticulous ligand selection by Zhao *et al.* (Zhao *et al.*, 2021). They screened a group of MIL-based MOFs to remove PFOS. MIL-53 (Al) emerged as the best performing material compared to MIL-101 (Cr) and MIL-53 (Fe) owing to its high density of coordinatively Al unsaturated metal sites, highest surface area and smallest pore size. They also discovered that by synthesizing the MIL-53 (Al) with longer organic ligand biphenyl-4,4'-dicarboxylic acid (BPDC), the new MIL-53 (Al)-BPDC contains larger skeletal pore sizes that allowed more PFOS entry.

To achieve higher porosity and density of coordinatively unsaturated metal sites (CUS) in a MOF, Clark and co-workers introduced framework defects into UiO-66 (Zr) by adding various amounts of HCl as a modulating agent (Clark *et al.*, 2019). The defective MOFs, UiO-66-10, and UiO-66-25 (the numeric suffix refers to the volume percent of HCl concentration used in the synthesis) showed increased porosity and CUS density according to their non-local density functional theory and TGA analyses, respectively. The defective UiO-66-10 and 25 have larger pores (16 and 20 Å) which contributed to an increase in pore volume and quantity of Zr-CUS relative to the defect-free UiO-66. The defective MOFs were then used to remove PFOS and its shorter-chain homologue perfluorobutanesulfonate (PFBS) from synthetic wastewater. The adsorption performance comparison was also made against a commercial powdered AC (Darco G-60, 100 – 325 mesh) and an anion exchange resin (Amberlite IRA-900, chloride form, 16 – 50 mesh).

The experimental results found by Clark *et al.* was quite surprising. Although the powdered AC possesses lower surface area than the defective MOFs, it exhibited a relatively similar adsorption rate. While for the MOFs, the introduced structural defects simultaneously led to missing linkers, which made them more hydrophilic. Increased framework hydrophobicity has been proven beneficial for adsorption of perfluorinated compounds. The ion exchange resin displayed a superior adsorption capacity, but this performance was hampered by a very slow rate of uptake (> 80 hrs). It has therefore become clear that the tested commercial adsorbents, powdered AC, and ion exchange resin, are each constrained by low adsorption capacity and slow equilibrium uptake rate, respectively (see Figure 2.5). In the presence of other solution ions like 25 mg/L sulphate and 100 mg/L chromate in the PFOS/PFBS mixture, the defective MOFs' sorption capacity decreased significantly due to adsorption site competition except when with 100 mg/L chloride, there was a negligible effect on the sorption. Overall, if MOFs are to be considered as an effective adsorbent for perfluorinated compounds, there should be a balanced approach between increasing the framework defects in a MOF and reducing the MOF's hydrophobicity. Also, despite the excellent performance shown by the defective MOFs and the powdered AC, they are still fabricated in powdered form, which is impractical for industrial deployment.

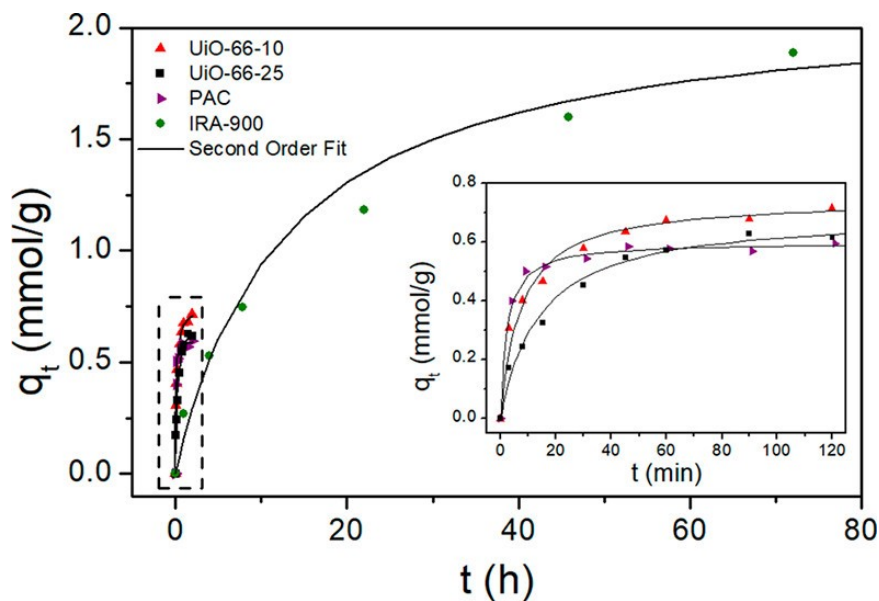


Figure 2.5: PFOS uptake rate (at pH 5) over 80 hrs of defective UiO-66 (Zr), powdered AC (PAC) and anion exchange resin IRA-900. Results were fitted with a pseudo-second order kinetics model. Inset image shows the sorption trend in the first 2 hrs. Reprinted with permission from (Clark *et al.*, 2019). Copyright 2019, ACS Publications.

The adsorption of endocrine disrupting compounds such as BPA, the synthetic hormone 17 α -ethynyl estradiol (EE2) and PFOA by an Al-based MOF was investigated by Jun *et al.* (Jun *et al.*, 2019). They used Basolite A100 or also known as MIL-53 (Al), and a commercial powdered AC (Evoqua Water Technologies, USA) to investigate the adsorbents' adsorption mechanisms for these EDCs. A wide range of experimental conditions were covered in the study including (1) optimum adsorbent dosage, (2) equilibrium sorption isotherm study, (3) adsorption kinetics, (4) solution properties such as temperature, pH, background ions, presence of natural organic matter (humic acid) and finally (5) adsorbent reusability. Generally, the PFOA adsorption by the MOF was negatively influenced by the presence of humic acid, as well as background salts including NaCl, CaCl₂ and Na₂SO₄. The MOF's PFOA removal rate also declined monotonically after each regeneration cycle, indicating an incomplete desorption due to the strongly adsorbed PFOA species. Although it is a comprehensive report, it still has some limitations. Firstly, the adsorbent concentration was not clearly stated in each experiment since different amounts were studied, ranging from 0.025 to 0.1 mg MOF/mL PFOA solution. Even with the maximum adsorbent concentration of 0.1 mg/mL, which is quite low, raises a slight suspicion on the reliability of the reported removal rate.

Secondly, the powdered AC's performance was only compared by Jun et al. once in the kinetics experiment, not in the rest of the study. Even though the powdered AC's adsorption capacity is lower than the MOF due to its lower surface area, comparisons for both adsorbents should have been performed in all experiments. Thirdly, for the regeneration tests, the drying temperature for the used MOF was not reported. The studied pollutants, BPA (360 °C), EE2 (457.2 °C) and PFOA (189 °C) all have very high boiling points, hence, knowing the drying temperature in between the ethanol washing cycles would be easier to pinpoint the exact cause of incomplete solute removal. The reusability datasets were also reported individually (one solute per one plot), although it would be more consistent to also supplement this investigation in a multi-solute condition like their earlier adsorption isotherm study. Along the same lines, the regeneration experiment could be further refined by trying out a desorption temperature > 360 °C, though the MOF's thermal stability might not be sufficient. Alternatively, since the PFOA adsorption by the MOF is mainly driven by electrostatic interactions, salts can be incorporated into the eluent solvent (ethanol) to weaken the solution's ionic strength and improve the desorption rate of the adsorbed PFOA.

Other than an increased electrostatic interaction, PFOA adsorption can be improved by using a hydrophobic material. A more hydrophobic UiO-66 (F4) has been prepared by Sini et al. using a fluorinated 1,4-benzene dicarboxylic acid (F4 BDC) linker in their UiO-66 (Zr) synthesis procedure (Sini *et al.*, 2018). Although they did not disclose the BET surface area of the UiO-66 (F4), judging by its maximum N₂ uptake of UiO-66 (F4), it is about 2.3 times higher than the unmodified UiO-66 (Zr). The authors also measured the UiO-66 (F4)'s FTIR spectra before and after being used for PFOA/PFOS adsorption. The PFOA/PFOS molecules were detected in the MOFs, but just from this finding, the authors directly concluded the UiO-66 (F4)'s superiority was due to its higher hydrophobicity interactions between the fluorinated linker and the PFOA/PFOS. Their evaluation is rather incomplete as the authors did not discuss the possible contribution of the UiO-66 (F4)'s higher surface area which may also have helped it to demonstrate higher q_e for both PFOA and PFOS. It would be better if the authors perform a quantitative analysis of the fluorine content in the UiO-66 (F4) and correlate that information with the two examined MOFs' adsorption performance. This analysis could rationalize the true contributor to the UiO-66 (F4)'s improved adsorption rate.

Continuing from this work, in 2019, Sini et al. then studied the effect of pore size to remove PFOA and PFOS from water (Sini *et al.*, 2019). They chose UiO-67 (Zr) which has a larger cavity size range (12 – 16 Å) than UiO-66 (Zr) (8 – 11 Å). Again, it is quite expected to see the former showing higher q_e . They also claimed that there is a change in the UiO-67 (Zr)'s sorption mechanism because of the increased cavity size, from a Langmuir monolayer to a Freundlich multi-layer instead. Surprisingly, a closer look at the fitting accuracy (R^2) values revealed that they are in closer agreement to the Langmuir model. No further reasonings were provided to support their assertion.

The existence of many environmental pollutants in their inherent anionic forms make them very mobile in the natural water systems. Development of a cationic material will be useful to capture these pollutants better like in the preparation of SCU-8 (Th) by Li et al. (Li *et al.*, 2017). SCU-8 (Th) is a mesoporous, cationic MOF that is proven very effective in removing PFOS anions, having displayed a high equilibrium capacity within a short contact period (2 mins). The SCU-8 (Th) was even capable of reducing an initially 1 µg/L PFOS concentration to lower than 21 ng/L, which is 3-times lower than the United States' Environmental Protection Agency's advisory standard of 70 ng/L. However, the use of slightly radioactive Th⁴⁺ as the metal building block is quite concerning and even more so for water purification purposes. The synthesis method will be difficult to scale up, as it demands strict adherence to protocols for using radioactive materials. Knowing these facts, it seems inadequate for them to investigate the material's hydrolytic stability only for 12 hrs. Furthermore, since the authors claimed that studies using Th-based MOFs are still underrepresented, longer duration soaking experiments perhaps lasting for months would be appropriate to quantify the leaching of SCU-8 (Th) or any radioactive actinide-ion-based MOF overall.

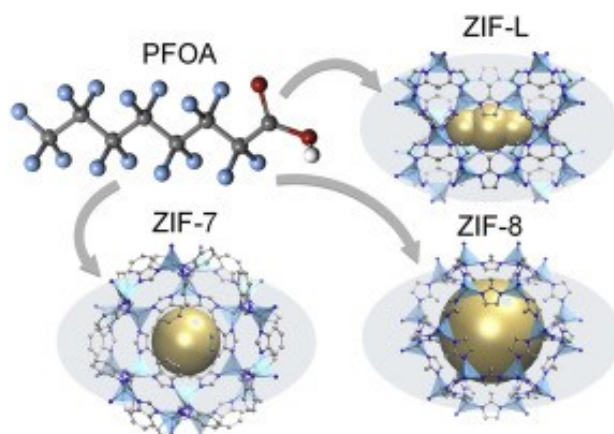


Figure 2.6: Structural topologies of ZIF-7 (Zn), ZIF-8 (Zn), and ZIF-L (Zn). The internal golden spheres represent the pore void. Reprinted with permission from (Chen et al., 2016). Copyright 2016, Elsevier.

Moreover, a MOF's unique forte is the ability to judiciously design its crystal topology and its interior surface functionality to target a specific pollutant. This concept was enlightened in the work by Chen et al. where three ZIF (Zn) family materials were studied comprising of ZIF-7, ZIF-8, and ZIF-L to remove PFOA (Chen *et al.*, 2016). ZIF-7 and ZIF-8 shared the same zeolite sodalite topology, but each was made from different ligands (ZIF-7 is with benzimidazole and ZIF-8 is with 2-methylimidazole respectively). ZIF-L is a homologue to ZIF-8 in the metal-linker combination. The difference is that the former has a 2-D layered structure while the latter is built from the original zeolite sodalite 3-D topology (Figure 2.6). All three ZIF materials exhibited higher PFOA sorption capacity than commercial zeolite 13X and AC with ZIF-L showing the highest equilibrium uptake. They believed this performance was due to the 2-D interlayer spacing that gives less constraint for PFOA molecules to enter the pores compared to the 3-D micropores of ZIF-8. ZIF-8 showed higher capacity than ZIF-7 which suggests a stronger interaction between the PFOA and the 2-methylimidazole than towards the benzimidazole linker. Although the lamellar structure of ZIF-L reduced the mass transfer resistance of PFOA, it has a low acidic stability, with pronounced crystallinity loss after a 24-hr immersion in pH 5 solution.

When discussing about the factors that can affect a MOF's adsorption performance, pore shape is another intertwined element. Yang et al. commenced a PFOA adsorption investigation using three Fe-based MOFs (Fe-BTC, MIL-100 and MIL-101), each composed of different pore geometries including triangular, hexagonal and pentagonal (Yang *et al.*, 2020). The order of

decreasing PFOA adsorption capacity is Fe-BTC > MIL-101 (Fe) > MIL-100 (Fe). Despite Fe-BTC having the lowest surface area among the three materials, the higher quantity of Lewis acidic sites on the Fe-BTC led to the highest capacity for this material compared to MIL-100 (Fe) and MIL-101 (Fe). The Fe centres also acted as the electron acceptor site whilst the benzene rings of the organic ligands become the electron donor in the adsorption process. Their XPS analysis also revealed that the Fe centres coordinated with the O of carboxyl PFOA group during the adsorption. To check the PFOA adsorption mechanisms into the MIL-101 (Fe) and the MIL-100 (Fe), the authors executed some computational calculations. For MIL-100 (Fe), it was observed that PFOA tends to adsorb into the smaller pentagonal pores (5.5 Å), but not in the larger hexagonal pores (8.6 Å). For MIL-101 (Fe), no PFOA was adsorbed in the wider pentagonal pores (16 Å), but they are present in the smaller triangular (10.8 Å) and the smaller pentagonal (12 Å) pores. These findings indicate that smaller and compacted triangular and pentagonal pores could provide better adsorption sites compared to the larger hexagonal ones, hence, why MIL-101 (Fe) shows a higher uptake than MIL-100 (Fe).

Barpaga et al. probed the role of a MOF's metal cations towards PFOS sorption by utilizing ^{19}F NMR, IR and XPS methods (Barpaga *et al.*, 2019). Using MIL-101 as a model MOF, both the chromium and the iron analogues of MIL-101 showed excellent capture of PFOS. Their XPS analysis revealed a preferential interaction by the MOF metal centres with the sulphur atoms of the polar head group of PFOS, though to a lower extent with the nonpolar fluorinated tail. Data from their *in situ* ^{19}F NMR experiments also showed that the MIL-101 (Cr) showed stronger interaction and twice as fast kinetics rate compared to the MIL-101 (Fe). It was also acknowledged in their report that the studied PFOS concentration is set very high (5000 mg/L) since their intention was to observe the MOFs' maximum potential at the highest PFOS solubility limit. Such high concentrations of PFOS will likely form micelles which can affect the sorption performance. This factor is also the reason to no equilibrium adsorption capacity values were mentioned anywhere in their report.

A full list of the studies is given in Table 2.4 which provides a summary of the removal studies of PFCs from water using MOFs.

Table 2.4: Comparison of MOFs used to adsorb PFCs from water at ambient condition (25 °C).

Pollutant	Adsorbent	Analyte concentration, pH, and instrument	Adsorbent concentration (mg/mL)	Results				Adsorption mechanism	Reference
				q_e (mg/g)	t_e (hr)	BET (m ² /g)	Pore volume (cm ³ /g)		
PFOS	MIL-53 (Al)	20 – 80 mg/L pH 7 UPLC-MS/MS	0.25	50	2	1336	N/S	Chemical bonding between the PFOS and the CUS. Fe ³⁺ in solution helped improved uptake due to bridging/complexation effect.	(Zhao <i>et al.</i> , 2021)
	MIL-53 (Al)-NDC			180		1132	N/S		
	MIL-53 (Al)-BPDC			220		1417	N/S		
	MIL-53 (Fe)			32		1247	N/S		
	MIL-101 (Cr)			10		874	N/S		
PFOA	Fe-BTC	500 mg/L pH 3.3	1	418	24	1051	N/S	π -CF interactions, Lewis acid/base complexation, H-bonding, electron donor-acceptor, hydrophobic interaction.	(Yang <i>et al.</i> , 2020)
	MIL-100 (Fe)			349		1237	N/S		
	MIL-101 (Fe)	HPLC		370		1811	N/S		
PFOS	MIL-101 (Fe)	5000 mg/L	10	N/S	24	3100	2.76	High sulphur-Cr affinity, chromium oxidation, stronger Lewis acid/base complexation.	(Barpaga <i>et al.</i> , 2019)
	MIL-101 (Cr)			N/S		2540	1.87		
PFOS	UiO-66-10	500 mg/L pH 5	0.5	375	1	1423	0.72	Electrostatic interactions with Zr ⁴⁺ and hydrophobic interactions.	(Clark <i>et al.</i> , 2019)
	UiO-66-25			350	1	1404	0.72		
	PAC			300	1	953	0.76		
	Amberlite IRA-900 (IX resin)	Using XRF TSA to measure PFOS.		1065	72	N/S	N/S		
PFBS	UiO-66-10	Using ICSC and UV-Vis for multi-ions.	0.5	162	2	1423	0.72		
	UiO-66-25			192	2	1404	0.72		
BPA	Basolite A100 or MIL-53 (Al)	1 mg/L of pollutant solutions.	0.1	138	4	630	N/S	Major PFOA adsorption mechanism is via electrostatic interactions.	(Jun <i>et al.</i> , 2019)

	PAC	Using HPLC for BPA and EE2.		75		470	N/S	The effect is in synergy with hydrophobic interactions.	
EE2	Basolite A100			201		630	N/S		
	PAC			90		470	N/S		
PFOA	Basolite A100	Using LC-MS for PFOA.		169		630	N/S		
	PAC			60		470	N/S		
PFOS	UiO-66 (Zr)	500 mg/L pH 4	1	160	1	682	N/S	Hydrophobic interactions between the pollutants and the MOF cavity.	(Sini <i>et al.</i> , 2019)
	UiO-67 (Zr)			580		N/S	N/S		
PFOA	UiO-66 (Zr)	¹⁹ F NMR.		388		682	N/S		
	UiO-67 (Zr)			700		N/S	N/S		
PFOS	UiO-66 (Zr)	500 mg/L pH 4	1	188	1	682	N/S	The incorporated F4 linker helped to accelerate PFOA and PFOS adsorption rate due to higher hydrophobicity interactions.	(Sini <i>et al.</i> , 2018)
	UiO-66 (F4)			262		N/S	N/S		
PFOA	UiO-66 (Zr)	¹⁹ F NMR.		327		682	N/S		
	UiO-66 (F4)			381		N/S	N/S		
PFOS	SCU-8 (Th)	1 mg/L PFOS solutions. For low concentration PFOS sorption experiment, 1 µg/L PFOS solution. UV-Vis.	For single-solute PFOS, 5 mg/mL. For trace PFOS sorption experiment, 1 mg/mL MOF.	45	0.03	1360	N/S	Strong hydrophobic interactions between PFOS and SCU-8. Hydrogen bonding between RSO ₃ ⁻ groups in PFOS. vDW interaction. Strong electrostatic interactions between the cationic SCU-8 frameworks with the PFOS anions.	(Li <i>et al.</i> , 2017)
PFOA	ZIF-L (Zn)	4 – 207 mg/L pH 5 HPLC	0.2	497	24	12	N/S	Layered structure reduces the resistance for PFOA diffusion than through cylindrical micropores.	(Chen <i>et al.</i> , 2016)

³ Abbreviations in Table 2.4 explained: PFOS = perfluoro octane sulfonate, RSO₃⁻ = alkyl sulfonate, F4 = 2,3,5,6-tetrafluoro-1,4-benzenedicarboxylic acid, NDC = dimethyl 2,6-naphthalene dicarboxylate, BPDC = biphenyl-4,4'-dicarboxylic acid, UPLC-MS/MS = ultra-performance liquid chromatography-tandem mass spectrometer, PFBS = perfluorobutanesulfonate, PAC = powdered activated carbon, IX = ion exchange resin, XRF TSA = x-ray fluorescence total sulphur analyser, ICSC = ion chromatography with suppressed conductivity detection, BPA = bisphenol A, EE2 = 17 α -ethinyl estradiol.

2.1.4 Water stability in MOFs

From thousands of available MOFs, the majority are made from divalent metal (M) cations such as Zn^{2+} , Cu^{2+} , Co^{2+} , Ni^{2+} , Cd^{2+} using carboxylates, phosphonates or N-donating linkers (L) or a combination of these linkers (Devic & Serre, 2014). However, those that are built from carboxylate-metal bonds have been reported to show varying degrees of water and moisture instability. When they are exposed to water or high humidity, structural disintegration takes place, causing partial or total porosity loss in the MOFs. This phenomenon hinders many of their commercial applications in various fields including gas storage, catalysis, molecular sensing, and liquid separation (DeCoste *et al.*, 2013; Van de Voorde *et al.*, 2014). Hitherto, the design of porous MOFs that are resistant to hydration remains a major challenge (Wang *et al.*, 2014, 2016). The term hydration stability can refer to the material's intactness after an aqueous immersion or moisture contact. Although the former state (aqueous immersion) involves greater degree of water exposure in a short period than the latter (moisture contact), whichever the case is, in this thesis, they can be assumed as interchangeably similar.

The methods used to assess a MOF's water stability differ between studies. Typically, a compromised MOF's water stability is reflected through the reduction of its BET surface area or changes in crystal structure (can be confirmed using PXRD) after exposure to prolonged and highly humid conditions (Gomes Silva *et al.*, 2010). Some other groups considered swelling resistance of MOFs under aqueous immersion as another criterion (Horcajada *et al.*, 2011; Taylor, Dawson & Shimizu, 2013). Furthermore, if a MOF is considered for any aqueous phase applications, an additional investigation is suggested to probe the dissolution of the solid phase, often indicated by the MOF's mass loss after filtration (Burtch, Jasuja & Walton, 2014).

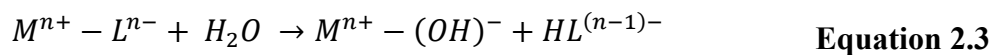
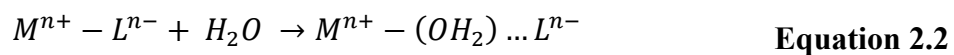
Therefore, prior to using any MOFs, it is imperative for one to evaluate potential MOFs and classify them according to their hydration stability level, either as being kinetically or thermodynamically stable (Jasuja *et al.*, 2013; Burtch, Jasuja & Walton, 2014). An extended recent review in 2020 by Batra *et al.* which used the datasets compiled by Burtch *et al.* (Burtch, Jasuja & Walton, 2014) provides clearer explanations of these stability states (Batra *et al.*, 2020).

Kinetically stable MOFs rely on a high activation energy (E_a) barrier to prevent hydrolysis reactions from taking place. Therefore, if they are exposed to high water/humidity for long periods, MOFs with low kinetic stability are still susceptible to degradation, yet those with high kinetic stability will survive under the same conditions.

In contrast, a MOF can be thermodynamically stable in the presence of water/humidity due to inadequate change in the system's free energy (ΔG) that can drive an irreversible hydrolysis reaction. A common feature embodied in many thermodynamically stable MOFs is their inert metal clusters that protect the material from hydrolysis. The oxygen in water/moisture is a nucleophile whereas the metal coordination centres of the MOFs are hydrophilic. If the metal centres are not sufficiently inert, water can coordinate with the metal cluster, and eventually disrupting the entire MOF's crystal framework. The thermodynamic stability of a material in the presence of water can be computationally quantified from its net free energy of a hydrolysis reaction. The relationship is shown in Equation 2.1:

$$\Delta G_{hydrolysis} = \Delta G_{prod(MOF+nH_2O)} - \Delta G_{react(MOF+nH_2O)} \quad \text{Equation 2.1}$$

Where ΔG_{prod} is the free energy of the MOF-water coordination complex after the hydrolysis occurs and ΔG_{react} is the free energy of the MOF and the water molecules before the hydrolysis occurs. When MOFs are exposed to water, data from computational chemistry models then confirmed from experiments have uncovered two main degradation mechanisms; (1) ligand displacement and (2) hydrolysis (Low *et al.*, 2009; Canivet *et al.*, 2014). In a ligand displacement reaction (Equation 2.2) water molecules can replace the metal-ligand (M-L) bond of the framework thus, forming a hydrated cation [$M^{n+}-(OH_2)$] and a free ligand (L^{n-}) While during a hydrolysis reaction (Equation 2.3), the intrusion of water molecules will break the M-L bond which later dissociates into a hydroxylated cation [$M^{n+}-(OH)^-$] and a free protonated ligand ($HL^{(n-1)-}$).



Several other factors can influence the stability of MOFs. For instance, the extent of basicity or pK_a values of the ligand can provide useful insights into a MOF's stability. According to the Lewis acid-base coordination theory, a strong base, described as having high electron density on the atoms is more favoured to donate electrons and correspondingly, creates stronger M-L bond (Choi *et al.*, 2010; Jasuja *et al.*, 2013; Lu *et al.*, 2014). A strongly covalent M-L bond can be formed as a result of the interaction between highly charged metal ions such as Al^{3+} , Cr^{3+} or Zr^{5+} with the O atoms from the carboxylate groups (Al-O, Cr-O or Zr-O) (Lu *et al.*, 2014; Feng *et al.*, 2012).

For the case of a fixed organic linker size, by choosing metals with higher valence cations (more than divalent, $2+$ ions), the resulting MOF will usually provide better hydrothermal stability (Devic & Serre, 2014). To recapitulate, a MOF's stability is highly influenced by the inertness of the metal ions used. Among a series of MIL-based MOFs, Kang *et al.* (Kang *et al.*, 2011) mentioned that Cr^{3+} is the most thermochemically stable ion followed by Al^{3+} , V^{3+} and V^{5+} in the order of decreasing ion inertness. Cr^{3+} -based MOFs prove to be very stable as they have a very slow ligand exchange rate constant of around $10^{-5} s^{-1}$; eight times slower than their Fe^{3+} analogues (Cheetham, Rao & Feller, 2006). This inertness is also responsible for its strong metal-oxygen octahedral coordination, as found in MIL-101 (Cr).

Ligand exchange or substitution is a condition when one ligand in a solution is replaced by another ligand, but the metal oxidation states, or the complex geometry are unchanged. Similarly, the original MOF's metal ions can be exchanged with other metal secondary building units (SBUs) from another solution without imparting significant changes in the framework structure. Taken together, this metathesis of metal ions or ligands from intact MOFs can be conveniently referred as post-synthetic exchange. Moreover, with respect to the kinetic inertness of the Cr^{3+} ions, the application of aerosol time-of-flight mass spectrometry (ATOFMS) by Kim *et al.* ascertained the absence of a ligand exchange on MIL-101 (Cr) (Kim *et al.*, 2012a).

However, it is not so well for the purportedly inert Zr (IV)-based UiO-66 (Zr) as the ATOFMS findings also by Kim et al. indicate this MOF's likelihood towards a ligand exchange (Kim *et al.*, 2012b). Nonetheless, as a general conclusion, they found that this post-synthetic ligand exchange process can be readily exploited on any eligible MOF to replace its unfunctionalized with functionalized ligands without causing appreciable loss in the MOF's crystallinity or porosity.

Before moving on to the shortlisting of potential water stable MOFs, it is apt to mention that despite the ongoing development of water stable MOFs, only a limited number have been studied thoroughly and classed as having high water stability including ZIF-8 (metal = Zn), HKUST-1 (Cu), UiO-66 (Zr) and MIL materials as documented by Liu et al. (Liu *et al.*, 2020). However, the ZIF and the UiO family members are microporous crystalline solids. Therefore, the size range of molecules that can be adsorbed into their pores will be limited compared to the MIL materials that generally exhibit both micro and to a greater proportion, mesoporosity. It is worth reiterating that the "assumed" inertness of Zr⁵⁺ contained in UiO-66 is solvent-dependent. From the assessment of UiO-66's inertness by Kim et al., they demonstrated that ATOFMS is a great tool to provide single-particle level insights on UiO-66 (Zr) that cannot be acquired through bulk analysis like PXRD or N₂ adsorption-desorption isotherms (Kim *et al.*, 2012b). Even though UiO-66 (Zr) displays good structural and chemical robustness in the bulk aqueous phase, the ATOFMS findings signal its vulnerability for ligand displacement especially in the presence of polar solvents like water. This work acts as a subtle reminder that a second evaluation of the "assumed" stability of other robust MOFs can be very useful.

HKUST-1 (Cu) is undoubtedly a MOF with low hydrolytic stability (Álvarez *et al.*, 2017). So, when used in aqueous media, the successive coordination of water molecules on the unsaturated Cu metal sites of HKUST-1 (Cu) can dramatically accelerate the hydrolysis reactions and the ligand displacement. Over time, the accretion of water on the sites will finally collapse the whole framework (Xue *et al.*, 2019).

Eventually, this shifts the attention on either MIL materials such as MIL-100 (Fe/Cr), MIL-101 (Fe/Cr). Based on previous explanations, MOFs made with Cr^{3+} ions are by far the most stable candidates for liquid application even when identical structures are made from Fe^{3+} or Al^{3+} (Rieth & Dincă, 2018). Plus, vis-à-vis the others in their structural properties, MIL-101 (Cr), which was first discovered in 2005 by Férey et al. displays a very porous crystal structure with super large pore sizes between 30 – 34 Å and a Langmuir surface area of $\sim 5900 \pm 300 \text{ m}^2/\text{g}$ (Férey *et al.*, 2005). Moreover, having two window openings of 12 Å (for the smaller cage) and 16 Å (for the larger cage) are enough for most small and large guest molecules to access and bind to the sites. It has therefore been clear among other MOFs, MIL-101 (Cr) has the upper hand and deemed reasonable to be further studied.

If MIL-101 (Cr) is meant to be used for liquid phase separation, the leaching potential of toxic Cr compounds from the MOF into the treated water may be contentious. Contrary to popular belief, MIL-101 (Cr) has actually been studied by Horcajada et al. as a drug carrier in human bodies, proving that it is a safe MOF (Horcajada *et al.*, 2006). Moreover, the solubility and toxicity of Cr in water are dependent on its oxidation state. The most prevalent states found in the environment are +6 and +3 although the Cr oxidation states can vary from +6 to -4. The commonly found hexavalent Cr (VI) is highly toxic, carcinogenic, and water-soluble whereas the Cr (III) that is used to make MIL-101 (Cr) has the opposite nature (Saha, Nandi & Saha, 2011; DesMarias & Costa, 2019). Plus, in the absence of complexing ligands, Cr (III) tends to form hydroxides that are less toxic to humans (Yadav & Xu, 2013). Finally and more importantly, in the interest of a MOF synthesis scalability, those that use ecologically benign and low-cost metals such as Mg, Ca, Al, or Fe are acceptable too (Kim *et al.*, 2019).

Before the discovery of MIL-101 (Cr), Férey et al. already developed a hydrothermal synthesis method to produce MIL-100 (Cr), using the same inert Cr^{3+} ions, but combined with a trimesic acid (benzene-1,3,5-tricarboxylate or BTC) linker (Férey *et al.*, 2004). Three years later, in 2007, Horcajada et al. introduced an iron-based MIL-100 (Fe) made from Fe (III) to make use of its low cost and toxicity, good redox properties, excellent water stability and ability to be produced in large scale (Horcajada *et al.*, 2007).

MIL-100 (Fe) is also notably known for its high porosity and high thermal stability, possessing a Langmuir surface area $> 2800 \text{ m}^2/\text{g}$ and a stable structure up to $270 \text{ }^\circ\text{C}$. In terms of its architecture, MIL-100 (Fe) comprises two types of mesoporous cages, 24 \AA and 29 \AA that can be accessed through microporous windows of 5.5 \AA and 8.6 \AA respectively. Figure 2.7 shows the pore structures available in Cr-based MIL-100 and MIL-101, though the Fe versions will be identical.

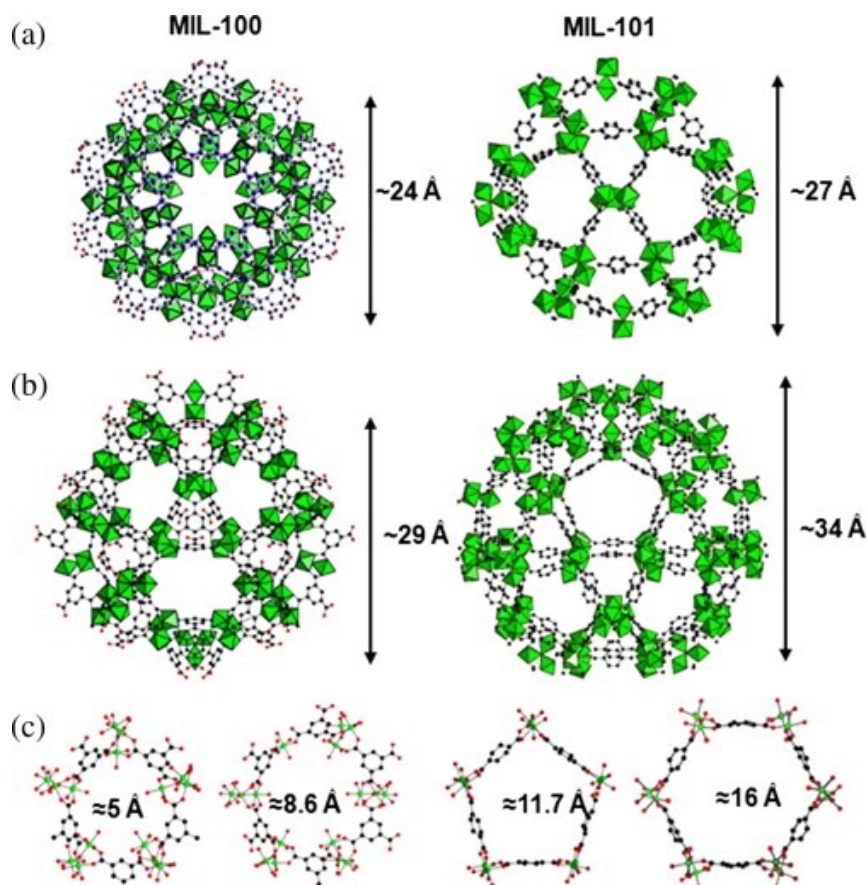


Figure 2.7: Structures of MIL-100 (Cr) and MIL-101 (Cr) showing their (a) small cages, (b) large cages, and (c) pentagonal and hexagonal windows. The chromium octahedra is in green whereas the carbon atoms are in black. Image is taken with permission from (Trung *et al.*, 2010). Copyright 2010, Elsevier.

2.1.5 Summary of literature gaps and the rational design of MOFs in water decontamination

Initially, it was anticipated that a high adsorbent porosity would be the most important material property in distinguishing an adsorbent's performance. However, for some MOFs with lower surface areas, based on the reports listed in Table 2.3 and Table 2.4, the chemical molecular-level interactions appear to be more prominent, especially in the presence of NH₂ functionality and coordinatively unsaturated metal sites. They function as a hydrogen bonding and a Lewis acid sites, respectively. Hydrophobicity and π - π interactions are the classic attractive factors for adsorbing hydrophobic solutes typically containing benzene rings in their chemical structures. The hybrid addition of graphene oxide with benzene rings into a MOF could help increase the π - π bonding interactions, which in turn accelerates the composite's adsorbate uptake rate while the formation of new small pores or layer-like structures can also boost its maximum adsorption capacity. In this regard, post-synthetic modification is the right technique that can be utilized to improve the MOF-adsorbate specificity and hydrophobicity.

Additionally, phenols and perfluorinated compounds are both partially ionic compounds. So, their uptake rate is dependent on (1) the MOF's surface charge at a particular pH and (2) the presence of competing ions within the same aqueous environment. Therefore, future studies on adsorptive removal of phenols and perfluorinated compounds should always be designed to incorporate these factors. Measuring the zeta potential of an adsorbent at a particular pH will provide information about its surface charge trend, leading to the identification of its point of zero charge which is the pH when the material's surface charge is zero. While the addition of common competing ions within a similar testing solution will simulate the adsorbent's removal effectiveness if it is used in real-world situations.

Even though AC is the currently preferred adsorbent used in aqueous phase remediation applications, the performance of the studied MOFs was only occasionally cross-referenced with AC's. Even when compared, much of the focus is on the adsorption mechanisms by MOFs. Little emphasis was placed on the corresponding adsorption mechanisms for AC, regardless of its superior or inferior performance. It is advisable to keep using AC's performance as a benchmark to understand the difference between the MOF's and the AC's adsorption mechanisms better.

Moreover, as far as a MOF's kinetics and uptake capacity is concerned, a batch-mode and a single-solute adsorption experiments can be used to generate preliminary data, but they are not indicative of its real-performance in industrial purification processes. Instead, testing them in packed or breakthrough columns with more complex wastewater mixture should be the baseline in future studies. Furthermore, fine powdered MOFs are not suitable for easy post-adsorption recovery and long-term reusability. The MOF particles should be developed into larger, granular shaped products just like AC.

It is highly crucial if MOFs were to be used in water remediation applications, the metal toxicity/leaching of the MOFs must be studied thoroughly. However, this leaching assessment is usually done once the MOFs have been synthesized. So, it will be better if the synthesis procedures for the MOFs are evaluated before even using them for adsorption. Particularly, by conducting a life cycle analysis as an initial MOF screening tool. Through this life cycle analysis, it will provide detailed information about the impacts of sourcing greener reactants (less toxic metal or linker substitutes), using less harmful solvents and adopting ambient reaction conditions (instead of using high temperature and pressure to synthesize the MOFs). When an eco-design methodology for a specific MOF has been found, it will increase their chances to be scaled up cost-effectively.

2.2 Air purification

2.2.1 Limitations of current indoor air VOC removal technologies

Among the range of available VOC removal technologies, gas phase adsorption using porous carbons is currently the most economic and established strategy. However, they have limited selectivity and adsorption capacity which worsen when being used under humid conditions (Zhang et al., 2017b; Zhu, Shen & Luo, 2020). AC-based adsorbents have low cost, high porosity, and chemical stability which result in their ubiquitous use for air filtration devices. However, their amorphous, heterogeneous chemical structures make targeted removal of specific hydrocarbon species challenging (Xie et al., 2018). Majority of the air purification filters are made of two components. The AC part is installed for removal of odour, VOCs, and ozone whereas the complementary high-efficiency particulate air glass fibres can deal with indoor particulate matter (Yang et al., 2017c). However, the efficiency of these combined filters for removing VOCs sharply decreases when operating in high humidity (Li et al., 2020d).

In addition, the regeneration of used AC results in gradual capacity loss. Since AC needs to be regenerated at high temperatures, it will experience progressive thermal degradation which can give rise to higher carbon deposition in the pores and cause blockage. Another issue with AC regeneration is the possibility of a heel build-up or irreversibly adsorbed species on its surface which can affect AC's performance. Some of the mechanisms causing a heel formation include strong physical adsorption, chemical adsorption, oligomerization, and decomposition of the captured adsorbates. Exposure to high regeneration temperatures also favourably shifts adsorbates' physisorption to chemisorption and later to total decomposition trapped within the pores (Lashaki et al., 2012; Niknaddaf et al., 2016).

An efficient adsorbent should exhibit high selectivity, high uptake capacity, and fast kinetics for targeted removal of a specific VOC species. These criteria are necessary because, in the atmosphere, water vapor exists at 10,000 times or higher than many VOC species concentrations. Consequently, relative to VOCs, the water molecules are favourably adsorbed onto the adsorbents at a higher concentration, resulting in poor VOCs uptake (Hunter-Sellers et al., 2020).

2.2.2 Developing MOFs to remove VOCs from humid air

Metal-organic frameworks (MOFs) are an important emerging class of adsorbent materials known to have high porosity, stability, tuneable properties, and excellent reusability. These new materials may be able to overcome the limitations of porous carbon and thus become an alternative adsorbent for VOC capture (Kumar *et al.*, 2015; Xie *et al.*, 2018). Also advantageous about MOFs is the wide range of structures that can be formed. With the myriad of organic linkers and metal ions to choose from, it can generate unlimited number of possible scaffolds and pore sizes in the resultant MOF structures, which in turn can be tailored for specific applications. This design scope is crucial as adsorption performance, both in terms of adsorption rate and capacity, is determined by a few key factors including pore size, accessible porosity, hydrophobicity and available functional groups (Li *et al.*, 2020d). MOFs already fulfilled part of these criteria with their large pore size and high porosity, so, their surface chemistry can be easily modified to impart specific functional groups.

Despite these promising features ascribed to MOFs, high water affinity for some MOF materials is one of the remaining significant challenges preventing their widespread industrial acceptance (Safy *et al.*, 2020). For instance, among the currently available MOFs, MIL-101 (Cr) is frequently studied for VOC capture as it has high surface area, tuneable surface properties, and excellent hydrothermal stability (Huang *et al.*, 2011; Zhao, Li & Li, 2011; Xian *et al.*, 2015; Wang *et al.*, 2018b). However, the natural hydrophilicity of MIL-101 (Cr) causes low selectivity for VOCs, especially in humid environments (Ko *et al.*, 2015b; Yanagita *et al.*, 2019).

The sister of MIL-101 (Cr), which is MIL-100 is also known to be very hydrophilic. A recent review by Feng *et al.* found that MIL-100 (Fe) displays good potential as an indoor moisture adsorbent (Feng *et al.*, 2018). The combination of high porosity and hydrophilicity, plus good water stability enable MIL-100 (Fe) to adsorb high water quantity (15 g water/m².RH), 33 times higher than laminated wood and other traditional building materials. Apart from these features, an ideal moisture adsorbent also needs to have a low regeneration temperature, so they can release the adsorbed moisture in room temperature or at low humidity levels.

Conventional desiccants such as silicates, aluminophosphates, zeolites and activated charcoal all have high water uptake capacity, but their regeneration temperature is normally $> 100\text{ }^{\circ}\text{C}$ (Ng & Mintova, 2008; Bauer *et al.*, 2009; AbdulHalim *et al.*, 2017; Wragg *et al.*, 2010). Unlike the others, MIL-100 (Fe) has a low regeneration temperature of $50\text{ }^{\circ}\text{C}$, which is not difficult to find a heat source within a building's heating, ventilation, and air conditioning system.

Although MIL-100 (Fe) has the conducive features for VOCs adsorption, reports on Fe-based MOFs are scarcely available. Realizing this gap, Ma *et al.* compared three Fe-based MOFs which are MIL-101 (Fe), MIL-53 (Fe) and MIL-100 (Fe) for removal of toluene (Ma *et al.*, 2021). The highest toluene adsorption capacity was shown by MIL-100 (Fe) (587 mg/g), about 3 and 5 times higher than MIL-101 (Fe) and MIL-53 (Fe) respectively. Apart from its highest porosity ($1399\text{ m}^2/\text{g}$) than other studied MOFs, further XPS analysis by the authors revealed the π - π interaction between the toluene and the benzene ring in the trimesic acid linker as the primary adsorption mechanism. This can actually be a good opportunity to investigate MIL-100 (Fe)'s potential as a VOC adsorbent just like MIL-101 (Cr). However, first and foremost, to enhance their VOC removal performance in humid conditions, both MIL-100 (Fe) and MIL-101 (Cr) need to be transformed from a hydrophilic into a hydrophobic material.

Recent developments of water-tolerant or hydrophobic MOFs have been achieved via hydrophobicity improvements either in their internal pores or on the external crystal surfaces (Jayaramulu *et al.*, 2019; Mukherjee, Sharma & Ghosh, 2019; Xie *et al.*, 2020). More specifically, a MOF's hydrophobicity can be improved using three modification strategies:

1. Ligand functionalization with hydrophobic moieties (Yang *et al.*, 2011a; Zhu *et al.*, 2017). This internal pore chemistry modification (Strategy 1) is noted for its efficacy in the generation of many hydrophobic MOFs. These syntheses rely on the use of niche hydrophobic linker molecules which necessitates bespoke synthesis procedures, or if commercially available tend to be costly. Examples include amino and fluoro-based organic linkers (Vellingiri *et al.*, 2017; Yang *et al.*, 2011a).

2. *In situ* hydrophobization (Karikkethu Prabhakaran & Deschamps, 2015; Chun *et al.*, 2014). However, this *in situ* hydrophobization method (Strategy 2) can produce undefined structures (Zhang *et al.*, 2019d, 2019a, 2019c).
3. Post-synthetic modification (Zhang *et al.*, 2017; Sun *et al.*, 2016; Bae *et al.*, 2014; Sun *et al.*, 2019). Clearly, out of these identified Strategies, post-synthetic modification (Strategy 3) using coatings is preferred because of its low cost, ability to develop controllable structure, simple and scalable fabrication process (Xie *et al.*, 2020; Zhang *et al.*, 2017). Simple and low-cost hydrophobic chemicals/polymers can be used to convert less hydrophobic or hydrophilic MOFs into a more hydrophobic form. These coatings can be imparted on the MOFs through vapour-phase deposition method or treated in a liquid phase, which in any case, is expected to enhance a MOF's selectivity and kinetics for VOCs adsorption from air.

2.2.2.1 Pristine MOFs as VOC adsorbents

This Section reviews reports that used only pristine MOFs to remove VOCs. In a recent 2021 report by Liu *et al.* on MOF-199 (Cu) (also known as HKUST-1) and UiO-66 (Zr)-NH₂'s ability to remove benzene vapour was reported (Liu, Younis & Kim, 2021). For air quality monitoring at ambient conditions or for this benzene vapour removal specifically, the authors proposed three universal metrics to assess the performance of a packed bed adsorbent. Firstly, 10% breakthrough volume (BTV) is a more meaningful criterion than 100% BTV (complete bed saturation), primarily looking at 10% BTV values > 100 L.atm.g⁻¹. Secondly, the partition coefficient (PC), whereby if pressure is very low ($P \sim 0$), this can be considered equivalent to the Henry's Law constant (K_H). Essentially, both PC and K_H can measure the distribution of a target adsorbate between the gas and solid interfaces. Thirdly, the maximum equilibrium adsorption capacity (Q) which is the typical and the most reported parameter in any studies concerning adsorptive VOC removal.

These parameters are defined in Table 2.5 where C is the sorbent capacity (mg/g) at bed inlet pressure P (Pa), C_m is the maximum sorbent capacity (mg/g), k is the Langmuir's constant (Pa⁻¹), and M is the adsorbate molar mass (g/mol).

Table 2.5: Performance metrics used to evaluate a packed adsorbent bed performance for air quality monitoring applications. Formulae are taken from (Szulejko & Kim, 2019; Szulejko, Kim & Parise, 2019).

Description	Unit	Formula
Langmuir isotherm	$\frac{mg}{g}$	$C = C_m \times k \times \frac{P}{(1 + kP)}$
Henry's coefficient	$\frac{mol}{kg.Pa}$	$K_H = C_m \times \frac{k}{M}$
Partition coefficient	$\frac{mol}{kg.Pa}$	$PC = \frac{C}{MP}$
Henry's Law ($P \sim 0$)	$\frac{mg}{g}$	$C = K_H \times P$
10% BTV at 298 K	$\frac{L.atm}{g}$	$BTV_{10} = PC \times 24.45 \times 10.1$
Maximum capacity	$\frac{mg}{g}$	$Q = \frac{Total\ mass\ adsorbed}{Adsorbent\ bed\ mass}$

At 0% RH, the two studied MOFs by Liu et al. which are MOF-199 (Cu) and UiO-66 (Zr)-NH₂ both exceeded the reference 10% BTV threshold when adsorbing low-level benzene (< 50 ppm). However, at higher benzene inlet concentrations (50 to 200 ppm), both MOFs failed to achieve the same threshold. At RH > 50% and with a benzene concentration < 50 ppm, the Q values of the MOFs suffered dramatic reductions. Specifically, an 85 – 99.9% performance reduction for MOF-199 (Cu) and 71 – 95% for UiO-66 (Zr)-NH₂ due to their strong intrinsic competitive adsorption with water. However, when the benzene concentration is above 50 ppm, further increase of RH led to relatively low reductions in the 10% BTV capacity of the MOFs. This fascinating trend suggests that by increasing the benzene concentration, the negative effects of water vapour on the MOFs' performance can be reduced. Nonetheless, irrespective of the high studied MOFs' porosities, for them to be employed in air purification systems, their obtained findings necessitate the use of hydrophobic adsorbents, which will help increase a VOC's selectivity and a MOF's structural robustness in humid environments.

Despite the relative abundance of data for formaldehyde (FA) adsorptive removal, Vikrant et al. identified two main issues (Vikrant et al., 2020). Firstly, the adsorption mechanisms of FA by MOFs were not studied in detail. Secondly, FA was investigated independently although in a realistic setting, FA exists together with other carbonyl compounds (CCs). So, they compared four MOFs which are MOF-5 (Zn), MOF-199 (Cu), UiO-66 (Zr) and UiO-66 (Zr)-NH₂ alongside AC, to remove a mixture of 6 CCs at low concentrations comprising 14 ppm FA, 10 ppm acetaldehyde (AA) and 0.2 ppm each of propionaldehyde (PA), butyraldehyde (BA), iso valeraldehyde (IA) and valeraldehyde (VA). The CC mixture was humidified with water at 5% RH to simulate real-world conditions, though 5% RH is a very low real-world humidity level. The authors expressed their preference on using BTV10 and PC as better evaluation metrics than Q alone. In their work, UiO-66 (Zr)-NH₂ showed the highest BTV10 and PC for FA at ~1 Pa, whereas for heavier CCs (PA, BA, IA, VA), MOF-199 (Cu) has higher BTV10 values. Additional DFT simulations suggested that the controlling factor for the CCs adsorption is the strong adsorbate-adsorbent interaction between the C=O groups of the CC molecules with the open metal centres and the amine functionality. Lighter CCs of FA and AA were preferably adsorbed by UiO-66 (Zr)-NH₂ because of the amino groups which covalently bonded to these CCs. On the other hand, MOF-199 (Cu) demonstrated favourable adsorption of heavier CCs given its open metal centres.

Chevalier et al. investigated the adsorption performance of HKUST-1 (Cu) with selected VOCs at low concentrations (Chevalier et al., 2019). VOCs of toluene, o-xylene, acetone, ethanol, and acetaldehyde were tested under several conditions including as a mono-pollutant, a multi-pollutant mode, under RH% of 0, 20, 40, and using three consecutive adsorption-desorption cycles. In mono-pollutant conditions, all pollutants were adsorbed in high quantities especially toluene with a maximum of 238 mg/g. As soon as the pollutant species were mixed in one dry gas stream (0% RH), toluene was poorly adsorbed and likewise for other pollutants. Each VOC's selectivity was said to be dependent on its steric selectivity with the HKUST-1 (Cu)'s side pockets and the Cu-O interactions. Further experiments with RH saw significant decreases in the MOF's adsorption capacities for the multi-component mixture, reaching close to 0% total capacity at 40% RH. In their reusability study, the total adsorption capacity of HKUST-1 (Cu) continued falling from the first to subsequent cycles. Thus, prompting the authors to

conclude that HKUST-1 (Cu) can only be adapted for removal of VOCs in dry air situation, an unrealistic practical environment.

Jafari et al. reported that different activation conditions for ZIF-8 (Zn) could impact its toluene vapor adsorption capacity (Jafari et al., 2018). They compared two conditioning environments, in air (300 °C) and in N₂ (300 °C and 400 °C). A thermal activation with inert gas N₂ seems to give temperature-dependent uptake improvement, with the ZIF-8 (Zn) activated from the higher temperature giving higher toluene adsorption capacity (with N₂ at 400 °C). However, the uptake capacity is still lower than the value obtained after activation in air at 300 °C (ZIF-8/air/300 °C). The strong oxidizing condition associated with air was claimed to be more favourable in the decomposition of trapped molecules in its cavities and pores unlike the more passive N₂-based activation process. Subsequent exposures to a range of humidities still affected ZIF-8 (Zn)'s toluene adsorption capacity, declining progressively as the humidity increases. Despite having a lipophilic 2-imidazole linker, the hydrophilic Zn metal sites in ZIF-8 (Zn) were identified as the main water adsorption sites.

Bahri et al. compared three different MOFs namely, MIL-101 (Cr), MIL-53 (Fe) and CPM-5 (In) to remove toluene vapor in dry and humid air (30% RH) (Bahri et al., 2017). By virtue of MIL-101's highest surface area and pore volume, it achieved the highest toluene and isobutanol adsorption capacity at 0% RH. Nevertheless, in the presence of 30% RH, MIL-101 (Cr) and CPM-5 (In) both experienced substantial reduction in their adsorption capacity due to high adsorbent polarity that favours water over the VOCs. MIL-53 (Fe) had a lower degree of reduction that was attributed to its flexible "breathing" framework. In the case of humidity exposure, it allowed the VOCs to still be adsorbed into the MIL-53 (Fe)'s empty pores. Although this ability appears beneficial, the maximum capacity of MIL-53 (Fe) is offset by about 3-fold lower surface area availability than MIL-101 (Cr). More detailed research is required to gain better control of the pore opening and closing response in MIL-53 (Fe).

Vellingiri et al. studied several MOFs which are UiO-66 (Zr), UiO-66 (Zr)-NH₂, MOF-199 (Cu) and ZIF-67 (Cr) in addition to 4Å zeolite to remove toluene vapor at atmospheric pressure (Vellingiri et al., 2017). In their study, they found that toluene capacity decreased with an

increase in temperature and RH. The rise in temperature from 293 K to 303 K also led to proportional decrease in Henry's constant, indicating loss of solute affinity for the adsorbent. When the adsorbents were tested for toluene adsorption at humid conditions (25% RH and 50% RH), UiO-66 (Zr) -NH₂ consistently showed the highest adsorption capacity, followed closely by ZIF-67. Vellingiri et al. also studied the cyclic adsorption-desorption of toluene at 99 ppm. In the experiments, UiO-66 (Zr)-NH₂ retained its adsorption capacity from the first cycle (147 mg/g) to the third cycle (139 mg/g) unlike both UiO-66 (Zr) and ZIF-67 (Cr) that lost 50% of their initial capacity by the end of the third cycle. Distinctively, the high performance shown by the NH₂-terminating UiO-66 (Zr) was claimed to have been contributed from its enhanced toluene physiochemical adsorption mechanisms; via H-bonding and π -complexation. However, there are issues in the thermal stability of the MOFs. UiO-66 (Zr)-NH₂ is unstable beyond 423 K while ZIF-67 (Cr) has a lower thermal stability of 373 K.

Yang et al. studied the removal of a series of VOCs using MOF-177 (Zn) (Yang et al., 2013). MOF-177 (Zn) showed higher preference to adsorb smaller VOCs, like benzene (800 mg/g) and acetone (589 mg/g). A negative linear relationship calculation that relates the volumetric adsorption capacity (Y-axis) and the molecular cross-sectional area (X-axis) showed that benzene, toluene, ethylbenzene, and xylene molecules could form stronger interactions with the MOFs primarily via π - π coupling, compared to acetone. In the presence of increasing humidity, MOF-177 (Zn)'s capacity sharply decreased between 0 to 50% RH, but lower reductions were observed above 50% RH. Specifically, it only experienced 35% capacity reduction from 0 to 90% RH. On the other hand, AC experienced 91% trichloroethylene capacity reduction when the humidity increased from 5 to 85%. This indirectly suggests that MOF-177 (Zn) has a good potential to remove VOCs at high humidity. However, further investigations on MOF-177 (Zn)'s water stability elucidated that it decomposed after a 3-day water immersion and 40% RH moisture contact thus, making it a less appealing adsorbent.

Table 2.6 combines the reports, which used native MOFs for humid adsorptive removal of airborne VOCs. By definition, humid conditions must involve an elevated level of water/RH alongside the VOC adsorption although some studies might not include discussions on the whole RH range (0 – 100%).

Table 2.6: Compilation of VOC capture reports at room temperature and in humid conditions using unmodified MOFs.

VOC	Adsorbent	Modification	VOC details and tested RH% range	Results				Reference
				RH%	q_c (mg/g)	BET surface area (m ² /g)	Pore volume (cm ³ /g)	
Benzene	MOF-199 (Cu)	None	50 ppm RH% (0, 20, 50, 80, 100)	0	101	N/S	N/S	(Liu, Younis & Kim, 2021)
				50	8			
				80	3			
	UiO-66 (Zr)-NH ₂			0	35	N/S	N/S	
				50	5			
				80	1			
Formaldehyde	MOF-5 (Zn)	None	14 ppm RH% (5)	5	4	424	0.22	(Vikrant <i>et al.</i> , 2020)
	MOF-199 (Cu)				3	1212	0.46	
	UiO-66 (Zr)				4	1210	0.73	
	UiO-66 (Zr)-NH ₂				24	963	0.58	
	AC				0	1004	0.71	
Toluene	HKUST-1 (Cu)	None	2.5 ppmv total or 1.25 ppmv each for a binary mixture RH% (0, 20, 40)	0	238	1122	0.47	(Chevalier <i>et al.</i> , 2019)
Acetone				40	0			
O-xylene				0	50			
				40	30			
Ethanol				0	147			
				40	0			
Acetaldehyde				0	165			
				40	0			
				0	14			
Toluene	ZIF-8/Air/300 °C	None.	1000 ppmv RH% (0, 40, 60, 80)	0	562	N/S	N/S	(Jafari <i>et al.</i> , 2018)
				40	411			
				60	354			
				80	203			
	ZIF-8 (Zn)			0	131			
Toluene	MIL-101 (Cr)	None	1 ppm RH% (0, 30)	0	2116	2728	0.289	(Bahri <i>et al.</i> , 2017)
				30	395			

	MIL-53 (Fe)			0	730	951	0.279		
				30	692				
	CPM-5 (In)			0	389	1140	0.284		
				30	40				
Iso-butanol	MIL-101 (Cr)	None		0	2060	2728	0.289		
				30	158				
	MIL-53 (Fe)			0	643	951	0.279		
				30	445				
	CPM-5 (In)			0	570	1140	0.284		
				30	20				
Toluene	UiO-66 (Zr)	None	0.0026 P/P ₀ RH% (0, 25, 50)	0	166	1414	0.68	(Vellingiri <i>et al.</i> , 2017)	
				25	157				
				50	66				
	UiO-66 (Zr)-NH ₂			0	252	1250	0.62		
				25	233				
				50	120				
	MOF-199 (Cu)			0	159	1237	0.47		
				25	151				
				50	32				
	ZIF-67 (Cr)			0	224	1401	1.22		
				25	185				
				50	63				
4 Å zeolite	0	31	N/S	N/S					
	25	38							
	50	10							
Toluene	MOF-177 (Zn)	None	N/S RH% (0, 30, 50, 70, 90)	0	290	2970	1.11	(Yang <i>et al.</i> , 2013)	
					30				240
					50				210
					70				~210
					90				189

4

⁴ Explanation of the used abbreviations in Table 2.6: q_c = maximum adsorption capacity or 100% breakthrough capacity, CPM = crystalline porous materials, N/S = not stated.

2.2.2.2 Synthetically modified MOFs as VOC adsorbents

Because of the performance deficiencies' shown by native MOFs in the presence of humidity, various types of modifications have been investigated to overcome this problem. These advancements will be described in this Section.

For example, ZIF-8 (Zn) belongs to the microporous MOF category that is widely studied for adsorptive applications. Li et al. experimented with different synthesis temperatures to produce an array of carbon frameworks derived from MOFs or termed henceforth as CF-T materials, where T is the carbonization temperature in °C (Li *et al.*, 2021). The adsorbents were first studied for dry toluene adsorption where the measured capacities follow the order of CF-1100 > CF-1000 > CF-1200 > CF-900 > CF-800 > ZIF-8. CF-1100 has the highest dry toluene uptake capacity (209 mg/g), followed by CF-1000 (180 mg/g), and ZIF-8 (6 mg/g) was the lowest. For treatments above 1100 °C, the dry toluene adsorption capacity started decreasing, making this temperature the optimum temperature. It seems like the higher carbonation temperature had significantly increased the adsorbents' dry toluene adsorption capacity. The authors attributed this improvement due to (1) the formation of hierarchical porous carbonaceous structure with newly generated narrower micropores (pore width 0.6 – 0.8 nm), mesopores above 10 nm and (2) higher degree of graphitization. Li et al. also found CF-1100 to have the highest dry toluene adsorption capacity compared to other carbonized MOFs such as MIL-101 (Fe) (8 mg/g), MIL-53 (Fe) (20 mg/g), UiO-66 (Zr) (45 mg/g) and ZIF-7 (Zn) (71 mg/g). At 75% RH, CF-1100 displayed outstanding humid performance, decreasing its capacity by only 10.4% relative to its 0% RH capacity. The breakthrough points for dry and wet toluene were also unchanged. Plus, the absence of roll up phenomenon when humidity was introduced could suggest its high toluene selectivity in humid conditions. This was further studied by running binary VOC species experiments involving toluene as the primary VOC alongside with cyclohexane and benzene. Here, both benzene and cyclohexane demonstrated roll-up phenomenon, confirming the preferential adsorption of toluene by CF-1100. When being reused for 3 cycles, it only experienced 84% capacity reduction in the 3rd cycle while the $t_{0.1}$ breakthrough times were nearly similar across the three cycles. Because CF-1100 showed excellent humidity resistance, toluene selectivity and reusability, it was further developed as a coating for a quartz crystal microbalance sensor. It exhibited very high sensitivity of 0.4004 Hz/ppm.

A novel post-synthetic modification strategy involving treatment of MIL-53 (Al) with alkyl phosphonic acids, creating MIL-53-Al@C_x (where x = carbon atoms of the PA) has been proposed by Shi et al. (Shi *et al.*, 2021). The grafted PA was hypothesized to have replaced the hydrophilic Al-OH sites on the original MIL-53 (Al), hence, reducing water interaction and increasing surface hydrophobicity. This view was supported from the 73% lower water adsorption capacity by MIL-53 (Al)@C₁₄ than the parent MOF (at a single fixed 75% RH). However, this presented data could be misleading as a quick comparison on each adsorbent's surface area suggests that this water capacity reduction might have been caused simply by a reduction in the MIL-53 (Al)@C₁₄'s surface area. Therefore, it is always advisable to report data from 0% RH to 100% RH to identify the adsorbents' water isotherm behaviour better. Nevertheless, compared to MIL-53 (Al), MIL-53 (Al)@C₁₄ appeared as a more hydrophobic and selective acetone adsorbent as it showed 39% and 103% higher capacity at 60% and 90% RH, respectively. Their regeneration datasets also affirmed the superiority of MIL-53 (Al)@C₁₄ as it remained stable after 10 adsorption-desorption cycles of acetone, losing minimal capacity of only 1 – 2 mg/g. The authors also claimed they have improved MIL-53 (Al)@C₁₄'s hydrophobicity for acetone removal. However, acetone is still a hydrophilic VOC (log K_{ow} = -0.24, more negative values indicate a more hydrophilic solvent). So, their claim would be more readily accepted if the treated MOF's performance remained higher than the pristine MIL-53 (Al) when adsorbing a more hydrophobic VOC.

To improve toluene vapor selectivity in humid air, Wang et al. chose to impregnate the pores of MIL-101 (Cr) with short-chained hydrophobic polyethylene glycol (PEG) (Wang *et al.*, 2021). The PEG/Cr³⁺ molar ratios (x) were varied accordingly (2.5, 5 and 10 moles%). The OH-groups of the PEG chains coordinated well with the Cr sites of MIL-101. Increased PEG loadings (5 mole %) was accompanied with a slight reduction in the pristine material's surface area as well as particle size. Uniquely, the PEG incorporation established a new isolate pore at 11.2 Å inside the modified MIL-101 (Cr). Through Grand Canonical Monte Carlo and molecular dynamics simulations, they observed that the PEG chains restricted the diffusion of water. The results agreed well with the materials' water adsorption isotherms, where the PEG₅@MIL-101 (Cr) showed 53.7% lower capacity than the pure MIL-101 (Cr) at 50% RH.

The crux of the work by Wang et al. is in the PEG₅@MIL-101 (Cr)'s 3.3 times higher toluene working capacity (Q_w) at high humidity (80% RH) compared to MIL-101 (Cr). The Q_w/Q_e ratio can reflect the utilization rate of the adsorbents, with higher values indicating there are more available adsorption sites for toluene. The Q_w/Q_e of the pristine MIL-101 (Cr) decreased with increasing RH, a sign of impeded toluene adsorption due to its natural hydrophilicity. On the contrary, the Q_w/Q_e values for PEG₅@MIL-101 (Cr) increased with increasing RH. The hydrophobic PEG chains prevented the entry and diffusion of water vapours and facilitated the diffusion rate of toluene into the pores. Based on these results, this form of composites could be a potential adsorbent for VOC abatement in humid conditions.

Pei et al. studied a series of MIL-100 (Fe) materials calcined at high temperatures (M-T where $T = 300, 350$ and 400 °C) for the removal of oxygenated VOCs; methanol, formaldehyde and acetone (Pei *et al.*, 2021). In their report, M-350 displayed superior adsorption performance to MIL-100 (Fe), having the longest breakthrough time and the highest adsorption capacities of 260 mg/g methanol, 18 mg/g formaldehyde and 197 mg/g acetone. An extra adsorption experiment involving propylene was performed since it has a similar molecular size to these oxygenated VOCs. However, there was no substantial difference in the adsorptive performance of MIL-100 (Fe) and M-350, indicating that pore size has little effect on its adsorption capacity. Under the influence of different relative humidities (0 to 70% RH), the methanol adsorption capacity for both MIL-100 (Fe) and M-350 decreased significantly, but M-350 maintained higher adsorbate uptakes than the MIL-100 (Fe). It was concluded that M-350 showed favourable adsorption capacity towards methanol or oxygenated VOCs in general due to several reasons. Firstly, the metal sites in the MOF played a pivotal role in adsorbing methanol. When calcined at 350 °C and after acid washing, the number of Fe coordinatively unsaturated sites increases, which concurrently acts as Lewis acid sites. Eventually, they can bind through strong acid-base interaction with the oxygen-containing groups or the Lewis bases on the oxygenated VOCs. Secondly, the higher capacity shown by M-350 was attributed from the creation of new hierarchical micro pores post-calcination, which increases its surface area by 22% than MIL-100 (Fe). Thirdly, the carbonization caused higher carbon content which helped lowered the M-350's hydrophilicity, indicated by its 2.2 times higher water contact angle than MIL-100 (Fe). At the same time, this improved hydrophobicity in M-350 would inhibit the presence of water molecules and increase methanol selectivity into its pores.

Khoshakhlagh et al. showed that via the simple addition of MIL-101 (Fe) precursors to oxidized AC (OAC), a series of MIL-101 (Fe)/OAC composites could be synthesized (Khoshakhlagh *et al.*, 2020). At the default test humidity of 30% RH, MIL-101 (Fe)/OAC adsorbed 127 mg/g: 1.3 and 2.3 times higher than MIL-101 (Fe) and OAC, respectively. Despite its lower surface area, higher toluene was adsorbed due to greater mesopore formation in the composite. The added OAC also helped to decrease the crystal agglomeration of MIL-101 (Fe), simultaneously providing more active sites to adsorb toluene. Nevertheless, at 50% and 80% RH respectively, the adsorption capacity of the composite still reduced by 8% and 20% compared to that at 30% RH. The breakthrough time also decreased, showing that the composite's hydrophobicity was not improved that much.

SION-82 (Sr) is a novel hydrophobic MOF reported by Sudan et al. which is composed of pyrene-based linker and Sr metal cores with an even pyrene spacing of 6.86 Å (Sudan *et al.*, 2020). They proposed that this MOF could be used to capture small hazardous aromatic molecules like benzene, pyridine and thiophene. The SION-82's dry equilibrium uptakes of these molecules were found at 107 mg/g, 140 mg/g and 160 mg/g respectively. Binding energy calculations found that benzene has the highest value of this set. Furthermore, upon activation (solvent exchange with CHCl₃ followed by vacuum outgassing at 85 °C for 12 hrs, hereafter termed as SION-82'), the Sr atoms still retained the coordinated water molecules. This led the authors to believe the unaltered water occupation on the open Sr metal sites and the ligand hydrophobicity will help to maintain the ability to capture aromatics even at a high relative humidity. Indeed, it was found that the amount of benzene adsorbed in the presence or absence of water vapor for SION-82' were very similar. Figure 2.8a shows the water vapor uptake capacity of SION-82' and three other studied MOFs: MOF-74 (Co), HKUST-1 (Cu), UiO-66 (Zr). Based on these MOFs' water adsorption isotherm trends and excluding the differences in the intrinsic properties of the MOFs that could influence the maximum uptake values, SION-82' showed the lowest affinity towards water. Arguably, because of its lower surface area, it has a lower and slower uptake of benzene. However, in the 6-cycle humidified benzene uptake study shown in Figure 2.8b, even though MOF-74 (Co) and HKUST-1 (Cu) showed higher uptake values than SION-82', their values dropped considerably to 93 and 98 mg/g in the sixth cycle. UiO-66 (Zr) also experienced a slight reduction from 127 mg/g (dry) to 106 – 112 mg/g (humid). SION-82' on the contrary, displayed a constant adsorption performance across the 6 cycles. Because of its high-water stability (the Sr metal sites that are already occupied with

water), SION-82' shows superior benzene capture under high humidity and even after being used and recycled multiple times, it did not experience any diminishing capacity.

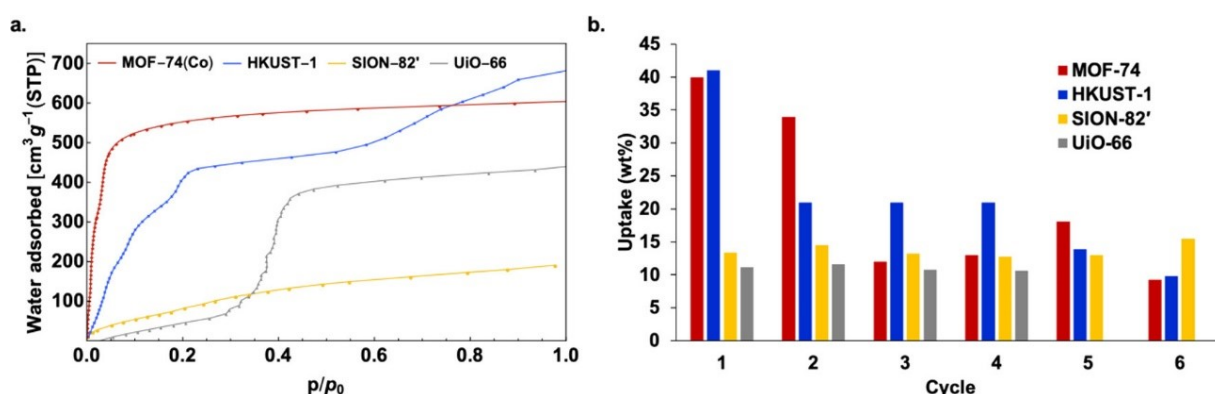


Figure 2.8: (a) Water adsorption isotherms measured at 298 K for MOF-74 (Co) (red), HKUST-1 (Cu) (blue), UiO-66 (Zr) (grey) and SION-82 (Sr)' (yellow) and (b) recyclability of benzene capture under humid atmosphere for the same adsorbents. Reproduced with permission from (Sudan *et al.*, 2020). Copyright 2020, ACS Publications.

When it comes to choosing the right adsorbents for humid VOC capture, their practical and physical structures are as equally important as their hydrophobicity. In this regard, an accelerated heating synthetic route was conceived by Zheng *et al.* to prepare a hydrophobic metal organic gel, denoted as CAU-3 (gel) with hierarchical micro/meso-porosity (Zheng *et al.*, 2020a). It has good water and thermal stability, high surface area, high hydrophobicity, and excellent removal performance of toluene, hexanal and p-xylene. Compared to commercial BPL AC, CAU-3 (gel) showed higher hexanal adsorption capacity under dry conditions, having longer breakthrough times. When tested at humid ambient conditions of 298 K and 50% RH, the CAU-3 (gel) demonstrated higher capacity when adsorbing 175 ppm hexanal than AC. It also exhibited the highest recorded capacity among other well-known adsorbents including zeolite 13X, MIL-101 (Cr), HKUST-1 (Cu), ZIF-8 (Zn), and UiO-66 (Zr). The self-assembly gelation process introduced defects which created more adsorption sites and helped created the highest surface area among many other metal organic gels so far. The CAU-3 (gel) can also be easily coated on a nonwoven fibre by a simple dip coating method without using extra binder (Figure 2.9). Additionally, it displayed an outstanding hexanal removal performance and easy reusability protocol using low temperatures (358 K) compared to AC filters. Moreover, after twice regeneration, the adsorption performance was similar, unlike AC which needs a higher temperature and a longer time to desorb the hexanal from its disordered micropore structure.

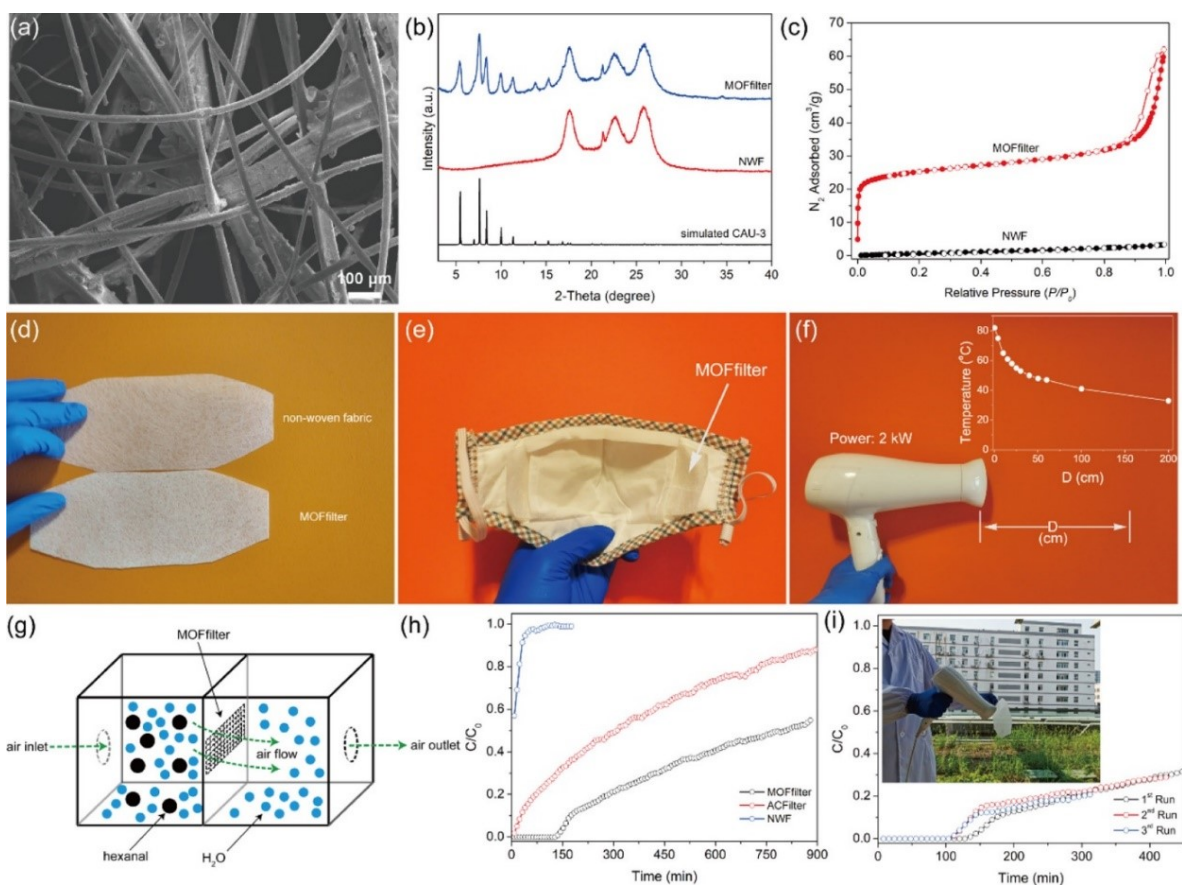


Figure 2.9: (a) SEM image of the MOF filter, (b) XRD spectra of simulated CAU-3, MOF filter and NWF, (c) N₂ adsorption-desorption plots of the MOF filter and NWF at 77 K, (d) image of NWF and MOF filter, (e) image showing the encapsulation of MOF particles into a face mask, (f) photograph of a household hair dryer (with the inset displaying the relationship between the outlet temperature and the distance), (g) schematic of the bespoke adsorption breakthrough experimental setup, (h) breakthrough curves of 2 ppm hexanal of the filters at 298 K and 50% RH, (i) breakthrough curves of 2 ppm hexanal of the MOF filter under 50% RH and after three regeneration cycles (adsorption and desorption temperatures are 298 K and 358 K respectively) whereas the inset shows the regeneration procedure using a hair dryer. Reproduced with permission from (Zheng *et al.*, 2020a). Copyright 2020, ACS Publications.

Another proven method to control a MOF's surface hydrophobicity is by introducing alkyl, aryl, or fluorinated groups onto the surface. The grafting of low-surface energy chemicals such as calixarenes by Jeong *et al.* has delivered great potential when they transformed a hydrophilic UiO-66 (Zr) into an oleophilic state for the purpose of increasing the MOF's colloidal stability as displayed in Figure 2.10. Counterintuitively, such inclusion is also expected to improve the adsorption rate of aromatic VOCs, but data from the current literature remains scarce.

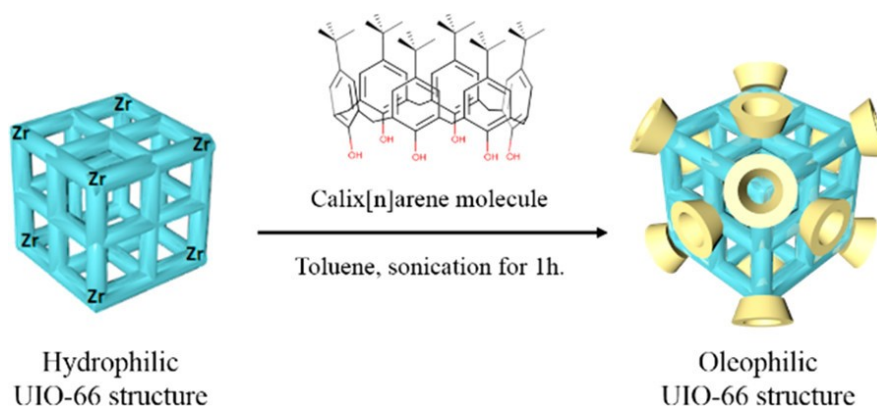


Figure 2.10: Attachment of calixarene molecules onto UiO-66 (Zr) framework to improve its oleophilicity. Figure from (Jeong *et al.*, 2019) with permission. Copyright 2019, ACS Publications.

Hydrophobic surface functionalization has alternatively been achieved with evaporation/coating method of several polymers including oligomeric silsesquioxane (Sanil *et al.*, 2015), triblock copolymer (Pluronic P-123) (Fernandez *et al.*, 2015), dimethylbenzimidazole (Liu *et al.*, 2013) and silanes/silicones. Generally, silanes and silicones are the most frequently used chemicals due to their super hydrophobic properties (Li *et al.*, 2016a). For instance, polydimethylsiloxane (PDMS) is a hydrophobic, silicon-based polymer that prevents liquids, but permits gases to diffuse through the surfaces (Thurgood *et al.*, 2017). With its excellent hydrophobicity, gas phase selectivity, and low cost, the commercial PDMS is emerging as a promising coating material in enhancing a MOF's hydrophobicity.

To date, research efforts have been focused on synthesizing MOF-PDMS composites, though not for VOC capture applications (Zhang *et al.*, 2014b; Huang *et al.*, 2016; Xu & Yan, 2016; Kang *et al.*, 2019; He *et al.*, 2020). Competitive benzene-moisture adsorption data is also available for activated carbon (AC)-PDMS composites and encouraging data was shown, but specific water sorption isotherms were not reported (Li *et al.*, 2020c). These data are necessary to evaluate the differences between the adsorbent's single and multi-component adsorption behaviour. Also, the authors used an unrealistic benzene concentration at > 1400 ppm. The United States' Occupational Safety and Health Administration (OSHA) has set a permissible exposure limit of 1 ppm for benzene in the workplace during an 8-hour workday, 40-hour workweek, and the UK has the same exposure limit (United States Department of Labor, 2021a).

Still in the same theme of VOC adsorption by AC, Liu et al. used environmentally relevant benzene concentration of 8 ppm (Liu, Yang & Xue, 2016). They also extensively compared two key aspects of their PDMS-coated ACs, namely in terms of the influence of the materials' hydrophobicity and their total micropore volume towards humid benzene adsorption (Figure 2.11). The pristine granular AC was heated with PDMS within a temperature range between 80 °C and 250 °C. A higher heating temperature positively correlates with a higher water contact angle. The hydrophobicity of the PDMS-coated ACs was defined from their high water contact angles and low amount of acidic functional groups. At 0% RH, all materials showed high benzene adsorption capacity due to their high hydrophobicity. At 50% RH, the benzene vapor adsorption capacities for PDMS/AC-150 (56 mg/g) and PDMS/AC-250 (9 mg/g) were far lower than the bare AC (84 mg/g) due to pore blockage. However, at 90% RH, both PDMS/AC-150 (320 mg/g) and PDMS/AC-250 (319 mg/g) displayed significantly higher benzene uptake than the bare AC (166 mg/g), further affirming its better benzene selectivity in humid environments after being coated with PDMS.

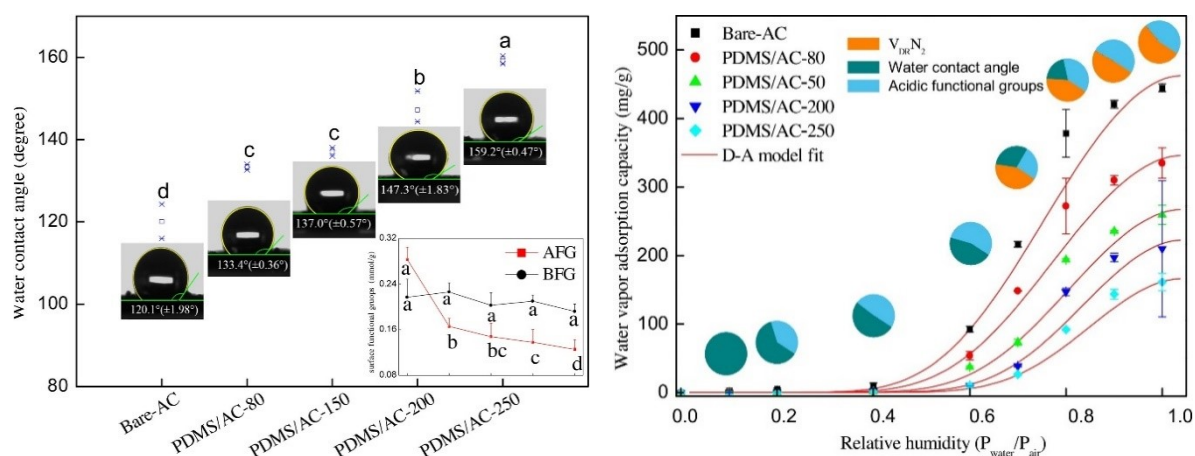


Figure 2.11: (Left) Measured water contact angle, acidic (AFG) and basic (BFG) functional groups of original AC and after a series of PDMS coating temperatures. (Right) The influence of total micropore volume, water contact angle and AFG towards the adsorbents' water vapour adsorption capacity. Reprinted with permission from (Liu, Yang & Xue, 2016). Copyright 2016, Elsevier.

Zheng et al. have recently carried out external surface modification on CAU-1 (Al) MOF using PDMS coating preceded with an anhydride-modification protocol (Figure 2.12), and later used this material to adsorb trace toluene in humid air (Zheng *et al.*, 2020b). Increasing the PDMS evaporation time resulted to a continuous decrease of specific surface area and pore volume in the studied materials, but surprisingly, they were not too significant. Two effective experimental practices were identified in this study. The injection of N₂ into the coating chamber which purged all residual O₂ before starting the reaction may have minimized the possibilities of side polymerization reactions that can cause severe unintended pore blockage. Secondly, the reaction between the anhydride with the amino group of the CAU-1 (Al) may have already formed hydrophobic functional groups inside the pores, so, only a minor portion of PDMS could be coated subsequently. Both the anhydride functionalization and the PDMS coating successively increased the treated CAU-1 (Al)'s water contact angles to a maximum of 140° – 150°. When all samples were tested for water adsorption, the best MOF was found to be p_{0.5}-CAU-1 (Al)-vale as it exhibited improved moisture resistance and showing only 1/5th of the original CAU-1 (Al)'s capacity below 50% RH. In their toluene breakthrough experiments at 50% RH nine other adsorbents were compared. It also turns out that p_{0.5}-CAU-1 (Al)-vale had the highest adsorption capacity (6.82 mg/g) for 1 ppm toluene, followed closely by ZSM-5 (6.26 mg/g). Despite the latter's lower surface area, its corresponding hydrophobicity has helped to overcome competitive adsorption in comparison to most MOFs, albeit them having higher surface area. Because most MOFs are hydrophilic, preferential water adsorption will eventually be apparent in their lower VOC adsorption capacities. Note that although they tested ZIF-8 (Zn), which is hydrophobic, its constricted pore window, being smaller than the toluene molecule makes the diffusion into its pores very difficult. The only missing piece of data within this useful report is data on AC as the reference VOC adsorbent.

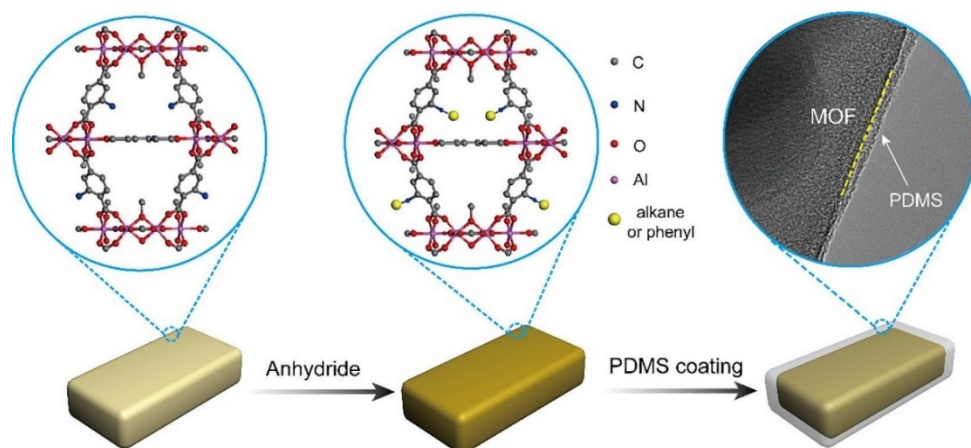


Figure 2.12: A schematic illustrating the sequential amide reaction and PDMS vapour coating on CAU-1 (Al) Reproduced with permission from (Zheng et al., 2020b). Copyright 2020, Elsevier.

Besides MOFs, silica has been extensively investigated as a prospective adsorbent for humid VOC removal too. For example, Liu et al. initially prepared mesoporous silica KIT-6 using tetraethoxysilane (TEOS) as a silica source (Liu *et al.*, 2018). In most studies that seek to improve silica's adsorption capacity, the base silica is normally surface functionalized with phenyl/methyl groups via chemical grafting. These treated silicas can sometimes display higher adsorption capacity, but not always, as significant pore steric hindrance from the added functionality may result. In this study, Li et al. opted for a single-step co-condensation method to introduce phenyl functionality (phenyltriethoxysilane or PTES) onto KIT-6. The modified KIT-6 samples (labels are affixed with their molar ratio of PTES to TEOS) all displayed consistent decreases in surface area, pore volume and pore diameter at higher PTES/TEOS ratio. These reductions were inferred due to the varying insertion degrees of organic TEOS into the samples' pores. Higher phenyl contents also resulted to a disruptive loss of mesoporosity as the phenyl-modified KIT-6 displayed smaller hysteresis loops than the untreated KIT-6. Data from their dry toluene adsorption tests show that all the phenyl-modified mesoporous silica KIT-6 maintained high toluene adsorption capacity resembling that of the pure KIT-6, although their porosities were variables. When these results are expressed in $Q_{\text{dry}}/\text{surface area}$, the order of increasing dry toluene uptake capacity is as follows: 1:6 (KIT-6) > 1:12 (KIT-6) > 1:18 (KIT-6) > 1:36 (KIT-6) > pure KIT-6. This order directly implies that the higher quantity of phenyl functional group is beneficial in increasing the dry toluene adsorption capacity of KIT-6.

All studied samples by Li et al. were subsequently tested for adsorption at 60% RH, 1000 ppmv of toluene at 25 °C. It was noted that for a 1 PTES:6 TEOS ratio in KIT-6, its $Q_{\text{wet}}/Q_{\text{dry}}$ substantially increased (78%) compared to the pristine KIT-6 (16%), indicating higher toluene and lower water affinity within the 1:6 (KIT-6) after phenyl functionalization. Overall, these findings have highlighted the success of phenyl surface functionalization in improving both an adsorbent's aromatic toluene selectivity and capacity. Though it is noted that the 1000 ppmv toluene concentration used for this study needs to be lowered to a more realistic concentration to make it closer to real world exposure conditions.

Zeolites could also potentially be used in conjunction with MOFs to form MOF composites. Li et al. prepared some Cu-BTC and ZSM-5 composites CZ_x, where x refers to the ZSM-5 wt% content, through the conventional hydrothermal method to produce a composite for adsorbing toluene in a moist ambience (Li *et al.*, 2020b). The hydrophobicity of the added ZSM-5 molecular sieves was postulated to enhance the composite's selectivity towards VOCs whilst reducing competition between the VOCs and water vapor. The Cu-BTC MOF was chosen based on its high surface area and low pore volume that can accommodate small VOC molecules. With a 5 wt% ZSM content, CZ5% showed 2.5 times higher adsorption capacity than Cu-BTC at 30% RH. Based on this result, the authors attributed this enhanced composite performance to the synergistic effects of enhanced hydrophobicity and higher resultant surface area. Nevertheless, the composite's performance was still inhibited by higher humidity levels, having its capacity reduced by 18% at 80% RH, and similarly poor in the reusability test, decreasing by 20% after six cycles.

By using polyvinylpyrrolidone (PVP) as a structure-directing agent, Zhang et al. modified UiO-66 (Zr) using a simple solvothermal method, creating PVP-U-x composites where x is the PVP/Zr⁴⁺ molar ratio (Zhang *et al.*, 2019a). The introduction of PVP (x = 0.1 to 1) during the synthesis stage slightly reduced the original BET surface area of pristine UiO-66 (Zr) as it affected the original self-assembly process between the organic ligand and the metal ions. No significant morphological change was detected except that the pores became more regular and uniform. In terms of their dry breakthrough performance, higher x values up to 0.5 (adsorbent label is PVP-U-0.5) directly improved the breakthrough time and the adsorption capacity.

However, as soon as humidity was accounted in the experiments by Zhang et al., all materials experienced a substantial decline in their toluene co-adsorption capacities due to their intrinsic hydrophilicity. Surprisingly, even though the surface area of PVP-U-0.5 is lower than its untreated version, it consistently showed higher competitive adsorption capacities. Given its lower water desorption activation energy (11.5 kJ/mol) than the pristine UiO-66 (Zr) (19.9 kJ/mol), the authors endorsed this as a sign of improved hydrophobicity by the PVP-U-0.5 sample. However, if the authors had included their water isotherm plots, it would enable a clearer evaluation of the corresponding materials' state of hydrophobicity.

In the same year, Zhang et al. once again applied the same structure-templating technique on UiO-66 (Zr), this time using non-ionic surfactant P123 (Zhang *et al.*, 2019c). As expected, the addition of P123 into the synthesis solution reduced the original microporous UiO-66 (Zr)'s specific surface area and it formed a mixture of micro and meso pores in the new UiO-66 (Zr) composites. The highest meso-microporosity proportion was found on the sample made with 0.2 P123/Zr⁴⁺ molar ratio (P-U-0.2). Their adsorption results proved that toluene was mainly adsorbed in the micropores, but due to UiO-66 (Zr)'s narrow pores, the adsorbate transportation is rather restricted. Defects created during the modified synthesis resulted in the formation of larger pores which increased the molecular diffusion rate, allowing toluene to penetrate further. This feature is evident in their regeneration study where the P-U-0.2 sample still has higher adsorption capacity than the pure UiO-66 (Zr). However, the drawback of having large pores is the weakened toluene-MOF attraction, given P-U-0.2's lower toluene desorption activation energy value (26.5 kJ/mol) compared to the UiO-66 (Zr) parent (30.2 kJ/mol) in the same adsorption conditions.

This group have been working on the same research theme as seen in four closely related publications. In this third of four reports in this series, Zhang et al. demonstrated that the presence of cetyltrimethylammonium bromide (CTAB) (CTAB/Zr⁴⁺ = 0.3 – 1) in the initial synthesis solution influenced the self-assembly process, reducing the original UiO-66's porosity (Zhang *et al.*, 2019d). The highest meso-microporosity ratio was obtained when adding 0.5 CTAB/Zr⁴⁺ (CTAB-U-0.5) which also formed slightly larger and more agglomerated spherical crystals. Interestingly, based on the SEM images acquired after toluene adsorption, the CTAB-U-0.5 particles evolved a distorted morphology before adsorption,

suggesting that the adsorbed toluene played a role in this morphology evolution. No further justification was provided by Zhang et al. though. The quantities of toluene captured by UiO-66 (Zr) and CTAB-U-0.5 declined significantly when humidity level increases, but as previously explained, the defective sites contributed to the nominally higher adsorption capacity than the former even at 70% RH. Calculations on their respective toluene desorption activation energy also seemingly indicate that CTAB-U-0.5 has stronger physical interaction with the adsorbed toluene. It has a slightly higher desorption activation energy (33.2 kJ/mol) than the pristine UiO-66 (Zr) (30.2 kJ/mol).

Also using CTAB, Shi et al. found that an appropriate CTAB concentration (0.5 CTAB/Zr⁴⁺ molar ratio) can form defects in UiO-66 (Zr)-NH₂ framework that led to more adsorption sites and 1.4 times higher surface area than the original UiO-66 (Zr)-NH₂ (Shi *et al.*, 2020). However, the defects in CTAB-U-N-0.5 caused an 88% capacity drop when the adsorption temperature increased from 298 to 348 K due to its lower thermal stability, compared to the parent MOF that lost 83%. When the humidity was increased to 80% RH, the uptake quantities by UiO-66 (Zr)-NH₂ and CTAB-U-N-0.5 reduced by 67 and 57% respectively. The authors claimed this to be due to the presence of CTAB that sterically hindered water molecules from being adsorbed. Their DFT calculations also indicate that the amino functional group contributed to the toluene adsorption by UiO-66 (Zr)-NH₂, combined with the synergistic effects of π - π , OH-CH₃, and OH- π bonds. The primary driving force in the adsorption was identified as the OH- π interactions.

The next article published by the prolific Zhang group involves the addition of MOF-5 (Zn) as a structural modifier for UiO-66 (Zr) (Zhang *et al.*, 2019b). When the Zr⁴⁺/MOF-5 molar ratio is at 0.01, the M-U-0.01 had the highest dry toluene adsorption capacity, more than the remaining defective MOFs, specifically 1.7 times higher than the pristine UiO-66 (Zr). Higher humidity and temperature further led to reductions of capacity due to lower π - π complexation with the defective sites. In a high humidity of 70% RH, M-U-0.01 still prevailed with higher capacity than UiO-66 (Zr), suggesting that the missing-linker defects helped to improve the adsorption performance. Just like before, the defects also caused lower thermal stability which is evident from M-U-0.01's higher capacity loss, 20% from the first cycle to the fifth cycle. The pristine UiO-66 (Zr) was more stable, losing only 4%.

Chu et al. proposed that the incorporation of sheet-shaped graphene oxide particles could improve the adsorption capacity of MOFs like ZIF-8 (Zn) (Chu *et al.*, 2018). This motivated them to prepare ZG-X composites (X refers to the weight percentage of the graphene oxide) for removal of toluene in humid environments. The ZIF-8 (Zn) particles were left to grow in situ on the added graphene oxide sheets, whilst the graphene oxide indirectly functioned as a structural directing agent. Interestingly, adsorption experiments at 55% RH (default tested humidity level) using ZG-4 demonstrated 19% higher and the highest toluene uptake quantity (116 mg/g) compared to the pure ZIF-8 (Zn) (97 mg/g). It showed consistently higher capacity than ZIF-8 (Zn) too for 5 regeneration cycles. Even at 80% RH, the reduction by ZG-4 is quite minor at only 11%. Although it has a 20% lower surface area than ZIF-8 (Zn), the authors believed this unusually higher uptake is due to the synergistic effects between the ZIF-8 (Zn) and the graphene oxide. The incorporated graphene oxide helped increased toluene affinity via π - π interactions stemming from both of their structures which contain benzene rings. In general, the ZG composites (up to 4 wt%) also showed longer breakthrough time, hence, indicating better adsorption performance. Thereafter, any increase in graphene oxide content further decreased the breakthrough time.

The construction of MOFs using normal long linear ligands often give large cavities which may not be favourable for capture of small molecules like VOCs. To solve this problem, Xie et al. suggested replacing the linear with angular ligands that contain uncoordinated aromatic bridging backbones (Xie *et al.*, 2018). In their report, two new highly stable MOFs were synthesized, named BUT-66 (Zr) and BUT-67 (Zr) using long, angular ligands to form small hydrophobic pores within the MOFs' structures (Figure 2.13). Their surface hydrophobicity was measured using water contact angles, resulting in 142.8° and 137.9°, respectively. Their water adsorption isotherms also indicate that the interior pore surfaces of both MOFs are moderately hydrophobic. Two adsorption temperatures were investigated, at 25 °C and at 80 °C, where the latter is meant to simulate using the MOF to capture harmful VOCs from a hot gas flow like in vehicle exhaust emissions. At low pressure (0.012 kPa) and at room temperature (25 °C), BUT-66 (Zr) demonstrated remarkably higher benzene adsorption capacity compared to other benchmark materials, including MCM-41, MIL-101 (Cr), ZIF-8 (Zn), PAF-1 and Carboxen 1000. It is important to mention that among all the studied adsorbents, only BUT-66 (Zr) and Carboxen 1000 showed an abrupt increase at low pressure.

BUT-66 (Zr) also performed excellently at low pressure (0.12 kPa) and at 80 °C. The superior performance of BUT-66 was more apparent when it was shown capable of adsorbing unchanged dry benzene quantity at moderate humidity (50% RH). Even when the humidity was increased to 80% RH, BUT-66 (Zr) still reached 70% of its dry capacity. The authors emphasized that its high performance for removal of aromatic VOCs is influenced by its small hydrophobic pores and sites as well as the rigid framework containing rotatable phenyl rings.

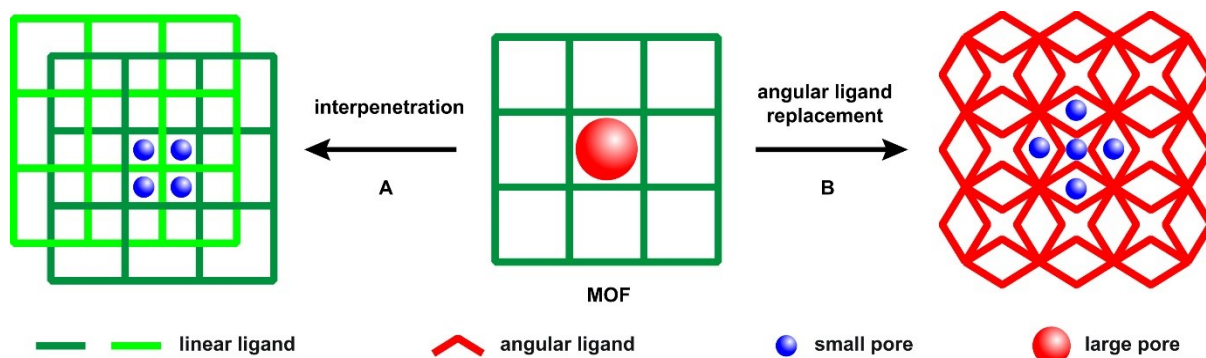


Figure 2.13: Two constructive approaches to build MOFs with constrained pores either (A) by network interpenetration with conventional linear ligands or (B) by substituting the linear types with angular ligands. Reprinted with permission from (Xie *et al.*, 2018). Copyright 2018, Elsevier.

Manipulation of the ligand mixing ratio is another method to obtain the maximum possible pore and cage sizes in a MOF synthesis. Yang *et al.* made a series of 15 new ZIFs (Zn) from a combination of various small and large various imidazolate linkers (Yang *et al.*, 2017a). Among the synthesized ZIFs, ZIF-412 (Zn) was found to possess the largest cage size (45.8 Å) and a very large aperture size (8.2 Å). Such porosity, together with its hydrophobicity, was expected to display exceptional separation of large-sized VOCs including aliphatic (octane) and aromatic VOCs (*p*-xylene) in the presence of water. Indeed, under dry conditions, the octane, and the *p*-xylene capacities for ZIF-412 (Zn) were 2.6 and 2.5 times higher compared to BPL activated carbon, respectively. The ZIF-412 (Zn)'s octane uptake was unaltered for 65% RH conditions and continued over three continuous cycles as displayed in Figure 2.14. ZIF-412 (Zn) performed similarly for *p*-xylene adsorption. Through this work, the authors proved that by using a mixture of linkers classed according to their steric index (defined by the linker's shape and size), it is possible to create MOFs with permanent porosity, expanded pore openings and internal pore size as well as giving the MOFs high hydrophobicity.

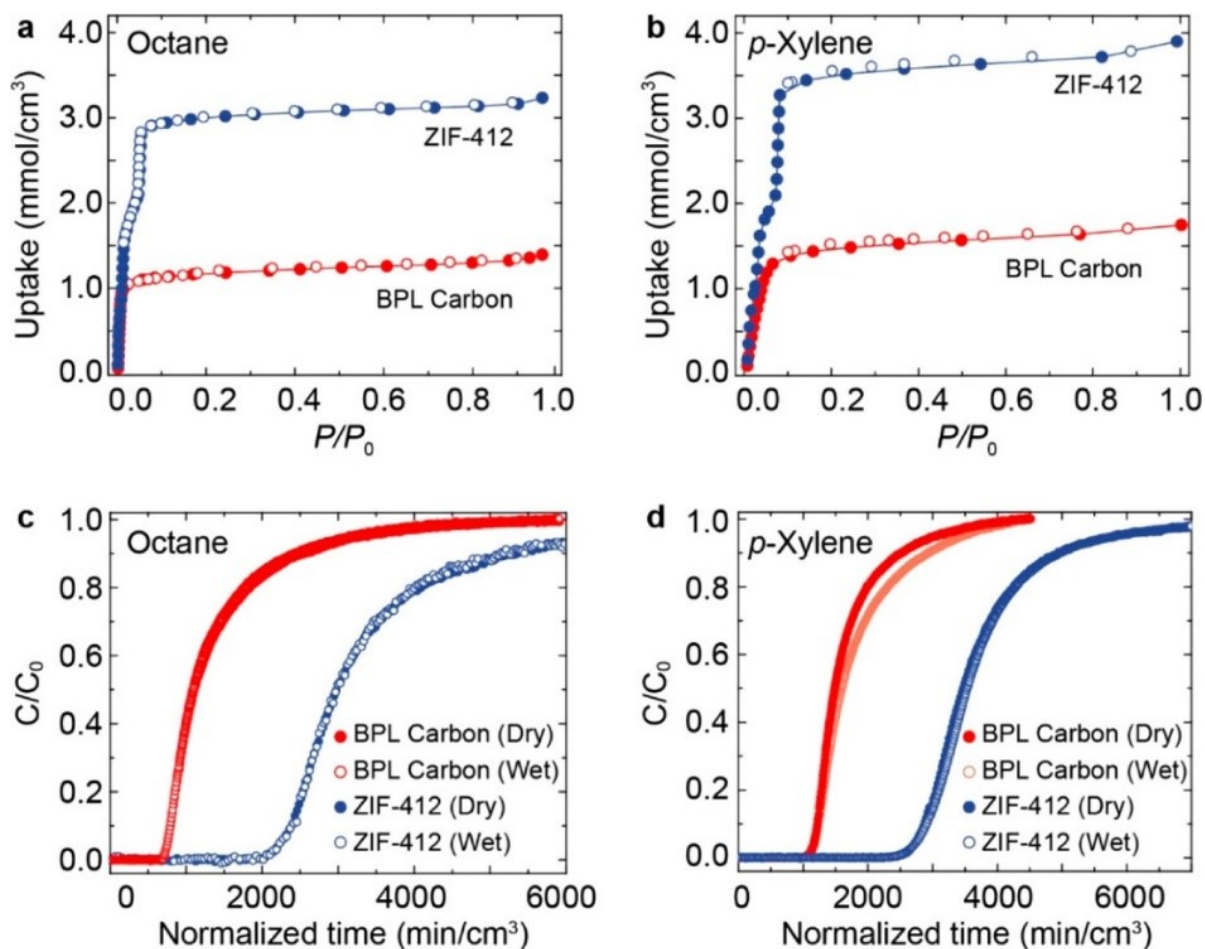


Figure 2.14: The removal performance of octane and *p*-xylene by ZIF-412 (Zn) and BPL carbon at 298 K. (a) Static octane vapor adsorption isotherm where ZIF-412 shows 260% higher uptake than BPL carbon, (b) static *p*-xylene vapor adsorption isotherm with 250% higher uptake by ZIF-412 (Zn) than BPL carbon, (c) breakthrough curves for octane in both dry (0% RH) and wet (65% RH) conditions, (d) breakthrough curves for *p*-xylene. Solid and empty circles in the breakthrough curves refer to adsorption and desorption points respectively. Reprinted with permission (Yang *et al.*, 2017a) Copyright 2017, ACS.

The most straightforward way of transforming a hydrophilic MOF into a hydrophobic one is by an appropriate ligand substitution. Zhu *et al.* used 1,4-naphthalene dicarboxylic acid as the ligand to synthesize MIL-101 (Cr) which eventually enhanced the hydrophobicity of the resultant MIL-Cr (Z1) (Zhu *et al.*, 2017). The novel MOF performance was systemically investigated through competitive adsorption between benzene and water. MIL-Cr (Z1) possessed smaller pore size openings (6.9 Å and 23 Å) than those of pristine MIL-101 (Cr) (12 Å and 16 Å micropore cages, as well as mesoporous cages are at 29 Å and 34 Å) mainly due to the naphthalene group that slightly occupied the pore space. The water vapor uptake (80% RH) by MIL-Cr (Z1) was remarkably only 13% lower from its original form. A single species

adsorption experiment of benzene at low pressure (1 kPa) indicates that the benzene diffused 30 – 40 times faster than water under similar conditions. This shows that the hydrophobic surface of MIL-Cr (Z1) helped increased diffusion resistance for water, needing much longer time to reach equilibrium than benzene. In a relatively dry atmosphere of 5% RH, the working capacity (Q_w or 95% breakthrough capacity) of MIL-Cr (Z1) was slightly lower than MIL-101 (Cr) due to its lower surface area. However, with increased humidity, it began showing higher Q_w values than MIL-101 (Cr). It is noteworthy to mention that the ratio of Q_w of MIL-Cr (Z1) to MIL-101 also increased proportionately with higher humidity. The calculated water desorption activation energy for MIL-Cr (Z1) was only 16.5 kJ/mol, while MIL-101 (Cr)'s value is 76.5 kJ/mol: a substantial difference. These findings further affirmed MIL-Cr (Z1) enhanced hydrophobicity and higher benzene selectivity.

Along the same approach, Padial and her co-workers capitalized on the enhanced stability of mixed pyrazolate/carboxylate linkers (L1 – L5) when combined with Ni^{2+} metal cluster, yielding a series of highly porous iso-reticular MOFs $[Ni_8(L)_6]$ (Padial *et al.*, 2013). Their N_2 adsorption data indicates the longer the linker, the higher the porosity. Notably, all materials showed type I isotherms, indicative of microporous crystalline solids except $Ni_8(L5)_6$ which features some 2.4 nm wide mesopores. The water stability of the materials was tested by soaking them in water for 24 hrs. Each material displayed minor changes in their XRD patterns. In terms of their water vapor adsorption isotherms, the partial pressures that marked the beginning of water vapor condensation into the porous frameworks increased proportionately from L1 to L5 with the highest shown by a fluoro-functionalized $Ni_8(L5)_6$ $[Ni_8(L5-CF_3)_6]$ at $P/P_0 > 0.8$, suggesting an increasing framework hydrophobicity trend. The functionalization with a fluorinated moiety yielded higher hydrophobicity than with CH_3 too ($P/P_0 > 0.65$).

The synthesized materials by Padiál et al. were later tested for the capture of diethylsulfide (DES), a simulant for mustard, under dry and humid conditions. Under dry conditions, all tested materials presented comparable capacity and kinetics to a commercial Blücher-10408 AC. However, in the case of a moist atmosphere, the AC still adsorbed significant quantity of water whereas $[\text{Ni}_8(\text{L5-CF}_3)_6]$ did not, proving its highly hydrophobic nature. Although the AC has slightly higher heat of adsorption and Henry's constant values, the values by the $[\text{Ni}_8(\text{L5-CF}_3)_6]$ are closely trailing behind, suggesting they both have similar hydrophobicity. In conclusion, this work rightly showcases the merit of using a fluoro-based linker to improve a MOF's hydrophobicity and adsorptive performance from highly competitive moist environments.

Table 2.7 shows a variety of modified MOFs used for VOC removal under humidified conditions.

Table 2.7: Synthetically modified MOFs for the removal of VOCs at room temperature and in humid conditions.

VOC	Adsorbent	Modification applied	VOC concentration and %RH range	Results				Reference
				RH%	q_e (mg/g)	BET (m ² /g)	Pore volume (cm ³ /g)	
Toluene	ZIF-8 (Zn)	None	120 ppm %RH (0, 75)	0	6	1791	0.614	(Li <i>et al.</i> , 2021)
	CF-1100	Carbonization of ZIF-8 at high temperature under N ₂ gas		0	209	1024	0.497	
				75	187			
Acetone	MIL-53 (Al)	None	1000 ppm %RH (0, 30, 60, 90)	0	164	1065	0.63	(Shi <i>et al.</i> , 2021)
				30	117			
				60	90			
				90	61			
	MIL-53 (Al)@C14	PSM with n-tetradecyl phosphonic acid		0	124	619	0.42	
				30	118			
				60	126			
Toluene	MIL-101 (Cr)	None	Inlet 727 ppm %RH (10, 60, 80)	10	*244	3368	1.65	(Wang <i>et al.</i> , 2021)
				60	*84			
				80	*38			
	PEG ₅ @MIL-101 (Cr)	Hydrothermal synthesis inclusive of PEG		10	*262	2939	1.88	
				60	*184			
				80	*126			
Methanol	MIL-100 (Fe)	None	300 ppm %RH (0, 30, 50, 70)	0	161	1567	1.54	(Pei <i>et al.</i> , 2021)
				30	70			
				50	7			
				70	5			
	M-350	High temperature post-synthesis calcination in N ₂ atmosphere		0	260	1908	1.77	
				30	154			
				50	65			
Toluene	OAC	None	350 ppm %RH (30, 50, 80)	30	56	632	0.277	(Khoshakhlagh <i>et al.</i> , 2020)
	MIL-101 (Fe)	None		30	98	681	0.363	
				30	127	578	0.347	

	MIL-101 (Fe)/OAC	Solvothermal synthesis inclusive of OAC		50	116			
				80	102			
Benzene	SION-82 (Sr)	Using H ₄ TBAPy ligand	N/S %RH (0, 100)	0	107	635	0.36	(Sudan <i>et al.</i> , 2020)
				100	107			
	HKUST-1 (Cu)	None		0	480	N/S	N/S	
	MOF-74 (Co)			100	401			
	UiO-66 (Zr)			0	280	N/S	N/S	
				100	400			
			0	127	N/S	N/S		
			100	106				
Hexanal	CAU-3 (gel)	Rapid heating-up synthesis procedure	2 ppm %RH (0, 50)	0	291	2050	N/S	(Zheng <i>et al.</i> , 2020a)
				50	26			
Toluene	CAU-1 (Al)	None	1 ppm %RH (0, 50)	0	113	1209	0.508	(Zheng <i>et al.</i> , 2020b)
				50	1			
	P _{0.5} -CAU-1 (Al)-vale	Internal PSM with anhydride followed by external PSM by vapor-phase PDMS coating.		0	95	786	0.387	
	ZSM-5	None		50	7			
				50	6	337	N/S	
Toluene	Cu-BTC	None	Inlet 31785 ppm %RH (30, 60, 80)	30	63	1252	0.59	(Li <i>et al.</i> , 2020b)
				30	159			
	CZ5%	Hydrothermal synthesis inclusive of ZSM-5		60	146	1485	0.6	
				80	130			
Toluene	UiO-66 (Zr)-NH ₂	None	1000 ppm %RH (0, 40, 60, 80)	0	162	568	0.36	(Shi <i>et al.</i> , 2020)
				80	54			
	CTAB-U-N-0.5	Hydrothermal synthesis inclusive of CTAB		0	228	795	0.39	
				80	98			
Toluene	UiO-66 (Zr)	None	1000 ppm %RH (0, 30, 50, 70)	0	151	1335	0.83	(Zhang <i>et al.</i> , 2019a)
				70	27			
	PVP-U-0.5	Hydrothermal synthesis inclusive of PVP		0	259	1259	0.69	
				70	84			
Toluene	UiO-66 (Zr)	None.	1000 ppm %RH (0, 30, 50, 70)	0	151	1335	0.83	(Zhang <i>et al.</i> , 2019c)
				70	27			

	P-U-0.2	Hydrothermal synthesis inclusive of P123		0	394	1183	0.79			
				70	70					
Toluene	UiO-66 (Zr)	None	1000 ppm %RH (0, 30, 50, 70)	0	151	1335	0.83	(Zhang <i>et al.</i> , 2019d)		
					70				27	
	CTAB-U-0.5	Hydrothermal synthesis inclusive of CTAB		0	275	885	0.47			
			70	47						
Toluene	UiO-66 (Zr)	None	1000 ppm %RH (0, 30, 50, 70)	0	151	1335	0.83	(Zhang <i>et al.</i> , 2019b)		
					70				27	
	M-U-0.01	Hydrothermal synthesis inclusive of MOF-5		0	257	1168	0.95			
			70	51						
Toluene	ZIF-8 (Zn)	None	N/S %RH (10, 55, 80)	55	97	1388	N/S	(Chu <i>et al.</i> , 2018)		
					10				123	
	ZIF-8/GO	Hydrothermal synthesis inclusive of GO		55	116	1112	N/S			
					80				110	
Benzene	BUT-66 (Zr)	Using H ₂ BDB ligand	10 ppm %RH (0, 50, 80)	0	21	1096	0.46	(Xie <i>et al.</i> , 2018)		
					50				~21	
	BUT-67 (Zr)	Using H ₂ NDB ligand		80	15				984	0.41
			50	12						
Octane	ZIF-412 (Zn)	Solvothelmal synthesis using combined linkers bIM, nIM and IM	910 ppm %RH (0, 65)	0	475	1520	N/S	(Yang <i>et al.</i> , 2017a)		
									65	475
<i>p</i> -xylene									850 ppm %RH (0, 65)	0
				65	500					
Benzene	MIL-101 (Cr)	None	2 ppm %RH (5, 40, 60)	5	*227	N/S	N/S	(Zhu <i>et al.</i> , 2017)		
					40				*132	
					60				*104	
	MIL-101-Z1	Hydrothermal synthesis using Z1 linker		5	*173	2086	1.23			
					40				*171	
			60	*164						
DES	B-101408 AC	None	DES 50% in dry Ar/N ₂	0	0.5	N/S	N/S	(Padial <i>et al.</i> , 2013)		
					80				0.5	
	Ni ₈ (L5-CF ₃) ₆	Synthesized with L5-CF ₃ linker		0	0.2	2195	N/S			

			DES 20% in wet Ar/N ₂ %RH (0, 80)	80	0.2			
--	--	--	--	----	-----	--	--	--

⁵

⁵ Abbreviations in Table 2.7 explained: PVP = polyvinylpyrrolidone, P = triblock copolymer P123, CTAB = cetyltrimethylammonium bromide surfactant, M-U-0.01 = molar ratio of Zr⁴⁺/MOF-5, N/S = not stated, * = working capacity or 95% capture efficiency, bIM = 2,2'-biimidazole, nIM = nitroimidazole, IM = imidazole, DES = diethylsulfide, B-101408 AC = Blücher-10408 activated carbon procured from Blücher GmbH, L5-CF₃ = 4,4'-(benzene-1,4-diyl-diethyne-2,1-diyl)bis(1H-pyrazole)-trifluoromethyl, Z1 = 1,4-naphthalene dicarboxylic acid, P_{0.5} = denotes the PDMS heating time of 0.5 hrs, vale = valeric anhydride, PEG₅ = 5 mole% of PEG impregnated into MIL-101's pores, H₂BDB = butadienedibenzoic acid, H₂NDB = 4-4'-nitrilodibenzoic acid, H₄TBAPy = 1,3,6,8-tetrakis(*p*-benzoic acid) pyrene, OAC = oxidized AC.

2.2.3 Summary of best approaches to designing adsorbents for humid VOCs capture

It is encouraging to see the abundance of reports considering the influence of relative humidity on VOC removal performance by MOFs. Unfortunately, under humid conditions, the uptake by pristine MOFs like those listed in Table 2.6 declines significantly mainly because of their intrinsic hydrophilicity. Although some reports emphasized the contributions of NH₂ functionality and open metal centres towards enhanced dry VOC uptake, they were inadequate to protect the MOFs from being saturated with water in high moisture levels. Furthermore, the original MOFs tend to show low thermal stability which adds another disadvantage for them to be adopted in industrial applications. Based on the variety of MOF modifications presented in Table 2.7, a few key design concepts for the improved capture of VOCs from humid air can be identified as:

1. Improved surface and ligand hydrophobicity either obtained through *in situ* or post-synthetic modifications such as silicone, fluoro, phenyl or methyl functionalization.
2. Restricted water diffusion into the pores.
3. Increased number of coordinatively unsaturated sites.
4. Ensure large enough pore sizes to capture the targeted VOC molecules.

Carbonization and hybridization with species such as with graphene oxide appear as viable methods to improve an original MOF's state of hydrophobicity, which in turn contributed to higher levels of VOC uptake. However, a higher capacity alone is not enough, but the MOF's adsorption kinetics should also be considered. Among the outlined methods, Method 1 that relies on the use of hydrophobic ligands in a MOF synthesis can generate the most promising results, both in terms of impeding water transport into the MOF pores whilst increasing its VOC selectivity. The improvement is more striking when the MOFs contain ligands with low-surface energy functional groups such as methyl and fluoro. Although the final MOF hydrophobicity is confirmed, most hydrophobic linkers are niche and need to be synthesized from scratch or if commercially available, can be extremely costly.

As an alternative to Method 1, one can opt for a surface functionalization using hydrophobic polymers which can be introduced by vapor or liquid phase chemical deposition or reaction. There are however some challenges associated with this technique. The reactions require precise process control including temperature, time, sample mass, polymer molecular weight/shape and chemical concentration to ensure that a homogeneously treated material is produced. While these treated materials will often show improved surface hydrophobicity, as indicated by a higher water contact angle compared with the untreated form, pore blockage is a common side-effect. This problem can consequently dramatically reduce the maximum adsorption capacity of the treated material. To reduce the risk of complete pore blockage, it is advisable to perform the deposition in an inert (N_2) atmosphere.

It is also realized that a MOF's porosity and surface area are rarely the highlight in these compiled VOC removal studies, but this observation does not necessarily mean they lack importance. For example, MIL-101 is a frequently used MOF for VOC removal by virtue of its high porosity and surface area, but it is strongly hydrophilic which ends up performing poorly when humidity is present. If MIL-101 is treated with super hydrophobic polymers like PDMS, the MIL-101-PDMS composites could potentially exhibit high selectivity while its high porosity will enable high uptake of VOCs. Within the same MIL material family, MIL-100 (Fe) is another budding MOF with high porosity, high hydrothermal stability, and environmentally benign properties. On top of these, due to its highly hydrophilic nature, the latest research has found MIL-100 (Fe) to offer promising performance as an indoor air dehumidifier. For this reason, it is not commonly considered for VOC removal applications. Regardless of the status quo, the current study provides an ideal opportunity to investigate the effects of surface functionalization on MIL-100 (Fe) towards its VOC removal efficiency, like what has been applied to MIL-101.

In terms of the kinds of VOCs tested, a single-species experiment is common, especially using toluene, but a multi-component mixture is recommended for a more realistic testing condition. Multi-component experiments are better in portraying the effects of competing VOC species and to identify the adsorption affinity of a specific species over another. On a separate note, a prominent subject expert recently pointed out that removal of very volatile organic compounds is

still neglected in indoor air studies although they also play a vital role in the evaluation of indoor air quality (Salthammer, 2016).

The different experimental measurement techniques used in the literature can complicate a fair comparison of their results. Some workers have used gravimetric measurements using a free form solid, while some others reported data measured from their breakthrough curves where the adsorbent is packed in a column. It is suggested that a gravimetric measurement can be used as an initial material screening tool to shortlist the materials which display the most optimum uptake capacity and kinetics. Once the best materials have been identified, one may proceed with breakthrough curve analysis as it is more suitable to represent industrial scenarios with competitive multicomponent adsorption. To assess the performance of an adsorbent in both gravimetric and breakthrough techniques, three parameters including the partition coefficient (PC), maximum adsorption capacity (Q) and 10% BTV (breakthrough volume) seem reasonable to be adopted. The parameter Q is a common comparison metric used in most studies. The PC value of an adsorbent can be calculated in both techniques too though presently, it is rarely being used in reports employing gravimetric measurements. The 10% BTV that is obtained from a breakthrough measurement comprises both equilibrium capacity and kinetics in a single adsorption profile. However, this 10% BTV cannot be obtained directly from a gravimetric measurement as the kinetics and the equilibrium capacity are provided separately. So, in a gravimetric measurement, the Q and PC values of an adsorbent must be complemented with its kinetics parameters to select the adsorbent for the right application.

Lastly, assembling suitably porous materials into monolithic or compacted forms is the next step for practical applications. This process is an area that is increasingly studied, but these adsorbent monoliths seem to find much interest in the gas storage domain with little attention being paid to VOC capture despite having many shared similarities in their operational requirements. It is hoped that by exploring strategies to manufacture denser MOFs, their reusability and mechanical stability can be properly optimized.

2.3 Structural stability in MOFs

In commercial water purification processes, adsorbents are generally deployed into a packed bed for continuous filtration. Fluids flowing through some packed beds may result in high pressure drops which directly increase the energy requirement to pump the fluid through the bed and decrease the operational lifetime of the pumps, impacting on the economics of the process (Gebald *et al.*, 2019). Although various factors are involved in an optimal bed design, lowering the pressure drop can be most easily achieved by increasing the adsorbent particle size (Mandić *et al.*, 2017). Larger particles also facilitate easier recovery in between the washing cycles.

Industrial gas separators or filters also have the same bed configuration. In this situation, the gradual fracture and fragmentation of the adsorbent particles from the incoming gas pressure will result in even higher mass resistance throughout the column, eventually, building significant pressure drops over time. Therefore, the material transformation from a powdered adsorbent into more robust and larger formats (i.e., sol-gel, monolith, granular, membrane) will not only solve issues related to mainly mass transfer restrictions, but this change can also address poor powder handling properties, and mechanical instability (Hou, Sapnik & Bennett, 2020). Dust emission is also a potential hazard due to the adsorbent's powdery nature (Woellner *et al.*, 2018). In fact, a recent study that used a mixed ligand-modulator (1-methylimidazole with *n*-butyl amine) approach to synthesize a series of dense monolithic ZIF-8 (Zn) and ZIF-67 (Co) fully supports the benefits of using monolithic adsorbents in lowering the packed bed pressure drop (Hunter-Sellars *et al.*, 2021). Taken together, both for the decontamination of liquid effluents and gas streams, the need is clear to scale up MOFs from common native particle size range which are within the nm/ μ m into mm/cm sizes which are closer to the industrial requirements.

In considering the formation of monolithic MOFs, the fundamental crystallization mechanisms must first be understood which comprise two successive stages: namely nucleation and growth. According to the classical nucleation theory, crystallization begins under supersaturated conditions, where a disparate number of small atoms, ions or molecules come together to form crystalline nuclei until they grow sufficiently large enough and irreversibly into well-faceted macroscopic crystals (Van Vleet *et al.*, 2018).

The classical nucleation theory also assumes that in a homogenous solution, the nucleation will lead to only products that are the most thermodynamically favourable (maximum system free energy), without amorphous or side crystalline phases. On the other hand, in heterogeneous systems, the presence of foreign substrates (solids or liquids) can alter the crystallization rate, allowing it to happen at much lower super saturation levels.

The use of additives in the manufacturing of MOFs, as well as in other materials' syntheses, is common for the precise control of particle sizes and crystal morphologies. This step may involve adding (Seoane *et al.*, 2016):

1. Initiation solvents.
2. Coordination modulators.
3. Surfactants.
4. Hard templates into the reacting mixture.

2.3.1 Addition of initiation solvents

Initiation solvents can be any non-polar solvents that precipitate the reacting particles due to their lower solubility than in the precursor solutions. The rate of addition, type of initiation solvent and mixing intensity are some of the factors that can dictate the final particle size (Wang *et al.*, 2018a) and to some extent, the absence, or the presence of the desired crystals. For example, Long and co-workers (Long *et al.*, 2011) reported the influence of different solvents such as ethanol, methanol, N,N-dimethylformamide and acetone on the hydrothermal (water as the base solvent) synthesis of two chromium trimesates; MIL-100 (Cr) and MIL-96 (Cr). Although both MOFs were derived from the same elements (Cr^{3+} and H_3BTC), the novel MIL-96 (Cr) was only favourably produced in the presence of methanol/water solution, while the MIL-100 (Cr) was able to form independently in water or when mixed with acetone. The variations observed indicate that when the reagent concentrations are fixed, the choice of solvents brought drastically different sets of reaction depending on their solubility and polarities in the reaction solutions

2.3.2 Addition of coordination modulators

The addition of certain chemicals known as modulators or capping agents into the reacting solution can induce competition among the nuclei clusters, which in turn inhibits and slows down the crystal growth rate. This concept can be understood from the work conducted by Guo et al. (Guo *et al.*, 2018). In their work, they introduced a general approach using 2-methylimidazole (2-MI) to control the morphology and the size of several MOFs including MOF-74 (Co), MOF-5 (Zn), HKUST-1 (Cu), MOF-74 (Ni) and MIL-101 (Fe)-NH₂. The addition of 2-MI as a modulator did not change the original x-ray diffraction patterns of the studied MOFs, suggesting the 2-MI-modulated samples are still the same MOFs. However, as the 2-MI concentration was increased, pronounced changes in the MOFs' sizes and morphologies were observed. They then selected MOF-74 (Co) as a model MOF to study the effect of 2-MI addition on the MOF's crystal growth. The results indicate that 2-MI had dual functions, as a ligand competitor and as a base for the ligand deprotonation. Higher 2-MI concentrations increased the availability of deprotonated ligands to coordinate with the metal ions. As a result, the nucleation rate is faster, and the MOF's crystal size becomes smaller. In a separate experiment, they also found that by increasing methanol concentration and reaction times, it led to the shrinking and enlargement of the crystal size respectively. The illustration in Figure 2.15 summarises the influence of reaction time, methanol, and 2-MI concentration to the crystal growth of MOF-74 (Co).

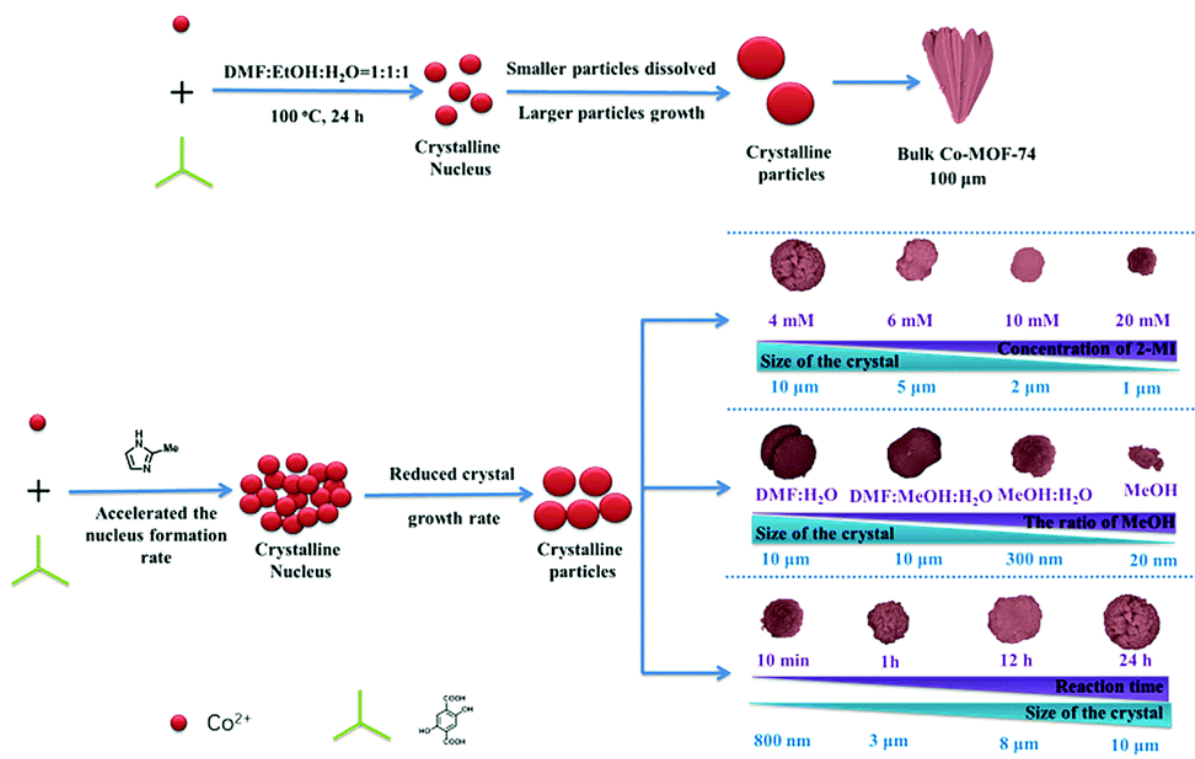


Figure 2.15: A schematic illustration showing the influence of reaction times, 2-MI and methanol concentrations on MOF-74 (Co)'s particle size evolution. Reproduced with permission from (Guo et al., 2018). Copyright 2018, RSC Publishing.

Sometimes, the need for the extra addition of modulators can be eliminated. Manipulating the ratio and type of reactants within the same reactant solution can also deliver the same outcome. Indeed, this approach was proven by Liu and his group in the modified synthesis of MIL-96 (Al) using a dual aluminium source system (aluminium nitrate-aluminium isopropoxide) and a dual ligand system (H₃BTC-Me₃BTC) (Liu *et al.*, 2015a). The concentration variations of aluminium isopropoxide and Me₃BTC had produced crystals with different size and morphology. With a higher ratio of aluminium isopropoxide/Me₃BTC, the modulated MIL-96 (Al) crystals transformed from a hexagonal spindle to a truncated form, ending as a micro hexagonal lump. Each added chemical gave a different growth mechanism, but they equally served the same function, that is, as an inhibitor to the overall crystal growth rate. The rapid hydrolysis of aluminium isopropoxide yielded abundant isopropanol that interfered with the ligand coordination process whereas the slower hydrolysis of Me₃BTC caused an initial shortage of ligands.

2.3.3 Addition of surfactants

The crystal size and shape of MOFs may also be tuned using surfactants. Depending on the reaction conditions, apart from acting as capping agents that slow down the crystal growth rate, their steric attachment to the crystals could provide the space for anisotropic growth, leading to formation of distinct nanocrystal facets. Using Ni-MOF as a reference MOF, Arul and John saw a drastic reduction in its spherical average particle size from 322 nm to 80 nm after introducing 600 mg of polyvinylpyrrolidone (PVP) into the synthesis solutions (Arul & John, 2018). However, at 800 mg PVP concentration, MOF agglomeration started occurring. The TEM images of the Ni-MOF also clearly showed a high-density PVP coverage on the surface. Given that PVP also has good electrical conductivity, the authors made use of this property by using the Ni-MOF-PVP composite as a gas chromatography electrode. The composite showed good success when it was used to detect nitrobenzene in tap and lake water samples.

Furthermore, when it comes to fabrication of hybrid materials, the ability to control a MOF particle size becomes a highly desirable property. For example, MOF particles can be dispersed into low-cost polymeric bases to create advanced functional mixed membranes. However, the two distinct phases should be properly integrated so as to remain free from material defects and to reap the maximum performance, physical and chemical property enhancement (Sosa *et al.*, 2018). Achieving a smooth inclusion of the MOF crystals into the polymers usually requires having the right MOF crystal orientation. This concept has been investigated by Avci and his team where they used a typical surfactant, cetyltrimethylammonium bromide (CTAB) to synthesize well-ordered truncated rhombic dodecahedral ZIF-8 (Zn) crystals (Avci *et al.*, 2019). They demonstrated that an increase in CTAB concentration was able to force the crystal orientation from the entropically favoured (111) to (100) and (110).

While in a different study by Pustovarenko *et al.*, the same application of CTAB effectively formed 1-dimensional nano-sheets of MIL-53 (Al)-NH₂ from its original 3-dimensional crystalline state (Pustovarenko *et al.*, 2018). These MOF nano-sheets even showed superior performance for alcohol sensing and CO₂/CH₄ separation than its original MOF form. Based on the nano-sheets' electron microscopy images and diffraction data, the authors asserted the reason to the nanosheets'

enhanced performance is due to the shorter solute diffusion/mobility pathways, especially along the shortest nanosheet dimension (crystallographic *a*-direction). It may be concluded that essentially, addition of initiation solvents, modulators, and surfactants (Method 1, 2 and 3 respectively) can be generalized as soft template approaches.

2.3.4 Addition of a hard template

Method 4 or preparation of pore-controlled MOFs may also be accomplished via hard templates which relies on the use of solid-state structures such as polystyrene spheres (Shen *et al.*, 2018), ZnO (Song *et al.*, 2017) and mesoporous silicas (Li *et al.*, 2018a) as shaping aids. The MOF crystals can be grown either inside or around the templates. Although this Method permits greater control over the final product, as it will inherit the features of the parent templates, certain limitations including difficult preparation of the original templates and their removal afterwards make it less favourable for large-scale production. Methods 1 – 3 have their own complexities including usage of harmful organic solvents and acidic or basic modulators that could increase the risk of safety hazards. On another note and slightly different than Method 1 – 4, physical synthetic techniques such as pyrolysis (Lee & Kwak, 2017), microreactor (Watanabe *et al.*, 2017), ultrasound and microwave (Burgaz *et al.*, 2019) could as well help accomplish the same objective of particle size and shape refinement.

In summary, it is obvious that any of the methods discussed previously could modify the morphology of MOF crystals. However, the common limitation of all these approaches is the formation of predominantly nanoparticle products, whereas the current sought goal is to enlarge the MOF particle size. The question remains whether the particle size decreasing effect of these techniques can potentially be reversed to create bigger particles while using the same methods.

2.3.5 Denser MOF formation

Apart from Method 1 – 4, developments on bulkier MOFs obtained either from mechanical shaping or sol-gel technique are growing steadily (Lorignon, Gossard & Carboni, 2020). There are two shape categories that can be produced namely in (1) cylindrical or spherical granules, pellets,

tablets and (2) in monoliths. As the former name suggests, the mechanical shaping technique can turn powdery MOFs into certain shape/size with the help of external tools/processes such as granulation, extrusion, spray drying and pressing. Figure 2.16 shows the photographs of several mechanically shaped MOFs. This method is relatively simple and fast, but because it involves high pressure, use of binders and wetting agents, the porosity and eventually, the performance of the resultant materials is always compromised (Liu, Xie & Wu, 2020).



Figure 2.16: Frequently studied MOFs that have been shaped using granulation and pressing methods. Reproduced with permission from (Lee et al., 2021). Copyright 2021, Springer.

Compared to other MOF shapes, monoliths are mechanically stronger. Plus, monoliths have other features such as good attrition resistance, uniform packing, and low pressure drop which make them more suitable for industrial applications. Monolithic MOFs can be prepared from two ways, firstly through *ex situ* (post synthetic techniques) such as extrusion and deposition on monolithic supports and secondly, via *in situ* techniques such as powder packing, sol, aero and xerogel synthesis. The second class of *in-situ* formed monoliths is advantageous than the first *ex-situ* class as they could have up to 1000 times higher Young's moduli values (Shah, Kundu & Zhao, 2019). To put this into context, by using the sol-gel synthesis strategy, Tian et al. obtained HKUST-1 (Cu) monolith, possessing remarkably higher bulk density than the single crystal. The monolith demonstrated a record volumetric methane uptake loading of 259 cm³ at STP (Tian *et al.*, 2018). Nano indentation tests performed on the monolith showed very high mechanical strength: 9.3 GPa

of elastic modulus (E) and 460 MPa of hardness (130% higher than its film counterpart). Another example can be observed in the work by Bueken and his co-workers (Bueken *et al.*, 2017). They were able to prepare extremely lightweight UiO-66 (Zr) aero and xero gels by using a solvent drying method in supercritical CO₂ and air accordingly. UiO-66 (Zr) monolithic spheres were then created from the gels by using an industrially approved oil granulation method. After performing some nano indentation measurements, the air-dried xero gels showed a range of E values between 9.3 and 10.5 GPa.

Furthermore, the mild gel synthesis conditions (no high pressure, no binder) could reduce the risks of structural amorphization and pore collapse (Lorignon, Gossard & Carboni, 2020) while enabling the formation of hierarchical porosity under different drying conditions. As an example, UiO-66 (Zr)-NH₂ is primarily a microporous MOF. Yet, Vilela *et al.* successfully created new meso and macro-porosities in the single centimetric-scale, monolithic aero and xerogels of the MOF after controlled drying with supercritical CO₂ and SiO₂ respectively (Vilela *et al.*, 2018). Also employing the same MOF, Hara *et al.* (Hara, Kanamori & Nakanishi, 2019) presented a two-step approach to impart trimodal pore structures within the monoliths. Initially, the UiO-66 (Zr)-NH₂ gels were formed in a DMF solution followed by the addition of polypropylene glycol into the system as a phase separator. By increasing the polypropylene glycol amount, more interconnected macro-porosities were observed in the samples. Besides the explained *ex* and *in-situ* strategies to prepare MOF monoliths, 3D printing technology is now an appealing option too (Duan *et al.*, 2021).

To summarise, the densification of MOFs certainly provides higher mechanical strength along with higher volumetric capacity, easier handling and low pressure drop. Additionally, the capability of introducing all three pores within gel-derived MOF monoliths is equally valuable as it can simultaneously increase its total pollutant uptake (capacity) and mitigate mass transfer limitations (kinetics) that are specific to each pore size range. Despite these presented benefits of sol-gel synthesis, there could still be plenty of opportunities available to incorporate specific chemical functionalities into the monoliths that may enhance their selectivity towards specific adsorbates.

2.4 Research objectives

Based on the research gaps that have been identified, the overarching aim of this project is to modify MOFs for the removal of toxic organic pollutants from aqueous and atmospheric environments. Their pristine and modified performance will always be compared with a commercial AC. The specific questions that are going to be addressed in this thesis are:

2.4.1 Research objective 1: Amine functionalised MOF for aqueous phase phenol removal

It is a recurrent theme in the literature that the NH_2 group is a useful functionality to help improve a MOF's performance for aqueous phase adsorption. Therefore, an NH_2 -grafted MOF will be compared with its pristine MOF and AC to evaluate their chemical property differences. While in terms of their physical properties, the MOF that will be selected must possess high porosity (technically higher than the AC) and an excellent hydrolytic stability. Note that in all experiments performed in this thesis, a commercial AC will permanently be used as the benchmark adsorbent. The differences in the chemical and physical properties between the MOFs and the AC will distinguish the influences of exemplary material properties on an adsorbent's removal performance. In this work, the adsorbents will be tested for aqueous phase phenol removal. The extracted findings will also be used to identify other possible contributors to an effective removal performance.

2.4.2 Research objective 2: Improving a MOF's moisture stability via a vapour phase hydrophobic surface treatment

PDMS is a frequently used polymer when it comes to transforming a hydrophilic surface into a hydrophobic state. Having trialled the liquid-phase deposition previously, here, the PDMS will be applied onto the MOF surface via a vapor-phase deposition method at an elevated temperature. Additionally, to minimize the implications of pore blockage, yet to be able to introduce the necessary hydrophobicity, two other factors will be included in this study for optimization. Firstly, different PDMS molecular weights will be used. Secondly, the deposition time will be controlled.

These two factors will be the anchor points for comparing their performance with AC. The testing conditions that are practiced here will be the same as in Section 2.4.3.

2.4.3 Research objective 3: Wet-phase hydrophobic treatments for MOFs

Low surface energy functional groups like those containing CH_3 and CF_3 are very appealing to increase a MOF's surface hydrophobicity. External surface treatments were chosen instead of synthesizing the MOF with ligands derived from these hydrophobic groups as the former is relatively cheaper and easier than the latter. Silanes, phosphorous oxyacids and calixarenes are some underexploited agents with great promise as hydrophobic surface treatments for MOFs. These chemicals can be attached to the MOF surface via a liquid-phase deposition technique. Moving on from adsorption in aqueous solutions, the impact of this hydrophobic modification may be evaluated better for adsorption of hydrophobic VOCs in a realistic water-saturated (humid) atmospheric condition. An aromatic/hydrophobic VOC molecule, a relevant trace VOC concentration and a gravimetric measurement method will be used to probe the studied adsorbents' performance.

2.4.4 Research objective 4: Role of surface chemistry, crystal morphology and particle size in MOFs for perfluorochemical removal

Another MOF's physical property improvement is to enlarge its particle size for a more convenient recovery after adsorption. Moreover, industrial filtration settings require the adsorbents to be packed in a column. Usage of larger-sized adsorbents in a column will help lower the column's pressure drop while also reducing pump energy costs. If the MOF size can be tuned into a granular form like AC, it will enhance its competitiveness for industrial applications. NH_2 remains the key moiety to be imparted on the MOF. This time, the performance of the adsorbents will be studied for the removal of a highly persistent organic contaminant PFOA to explore other mechanisms that may assist its adsorption and desorption processes.

Chapter 3: Experimental Materials and Methods

This Chapter begins by introducing the general measurement methods used in this thesis followed by more detailed explanations of the experiments involved in Chapter 4, 5, 6 and 7.

3.1 Powder x-ray diffraction (PXRD)

X-ray diffraction (XRD) is a non-destructive technique used to characterize a material's crystallinity, purity, crystallite size, phase identification, and in some cases, morphology based on its unique x-ray diffraction patterns (Holder & Schaak, 2019). Figure 3.1 shows the operating principle of an x-ray diffractometer.

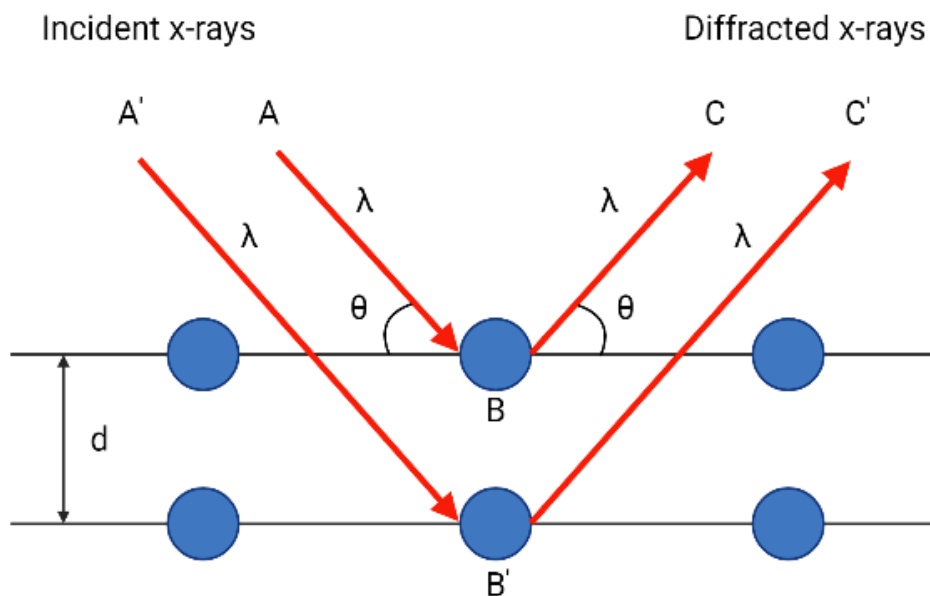


Figure 3.1: A 2-dimensional schematic of XRD principle.

X-rays are high-energy light with a repeating period called the wavelength (λ). Since the λ of an x-ray is equivalent to the distance between atoms in a crystal, an interference effect called diffraction can be used to measure the distance (d) between the planes of atoms. Most materials contain tiny crystals that are made up from regularly arranged atoms. When x-ray is directed to a sample's surface (incident x-ray), the diffracted x-ray from the atoms in the crystal will produce different degree of scattering or interferences. If the diffracted x-ray waves are in alignment, the

signal is amplified, and they produce constructive interferences. Some of the diffracted x-ray waves may be out of alignment, cancelling out each other, or known as destructive interferences. The half scattering angle between the diffracted x-ray beam and the crystal planes is called θ . For the constructive interferences to happen, two conditions must be fulfilled:

1. The angle of incidence = the angle of diffraction.
2. The travelled x-ray path length difference equals to an n integer number of wavelengths. The second wavelength must travel a whole number of wavelengths. For instance, in Figure 3.1, the path that ABC has travelled on the incident side and on the diffracted side will be different by a factor of $n\lambda$ compared to path A'B'C'.

Essentially, the relationship between the diffraction angle, the x-ray wavelength and the spacing between the atoms can be expressed through Bragg's Law (Equation 3.1). The specific directions of these constructive interferences will resultantly generate the material's unique diffraction patterns. Sometimes, the same diffraction patterns may be projected as spots or also known as reflections. Each spot represents the position of an atom which can then be used to determine a crystal structure.

$$n\lambda = 2d \sin \theta$$

Equation 3.1

There are two other physical conditions that allow constructive interferences or a display of diffraction patterns. Firstly, the sample must be crystalline which means it possesses a regular structure. So, amorphous sample will not show up any diffraction patterns. Secondly, the d spacing between the atom layers must be close to the x-ray's λ because if the diffracted x-ray is out of phase, destructive interferences will occur, and no peak will be produced. XRD techniques are also divided into two primary types, depending on the bulk particle size of a sample:

1. For samples with crystal sizes generally between 30 and 300 μm , single crystal XRD can be used to determine the unit cell, bond lengths and atom positioning in a crystal lattice (Clark, Christine M., Dutrow, 2021). Other applications include identification of new minerals, cation-anion coordination, and the variations of crystal lattice with changing chemistry or other stimuli like high pressure/temperature.

2. For materials that are smaller than 30 μm , they are analysed using powder XRD (PXRD). A pure, finely ground, and homogenized sample are crucial pre-requisites for a PXRD analysis. Although PXRD provides less information than single crystal XRD, it is simpler and faster. PXRD is commonly used to confirm the identity of a solid material, its crystallinity and purity.

In this thesis, only the PXRD technique was used since the synthesized crystalline materials (MOFs) are made up of fine grain sizes. To identify the right material phase and its purity, the experimentally scanned PXRD patterns are compared against the reference pattern usually obtained from a database in Crystallographic Information File (CIF) file format. An unambiguous and a complete match is expected between the two patterns to confirm the right material has been synthesized. However, it is worth noting that the PXRD patterns from a database can sometimes differ from those that are measured experimentally. To help solve this issue, (1) the reference of the downloaded CIF files should be clearly stated as there can be many CIF files bearing almost similar structures, yet there might be some minor differences in their registered crystallographic data. (2) Unknown phases or unlikely introduced impurities can be detected through the missing of some original peaks or newly formed arbitrary peaks compared to the simulated PXRD patterns. Any deviations from the simulated PXRD patterns must be justified with the right rationale.

In this thesis, the PXRD patterns of the studied materials were measured using X'Pert Pro PANalytical diffractometer with a Cu $K\alpha$ radiation source (40 kV, 20 mA). The materials were ensured to be finely ground prior to starting the PXRD measurement. The scattering angle range (2θ) was set between 5° and 30° with a scan speed of $0.0005^\circ/\text{s}$. The scans will be juxtaposed with the simulated PXRD patterns of the material, either obtained from a direct PXRD scan or relevantly retrieved from the Cambridge Crystallographic Data Centre (CCDC) repository. Up to date Mercury freeware could also be used to extract more details from the crystallographic information such as assignments of specific PXRD peaks to their corresponding planes (i.e., (100), (002), etc.). Specific CCDC identifier of the material in discussion will be mentioned under each experimental chapter's (Chapter 4, 5, 6, and 7) material characterization section.

3.2 Thermogravimetric analysis (TGA)

Thermogravimetric analysis (TGA) is a technique that measures the mass change (gravimetric method) of a solid material as a function of temperature or time when it is heated in a temperature-controlled and gas-specified atmosphere (furnace). In this thesis, the main objectives of using TGA are to determine a solid material's decomposition behaviour, its compositional analysis, and the optimum degassing temperature so that during activation, they will not degrade permanently. Apart from these, TGA can also provide various physical and chemical information of the samples such as (Netzsch, 2021):

1. Phase transitions (dehydration, oxidation, reduction, etc.).
2. Aging in polymer samples.
3. Determination of moisture/plasticizer/filler/ash content and other additives.
4. Reaction kinetics.
5. Purity check.
6. Detection of Curie transition temperature in ferromagnetic materials. The magnetic attributes of some of these materials can change with temperature.
7. Corrosion studies.

Besides TGA, other commonly used thermal analysis techniques include differential scanning calorimetry (DSC) and differential thermal analysis (DTA), all of which are complementary to each other (Hammer *et al.*, 2021). Sometimes, only a combination of the techniques could provide comprehensive insights into a sample. Both DSC and DTA techniques can be used for detection of endothermic (caused by most phase transitions like melting) and exothermic peaks (e.g., crystallization, oxidation, decomposition), determination of temperatures that characterize specific thermal effects (glass transition, melting, crystallization), calculation of specific heat capacity and change in enthalpies. However, there are some differences as explained in Table A10.1.

In a TGA instrument, three kinds of gases are involved namely protective, reactive and purge gas:

1. A protective gas can be any dry gas (usually N₂ but may also be Ar or He) consistently flowing at 20 mL/min during the operation. It is mandatory to protect the balance from out-gassed products (gases that are released when the solid is exposed to heat or vacuum treatment).
2. A reactive gas is the gas that occupies the testing chamber and will only be switched on during the experiment. It is selected depending on the study nature. An inert atmosphere (using typically N₂ or He) can show the material's thermal decomposition and the gaseous products that are formed, while in the presence of air or O₂, it simulates an oxidative decomposition. Either way of the reactive gas environment is chosen, the sample decomposition can generate organics/volatiles/gaseous products. These gases can be identified and measured precisely by combining TGA with other accessories such as a mass (MS) or an infrared (FTIR) spectrometer.
3. A purge gas, usually unnecessary, but for conditions requiring the reaction products to be eliminated from the system, either N₂ or air can be flown at the same flow rate with the reactive gas.

Additionally, different temperature settings can give different types of information such as:

1. Dynamic mode where the temperature rises at a constant heating rate. Apart from knowing the material's decomposition behaviour, it allows simultaneous identification of how much gases are evolved and at which temperature it occurs.
2. Static mode where the furnace temperature is kept constant (isothermal). From this setting, a material's decomposition behaviour or its thermal stability at a specific withheld temperature can be investigated.
3. Quasi-static mode where the sample is heated in various temperature intervals and held at those intervals for a certain period, usually until a stable mass is reached. This method is suitable for materials that might decompose in different ways when subjected to different temperatures.

After the temperature and the reactive gas have been specified, the solid material is placed on a sample pan which is supported by a balance, either in a top, bottom, or horizontal loading configuration (Figure 3.2). The more commonly used in laboratories is the top loading TGA where the sample pan is positioned above the balance and connected via an upright “stem” support rod. On the contrary, the sample pan in a bottom loading TGA is located below the balance, supported via a “hang-down”. The horizontal arrangement is less commonly used nowadays. It contains a simple moving coil microbalance system. The disadvantage is that it can generate an apparent change in mass during the heating process, usually compensated for by co-installing a parallel-guided system (Gabbott, 2008).

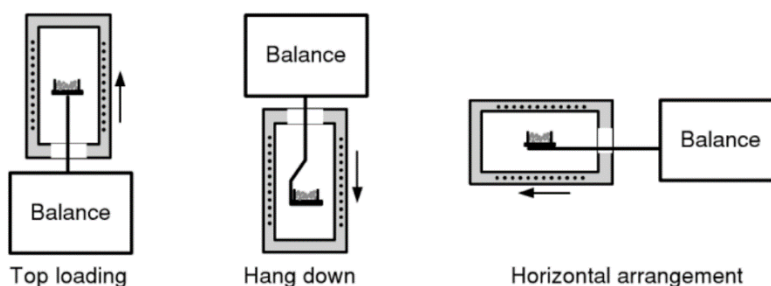


Figure 3.2: The three balance designs in a TGA instrument (from left to right): top, bottom-loading, and horizontal arrangement (Gabbott, 2008).

Throughout this thesis, the thermal stability of the samples was mainly investigated using Netzsch STA 449 F5 Jupiter[®]. Each measurement uses about 20 mg of sample to be filled in an Al₂O₃ crucible pan, then heated from 30 to 900 °C under flowing reactive gas (40 mL/min) at a heating rate of 20 °C/min. By the end of the heating process, a safe maximum temperature was also set at 920 °C to ensure complete disintegration of all residual contents. The type of reactive gas used was either air or N₂ and is specified in the respective experimental chapters. At the same time, a N₂ protective gas (20 mL/min) was supplied continuously during the operation.

3.3 Surface area and pore measurement

3.3.1 Surface area analysis

Adsorption is defined as the adhesion of atoms or gas molecules to a surface. It is different to absorption where a fluid permeates into a solid, usually dissolving in the solid phase. In 1916, Irving Langmuir proposed a theory to model a monolayer adsorption of gas molecules (adsorbates) onto a solid surface at a specific gas pressure and fixed temperature (Langmuir, 1916). The key assumptions are:

1. All adsorption sites have the same heat of adsorption value (each site has equal affinity for the adsorbate).
2. Only one molecule can occupy a single vacant adsorption site (1:1 stoichiometric ratio).
3. Adsorbates form a monolayer.
4. The activity of the adsorbate is directly proportional to its concentration.
5. Adsorption at one site happens independently of adsorption at neighbouring sites.

$$\theta_1 = \frac{\alpha \cdot P}{1 + \alpha \cdot P} \qquad \text{Equation 3.2}$$

Equation 3.2 shows the Langmuir equation where θ_1 is the surface coverage fraction (0 to 1), α is the Langmuir constant, and P is the gas pressure. As P increases, θ_1 will increase accordingly until it finally reaches saturation ($\theta_1 = 1$). However, the Langmuir theory is strictly limited to monolayer adsorption. To account for multilayer adsorption, Brunauer, Emmett and Teller (BET) jointly developed the BET theory in 1938, adding three more assumptions to the original Langmuir theory (Brunauer, Emmett & Teller, 1938):

1. Gas molecules will be physically adsorbed on a solid into multilayers.
2. The different adsorption layers have negligible interaction between one another.
3. The heat of adsorption is different for the first adsorbed layer compared to subsequent adsorbed layers multilayers.

The BET formula (Equation 3.3) relates the volume of “physically” adsorbed gas (Q) by a solid material at a specific relative gas pressure (P/P_0). By “physical”, it means that the adsorption is reversible, with no chemical interaction/bonding involved during the process. N_2 is typically used as the adsorbate gas due to its easy availability and high purity. Argon (used at 87 K) is actually a better adsorbate than N_2 due to its slightly smaller size and absence of quadrupole moment, though it is slightly more expensive (De Lange *et al.*, 2014).

$$\frac{1}{Q[(P_0/P) - 1]} = \frac{1}{Q_m C} + \frac{C - 1}{Q_m C} \left(\frac{P}{P_0}\right) \quad \text{Equation 3.3}$$

Prior to a BET analysis, samples must be thermally cleaned under vacuum condition to free the pores from adsorbed gas molecules, before cooling to 77 K using liquid N_2 . Because most solids have weak interaction with gases, this low temperature allows the inert gas to physically adsorb onto the solid’s surface. A known amount of N_2 at specific P is dosed stepwise into the sample container. More N_2 molecules will adsorb on the solid’s surface until they form a single monolayer and consequently, into multiple monolayers. The process continues until the saturation pressure (P_0), thereafter, no more adsorption happens regardless of further P increase. C is the BET constant which is related to the adsorption energy of the first monolayer on the solid while Q_m is the BET monolayer capacity, which is the volume of N_2 adsorbed (cm^3/g) at standard temperature and pressure (STP).

In the final step, after all multilayers completely formed ($P/P_0 \approx 1$), the pressure is reduced, and the desorption experiment is run. To measure the solid’s surface area, the data can be plotted as a linear plot with $\frac{1}{Q_m[(P_0/P)-1]}$ (y-axis) versus $\frac{P}{P_0}$ (x-axis). Once Q_m is determined, the BET surface area (S_{BET}) can be calculated using Equation 3.4 together with other information like the Avogadro’s number ($N_{Av} = 6.02 \times 10^{23}$), the N_2 molar volume at STP ($M_v = 22.414$ L) and the molecular cross-sectional area of N_2 ($A_m = 0.162$ nm²).

$$S_{BET} = \frac{Q_m N_{Av} A_m}{M_v} \quad \text{Equation 3.4}$$

Alternatively, the data can also be displayed as a plot of Q (y-axis) against P/P_0 (x-axis), known as a BET isotherm. As a side note, because the BET equation is based on a manometric (vacuum-volumetric) approach, the volume of gas adsorbed by the sample (Q) is equivalent to the difference between what has been dosed into the sample tube and what is left un-adsorbed in the free space (dead volume). The dead volume is measured at the end of each analysis by dosing helium into the sample tube. The International Union of Pure and Applied Chemistry (IUPAC) have classified six possible isotherms for gas adsorption into porous solids as shown in Figure 3.3:

1. Type I: Mostly displayed by microporous solids with low surface area like AC, zeolites, and some porous oxides. A Type I(a) isotherm indicates that the microporous materials have mostly narrow micropores (< 1 nm) while Type I(b) is given by materials that have larger pore size distributions, comprising of wider micropores and some narrow mesopores (< 2.5 nm).
2. Type II: The materials are either nonporous or macroporous as they continue having unrestricted monolayer-multilayer adsorption up to high P/P_0 . If the inflection point B is sharp, it indicates the completion of a monolayer coverage. If point B is flatter, then it means the monolayer coverage is significantly overlapping, leading to the prologue of a multilayer adsorption.
3. Type III: Point B is non-existent due to no monolayer formation, so, the BET equation is not applicable. The weak gas-solid interactions cause the gas molecules to only cluster around the most favourable sites on a nonporous or a macroporous solid's surface.
4. Type IV: A characteristic feature of mesoporous materials showing two adsorption behaviours. At low P/P_0 , a monolayer, then multilayer adsorption takes place which is followed by pore or capillary condensation. This process is a phenomenon whereby gases can condense to liquids inside the tiny pores of a solid when $P < P_0$. Typically, the isotherm ends with a saturation plateau. Type IV(a) is followed by a desorption hysteresis (adsorption and desorption plots do not overlap) while Type IV(b) does not. Usually, a hysteresis can occur when the pore width of a mesoporous material exceeds a certain critical width (> 4 nm), but it may change depending on the adsorption system and temperature too.

5. Type V: In the initial P/P_0 range, it resembles a Type III isotherm due to the relatively weak gas-solid interactions. At higher P/P_0 , molecules are clustered, followed with pore filling.
6. Type VI: Signifies a layer-by-layer adsorption on a uniform, nonporous surface. Each step height represents the capacity of each adsorbed layer whereas the sharpness of the successive step is a function of the adsorption system and the temperature.

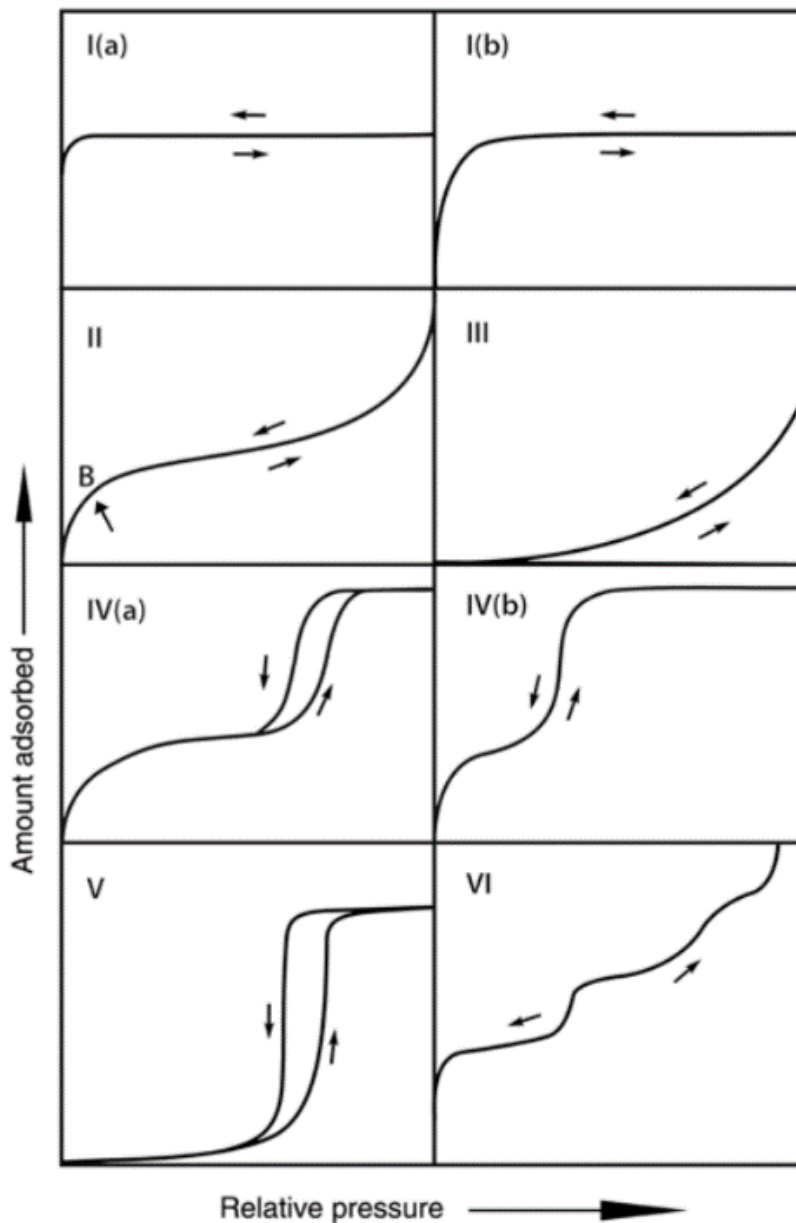


Figure 3.3: Six classifications of physisorption isotherms. Image is taken with permission from (Thommes *et al.*, 2015). Copyright 2015, IUPAC and De Gruyter.

3.3.1.1 Limitations of BET method for microporous materials

It should be reminded that the BET method is very suitable to estimate the surface area of materials with well-defined Type II and IV isotherms (non, meso, and macroporous). However, in the presence of micropores (Type I, combined Type I-II, or Type I-IV), the micropore filling that happens at really low P/P_0 is often indistinguishable from the mono-multilayer adsorption. This makes it challenging to locate the linear range for the BET plot. Notwithstanding, if a BET surface area can be calculated from the isotherms of the microporous materials, it should only be treated as an *apparent* surface area. Best practices of N_2 adsorption isotherm analysis have been elaborated by De Lange et al. in their review (De Lange *et al.*, 2014). They performed an extensive analysis on errors that may occur when one is calculating a material's pore volume and surface area using the BET equation. Several archetypical adsorbents (MOFs, zeolite, AC, alumina) were studied and compared in their work. Also, according to De Lange et al., to ensure the BET-derived properties are valid, these guidelines should be followed:

1. It can only be applied within the linear BET model regime, usually between 0.05 P/P_0 and 0.35 P/P_0 , although the range can be adjusted narrower to give the highest linear regression coefficient ($R^2 \approx 1$).
2. The y-intercept or C value must be positive as a negative value directly implies that it no longer follows a linear profile.

3.3.2 Pore size distribution analysis

From the measured N_2 adsorption isotherms, the pore size distribution (PSD) of the samples can be estimated using several models based on slit, cylindrical or spherical pore shapes. The most commonly applied model is the BJH model (Barrett, Joyner & Halenda, 1951). However, De Lange et al. found that BJH-pore size distributions could be problematic due to the overlooked desorption hysteresis in a sample, caused by different material's tensile strength effect. For the conclusions to be quantitatively acceptable, De Lange et al. suggested:

1. To compare the pore size distribution of both the adsorption and the desorption branch to ensure any tensile strength effect-related artefact is absent.
2. To avoid introducing artificial desorption hysteresis and erroneous pore size distribution, one needs to use an optimum ratio of manifold and cell volume, preferably between 2 and

3. In other words, a large sample cell volume (> 10 mL) or small sample mass (< 0.5 g for a weakly adsorbing material, $< 0.2 - 0.3$ g for a moderately adsorbing material and < 0.1 g for a strongly adsorbing material) will increase the possibility of widening the hysteresis gap between the adsorption and the desorption curves.

The BJH method is underpinned by the Kelvin equation of pore filling which has been modified to include multilayer adsorption. For materials with cylindrical pores, the Kelvin equation is shown as Equation 3.5 where γ is the surface tension of the bulk fluid, V_m is the molar liquid volume, r_p is the pore radius and t_c is the thickness of the adsorbed multilayer film before capillary condensation happens.

$$\ln\left(\frac{P}{P_0}\right) = -\frac{2\gamma \cdot V_m}{RT(r_p - t_c)} \quad \text{Equation 3.5}$$

3.3.2.1 Limitations of BJH method for microporous materials

The BJH method (based on the Kelvin equation) is suitable to simulate the pore size distribution of most meso and macroporous materials, but it becomes erroneous for microporous materials. This limitation is because as the pore radius gets smaller, the intra-pore adsorptive forces are enhanced and the gas property deviates from a typical bulk liquid-like behaviour, thus, requiring a more complex model to determine the porosity accurately. Normally, for microporous materials with a pore size < 2 nm, the Horvath-Kawazoe method is used.

Sophisticated modelling methods such as the density functional theory (DFT) and Monte Carlo simulation have been developed for deeper understanding of the adsorption phenomena in complex scenarios. For instance, a refined version of DFT for gas adsorption analysis, known as the non-local DFT model is now a default method in most commercial porous analysis software due to its good applicability to visualize a material's pore size distribution across all three porosity hierarchies (Micromeritics, 2020).

The implementation of a non-local density functional theory model is a two-step process, all handled by the software. Firstly, users need to choose a reference, theoretical isotherm model, known as a kernel. Then, the software will use a series of complex mathematical algorithms to fit the experimental data to the chosen kernel.

In this thesis, the porosity of the synthesized materials was measured on 3Flex (Micromeritics, UK) BET analyser using N₂ at 77 K. The Tristar (Micromeritics, UK) analyser was only used to collect the N₂ isotherms for silane-coated MIL-100 samples in Chapter 6. Unless otherwise stated, the sample pre-treatment usually involves activation at 150 °C under vacuum overnight followed by an *in-situ* degassing at 120 °C. All N₂ measurements were performed between 0 and 0.99 P/P₀. For the pore size distribution analysis, a non-local density functional theory based on Tarazona model was chosen. The materials were assumed to have a cylindrical pore geometry.

3.4 Fourier-transform infrared (FTIR) spectroscopy

Fourier-transform infrared spectroscopy (FTIR) is a simple non-destructive technique that uses infrared radiation (IR) to determine the functional groups in a sample. FTIR can also be used to identify unknown compounds and to study a reaction's progress. Compared to the visible light, IR has a longer wavelength and a lower frequency which enables IR to pass through an object with less scattering and absorption. FTIR technique is also known as absorption spectroscopy whereby the emission of the IR light through a sample can cause the molecular bonds to experience measurable vibrational transitions. Depending on the types of chemical bond available in a molecule, they will selectively absorb or transmit some wavelengths from the emitted IR. If the energy of the IR light matches with the energy needed to initiate the molecular vibrations, the IR light will be absorbed and vice versa. Each functional group (such as carboxylic acids, alcohols, ketones) has its own characteristic vibrations which are represented by different bands in an IR spectrum. The region where most of these characteristic vibrations are present is also termed the fingerprint region, located at the lower end of the mid-IR region (4000 to 400 cm⁻¹).

In the early days of IR spectroscopy developments, the dispersive spectrometer was the main instrument type until the FTIR spectrometer was introduced and later became the standard of modern IR analysis. The FTIR spectrometer has three main advantages over the dispersive design:

1. Faster data collection since the interferometer in a FTIR spectrometer does not separate the incident IR into individual spectral components to measure the IR spectrum like the dispersive system. A dispersive spectrometer uses a diffraction grating to measure each wavelength individually. In FTIR, the simultaneous measurement of all IR frequencies makes it a much faster spectral acquisition process than a dispersive instrument.
2. Higher sensitivity due to higher signal-to-noise ratio. As a result, small peaks on the FTIR spectrum can be observed clearer. Because the dispersive instrument uses a slit to limit the individual wavelength, there can be significant losses of IR energy projected to the sample, hence, transmitted light to the subsequent detector. Less mirrors in a FTIR spectrometer also helps to lower reflection losses compared to dispersive instruments.
3. Higher accuracy and precision due to the use of laser in controlling the velocity of the moving mirror. The laser also has a constant wavelength that simultaneously acts as an internal wavelength calibrator in which the measured x-axis data points in a FTIR spectrum are always referenced to. This minimizes data fluctuation even when measuring the same sample on different days apart. Such laser precision capability is not available on a dispersive instrument as it requires external calibration standards to improve its measurement accuracy.

At the core of every FTIR spectrometer is the interferometer system. It comprises an IR radiation source, beam splitter, two mirrors, a laser, and a detector. IR radiation sources are usually thermally stable solids that can be electrically heated to release IR radiation. The most ubiquitous in use is the silicon carbide rod (Globar) given its high thermal stability and ability to produce significant quantities of IR radiation. The radiated IR then reaches the beam splitter, which as the name suggests, separates the IR towards two mirrors, a fixed and a moving mirror. The moving mirror's movement velocity is timed and adjusted by the internal system in accordance with the precise laser wavelength. The reflected beams from the two mirrors eventually meet again at the beam splitter.

However, the different distances (optical path difference, OPD) travelled by the two reflected beams from the fixed and moving mirror respectively will result in constructive (visible) and destructive wavelength (not visible) interferences, giving rise to an interferogram signal. It is a function of signal intensity versus time (derived from the OPD, cm).

The interferogram then moves from the beam splitter to the sample which absorbs some of the energy while the remainder is transmitted to the detector. The most widely used detector materials are deuterated L-alanine doped triglycine sulphate (DLATGS) and cooled mercury cadmium telluride (MCT), with the MCT detectors offering superior detection sensitivity.

In the final stage, the interferogram signal that reaches the detector is converted by the software via Fourier transform algorithm to generate its fingerprint spectrum, displayed in the form of intensity of signal/transmittance (%T) against wavenumber (cm^{-1}). A Fourier transform is a mathematical approach to modify a function into a new function. In this case, the Fourier transform of the interferogram can be regarded as the inversion of OPD (cm) into inverse centimetres (cm^{-1}) as the x-axis. The inverse centimetres are also known as wavenumber.

Table 3.1: Specifications of the FTIR spectrometer used in this thesis.

Instrument	Cary 630 FTIR (Agilent, USA)	Spectrum 100 FTIR (Perkin Elmer, USA)
Sampling technique	Attenuated total reflection (ATR) sampling technique with a diamond tip	
When it was used	To characterize the materials in Chapter 6 and 7	To characterize the materials in Chapter 4 and 5
Resolution (cm^{-1})	0.93	0.5
Scanning range (cm^{-1})	650 – 4000	450 – 4000

Table 3.1 shows the specifications of the FTIR spectrometers used in this thesis. Note that FTIR sampling techniques can vary between transmission, attenuated total reflectance (ATR), spectral and diffuse reflection. A spectral reflection technique suits measurement of liquids, thin films, and bulk materials while a diffuse reflection works best on powders.

Transmission technique was mostly used in the initial FTIR spectroscopy developmental stages, but the usage of sample cells for analysis is prone to errors and time-consuming. Nowadays, ATR is the mainstream technique due to its quick measurement process and ability to measure a broad range of sample types.

During an ATR experiment, the incident IR light is internally reflected at the crystal-sample interface and the reflected light is directed to the FTIR detector (Figure 3.4). The un-reflected portion of the light is absorbed by the sample and is also termed as the evanescent wave. The penetration depth of the evanescent wave into the sample is dependent on the reflective index difference between the ATR crystal and the sample. So, different crystal types can be chosen to measure different sample types. By and large, diamond is the most used crystal given its high chemical resistance and wide detection limits although germanium and zinc selenide may also be used for certain materials.

For the measurement protocol, the ATR tip should first be cleaned with a tissue wetted with isopropanol to remove residual contaminants. Then, very little quantity of liquid (1 drop from a plastic pipette) or solid samples (1 scoop of a small spatula resembling 1 grain of sand) can be placed on the ATR tip. To start the measurement, a background scan (without a sample) is performed prior to measuring the sample. The software will subtract the background spectrum to produce only the sample's transmittance (%T) spectrum.

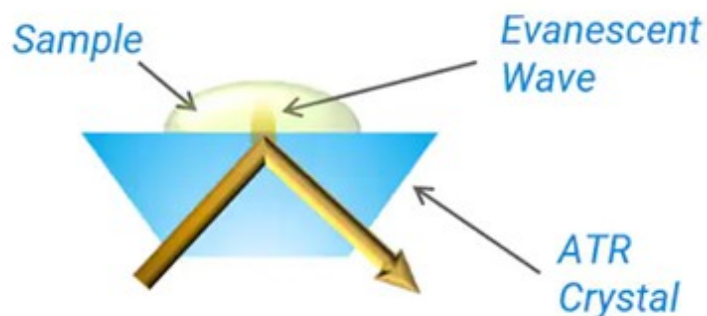


Figure 3.4: A sample image of an ATR sampling method in a modern FTIR spectrometer (Agilent, 2021).

3.5 Scanning electron microscopy (SEM)

A scanning electron microscope (SEM) uses reflected electrons on a sample to create a high-resolution image under vacuum. The electrons are produced from an electron source which are further accelerated by the anode and the various internal lenses adjust their pathways to help focus the electron beam onto the sample. As the electrons reach the sample surface, many different types of electrons are produced, but in the case of SEM imaging, they are primarily backscattered and secondary electrons. Backscattered and secondary electrons can provide insights into the deeper and surficial (topography) regions of a sample, respectively. Additionally, the sample-electron interactions could also generate element specific x-rays that can be used to analyse the sample's elemental compositions. This method is commonly called energy dispersive x-ray analysis – EDAX or EDXA.

To improve the image quality, non-conductive samples need to be coated with electrically conductive materials such as gold, palladium, platinum, silver, chromium, or iridium. The coated samples will inhibit static electricity collection and thus, avoiding artefact formation in the SEM images as well as reducing beam damage. To prepare for SEM imaging, the samples synthesized and studied in this thesis were mounted on specimen holders covered with carbon tape and then sputter-coated with a 15 nm-thick chromium layer. The SEM images were acquired using a field emission gun (FEG) SEM Zeiss Leo Gemini 1525 operated in secondary electron imaging mode at 5 kV accelerating voltage.

3.6 Water contact angle

The contact angle a liquid droplet makes when placed on a solid surface provides an indicator of a solid sample's surface wettability. By measuring the water contact angle (θ_c) at the three-phase contact line (between the liquid droplet, the solid surface, and the atmosphere), one can determine whether the solid surface is hydrophilic ($< 90^\circ$), hydrophobic ($90^\circ - 150^\circ$) or superhydrophobic ($> 150^\circ$). The θ_c of a liquid droplet on an ideal solid surface is governed by Young's equation shown in Equation 3.6.

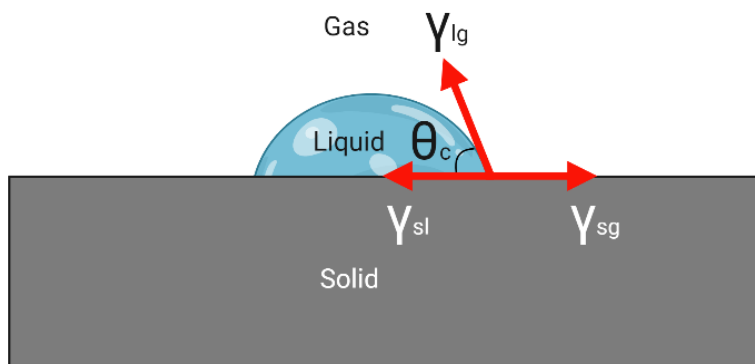


Figure 3.5: Contact angle forces.

$$\cos \theta_c = \frac{\gamma_{sg} - \gamma_{sl}}{\gamma_{lg}} \quad \text{Equation 3.6}$$

Where γ_{sg} is the solid's surface free energy, γ_{lg} is the liquid's surface tension, and γ_{sl} is the solid-liquid interfacial tension. A simplified illustration of the variables involved is shown in Figure 3.5. When the liquid is water, it has a constant surface tension (γ_{lg}) for a specific temperature, thus, the water's θ_c is dependent on γ_{sg} and γ_{sl} . Equation 3.6 assumes that the three forces must be in equilibrium at the three-phase contact line. Therefore:

1. If $\gamma_{sg} < \gamma_{sl}$, then $\cos \theta_c$ is negative where $\theta_c < 90^\circ$, hence, the droplet wets. This behaviour can happen on a high-surface energy solid.
2. If $\gamma_{sg} > \gamma_{sl}$, then $\cos \theta_c$ is positive which gives $\theta_c > 90^\circ$, a common feature of a hydrophobic and a low-surface energy solid. Since this property is the desired goal in this thesis, treating the adsorbent solids with low-surface energy compounds such as $-\text{CF}_3$ or $-\text{CH}_3$ groups or with nonpolar hydrocarbon fragments having γ_{sg} values between 10 and 30 mJ/m^2 can be a feasible idea (Jayaramulu *et al.*, 2019).

Ideally, the Young's equation assumes the solid surface to be homogenous, smooth, and inert. However, surfaces of MOF samples either in their crystals forms, or as a loose powder, or pelletized forms, differ considerably from these assumptions due to their innate roughness and/or chemical reactivity. As a result, the force balance at the three-phase contact line can be severely

affected, thus, giving inconsistent θ_c measurements. Implementation of other equations such as the Wenzel and Cassie-Baxter equations may be able to account for their roughness and surface heterogeneity (Xie *et al.*, 2020), altogether, providing more accurate θ_c values. It is also pertinent to reiterate that a static contact angle measurement, despite its frequent use, may vary considerably even when testing the same sample as it can be easily influenced by many factors such as surface deformation, liquid evaporation, slow spreading of the liquid and the manner how the drop is deposited onto the surface. Advancing and receding contact angle techniques are better options to measure a sample's contact angle (Figure 3.6).

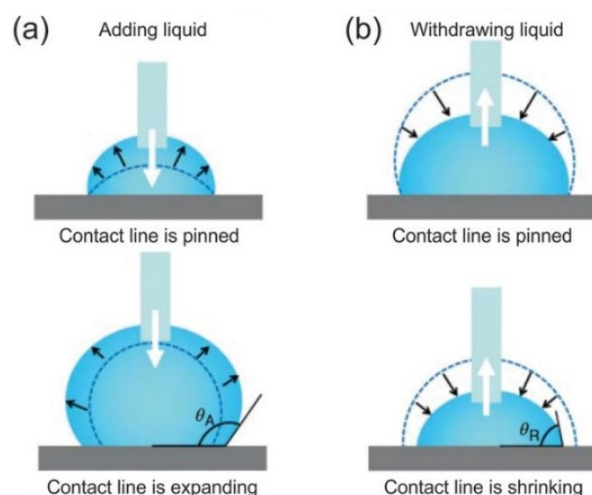


Figure 3.6: Illustrations showing (a) the advancing contact angle measurement technique involving liquid addition to an existing droplet and (b) the receding contact angle measurement technique that removes the liquid from an existing droplet. Image is reproduced with permission from (Jayaramulu *et al.*, 2019). Copyright 2019, Wiley-VCH.

In an advancing contact angle technique (Figure 3.6a), the liquid is added at a rate of around 0.5 $\mu\text{L/s}$ or less onto the existing droplet. As the addition proceeds, the droplet continues expanding until the base three-phase contact line moves outwards from its critical advancing contact angle (θ_A). Figure 3.6b shows the receding contact angle technique, where the liquid is instead removed at the same rate from an expanded droplet until the base contact line moves inwards from its critical receding angle (θ_R). However, a sample's θ_c value is only representative of its degree of surface hydrophobicity. What is more imperative is to investigate the surface treatment advantages on a MOF's internal hydrophobicity for VOC capture. The static water contact angle measurement

technique (labelled as θ_c) was used only for preliminary/material screening experiments whereas in other circumstances, the advancing technique (labelled as θ_A) was opted.

In this thesis, KRÜSS drop shape analyser was used to measure the samples' θ_c and θ_A at ambient temperature. The samples were measured either in their pelletized or loose form. To prepare a cylindrical pellet with a flat face, about 150 mg of MOF sample was placed into a powder pelletizer (13 mm diameter pellet dies, Specac Ltd., UK). An external pressure up to 9 tonnes was applied on the pelletizer using a manual hydraulic press and held for about 30 seconds to yield a uniformly pressed pellet. It is well understood that a surface's contact angle can be influenced by the surface roughness, especially, in the case of a pelletized MOF. Therefore, a pelletized MOF was no longer used for subsequent measurements, but was instead substituted with the original MOF loose form. Where a pellet was not used, the MOF powder was placed on a glass slide with 1.5 cm \times 1.5 cm double-sided tape attached to it. The MOF powder was flattened on the tape segment by pressing it with another slide on the top, and non-adhered powder was tapped free from the slide to create a cleaner surface. See Figure 3.7 which shows a MOF pellet and a slide coated with MOF powder.

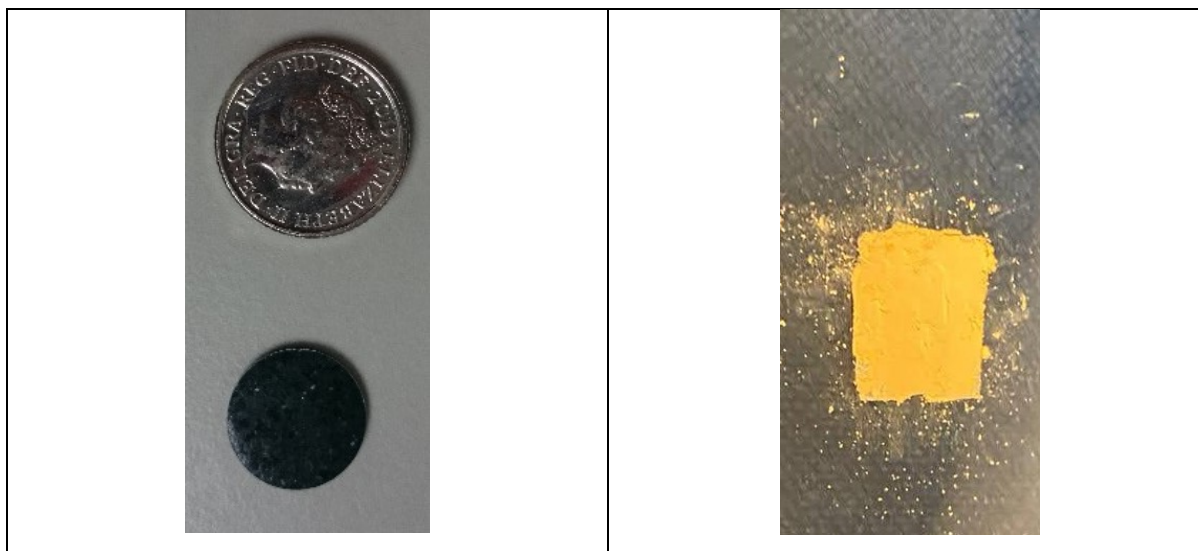


Figure 3.7: Images of (left) a pelletized, green-coloured MIL-101 (Cr) and (right) a uniformly pressed, orange-coloured MIL-100 (Fe) powder on a glass slide.

3.7 Static vapor sorption

Single-solvent sorption experiments were performed at 25 °C in static and vacuum mode using IGA-002 gas and vapor sorption analyser (Hiden Isochema, UK). Vapour sorption analysis is usually performed at low pressures (< 100 mbar) whereas a gas sorption experiment almost always involves higher pressures (> 1000 mbar). In this thesis, only the vapor operation under vacuum will be covered. Figure 3.8 shows the schematic of an IGA system. The system can be set with an operating temperature ranging between 77 K (-196 °C) to 1273 K (1000 °C). This function is also useful to conduct in situ sample degassing. However, in this thesis, all samples tested on IGA-002 were preheated overnight at 150 °C in a vacuum oven to eliminate the time for an additional degassing here.

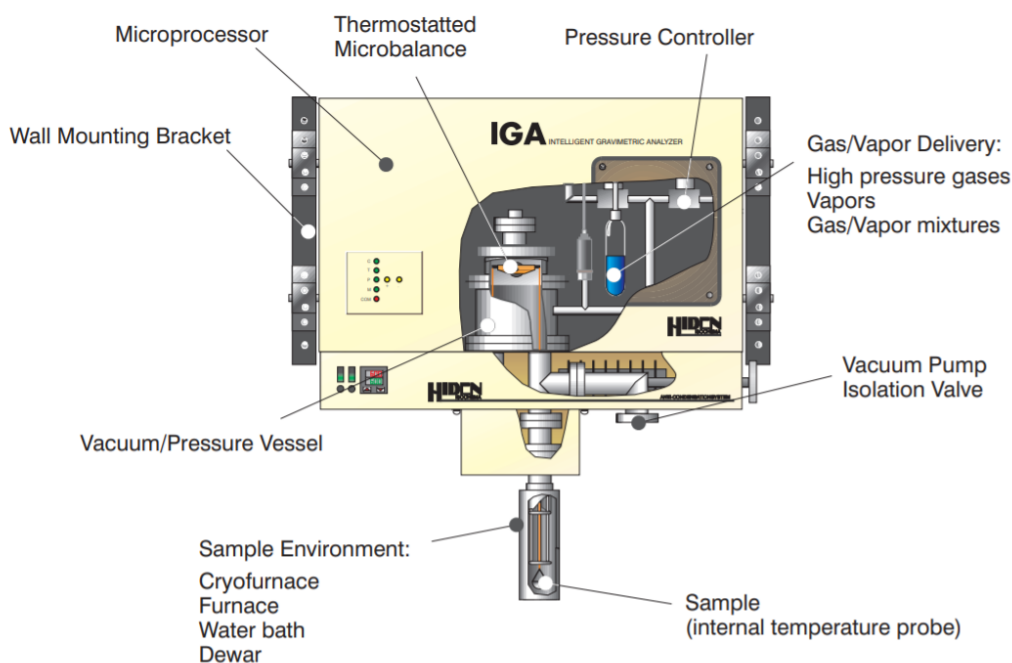


Figure 3.8: A disassembled picture of an Intelligent Gravimetric Analyser (IGA). Image is taken from (Hiden Isochema, 2021).

For experiments using operating temperatures lower than 333 K (60 °C), an isothermal environment is provided by immersing the sample holder in a water bath filled with polyethylene glycol antifreeze solution, whereas a furnace is used to maintain it at higher temperatures. When selecting the vapour adsorbate to be analysed, it is instrumental to know the vapour's saturation

pressure (P_0) at the temperature of investigation. For example, at 25 °C, the P_0 for water and toluene are 31.7 mbar and 37.5 mbar, respectively. Next, the system will request a series of pressure setpoints, a minimum and a maximum measurement time. Note that the IGA software attempts to predict the kinetics of a tested solid when the solid's mass change approaches 99 wt% or known as the asymptote relaxation. After it achieves 99 wt%, the system will move on to the next pressure setpoint. Figure 3.9 shows an example of a toluene sorption isotherm method development on the IGA software.

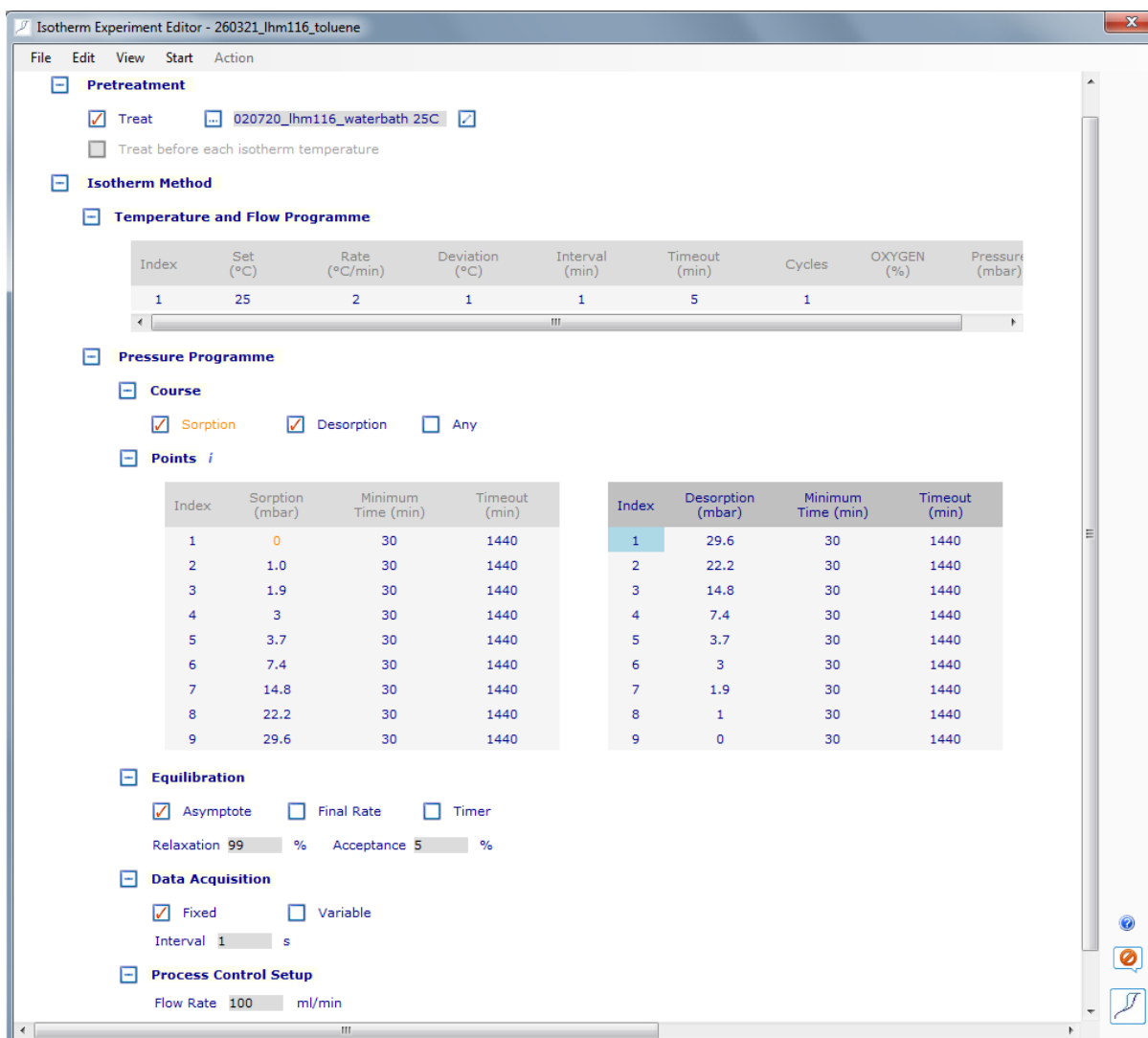


Figure 3.9: A sample image of the user interface on the IGA software when setting a toluene vapour adsorption and desorption isotherm experiment at 25 °C.

In the “Isotherm Method” tab, users can choose to conduct either an adsorption or a desorption isotherm only, in single or multiple cycles (e.g., for reusability study). The maximum experimental pressure setpoint is best kept lower than 80% P_0 to avoid condensation in the sample chamber. For toluene at 25 °C, this will be ≤ 30 mbar. Any experimental problems such as out of range maximum pressure setpoint (e.g., setting a toluene pressure setpoint at 40 mbar although it has a maximum $P_0 = 37.5$ mbar at 25 °C) or incorrect valve positioning (e.g., opening the wrong valve meant for a high-pressure gas sorption analysis instead) will be alerted by the software before initiating the measurement.

Figure 3.10 displays the main sensor readings on the IGA software. For sample preparation, the sample pan is tared and later, between 30 – 100 mg of porous material is placed inside the mesh pan (shown in the “Total Weight” column). As soon as the microbalance detects a stable reading (± 0.01 mg), air needs to be evacuated from the system, as the system is initially at atmospheric pressure (1013 mbar) to decrease to 0 mbar (current system pressure is shown in “Pressure(1)”).

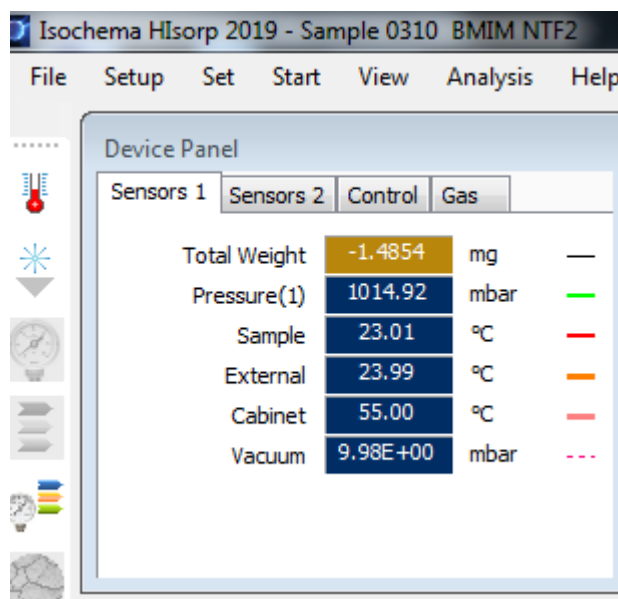


Figure 3.10: The main sensor display window of the IGA software.

The first air evacuation process by a rotary vane vacuum pump will take a while, but there could be a situation when it is really close to 0 mbar, yet seemingly not going to reach 0 mbar. So, the vacuum pump isolation valve (PIV-1) at the bottom of the IGA machine could be opened slowly to re-zero the pressure. Only if the “Pressure(1)” has reached 0 mbar, then the turbo vacuum pump can be activated. Once the turbo vacuum pump is in operation, it will create a sufficiently vacuum condition (10^{-6} mbar) which is shown in “Vacuum” tab. While waiting, the solvent of interest can be filled into the solvent container. This is the blue reservoir in Figure 3.8 that houses the solvent to be vaporized. The IGA system will next prompt the user to conduct an inlet decontamination protocol to clear the pipelines from residual solvents.

By now, the system is ready to run. The adsorbate pressure in the sample chamber will start to increase to the specified initial P setpoint. Once the pressure sensors confirm a steady setpoint, then the weight data is recorded within the stipulated time (1440 mins) and equilibrium limits (99%) before moving on to the next pressure setpoint until the whole isotherm cycle completes. From the real-time sample weight data, the software can generate kinetics parameters and make prediction of the equilibrium uptake. All equilibrium mass uptakes are then plotted as an isotherm either as sample mass change (wt%) (y-axis) against pressure (mbar) or against time (min) as the x-axis.

On a separate occasion, to validate the accuracy of the IGA-002 instrument and its associated measurements, a water sorption experiment at 25 °C was repeated for 3 times using an industrial-standard activated carbon (AC) F400. Figure 3.11 displays the water sorption measurements to be within a standard deviation range of 4.4% (at the highest water % $P/P_0 = 79\%$) to 22.0% (at the lowest water % $P/P_0 = 3.2\%$). It is reasonable to observe that the standard deviation is the highest at low % P/P_0 and vice versa. In other words, this indicates that the IGA machine has better precision in controlling the solvent pressure when operating at higher % P/P_0 compared to at a low % P/P_0 . The full details of the standard deviation values can be found in Section 10.1.2.

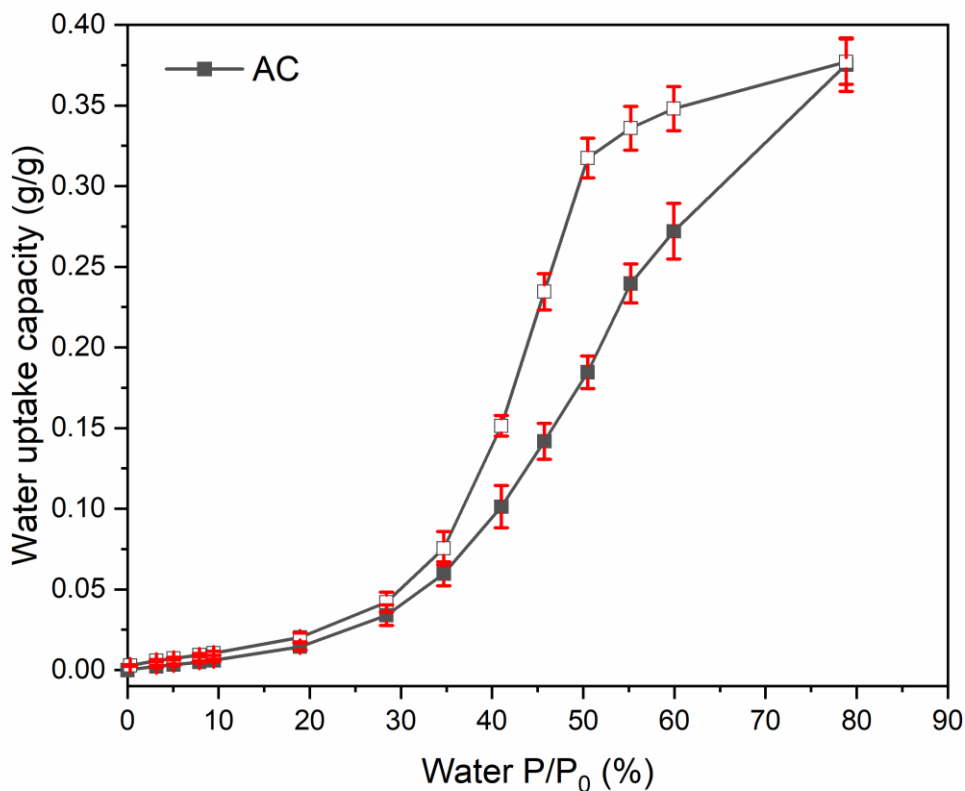


Figure 3.11: IGA measurement validation based on water sorption isotherms by AC at 25 °C. Filled symbols are the adsorption isotherms whereas empty symbols shapes are for desorption.

Despite the well-accepted hydrophobicity of AC, the presence of polar functional groups mainly at the surface can act as the nucleating sites for water to attach and consequently form clusters, thus, leading to high water adsorption capacity and poor VOC adsorption in highly humid conditions. In this regard, Do et al. have developed a model to describe the adsorption and desorption of water in AC (Do, Junpirom & Do, 2009). Do et al. tried improving the previous models' accuracy by considering the isotherm hysteresis to be due to the difference in water clustering mechanisms during the adsorption and the desorption processes. Specifically, due to the slow relaxation and reorientation of water clusters inside the micropore.

Do et al. tested their proposed model's applicability by fitting the experimental water sorption data at 25 °C on BPL AC (also another industrial-standard material) obtained from the original work by Barton et al. (Barton *et al.*, 1984). Figure 3.12 shows the original water adsorption and desorption data by Barton et al. that is fitted with the proposed model by Do et al. Generally, the water sorption behaviour on the BPL AC (Figure 3.12a) matches closely with the data from the AC F400 studied in this thesis (Figure 3.11), suggesting that both materials have met the same strict industrial production quality controls. Therefore, making them eligible to be used as a reference adsorbent in this thesis.

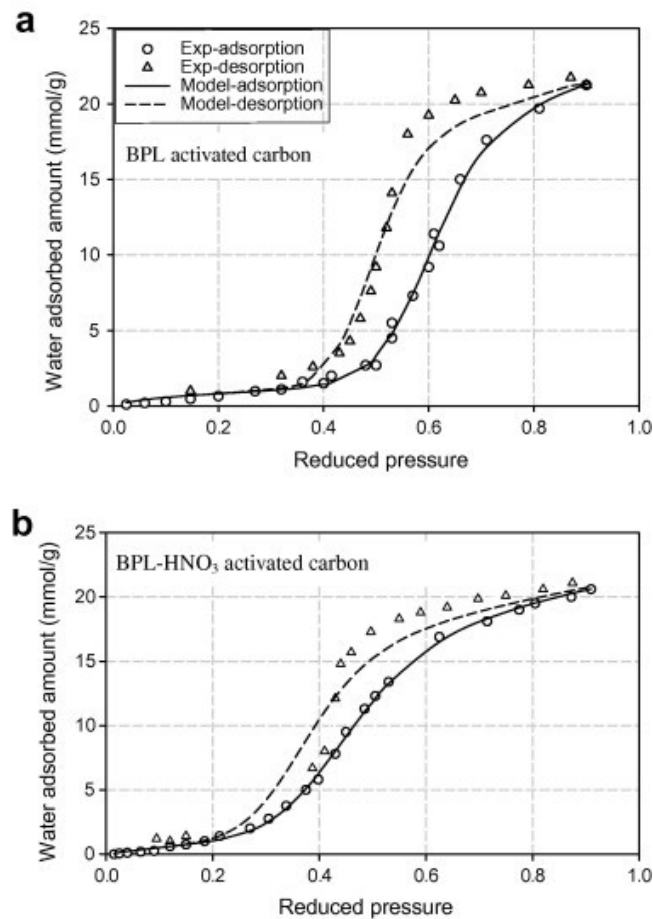


Figure 3.12: Experimental and model-fitted water sorption data at 25 °C of (a) BPL activated carbon and (b) nitric acid-treated BPL activated carbon. Image is reproduced with permission from (Do, Junpirom & Do, 2009). Copyright 2009, Elsevier.

3.8 Dynamic vapor sorption

The dynamic and competitive sorption isotherms were collected using DVS Resolution (Surface Measurement Systems, UK). Like IGA-002, this instrument also uses a gravimetric sorption technique to measure the change of adsorbent mass after being exposed to a specific vapor concentration at ambient pressure, but the DVS operates without using vacuum. The technical advantages of a DVS equipment over the IGA are as follows:

1. A broader range of organic solvents can be studied.
2. The pre-drying and the sorption experiments are performed under continuous air/nitrogen flow that reflects a more realistic operational setting.
3. The binary solvent operation permits competitive adsorption experiments through manipulation of the humidity levels (solvent reservoir 1) whilst adsorbing any organic solvent (solvent reservoir 2). This setup can be adjusted accordingly to suit the nature of a material's application.
4. Another related model, DVS Endeavour allows parallel running of 5 samples which can substantially reduce analysis time.
5. The DVS software package combines multiple quantitative analysis models for a comprehensive visualization and evaluation.
6. The built-in preheater and an ultra-sensitive microbalance provide a well-controlled experimental temperature and minimal requirement of sample mass as low as 10 mg. For information, the measurement temperature of this current work was maintained at 25 °C.

Figure 3.13 shows the schematic of a DVS Resolution, a dual-vapor gravimetric analyser that can measure a solid's (only 1 solid for one measurement) uptake capacity of an organic solvent across a range of organic vapour pressures. Typically, in a competitive experiment mode, a known concentration of water vapor is passed over a sample placed inside a sample pan. The pan is connected to an ultra-sensitive mass balance that can measure real-time mass changes either caused by adsorption or desorption of gas molecules. Dry air was used as the carrier gas for each solvent reservoir with an equivalent individual flow of 200 sscm, totalling the system to 400 sscm. The unit's mass flow controllers (MFC) control both the air and the solvent vapour flow rates.

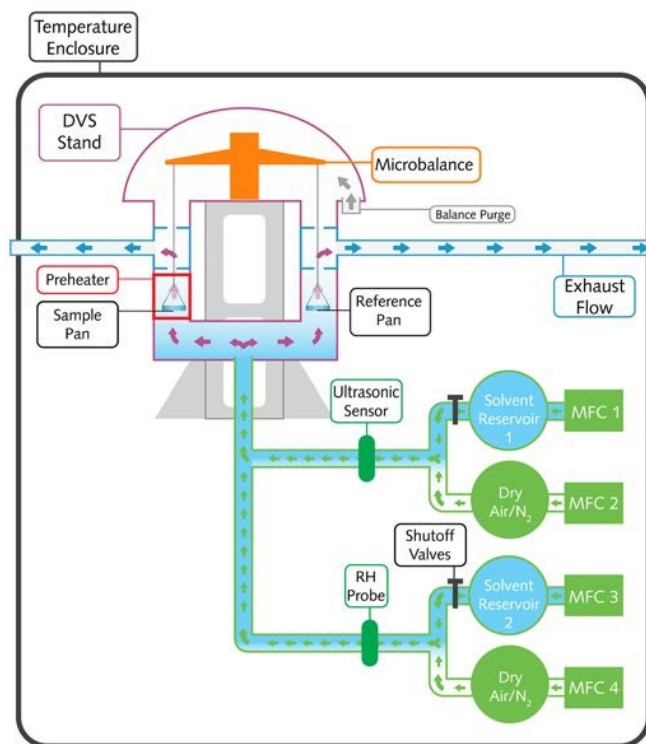


Figure 3.13: A schematic diagram of the working principles inside a DVS Resolution.

In this thesis, samples weighing around 15 – 100 mg were used for analysis. The sample pans were first calibrated with 100 mg standard weights and tared prior to transferring the samples. All samples studied with the DVS were already preheated overnight under vacuum condition at 150 °C. At each partial pressure (% P/P₀) setpoint, the mass stability limit (dm/dt) was set at 0.001 with a maximum measurement time of 1440 mins (1 day) for each pressure setpoint. When a sample displays a mass change of ± 0.001 wt%/min, this will ensure that the sorption process at a particular % P/P₀ has fully reached equilibrium. However, in certain situations, for example, when testing a very hydrophilic material, it may continue adsorbing water for a very long period before it could reach the specified dm/dt , possibly more than 1440 mins. Although it may have a high water uptake capacity, but if the uptake rate has not reached equilibrium within 1440 mins, it is too slow to be considered as an effective adsorbent for real-world scenarios. So, by specifying this time threshold, it will allow better identification of an ideal adsorbent: possessing a high uptake capacity alongside a fast uptake rate. After the sample achieves whichever of the two conditions first, only then the DVS system will move on to the next setpoint.

Before starting any adsorption experiment, the samples were dried at 0% RH until they reached a constant mass. For a competitive adsorption, to mimic real-world conditions, the samples were pre-exposed in separate experiments at 40 and 80% P/P₀ or RH of water vapor. It is acknowledged that factors such as geographical, seasonal, and building environments can influence the average building humidity levels. However, 40% RH can be reasonably considered as a typical daily average indoor value and is the focus for the current study. At the higher humid condition of 80% RH, the samples showed negligible toluene uptake because water adsorption process has occupied virtually all the available adsorption sites.

Therefore, the performance of all adsorbents was only evaluated at 40% RH for two separate toluene concentrations of 0.5% P/P₀ (188 ppm) and at 10% P/P₀ (3750 ppm), representing an environmental VOC concentration of interest, and concentration from an industrial solvent separation/recovery process, respectively. Toluene was chosen as a hydrophobic VOC model molecule. It is a relatively common environmental VOC with Occupational Safety and Health (OSHA) toxicity exposure limits in the 100 to 500 ppm range. Specifically, the 188 ppm toluene concentration is in the mid-range of the environmental concentration for human exposure; the OSHA Permissible Exposure Limit is 200 ppm while the National Institute for Occupational Safety and Health (NIOSH) Recommended Exposure Limit (REL) is 100 ppm (United States Department of Labor, 2021b). The desired relative humidity is generated by mixing the dry air and saturated water (solvent reservoir 1) in certain flow ratios with calculation examples shown below:

If solvent reservoir 1 contains water, to achieve 20% RH or 0.2 P/P₀ in the system:

$$\frac{\text{wet solvent 1 flow (sscm)}}{\text{total flow 1 (sscm)}} + \frac{\text{wet solvent 2 flow (sscm)}}{\text{total flow 2 (sscm)}} = \frac{80(0.5)}{200} + \frac{0(0.5)}{200} = 20\% RH$$

The 0.5 multiplication factor on the numerators is necessary because Flow 1 and Flow 2 each contributes 50% to the total 400 sscm flow.

Similar steps are applied to generate a desired relative pressure for toluene (solvent reservoir 2). When solvent reservoir 2 contains toluene, to get 0.5% or 0.005 toluene P/P_0 in the system:

$$\frac{\text{wet solvent 1 flow (sscm)}}{\text{total flow 1 (sscm)}} + \frac{\text{wet solvent 2 flow (sscm)}}{\text{total flow 2 (sscm)}} = \frac{0(0.5)}{200} + \frac{2(0.5)}{200}$$

$$= 0.005 P/P_0$$

To convert 0.5% toluene P/P_0 at 25 °C into parts per million (ppm):

$$\frac{\text{pressure of toluene at 25 °C (Pa)}}{\text{toluene saturation pressure at 25 °C (Pa)}} = \frac{19}{3800} = 0.005 P/P_0$$

$$\frac{\text{pressure of toluene at 25 °C (Pa)}}{\text{atmospheric pressure at 25 °C (Pa)}} = \frac{19}{101325} \times 10^6 = 188 \text{ ppm}$$

For single-solvent adsorption experiments, using either only water or an organic solvent, all steps will be the same except that only the respective solvent reservoir is used in an experiment. To help readers understand the experimental procedures better, Section 0 describes the steps involved in setting up a competitive adsorption experiment on a DVS.

As previously stated, to validate the precision of the DVS measurements, triplicate sorption experiments were performed on AC covering competitive water-toluene adsorption at 40% RH/0%, 0.5% and 10% toluene P/P_0 . It has been stated previously in Section 3.7 that the reason to choosing AC as a model adsorbent is due to its highly standardized bulk properties. A commercially sold AC will always go through rigorous quality control checks in its industrial manufacturing processes. So, it is reasonable to only account for the AC's final equilibrium adsorption capacities to quantify the standard deviation values.

Figure 3.14 shows that the DVS measurements on AC's uptake capacity have a standard deviation of 3.4% (at 40%RH/0% toluene P/P₀), 6.7% (at 40%RH/0.5% toluene P/P₀) and 0.7% (at 40%RH/10% toluene P/P₀). By extension and for simplicity, these standard deviation values may be applied to all experiments that employ the same toluene concentration irrespective of the material studied.

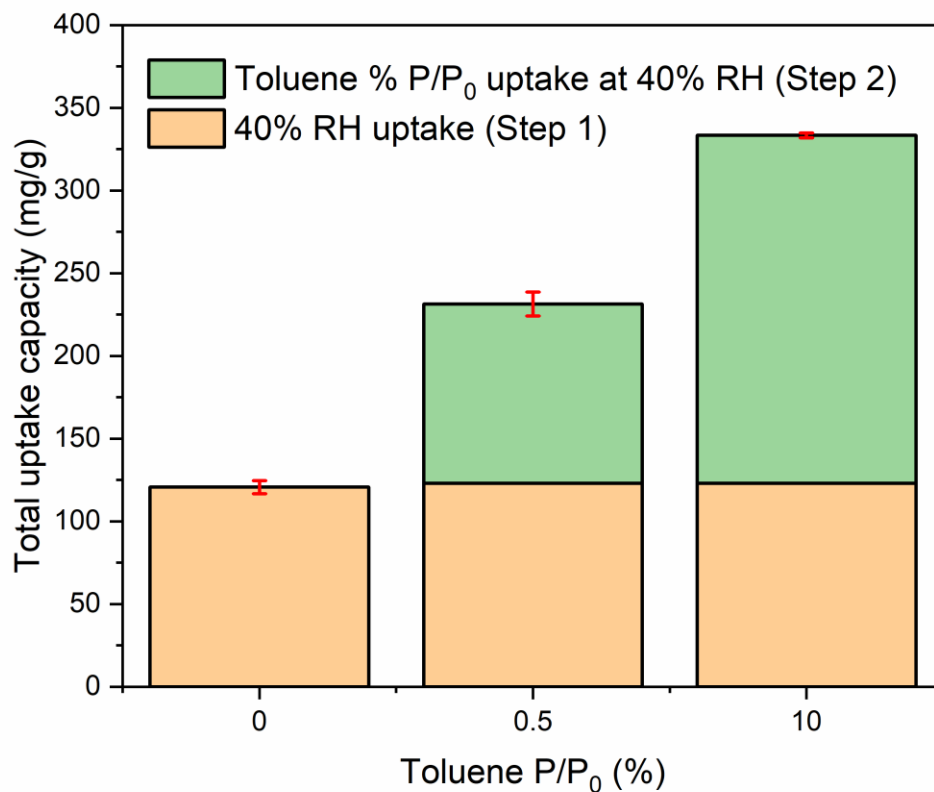


Figure 3.14: DVS measurement validation involving triplicate competitive adsorption experiments by AC at 25 °C and 40% RH using 0%, 0.5% and 10% toluene P/P₀.

3.9 Liquid-phase chlorophenol adsorption experiments (Chapter 4)

3.9.1 Materials

All chemicals used in this work were purchased from commercial suppliers and used without further purification. Chromium (III) nitrate nonahydrate ($\text{Cr}(\text{NO}_3)_3 \cdot 9\text{H}_2\text{O}$, 98.5%) was obtained from Alfa Aesar. Terephthalic acid (H_2BDC , 98%) and chromium (III) chloride hexahydrate ($\text{CrCl}_3 \cdot 6\text{H}_2\text{O}$, 96%) were purchased from Sigma-Aldrich. Anhydrous tin (II) chloride (SnCl_2 , 98%) and 2-chlorophenol (2-CP, 98%) were purchased from Acros Organics. 2-nitroterephthalic acid ($\text{NO}_2\text{-BDC}$, 95%) was purchased from Fluorochem. Solvents including ethanol (EtOH, 100%), N, N-Dimethylformamide (DMF, 99.9%) glacial acetic acid (AcOH, 100%), hydrochloric acid (HCl, 37%) and sodium hydroxide (NaOH, 50%) were all procured from VWR Chemicals. Working solutions were diluted accordingly with ultrapure water obtained from PURELAB Chorus ELGA. Granular AC F400, supplied by Chemviron Carbon was prepared from high grade bituminous coal and steam activated (Morlay *et al.*, 2005; Chemviron Carbon, 2013).

3.9.2 Hydrofluoric acid-free synthesis of MIL-101 (Cr) and MIL-101- NH_2

Synthesis of MIL-101 (Cr) was adapted from a previously reported method (Karikkethu Prabhakaran & Deschamps, 2015). $\text{Cr}(\text{NO}_3)_3 \cdot 9\text{H}_2\text{O}$ (2 g), H_2BDC (0.83 g), AcOH (0.29 mL) and 25 mL of ultrapure water were mixed in a 50 mL Teflon-lined bomb. The mixture was later sealed and heated in an oven at 220 °C for 8 hrs. When it cooled down to room temperature, the resultant fine, green crystals were thoroughly washed with DMF (20 mL \times 3) and EtOH (20 mL \times 3). Washing with each solvent was repeated thrice to clear unreacted H_2BDC from the product. The suspensions were centrifuged and then vacuum dried at 120 °C for 12 hrs to obtain dehydrated MIL-101 (Cr).

Amino-functionalized MIL-101 (Cr)-NH₂ was synthesized according to Bernt *et al.* (Bernt *et al.*, 2011). CrCl₃.6H₂O (0.27 g) and NO₂-BDC (0.21 g) were suspended with 5 mL ultrapure water in a 25 mL Teflon-lined bomb. The bomb was left in a preheated oven for 96 hrs at 180 °C. The resultant green solid was centrifuged, washed, and dried according to the aforementioned steps. The final product was designated as MIL-101 (Cr)-NO₂ which serves as an intermediate to obtain MIL-101 (Cr)-NH₂. Continuing from the previous synthesis, 0.1 g of MIL-101 (Cr)-NO₂, 3.3 g of SnCl₂.2H₂O and 20 mL EtOH were mixed, heated, and continuously stirred in an oil bath kept at 70 °C for 6 hrs. After it cooled down, it was centrifuged, washed with concentrated HCl (20 mL × 1), water (20 mL × 3) and EtOH (20 mL × 1) before finally dried under the same condition mentioned before.

3.9.3 Material characterizations

The simulated PXRD patterns for MIL-101 (Cr) was obtained from Mercury version 3.9 software suite using a CCDC code of OCUNAC (Zorainy *et al.*, 2021). The BET surface areas were calculated from the materials' N₂ sorption isotherms measured with Micromeritics 3Flex (for MIL-101 (Cr), MIL-101 (Cr)-NH₂, and AC) and Tristar (for MIL-101 (Cr) immersed in pH 1 and 11 for 3 days). The reported total pore volume was based on single point adsorption method. The materials' pore size distribution analysis was completed using the non-local density functional theory Tarazona model, assuming the pores are cylindrical. The FTIR spectra were analysed using Perkin Elmer Spectrum 100 FTIR spectrometer. Ultraviolet-visible (UV-vis) analysis was performed on Perkin Elmer Lambda 35 UV-Vis spectrophotometer. A background run was scanned between a wavelength spectrum (λ) of 200 and 300 nm using water as the base solvent. Around 1 – 1.5 mL of liquid solution was filled in the quartz cuvette for this analysis. The thermal stability of all adsorbents was investigated using thermogravimetric analysis (TGA) instrument Netzsch STA 449 F5 Jupiter[®] in N₂ atmosphere. The temperature was ramped from 20 °C to 1000 °C with a heating rate of 20 °C/min. The zeta potential and the particle size distribution of the adsorbents were measured using NanoBrook ZetaPALS (Brookhaven Instruments, USA) in 500 ppm 2-CP solution with 0.01 M NaCl as the electrolyte.

The morphology of the MOFs was studied using scanning electron microscopy (SEM). SEM images were collected with a high-resolution Schottky FEG-SEM (Zeiss Auriga Cross Beam) operating at 5 kV after the samples had been coated with chromium (15 nm thick). Elemental analyses for carbon, hydrogen, nitrogen, and sulphur (CHNS) were conducted with a CHNS analyser Vario MICRO cube (Elementar, Germany). The instrument uses helium as a carrier and flushing gas and the combustion is carried out by pulse injection of oxygen. KRÜSS drop shape analyser was used to measure water contact angle of MIL-101 (Cr) at ambient temperature. To prepare the sample, about 150 mg of MIL-101 (Cr) was pressed into a pellet. Generally, prior to conducting any characterizations or experiments, the samples were activated at 120 °C under vacuum for 12 hrs to clear the pores of any adsorbed solvent or gas molecules.

3.9.4 Batch adsorption of 2-chlorophenol (2-CP)

The 2-CP pollutant experiments were designed based on a reported method by Hasan et al. with some modifications (Hasan, Choi & Jhung, 2013). A stock 2-CP solution (1000 ppm) was prepared and diluted successively with ultrapure water to obtain the desired concentrations. First and foremost, a calibration curve (Figure 3.15) was generated by plotting the UV-vis spectra of self-prepared standard 2-CP solutions against its corresponding measured 2-CP's maxima absorbance wavelength (at $\lambda = 274$ nm). At least five 2-CP solutions (5 – 50 ppm) were measured with the UV-vis spectrometer to construct the calibration curve. The slope of the calibration plot in Figure 3.15 is directly taken as the molar absorptivity (L/mol.cm) or ϵ . This value is required in the Beer-Lambert's Law (Equation 3.7) to calculate the initial and the final concentrations of 2-CP in the solution. Parameter A is the absorbance, l is the path length of the cuvette (cm), and c is the concentration of the compound in the solution (mol/L). However, it must be reminded that Equation 3.7 is only valid at dilute concentration ($A < 1$). The molar absorptivity values will deviate at higher than 0.01 M concentrations due to electrostatic interactions between the molecules in close proximity. Therefore, if a solution's UV-vis measurement gives $A > 1$, it is too concentrated and needs to be diluted further.

$$A = \epsilon lc$$

Equation 3.7

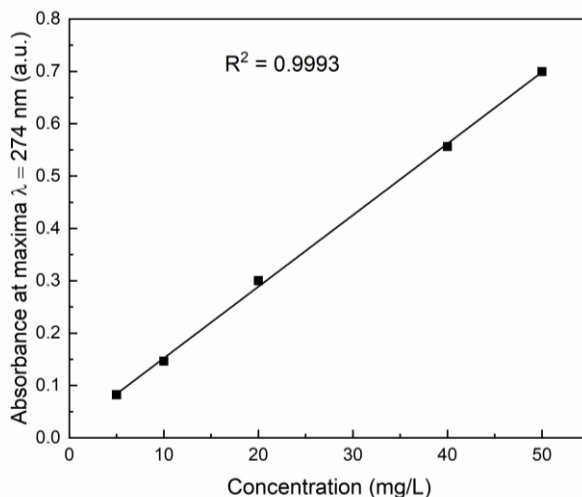


Figure 3.15: Calibration plot of 2-CP solutions with a molar absorptivity (ϵ) = 0.0137 L/mol.cm.

To set up the batch adsorption experiment, 5 mL 2-CP solution of different concentrations and 5 mg of each adsorbent (AC, MIL-101 (Cr), MIL-101 (Cr)-NH₂) were added respectively into glass vials containing magnetic stir bars. The solutions were continuously stirred and left to reach equilibrium for 24 hrs under ambient temperature. After the designated period, the mixtures were filtered with 0.22 μ m syringe filters. The filtrate was then diluted (0.5 mL aliquot: 10 mL ultrapure water). The residual 2-CP concentration for the samples was measured using UV-vis spectroscopy technique. All experiments were carried out in triplicate. The amount of 2-CP adsorbed was calculated using Equation 3.8 where C_0 and C_t (mg/L) are the initial concentration and the concentration of the solution at time t (min) accordingly. V (L) and m (g) represent the solution volume and the mass of adsorbent, respectively.

$$q_t = (C_0 - C_t) \frac{V}{m} \quad \text{Equation 3.8}$$

3.9.5 Adsorption isotherm modelling

Various adsorption isotherm models are available in the literature to analyse the liquid phase adsorption isotherms, the adsorbents' properties and most importantly, to estimate the maximum adsorption capacity of an adsorbent (Foo & Hameed, 2010).

In a recent review by Wang and Guo, 13 isotherm models were discussed in depth, as listed in Table 3.2. The models were further categorized into 5 main groups namely: (1) empirical, (2) based on Polanyi’s potential theory, (3) chemical adsorption, (4) physical adsorption and (5) ion-exchange (Wang & Guo, 2020).

Table 3.2: Classification of the 13 adsorption isotherm models (Wang & Guo, 2020).

Classification	Isotherm model name
Empirical adsorption isotherm models	Linear (Henry’s Law)
	Freundlich
	Redlich-Peterson (R-P)
	Sips
	Toth
	Temkin
Adsorption models based on the Polanyi’s potential theory	Dubinin-Radushkevich (D-R)
	Dubinin-Astakhov (D-A)
Chemical adsorption models	Langmuir
	Volmer
Physical adsorption models	Langmuir
	Brunauer Emmett Teller (BET)
	Aranovich
Ion exchange isotherm models	Homovalent ion exchange
	Monovalent and bivalent ions exchange

After surveying over 200 experimental adsorption datasets and the isotherm models that were used, Wang and Guo found the most common was the Langmuir isotherm model. It is usually used to model adsorption of metal ions, dyes, pharmaceuticals, and other types of organic pollutants onto adsorbents. The second most frequently used is the Freundlich model. Three reasons were identified for the preference of these two isotherm models. Firstly, owing to the simplicity of both methods (availability of linear model forms). Secondly, the Langmuir model describes an equilibrium condition consisting of a monolayer and homogenous adsorption which is the case for

most adsorption processes. The term “homogenous” refers to the macroscopic, uniform blending between the adsorbent and the solution due to rapid agitation. So, even though certain adsorbents have irregular shapes and non-uniform shapes from a microscopic perspective, their adsorption can still be represented by the Langmuir isotherm model. Thirdly, many adsorption processes are fundamentally driven by monolayer chemisorption (related to surface bonding) which agrees well with the Langmuir model’s assumptions. Therefore, based on these reasons, the adsorption data obtained in this Chapter will also be fitted using the Langmuir and the Freundlich isotherm models.

3.9.5.1 Langmuir adsorption isotherm model

Equation 3.9 presents a more specific nonlinear form of the Langmuir isotherm model compared to Equation 3.2 outlined in Section 3.3.1 earlier. Equation 3.9 requires two experimentally measured parameters, q_e and C_e , which are the equilibrium uptake capacity (mg/g) and the equilibrium concentration of the fluid (gas or liquid) phase (mg/L) respectively. With these inputs, the equation will be able to estimate two other parameters, q_m or the maximum Langmuir uptake capacity (mg adsorbate/g adsorbent) and K_L which stands for the Langmuir constant (L/mg). Since q_m is closely related to the adsorbent’s physical properties such as surface area and its affinity towards an adsorbate, its value is not dependent on the system temperature. However, q_m is subject to change for a range of reasons such as the solution pH values that can modify the existing adsorbate-adsorbent adsorption process.

$$q_e = \frac{q_m K_L C_e}{1 + K_L C_e} \quad \text{Equation 3.9}$$

On the contrary, K_L is a temperature-dependent parameter that indicates the extent of interaction between an adsorbate and an adsorbent. Higher K_L values usually imply a more favourable adsorption. The temperature dependence of K_L is described through the van’t Hoff equation, as shown in Equation 3.10, where ΔH and ΔS are the adsorption enthalpy and entropy respectively. R is the molar gas constant (8.3145 J/mol.K) and T is the system temperature in Kelvin (K).

$$K_L = \exp\left(\frac{\Delta S}{R} - \frac{\Delta H}{RT}\right) \quad \text{Equation 3.10}$$

The Langmuir adsorption nonlinear equation (Equation 3.9) may be variably expressed in six different linear forms (Osmari *et al.*, 2013) as shown in Table 3.3. From these six variants, the most widely used is the Langmuir-1 type model given its closest parameter estimation relative to the ones derived from the original nonlinear form regression. However, despite the frequent use of the linearized forms, the errors within the estimated parameters can propagate up to 40%, for instance, when using the Langmuir-4 form (Guo & Wang, 2019).

Table 3.3: The six linearized variations of the nonlinear Langmuir isotherm model.

Isotherm name	Linear form ($y = mx + c$)	Plot (y-axis vs x-axis)	Slope	y-intercept
Langmuir-1	$\frac{C_e}{q_e} = \frac{1}{q_m}(C_e) + \frac{1}{q_m K_L}$	$\frac{C_e}{q_e}$ vs C_e	$\frac{1}{q_m}$	$\frac{1}{q_m K_L}$
Langmuir-2	$\frac{1}{q_e} = \frac{1}{q_m K_L} \left(\frac{1}{C_e}\right) + \frac{1}{q_m}$	$\frac{1}{q_e}$ vs $\frac{1}{C_e}$	$\frac{1}{q_m K_L}$	$\frac{1}{q_m}$
Langmuir-3	$q_e = -\frac{1}{K_L} \left(\frac{q_e}{C_e}\right) + q_m$	q_e vs $\frac{q_e}{C_e}$	$-\frac{1}{K_L}$	q_m
Langmuir-4	$\frac{q_e}{C_e} = -K_L(q_e) + q_m K_L$	$\frac{q_e}{C_e}$ vs q_e	$-K_L$	$q_m K_L$
Langmuir-5	$\frac{1}{C_e} = q_m K_L \left(\frac{1}{q_e}\right) + (-K_L)$	$\frac{1}{C_e}$ vs $\frac{1}{q_e}$	$q_m K_L$	$-K_L$
Langmuir-6	$C_e = q_m \left(\frac{C_e}{q_e}\right) + \left(-\frac{1}{K_L}\right)$	C_e vs $\frac{C_e}{q_e}$	q_m	$-\frac{1}{K_L}$

The fundamental differences between using a linear and a nonlinear adsorption isotherm model have been described elsewhere by Subramanyam & Das (Subramanyam & Das, 2014) and Khandelwal *et al.* (Khandelwal *et al.*, 2020). In summary, and backed with multiple statistical evaluations, the authors proved that the transformation from an originally nonlinear to a linear form caused implicit addition of errors which amplify at higher solute concentrations, hence, the

reason to why regression using nonlinear models is preferred. However, if in instances when the linear form needs to be used, a R^2 close to unity (~ 1.00) should be sought. On the other hand, the fitting accuracy for nonlinear models is best described by their lower residual sum of squares (RSS) or reduced Chi-square (χ^2) error values.

3.9.5.2 Freundlich adsorption isotherm model

The Freundlich isotherm is an empirical model widely used to describe a non-ideal, reversible, and multilayer adsorption over a heterogeneous surface as opposed to the monolayer theory utilized by Langmuir (Freundlich, 1906). It is considered an empirical model due to the lack of physical meaning in its parameters and theoretical support (Wang & Guo, 2020). The equations can be seen in Table 3.4 where K_F is the Freundlich constant related to the adsorption capacity ($\text{mg/g}(\text{mg/L})^n$). $1/n$ is a parameter ranging from 0 to 1 which represents the adsorption intensity or surface heterogeneity with values approaching 0 as an indicator of the surface becoming more heterogeneous (Haghseresht & Lu, 1998).

Table 3.4: Details of the Freundlich adsorption isotherm model used in this study.

Isotherm	Nonlinear form	Linear form	Plot (y-axis vs x-axis)	Slope	y-intercept
Freundlich	$q_e = K_F C_e^{\frac{1}{n}}$	$\ln q_e = \frac{1}{n} \ln C_e + \ln K_F$	$\ln q_e$ vs $\ln C_e$	$\frac{1}{n}$	$\ln K_F$

3.9.6 Kinetics study for 2-chlorophenol adsorption

To study the uptake rate of the adsorbents, a 2-CP stock solution of 500 ppm was used. Only AC and MIL-101 (Cr) were tested. 5 mg of dried adsorbents were added into the glass vials and then topped up with 10 mL of the pollutant stock solution. The contents were stirred and after specific time intervals, 2 mL aliquot of the suspension was extracted using a syringe and immediately filtered with 0.22 μm syringe filters. The filtrate was further diluted (1 mL aliquot: 10 mL ultrapure water) to prepare for UV-vis spectroscopy measurements. The adsorption capacity (q_t) at each reaction time (t) was calculated using Equation 3.8.

Before discussing the calculation of a kinetics coefficient, it is useful to review the original concept. In a reaction, let's assume A as the sole reactant that gradually converts to a single or multiple products. The rate of concentration reductions (Equation 3.11) of reactant A when converting into its product constituent can be expressed through a general differential rate law (Equation 3.12). Parameter n is the order of the reaction either as 0, 1 or 2 whereas k_n is the rate constant according to its reaction order. When A fully converts at final time t , the integrated laws for a 0th, 1st and 2nd order reactions are shown in Equation 3.13, Equation 3.14 and Equation 3.15 respectively.



$$-\frac{d[A]}{dt} = k[A]^n \quad \text{Equation 3.12}$$

$$[A] = [A]_0 - k_0 t \quad \text{Equation 3.13}$$

$$\ln[A] = \ln[A]_0 - k_1 t \quad \text{Equation 3.14}$$

$$\frac{1}{[A]} = \frac{1}{[A]_0} + k_2 t \quad \text{Equation 3.15}$$

In the context of an adsorption process, the adsorbate concentration can be used as a substitute to $[A]$. However, instead of expressing the rate law in terms of the adsorbate concentration reduction, it is more relevant to calculate the amount of adsorbate being adsorbed, hence, the establishment of “pseudo” kinetics models. Lagergren (Lagergren, 1898) and Ho and McKay (Ho & McKay, 1999) were the pioneers of the pseudo first order (PFO) and the pseudo second order (PSO) model respectively. Although both are empirical equations, they can still be used to estimate the rate of adsorption of an adsorbent (Equation 3.16) based on the difference between the adsorption capacity at any time t (q_t) and the equilibrium capacity (q_e).

$$\frac{dq_t}{dt} = k_{n-pseudo} (q_e - q_t)^{n-pseudo} \quad \text{Equation 3.16}$$

Where n -pseudo is an integer equals to 1 (for PFO) or 2 (for PSO). The value of $k_{n\text{-pseudo}}$ is simply understood as the measure of the speed at which an adsorbent can adsorb a molecule. By integrating Equation 3.16 with the equilibrium boundary limits (from $t = 0$ to $t = t$ and from $q_t = 0$ to $q_t = q_t$), the PFO (using $n = 1$) and PSO (using $n = 2$) nonlinear equations can be rewritten as Equation 3.17 and Equation 3.18 respectively. Table 3.5 shows the nonlinear and linear equations of both PFO and PSO kinetics equations. Where k_{PFO} is the PFO kinetics rate constant, k_{PSO} is the PSO kinetics rate constant (mg/g.min), q_e is the equilibrium amount of solute adsorbed at equilibrium (mg/g), t is time (min), and q_t is the adsorption capacity at a specific time t .

Table 3.5: Nonlinear and linear forms of pseudo first and second order kinetics equations

Type	Nonlinear form	Linear form	Plot (y-axis vs x-axis)	Linear parameters		Nonlinear equation no.
				Slope	Y-intercept	
PFO	$q_t = q_e(1 - e^{-k_{PFO}t})$	$\ln(q_e - q_t) = \ln q_e - k_{PFO}t$	$\ln(q_e - q_t) vs t$	$-k_{PFO}$	$\ln q_e$	Equation 3.17
PSO	$q_t = \frac{k_{PSO}q_e^2t}{1 + k_{PSO}q_e t}$	$\frac{t}{q_t} = \frac{1}{k_{PSO}q_e^2} + \frac{t}{q_e}$	$\frac{t}{q_t} vs t$	$\frac{1}{q_e}$	$\frac{1}{k_{PSO} \cdot q_e^2}$	Equation 3.18

The intricacies of using a PFO or a PSO kinetics model, as well as the nonlinear or the linear form, have been discussed in a study by Simonin who analysed the differences between the two models and their kinetics parameters (Simonin, 2016). Several interesting conclusions were found. First, Simonin replotted a wide range of experimental data reported in the literature using the linear forms of the two models. It was discovered in many of the studies, the linear PSO equation was used more often. However, the used experimental datasets were nearly at or already reached equilibrium. This makes little sense for the data to be fitted with a kinetics model as a model is supposed to predict the final equilibrium fractional uptake between 0 and 1. Moreover, based on the linearized Equation 3.18, as q_t approaches q_e , the value of t/q_t will be almost equal to the gradient of t/q_e , resulting to points in this range being naturally well aligned. This leads to an overestimation in the PSO's accuracy to predict the kinetics profile of an adsorbent. As an example, Figure 3.16 shows the alignment tendency when the linear PSO equation was used to model this work's data.

In a different report by Kajjumba et al., despite using a linearized PFO (Equation 3.17) equation, they encountered a similar error (Kajjumba *et al.*, 2019). As the system approaches equilibrium, the $(q_e - q_t)$ gradient tends to zero, thus, causing $\ln(q_e - q_t)$ to have an abnormally high negative value and consequently, reducing the accuracy. Therefore, to alleviate this issue, Simonin and Kajjumba et al. highly recommend: (1) the use of nonlinear forms to minimize various implicit error functions and (2) the upper limit q_e needs to be set to 0.85 to avoid the erroneous influence of near-equilibrium data in the model fitting accuracy. Simonin's work also found that PFO has a slightly lower fitting accuracy (~33%) than the PSO (~35%). PSO is deemed as a more suitable kinetics model to describe diffusion-controlled processes although it is nonetheless unable to account for the steep initial uptake increments within a short timeframe.

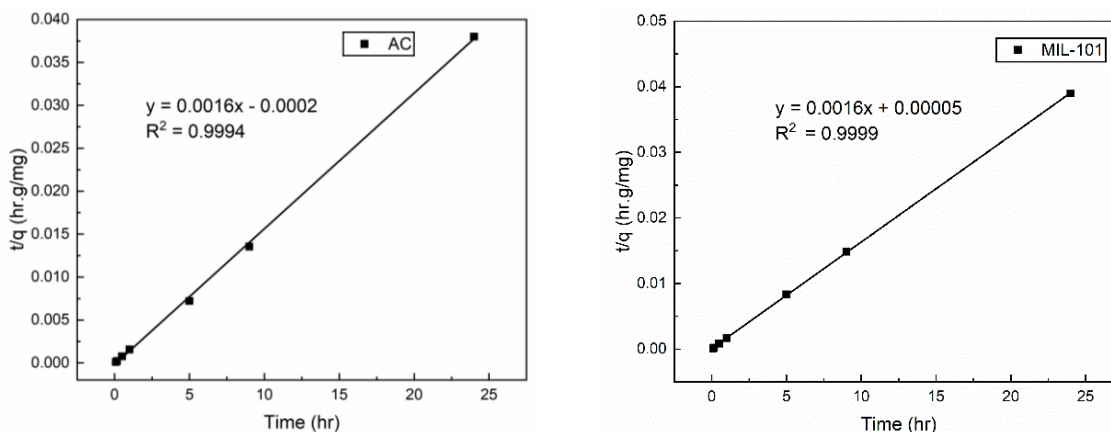


Figure 3.16: Rate of 2-CP uptake data (left) by AC and (right) by MIL-101 (Cr) fitted with a linear pseudo second order (PSO) kinetics equation.

3.9.7 Influence of pH and zeta potential in 2-chlorophenol batch adsorption

Given that 2-CP is an ionic compound, its adsorption affinity can be influenced by the solution pH and the adsorbent's corresponding zeta potential (surface charge). So, separate adsorption experiments were performed at different pH values (1 – 13) using 500 ppm 2-CP as the stock solution. The adsorption experimental setup and calculation for adsorption capacity can be referred to the template mentioned in Section 3.9.4.

3.9.8 Adsorbent reusability study

To demonstrate the adsorbents' reusability after being used for adsorption, the used MIL-101 (Cr) and AC were regenerated using ethanol. Initially, 100 mg (m_1) of pre-activated adsorbent was weighed and added into a closed-cap vial containing 100 mL of 100 ppm (C_0) 2-CP solution. The mixture was continuously stirred for 2 hrs to allow adsorption to occur. Next, the suspension was centrifuged to separate the solids and the aqueous phase. The supernatant was then filtered with a 0.22 μm syringe filter and the filtrate was kept aside to determine the 2-CP residual concentration (C_e) via UV-vis analysis.

Meanwhile, the centrifuge tube containing the settled solids was filled with 20 mL ethanol and later stirred for 30 mins (desorption). It was then centrifuged again, but this time, the ethanol supernatant was disposed while the settled solids were dried overnight in the vacuum oven at 120 $^{\circ}\text{C}$. This experiment is considered as a complete regeneration cycle. The dried solids were decanted, weighed (m_2) and placed into a new tube. After recording m_2 , the upcoming procedures followed what have been described earlier until m_3 was obtained. The adsorbent's 2-CP adsorption capacity (q_i) after each regeneration cycle was calculated using Equation 3.8.

3.10 Toluene vapour capture experiments from humid air by PDMS-treated MIL-101 (Cr) (Chapter 5)

3.10.1 Materials

Chromium (VI) nitrate nonahydrate (98%), terephthalic acid (99%), PDMS-Sigma (dynamic viscosity, $\mu = 10$ cST), were supplied by Sigma-Aldrich. Glacial acetic acid (100%) was purchased from VWR, and toluene (99.5%) was purchased from Alfa Aesar. Silicone elastomer kit SYLGARDTM 184 was ordered from Dow Chemical Company. This 2-part kit contains PDMS and a curing agent, but only the PDMS was used. Herein denoted as PDMS-Dow ($\mu = 3500$ cST). The reference adsorbent is a commercialized, granular activated charcoal (AC) F400 procured from Chemviron Carbon.

3.10.2 Synthesis of MIL-101 (Cr)

Hydrofluoric acid-free MIL-101 (Cr) was synthesized by preparing equimolar quantities of chromium (VI) nitrate nonahydrate (5 mmol, 2 g), terephthalic acid (0.83 g) and acetic acid (0.29 mL) to be dissolved in 25 mL of water (Azmi, Williams & Ladewig, 2020). The mixture was later sealed in a Teflon-lined reactor and heated in an oven at 220 °C for 8 hrs. The resultant green crystals were centrifuged and thoroughly rinsed with water (20 mL × 2) and ethanol (20 mL × 1) to remove unreacted terephthalic acid from the product. The suspension was finally dried overnight in a vacuum oven at 120 °C to obtain the dehydrated MIL-101 (Cr) product.

3.10.3 PDMS coating method

Between 50 – 100 mg of activated MIL-101 (Cr) was spread in a small glass petri dish to form a thin powder layer. The dish containing the substrate was placed inside a larger dish filled with liquid PDMS. Both dishes were covered with aluminium foil and then heated in an oven. The dish containing PDMS-Dow was heated at 235 °C whereas for PDMS-Sigma at 180 °C, for a series of coating times. After the coating time was completed, the sample was allowed to cool, yielding a range of coated MIL-101 (Cr) samples designated as MIL-PDMS-XXX-T. The suffix XXX describes the PDMS source and T represents the time spent in the oven (hr). Different heating temperatures were used depending on the PDMS boiling points to ensure polymer volatility (Clearco, 2015). Figure 3.17 shows the gas-phase deposition experimental setup described here.

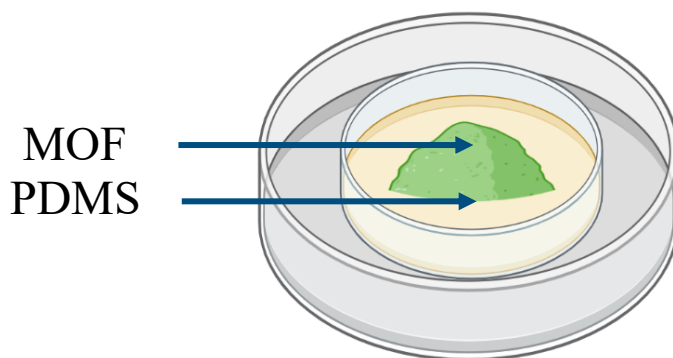


Figure 3.17: An illustration of the sample preparation before it is heated in the oven for PDMS vapor deposition.

3.10.4 Material characterizations

The theoretical PXRD patterns of MIL-101 (Cr) were derived from CCDC code OCUNAC. The FTIR spectra were measured with Cary (Agilent, USA) spectrometer. The thermal stability of the coated samples was examined using a thermogravimetric analysis (TGA) instrument Netzsch STA 449 F5 Jupiter[®] from 30 to 900 °C under flowing air (40 mL/min) at a heating rate of 20 °C/min. Nitrogen (N₂) adsorption-desorption measurements were conducted with 3Flex Micromeritics analyser at 77 K from partial pressure (P/P₀) 0 to 0.99. Prior to testing, the samples were degassed overnight in vacuo at 150 °C. The x-ray fluorescence (XRF) measurements for the samples were performed on PANalytical Epsilon 3XLE XRF spectrometer. The SEM images were acquired using Zeiss Leo Gemini 1525 operated at 5 kV. Brunauer Emmett Teller (BET) method was used to calculate the specific surface area of the adsorbents. Total pore volume and pore size distribution were estimated according to Tarazona non-local density functional theory (N₂) model by assuming a cylindrical pore geometry. A KRÜSS drop shape analyser was used to measure the samples' advancing water contact angle at ambient temperature. The powdered samples were pressed onto a small double-sided tape segment attached on a glass slide.

Additional water and toluene contact angle measurements were also conducted on PDMS-coated thin films. To prepare a thin film sample, a dust-free microscope slide (2 cm × 1.5 cm) was first placed onto the coating platform of a spin coater (Ossila, UK). Then, 30 µL of PDMS-Sigma was carefully pipetted onto the slide centre. The slide was spun at 3000 rpm for 180 seconds. After this round, another layer of equivalent PDMS-Sigma quantity was added, and it was spun again with the same settings.

3.10.5 Hydrophobicity index

Please refer to Section 3.11.8 for explanations on the calculation of molar hydrophobicity index.

3.10.6 Single and dual component vapor sorption setup

The experimental details are listed in Section 3.11.9.

3.10.7 Moisture stability and adsorbent reusability tests

The experimental details are listed in Section 3.11.10.

3.11 Toluene vapour capture experiments from humid air by modified MIL-100 (Fe) (Chapter 6)

3.11.1 Materials

All solvents and reagents were used as received. Iron (III) nitrate nonahydrate (98%), iron (II) chloride tetrahydrate (99%), ammonium fluoride (NH₄F, 98%), trimesic acid (95%), sodium hydroxide pellets (NaOH, 97%), dimethyldichlorosilane (DMDCS, 99.5%), trichloro (3,3,3-trifluoropropyl) silane (TCTFPS, 97%), methoxytrimethylsilane (MTMS, 99%) and diphenylphosphinic acid (DiPPA, 98%) were purchased from Sigma Aldrich. Toluene (anhydrous, 99.8%), 1-decylphosphonic acid (DPA, 98%), n-octadecyl phosphonic acid (ODPA, 97%), methyl phosphonic acid (MPA, 98%), 4-tert-butylcalix[4]arene (Cx4, 98%), 4-tert-butylcalix[6]arene (Cx6, 98%), 4-tert-butylcalix[8]arene (Cx8, 98%) were supplied by Alfa Aesar. Dichloromethane (DCM, 100%) was bought from VWR Chemicals. Nonafluorohexyltrimethoxysilane (95%, NS) and 3-(heptafluoroisopropoxy)-propyltrimethoxysilane (95%, HS) were bought from Fluorochem.

3.11.2 Synthesis of high temperature MIL-100-HT (Fe)

The hydrothermal synthesis procedure of MIL-100 (Fe) free from hydrofluoric acid was taken from the literature (Seo *et al.*, 2012). Iron (III) nitrate nonahydrate, trimesic acid and water were mixed in 1: 0.66: 56 molar ratio and stirred for 1 hr. The reactant mixture was transferred into a Teflon-lined reactor to be heated in an oven at 160 °C for 12 hrs. After the reaction ended, the solid was filtered and washed copiously with deionized water. Further purification steps included washing with hot water and ethanol, followed by a rinse with an aqueous 38 mM NH₄F solution. The final product termed here as MIL-100-HT (Fe) was obtained after overnight drying at 120 °C

in a vacuum oven. MIL-100-HT (Fe) was only used as a precursor for the silane surface modification explained in Section 3.11.3.

3.11.3 Preparation of silane-coated MIL-100 (Fe) particles

Several silane reagents with different carbon chain lengths namely NS, HS, DMDCS, TCTFPS, and MTMS (refer to Section 3.11.1 for full descriptions) were dissolved in dichloromethane at various concentrations ranging from 1.0, 2.5, 5.0 and 7.5 vol%. About 200 mg of activated MIL-100-HT (Fe) was later dispersed into 10 mL silane solution and held refluxed at 50 °C overnight. The reflux is necessary to prevent dichloromethane from evaporating (boiling point = 39.6 °C). After the reaction, the slurry was dried in the oven by keeping it at 80 °C overnight to complete the functionalisation. Table A10.7 provides the chemical structure and the calculated diameter for all silanes used.

3.11.4 Synthesis of room temperature MIL-100 (Fe)

The classic hydrothermal synthesis of MIL-100-HT (Fe) involves heating the solution at 160 °C for 12 hrs. Therefore, motivated by the need for a more environmentally friendly method, an alternative room-temperature synthesis was sought. This experimental synthesis was performed according to a previously described method (Guesh *et al.*, 2017). Two different solutions were first prepared. Solution 1 contains 1.7 g (7.6 mmol) of trimesic acid dissolved in 23.7 g of 1 M NaOH aqueous solution (22.8 mmol). Solution 2 was obtained by dissolving 2.3 g (11.4 mmol) of iron (II) chloride tetrahydrate in 97.2 g of H₂O.

Both solutions were stirred separately overnight to ensure complete dissolution. Then, Solution 1 was added dropwise into Solution 2. The mixture was stirred at room temperature for 24 hrs. Time zero ($t = 0$ hr) was considered when the last drop of Solution 1 was added into Solution 2. The formed solid was recovered from the suspension by centrifugation at 6500 rpm, washed with water (20 mL \times 3), and a final equivalent rinse with ethanol. Overnight vacuum drying at 150 °C afforded the MIL-100 (Fe) product as reddish-brown crystals. The coated MIL-100 (Fe) samples were labelled as MIL-CA-LQ where CA is the type of coating agent applied, either phosphorous oxyacid

(PA) or calixarene (Cx). LQ refers to the loading quantity of the coating agents expressed in mM or wt% respectively.

3.11.5 Preparation of phosphorous oxyacid-treated MIL-100 (Fe) particles

The MOF surface modification using PA was performed based on a reported work by Sun et al. (Sun *et al.*, 2017). Typically, 100 mg of activated MIL-100 (Fe) was mixed in 50 mL of 5 mM DPA ethanol solution. The mixture was stirred for 24 hrs at room temperature. Then, the solution was filtered followed by washing the filtered solid with ethanol thrice to remove any excess DPA. The filtrate was dried overnight in a vacuum oven at 120 °C to produce MIL-DPA. Similar steps were applied to prepare MIL-ODPA, MIL-MPA, and MIL-DiPPA except that the latter was synthesized with three different DiPPA concentrations; 5 mM, 10 mM, and 50 mM. Table A10.7 provides the chemical structures and the calculated diameter for all PA chemicals used. Please refer to Section 3.11.1 for full descriptions of the PA chemicals.

The reasons for testing four PA variants are to determine the influence of the PA's chain length, its functional group and substrate concentration to the treated MIL-100's porosity and hydrophobicity. Alkyl PAs, DPA and ODPA each has different chain lengths which is useful to predict the degree of pore blockage. On the other hand, DiPPA has two phenyl rings while MPA has a methyl (CH₃) group. These functional groups with low surface free energy are expected to increase the treated surface's hydrophobicity. Additionally, it is important to clarify that the double phenyl rings in DiPPA (phosphinic acid) are not available on a phosphonic acid molecule, hence, why DiPPA was chosen.

3.11.6 Preparation of calixarene-treated MIL-100 (Fe) particles

The calixarene coating process was adapted from another report (Jeong *et al.*, 2019). Approximately 50 – 100 mg of MIL-100 (Fe) was dispersed in 10 mL toluene prepared with varying proportions (1, 3, 5 wt%) containing 4-tertbutylcalix[n]arene (Cx with n = 4, 6 or 8) and stirred for 1 hr. The solutions were then filtered to retrieve the solids, then they were rinsed with

toluene to remove excess Cx. The samples were finally dried overnight at 150 °C under vacuum. Table 6.1 in Section 6.2.1 provides the chemical structures and the calculated diameter for all Cx chemicals used.

3.11.7 Material characterizations

The simulated PXRD patterns for MIL-100 (Fe) were derived from CCDC ID 640536. The samples' N₂ adsorption and desorption isotherms were collected on 3Flex Micromeritics BET analyser at 77 K. The samples were degassed at 150 °C overnight under vacuum before starting the measurements. Brunauer Emmett Teller (BET) method was used to calculate the specific surface area of the adsorbents. The total pore volume and pore size distribution were estimated according to Tarazona non-local density functional theory (N₂) model by assuming a cylindrical pore geometry. Note that the N₂ isotherms for silane-coated MIL-100 (Fe) samples were measured using Micromeritics BET Tristar.

The TGA experiment was conducted on instrument Netzsch STA 449 *F5 Jupiter*[®] from 30 to 900 °C under flowing air (40 mL/min) at a heating rate of 20 °C/min to compare the thermal stability between the modified MIL-100 (Fe) particles and the original sample. A KRÜSS drop shape analyser was used to measure the samples' advancing water contact angle at ambient temperature. The samples were dispersed on a glass slide attached with double-sided tape and pressed uniformly with another glass slide on top of it. The SEM images were obtained using Zeiss Leo Gemini 1525 operated at 5 kV.

The solvent adsorption experiments were performed at 25 °C with water and toluene in static mode using IGA-002 (Hiden Isochema, UK). The dynamic and competitive isotherms were obtained using DVS Resolution (Surface Measurement Systems, UK). Toluene was chosen as a hydrophobic VOC molecule model. It is a relatively common environmental VOC with toxicity exposure limits in the 100 to 500 ppm range.

3.11.8 Hydrophobicity index

An effective VOC adsorbent requires hydrophobicity on both internal pore surfaces as well as external surfaces for optimal organic molecules adsorption (Xie *et al.*, 2020). However, the traditional contact angle method only provides the extent of hydrophobicity for the outer surface, but not for the surface of the internal pores (Jayaramulu *et al.*, 2019). Furthermore, contact angle measurements do not consider factors specific to adsorption performance including differences in size, volume, and shape of the pores. To address this gap, the internal adsorbent hydrophobicity was evaluated through water and toluene adsorption isotherms.

A hydrophobicity index (HI) was used in this study as a quantitative descriptor of pore hydrophobicity. Different types of HI can be used to determine a material's hydrophobicity based on its adsorption capacity in. These include the ratios for the adsorption of a hydrophobic molecule such as toluene (Hunter-Sellars *et al.*, 2021) or cyclohexane (Halasz *et al.*, 2005) relative to water, or as obtained from specific single (Hunter-Sellars *et al.*, 2021) or dual component adsorption experiments (Bhadra *et al.*, 2015). Alternatively, HI can also be estimated through pore volume measurement from N₂ adsorption and volume of desorbed water from TGA analysis (Giaya, Thompson & Denkwicz Jr, 2000). To provide a fair comparison on the reported HI values, the mode of the experiment must be specified, either conducted in dynamic (simultaneous exposure of competing species) or static (separate exposure). Equation 3.19 shows the preferred molar hydrophobicity index (HI) calculation formula used in the current study (Hunter-Sellars *et al.*, 2020).

$$HI_{\text{static}}(x) = \frac{Q_{\text{toluene-0.05}}}{Q_{\text{water-x}}} \quad \text{Equation 3.19}$$

Where $HI_{\text{static}}(x)$ (mol/mol) is the material's molar hydrophobicity index calculated using the quantity of toluene adsorbed at a 5% P/P₀ ($Q_{\text{toluene-0.05}}$, mol/g) as a function of adsorbed water quantity ($Q_{\text{water-x}}$, mol/g) at different values of water P/P₀ or relative humidity (x).

3.11.9 Single and dual component vapor sorption setup

Please refer to Section 3.7 for descriptions on single-solvent and Section 3.8 on dual-solvent vapor sorption experimental setups.

3.11.10 Moisture stability and adsorbent reusability tests

The MIL-100 materials were assessed for their short-term stability at a high RH condition when other MOF adsorbents such as HKUST-1 (Cu) (Álvarez *et al.*, 2017) and MOF-177 (Zn) (Yang *et al.*, 2013) are known to be unstable. The DVS test protocol is as follows:

1. The samples were first saturated at a 40% RH background, followed by the introduction of 0.5% toluene P/P₀ until the sample reaches adsorption equilibrium: constant mass.
2. Then, the samples were exposed to 90% RH at 0% toluene P/P₀ for 24 hrs.
3. The samples were finally tested at 40% RH and 0.5% toluene P/P₀ again.

The toluene uptake at the end of (1) and after (3) the second 40% RH and 0.5% toluene P/P₀ exposure was reported. There are several objectives to be gained from this experiment. Firstly, the 90% RH in step (2) represents a highly humid condition which will certainly fill the entire adsorbent's pores with water. The same explanation can be said as to why the toluene concentration is set at 0% toluene P/P₀. Secondly, the repeat of step (3) after the 90% RH exposure can instantly test the coating's resistance and efficacy compared to the samples' initial uptake in step (1). Thirdly, one may contend about the reversed experimental design in step (1), by starting with toluene saturation first, then followed by water equilibrium. However, since MIL-100 (Fe) is originally a hydrophilic material, it has a very strong water affinity and a low affinity towards a VOC like toluene. So, the current water-then-toluene protocol will specifically measure the “real” treated MIL-100 (Fe) samples' toluene affinity when its pores are saturated with 40% RH. On the contrary, in a hypothetical toluene-then-water protocol, it does not reflect a realistic setting since it implies that the toluene adsorption occurs in a moisture-free, dry condition.

In the reusability experiment, also with a 40% RH background, the samples were exposed to 10% toluene P/P₀ for 3 hrs followed by 1 hr of desorption and repeated for 10 experimental cycles. The

10% toluene P/P_0 was chosen as the studied toluene concentration in lieu of the 0.5% toluene P/P_0 on the basis that the former condition will show faster adsorption rate, thus, making easier materials' performance comparison than the latter. All experiments were conducted at 25 °C.

3.12 Liquid-phase PFOA adsorption experiments (Chapter 7)

3.12.1 Materials

Polyacrylamide (PAM) (FLOPAM FA 920 SH, non-ionic, molecular weight (M_w) = 10 – 12 MDa) and partially hydrolysed polyacrylamide (HPAM) (FLOPAAM FP 3630 S, anionic, 25–35 mol% hydrolysed, M_w = 18 MDa) were supplied by SNF Floerger (France). Polyacrylic acid sodium salt (PAA, average M_w ~2100), 2,2,2-trifluoroethanol (TFE, 99.5%), perfluorooctanoic acid (PFOA, 95%), ammonium acetate (AA, 99.0%), trimesic acid (TMA, 95%), sodium chloride (NaCl, 99%) were purchased from Sigma Aldrich. Deuterium oxide (D_2O , 99.9%) and aluminium nitrate nonahydrate ($Al(NO_3)_3 \cdot 9H_2O$, 98%) were purchased from Fluorochem and Alfa Aesar respectively. All other chemicals and solvents were from reagent grade and used without further purification. Ultrapure water (H_2O) used throughout the study was obtained from PURELAB Chorus ELGA unit. Granular activated carbon (AC) F400 was procured from Chemviron Carbon as a high-grade, steam-activated bituminous coal.

3.12.2 Synthesis of MIL-96 (Al)

MIL-96 (Al) was synthesized according to the original method described previously (Loiseau *et al.*, 2006) and the protocol for the polymer addition was adapted from another study (Nandiyanto, He & Wang, 2019). A typical hydrothermal synthesis solution contains $Al(NO_3)_3 \cdot 9H_2O$ (1.3 g, 3.5 mmol), TMA (0.1 g, 0.5 mmol) and H_2O (5 mL, 278 mmol) in a 23-mL Teflon liner. Firstly, to induce particle aggregation, HPAM solution (1000 mg/L) was poured into the reacting solution containing only the dissolved linker in H_2O . The solution was later sonicated for 15 mins prior to adding the metal precursor. The ratio between the volume of polymer solution added to the volume of water (R) is defined in Equation 3.20. The mixture was heated to 210 °C for 24 hrs. After cooling to ambient conditions, the resulting solid product was recovered via filtration and consequently

washed with copious amount of H₂O. The washed residue was dried at 120 °C in vacuo overnight. Similar steps were implemented when using other polymer solutions (PAM and PAA).

$$R = \frac{\text{Volume of polymer added (mL)}}{\text{Volume of water used as solvent in the reaction (mL)}} \quad \text{Equation 3.20}$$

3.12.3 *Material characterizations*

To prepare for the SEM imaging, the samples were mounted on specimen holders and sputter coated with 15-nm thick chromium to inhibit charging during examination. Then, the SEM images were acquired using Zeiss Leo Gemini 1525 operated at 5 kV. Fluorine (¹⁹F) nuclear magnetic resonance (NMR) spectra were recorded on Jeol 400 MHz NMR spectrometer with deuterium oxide (D₂O) as the analysis solvent. Particle size measurements were performed on Malvern Mastersizer 2000 particle size analyser using laser light diffraction. As a standard procedure, the samples were sonicated before the measurements. Dilute aqueous suspensions were prepared by dispersing the adsorbents in H₂O and sonicated to ensure homogeneity. Measurement time was set to 30 seconds with a total of 5 runs performed for each sample. Only the average values are reported here.

Elemental analysis for the polymer-modified samples was performed on Vario MICRO cube analyser supplied by Elementar, Germany. Runs were carried out in triplicate to yield average values. The FTIR spectra were measured with Perkin Elmer Spectrum 100 FT-IR spectrometer. The simulated PXRD patterns for MIL-96 (Al) and trimesic acid were generated using CCDC codes of KENKOE and BTCOAC accordingly. The identity of gases evolved from the material's decomposition and their respective thermal stability were assessed on Netzsch STA 449 *FI Jupiter*[®] TGA/DSC hybrid system with mass spectrometer (MS). The solids were heated from 30 °C to 800 °C with a heating rate of 3 °C/min under inert gas (N₂) atmosphere.

Sample porosity was evaluated using N₂ gas adsorption at 77 K on Micromeritics 3Flex surface analyser. Before starting the N₂ adsorption, the samples were outgassed at 150 °C under vacuum overnight. Sample properties including apparent and external surface area, as well as microporous

volume were then derived. Vapor adsorption of n-octane (C_8H_{18}) was measured in an intelligent gravimetric analyser (IGA-002, Hiden Isochema, UK) at 303 K (30 °C). Prior to IGA measurement, around 50 mg sample was outgassed at 150 °C for 24 hrs. The isotherms were recorded by increasing the vapor pressures of C_8H_{18} from 0 to 15 mbar. The highest vapor pressure was maintained below 80% of the upper limit or the saturation vapor pressure ($P_{0,octane}$ at 300 K = 21 mbar) to avoid condensation in the operating chamber. The minimum and the maximum measurement time for each step is 60 and 1000 mins accordingly.

3.12.4 ^{19}F NMR analysis

The concentration for the internal standard (TFE) solution was set to 2.3 mM by transferring 0.42 mL TFE into 1 L H_2O . The NMR analyte consists of 0.25 mL D_2O , 0.25 mL filtrate and 0.2 mL TFE. Quantification was performed according to the literature (Sini *et al.*, 2018). The integrated area under the characteristic peaks of the terminal CF_3 groups for PFOA (-80 ppm) was compared relative to the TFE peaks (-76 ppm). The residual PFOA concentration after adsorption was calculated from the linear calibration equation obtained.

3.12.5 PFOA adsorption

Prior to adsorption, the adsorbents were activated overnight at 120 °C under vacuum. All solution adsorption experiments were conducted at room temperature. A PFOA stock solution (1000 mg/L) was prepared using ultrapure H_2O . The adsorbent (20 mg) was added with 20 mL PFOA solution into a screw cap vial, stirred for 72 hrs and then, the solution was filtered. The filtrate was collected for NMR analysis while the filtered solids were reused for desorption. The experiments were performed in duplicate, and the average values are reported.

3.12.6 PFOA desorption

Based on the results from the desorption solvent screening (Figure 7.12), the solvent composition was adjusted to provide a methanol/water mixture (3:1, v/v) stabilized with 10 mM AA buffer solution. To study the influence of NaCl on the desorption efficiency, four desorption solvents

were prepared with varying NaCl concentrations namely: RS1 (no salt), RS2 (10 mM NaCl), RS3 (50 mM NaCl) and RS4 (500 mM NaCl).

After 72 hrs of adsorption, the adsorbent was recovered by filtration and placed respectively in 20 mL desorption solvent containing the above NaCl concentrations to be continuously stirred for another 72 hrs at room temperature. The sample mass used for desorption was assumed the same with the initial mass. Sample preparation for NMR analysis followed the steps mentioned previously.

3.12.7 PFOA homologue: n-octane vapor adsorption kinetics analysis

Besides the extensively used PFO and PSO analyses, a number of adsorbates have been reported to display better fitting with an Elovich kinetics model including lead sorption on AC (Largitte & Pasquier, 2016), flue gas VOC capture by pistachio nutshell-derived AC (Cheng *et al.*, 2021), and xylene removal on biochar (Rajabi *et al.*, 2021). The Elovich equation was initially proposed by Roginsky and Zeldovich (Roginsky & Zeldovich, 1934) to describe the kinetics of gases onto a heterogenous solid surface with negligible desorption. Nowadays, its applicability has been extended for liquid-phase sorption applications. The Elovich model (Equation 3.21) predicts an exponential decrease of the solute adsorption rate as the amount of adsorbed solute increases, where α is the initial adsorption rate (mg/g.min) and β is desorption constant. However, as it is based on an exponential function, the adsorption rate will never achieve a saturated level (Hubbe, Azizian & Douven, 2019).

$$\frac{dq_t}{dt} = \alpha \cdot e^{-\beta \cdot q_t}$$

Equation 3.21

Chapter 4: Aminated MIL-101 for aqueous-phase phenol removal⁶

4.1 Introduction

Activated carbon (AC) is the normal industrial adsorbent which is used to remove many persistent organic contaminants like phenols, from water (Moura, Rios & Galvão, 2018). But more recently, new porous materials, including specifically metal organic frameworks (MOFs), are taking centre stage with their ability to surpass AC's performance in some separation processes (Hasan & Jhung, 2015; Khan et al., 2015; Dias & Petit, 2015). MOFs are attractive with their superior properties including high surface area, good thermal stability and the versatility of in-pore or outer-surface modification to suit diverse form of applications (Gu et al., 2012; Seo et al., 2016). Apart from that, MOFs can be reused using a very simple solvent exchange technique (Han & Lah, 2015) in comparison to incineration or high-temperature activation (up to 800 °C) for spent AC. Indeed, the costly thermal AC regeneration process sometimes yields little benefit over the cost of buying fresh AC (Sühnhholz, Kopinke & Weiner, 2018). In this Chapter, a high surface area and a highly water stable MOF, MIL-101 (Cr), will be studied alongside its amine-functionalized analogue, MIL-101 (Cr)-NH₂ to remove a phenolic pollutant model, 2-chlorophenol (2-CP) from dilute aqueous solutions. The adsorption performance of the MOFs and their reusability will be compared with a commercial AC as the benchmark adsorbent.

4.2 Results and discussion

4.2.1 PXRD

MIL-101 (Cr) is commonly synthesized based on a hydrothermal method using hydrofluoric (HF) acid as an additive. HF is a very corrosive acid with a pK_a of 3.45 (Burgher *et al.*, 2011) and the

⁶ Part of this Chapter has been published as “Azmi, L. H. M.; Williams, D.; Ladewig, B. P. Can Metal Organic Frameworks Outperform Adsorptive Removal of Harmful Phenolic Compound 2-Chlorophenol by Activated Carbon? *Chem. Eng. Res. Des.* **2020**, *158*, 102–113.”

associated human injuries from accidental exposure can be horrendous. To reduce potential hazards, acetic acid has been regularly used as a substitute (Zhao *et al.*, 2015; Rallapalli *et al.*, 2016; Zhao *et al.*, 2017) including in this study. The successful synthesis of MIL-101 (Cr) using acetic acid can be confirmed from the same PXRD patterns of the prepared MIL-101 (Cr) with the simulated patterns as shown in Figure 4.1. Similar PXRD patterns were also observed for MIL-101 (Cr)-NH₂, indicating that this modified version of MIL-101 (Cr) retained material crystallinity after modification. Meanwhile, for AC, the only peak appearing at 27° indicates the presence of quartz or silica impurities (Ismail, Khulbe & Matsuura, 2015). The aqueous stability of the synthesized MIL-101 (Cr) was also investigated by immersing the MOF for 3 days in pH 1 and pH 11 solutions (Figure A10.5).

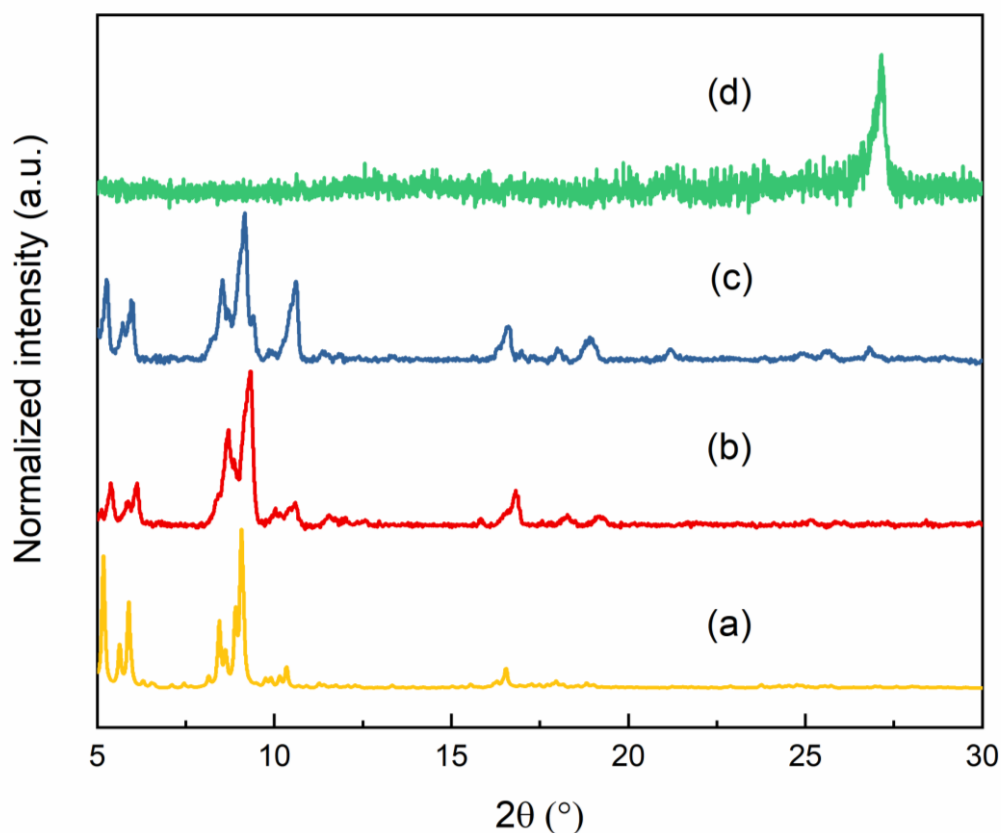


Figure 4.1: PXRD patterns of (a) simulated MIL-101 (Cr), (b) as-prepared MIL-101 (Cr), (c) as-prepared MIL-101 (Cr)-NH₂ and (d) AC.

4.2.2 SEM

The SEM images of MIL-101 (Cr) and MIL-101 (Cr)-NH₂ shown in Figure 4.2 show a good distribution of octahedral-shaped crystals, which is the typical morphology of MIL-101 (Cr) (Zhao *et al.*, 2017).

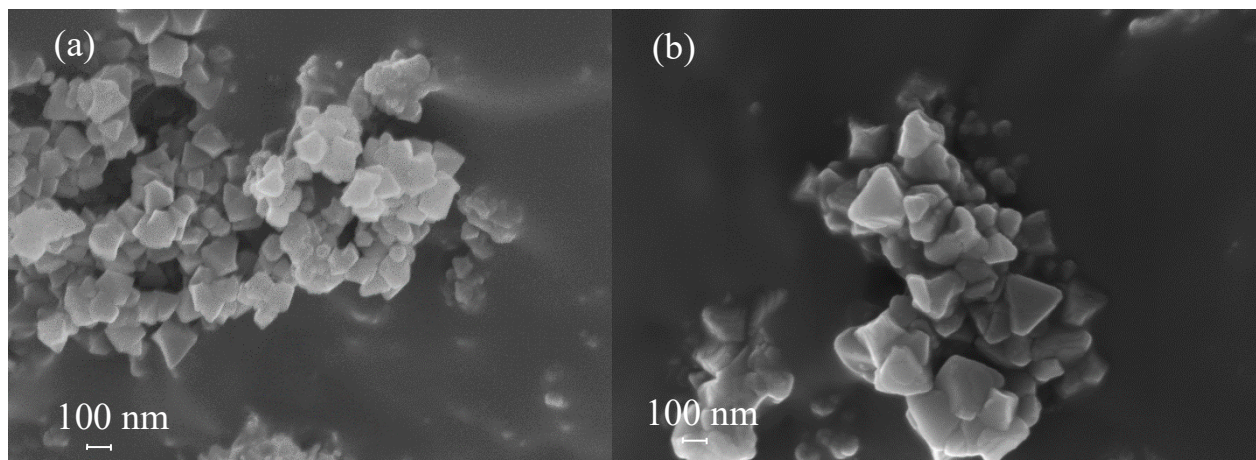


Figure 4.2: SEM images for (a) MIL-101 (Cr) and (b) MIL-101 (Cr)-NH₂ nanocrystals.

4.2.3 Porosity analysis

Table 4.1 shows the calculated BET surface area and pore volume of the studied adsorbents. In the order of decreasing surface area, MIL-101 (Cr) has the highest BET surface area (2710 m²/g) followed by MIL-101 (Cr)-NH₂ (1392 m²/g) and lastly AC (1179 m²/g). Post-liquid immersion surface area data shows the MOF's outstanding resistance towards acidic environments given its negligible surface area reductions. In contrast, a highly alkaline solution is detrimental to the framework as it started to lose some of its porosity. It is believed that MIL-101 (Cr) is stable in acidic condition because acetic acid was used as an additive. However, when the alkalinity level increases, the Cr³⁺ metal sites are prone to degradation, hence, the partial collapse of the framework. The pore size distribution plots of all investigated adsorbents are shown in Figure 4.3 while the complete N₂ adsorption and desorption isotherms of the adsorbents can be found in Figure A10.6.

Table 4.1: Surface area and pore volume analysis of all studied adsorbents.

Sample	BET surface area (m ² /g)	Total pore volume (cm ³ /g)
Pristine MIL-101 (Cr)	2710 ± 40	2.146
MIL-101 (Cr) after 3 days in pH=1	2525 ± 49	1.564
MIL-101 (Cr) after 3 days in pH=11	1835 ± 28	1.176
MIL-101 (Cr)-NH ₂	1392 ± 28	1.250
AC	1179 ± 20	0.805

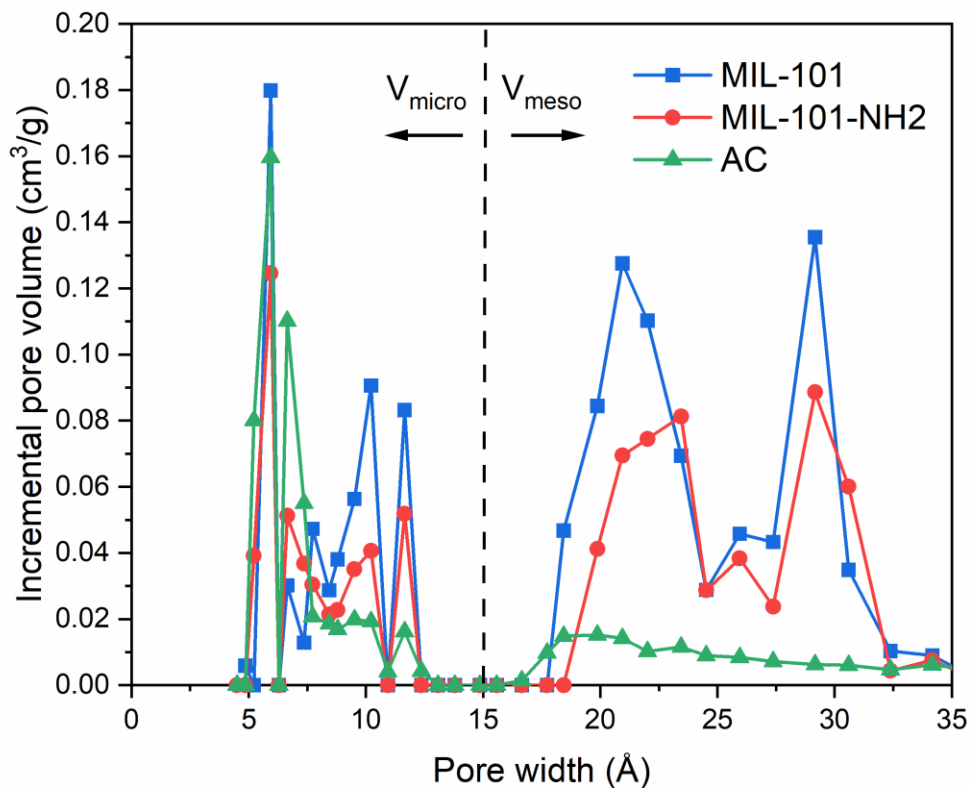


Figure 4.3: Pore size distribution plots for MIL-101 (Cr), MIL-101 (Cr)-NH₂ and AC adsorbents.

4.2.4 FTIR

A comparison between the Fourier-transform infrared (FTIR) spectra of pristine MIL-101 (Cr) and 2-chlorophenol (CP) saturated MIL-101 (Cr) is shown in Figure A10.7. The 2-CP saturated MIL-101 (Cr) was recovered after using it for a 24-hr batch adsorption experiment where $C_0 = 1000$ mg/L. To prepare the used MOF sample for the FTIR measurement, it was dried in a vacuum oven at 120 °C for 12 hrs. Although the 2-CP adsorption isotherms in Figure 4.6 indicate that 2-CP is certainly adsorbed by MIL-101 (Cr), but the measured FTIR spectra cannot confirm the presence of adsorbed 2-CP in the sample. The characteristic signals for MIL-101 (Cr)-NH₂ can also be observed in its measured FTIR spectra, signifying a complete amine functionalization on the MIL-101 (Cr). Details can be found in Appendix Section 10.2.3.

4.2.5 TGA

Figure 4.4 shows the change in mass for the studied adsorbents when heated in N₂ from 20 to 1000 °C. The mass of AC only decreased slightly throughout the measurement, remaining stable up to 700 °C before showing signs of decomposition. The relatively constant sample mass also indicates AC's low hygroscopicity since limited removal of weakly adsorbed water was observed before 150 °C (Krahnstöver, Plattner & Wintgens, 2016). AC's mass loss above 700 °C corresponds to the decomposition of its functional groups and the result of partial gasification of the least thermally stable fragments contained in the carbon structure (Bazan *et al.*, 2016).

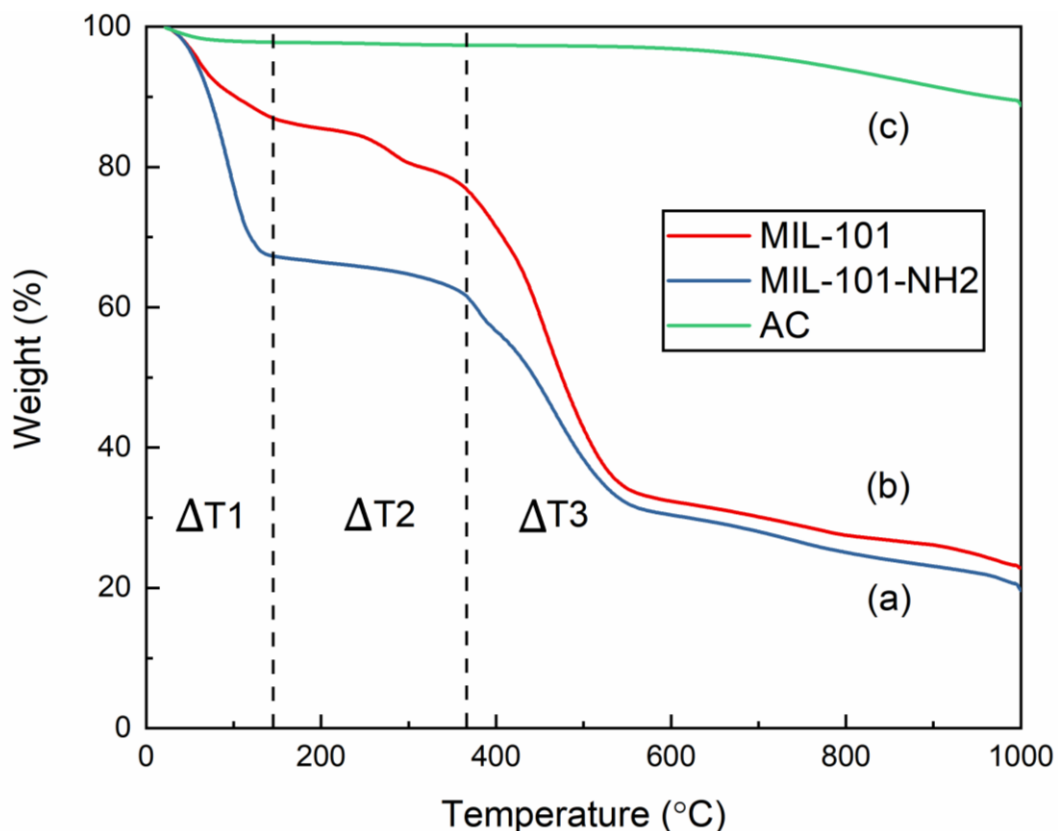


Figure 4.4: Thermal weight loss profiles of (a) MIL-101 (Cr)-NH₂, (b) MIL-101 (Cr) and (c) AC.

As for the MOFs, generally, there are three distinct weight loss steps. The first step between 30 °C and 150 °C refers to the loss of moisture physically adsorbed from air and residual solvents used for washing (EtOH) during synthesis (Jhung *et al.*, 2007). Secondly, strongly adsorbed water molecules were removed from the molecular cages between 150 °C to 370 °C range. Above 370 °C, compounds such as –OH and other coordinated groups were degraded, causing MIL-101 framework decomposition (Bernt *et al.*, 2011; Jhung *et al.*, 2007; Hong *et al.*, 2009; Karikkethu Prabhakaran & Deschamps, 2015).

Summaries of the materials' respective weight loss in the three stages can be found in Table 4.2. AC exhibited the least weight loss across the overall tested temperature range (20 °C to 1000 °C), indicating its low hygroscopicity. It also shows that MIL-101 (Cr) is more hygroscopic than MIL-101 (Cr)-NH₂ as the latter experienced greater weight loss (< 150 °C). TGA is a suitable technique

to determine a material's hygroscopicity as the loss of bound water molecules from the adsorbents can be accurately quantified from their thermal decomposition profiles.

Table 4.2: Detailed descriptions of the adsorbents' TGA profiles.

Temperature gradient, ΔT	Chemical phenomena	Range (°C)	Sample weight loss (%)		
			MIL-101 (Cr)	MIL-101 (Cr)-NH ₂	AC
$\Delta T1$	Water/solvent loss	20 – 150	13	33	2
$\Delta T2$	Linker decomposition	150 – 370	10	6	0.4
$\Delta T3$	Structural decomposition	370 – 1000	53	42	9

4.2.6 Water contact angle

While hygroscopicity is a bulk property, the surface energy of a material can be determined from its water contact angles. Surfaces can be classed as hydrophobic or hydrophilic, depending on their contact angles with water. To check MIL-101 (Cr)'s state of hydrophobicity, it was pelletized prior to performing the water contact angle measurement. Figure 4.5 shows the initial and final water contact angle measurement of the pelletized MIL-101 (Cr). It took about 15 seconds for the water droplet to penetrate its pores, finally displaying a contact angle of 0°. The initial contact angle of 48° confirms that MIL-101 (Cr) is a hydrophilic sample. The same measurement cannot be performed on AC due to its rough surface. However, AC's hydrophobicity is well-known and has been reported elsewhere where θ_c is 120° (Liu, Yang & Xue, 2016).

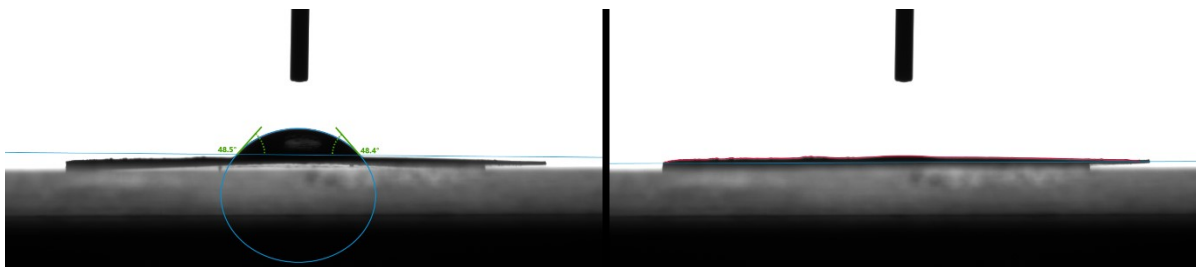


Figure 4.5: Static water contact angle measurement on MIL-101 (Cr) pellet at (left) $t = 0$ second and when the liquid has penetrated the porous pellet (right) at $t = 15$ seconds.

4.2.7 Adsorption isotherm modelling

4.2.7.1 Langmuir adsorption isotherm model

The adsorption isotherm data were modelled with the nonlinear and linearized Langmuir-type 1 equations. Detailed explanations for these equations have been outlined in Section 3.9.5. Table 4.3 lists the estimated parameters obtained from the Langmuir-1 linear type and the nonlinear Langmuir equations. The graphical results for the linear fitting equation are presented in Table A10.5 and Figure A10.8. By comparing the K_L values in Table 4.3, there are two issues noted:

1. A negative K_L value by MIL-101 (Cr)-NH₂ from its linear fitting. Despite its high R^2 fit to the linear model, an initial suspicion was that MIL-101 (Cr)-NH₂ does not follow the monolayer Langmuir assumptions, or it may have not reached its equilibrium capacity even after 24 hrs of adsorption. If multilayer solute formation occurs, the data needs to be fitted with a Freundlich isotherm model.
2. AC exhibited contrasting K_L values, high RSS and reduced χ^2 values from its nonlinear estimation. So, because the AC's adsorption isotherm seems to be better modelled with a linear Langmuir model, these linear-modelled values will be taken forward for discussion. Whereas for MIL-101 (Cr)-NH₂, the nonlinear data will be used. Higher K_L values usually imply a more favourable adsorption. The K_L data suggests that AC has the strongest interaction with the solute.

Table 4.3: Isotherm parameters from a linear Langmuir-1 and a nonlinear Langmuir model

Adsorbent	Linear Langmuir-1			Nonlinear Langmuir			
	q_m (mg/g)	K_L (L/mg)	R^2	q_m (mg/g)	K_L (L/mg)	RSS	Reduced χ^2
MIL-101 (Cr)	121	0.03	0.9942	125	0.024	7.457	1.864
MIL-101 (Cr)-NH ₂	84	-0.04*	0.9764	99	0.08	73.31	18.33
AC	345	0.74	0.9990	422	0.01 [‡]	911.9	228.0

*This value was not used due to negative estimation

[‡]This value was not used due to high RSS and reduced χ^2 values.

Based on the Langmuir equation, Weber and Chakravorti (Weber & Chakravorti, 1974) introduced a dimensionless constant known as the separation factor (R_L) which can be used to describe the nature of the adsorption process – see Equation 4.1. R_L values of $0 < R_L < 1$ indicates a more favourable adsorption process, a $R_L > 1$ indicates an unfavourable process, and $R_L = 0$ is an irreversible process. K_L is the Langmuir constant (L/mg) and C_0 refers to the initial adsorbate concentration (mg/L).

$$R_L = \frac{1}{1 + K_L C_0} \quad \text{Equation 4.1}$$

The R_L values calculated for all studied adsorbents in Table 4.4 are between 0 and 1, signifying a favourable adsorption process which follows an increasing order of; AC > MIL-101 (Cr)-NH₂ > MIL-101 (Cr). The initial concentration of 2-CP, C_0 (mg/L) was calculated based on the previously obtained calibration data shown in Figure 3.15. Note that MIL-101 (Cr)-NH₂ has comparatively lower R_L values than the unmodified MIL-101 (Cr), meaning that the NH₂ functionality results in enhanced chemical interactions with 2-CP. However, it is still unable to outperform the excellent adsorptive performance by AC. Generally, the R_L values gradually become lower as the initial

solute concentration increases, mainly due to the greater concentration gradient that allows faster adsorption by the studied sorbents.

Table 4.4: Dimensionless separation factor values (R_L) calculated for each adsorbent.

C_0 (mg/L)	R_L values for samples		
	MIL-101 (Cr)	MIL-101 (Cr)-NH ₂	AC
98	0.299	0.113	0.0140
191	0.179	0.0614	0.0070
416	0.091	0.0292	0.0032
789	0.050	0.0156	0.0017
998	0.040	0.0124	0.0014

4.2.7.2 Freundlich adsorption isotherm model

Data fitting for MIL-101 (Cr)-NH₂ using a linear ($R^2 = 0.342$) and a nonlinear Freundlich model (RSS = 1134, reduced $\chi^2 = 284$) led to poorer fitting accuracy values compared to using Langmuir's. This might be because the minimal divergence seen at higher solute concentrations may slightly alter the Langmuir-1 model linearity. So, the initial suggestion about potential multilayer adsorption is not supported. Therefore, it was decided to revert to the initial Langmuir isotherm model for the MIL-101 (Cr)-NH₂.

4.2.8 Batch adsorption of 2-chlorophenol

The batch adsorption isotherm plots of 2-CP uptake by MIL-101 (Cr) and MIL-101 (Cr)-NH₂ as shown in Figure 4.6 are Langmuir in shape. According to Sparks, a Langmuir isotherm can be easily identified by a decreasing slope with the increase in solute concentration. This happens as more vacant adsorption sites are gradually being occupied (Sparks, 2003). In comparison to AC in Figure 4.6, it presents the characteristic of a high affinity adsorption isotherm as there is a steep uptake at very low solute concentrations due to the extremely strong adsorption interactions between AC and 2-CP (Hinz, 2001; Dąbrowski *et al.*, 2005) which eventually tapers off to become a Langmuir type curve at higher solute concentrations.

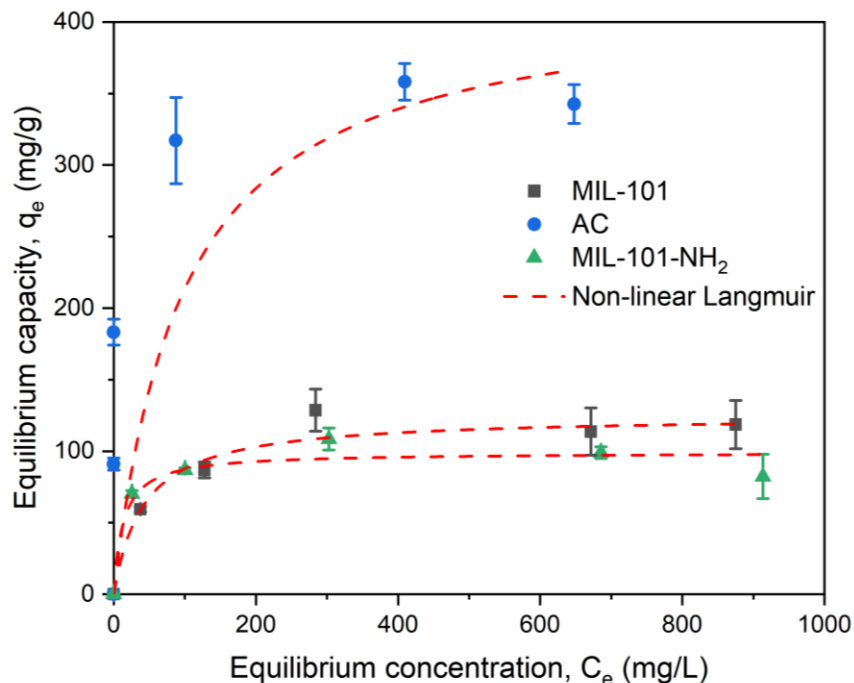


Figure 4.6: 2-CP uptake capacity versus concentration after 24 hrs of adsorption. Dashed lines are the fitted data using a nonlinear Langmuir isotherm model.

In Table 4.3, the estimated q_m values are 345, 125 and 99 mg/g respectively for AC, MIL-101 (Cr) and MIL-101 (Cr) -NH₂. Despite having the lowest surface area amongst all studied adsorbents, AC shows the highest Langmuir adsorption capacity in this work. However, compared to the literature, capacities as low as 95 mg/g (Machado *et al.*, 2020) and as high as 550 mg/g have been reported (Gokce *et al.*, 2021). Differences in the initial solute concentrations and the types of AC used make direct comparisons difficult. Moreover, according to Perrich, high surface area does not guarantee high adsorptive capacity by a material due to a range of reasons which include (Perrich, 2018):

1. In liquid-phase adsorption, only the wetted surface area of the adsorbent is effective, and this value is never equal to the total surface area.
2. The bulk of a material's surface area may be provided by the micropores. Since most molecules are too large to fit into these micropores, this renders the high surface area proportion within a material inaccessible.

3. There seems to be little attention paid to correlating the adsorbent's surface area, pore volume and surface properties with regards to the adsorbate properties such as concentration, physical and chemical descriptors. Note that even if both the adsorbent and the adsorbate's physicochemical properties are known, many other chemical factors can influence the adsorbate's affinity to an adsorbent.

It has been reported by Hasan and Jhung that liquid-phase adsorption of adsorbate molecules by MOFs can occur via several molecular mechanisms including: (1) electrostatic interaction, (2) acid-base interactions, (3) hydrogen bonding, (4) influence of framework metal, (5) π - π stacking/interaction and (6) hydrophobic interactions (Hasan & Jhung, 2015). In addition, external factors like adsorbate molecular structure, solubility, ionization, reaction temperature and presence of multiple solutes can also affect both the rate and the magnitude of adsorption by an adsorbent (Perrich, 2018).

4.2.8.1 Acid-base interactions

From 2-CP molecular structure and the excellent adsorption capacity shown by AC, it is deduced that the acid-base interaction between the acidic phenol molecules and the basic surface functionalities on AC are key (Okolo, Park & Keane, 2000). The existence of electron withdrawing groups like Cl and NO₂ will make the hydroxyl groups in phenol more acidic, which will then form stronger interactions with AC's basic or amphoteric oxygen surface groups. Although the respective concentrations of basic and acidic surface groups on AC were not quantified in this work, the values can be obtained by using Boehm titration technique.

The selection of a post-synthetically modified MIL-101 (Cr) -NH₂ for this study was done to investigate the effect of adding -NH₂ on the 2-CP adsorption performance compared to the pristine MIL-101 (Cr). A similarly functionalised MOF was used by Hasan et al. to remove hazardous pollutants like naproxen and clofibric acid (Hasan, Choi & Jhung, 2013). Their results demonstrated higher adsorption capacities on their ED-MIL-101 (Cr) (ethylene diamine modified) compared to pristine MIL-101 (Cr) and AMSA-MIL-101 (Cr) (aminomethanesulfonic acid). The

-NH_2 functionalization of MIL-101 (Cr) with ED made the MOF more basic, and the interactions with acidic -COOH group in the pollutants led to a stronger acid-base link between them.

4.2.8.2 Hydrophobic interactions

Additionally, adsorption of organic molecules often involves a complex balance between non-electrostatic (dispersion and hydrophobicity) and electrostatic interactions. Hydrophobic interactions, sometimes described as hydrophobic bonding, describes the unusual strong attraction between hydrophobic molecules and hydrophobic surfaces (Moreno-Castilla, 2004). AC demonstrated good 2-CP uptake possibly due to the low $\log K_{\text{OW}}$ value of 2-CP (2.15) which enabled strong hydrophobic-hydrophobic interactions between the adsorbate and the adsorbent (Chuang *et al.*, 2008).

4.2.8.3 Hydrogen bond formation

The -NH_2 functionalization strategy also aims to bring forward the establishment of H-bonding with 2-CP as depicted in Figure 4.7. As expected, after modification, the surface area of MIL-101 (Cr) -NH_2 decreased significantly compared to pristine MIL-101 (Cr). The addition of -NH_2 groups occupied some space in the pores. Thus, reducing the original MIL-101 (Cr)'s pore volume from $2.146 \text{ cm}^3/\text{g}$ to $1.250 \text{ cm}^3/\text{g}$. Among the MOFs, data from the batch adsorption isotherms in Figure 4.6 confirms that higher surface area, represented by MIL-101 (Cr) is key as it provides more vacant adsorption sites. Here, the extrinsically introduced H-bond surface groups ($\text{NH}_2\text{-H}_2\text{BDC}$) did not show more prevalent benefit than the available surface area unlike the case found by Hasan *et al.* (Hasan, Choi & Jhung, 2013). It could be because the lone pair of $\text{NH}_2\text{-H}_2\text{BDC}$ also has higher possibility of forming H-bond with the surrounding water molecules, thus, interfering with the overall 2-CP adsorption effectiveness (Gao *et al.*, 2013).

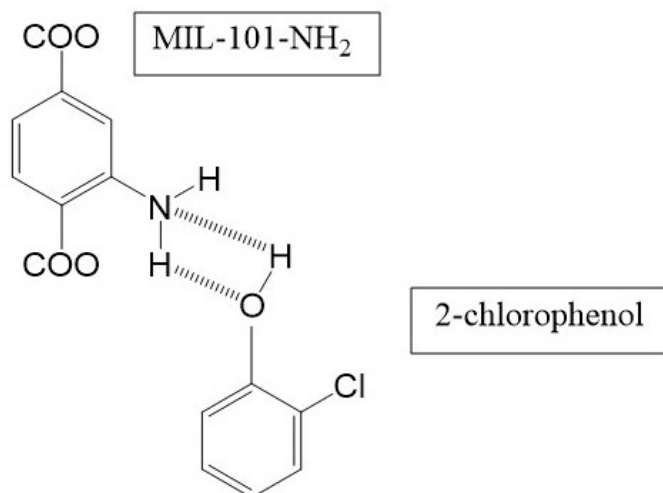


Figure 4.7: The author’s proposed hydrogen bond formation between 2-CP and the coordinated linker of MIL-101 (Cr)-NH₂ during the adsorption process.

MIL-101 (Cr) is already widely acknowledged as a water stable MOF. Previous studies for MIL-101 (Cr) have demonstrated high water uptake capacity at a moderate humidity (1.0 – 1.4 g H₂O/g MOF at P/P₀ = 0.9). The hydrophilicity of MIL-101 (Cr) is largely provided by the –COOH groups in the BDC linker (Ko *et al.*, 2015a). However, by introducing additional hydrophilic groups like –NH₂ and –SO₃H, it promotes more hydrophilic surface properties inside the pore, likely resulting to higher affinity of water molecules towards the pores (Akiyama *et al.*, 2012). Therefore, it can be asserted that the MIL-101 (Cr) -NH₂ derivative has become more hydrophilic after –NH₂ functionalization. Such a hydrophilic MOF, when exposed to room air containing moisture, is likely to result in the formation of water surface layers which will impede the mass transfer rates of guest molecules the pores, as well as occupying potential adsorption sites (Heinke, Gu & Wöll, 2014).

It has been reported for AC when molecular oxygen is present in the test environment, known as an “-oxic” condition, phenols are reported to undergo oligomerization. Consequently, the oligomerized phenols will develop an irreversible bond to the carbon surface and this may consolidate the high 2-CP uptake demonstrated by AC (Lu & Sorial, 2007).

Reported adsorption kinetics of 2-CP on a solid TiO₂ catalyst also demonstrated the existence of competitive adsorption between the solvent (water in their case) and the pollutant at the same sites (Rideh *et al.*, 1999). Therefore, it is understood that MIL-101 (Cr)'s hydrophilicity, as characterised by its high surface wettability as observed in Figure 4.5 seems to be the most important deterrent for an efficient 2-CP adsorption in contrast to hydrophobic AC, which can repel surrounding water molecules and facilitate preferential adsorption of the hydrophobic pollutant.

4.2.9 Kinetics study for 2-chlorophenol adsorption

Since MIL-101-NH₂ did not yield higher 2-CP uptake than the pristine MIL-101 (Cr), it was not studied any further. The adsorption kinetics 2-CP by MIL-101 (Cr) and AC as a function of time is shown in Figure 4.8 where both plots indicate a rapid adsorption of 2-CP into the adsorbents.

It has been presumed that the MIL-101 (Cr)'s hydrophilicity is the main element that causes it to demonstrate an inferior 2-CP adsorption compared to AC. To investigate other reasons behind MIL-101 (Cr)'s inferiority, it could be interesting to compare the pore size of the adsorbents with the adsorbate diameter (Jung *et al.*, 2001). From the porosity analysis in Table 4.1, MIL-101 (Cr) has the highest pore volume and the pore size distribution plots in Figure 4.3 also show that MIL-101 (Cr) has more mesoporosity (17 – 35 Å) compared to AC which is primarily microporous (5 – 15 Å). Meanwhile, the computationally calculated 2-CP molecular diameter is 5.6 Å. It could be expected that micropores would provide strong adsorption sites, relative to surface sites, but the pollutant's access to these micropores might be diffusion constrained. For the case of AC, the AC's higher microporosity could have helped it adsorb 2-CP more efficiently due to the closer match between the AC's micropore and the molecular size of 2-CP. The 2-CP removal kinetics plots in Figure 4.8 show that the adsorbents reached an adsorption equilibrium within the first hour, with no obvious diffusion constraints for either material.

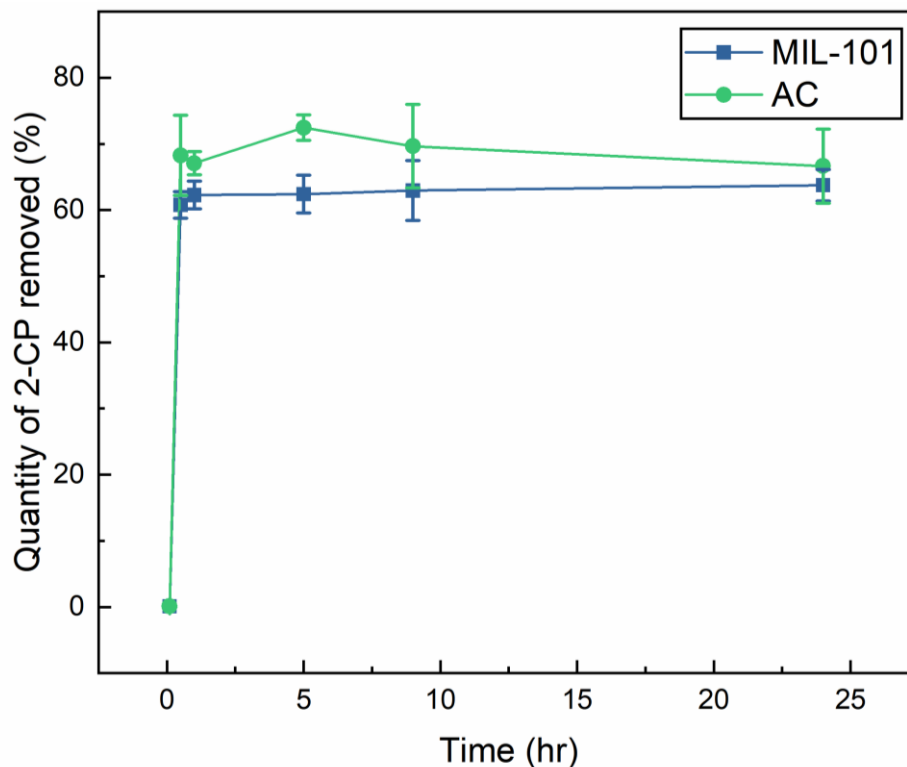


Figure 4.8: Amount of adsorbed 2-CP by MIL-101 (Cr) and AC at 25 °C after specific time intervals using [2-CP] = 500 mg/L, [MOF] and [AC] = 1 mg/mL solution.

4.2.10 Influence of pH and zeta potential on 2-CP adsorption

Figure 4.9 shows the quantity of 2-CP removed by MIL-101 (Cr) and AC as a function of solution pH range between 1 to 13 using batch experiments. As illustrated in Figure 4.9, irrespective of the adsorbent, there is no significant influence of solution pH from pH 1 to 6 on the adsorption of 2-CP. However, within this acidic pH range, AC once again surpassed the adsorption capacity of MIL-101 (Cr) due to the AC's hydrophobicity.

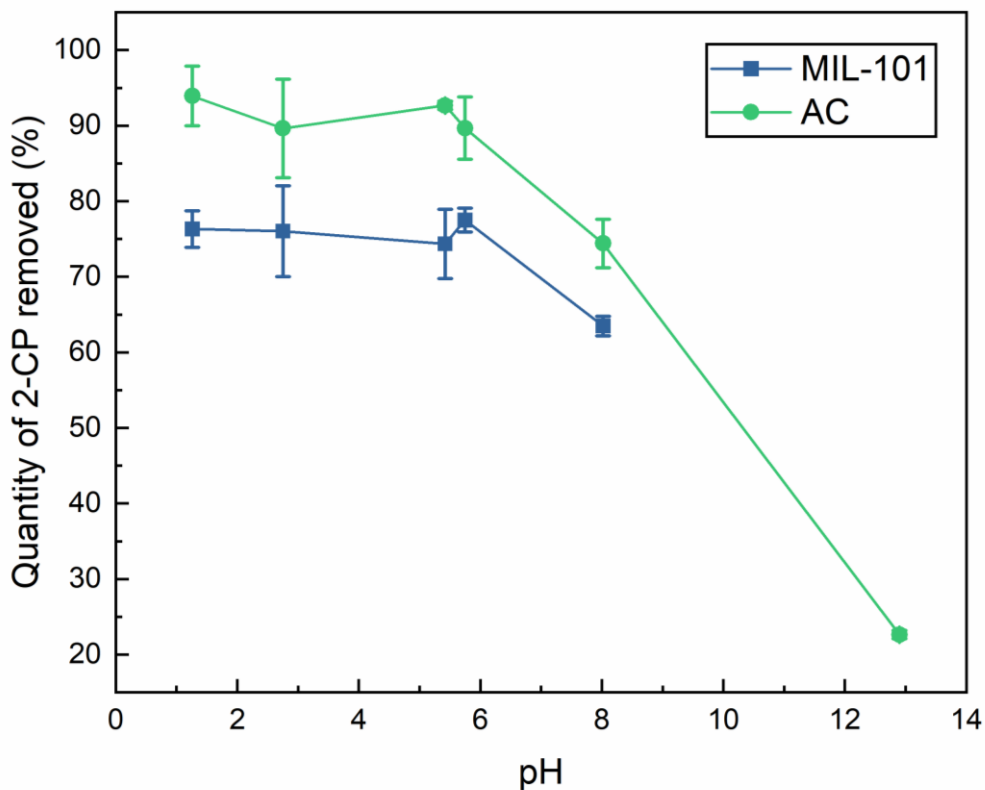


Figure 4.9: Influence of solution pH on the uptake of 2-CP by MIL-101 (Cr) and AC.

Phenols and their chlorinated forms are representatives of ionisable organic compounds (Kim *et al.*, 2005). This means, the variation of solution pH can affect 2-CP speciation (Figure 4.10) as well as the surface charge on the adsorbents. 2-CP has a dissociation constant (pK_a) value of 8.56. If solution $pH > 8.56$, the dominating species in the solution will be the anionic chlorophenolate. Conversely, when $pH < 8.56$, molecular 2-CP will be the dominant solution species (Chuang *et al.*, 2008). An increase in solution pH increases the number of negatively charged surface sites. Unfortunately, the effects of surface charge destabilization on MIL-101's 2-CP removal performance (Figure 4.9) after its pH_{PZC} could not be observed as MIL-101 degradation happens in an extremely basic condition ($pH = 13$), forming a green-coloured suspension. Early signs of MIL-101 (Cr) degradation were already observed from the material's porosity analysis in acidic and basic solutions, as shown in Table 4.1. Since a UV-Vis spectroscopic measurement can only be conducted on a homogenous solution, even after multiple filtrations, the degraded MIL-101 (Cr) particles could not be segregated from the pH 13 solution. Due to this reason, it is not possible to measure MIL-101 (Cr)'s uptake capacity at pH 13 on Figure 4.9.

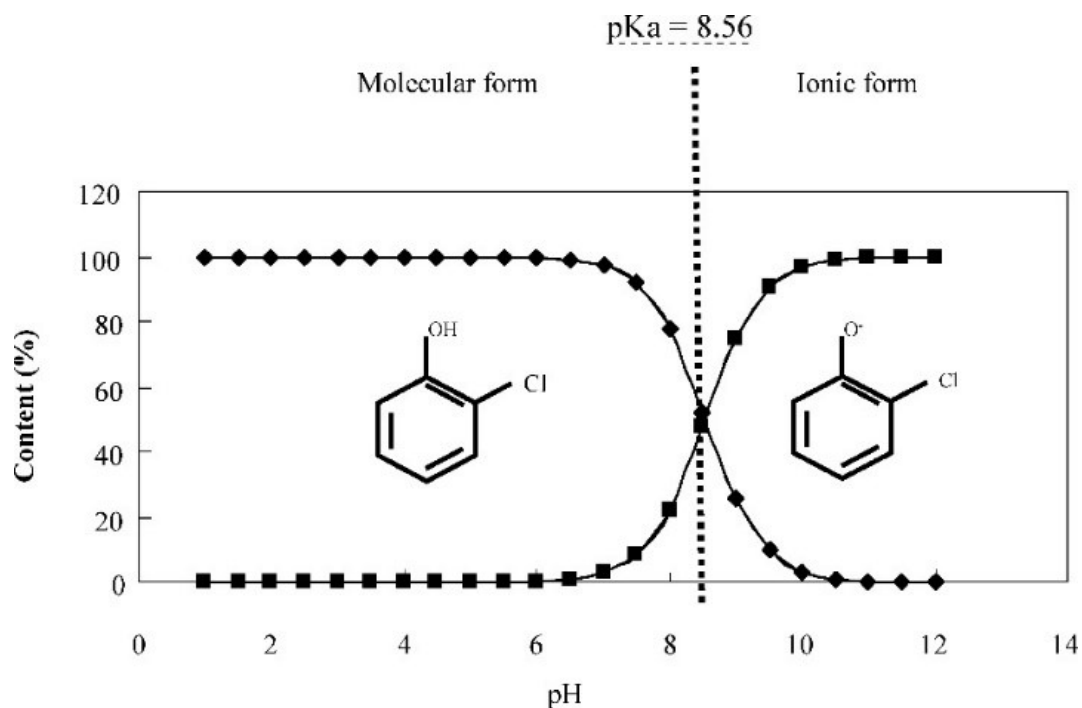


Figure 4.10: 2-CP speciation as a function of pH. Image from (Chuang *et al.*, 2008) with permission. Copyrights 2008, ACS Publications.

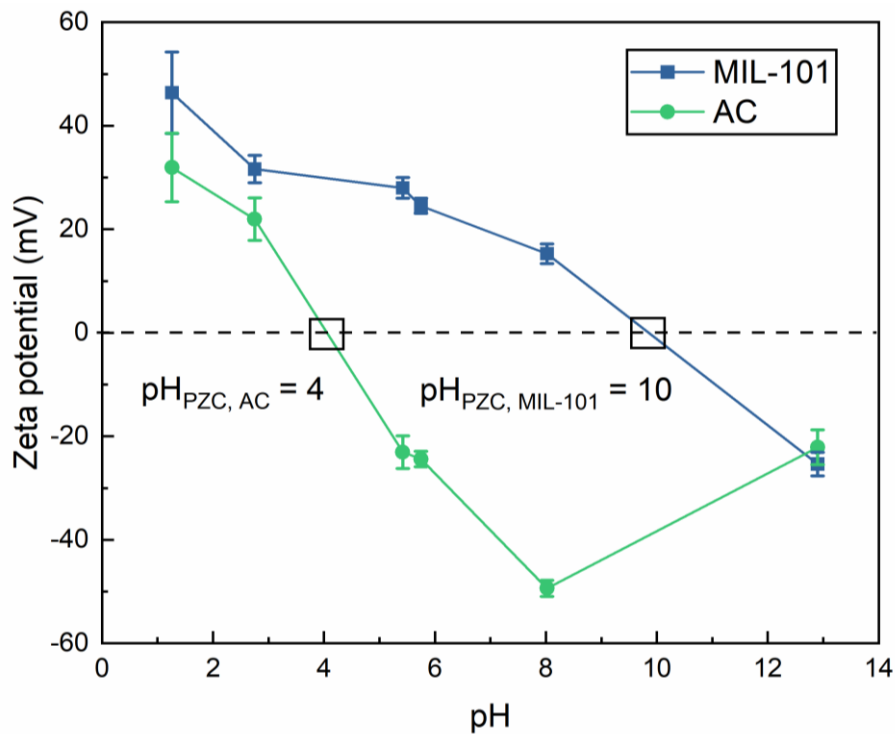


Figure 4.11: Zeta potential distribution for MIL-101 (Cr) and AC.

Figure 4.11 shows the change in the zeta potential (surface charge) of MIL-101 (Cr) and AC as a function of solution pH. Figure 4.9 shows AC with declining uptake especially after passing its estimated point of zero charge (PZC) at pH = 4. MIL-101 (Cr) also showed a similar downward trend at pH > 6, though it still has a positive surface charge. The decreases in 2-CP uptake by both adsorbents above pH 6 may be explained by the presence of stronger electrostatic repulsions interaction on their surfaces as these surfaces become less positively charged. At pH 8, close to the pK_a of 2-CP, significant concentrations of anionic 2-CP species exist in solution which will further impede the adsorption of increasing anionic solutions species onto more negative surfaces. Then, at pH 13, the solution becomes dominated by chlorophenolate ions. Consequently, the electrostatic repulsion between the negatively charged adsorbent surfaces and the anionic chlorophenolate species greatly reduced the adsorption ability to 25%, from an initial 90%.

Even though AC's adsorption capacity is very low at high pHs, some 2-CP can still be adsorbed. The result could be ascribed to the presence of residual silica on the AC surface which contains surface hydroxyl sites in which 2-CP could chemisorb to (Namasivayam & Kavitha, 2003; Alderman & Dellinger, 2005). The scanned PXRD patterns of AC in Figure 4.1 fully confirm the presence of some silica on AC.

4.3 Conclusions

Removal of persistent organic pollutants like phenols from aqueous solutions is generally achieved using adsorbent like activated carbon (AC), but it suffers from limited adsorption capacity due to its low surface area. In this Chapter, the adsorption performance of a model phenolic pollutant (2-CP) was studied using three different adsorbents namely MIL-101 (Cr), MIL-101 (Cr)-NH₂, and a commercial AC. The main findings can be summarised as follows:

1. The Langmuir maximum 2-CP uptake by AC is the highest (345 mg/g), followed by MIL-101 (125 mg/g) and MIL-101 (Cr)-NH₂ (99 mg/g) although the decreasing order of material surface area is MIL-101 (Cr) (2710 m²/g) > MIL-101 (Cr)-NH₂ (1983 m²/g) > AC (1179

m²/g). This means that high external surface area as in the case of these MOFs does not guarantee 2-CP adsorbate higher uptake.

2. The uptake quantity is more dependent on the strength of the adsorbate-adsorbent interaction. AC showed excellent removal performance as its adsorption mechanisms are governed by its abundance of basic/amphoteric oxygen surface sites such as -OH and -COOH that can adsorb the acidic 2-CP combined with AC's high material hydrophobicity. The introduced -NH₂ functionality into MIL-101 (Cr) was not able to form effective H-bonding with the 2-CP.
3. Native MIL-101 (Cr) is a highly hydrophilic material, as indicated from its 48° water contact angle measurement, which is the main reason for its inferior 2-CP uptake.
4. To utilize the high surface area of MOFs, the selected MOFs must exhibit high hydrophobicity to minimize the risk of competitive pollutant adsorption with water. Chapter 5 and 6 will investigate this idea in detail.

Chapter 5: Hydrophobic MOFs from vapour phase coating⁷

5.1 Introduction

This Chapter uses vapour-phase deposition to create hydrophobic MOFs. The commercial polymer polydimethylsiloxane (PDMS) was chosen due to its excellent hydrophobicity, gas phase selectivity and low cost. MIL-101 (Cr) is a frequently studied MOF for VOC capture because it has high surface area and pore volume. Unfortunately, MIL-101 (Cr)'s natural hydrophilicity results in low selectivity for common hydrophobic VOCs, especially in humid environments. Therefore, PDMS is emerging as a promising coating material for enhancing MIL-101 (Cr)'s hydrophobicity.

Given MIL-101 (Cr)'s high porosity and surface area, and the super hydrophobicity of the PDMS, MIL-101-PDMS composites could potentially exhibit high selectivity and uptake of VOCs. In this Chapter, a series of PDMS-coated MIL-101 (Cr) materials were prepared by tuning the PDMS vapour coating times and the PDMS molecular weights, followed by an evaluation on their effectiveness for competitive adsorption between toluene and water vapor. Toluene co-adsorption studies were performed at 0.5% P/P₀ (188 ppm) and 10% P/P₀ (3750 ppm) with 40% relative humidity (RH) at 25 °C. The 188 ppm is in the mid-range of the environmental concentration for human exposure; the OSHA Permissible Exposure Limits are 200 ppm while the National Institute for Occupational Safety and Health (NIOSH) Recommended Exposure Limit (REL) is 100 ppm (United States Department of Labor, 2021b). 3750 ppm represents a nominal industrial solvent-recovery scenario. All tests were conducted alongside the pristine MIL-101 (Cr) as well as AC for a more comparative understanding.

⁷ Part of this Chapter has been published as “Azmi, L. H. M.; Cherukupally, P.; Hunter-Sellars, E.; Ladewig, B.P.; Williams, D. R.. Fabrication of MIL-101-polydimethylsiloxane composites for environmental toluene abatement from humid air. *Chem. Eng. Jour.* **2022**, *429*, 132304.”

5.2 Results and discussion

5.2.1 PXRD and SEM

Figure 5.1 shows the PXRD patterns of the samples. The identical 2θ peaks at 8.7° , 9.3° , 10.6° and 16.9° exhibited by all coated materials signify their intact crystallinity relative to the theoretical peaks of MIL-101 (Cr) except for MIL-PDMS-Dow-6 which exhibited slightly degraded peaks. The high coating temperature of 235°C could be the reason for its crystallinity loss in this specific sample. This assumption was checked using SEM and Figure A10.9 shows the SEM images of the PDMS-coated samples. However, irrespective of the heating temperature, all samples display the typical octahedral morphology of MIL-101 (Cr) crystals, suggesting they are still stable even after being heated at 235°C .

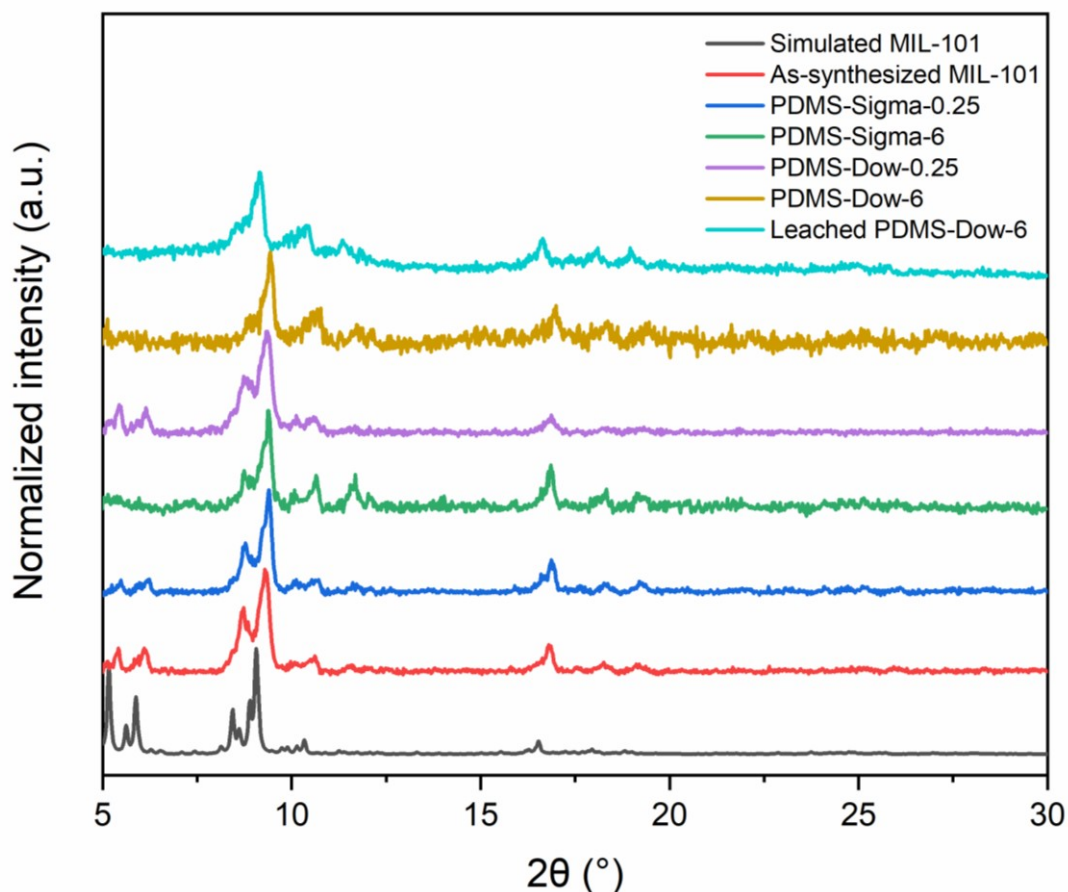


Figure 5.1: PXRD patterns of PDMS-coated MIL-101 (Cr) samples.

5.2.2 FTIR

The PDMS coating presence on MIL-101-PDMS composites was identified using FTIR spectroscopy. The FTIR spectra in Figure 5.2 of all PDMS-coated samples display the characteristic skeletal vibration of Si-O-Si bonds within 1130 cm^{-1} and 1000 cm^{-1} (Qin *et al.*, 2011). The chemical stability or leaching of the coating was also studied. Additional peaks formed at 800 cm^{-1} and 1264 cm^{-1} are associated with the $\text{CH}_3\text{-Si}$ stretching of the PDMS (Launer, Phillip J.; Arkles, 2013). There is no evidence of a covalent bond comprising of Si-O-Cr as the respective band that should appear as a strong, explicit band between 900 cm^{-1} and 1000 cm^{-1} (Selvaraj, Kim & Lee, 2005). Studies that employed similar deposition technique with PDMS reported no change in the elemental oxidation states of their treated materials' surface (Yuan *et al.*, 2008; Zhang *et al.*, 2014b; Huang *et al.*, 2016; Xu & Yan, 2016; Kang *et al.*, 2019; He *et al.*, 2020), indicating the PDMS is physically deposited on the surface.

The chemical stability or leaching of the coating was evaluated by soaking MIL-PDMS-Dow-6 in water for 24 hrs. The IR spectrum after the leaching test displays an increased intensity and broadening of the abovementioned peaks. The broadened peaks suggest the sample's hydrogen bonding with water molecules, possibly occupying the pores of the material where PDMS layer is absent. Besides, all samples irrespective of their coating time displayed a consistent peak at 1625 cm^{-1} arising from H-O-H bending bands of water (Xie *et al.*, 2020). The matching trends confirm there are still hydrophilic pore sites that were excluded from the coating.

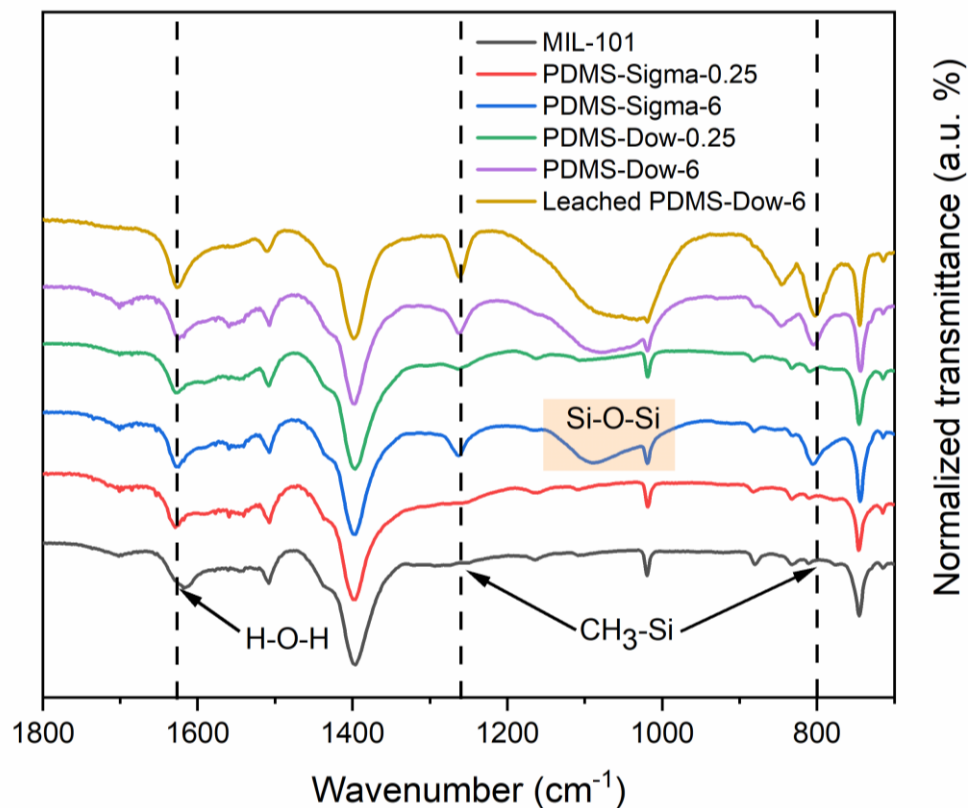


Figure 5.2: FTIR spectra of the MIL-101 (Cr)-PDMS composites.

5.2.3 XRF

The XRF analysis in Figure 5.4 shows the cumulative PDMS deposition (represented by elemental Si wt%) for different coating times. Generally, the Si coating quantities for both PDMS types had plateaued at about 1 hr. Figure 5.3 shows the n repeating monomer unit of $[\text{SiO}(\text{CH}_3)_2]$ that forms the polymer PDMS.

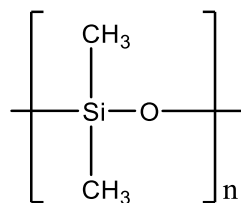


Figure 5.3: Repeating unit of PDMS polymer.

$$\text{Max. Si wt\% content} = \frac{\text{MW of Si}}{\text{MW of PDMS repeat unit}} \times 100 \quad \text{Equation 5.1}$$

$$\text{Wt\% of PDMS in MOF} = \frac{\text{Measured Si wt\% from XRF}}{\text{Max. Si wt\% content}} \times 100 \quad \text{Equation 5.2}$$

Equation 5.1 shows the maximum hypothetical content of Si on a treated surface where MW is molecular weight (g/mol). By using the formula, if all Si from the PDMS repeating unit is incorporated in the treated MIL-101 (Cr), the maximum Si content that should be detected by XRF is 37.8 wt%. Equation 5.2 shows the use of the measured Si wt% from XRF to generate the PDMS wt% in the treated samples. Table 5.1 shows the calculated PDMS wt% content in each treated MOF.

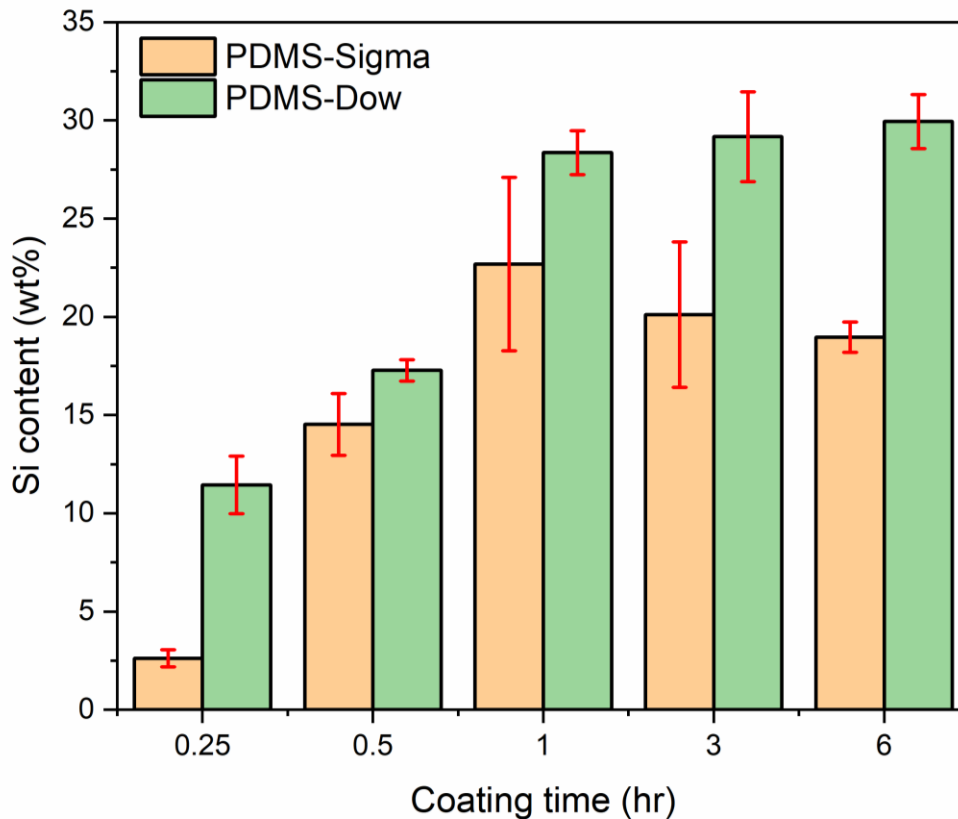


Figure 5.4: Elemental Si wt% quantification of all samples using XRF.

Table 5.1: Calculated PDMS wt% content from XRF data.

Sample	Deposition time (hr)	Measured Si wt% content from XRF	Calculated wt% of PDMS in MOF
MIL-PDMS-Sigma	0.25	2.6 ± 0.4	6.9 ± 1.1
	0.50	14.5 ± 1.6	38.4 ± 4.2
	1	22.7 ± 4.4	60.0 ± 11.6
	3	20.1 ± 3.7	53.2 ± 9.8
	6	19.0 ± 0.8	50.2 ± 2.1
MIL-PDMS-Dow	0.25	11.5 ± 1.5	30.3 ± 4.0
	0.50	17.3 ± 0.6	45.7 ± 1.6
	1	28.4 ± 1.1	74.9 ± 2.9
	3	29.2 ± 2.3	77.1 ± 6.1
	6	30.0 ± 1.4	79.1 ± 3.7

5.2.4 Porosity analysis

In a chemical vapour deposition method, the coating time would directly influence the amount of coating deposited on the outer surface and potentially in the pore surface of the MOFs. Therefore, the effect of PDMS exposure time to the MOF's pore volume was evaluated at 0.25 and 6 hrs. The complete (up to 0.99 N₂ P/P₀) and the low P/P₀ range (maximum of 0.1 N₂ P/P₀) N₂ adsorption and desorption isotherm plots are shown in Figure 5.5 and Figure 5.6 respectively.

In Figure 5.5, MIL-PDMS-Dow-6 and MIL-PDMS-Sigma-6 both seem to have lost their mesoporosity, since there is no characteristic abrupt mesopore filling (after capillary condensation) at around 0.2 N₂ P/P₀. Instead, after this point, their adsorption isotherms became quite flat which supports their major loss of mesoporosity. Below 0.1 N₂ P/P₀ (Figure 5.6), the first group (MIL-101 (Cr), MIL-PDMS-Sigma-0.25, MIL-PDMS-Dow-0.25) showed higher microporous adsorption quantity than the second group (MIL-PDMS-Sigma-6, MIL-PDMS-Dow-6). The micropores of the adsorbents in the second group are likely to be severely blocked.

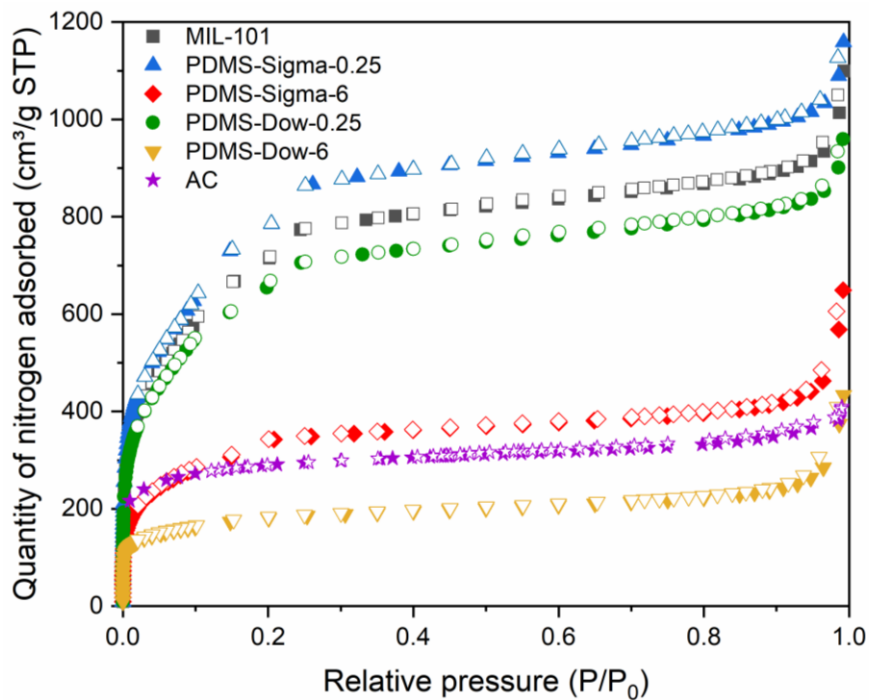


Figure 5.5: N_2 adsorption (full symbols) and desorption (empty symbols) isotherms.

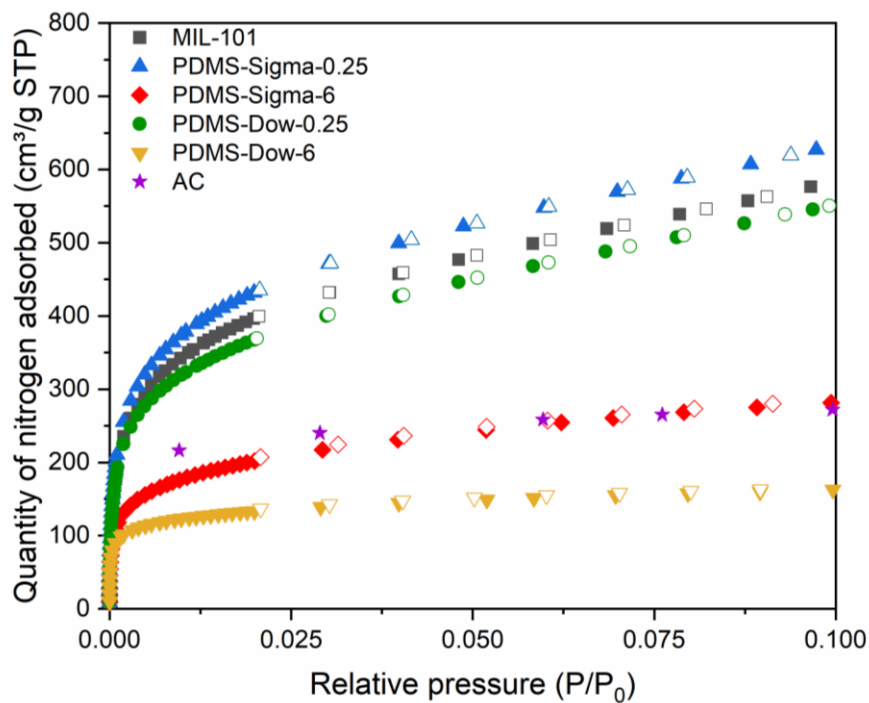


Figure 5.6: 0 to 0.1 P/P_0 of the N_2 adsorption (full symbols) and desorption (empty symbols) isotherms.

Table 5.2 provides the details of the BET surface area and total pore volume measurements whereby increasing the deposition time from 0.25 hr to 6 hrs of coating reduced the $V_{\text{micro}}/V_{\text{total}}$ ratio. This change is also visually identifiable from the adsorbents' pore size distribution plots (Figure 5.7). AC is a microporous material whereas the MOFs have a series of pores within the micropore and mesopore regions, but primarily mesoporous in nature. After 0.25 hr coating time, the PDMS-coated MOFs experienced lesser reduction in their available porosity as opposed to after 6 hrs of coating time, where the pore blockage was more pronounced.

Table 5.2: Surface area, pore volume and water contact angles for MIL-101 samples and AC.

Sample	BET surface area (m ² /g)	V _{total} (cm ³ /g)	V _{micro} (cm ³ /g)	V _{micro} /V _{total}	Water contact angle (°)
MIL-101 (Cr)	2607 ± 56	1.705	1.127	0.661	48 ± 2
MIL-PDMS-Sigma-0.25	2865* ± 76	1.797*	1.231*	0.685*	48 ± 2
MIL-PDMS-Sigma-6	1192 ± 17	1.006	0.477	0.474	131 ± 3
MIL-PDMS-Dow-0.25	2398 ± 35	1.488	0.979	0.658	48 ± 2
MIL-PDMS-Dow-6	656 ± 10	0.672	0.237	0.353	133 ± 3
Activated carbon (AC)	1179 ± 20	0.805	0.470	0.584	120 ± 2 [#]

* Slightly higher values than MIL-101 (Cr) due to batch-to-batch variations in synthesis process.

[#] Taken from (Liu, Yang & Xue, 2016).

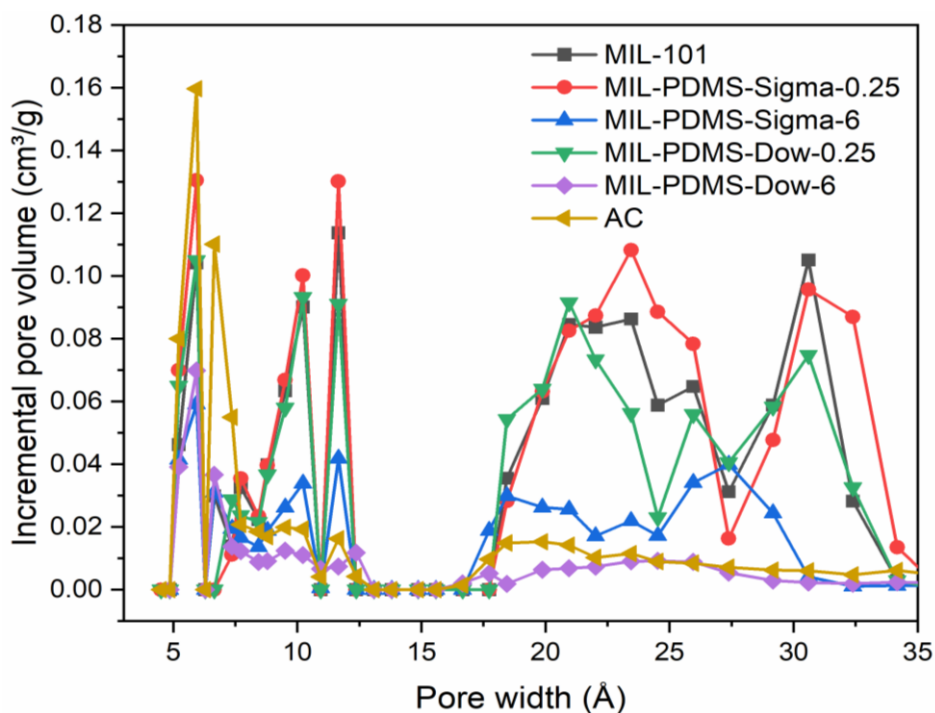


Figure 5.7: Pore size distribution analysis for all samples estimated from Tarazona non-local density functional theory model (N₂) using a cylindrical pore geometry assumption.

Based on Table 5.2, for MIL-PDMS-Sigma, the total surface area and the pore volume were each 140% and 79% higher for 0.25 hr relative to 6 hrs coating. Whilst for MIL-PDMS-Dow, the total surface area and the pore volume were 266% and 121% higher for 0.25 hr relative to 6 hrs. These combined results confirm that the longer exposure times filled the pores with PDMS. Notably, when the lower molecular weight Sigma PDMS was used with a 0.25 hr coating time, both the surface area as well as the pore volume were preserved. MIL-PDMS-Dow-0.25 exhibited some pore volume reduction which may be associated with greater pore space occupation by this higher molecular weight PDMS. To further assess their adsorption performance corresponding to the available surface area, MIL-PDMS-0.25 and MIL-PDMS-6 samples were compared. Note that this study only considered the impact of PDMS molecular weight on adsorbent's pore blockage. According to a previous report, fine tuning the polymer chain architecture was a proven option to achieve excellent PDMS coating without compromising adsorbent porosity (He *et al.*, 2020).

5.2.5 Water contact angle

Changes in the hydrophobicity on the MOF's outer surface and in its internal pores was evaluated using water contact angles and vapour adsorption-based hydrophobicity index (HI), respectively. The static contact angles in Table 5.2 were measured using sessile drop method with water, though these measurements were not possible for AC due to its granular nature and surface roughness. However, AC is well accepted to be a hydrophobic material with a high water contact angle value ($120 \pm 2^\circ$) (Liu, Yang & Xue, 2016) whereas MIL-101 (Cr) has a $48 \pm 2^\circ$ contact angle with water because of its innate hydrophilicity. After 0.25 hr coating time, both MIL-PDMS-Sigma and MIL-PDMS-Dow samples have contact angles similar with the unmodified MIL-101 (Cr). This result is slightly surprising and is most likely due to incomplete external surface coverage by the PDMS coating (e.g., patch wise coating). However, after 6 hrs of coating, the deposited PDMS resulted in an increased contact angle $> 130^\circ$, confirming successful external surface modification from a hydrophilic to a superhydrophobic surface (Figure 5.8). The influence of prolonged coating time on the sample's hydrophobicity agrees well with other reports in the literature (Huang *et al.*, 2016; Gao *et al.*, 2020b). Although controlling the PDMS layer thickness uniformity can certainly improve the adsorbents' surface hydrophobicity, it is considered more essential to assess the impact of the treatment on MIL-101 (Cr)'s internal hydrophobicity for VOC adsorption applications.

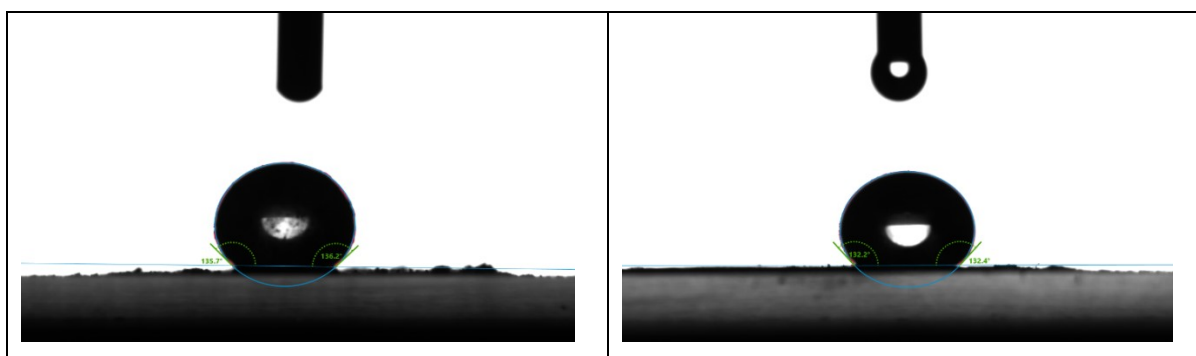


Figure 5.8: Images of the static water contact angle measurements for (left) MIL-PDMS-Dow-6 and (right) MIL-PDMS-Sigma-6 at ambient temperature.

5.2.6 Water sorption isotherms

Figure 5.9 shows the water adsorption and the desorption isotherms of all samples. Details on water adsorption mechanisms for MIL-101 (Cr) have been reported previously in which the water molecules initially bind to the metal sites on the MOF scaffold, followed by gradual occupation of the mesopores. During this initial adsorption stage, additional water build-up leads to formation of small hydrogen-bound water clusters. Finally, the water uptake proceeds at a slower rate as the molecules transfer into the large molecular cages and the remaining inter particulate voids before reaching uptake saturation (Küsgens *et al.*, 2009; Ko *et al.*, 2015a). The water adsorption isotherm for MIL-101 (Cr) displays two distinct adsorption steps: a first step from 40 to 45% water P/P₀ and a second step between 45 to 50% water P/P₀, confirming the presence of two mesoporous cages with different aperture sizes (Yanagita *et al.*, 2019).

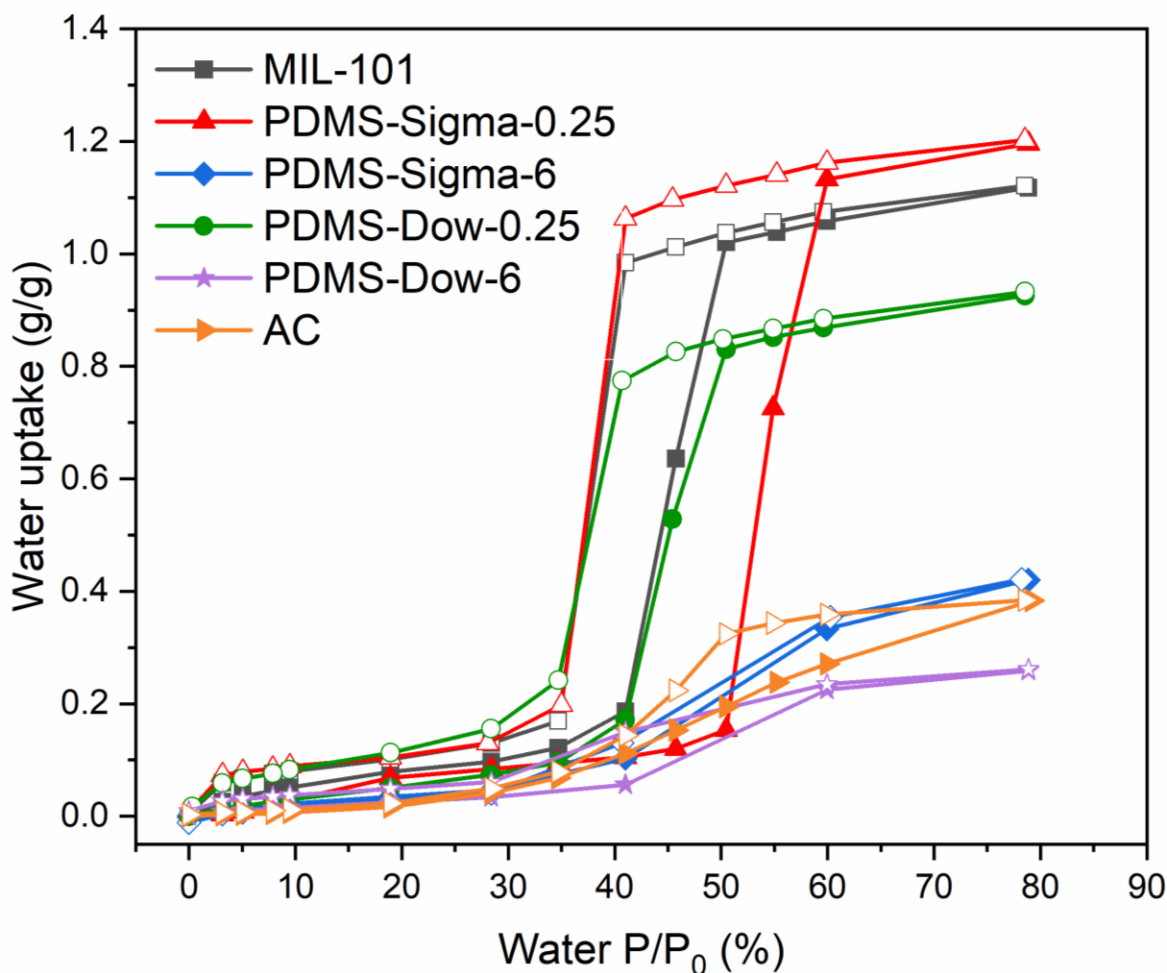


Figure 5.9: Water adsorption-desorption isotherms at 25 °C. Filled symbols and empty symbols are the adsorption and the desorption data points, respectively.

After 0.25 hr coating time, MIL-PDMS-Sigma-0.25 exhibited no decrease in its Type-V water uptake isotherm compared with the pristine form. Even though Table 5.2 shows MIL-PDMS-Sigma-0.25 has a 10% higher BET surface area than the pristine MIL-101 (Cr), this increase is fortuitous due to some small variations in the MOF batches produced. For the 6-hr coated MIL-101 (Cr) samples, their reductions in water uptake capacity correlated with their respective surface area reduction. Despite this chemical vapour deposition technique being commonly used from time to time (Zhang *et al.*, 2014b; Huang *et al.*, 2016; Kang *et al.*, 2019; He *et al.*, 2020; Zheng *et al.*, 2020b), the risks of severe pore blockage reported here highlight the need for a careful application process to be an effective means to enhance MIL-101 (Cr)'s hydrophobicity.

Whilst longer coating times yielded greater surface hydrophobicity, excessive duration negatively impeded pore access (Huang *et al.*, 2016). Both 6 hr-coated MIL-101 (Cr) samples exhibited substantial pore blockage. MIL-PDMS-Dow-6 suffered the greatest porosity loss, hence, its low water uptake at 80% P/P₀.

There appears to be a divergence between a material's external surface hydrophobicity and its water adsorption isotherms. The reason is because a water contact angle measurement can only interrogate the external surface chemistry that highly depends on the surface morphology and structure (i.e., grain size and arrangement), as well as the uniformity of any surface treatments being used. On the other hand, a material's water isotherms are representative of the adsorption chemistry arising from its intrinsic hydrophobicity. Furthermore, water contact angles on irregular surfaces, such as particulate substrates, are partially dependent on the substrate's roughness (Jayaramulu *et al.*, 2019; Gao *et al.*, 2020b). This behaviour is demonstrated by AC as the intrinsically hydrophobic pores resulted in a slower, gradual water uptake until it is capped by the material surface area. The 80% water P/P₀ uptake performance of the adsorbents can therefore be ranked as follows: MIL-PDMS-Dow-6 < AC < MIL-PDMS-Sigma-6 < MIL-PDMS-Dow-0.25 < MIL-101 (Cr) < MIL-PDMS-Sigma-0.25.

5.2.7 Toluene sorption isotherms

Figure 5.11 shows the amount of dry toluene adsorbed and desorbed by all samples as a function of toluene concentration. MIL-PDMS-Sigma-0.25 and MIL-101 (Cr) have almost identical and the highest adsorption capacity at 80% toluene P/P₀; 110 wt%. This result is also 260% higher than the performance industrial AC, even though MIL-PDMS-Sigma-0.25 and MIL-101 (Cr) have hydrophobic and hydrophilic pores respectively. Toluene, which has a low surface tension (28.5 mJ/m² at 20° C) will exhibit a contact angle of close to 0° for the hydrophilic MIL-101 (Cr). Similarly, for PDMS, which is swellable by toluene, will also exhibit a low contact angle of about 20° (see Figure 5.10). These low contact angles exhibited by toluene for both substrates are the reason for the identical isotherms, including the mesopore filling regions as observed in Figure 5.11. Reductions in toluene adsorption capacity for the other MIL-101-PDMS materials generally

scale with their available surface area and pore volume. For instance, MIL-PDMS-Dow-6 has the lowest toluene uptake due to its lowest surface area and lowest pore volume.

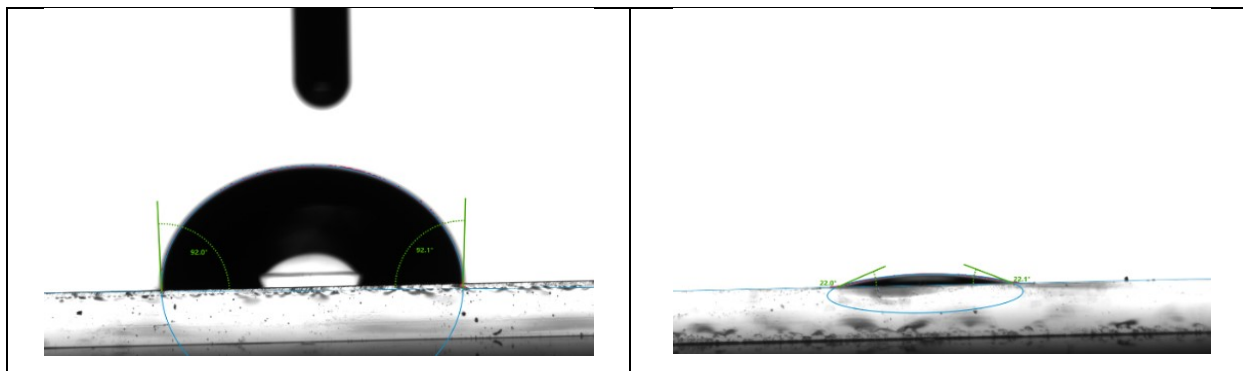


Figure 5.10: Advancing contact angle measurements for PDMS-Sigma-coated microscope slide at 25 °C. (Left) Water contact angle is $92 \pm 3^\circ$. (Right) Toluene contact angle is $22 \pm 3^\circ$.

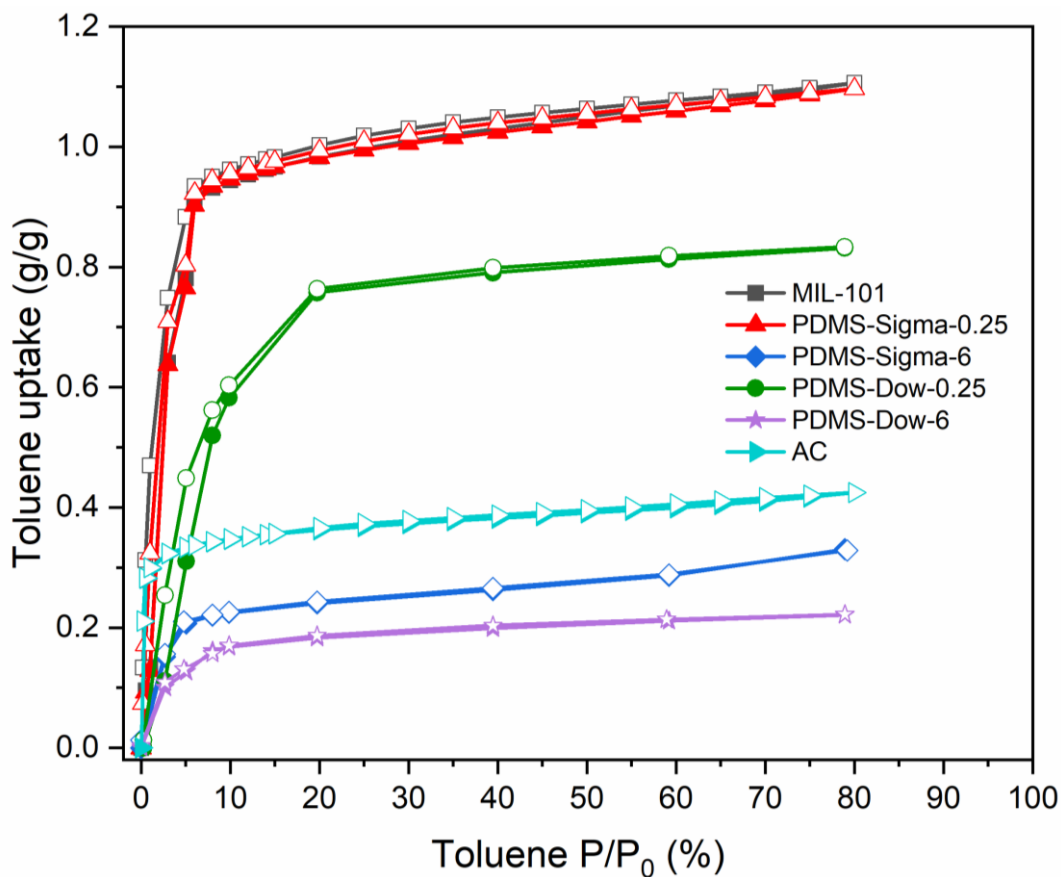


Figure 5.11: Dry toluene adsorption-desorption isotherms at 25 °C. Filled symbols and empty symbols are the adsorption and the desorption data points, respectively.

To examine the adsorption rate for low toluene concentrations ($< 10\%$ toluene P/P_0), the quantity of toluene adsorbed was plotted against the adsorption time, and the plots are shown in Figure 5.12. Overall, adsorption rates are rather slow. Interestingly, AC showed faster adsorption rate and higher capacity which confirms the utility of AC for low toluene P/P_0 ($< 5\%$) concentrations when only a single adsorbate is present. Once P/P_0 was above 5%, both AC and the MOF variants had similar kinetics and adsorption capacity in these single component toluene experiments. MOFs are preferred for adsorbing higher toluene quantities due to their high 80% toluene P/P_0 adsorption capacity (Kim *et al.*, 2019). AC's low surface area is its major limitation to capture any higher toluene quantity.

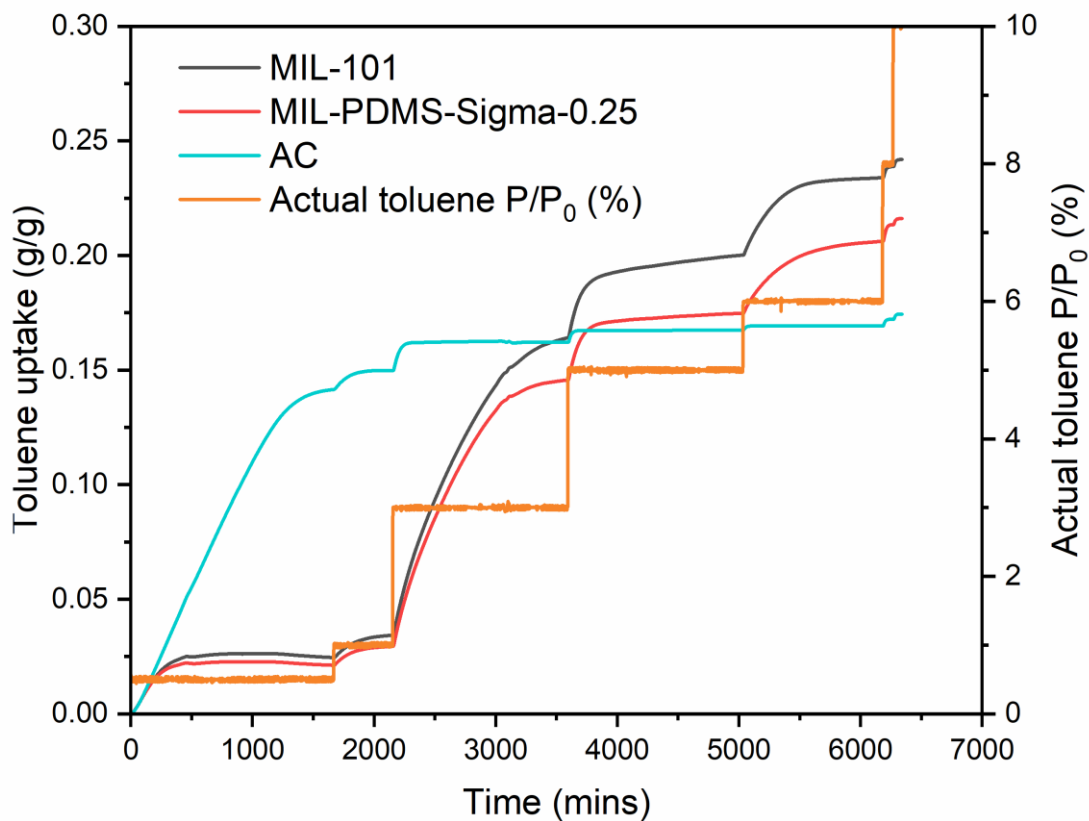


Figure 5.12: Dry toluene adsorption kinetics for MIL-101 (Cr), MIL-PDMS-Sigma-0.25 and AC at $< 10\%$ toluene P/P_0 region.

5.2.8 Hydrophobicity index

Figure 5.13 shows the experimentally estimated HI values as a function of humidity for all samples. Below 10% RH, the HI value of MIL-PDMS-Sigma-0.25 is between 2 and 8 times higher than MIL-101 (Cr). Therefore, MIL-PDMS-Sigma-0.25 is expected to offer superior VOC capture in low RH environment. Above 10% RH, AC exhibits the highest HI values. This suggests that AC could perform better if the application involves higher humidity between 10% and 50% RH. Nevertheless, as the humidity level increases, all samples will become fully saturated with adsorbed water, eventually losing some of their capability to readily adsorb hydrophobic organic molecules (Hunter-Sellars *et al.*, 2020).

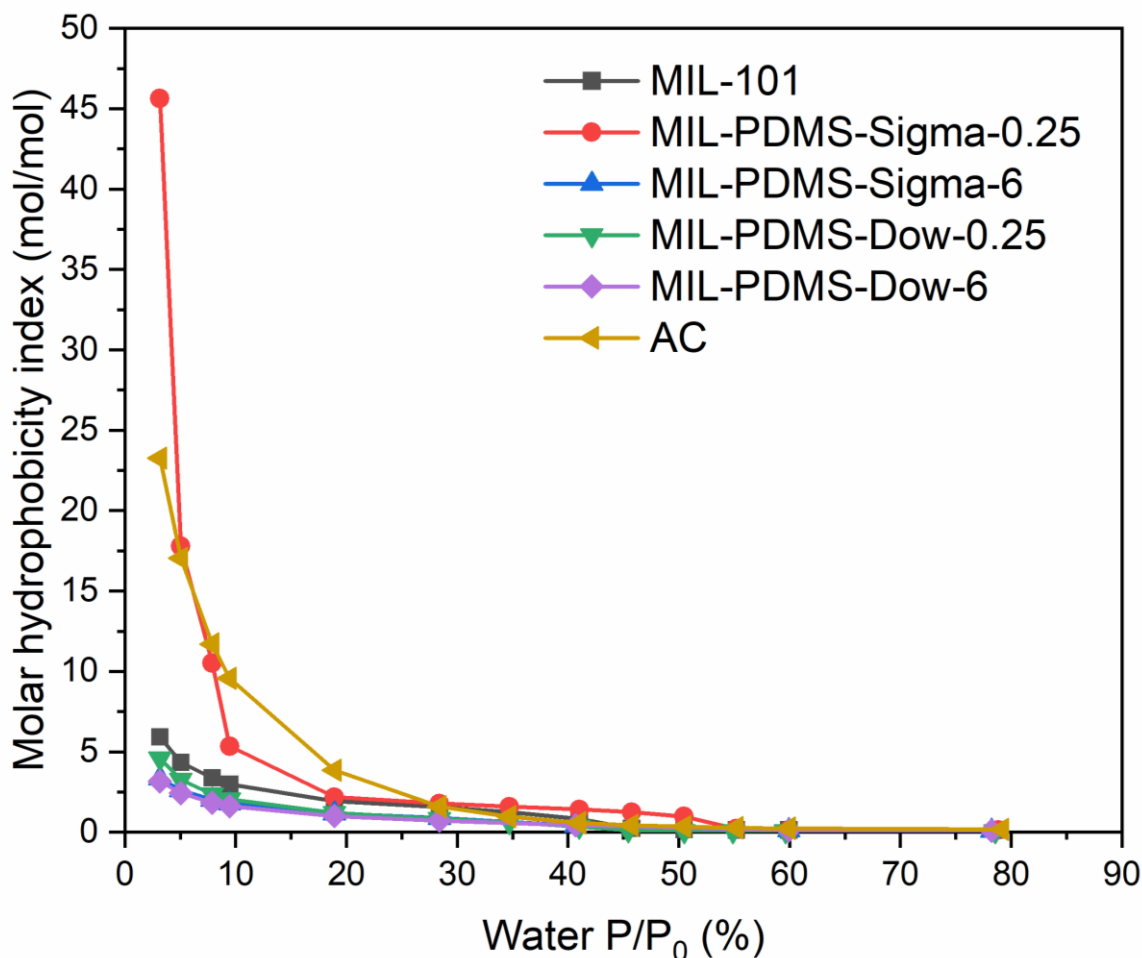


Figure 5.13: Calculated molar hydrophobicity index (HI) for selected adsorbents as a function of % water P/P₀ at 25°C.

5.2.9 Water and toluene co-adsorption experiments

The increased hydrophobicity of the mesopores in MIL-PDMS-Sigma-0.25 has a profound impact on the water mesopore filling events as shown by the water isotherms in Figure 5.9. A careful examination of Figure 5.9 shows that the mesopore filling by water starts at around 35 to 40% water P/P_0 for MIL-101 (Cr). However, for MIL-PDMS-Sigma-0.25, the start of its pore filling is delayed to between 45 and 50% water P/P_0 . This delay in pore filling can be directly ascribed to the change in contact angle for water condensing in these pores and the Kelvin equation that describes the condensation vapor pressures. In the case of the original MIL-101 (Cr) surface, the contact angle between water and MIL-101 (Cr) is $48 \pm 2^\circ$, whilst for water on a homogeneously PDMS-coated surface such as a mesopore, the contact angle would be $> 90^\circ$ as shown in Figure 5.10. The Kelvin equation which broadly governs condensation events within pores and the vapor pressures at which these events occur, depends directly on the contact angle the liquid makes with the pore surface. This angle then determines the resultant local capillary curvature and vapor pressure. Higher liquid contact angles result in lower radii of curvature for condensing droplets in pores, which results in higher vapour pressures for the onset of pore condensation to occur.

To help understand this concept better, readers are referred to a study by David et al. on hydrophobic (methylated) and hydrophilic (hydroxylated) variants of silica MCM-41 (David *et al.*, 2020). They reported an increase in pore filling humidity from 45% to 70% water P/P_0 for the hydrophobic 2.4 nm-pore samples compared to the hydrophilic ones, for nominally identical pore sizes. In the case of hydrophobic 9-nm pore samples, they exhibited no pore filling below 80% water P/P_0 , both in their adsorption and desorption plots. That is, whenever the humidity was under 80% water P/P_0 , the mesopores were effectively empty. This work shows that methyl functionalized-MCM 41 can form hydrophobic mesopores which eventually delay the samples' water vapour condensation to higher vapour pressures.

5.2.10 Uptake capacity at 40% RH and 0% toluene P/P_0

Previously, the water (Figure 5.9) and the dry toluene (Figure 5.11) adsorption experiments of all studied adsorbents were performed as single component experiments. So, the next important question is to understand whether the hydrophobic coating contributes positively to the materials'

competitive two vapour adsorption performance. Competitive adsorption experiments involve the co-existence of water and toluene at an average operating humidity (40% RH) and at two different toluene concentrations (0.5% and 10% toluene P/P₀). Comprehensive material screening was performed by using the materials' corresponding 40% RH/0% toluene P/P₀ adsorption capacity (Figure 5.14) as an estimate of their extent of pore blockage. Generally, across the coating time range of 0.25 hr to 6 hrs, there is a consistent decrease in the adsorbents' equilibrium capacity due to the increasing severity of pore blockage.

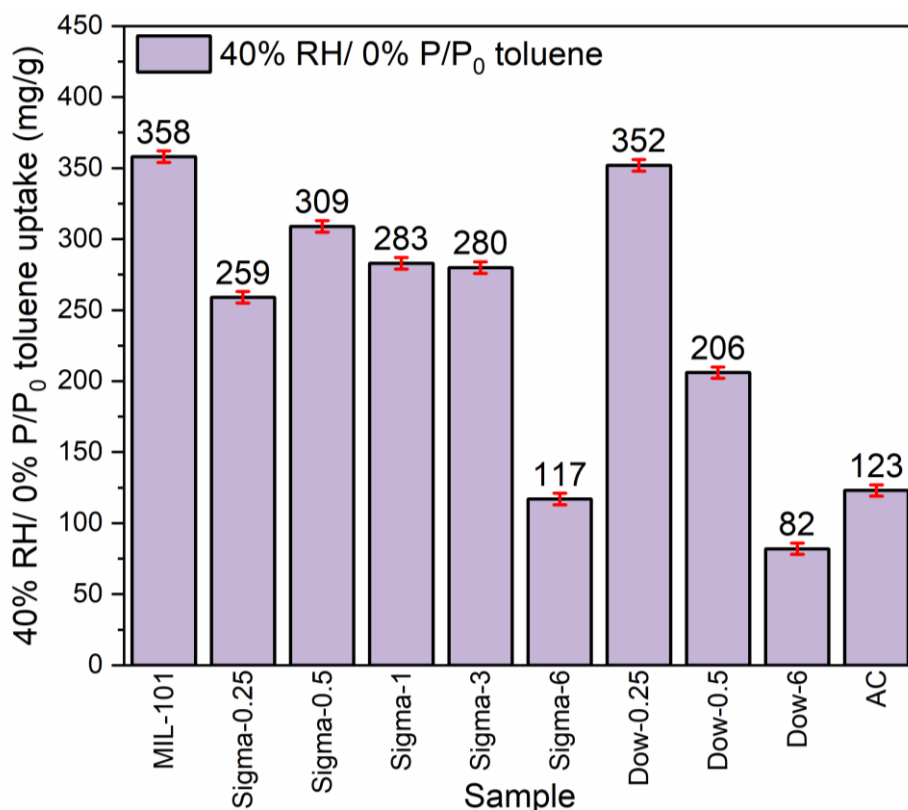


Figure 5.14: Adsorption capacity of all studied adsorbents at 40% RH and 0% toluene P/P₀.

The materials presented in Figure 5.14 all have lower surface areas and pore volumes than the untreated MIL-101 (Cr) except for MIL-PDMS-Sigma-0.25 and MIL-PDMS-Dow-0.25. Therefore, the lower levels of water uptake at 40% RH would be expected. However, the MIL-PDMS-Sigma-0.25 exhibits a 25% lower water uptake compared to pristine MIL-101 (Cr), which is ascribed to the hydrophobic mesopores created. Overall, the water adsorption at 40% RH is a

balance between pore volume and pore accessibility for the adsorbent by the adsorbate, and pore wettability by the adsorbate.

5.2.11 Uptake capacity at 40% RH and 0.5% toluene P/P₀

Figure 5.15 shows the co-adsorption uptake results corresponding to 40% RH/0.5% toluene P/P₀. The PDMS coating on MIL-PDMS-Sigma-0.25 achieved a 60% higher toluene uptake level compared to the standard MIL-101 (Cr): at 170 mg/g and 107 mg/g respectively. AC's uptake capacity fell slightly behind these two MOFs, adsorbing about 100 mg/g, but AC's pore diffusion kinetics is very slow as shown in Figure 5.16. It is also apparent that even for the shortest coating time on the Dow-coated PDMS, MIL-PDMS-Dow-0.25's performance at 40% RH/0.5% toluene P/P₀ is inferior to the substantial improvement exhibited by MIL-PDMS-Sigma-0.25. For this reason, this former material was not taken forward for more detailed studies at 40% RH/10% toluene P/P₀ (Figure 5.17). Also, from this data, only MIL-PDMS-Sigma-0.25, MIL-PDMS-Sigma-6 and MIL-PDMS-Dow-6 samples were selected for comparison with the pristine MIL-101 (Cr) and AC.

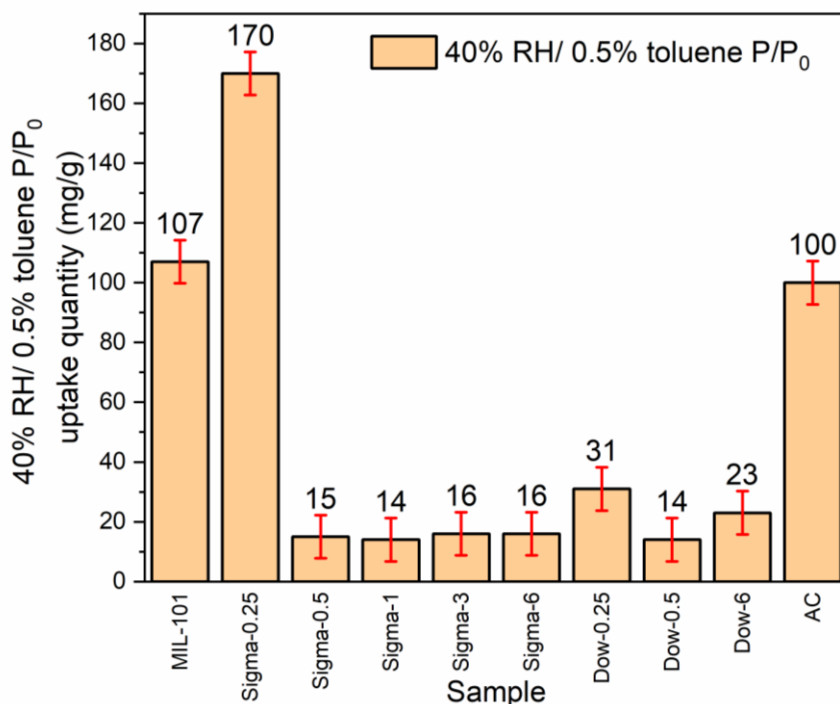


Figure 5.15: Toluene uptake quantity by PDMS-coated MIL-101 samples at 0.5% toluene P/P₀. All experiments were performed at 40% RH saturation and at 25 °C.

5.2.12 Adsorption kinetics for 40% RH and 0.5% toluene P/P₀

Figure 5.16 shows the adsorption kinetics by all modified MIL-101 (Cr) samples at 40% RH/0.5% toluene P/P₀. The data in Figure 5.16 (left) was analysed with a nonlinear pseudo first order kinetics model. Typically, if a nonlinear kinetics model is used, there are two main parameters that can be derived from the model namely, the sample's maximum theoretical equilibrium capacity (q_m) and its kinetics coefficient (k). Ideally, for practical and industrial applications, a material should have high values in both categories, meaning it will be able to adsorb a high quantity of adsorbate at a fast rate. For a better understanding of each material's performance and a convenient ranking assortment, a new metric is proposed by taking the product of the experimental adsorption capacity (q_e) and the k : $q_e.k$. The term is referred to in this thesis as the *aggregate adsorption rate*.

Based on the $q_e.k_1$ values at 40% RH/0.5% toluene P/P₀ shown in Table 5.3, the increasing order from worst to best material is:

AC < MIL-PDMS-Dow-6 < MIL-PDMS-Sigma-6 < MIL-101 (Cr) < MIL-PDMS-Dow-0.25 < MIL-PDMS-Sigma-0.25.

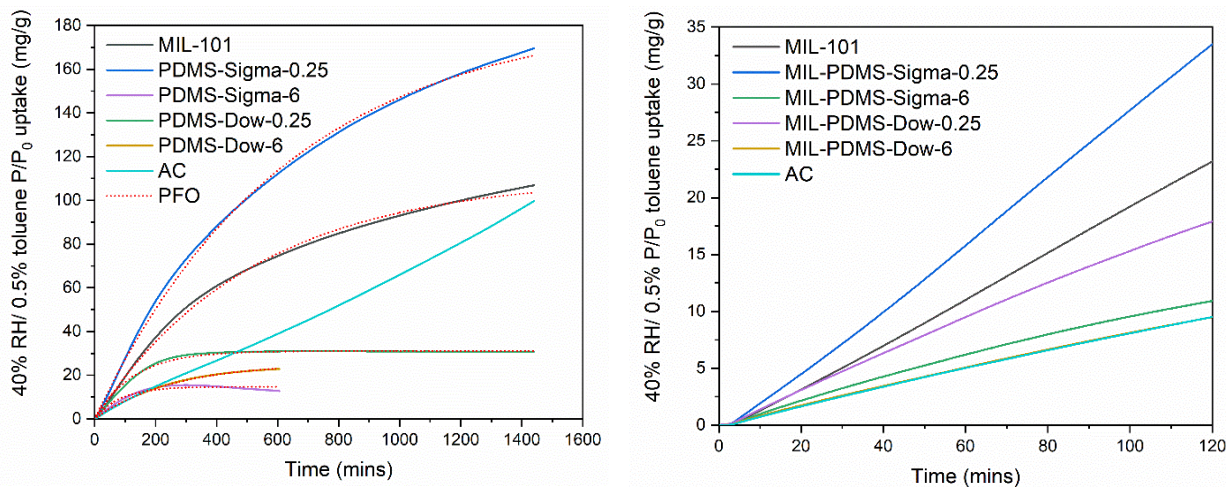


Figure 5.16: (Left) Adsorption kinetics at 40% RH and 0.5% toluene P/P₀ by MIL-PDMS samples. Solid lines are the experimental data whereas dotted lines are the fitted values derived from pseudo first order (PFO) kinetics model. (Right) The initial adsorption plot.

The best adsorbents generally demonstrate high uptake capacity and high uptake rates which can be determined from the material's initial adsorption stage behaviour. So, the data in Figure 5.16 (right) is modelled using a linear fitting equation to evaluate the materials' performance. For the case of 40% RH/0.5% toluene P/P₀, it is restricted to the first 120 mins of adsorption. Since the plots are highly linear in this regime ($R^2 > 0.98$), the *slope* conveys the same relative performance information as $q_e \cdot k_1$. The calculated linear parameters are shown in Table 5.3. Note that no q_e value is reported for AC at 40% RH/0.5% toluene P/P₀ as it did not reach equilibrium. By virtue of the *slope* values at 40% RH/0.5% toluene P/P₀, the increasing order of the best material is:

MIL-PDMS-Dow-6 \approx AC < MIL-PDMS-Sigma-6 < MIL-PDMS-Dow-0.25 < MIL-101 (Cr) < MIL-PDMS-Sigma-0.25.

Table 5.3: Experimental and estimated kinetics parameters at 40% RH/0.5% toluene P/P₀.

Sample	Experimental values and their linear-fitted parameters			Experimental values and their pseudo first order-fitted parameters			
	40% RH/0.5% toluene P/P ₀						
	q_e (mg/g)	<i>slope</i> (mg/g.min)	R^2	q_m (mg/g)	$k_1 \times 10^3$ (min ⁻¹)	$q_e \cdot k_1$ (mg/g.min)	R^2
MIL-101 (Cr)	107	0.200	0.999	111	1.9	0.203	0.997
MIL-PDMS-Sigma-0.25	170	0.288	0.999	185	1.6	0.272	0.998
MIL-PDMS-Sigma-6	16	0.0927	0.994	15	11.8	0.189	0.927
MIL-PDMS-Dow-0.25	31	0.153	0.998	31	7.8	0.242	0.989
MIL-PDMS-Dow-6	23	0.0801	0.998	25	4.0	0.092	0.999
AC	-	0.0805	0.998	-	-	-	-

Although MIL-PDMS-Dow-0.25 exhibited a low q_e value, it also has a high *slope* and k_1 which makes it additionally suitable for applications where fast adsorption is required. The promising MIL-PDMS-Sigma-0.25 topped the list and displayed 44% higher *slope* than MIL-101 (Cr). From these observations on both samples' improved toluene kinetics, it is evident that the PDMS coating is effective. Therefore, a PDMS coating which is optimized properly (0.25 hr) by minimizing pore blockage, is envisioned to produce a very competitive adsorbent for real world toluene VOC capture.

However, there is a notable ranking difference between the linear-derived experimental *slopes* and the PSO-fitted $q_e.k_1$ values in Table 5.3. Especially, in the swapped order of the top three samples. Based on the $q_e.k_1$ values, MIL-PDMS-Dow-0.25 came second, albeit possessing a much lower q_e (79% lower) than MIL-101 (Cr). Its high k_1 seemingly overpowers the $q_e.k_1$ metric, thus, giving it a higher aggregate adsorption rate than MIL-101 (Cr). Essentially, this means is that if one solely relies on the $q_e.k_1$ values, there are chances of comparing the materials with a biased metric. To help reduce such potential misjudgement, the best approach to use when evaluating a material's aggregate adsorption performance is by fitting the initial experimental adsorption stage with a linear model. The adsorption time window can be freely chosen provided the linear plots' fitting accuracy (R^2) within the regime is greater than 0.98. Nevertheless, this linear modelling approach has its own caveats:

1. Should a plot's R^2 is substantially lower than 0.98 or deviates significantly from a linear plot, it may indicate the adsorbent has nearly achieved equilibrium, hence, is more suitable to be fitted with a nonlinear kinetics model.
2. The obtained linear *slope* is not applicable for the whole experimental time range, but only within the specified time range unlike the estimated k parameter from a nonlinear kinetics model.

In conclusion, to make use of the linear and the nonlinear PFO estimations, the kinetics parameters obtained from the PFO kinetics model can be used to predict q_m and material's k_1 at adsorption equilibrium. Whereas the linearly obtained *slope* can provide insights of the material's performance during the initial adsorption stage.

5.2.13 Uptake capacity at 40% RH and 10% toluene P/P₀

Figure 5.17 shows the co-uptake capacity results of select samples at 40% RH/10% toluene P/P₀. Contrary to the previous trend, the pristine MIL-101 (Cr) (507 mg/g) outperformed the MIL-PDMS-Sigma-0.25 (426 mg/g) uptake by 19%. This result is somewhat surprising as it might have been anticipated that MIL-PDMS-Sigma-0.25, which at 40% RH has a significant amount of mesopores unoccupied, would have performed best, just as it did for 40% RH/0.5% toluene P/P₀.

Clearly, the 20 times higher toluene concentration at 10% P/P₀ versus 0.5% P/P₀ has its own significant influence. One potential explanation for this behaviour is the stronger toluene affinity for the pristine MIL-101 (Cr) adsorbent at the much higher concentration of 10% toluene P/P₀, which highlights the importance of intrinsic chemical interactions between the adsorbate and the adsorbent. Specifically, this strong adsorption may be linked to the donor-acceptor bonding and the π - π interactions taking place between the original MIL-101 (Cr) ligands and the toluene molecules (Li *et al.*, 2020e). However, the importance of these hydrogen bonding and π - π interactions for toluene adsorption on the MIL-PDMS-Sigma-0.25 composite will be compromised by the low surface energy PDMS coating. The PDMS coating will partly shield these original chemical interactions, resulting in a lower toluene uptake compared to the pristine MIL-101 (Cr).

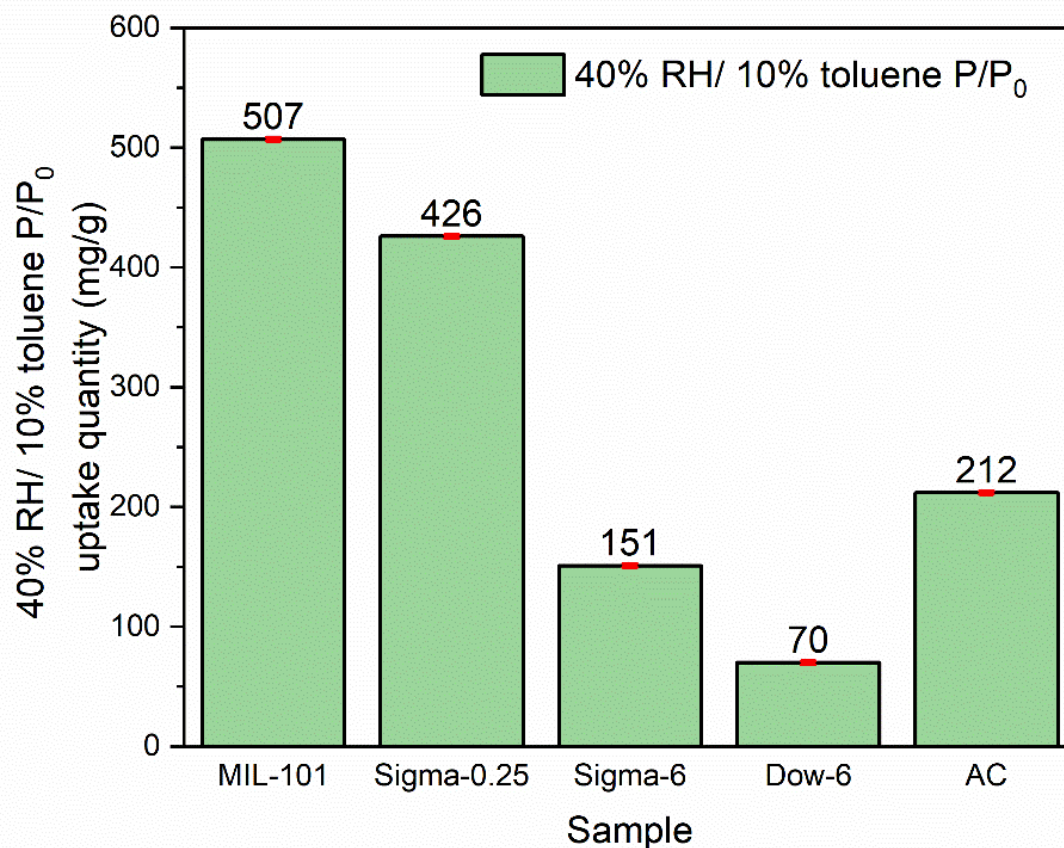


Figure 5.17: Toluene uptake quantity by PDMS-coated MIL-101 samples at 10% toluene P/P₀. All experiments were performed at 40% RH saturation and at 25 °C.

5.2.14 Adsorption kinetics for 40% RH and 10% toluene P/P₀

Figure 5.18 displays the adsorption kinetics plots by selected adsorbents at 40% RH and 10% toluene P/P₀. The data in Figure 5.18 (left) was analysed with nonlinear pseudo first order kinetics model. Based on the $q_e.k_1$ values shown in Table 5.4, the order from worst to best material is:

AC < MIL-PDMS-Dow-6 < MIL-PDMS-Sigma-6 < MIL-PDMS-Sigma-0.25 < MIL-101 (Cr).

Figure 5.18 (right) shows selected samples' adsorption kinetics plots at 40% RH/10% toluene P/P_0 during the first 30-minute adsorption time. Because the toluene concentration is higher, 30 minutes was chosen due to the faster materials' adsorption rate. Based on the linear *slope* values in Table 5.4, the increasing order of the best material is:

$$\text{MIL-PDMS-Dow-6} < \text{AC} < \text{MIL-PDMS-Sigma-6} < \text{MIL-PDMS-Sigma-0.25} < \text{MIL-101}$$

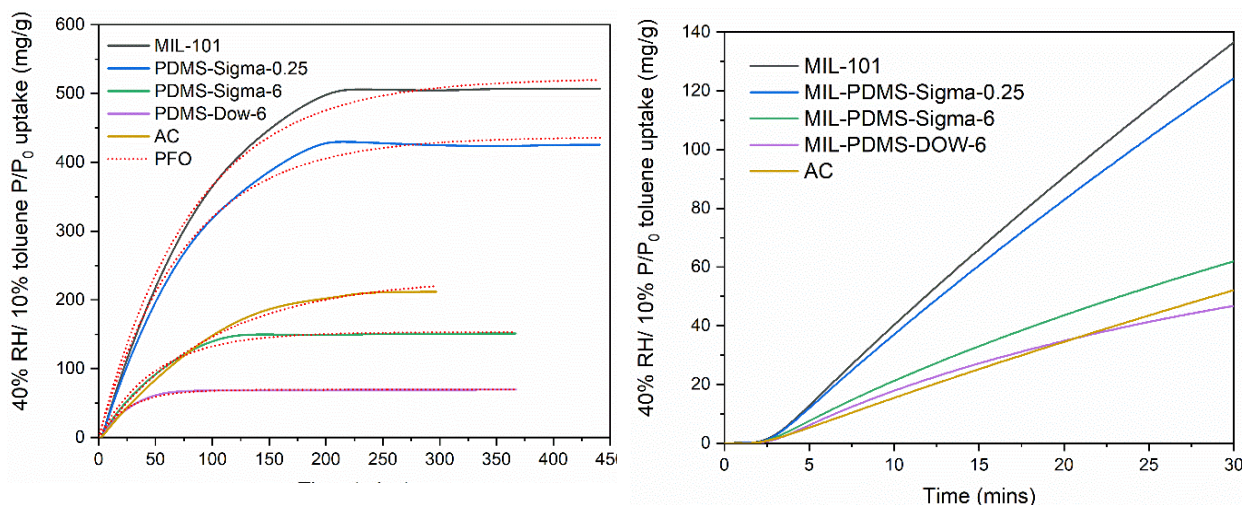


Figure 5.18: (Left) Adsorption kinetics at 40% RH and at 10% toluene P/P_0 . Solid lines are the experimental data whereas dotted lines are the fitted values derived from pseudo first order (PFO) kinetics model. (Right) The initial adsorption plot.

Remarkably, based on the information in Table 5.3 and Table 5.4, MIL-PDMS-Sigma-0.25 has good, not the best, performance at 40% RH for both 0.5% and 10% toluene concentrations, suggesting this material may be the right starting point for further optimization work. Compared to the MOFs, AC offers relatively modest performance, which is only compensated for by its very low cost.

Table 5.4: Experimental and estimated kinetics parameters at 40% RH and 10% toluene P/P₀.

Sample	Experimental values and their linear-fitted parameters			Experimental values and their pseudo first order-fitted parameters			
	40% RH/10% toluene P/P ₀						
	q_e (mg/g)	<i>slope</i> (mg/g.min)	R ²	q_m (mg/g)	$k_1 \times 10^3$ (min ⁻¹)	$q_e.k_1$ (mg/g.min)	R ²
MIL-101 (Cr)	507	4.909	0.998	522	12.1	6.135	0.991
MIL-PDMS-Sigma-0.25	426	4.470	0.9979	437	13.2	5.623	0.989
MIL-PDMS-Sigma-6	151	2.221	0.9946	153	20	3.020	0.987
MIL-PDMS-Dow-0.25	-	-	-	-	-	-	-
MIL-PDMS-Dow-6	70	1.701	0.9848	70	37.9	2.653	0.991
AC	212	1.864	0.9985	232	9.9	2.010	0.994

5.2.15 High humidity test

Since MIL-PDMS-Sigma-0.25 performs better than MIL-101 (Cr) at 40% RH/0.5% toluene P/P₀, both MOFs were further investigated to assess their moisture stability. Table 5.5 shows the moisture stability test results of the MOFs and AC. The brief 90% RH exposure led to very high moisture uptake levels for both MIL-101 (Cr) and MIL-PDMS-Sigma-0.25. This clearly verifies the intrinsic hydrophilicity of both materials. This performance was followed by negligible, toluene uptake in the second 40% RH/0.5% toluene P/P₀ cycle.

On the other hand, the hydrophobicity of AC enables AC to exhibit relatively low water uptake quantity at 90% RH, yet still able to maintain equivalent toluene uptake before and after the extreme humidity exposure. Once these MOFs are exposed to high humidity, which results in pore filling, their ability for VOC capture is severely compromised. So, AC appears as a better material

at very high humidity as its performance is unaffected by the transient extreme humid environment (Liu, Younis & Kim, 2021).

Table 5.5: Adsorption of 0.5% toluene P/P₀ following high humidity exposure.

Sample	Uptake quantity (mg/g)		
	1 st 40% RH/ 0.5% toluene	90% RH/ 0% toluene	2 nd 40% RH/ 0.5% toluene
MIL-101 (Cr)	42	425	5
MIL-PDMS-Sigma-0.25	91	366	2
AC	113	139	112

5.2.16 Adsorbent reusability study

Figure 5.19 shows the amount of toluene adsorbed by the adsorbents after being subjected to 10 adsorption-desorption cycles for toluene. AC adsorbed a comparatively moderate toluene quantity because it has lower surface area and pore volume. The cyclic toluene test also revealed that MIL-PDMS-Sigma-0.25 demonstrated superior uptake capacity than MIL-101 (Cr). All studied materials exhibited good reusability data across the test regime.

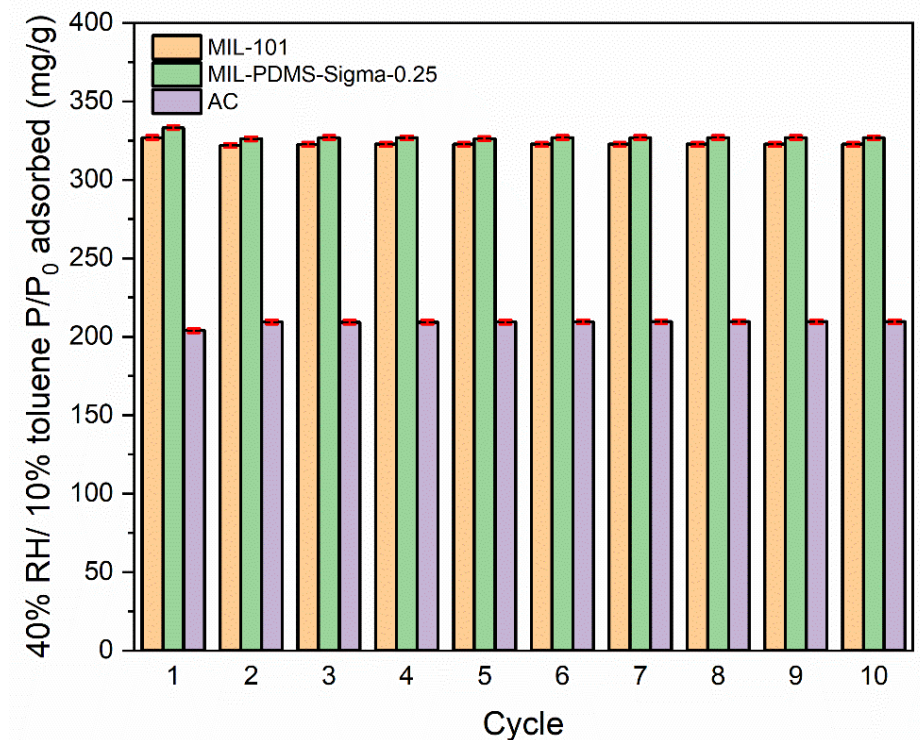


Figure 5.19: Reusability study of MIL-101 (Cr), MIL-PDMS-Sigma-0.25 and AC at 10% toluene P/P₀ and 40% RH, 25°C for 10 cycles.

5.2.17 Toluene co-adsorption mechanisms after PDMS treatment

The overall outstanding performance of MIL-101 (Cr) and its MIL-PDMS-Sigma-0.25 variant are significantly due to the fact that MIL-101 (Cr) has a high surface area and pore volume, thus, providing a higher number of potential adsorption/condensation sites (Yang *et al.*, 2011b). In practice, at a typical room's RH of 40%, MIL-101 (Cr) will have significant amounts of its mesopores already filled by water, whilst for MIL-PDMS-Sigma-0.25, far fewer mesopores will be filled. So, in turn, when the MIL-101 (Cr) is exposed at 40% RH and then to 0.5% toluene P/P₀ of toluene vapour, it exhibits a lower level of empty pores to adsorb toluene in the remaining vacant sites.

Whilst MIL-PDMS-Sigma-0.25 can in contrast, offer a significantly higher toluene sorption capacity at 0.5% toluene P/P₀ as its PDMS-coated mesopores are substantially unfilled by water at 40% RH. Figure 5.20 shows the amount of 0.5% toluene P/P₀ adsorbed by MIL-101 (Cr) at

different % RH from 0%, 20%, 40%, 60% to 80%. With virtually no toluene being adsorbed above 60% RH, this observation fully supports the complete filling of MIL-101 (Cr)'s mesopores with water at this humidity. This result itself is not surprising, but it encourages the development of MOF materials with larger hydrophobic pores, which can delay moisture condensation to even at high room humidity levels, just as was reported on hydrophobic (methylated) variants of silica MCM-41 by David et al. (David *et al.*, 2020).

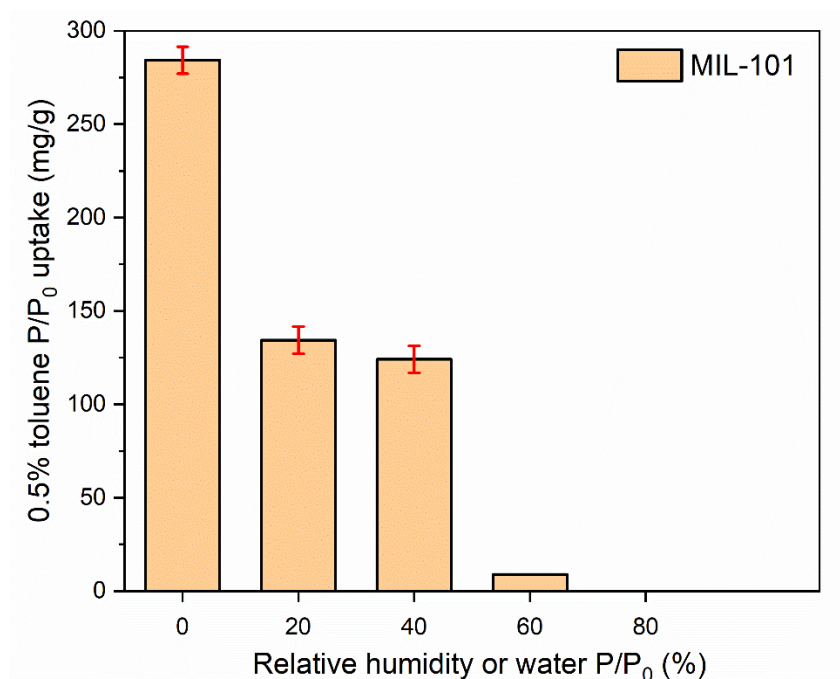


Figure 5.20: 0.5% toluene P/P₀ uptake quantity by MIL-101 (Cr) after exposure to varying relative humidity ranging from 0% to 80%.

5.3 Conclusions

In summary, a series of MIL-101-PDMS composites were fabricated by optimizing the polymer vapour deposition time and molecular weights. Longer coating times of > 0.25 hrs led to pore blockage as evident from the substantial decrease in the composites' surface area and pore volume. Alternatively, a 0.25 hr coating time using a lower molecular weight PDMS produced the best MIL-101 (Cr) composite (MIL-PDMS-Sigma-0.25) which exhibited an equivalent surface area and porosity to the unmodified MIL-101 (Cr). This composite has the highest hydrophobicity index values among all samples evaluated for humidity levels less than 10% RH. MIL-PDMS-

Sigma-0.25 and MIL-101 (Cr) were assessed for competitive adsorption of toluene (0.5% P/P₀ and 10% P/P₀) at 40% RH and 25 °C.

At 40% RH and 0.5% toluene P/P₀, which corresponds to 188 ppm, a concentration commonly seen in practical VOC capture applications, the composite demonstrated a 60% higher toluene uptake (170 mg/g) compared to the regular MIL-101 (Cr) (107 mg/g), as well as a 34% increased aggregate adsorption rate (inclusive of both toluene uptake capacity and adsorption kinetics). The composite's superior performance at 40% RH/0.5% toluene P/P₀ could be directly attributed to the shift in the mesopore condensation/ pore filling processes in its now hydrophobic mesopores.

At 40% RH/10% toluene P/P₀, MIL-101 (Cr) exhibited a higher uptake (507 mg/g) than the composite (426 mg/g) which highlights the importance of uncoated, native MOF framework's strong chemical interactions with toluene for this higher toluene concentration. Additionally, this composite demonstrated a 2.8 times higher aggregate adsorption rate than activated carbon, the industry reference material. Optimized MIL-101-PDMS composites of the type described in this work could form the basis of future adsorbent materials for the environmental capture of hydrophobic VOCs in real world conditions.

5.3.1 Future Work

After seeing the efficacy of this coating technique especially in the improved molar HI values at < 10% RH and the adsorption kinetics of the MIL-101-PDMS composites, it would be interesting to implement the same technique on originally hydrophobic adsorbents like zeolites, as well as other hydrophobic MOFs. Despite having optimized the PDMS molecular weight and deposition time, there is scope for more improved processes such as using lower PDMS molecular weights as well as shorter coating times. Other opportunities to refine this coating process include fine-tuning the PDMS polymer molecular shape and the deposition temperature. Of course, compared to the costlier yet efficacious alternative of using hydrophobic linkers in the MOF synthesis, these optimizations are only beneficial should the final PDMS-coated composites perform well in competitive adsorption experiments.

Chapter 6: Hydrophobic MOFs from wet phase coating

6.1 Introduction

Surface hydrophobicity can be created by introducing alkyl, aryl, or fluorinated groups onto the surface of a material. The low surface energies exhibited by these groups will lower the surface wettability, causing a significant increase in water contact angles to $> 90^\circ$ (Sun *et al.*, 2017; Jayaramulu *et al.*, 2019; Mukherjee, Sharma & Ghosh, 2019; Xie *et al.*, 2020). Silanes (Choe *et al.*, 2021), phosphonic acids (Sun *et al.*, 2017), phosphinic acids (Hynek *et al.*, 2017) and calixarenes (Jeong *et al.*, 2019) are some of the chemicals that have been employed successfully to create hydrophobic MOFs. Although there are numerous reports on the preparation of these new hydrophobic MOFs, the performance of these new materials for humid VOC capture has not been specifically reported. For example, MOF-calixarene composites have recently shown potential applications in NO_2 sensing (Schulz *et al.*, 2018) and gas separation processes (Wu, Liu & Chung, 2018). Calixarene's unique supramolecular open-cavity conformation on the MOF substrate is thought to facilitate host-guest interactions.

Figure 6.1 shows a typical calixarene structure. It resembles a 3-dimensional cup with a hydrophilic base due to the phenolic functionalities and an upper rim lined with hydrophobic species, forming a hydrophobic cavity of specific dimensions. By immobilising the calixarene base on a MOF's open metal sites, the exposed hydrophobic part could provide a selective entry to trap guest molecules. Such a feature would be expected to improve the adsorption rate of hydrophobic VOCs.

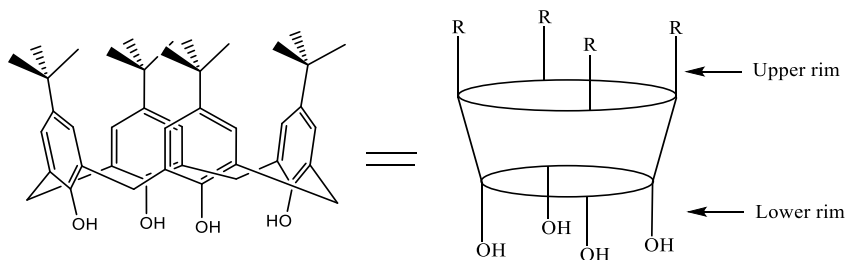


Figure 6.1: Diagrammatic representation of a calix[4]arene supramolecule.

This Chapter reports on a series of wet surface chemical modification protocols using silanes, phosphonic acids, phosphinic acids and calixarenes, onto the surface of MIL-100 (Fe). Besides having both micro and meso-porosities suitable for adsorbing small VOC molecules, MIL-100 (Fe)'s high hydrophilicity (Xie *et al.*, 2020) will enable better comparison on its external surface and internal pore chemistry improvement after being treated. Toluene was chosen as a model hydrophobic VOC probe molecule again. After characterisation, the treated MIL-100 (Fe) samples will be assessed for a realistic and competitive water-toluene adsorption. Two toluene concentrations are studied: 0.5% and 10% P/P₀, both with a constant 40% RH background, each represents a mid-range environmental VOC level and a concentration encountered in industrial solvent separation processes, respectively. The best performing samples from this first assessment will be further investigated for their water stability and reusability. More importantly, all the experiments are benchmarked with an industrial-standard activated carbon (AC) to rank and rate their adsorption performance.

6.2 Results and discussion

The following Sections show some of the results of MIL-100 (Fe) surface modifications using silanes, phosphonic acids and phosphinic acids, as well as calixarenes. Preliminary experiments were performed on all three reaction classes. Based on these results, successful methods are detailed in this Chapter, whilst methods which were not successful are reported in the Appendices.

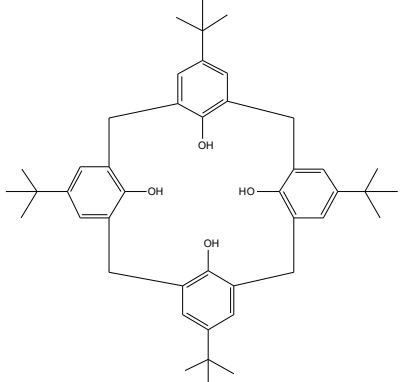
Preliminary results for MIL-100 (Fe) surface modification using silanes are presented in Appendix Section 10.4.2. Most silane-treated samples exhibited severe pore blockage and unchanged surface hydrophobicity, except for a few samples. So, because of these poor outcomes, this specific reaction was not studied further. The preliminary results from the phosphonic and phosphinic acids treatments are available in Appendix Section 10.3. Table A10.6 lists the differences between phosphonic acids and phosphinic acids. Together, these acids will be generally referred to as phosphorous oxyacids (PA). In summary, the implemented PA treatment did not improve the MIL-100 (Fe)'s adsorption kinetics or capacities. These investigations are included in the Appendices and not in this Chapter. Table A10.7 lists the structures of the hydrophobic silanes as well as the phosphonic acids and phosphinic acids used in this work.

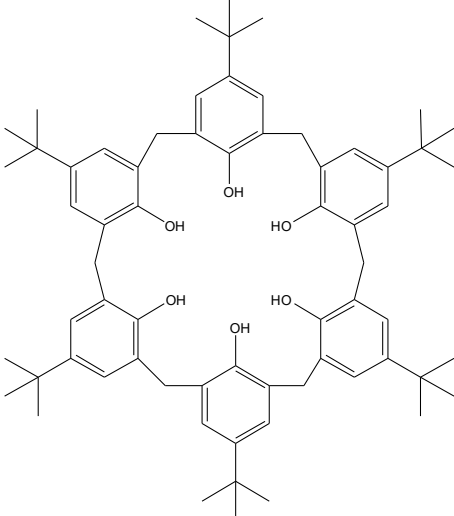
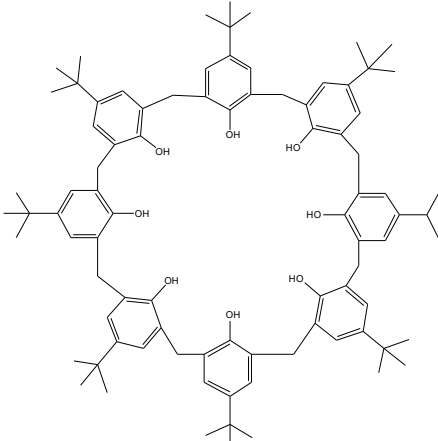
In short, the focus of Chapter 6 is mainly on the calixarene surface treatment results due to their overall successful implementation.

6.2.1 Calixarene structural properties

Table 6.1 lists the properties of the calixarene molecules used in this work. The sizes stated are their internal diameter (Saponar *et al.*, 2012).

Table 6.1: The chemical structures of the supramolecule calixarenes

Chemical	Chemical structure	Size (Å)
4-tert-butylcalix[4]arene (Cx4)		3.0

<p>4-tert-butylcalix[6]arene (Cx6)</p>		<p>7.6</p>
<p>4-tert-butylcalix[8]arene (Cx8)</p>		<p>11.7</p>

6.2.2 PXRD patterns of calixarene-treated MIL-100 (Fe)

Figure 6.2 shows the PXRD patterns for all calixarene-grafted samples. Generally, with higher number of calixarene carbon atoms and loading quantity (wt%), there is a downward shift in the characteristic MIL-100 (Fe) peak originally at 7° . In terms of the loading quantity, low loadings such as in MIL-Cx4-1 wt% and MIL-Cx6-1 wt% still retained the overall sample crystallinity, but increased loadings begin to deteriorate the crystallinity, as observed from the loss of many peaks. The shifting of adjacent PXRD peaks to lower 2θ could possibly be due to the chelation between the calixarene molecules and the Fe metal centres on the MOF (Arbaoui *et al.*, 2010). Specifically, these metal centres are Fe^{2+} that were formed on the MIL-100 (Fe) pores as a result of 150°C drying prior to calixarene immobilization (Hall & Bollini, 2019).

According to Bragg's relationship where $2d \sin(\theta) = n\lambda$, the change in θ values implies that there is also a change on the d-spacings/lattice parameters. Moreover, the sample *colour* also varied with incremental calixarene loadings especially for the MIL-Cx8 samples that were prone to both crystallinity and colour changes even at a low loading (1 wt%). Higher Cx8 loadings gradually levelled the intensity of the characteristic peaks, suggesting a major lattice transformation. Figure A10.14 corroborates the noticeable colour change of the MIL-Cx samples while Figure A10.15 contrasts the morphological changes of the calixarene-treated MIL-100 (Fe) based on their SEM images. FTIR spectra were then collected to identify the formation of these calixarene-MOF complexes.

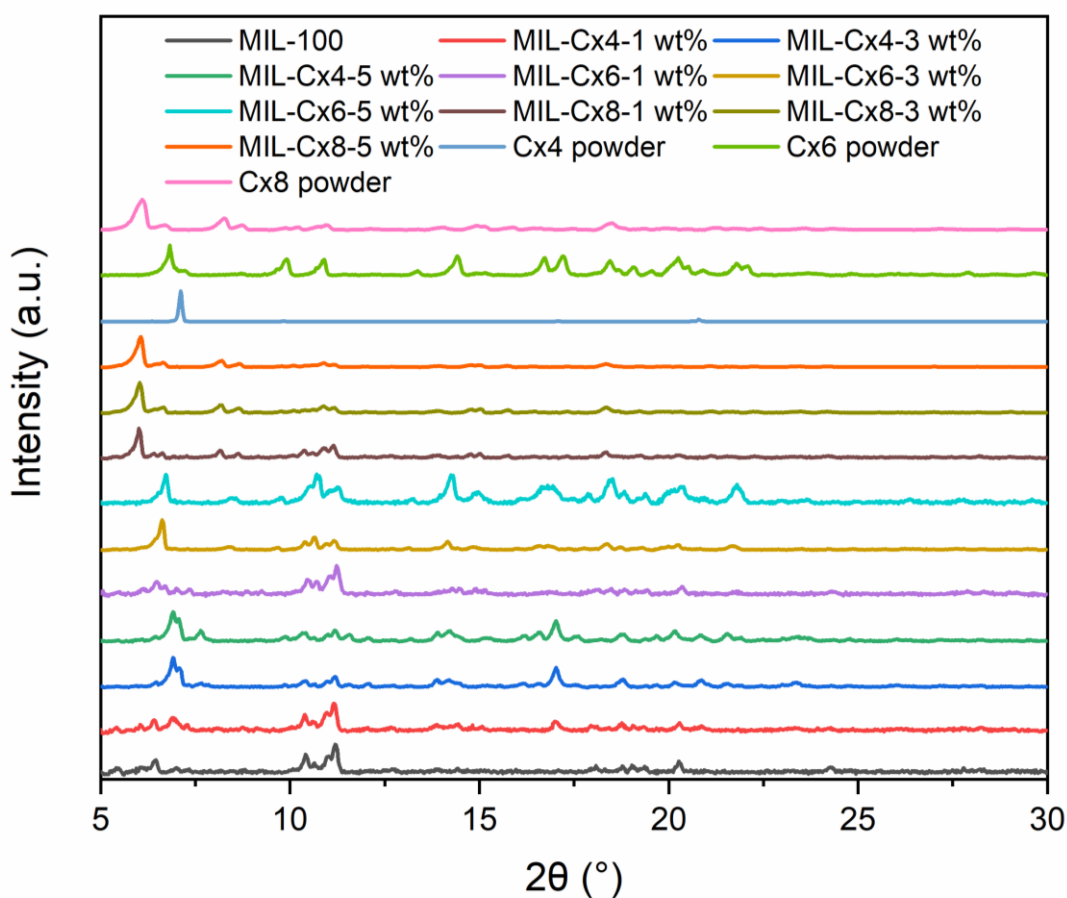


Figure 6.2: PXRD patterns of calixarene-treated MIL-100 (Fe).

6.2.3 FTIR spectra of calixarene-treated MIL-100 (Fe)

Figure 6.3 shows the FTIR spectra of all calixarene-treated MIL-100 (Fe) materials. The calixarene-functionalised particles display C-O stretching signals between $1100 - 1300 \text{ cm}^{-1}$ and O-H bending from the lower rim -OH groups of the calixarene between 1361 and 1385 cm^{-1} . The C-H bending peaks of $-\text{CH}_2$ and $-\text{CH}_3$ from the calixarene are found between 1449 cm^{-1} and 1484 cm^{-1} . The characteristic OH stretching absorption band attached on the calixarene's carboxylic acid appears at around 2866 cm^{-1} and 2953 cm^{-1} , followed by a broad shoulder at 3154 cm^{-1} . One point to note, the lack of these -OH stretching signals on MIL-Cx4-1 wt% and MIL-Cx6-1 wt% samples most probably indicates that the -OH groups of the calixarene are involved in the nucleophilic substitution reaction with the Fe (II) metal centres (Wu, Liu & Chung, 2018). All the described peaks became stronger with higher loadings, as demonstrated by the MIL-Cx-5 wt% variants.

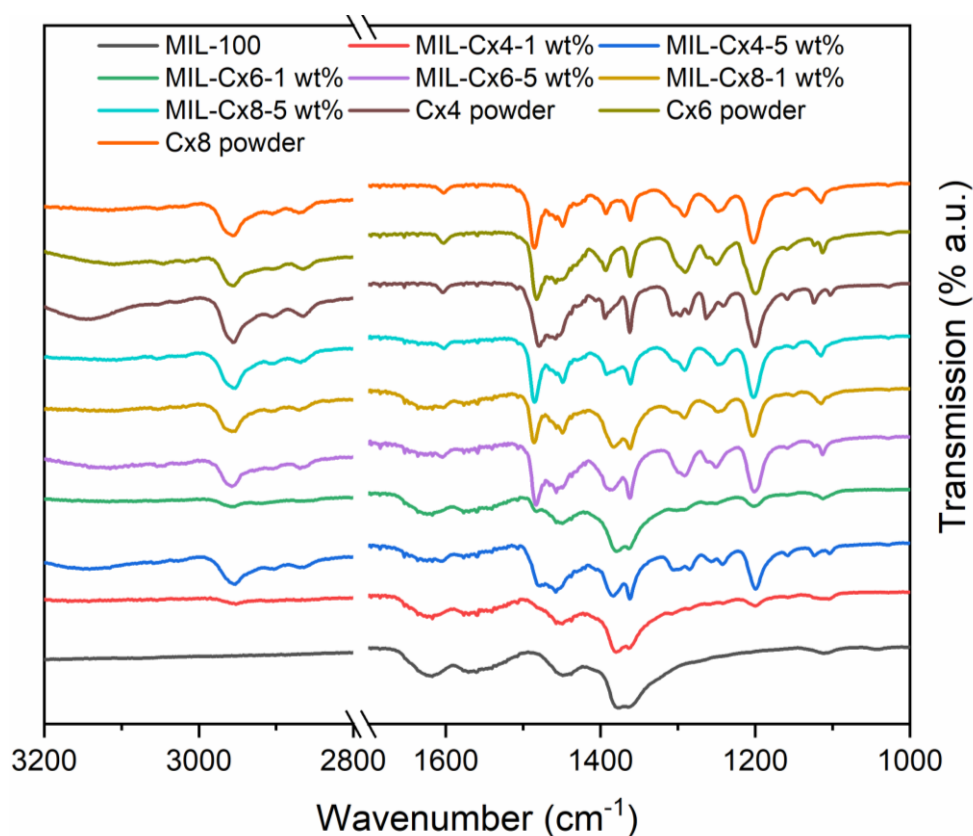


Figure 6.3: FTIR spectra of calixarene-treated MIL-100 (Fe).

6.2.4 TGA data for calixarene and PA-treated MIL-100 (Fe)

Figure 6.4 combines the thermal decomposition profiles of selected PA and calixarene-treated MIL-100 (Fe). MIL-DPA has a major weight loss in the first decomposition step before 100 °C. Because DPA has a relatively low melting temperature, at around 100 – 101 °C, it may have decomposed alongside evaporated water and residual bound ethanol from the synthesis. Although the PA is bonded to the metal (M) via strong covalent M-O-P bonds (Deria *et al.*, 2015; Hynek *et al.*, 2017; Sun *et al.*, 2017), there is a risk that even a mild activation temperature (< 100 °C) could degrade the functionalised PA.

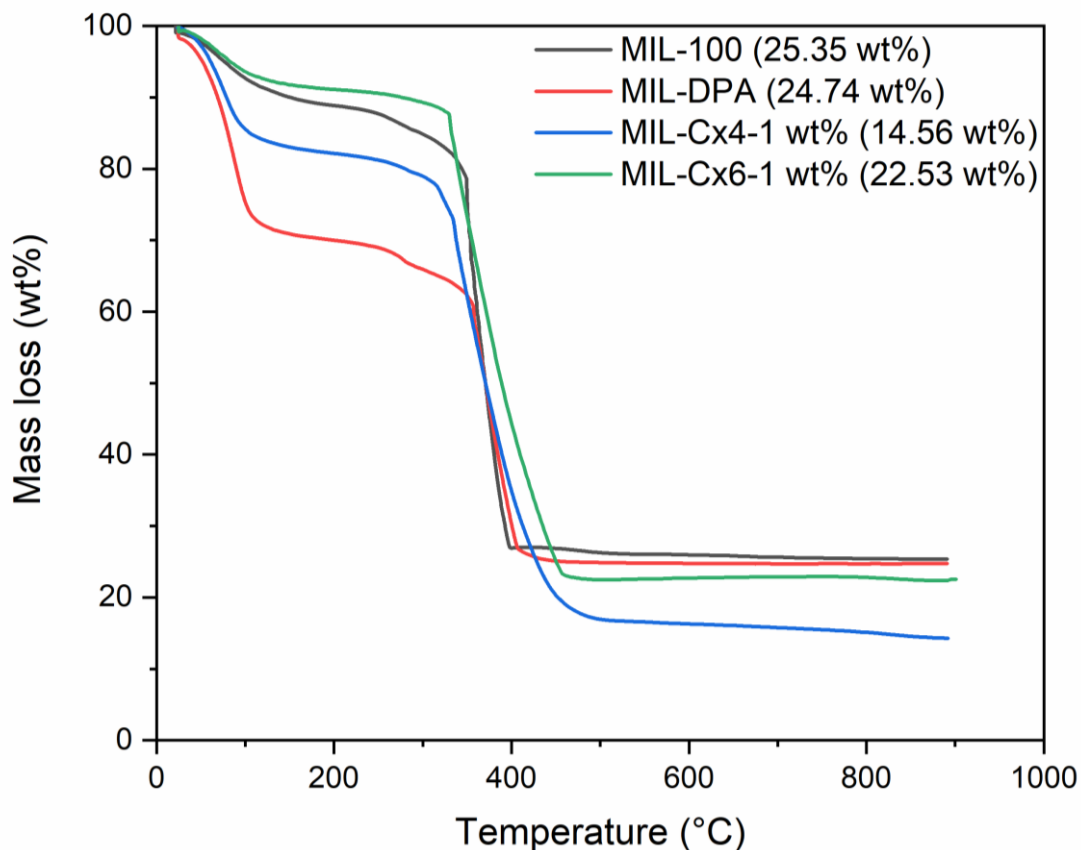


Figure 6.4: TGA profiles of PA and calixarene-treated MIL-100 (Fe). Values denoted in the brackets are the final residual masses.

In Figure 6.4, the initial weight loss up to 100 °C is noticeably higher for MIL-Cx4-1 wt% functionalised particles compared to MIL-100 (Fe), whilst for the MIL-Cx6-1 wt%, it is very similar to MIL-100 (Fe). In addition to water loss, this decrease could be associated with the removal of the carrier solvent (toluene size 5.5 Å) trapped in the small internal cavity of the MOF. The loss may also come from residual toluene molecules that are embedded in the internal cavity diameters of Cx4, Cx6 and Cx8 species estimated as 3.0 Å, 7.6 Å and 11.7 Å, respectively (Saponar *et al.*, 2012).

To calculate the quantity of coating agent on the treated MIL-100 (Fe), the difference of the samples' residual masses relative to the pristine MIL-100 (Fe) can be used. Equation 6.1 shows the relationship between the MIL-100 (Fe)'s residual wt% (m_i) and the treated MIL-100 (Fe) samples' residual wt% (m_t) to obtain the wt% of coating agent on the MOF. Table 6.2 shows the calculated wt% values of the studied coating agents.

$$\text{Wt\% coating agent on MOF} = \left(1 - \frac{m_i}{m_t}\right) \times 100 \quad \text{Equation 6.1}$$

Table 6.2: Quantity of coating agent on treated MIL-100 (Fe).

Sample	Residual mass wt%	Inorganics loss wt%	Wt% coating agent grafted on the MOF
MIL-100 (Fe)	25.4 ± 0.3	100 ± 0.3	0 ± 0.3
MIL-DPA	24.7 ± 0.3	97.2 ± 0.3	2.8 ± 0.6
MIL-Cx4-1 wt%	14.6 ± 2.0	57.5 ± 2.0	42.5 ± 2.3
MIL-Cx6-1 wt%	22.5 ± 0.5	88.9 ± 0.5	11.4 ± 0.8

6.2.5 Porosity analysis of calixarene-treated MIL-100 (Fe)

Table 6.3 shows the BET surface area and the total pore volume of calixarene-treated samples. These coated samples presented minimal surface area and total pore volume reductions, indicating that this approach is a viable material coating technique.

Interestingly, at 1 wt% calixarene loading, MIL-Cx4-1 wt% shows lower surface area than MIL-Cx6-1 wt% which indicates that the smaller Cx4 molecule blocked more pore spaces than the larger Cx6 molecule. Consistent with the calixarene dimensions and loading variation, MIL-Cx6-0.5 wt% exhibited the lowest decrease in surface area and pore volume by this coating method. It can be concluded that the calixarene coatings have been successfully grafted onto the MOF as evident in the FTIR and TGA analysis albeit with limited calixarene surface densities. The grafted calixarene is tentatively expected to offer stronger guest binding to any aromatic/hydrophobic guest molecule.

Table 6.3: Porosity analysis for selected calixarene-treated MIL-100 (Fe).

Sample	BET surface area (m ² /g)	V _{total} (cm ³ /g)	V _{micro} (cm ³ /g)	V _{micro} /V _{total}
MIL-100 (Fe)	1805 ± 17	0.81	0.74	0.91
MIL-Cx4-1 wt%	1414 ± 19	0.64	0.56	0.87
MIL-Cx6-0.5 wt%	1725 ± 19	0.80	0.69	0.86
MIL-Cx6-1 wt%	1556 ± 13	0.72	0.60	0.83
AC	1179 ± 20	0.81	0.47	0.58

Generally, the pore size distribution plots of the calixarene-treated MOFs in Figure A10.18 contain disproportionate amounts of micro and mesopores as opposed to the AC investigated here which has similar volumes of micro and mesopores. The micro-mesoporous nature of the MOFs also permits higher quantities of adsorbed N₂ as shown in their N₂ sorption isotherms (Figure A10.19).

6.2.6 Water contact angles of calixarene-treated MIL-100

The calixarene-treated MIL-100 (Fe) samples exhibited excellent hydrophobic surface properties, as shown in Table 6.4. The water contact angles for calixarene treated MIL-100 (Fe) could not be exactly measured as the superhydrophobicity caused the water droplets to roll off from the substrates very easily. Nevertheless, these surfaces are now obviously superhydrophobic. Still images of water droplets on these samples are shown in Figure A10.20. The considerable increase

in the calixarene-treated samples' water contact angles proves the potential efficacy of these chemicals in providing an intermediary barrier towards water.

Table 6.4: Water contact angles of some calixarene-treated MIL-100 (Fe) samples.

Sample	Water contact angle (°)
MIL-100 (Fe)	34.2 ± 2.0
MIL-Cx4-1 wt%	Superhydrophobic (> 150)
MIL-Cx6-1 wt%	Superhydrophobic (> 150)

6.2.7 Water sorption isotherms of calixarene-treated MIL-100 (Fe)

Figure 6.5 shows the water adsorption and desorption isotherms for selected calixarene-treated MIL-100 (Fe) samples. Both calixarene-coated materials exhibited significantly lower water sorption than pristine MIL-100 (Fe), as well as lower levels of water sorption hysteresis. These adsorption capacities are about 22% lower than the pristine MIL-100 (Fe), which is broadly consistent with the decrease in micropore volumes reported in Table 6.3. Figure 6.5 also shows that the calixarene-treated samples did not demonstrate improved pore hydrophobicity except for only a minor deviation from the pristine MIL-100 (Fe) water adsorption isotherm, located between 30 and 45% water P/P₀. It is surprising as their water adsorption trend appears independent from the high water repellency as inferred from their high water contact angle values.

Based on an earlier report by Notestein et al., they discovered although the ostensibly hydrophobic calixarene cavities promote host/aromatics guest complexation via van der Waals interaction, the same sites still preferentially adsorb water in the presence of aromatic guests (Notestein, Katz & Iglesia, 2006). The high-water affinity on the calixarene-treated MOF sites is likely the reason for the close resemblance in their water adsorption isotherm to that of pristine MIL-100 (Fe). Nevertheless, the slightly higher inflection point shown by MIL-Cx samples within 30% and 50% water P/P₀ boundary indicates the calixarene coatings happen to also be in the vicinity of the MIL-Cx's mesopores.

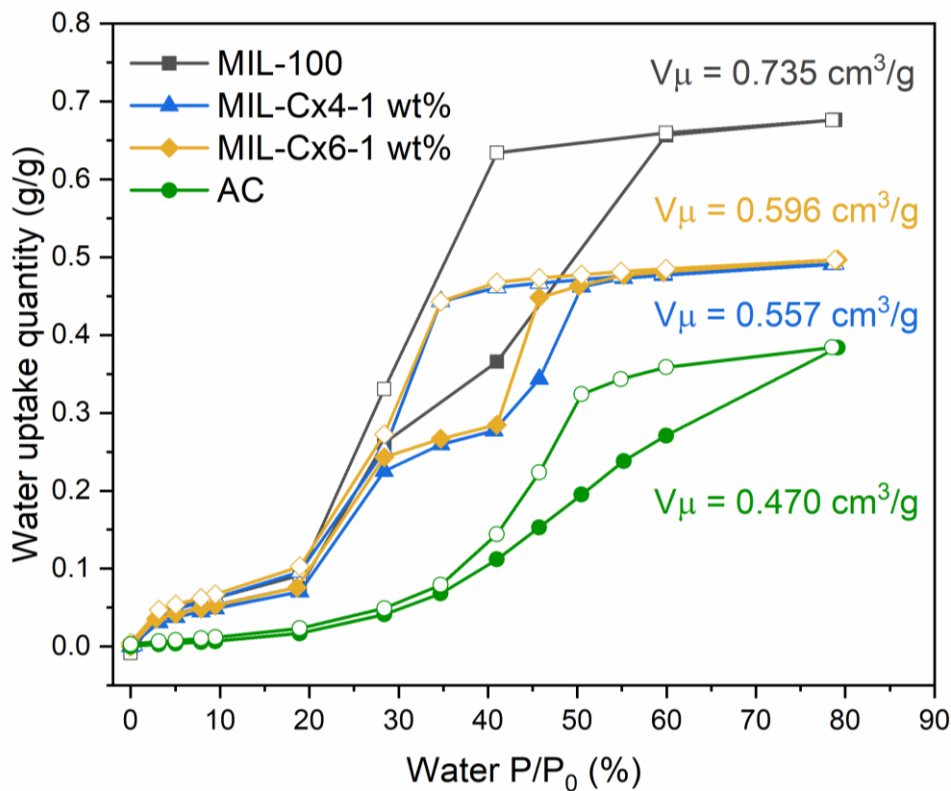


Figure 6.5: Water adsorption and desorption isotherms of calixarene-treated MIL-100 (Fe). Filled symbols are for adsorption while empty symbols are for desorption. Multi-coloured texts on the figure's right-hand side refer to the micropore volume of each adsorbent.

6.2.8 Toluene sorption isotherms of calixarene-treated MIL-100 (Fe)

Figure 6.6 shows the dry toluene adsorption and desorption isotherms of selected calixarene-treated MIL samples. Again, like water, the modified MIL-100 (Fe) materials have decreases in toluene uptake relative to the unmodified MIL-100 (Fe), which broadly follow their decreases in micropore volume accordingly.

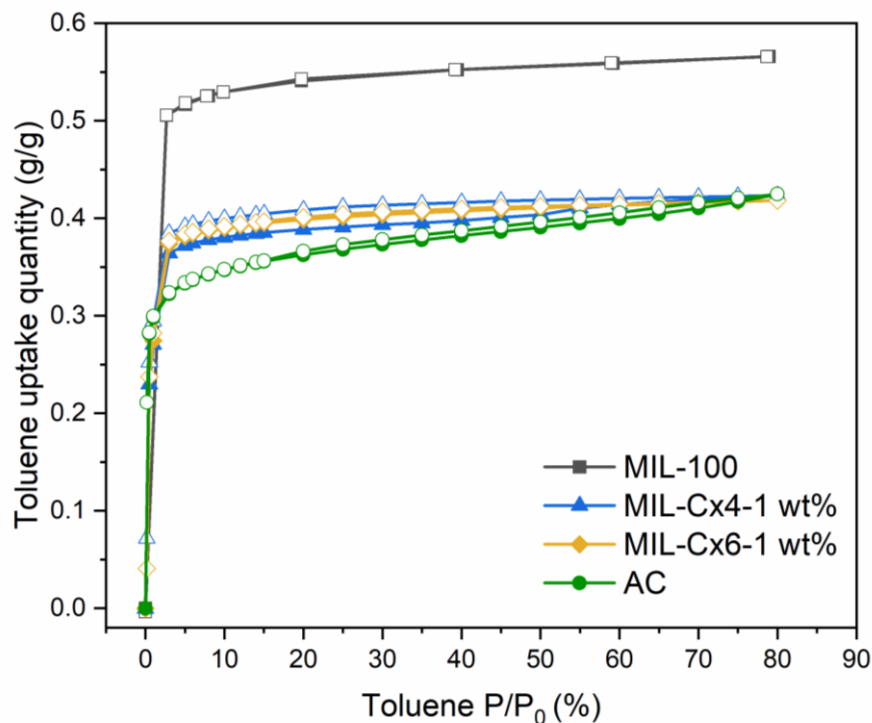


Figure 6.6: Dry toluene adsorption and desorption isotherms of calixarene-treated MIL-100 (Fe). Filled symbols are for adsorption while empty symbols are for desorption.

Some calixarene-treated materials were assessed for their toluene co-adsorption performance at low toluene P/P_0 range ($< 10\%$), as shown in Figure 6.9. The data indicates similar uptake levels and adsorption kinetics for both modified MIL-100 (Fe) materials compared to AC. None of the expected adsorption benefits from these two calixarene-modified, hydrophobic MIL-100 (Fe) materials are apparent in the single component sorption studies with toluene. The unexpected lack of performance from the calixarene-treated MIL-100 (Fe) may be because the toluene-calixarene complexation involves relatively weaker dispersion force compared to π - π stacking or CH- π interactions (Benevelli, Khimyak & Klinowski, 2004). Therefore, it is reasonable to claim that the MIL-Cx adsorbents still have weak affinity to bind toluene.

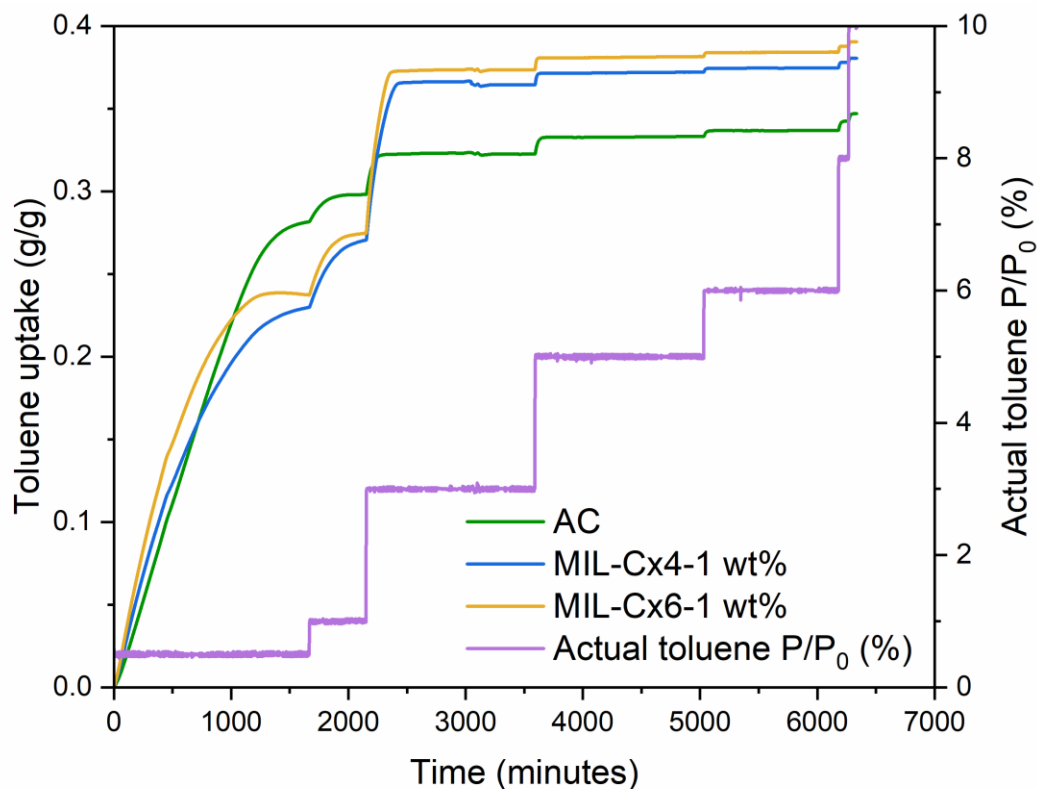


Figure 6.7: Dry toluene adsorption kinetics of AC and calixarene-treated MIL-100 (Fe) at low P/P_0 .

On the other hand, AC showed slightly faster adsorption kinetics than the MIL-Cx adsorbents as AC is intrinsically hydrophobic given the multiple stacks of benzene rings in AC's structure. Between 3 and 10% toluene P/P_0 , the Cx-treated MIL-100 (Fe) surpassed AC's uptake capacity solely because of their higher surface area. Indeed, the observed external surface hydrophobicity of these calixarene-treated MIL-100 (Fe) adsorbents is not translating to any comparable improvements in single toluene adsorption performance.

6.2.9 Hydrophobicity index of calixarene-treated MIL-100 (Fe)

Figure 6.8 shows the calculated HI for the calixarene-treated MIL-100 (Fe) as well as pristine MIL-100 (Fe) and AC. All MIL-100 (Fe) materials exhibit low HI values for all humidity levels. The markedly higher HI values by AC affirms the material's intrinsic hydrophobicity and highlights the poor hydrophobicity of all MIL-100 (Fe) variants tested. This preliminary finding

may predict their susceptibility towards water adsorption and their possible poor performance on co-adsorption experiments with water and toluene.

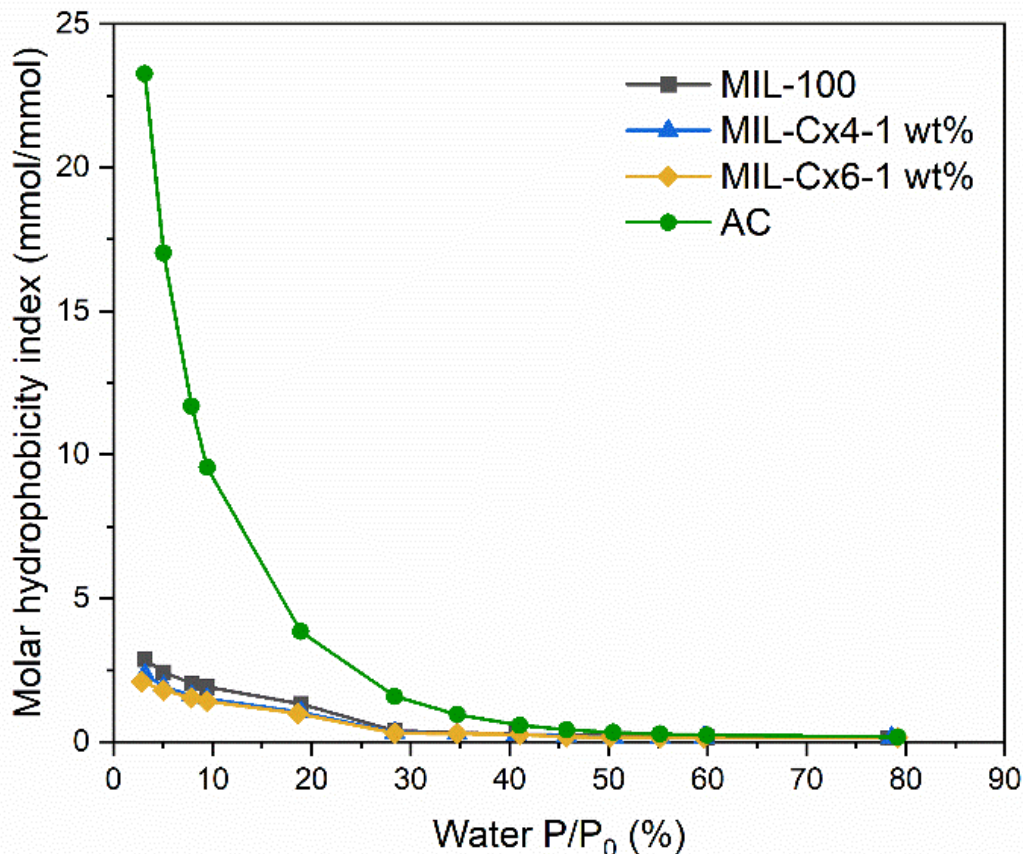


Figure 6.8: Molar hydrophobicity index (HI) of calixarene-treated MIL-100 (Fe).

6.2.10 Toluene co-adsorption by calixarene-treated MIL-100 (Fe) at 40% RH

The figures presented in Section 6.2.10, 6.2.11 and 6.2.12 summarise the measured equilibrium toluene adsorption quantity and kinetics by all calixarene-treated samples at 0%, 0.5% and 10% toluene P/P₀ concentrations with 40% RH background. The samples that demonstrate high toluene co-uptake capacity will be assessed in further kinetics studies.

Figure 6.9 shows the 40% RH and 0% toluene P/P_0 uptake capacity by all studied calixarene-treated samples. There is a general trend with higher calixarene coating loadings, the toluene adsorption capacity decreases. This trend can be expected since more molecules will occupy the pores and reduce the overall number of adsorption sites. The choice of the calixarene coating molecular size also has important ramifications to the extent of pore blockage. For example, the MIL-Cx8 samples, showing a substantial decline in their 40% RH adsorption capacity as low as 1 wt% loading from 383 mg/g to 120 mg/g. Meanwhile, low levels of calixarene coating, at 0.3 wt% and at 0.5 wt%, generally resulted in little change in water uptake at 40% RH relative to pristine MIL-100.

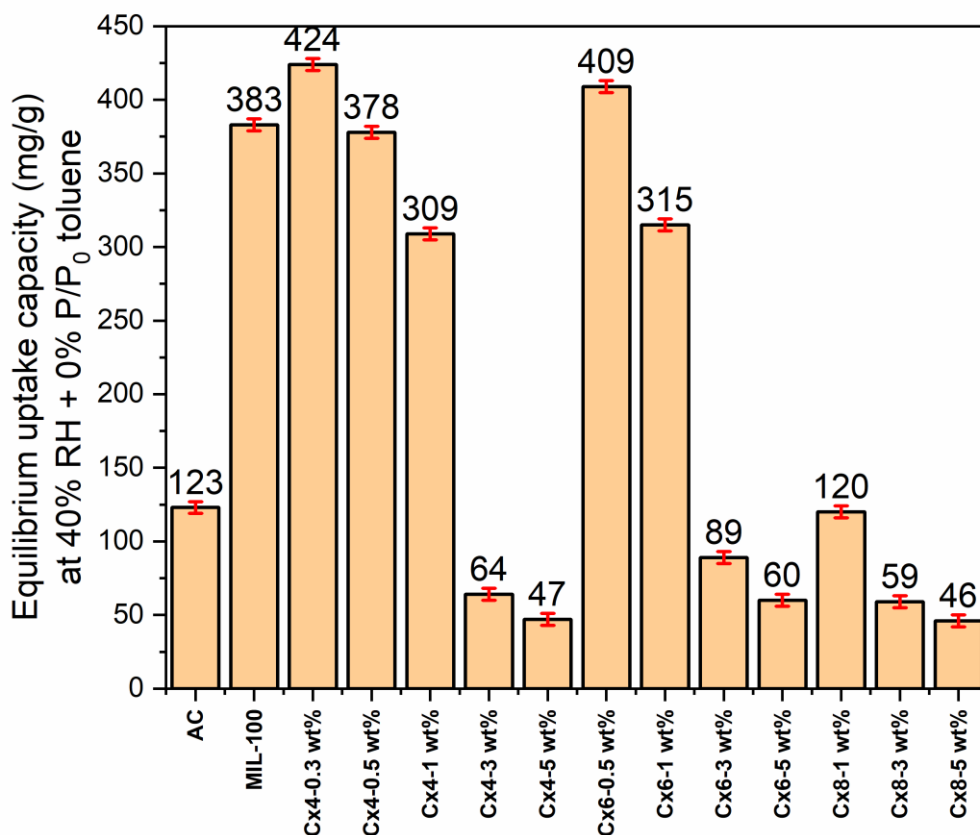


Figure 6.9: 40% RH and 0% toluene P/P_0 adsorption capacity of calixarene-treated MIL-100 (Fe).

6.2.11 Toluene co-adsorption by calixarene-treated MIL-100 (Fe) at 40% RH and 0.5% toluene

Figure 6.10 shows the 40% RH and 0.5% toluene P/P_0 adsorption capacity exhibited by MIL-100 (Fe) and all calixarene-treated samples. Among the calixarene-treated samples, MIL-Cx4-1 wt% and MIL-Cx6-1 wt% displayed the highest uptake increase relative to MIL-100 (Fe). Though when experimental errors are considered, these may not be statistically significant. The uptake capacity of these MIL-100 (Fe) materials is also disappointingly much lower than AC too. Some of these materials will be further assessed at 40% RH and 10% toluene P/P_0 later in this Chapter.

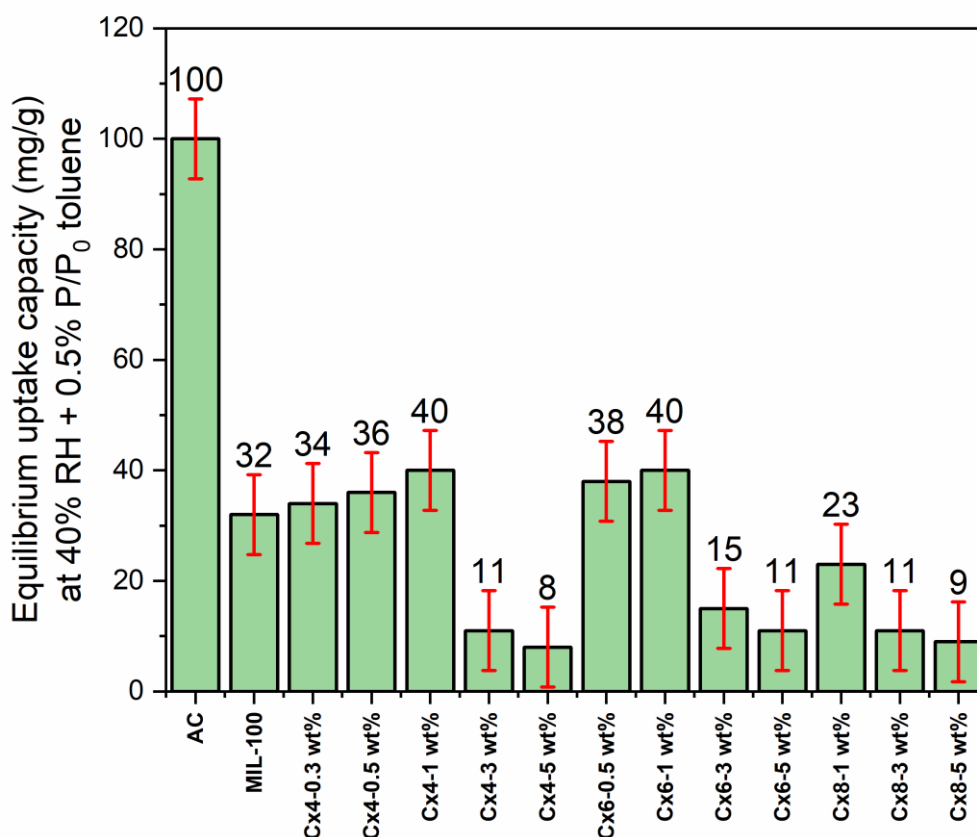


Figure 6.10: 40% RH and 0.5% toluene P/P_0 adsorption capacity of calixarene-treated MIL-100 (Fe).

Although high adsorption uptake level is the natural focus in many MOF studies, to facilitate a MOF's industrial use within adsorption systems, the kinetics of adsorption is also an important consideration. The following discussion evaluates the adsorption kinetics for the materials at 40% RH and 0.5% toluene P/P_0 . To compare the kinetics performance of these adsorbents, the samples' uptake rate was fitted with two separate models at two different adsorption regimes:

1. Firstly, within the first few hours of the adsorption process when there is a rapid adsorption, a linear equation ($y = mx + c$) can be used to quantify the initial kinetics parameters. Specifically, a 120-minute window was chosen for the case of 40% RH and 0.5% toluene P/P_0 . At 10% toluene P/P_0 , because of the higher toluene concentration gradient, it leads to faster adsorption. Therefore, the measurement window is reduced to 30 minutes. When a linear fitting equation is used, it provides the initial kinetics *slope* value.
2. Secondly, after the adsorption uptake plots reached an adsorption plateau, a pseudo first order (PFO) kinetics model is used to obtain the overall equilibrium kinetics coefficients. Figure 6.11 shows an illustrative sample's adsorption profile that is modelled with a nonlinear PFO kinetics equation, giving theoretically estimated maximum adsorption capacity, or q_m , which may be different to the experimentally determined capacity or q_e .

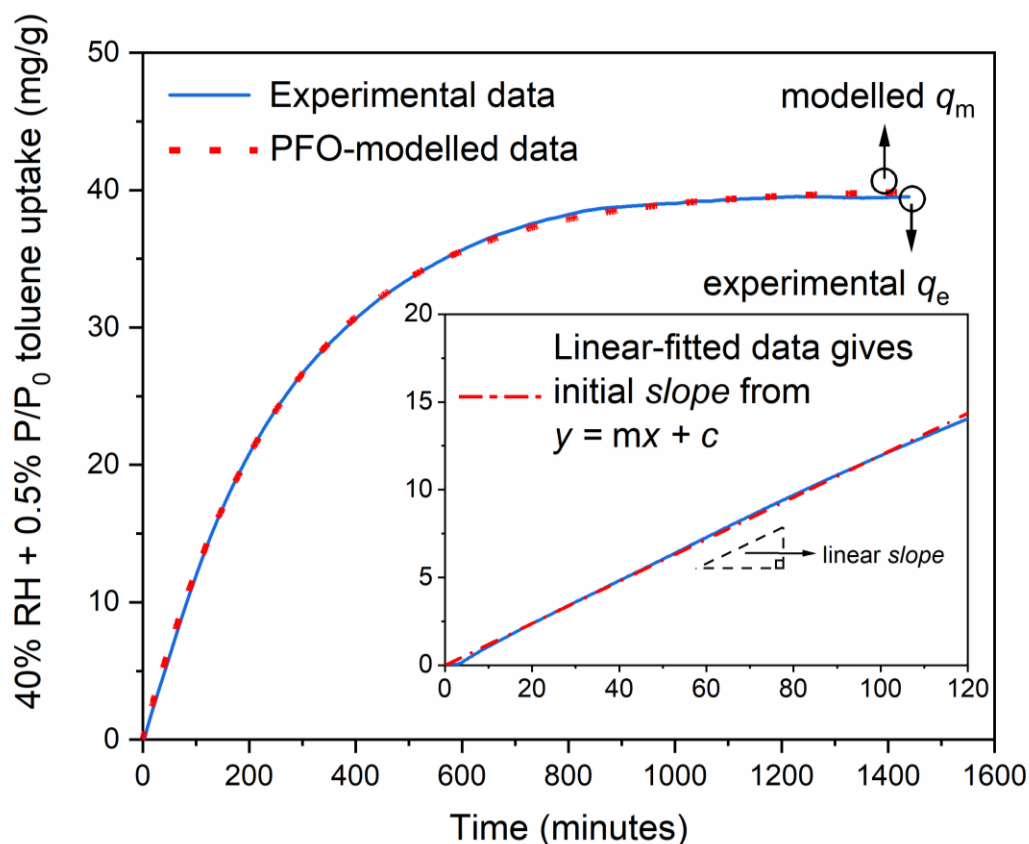


Figure 6.11: A sample plot showing the use of nonlinear pseudo first order kinetics model which generates q_m on experimentally measured adsorption data or q_e . Inset shows the linear-fitted kinetics plot during the initial 120 minutes of adsorption time.

Figure 6.12 (left) below shows the 40% RH and 0.5% toluene P/P_0 adsorption kinetics exhibited by MIL-100 (Fe), AC, and selected calixarene-treated samples. Compared to all tested MIL-100 (Fe) samples and AC, MIL-Cx6-1 wt% exhibited the fastest initial adsorption kinetics. AC's kinetics increased linearly until it achieved the highest uptake quantity, but the slow adsorption kinetics reflects the role played by its microporosity. However, as far as the time it takes to reach adsorption equilibrium is concerned, microporous AC is clearly not the right choice for quick adsorption applications.

Somewhat surprisingly, despite the lower toluene uptake capacity by all these MOFs compared to AC, the calixarene-treated MIL-100 (Fe) samples have much higher adsorption rate in the first 120 minutes of adsorption as shown in Figure 6.12 (right). This highlights the contribution of tailored

surface chemistry to achieve faster co-toluene adsorption kinetics at 0.5% toluene P/P_0 concentration. So, the increasing order of 40% RH/0.5% toluene P/P_0 by MIL-Cx samples is as follows (values in bracket are the linear initial *slopes*):

MIL-Cx6-1 wt% (0.167) > MIL-Cx4-0.5 wt% (0.156) > MIL-Cx6-0.5 wt% (0.155) > MIL-Cx4-1 wt% (0.120) > MIL-100 (Fe) (0.104) > AC (0.081).

So, it can be concluded, that in the short adsorption term of 2 hours until 4 hours, a relevant timeframe for some industrial processes, select calixarene-treated MIL-100 (Fe) samples adsorbed toluene vapour twice as fast as AC, and 60% faster than pristine MIL-100 (Fe), despite their lower pore volumes and surface areas.

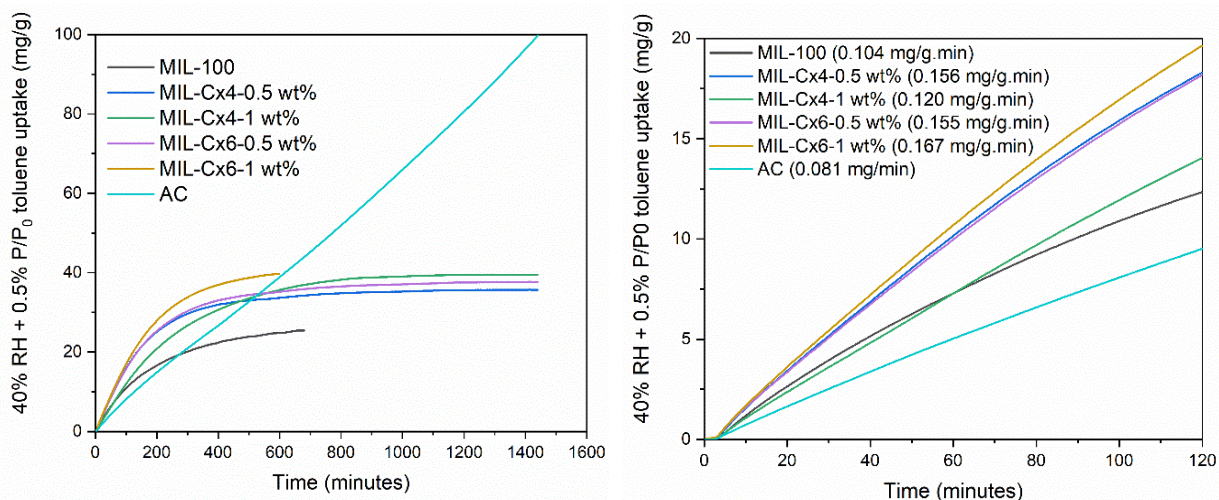


Figure 6.12: (Left) 40% RH and 0.5% toluene P/P_0 full range adsorption kinetics of calixarene-treated MIL-100 (Fe) samples. (Right) The first 120-minute adsorption rate is inclusive of the linear-fitted slope values given in the legend brackets.

6.2.12 Toluene co-adsorption by calixarene-treated MIL-100 (Fe) at 40% RH and 10% toluene

Figure 6.13 shows the 40% RH and 10% toluene P/P_0 adsorption capacity exhibited by MIL-100 and selected calixarene-treated MIL-100 (Fe) samples. The toluene uptake quantities by MIL-Cx samples fell below the pristine MIL-100 (Fe) due to their lower surface area and pore volume.

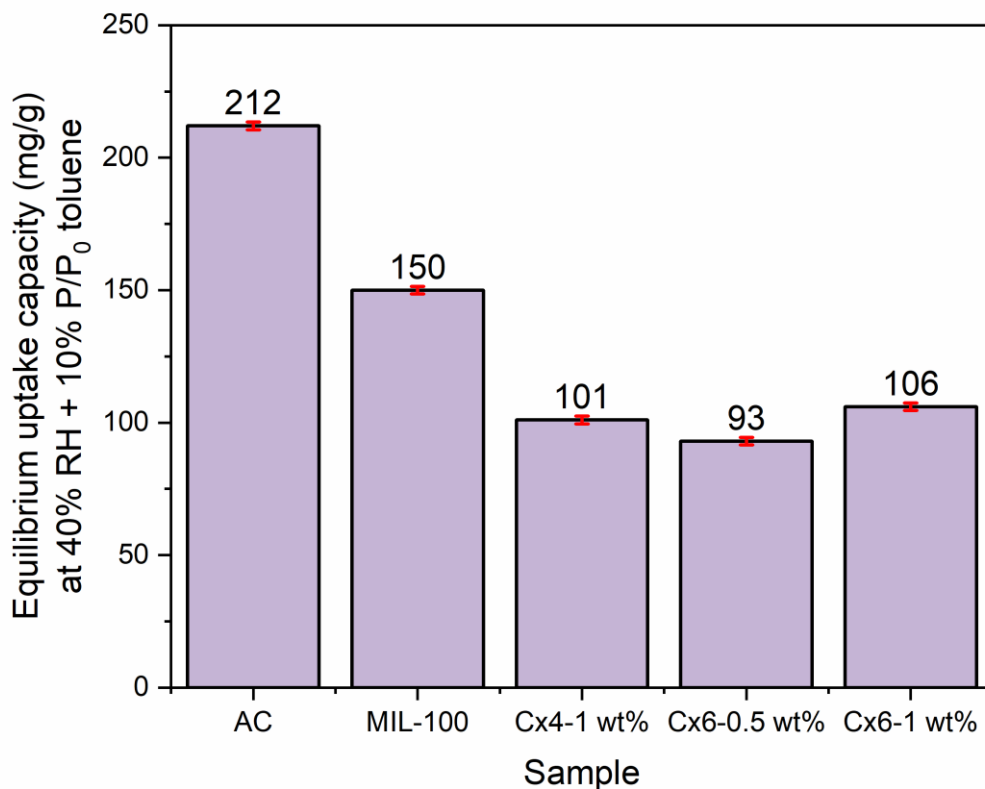


Figure 6.13: 40% RH and 10% toluene P/P_0 equilibrium adsorption capacity of calixarene-treated MIL-100 (Fe) samples.

Figure 6.14 shows the 40% RH and 10% toluene P/P_0 adsorption kinetics exhibited by MIL-100 (Fe) and select calixarene-treated samples. Figure 6.14 (left) shows some decreases in uptake with time for the MIL-100 (Fe) samples at about 50 minutes. This unusual effect is likely to be due to adsorbate displacement phenomenon in which slow adsorption of water molecules results in the slow displacement of toluene molecules. This phenomenon may be linked to MIL-100 (Fe) structure which comprises both micro and meso porosity. Though a full investigation of the displacement mechanism is outside the scope of the current work, it is possible to propose a potential mechanism. Figure 6.6 shows that for MIL-100 (Fe), 40% RH corresponds to the mesopore filling part of the isotherm. Therefore, as these mesopores slowly fill with water during adsorption, that will cause some toluene molecules that are co-adsorbed to be slowly desorbed as

some adsorption sites are gained by water molecules; resulting in the so-called displacement effect observed in Figure 6.14 (left).

Figure 6.14 (right) shows that MIL-Cx6-0.5 wt% is twice as effective kinetically as AC for short adsorption times of at least 30 minutes, and probably up to 60 minutes. It is also 15% faster than pristine MIL-100 (Fe), despite its lower pore volume and surface. It is also observed here that MIL-Cx6-1 wt% demonstrated similarly higher linear initial *slope* compared to the pristine MIL-100 (Fe) and AC. So, the increasing order of 40% RH/10% toluene P/P₀ by MIL-Cx samples is as follows (values in bracket are the linear initial kinetics *slopes*):

$$\text{MIL-Cx6-0.5 wt\% (3.629)} > \text{MIL-Cx6-1 wt\% (3.526)} > \text{MIL-100 (Fe) (3.227)} > \text{MIL-Cx4-1 wt\% (2.851)} > \text{AC (1.864)}$$

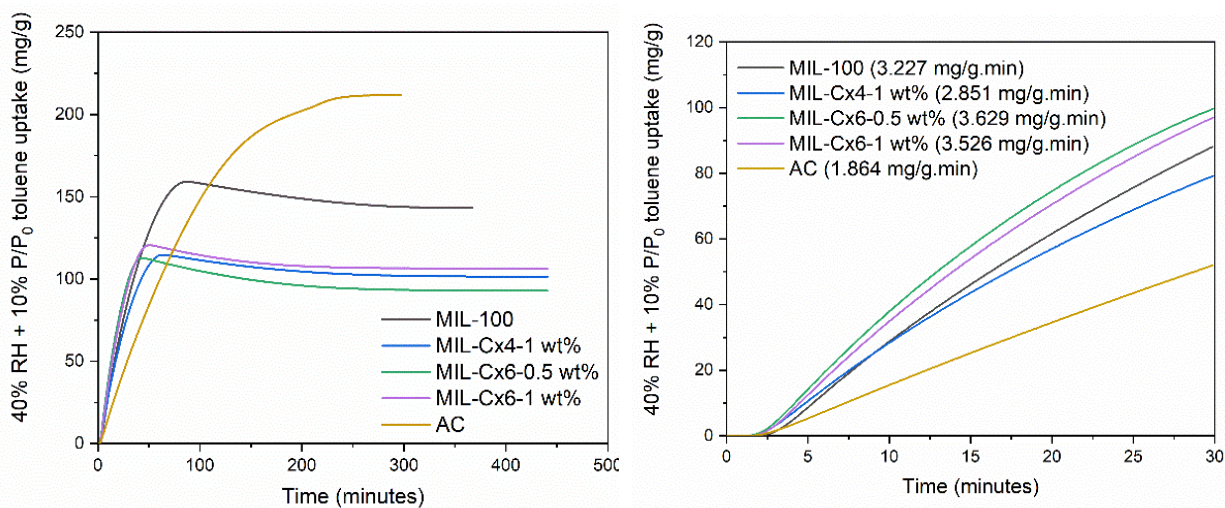


Figure 6.14: (Left) 40% RH and 10% toluene P/P₀ adsorption kinetics of calixarene-treated MIL-100 (Fe). (Right) Initial 30-minute adsorption data with linear-fitted slope values given in the legend brackets.

6.2.13 Adsorption kinetics for calixarene-treated MIL-100 (Fe)

Table 6.5 shows the estimated linear initial kinetics *slope* values for all calixarene-treated MIL-100 (Fe) samples. MIL-Cx6-1 wt% exhibited the highest *slope* value at 0.5% toluene P/P₀, which makes it one of the best sample candidates for further investigation. Also, MIL-Cx6-0.5 wt% and MIL-Cx6-1 wt% each exhibits a 12.5% and a 9.3% higher *slope* value than the pristine MIL-100 (Fe) at 10% toluene P/P₀. Experimental findings from these two toluene concentrations clearly show that the calixarene treatment, especially on MIL-Cx6-1 wt%, is more advantageous in accelerating the initial toluene adsorption kinetics than either pristine MIL-100 (Fe) or AC.

Table 6.5: Linear-fitted parameters of all calixarene-treated MIL-100 (Fe) samples.

Sample	Experimental q_e values and their linear-fitted <i>slopes</i>					
	40% RH/0.5% toluene P/P ₀			40% RH/10% toluene P/P ₀		
	q_e (mg/g)	<i>slope</i> (mg/g.min)	R ²	q_e (mg/g)	<i>slope</i> (mg/g.min)	R ²
MIL-100 (Fe)	26	0.104	0.989	150	3.227	0.995
MIL-Cx4-0.5 wt%	36	0.156	0.996	-	-	-
MIL-Cx4-1 wt%	40	0.120	0.999	101	2.851	0.993
MIL-Cx6-0.5 wt%	38	0.155	0.997	93	3.629	0.987
MIL-Cx6-1 wt%	40	0.167	0.997	106	3.526	0.991
AC	100*	0.081	0.998	212	1.864	0.999

* The value may not represent AC's equilibrium uptake due to its slow adsorption rate.

6.2.14 Adsorption kinetics for calixarene-treated MIL-100 (Fe) using a nonlinear pseudo first order kinetics model

The kinetics of the samples' adsorption curves can also be described with a pseudo-first order (PFO) model provided the adsorption has reached its equilibrium. Table 6.6 reports the calculated PFO kinetics parameters of all calixarene-treated samples at 0.5% and 10% toluene P/P₀ concentrations. At 0.5% toluene P/P₀, the nonlinear PFO equation is not valid for AC as it did not reach equilibrium. Meanwhile, at 10% toluene P/P₀, the adsorbate displacement occurrence on the MIL-100 (Fe) samples results in a poorer fit which gives lower R² values.

Table 6.6: Fitted values of the calixarene-treated MIL-100 (Fe) samples' adsorption kinetics profiles using a nonlinear pseudo-first order equation.

Sample	Experimental q_e and pseudo first order-fitted model parameters							
	40% RH/0.5% toluene P/P ₀				40% RH/10% toluene P/P ₀			
	q_e (mg/g)	$k_1 \times 10^3$ (min ⁻¹)	$q_e.k_1$ (mg/g.min)	R ²	q_e (mg/g)	$k_1 \times 10^3$ (min ⁻¹)	$q_e.k_1$ (mg/g.min)	R ²
MIL-100 (Fe)	26	5.2	0.135	0.999	150	35.7	5.36	0.932
MIL-Cx4-0.5 wt%	35	6.0	0.210	0.998	-	-	-	-
MIL-Cx4-1 wt%	40	3.7	0.148	0.999	105	50.3	5.28	0.902
MIL-Cx6-0.5 wt%	37	5.5	0.204	0.998	98	78.5	7.69	0.785
MIL-Cx6-1 wt%	42	5.4	0.227	0.999	110	62.2	6.84	0.886
AC	100*	-	-	-	212	9.98	2.32	0.994

* The value may not represent AC's equilibrium uptake due to its slow adsorption rate.

The PFO model supplies two key parameters. Namely the theoretical maximum equilibrium adsorption capacity (q_m), and PFO-kinetics coefficient (k_1) or rate of adsorption. An ideal adsorbent needs to score high values in each criterion to be suitable for practical applications. Therefore, by assuming an equal weighting to each parameter and for the purpose of convenient material comparison, the product of the experimentally measured equilibrium adsorption capacity (q_e) and k_1 or $q_e.k_1$ could provide a good selection basis. The $q_e.k_1$ term can be referred to also as the aggregate adsorption rate which is proposed as a metric reflecting potential practical utility of an adsorbent.

At 0.5% toluene P/P₀, AC is eliminated from the material shortlist due to its very slow kinetics despite its high final capacity. For other samples, there seems to be one distinct observation. The calixarene-treated samples showed at least 10% and up to 68% higher aggregate adsorption rate than the pristine MIL-100 (Fe) although the calixarene treatment reduced the surface areas and the pore volumes of the treated MIL-100 (Fe) samples.

Meanwhile, at 10% toluene P/P₀, AC appears superior with its high capacity, but it is significantly restricted by its slow kinetics, hence, the very low $q_e.k_1$. On the other hand, the slightly lower capacity by MIL-100 (Fe) than AC is compensated with its faster kinetics, as reflected in its 131% higher $q_e.k_1$ value. This advantage was amplified with the addition of calixarene coatings. Note that the data at this higher toluene concentration can potentially be overestimated as observed from the poor fitting values ($R^2 < 0.98$) obtained from the PFO model. It is believed that if breakthrough experiments are used for future work, followed by applying the appropriate breakthrough equations, these experiments will provide a more accurate depiction of their kinetics' standing. Although the calixarene-treated MIL-100 (Fe) samples showed faster adsorption kinetics than pristine MIL-100 (Fe), they fell way behind the uptake capacity of AC. Therefore, the calixarene-treated MIL-100 (Fe) may not have sufficient merit to be tested for breakthrough experiments.

6.2.15 High humidity test for calixarene-treated MIL-100 (Fe)

The kinetics analysis has demonstrated that the introduction of calixarene coating accelerated the rate at which 0.5% toluene P/P₀ is adsorbed into the pores. The next important parameter to investigate is the short-term water stability of these calixarene-treated MOFs at a high humidity condition: 90% RH. Pristine MIL-100 (Fe), MIL-Cx4-1 wt% and MIL-Cx6-1 wt% were chosen for this assessment, using AC as a benchmark.

Table 6.7 details the amount of 0.5% toluene P/P₀ uptake before and after 90% RH exposure. These results agree with their water adsorption isotherms. Despite the existence of the calixarene coating, the pores of the coated samples remained hydrophilic and could not prevent water adsorption at 90% RH. This strong water occupation in the calixarene-treated samples' pores thus prevents any

toluene capture in the second 0.5% toluene P/P₀ adsorption cycle. In short, after 90% RH exposure, these MOFs were unable to capture toluene at 0.5% P/P₀.

Table 6.7: Adsorbed 0.5% toluene P/P₀ amount for MIL-Cx4-1 wt%, MIL-Cx6-1 wt% and AC, before and after 90% RH exposure.

Sample	Uptake quantity (mg/g)		
	1 st 0.5% toluene	90% RH	2 nd 0.5% toluene
MIL-Cx4-1 wt%	22	104	0
MIL-Cx6-1 wt%	23	110	0
AC	113	139	112

In contrast, AC responded well to the high humidity challenge, as its hydrophobic pores help to repel the adsorbed water and to still reserve the space for toluene adsorption. It also displays consistent 0.5% toluene P/P₀ uptake measured before and after the humidity surge, verifying its hydrophobic utility.

6.2.16 Adsorbent reusability study on calixarene-treated MIL-100 (Fe)

MIL-Cx6-1 wt%, which has a higher $q_e.k_1$ value at 10% toluene P/P₀ than the pristine MIL-100 (Fe), was subjected to reusability test at the same concentrations. Figure 6.15 shows the quantity of 10% toluene P/P₀ adsorbed in 10 adsorption-desorption cycles. In Cycle 1, AC started with a slightly lower adsorption quantity before maintaining its adsorption capacity throughout the remaining cycles. Meanwhile, MIL-100 (Fe) experienced a higher uptake in the beginning, but it continued to slowly decrease from one cycle to the next. MIL-Cx6-1 wt% retained almost equal capacity for the entire 10 cycles trial. Two reasons can be outlined here:

1. Precursor MIL-100 (Fe)'s mesoporosity boosted its initial toluene co-uptake compared to the microporous AC which needs a longer time to adsorb the toluene under the same condition.

- The 40% RH background forces the hydrophilic nature of MIL-100 (Fe) to yield to water occupation. Since the calixarene coating is present on the MIL-Cx6-1 wt%, it helped protect the surface from complete water occupation, but due to its lower surface area, its maximum capacity is lower than MIL-100 (Fe).

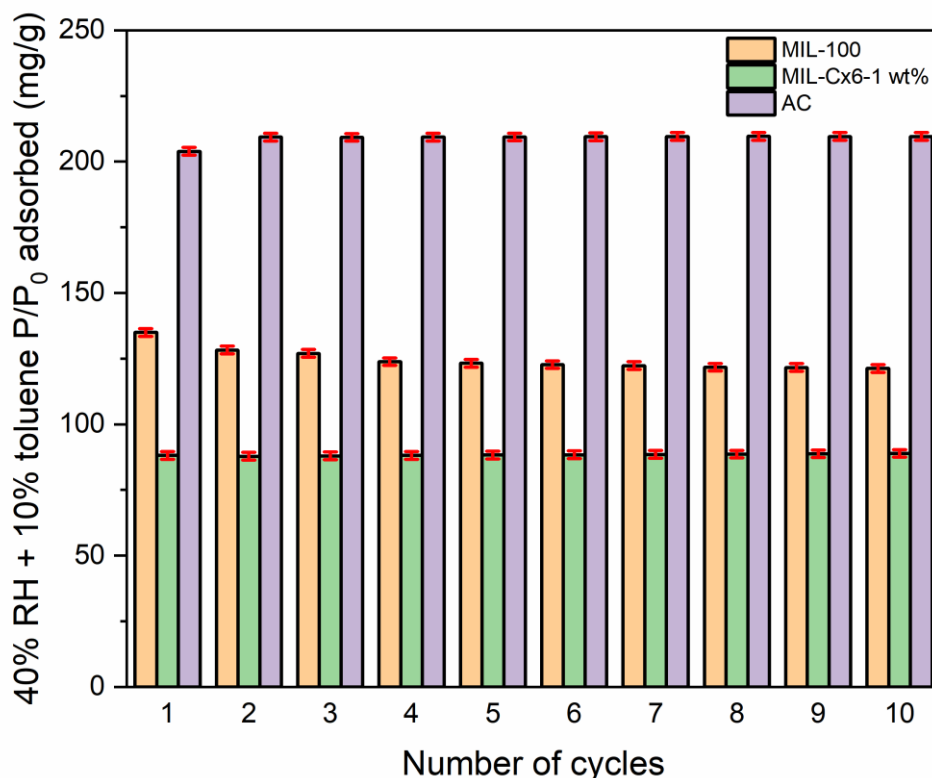


Figure 6.15: Quantity of toluene adsorbed at 40% RH and 10% toluene P/P_0 concentration by MIL-100 (Fe), MIL-Cx6-1 wt% and AC for a duration of 10 adsorption-desorption cycles.

6.2.17 Toluene co-adsorption mechanisms after calixarene surface treatment

Table 6.1 shows that the molecular diameters of the tested calixarene molecules are small enough to penetrate the micropores of MIL-100 (Fe) after the surface treatment. Following the calixarene treatment, there are nominal reductions in their surface area and pore volume compared to the pristine MIL-100 (Fe). Table 6.5 also shows that the linear initial kinetics *slope* values for the calixarene-treated samples are relatively higher than the pristine MIL-100 (Fe). So are their

aggregate adsorption rate ($q_e.k_1$) as displayed in Table 6.6, indicating some modest performance improvements in the modified materials for those treated with low concentrations of calixarene.

Since the competitive adsorption experiments were performed after 40% RH saturation, water molecules have already occupied a significant proportion of the MOF's pores. When the toluene molecules are introduced into the binary solvent system, they will first be adsorbed on the remaining vacant MOF surface sites until the monolayer formation of water and toluene completes. Then, the toluene will gradually fill in any vacant pores and subsequently, transferring into the two larger mesopores of the MOF. However, because neither the MOF's micro nor the mesopores are severely blocked, surface adsorption is postulated to be the main adsorption mechanism, followed by pore filling. Therefore, the high calixarene hydrophobicity on the surface of calixarene-treated samples lowers the overall surface site competition between water and toluene. Consequently, the calixarene-treated samples prefer to adsorb toluene in the surface adsorption stage which impacts on their faster toluene co-adsorption equilibrium. Hence, the reason to their higher linear *slope* and $q_e.k_1$ values.

Despite the surface of the calixarene-treated samples has turned hydrophobic, it appears that the pores remain significantly hydrophilic. This point is inferred from the data in Table 6.7 that indicates even a single-time exposure to a high humidity of 90% RH is enough fill all the pores and to severely restrict the calixarene ability to adsorb toluene. This proves that the calixarene-treated samples still possess significant amounts of the original MIL-100 (Fe)'s pore hydrophilicity.

6.3 Conclusions

The wet-phase hydrophobic coating methods using calixarenes (Cx) described here successfully increased MIL-100's water contact angles. However, this treatment appears to have been a predominantly external surface modification, with the coatings yielded no significant benefits to the internal pore chemistry, as indicated by their closely similar water isotherms to pristine MIL-100 (Fe) and their low hydrophobicity index values. Compared to MIL-100 (Fe), the calixarene-

treated MIL-100 (Fe) samples showed encouragingly faster toluene co-adsorption kinetics when tested at 40% RH/0.5% and 40% RH/10% toluene P/P₀ concentrations. Based on the kinetics modelling analysis that considers both adsorption capacity and rate, MIL-Cx6-1 wt% was one of the most promising candidates.

It was later investigated for its water stability and its reusability. In the water stability study, the pore hydrophilicity of MIL-Cx6-1 wt% became apparent as no toluene was adsorbed after exposure to high humidity (90% RH). On the contrary, AC showed equivalent toluene uptake under the same environmental stresses.

Over the course of 10 repeated adsorption-desorption cycles at 40% RH/10% toluene P/P₀, the MIL-Cx6-1wt% maintained a stable toluene uptake compared to MIL-100 (Fe) which shows constantly declining uptake due to its high hydrophilicity. AC demonstrated extremely slow adsorption kinetics due to its microporosity, yet its intrinsic hydrophobicity is believed to be the fundamental factor contributing to higher toluene adsorption capacity than the MOFs that have higher surface area. Overall, this study outlines the key criteria to rely on when selecting adsorbents for humid VOC capture in the order of highest priority:

1. First, the adsorbent framework needs to be intrinsically hydrophobic to selectively not adsorb water in competitive adsorption processes and to favour hydrophobic VOCs.
2. A high surface area, with a balance of micro-mesoporous material should be sought to attain a highly competitive VOC uptake capacity and superior kinetics. Usage of a microporous adsorbent *per se* can lead to extremely slow adsorption rate, making them ineffective for certain industrial applications.
3. If these requirements are met, then additional surface chemistry modifications can improve the treated adsorbent's adsorption performance. The findings from this Chapter prove that some calixarene-treated MOFs demonstrated faster adsorption kinetics than the pristine MIL-100 (Fe) even though with reduced pore volumes and surface areas.
4. Targeted chemical interactions between the adsorbate and the functionalized adsorbent improves the mutual molecular affinity despite the adsorbent possessing limited porosity.

Chapter 7: Modified MIL-96 (Al) particles for perfluorooctanoic acid removal⁸

7.1 Introduction

Chapter 4 raised an important point that fine powdered MOFs commonly in the nm/ μ m range need to be fabricated into larger particle sizes for their ultimate industrial utilization. Moreover, in commercial water purification processes, the adsorbents are usually packed into beds/columns, which in the case of fine particles, will be prone to high column pressure drops, and consequently have larger energy usage in operational pumping. Enlarging the adsorbent's particle size is one of the best design options for minimizing the pressure drops in the adsorbent beds.

The size and crystal morphology of MOFs particles can be precisely controlled by adding specific chemical additives in the synthesis reactions including (1) initiation solvents, (2) coordination modulators, (3) surfactants or (4) hard templates into the precursor reactants (Seoane *et al.*, 2016). However, these approaches are mainly used to create smaller nanoparticles.

In this Chapter, a new one-pot surfactant-based MOF synthesis method is developed to increase the particle size and to control the morphology of the MOF crystals. This method utilizes a synthetic surfactant/polymer known as hydrolysed polyacrylamide (HPAM). A non-toxic and hydrothermally stable aluminium-based MOF, MIL-96 (Al), was chosen as the precursor material to be subsequently tested for liquid phase adsorption of PFOA. Due to MIL-96 (Al)'s positive surface charge (Azhar *et al.*, 2018), the addition of anionic HPAM can facilitate particle aggregation. HPAM has a low cost and it is a water-soluble polymer widely used for enhanced oil recovery in petroleum drilling processes, as well being used as a flocculant for wastewater treatment (Rellegadla, Prajapat & Agrawal, 2017). Its benign impacts on water quality are also noted (Edomwonyi-Otu & Adelokun, 2018). Finally, to understand the adsorption mechanisms

⁸ Part of this Chapter has been published as "Azmi, L. H. M.; Williams, D. R.; Ladewig, B. P. Polymer-Assisted Modification of Metal-Organic Framework MIL-96 (Al): Influence of HPAM Concentration on Particle Size, Crystal Morphology and Removal of Harmful Environmental Pollutant PFOA. *Chemosphere*. **2021**, 262, 128072."

better for this MOF, the PFOA adsorption performance by the modified MOF material in this work was benchmarked with a commercial AC.

7.2 Results and discussion

7.2.1 SEM

For MIL-96 (Al), HPAM is proven effective in changing the MOF particle morphology as observed in Figure 7.2a-d. Generally, starting from the normally reported small hexagonal bipyramidal shaped crystals (Benzaqui *et al.*, 2017), higher HPAM concentrations facilitate incremental increases in the aspect ratio (length: diameter), transitioning from hexagonal spindles to elongated hexagonal rods, particularly when 20 mL HPAM was used (MIL-96-RHPAM2). Upon closer inspection from out-of-plane PXRD measurements, the apparent hexagonal spindle morphology was revealed to be a hybrid form of two elongated hexagonal pyramids seamlessly connected at the long axis (Sindoro, Jee & Granick, 2013).

It was reported that the hydrothermal synthesis conditions for MIL-96 (Al) must be strictly controlled given the possibility of forming two larger pore Al trimesates, MIL-100 (Al) and MIL-110 (Al), in the same reaction system despite all having their distinct crystal structures. MIL-100 (Al) is the kinetically stable product which forms at short reaction times and low pH condition whereas the thermodynamically favoured MIL-96 (Al) can be obtained after longer reaction times. MIL-110 (Al) on the other hand, crystallizes in a much more acidic or basic media (Haouas *et al.*, 2009). Their corresponding crystal morphologies have also been solved by Haouas *et al.* (Haouas *et al.*, 2012). They found that MIL-96 (Al), MIL-100 (Al) and MIL-110 (Al), each presents a flat hexagonal, an octahedral and a hexagonal needle-like habits respectively. In summary, the influence of HPAM on the crystal morphology agrees well with the stability order of these phases; MIL-96 (Al) > MIL-110 (Al) > MIL-100 (Al).

The addition of HPAM seems to play multiple roles in the crystal elongation phenomenon, though primarily as a competing modulator. Since the pK_a value for HPAM is 4.5 (Li *et al.*, 2002) which is similar to that of trimesic acid ($pK_{a1} = 3.51$, $pK_{a2} = 3.89$, $pK_{a3} = 4.70$), there will be competition with the linker to form coordination bonds with available Al^{3+} species. As a result, nucleation rate

slows down and concurrently permits the slower growth of larger MOF crystals (Morris *et al.*, 2017). Secondly, the amine (-NH₂) groups from the amide in both HPAM and PAM increase the basicity of the reaction solution, providing ideal conditions for the formation of MIL-110 (Al) as ascribed by the existence of the elongated hexagonal rod-like crystals. For reader's information, HPAM is a copolymer composed of PAM and PAA. Figure 7.1 illustrates the repeating units of the polymer additives that were used in these experiments.

So, to identify the dominant functional groups responsible for the formation of the elongated hexagonal rods, MIL-96 (Al) was synthesized using equivalent concentrations of PAM (Figure 7.2e) and PAA (Figure 7.2f) separately. Before the reaction, the solutions were very acidic upon addition of PAM (pH = 2), PAA (pH = 2.4) and HPAM (pH = 2.2). Such acidic environments could increase the likelihood of -NH₂ groups in the amide protonating to form primary ammonium ions (-NH₃⁺) in preference to the ionization of the -COOH groups on the trimesic acid due to higher pK_a values. It is therefore expected to see the -NH₂ groups contained in the amide-based polymers of HPAM and PAM to govern the crystal elongation mechanism, transforming from the hexagonal bipyramidal shape into the elongated hexagonal rods more so than using PAA.

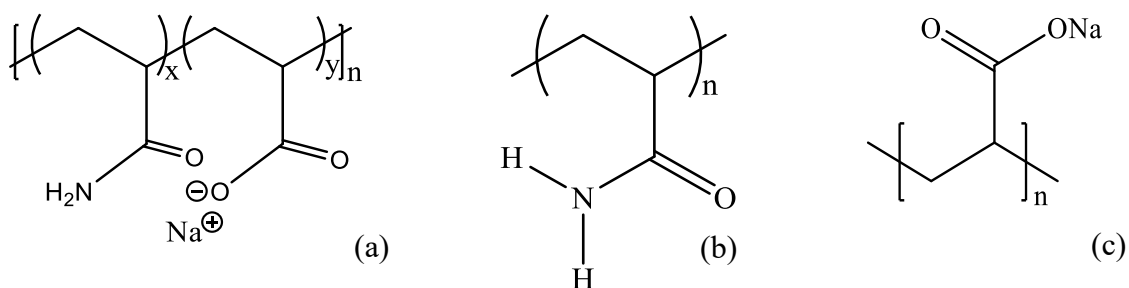


Figure 7.1: Chemical structures of the polymers used: (a) HPAM, (b) PAM and (c) PAA.

After adding 20 mL PAA (Figure 7.2f), it is unclear what properties drive the formation of new hexagonal particles, with some truncated and larger in dimension than the elongated hexagonal rods. One potential explanation could be that after mixing PAA in water, the dissociated Na⁺ cations may compete with Al³⁺ species to form bonds with the linker, causing deceleration in the crystal growth and altering the original template. Another factor that may have undermined PAA's influence is due to its low molecular weight (~2100 g/mol). By substituting higher molecular

weight PAA for the synthesis, thus, supplying higher PAA concentration in the reaction solution, it may amplify the PAA's influence towards the formation of the hexagonal particles.

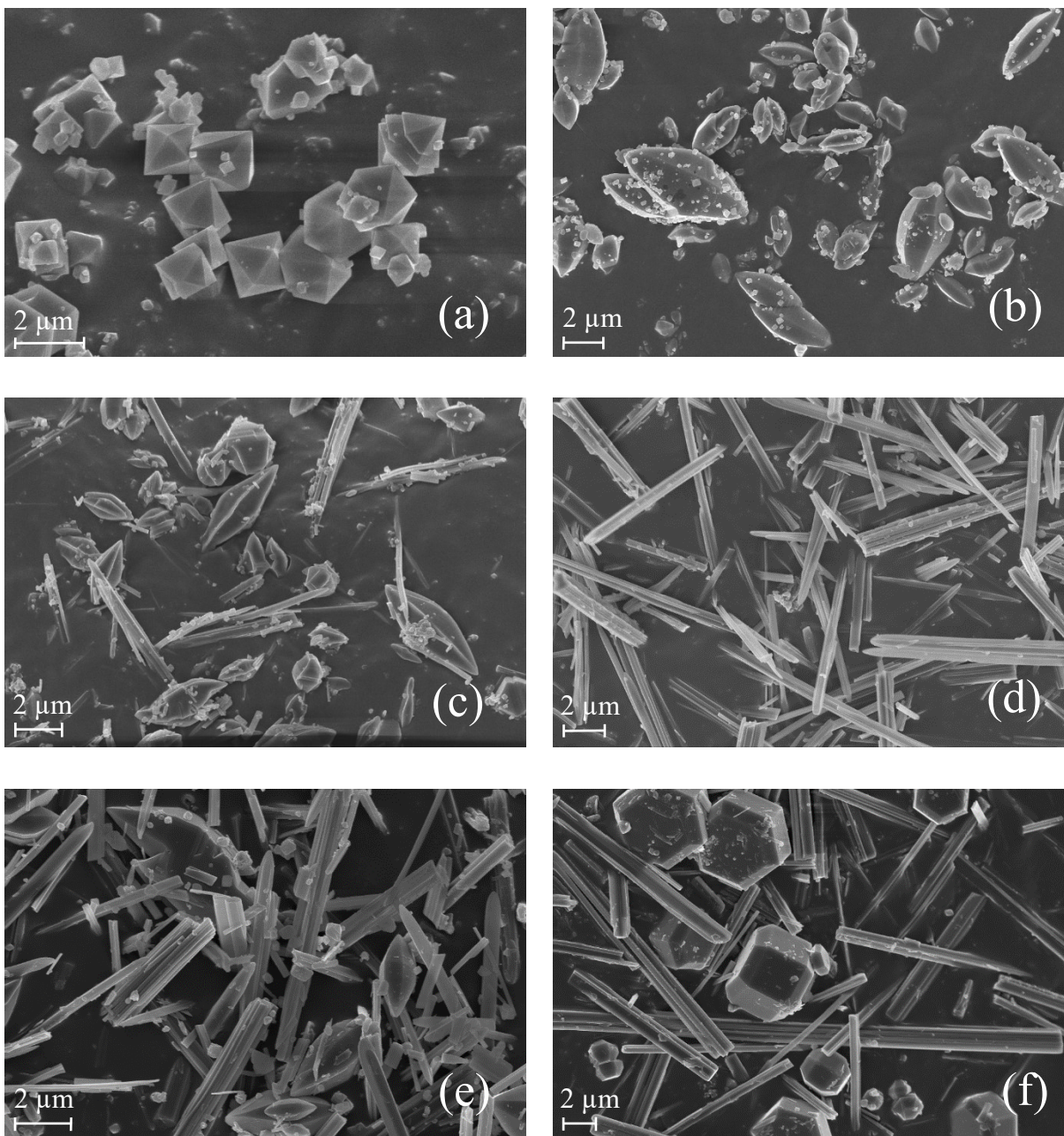


Figure 7.2: Modified MIL-96 (Al) crystals with (a) no polymer, (b) 2 mL HPAM ($R_{HPAM} = 0.2$), (c) 6 mL HPAM ($R_{HPAM} = 0.6$), (d) 20 mL HPAM ($R_{HPAM} = 2$), (e) 20 mL PAM ($R_{PAM} = 2$), and (f) 20 mL PAA ($R_{PAA} = 2$).

Finally, the successes in the morphological changes shown in the MIL-96 (Al) samples can be attributed to the solubility of the trimesic acid linker in water. Simultaneous dissolution of both trimesic acid and HPAM during the pre-mixing stage facilitates smooth integration of the latter species into the reaction solution, which subsequently changes the MOF crystal morphology. On a side note, identical experiments were performed involving similar chemical modification on MIL-101 (Cr). Readers are referred to Figure A10.29 in the Appendix for further information.

7.2.2 PXRD

As shown in Figure 7.3, the PXRD patterns of each sample vary slightly compared to the simulated MIL-96 (Al) spectra, with the peaks being shifted to slightly higher diffraction angles. The shift may be attributed to the presence of free trimesic acid inside the pores of the samples (Abid *et al.*, 2016). The crystal shape changes can be defined using the Bravais, Frisdel, Donnay and Harker (BFDH) theory which describes the three main planes that make up the morphology of MIL-96 (Al); they are (002), (100) and (101) at $2\theta = 5.7^\circ$, 7.1° and 7.7° respectively (Liu *et al.*, 2015a). However, in this work, the obtained experimental observations are different with facets (100), (101) and (102 at $2\theta = 9.1^\circ$) being the most prominent in the investigated MIL-96 (Al) adsorbents' PXRD peaks.

Except for the subtly present (002), other key characteristic peaks including (102) match well with the simulated MIL-96 (Al) spectra, indicating that the core crystalline structure is retained. Although by visual inspection, MIL-110 (Al) was mainly present at higher HPAM loading as evident by the hexagonal rod formation, due to instrument limitation (minimum $2\theta \geq 5^\circ$), the characteristic PXRD peaks of MIL-100 (Al) ($2\theta = 4^\circ$) and MIL-110 (Al) ((001) facet; $2\theta = 5^\circ$) (Lin, Kong & Chen, 2013) could not be clearly detected and thus, have to be omitted from subsequent discussion.

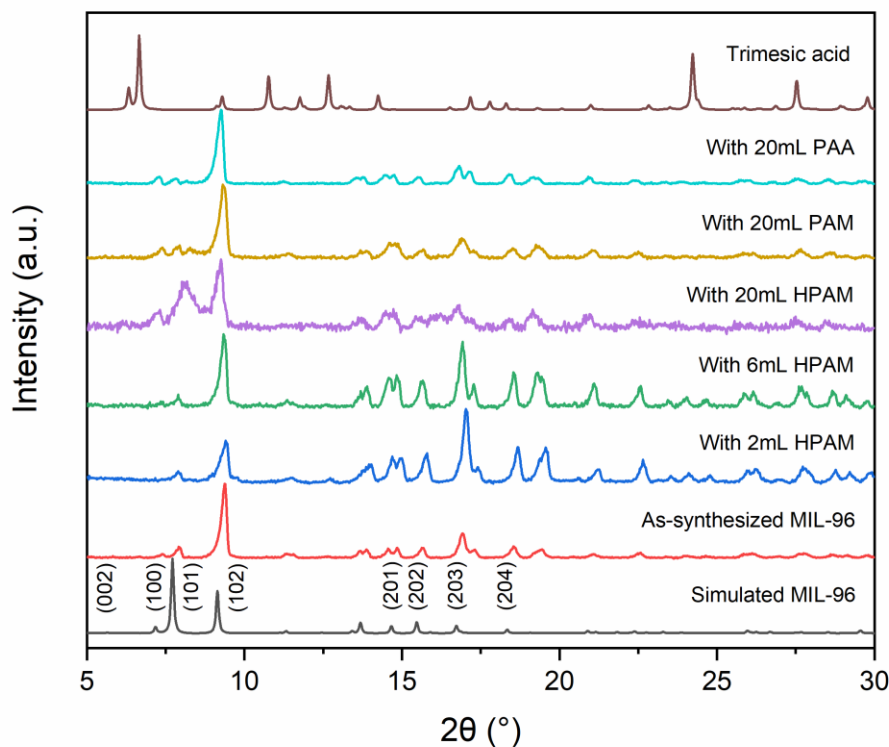


Figure 7.3: PXRD patterns of the simulated MIL-96 (Al) compared to the as-synthesized MIL-96 (Al) samples modified with different types and proportions of polymers.

With higher concentrations of HPAM, the increased intensity for the (100) facet indicates HPAM enhances the growth rate of the (100), resulting in narrowed edge and the lengthening of the crystals. Furthermore, a higher proportion of HPAM accentuates the growth of the (101) crystal plane as shown by the gradual peak increase alongside with (100). Thus, completing the formation of hexagonal rod crystal morphology. This change is consistent with the reported SEM images. The -NH_2 groups of the amide in HPAM function like OH^- ions, increasing solution basicity and speeding up the growth rate along the (101) facet, consequently forming the hexagonal rod habit (Lin, Kong & Chen, 2013).

After the addition of PAA, the (002) facet that is responsible for the formation of HL is only weakly observed in the PXRD, as with the simulated MIL-96 (Al). Although the BFDH theory also states that the growth rate of the (002) facet can be relatively unaffected, the number of products containing the (002) plane may be minor compared to the bulk phase which is dominated with (100) and (101)-directed crystals. In short, the preferential crystal growth along the (100) and (101) planes, which is a function of higher polymer concentrations, transformed the crystal anisotropy by promoting crystal elongation from its original hexagonal bipyramidal shape. In terms of a hexagonal lattice system, the impact of polymer presence in the reaction is acceleration of growth along the c axis (Sindoro, Jee & Granick, 2013). Moreover, with a higher quantity of added polymers reported here, there is a subtle width broadening of the strongest peak corresponding to the (102) crystal face implies a slight decrease in particle size. In addition, the relative Bragg peaks of (200) and (201) also become broader and less intense compared to the original MIL-96 (Al), supporting a minor reduction in particle size and crystallinity.

7.2.3 FTIR

FTIR spectroscopy was used to understand PFOA adsorption mechanism onto MIL-96-RHPAM2 (Figure 7.4) and the interactions between the linker and the added polymer during synthesis (Figure A10.30, Appendix). Examining Figure 7.4, HPAM addition to MIL-96 (Al) has no effect on the frequencies and relative absorption intensities with respect to the pristine sample, whereas the collected spectra of spent MIL-96-RHPAM2 confirm that PFOA was adsorbed, probably through electrostatic interaction with the MOF. A previous study also inferred the increased intensities of asymmetric (ν_{as}) than symmetric (ν_s) COO^- stretch after PFOA adsorption to be related with an inner-sphere complexation with the metal centres. In this case, the carboxylate head groups of PFOA may have formed electrostatic bonds to the surface of MIL-96-RHPAM2 (Gao & Chorover, 2012). Additionally, the consistent N-H peak on both spectra of MIL-96-RHPAM2 after PFOA adsorption and desorption indicates minimal leaching of the HPAM functionality.

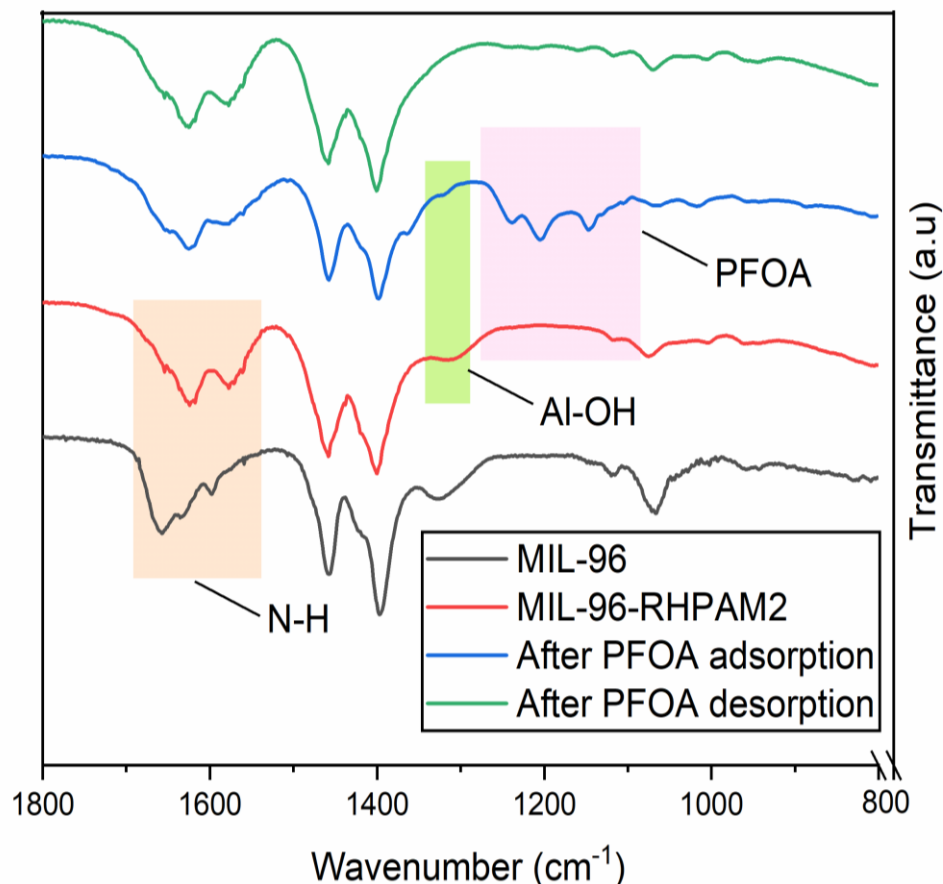


Figure 7.4: The FTIR spectrum for the parent MIL-96 (Al) is in black. The spectra of as-synthesized MIL-96-RHPAM2 is in red. The blue line refers to MIL-96-RHPAM2's spectra after PFOA adsorption whilst the green line is the spectra after PFOA desorption.

Details of the IR peaks involved in PFOA adsorption and desorption are described in Table 7.1. An interesting phenomenon to note after PFOA adsorption on MIL-96-RHPAM2 is the gradual disappearance of Al-OH peak at 1300 cm⁻¹. In a prior study by Zhang *et al.* (Zhang *et al.*, 2014a), they also used MIL-96 (Al) to remove fluoride through an ion exchange process. In that work, they identified another peak at 1123 cm⁻¹, for Al-F which replaced the weakened Al-OH peak. However, in this case, the proposed peak of 1123 cm⁻¹ was not evident on MIL-96-RHPAM2's spectra after adsorbing PFOA, indicating that it may be dominated by other adsorption mechanisms such as Lewis-acid base interaction or electrostatic forces. These mechanisms will require further investigations as their dominance is pH-dependent (Li *et al.*, 2016b).

Table 7.1: Band assignments for FTIR spectra of MIL-96 samples synthesized with HPAM.

Wavenumber (cm ⁻¹)	Mode assignment	Description	Reference
1658	Overtone of C-H bending from aromatic compound.	Multiple bands of the fundamental absorption frequency originating from MIL-96 (Al)'s linker benzene rings.	(Fu & Schlup, 1993; Linder <i>et al.</i> , 2008)
1620	C-H and primary amine N-H in-plane bending.	HPAM and PAM polymers are grafted to the MOF by H-bonding given the newly formed bands.	
1570	Asymmetric ν_{as} (COO ⁻) and ν_{as} (C-H) stretching.	Newly formed bands when the polymers are added indicate strengthened H-bonding between the carboxylate radical and C-H groups. The peaks might also be superpositioned from the N-H in-plane bending. After PFOA adsorption, the ν_{as} (COO ⁻) shifted to slightly lower wavenumber, but it showed an increased intensity.	(Xue <i>et al.</i> , 2016; Yu <i>et al.</i> , 2019)
1455 – 1500	Symmetric ν_s (COO ⁻) stretching.	The characteristic ν_s (COO ⁻) vibration strengthened upon addition of polymers suggesting change in vibration mode to asymmetric. After PFOA adsorption, the ν_s (COO ⁻) peaks displayed lower intensities, ascertaining the inner-sphere complexation phenomenon between the PFOA molecules and the MIL-96-RHPAM2's metal centres.	
1395 – 1440	O-H bending of carboxylic acid.	The origin of this vibration is from the trimesic acid linker built within the MOF.	(Zhang <i>et al.</i> , 2014a)
1300	Stretching of Al-OH.	Coordinated trimesic acid to the aluminium atoms.	
1146	ν_s (CF ₂).	Electrostatic interaction between all characteristic peaks ascribed to PFOA molecules and the MOF.	(Gao & Chorover, 2012)
1204	ν_{as} (CF ₂) and ν_{as} (CF ₃).		
1238	ν_{as} (CF ₂).		
1319, 1364	ν_{ax} (CF ₂).		

Note: ν_{as} , asymmetric stretch; ν_s , symmetric stretch; ν_{ax} , axial stretch.

7.2.4 Elemental analysis

Figure 7.5 shows the wt% quantity of C, H, N and S in all studied samples. All samples despite their polymer modifications, did not display any major changes in their elemental compositions. Therefore, it is reasonable to conclude the polymers are physically bonded to the external surface of the MOFs at low concentrations and are not chemically bonded in the main linkage structures. A trace contaminant level quantity of S (< 0.1 wt%) was detected in the MIL-96 (Al) control sample. The remaining samples do not contain any S, indicating the possibility of slight sample contamination in this one sample.

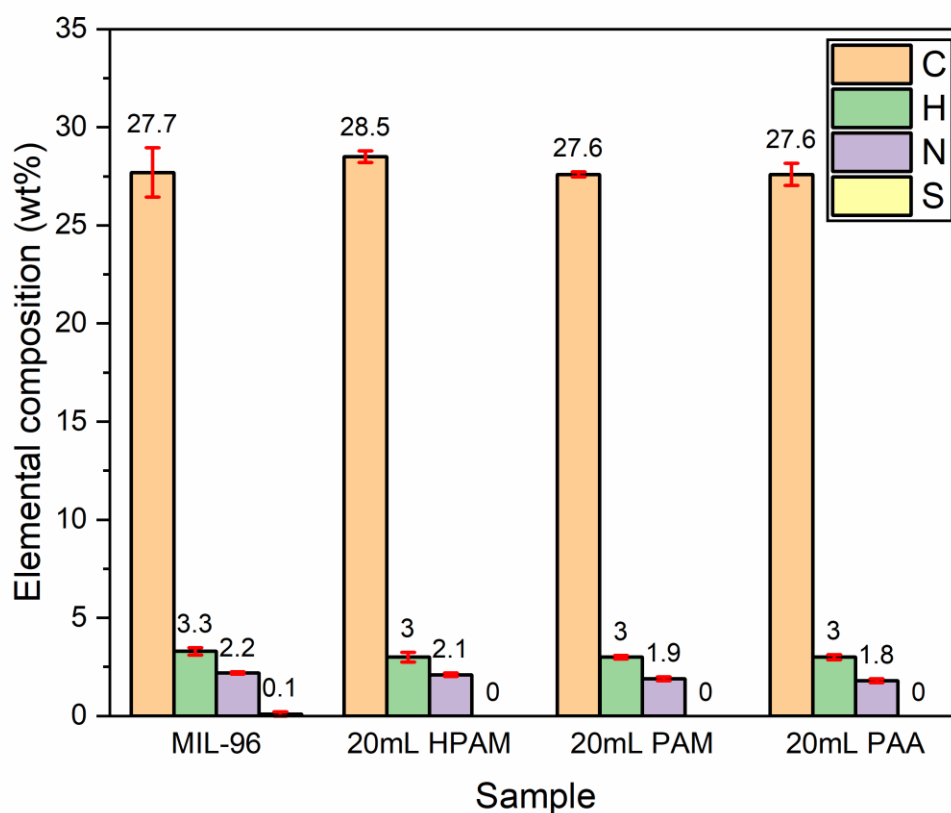


Figure 7.5: Elemental analysis for C, H, N and S in modified MIL-96 (Al) samples (n = 3).

7.2.5 TGA

The thermal stability of the HPAM-modified samples was studied using a thermogravimetric analyser coupled with MS analysis to detect the evolved gases from the materials' decomposition. These are referenced from the NIST Chemistry Web Book and the specific signal for H₂O was traced at m/z 18. Combined information from Table 7.2 and Figure 7.6 show that all MIL-96 (Al) samples exhibited three key stages of weight loss. The insertion of HPAM into the MIL-96 (Al) framework involves occupation of some of the pore space that is initially occupied by free water molecules. This point is supported by Figure 7.7 where, after sample drying at 150 °C, MIL-96 (Al) exhibits a higher (17%) mass loss whereas MIL-96-RHPAM2 loses only 11% in weight. This water loss is confirmed by the lower MS signal response at m/z 18 (H₂O). Along with trapped water molecules in the cavities, the signal also comprises water molecules that are bonded to the aluminium atoms in the MOF. The second weight loss event comprises a two-step process between 300 °C to 580 °C and is a result of gradual structural decomposition associated with the loss of the trimesate species. Addition of 20 mL HPAM might have caused slight shift in the bond strengths connecting the overall framework, as the decomposition no longer follows a stepwise trend. The final mass loss above 580 °C results in an Al₂O₃ residue (Loiseau *et al.*, 2006).

Table 7.2: Details about the distinct material decomposition stages up to 800 °C in N₂.

Temperature gradient	Range (°C)	Sample weight loss (wt%)	
		MIL-96 (Al)	MIL-96-RHPAM2
$\Delta T1$	20 – 150	17	11
$\Delta T2$	150 – 580	48	23
$\Delta T3$	580 – 800	5	25

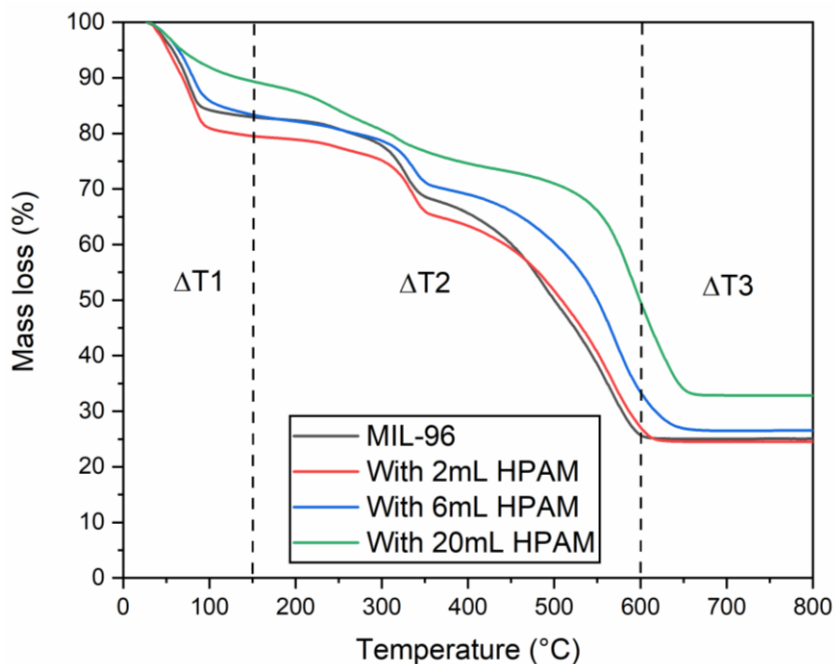


Figure 7.6: TGA results for MIL-96 (Al) samples containing various HPAM quantities.

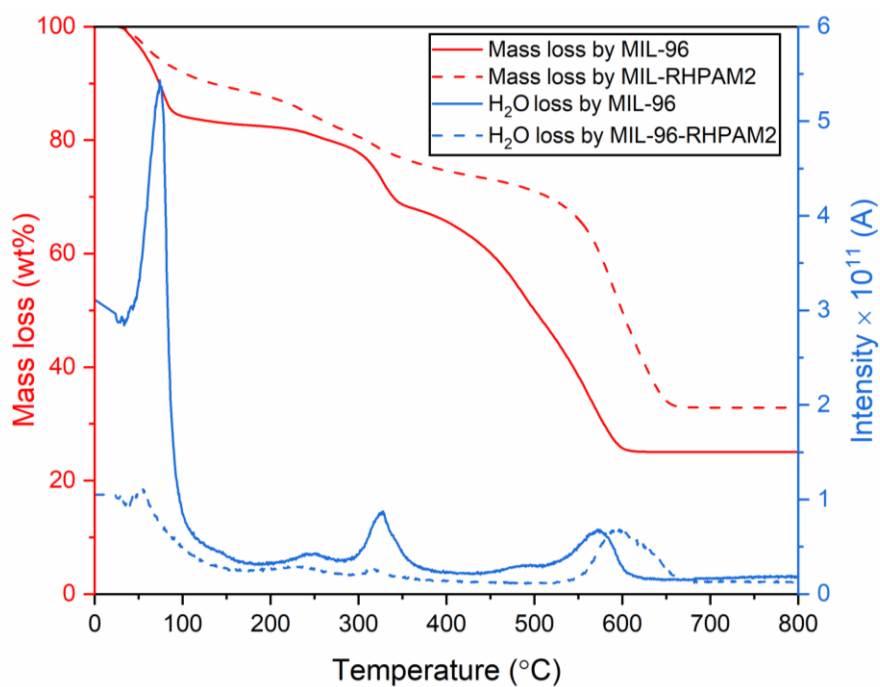


Figure 7.7: Compiled TGA-MS %mass loss spectra (left y-axis) as a function of temperature for MIL-96 (Al) (solid red line) and MIL-RHPAM2 (dotted red line). The quantity of H₂O desorbed over temperature is represented by the $m/z = 18$ current intensity on the right y-axis. The quantity of H₂O desorbed by MIL-96 (Al) is shown in solid blue line whereas by MIL-96-RHPAM2, it is the dotted blue line.

7.2.6 Porosity analysis

The use of PAM, PAA and HPAM for this particle size modification led to a significant reduction in the apparent surface area (S_{BET}), see Figure 7.8 and Table 7.3. The pore size distribution plots in Figure 7.9 clearly show complete pore blocking when HPAM was used, confirming its presence inside the pores.

Table 7.3: BET surface area and pore volume measurements of all studied samples.

Sample	BET surface area (m^2/g)	V_{total} (cm^3/g)	V_{micro} (cm^3/g)	$V_{\text{micro}}/V_{\text{total}}$
MIL-96 (Al)	714 ± 12	0.32	0.23	0.73
MIL-96-RPAA2	158 ± 3	0.089	0.052	0.59
MIL-96-RPAM2	114 ± 2	0.085	0.034	0.41
MIL-96-RHPAM2	75 ± 2	0.092	0.016	0.17
AC	1179 ± 20	0.81	0.47	0.58

V_{micro} values were obtained from t-plot measurements.

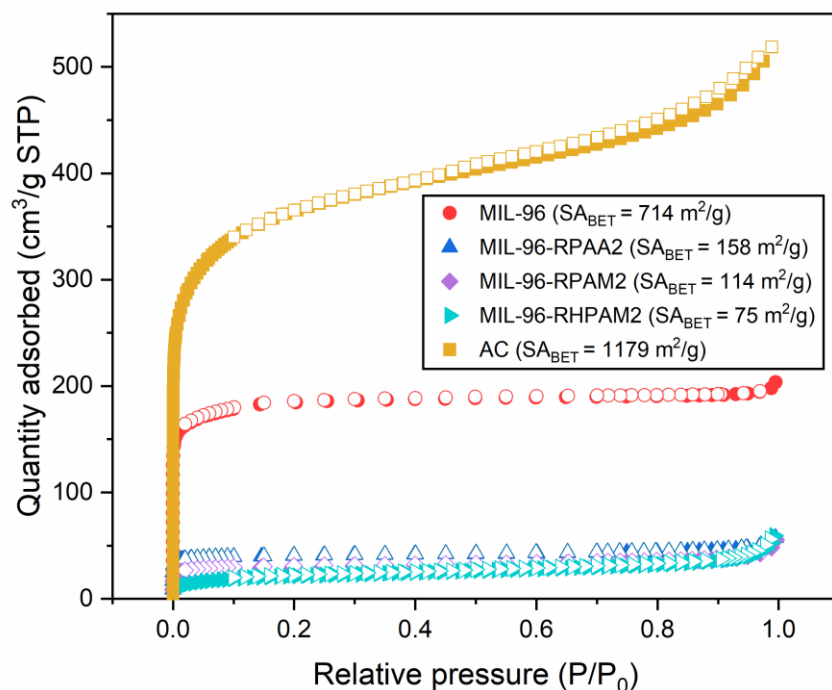


Figure 7.8: N_2 adsorption and desorption isotherms performed at 77 K on AC and modified MIL-96 (Al) materials. Filled symbols ■ adsorption whereas unfilled symbols □ desorption.

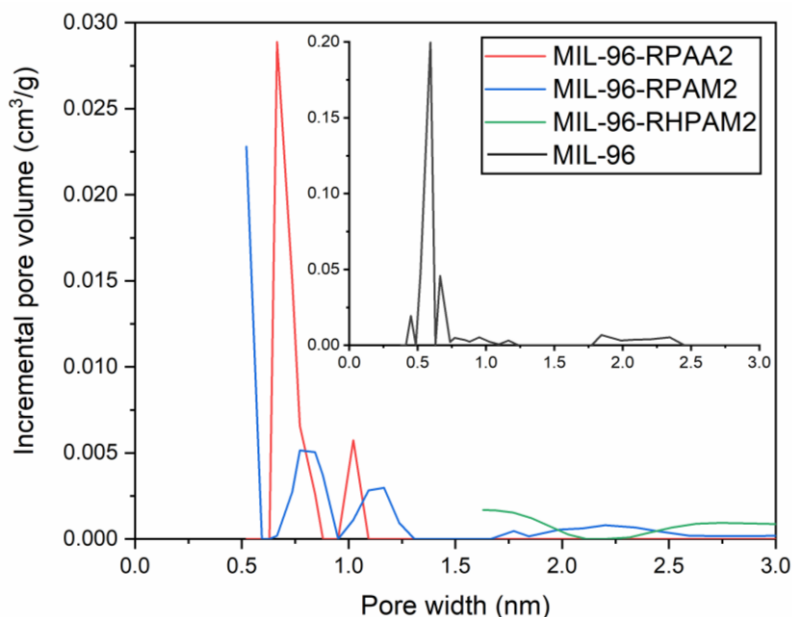


Figure 7.9: Pore size distribution plots for MIL-96 (Al) samples modified with HPAM, PAM and PAA compared to the unmodified MIL-96 (Al) (inset).

7.2.7 Particle size analysis

The particle size ranges shown in Figure 7.10 reflect the average volumetric size as the primary particles, which were pre-sonicated prior to a laser light diffraction measurement. Particle size measurements using laser light diffraction technique relies on Mie theory of light scattering to calculate the particle size distribution which is reported as volume equivalent sphere diameter, but it is still applicable for rod-like particles (Agimelen, Mulholland & Sefcik, 2017). The very broad pore size distribution reported in Figure 7.10 for 20 ml PAA, 20 ml PAM and 20 ml HPAM are due to the formation of significant amounts of rod-like crystals in these three formulations, as confirmed by the SEM images in Figure 7.2 (d), (e) and (f). Addition of 20 mL HPAM effectively formed the largest MIL-96 (Al) particles with 225% diameter increase from 3.2 μm to 10.4 μm . The BET results show that although increasing the HPAM content increases the particle size (as seen in Figure 7.10), it has compromised the material's porosity.

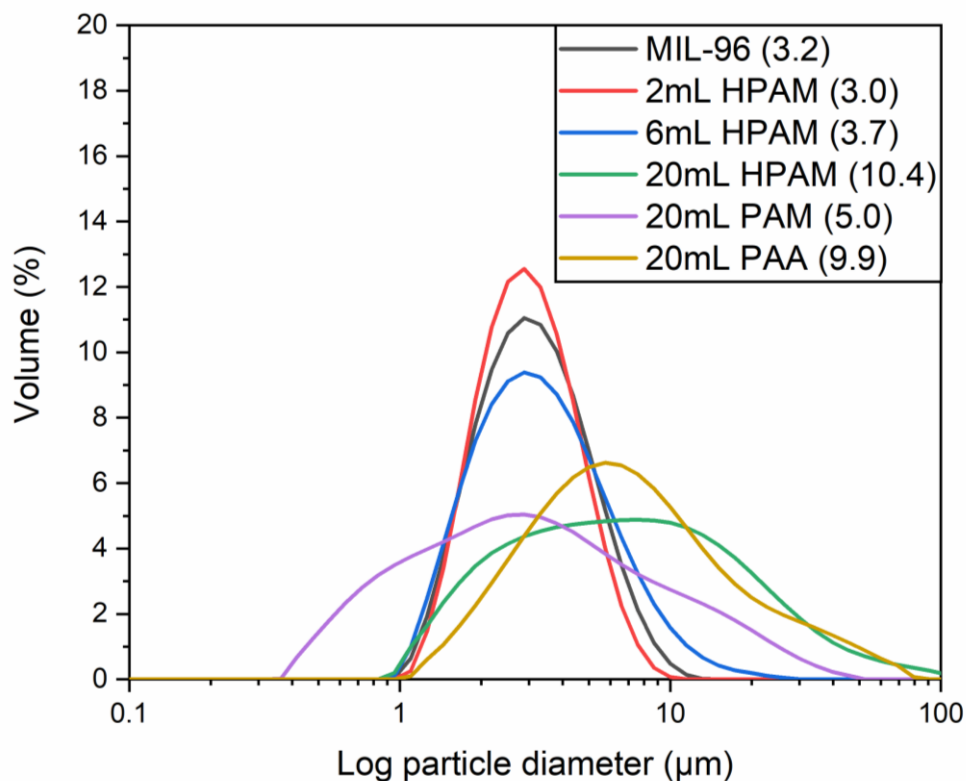


Figure 7.10: Hydrodynamic particle size distribution (mean volume equivalent sphere diameter in bracket) of polymer-modified MIL-96 (Al) in water by laser light diffraction (n = 5).

7.2.8 Batch adsorption of perfluorooctanoic acid using MOFs

Preliminary screening experiments were performed to select a MOF with the highest adsorption capacity for PFOA. Figure 7.11 shows the quantity of PFOA adsorbed by all investigated samples from different PFOA solution concentrations after 18 hrs of stirred batch adsorption experiment at 25 °C.

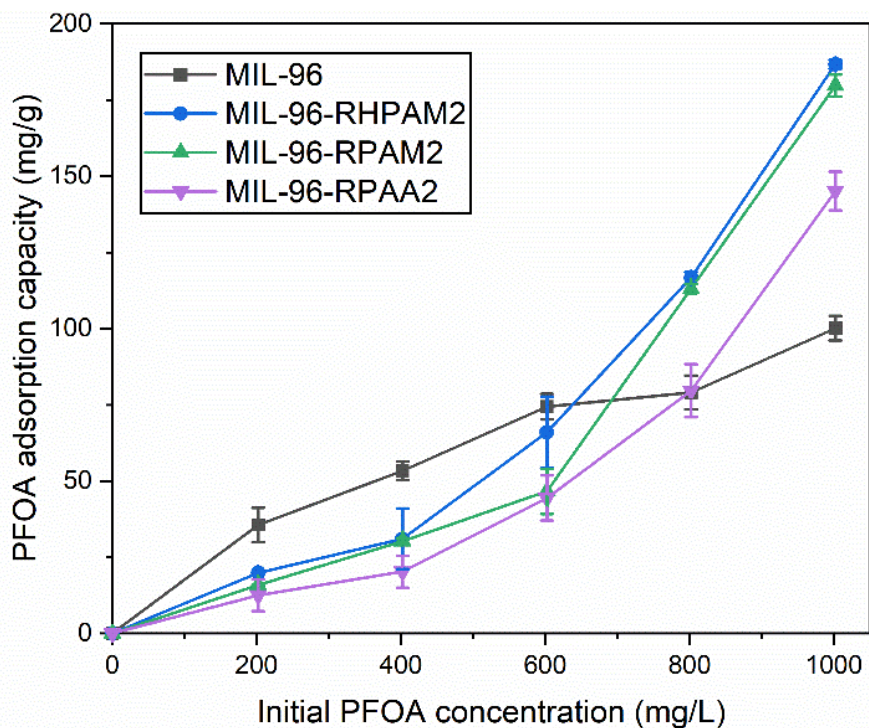


Figure 7.11: Batch PFOA adsorption isotherm plots by modified MIL-96 adsorbents after 18 hrs.

The PFOA isotherms in Figure 7.11 do not show classic Langmuir isotherm behaviour. MIL-96 (Al) showed higher adsorption capacity in the lower concentration range (< 600 mg/L), but at higher concentrations, the modified MIL-96 (Al) forms performed better. This performance is deemed superior because these modified MIL-96 (Al) materials have surface areas of 5 – 10 times lower than pristine MIL-96 (Al), see Table 7.3. On the one hand, the adsorption capacity shown by MIL-96-RHPAM2 was the highest, even though this material has the lowest surface area (75 m²/g) amongst those three modified MIL-96 (Al) materials. Pristine MIL-96 (Al) only displayed twice the adsorption capacity than the modified MIL-96 (Al) variants even though it has a 5 – 10 times higher surface area.

The PFOA adsorption process may involve the electrostatic interaction between the protonated amide (NH_3^+) of MIL-96-RHPAM2 and the anionic PFOA (Ateia *et al.*, 2019; Du *et al.*, 2014). Moreover, as adsorption is a combined activity of pore and surface diffusion (Kumar *et al.*, 2019b), despite MIL-96-RHPAM having much lower surface area compared to the control MIL-96 (Al),

it seems like the NH_3^+ on MIL-96-RHPAM2 gives it an added advantage in terms of PFOA adsorption behaviour.

The 18 hr-batch adsorption experiment was immediately followed by a desorption study where the used MIL-96-RHPAM2 underwent desorption for 24 hrs using three different solvents: water, ethanol, and methanol. This test was performed to evaluate regeneration of the MIL-96 (Al) materials after being used for PFOA adsorption. Different solvents were selected based on the level of PFOA solubility in each solvent. On the one hand, the results in Figure 7.12 show that methanol is the best solvent for desorption, although its limited desorption capacity of around 50% is noted. On the other hand, this highlights the fact that some PFOA is strongly adsorbed on the MIL-96-RHPAM2.

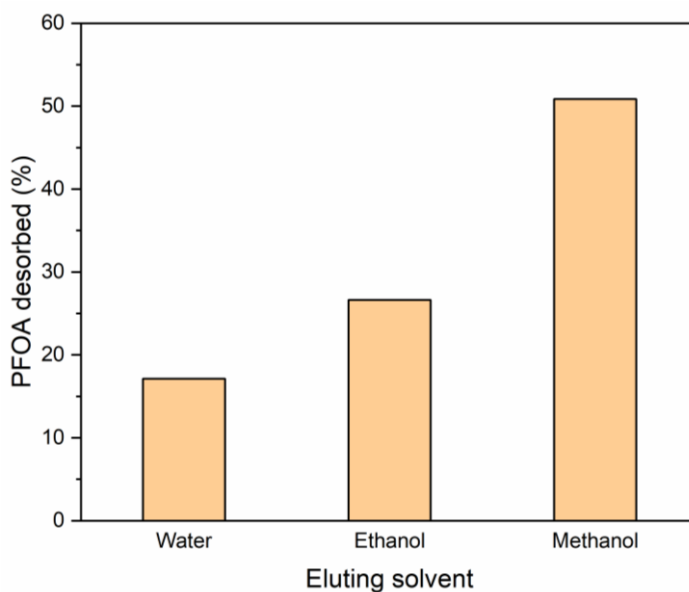


Figure 7.12: Solvents tested for desorption of PFOA from used MIL-96-RHPAM2 adsorbent.

Water, ethanol and methanol are protic solvents which means there will be variations in their hydrogen bonding strength for the desorption of PFOA from MIL-96-RHPAM2 (Shimadzu, 2012). Methanol shows higher PFOA desorption efficiency given its higher PFOA solubility (37,100 mg/L) compared to in water (Kutsuna *et al.*, 2012; Meng *et al.*, 2017). However, since PFOA also has high water solubility (3400 mg/L) (Bao *et al.*, 2014), a desorption solvent composition was formulated with the following methanol/water ratio (3:1, v/v). From this point onwards, due to the

highest PFOA uptake capacity demonstrated by MIL-96-RHPAM2 from Figure 7.11, it will be studied in more detail.

However, since 18 hrs was insufficient to reach full adsorption equilibrium, as deduced from the data in Figure 7.11, adsorption experiments were extended to 72 hrs, Surprisingly, MIL-96-RHPAM2 showed a substantial further increase in PFOA removal by about 46% higher, the capacity rising from 185 mg/g rising to 270 mg/g. To further investigate the slow adsorption kinetics by MIL-96-RHPAM2, the adsorption experiment was left running longer, for 186 hrs. Subsequently, the PFOA removal capacity increased to 318 mg/g and only then was a plateau adsorption uptake observed. However, for practicality of both the adsorption and desorption studies, an adsorption contact time of 72 hrs was selected.

7.2.9 Perfluorooctanoic acid adsorption kinetics analysis

It is important to understand the adsorption kinetics involved in the PFOA removal by MIL-96-RHPAM2. The experimental data obtained is fitted using pseudo second order (PSO) and Elovich kinetics models, which are shown in Figure 7.13. This figure highlights the severe diffusion limitation exhibited by MIL-96-RHPAM2 as the material's adsorptive capacity is only reached after 186 hrs of contact time. This PFOA adsorption data can also be described by the Elovich kinetics model. Please refer to Section 3.12.7 for elaborate justifications on choosing this kinetics model. Nonlinear plots using both models showed high regression coefficients with PSO ($R^2 = 0.983$) and Elovich ($R^2 = 0.996$). The Elovich equation gave superior agreement with the experimental data, it may be concluded that the adsorption proceeded in a highly heterogeneous mode (Riahi, Chaabane & Thayer, 2017). Earlier discussions have highlighted the heterogeneity coming from the abundance of multiple chemical functional groups comprising of $-NH_2$, $-OH$, $-COOH$, $-NH_3^+$ and the Al^{3+} metal centres on MIL-96-RHPAM2. All these groups may readily bind to PFOA, as also supported by the FTIR analysis.

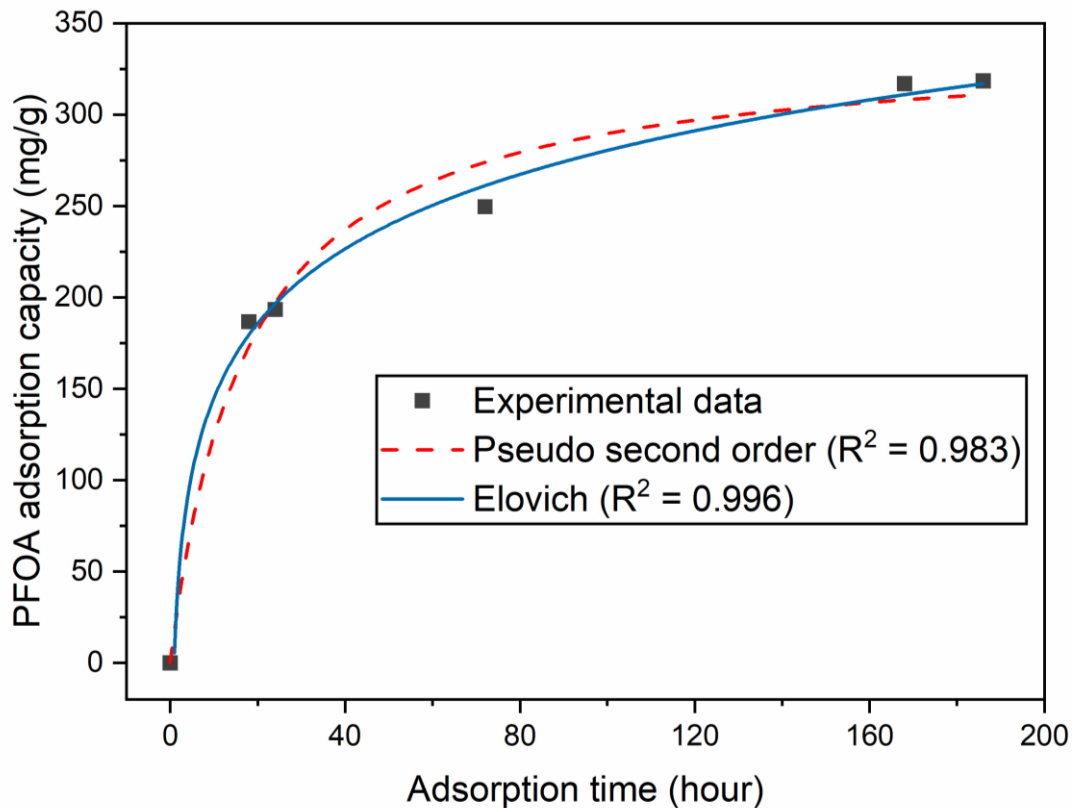


Figure 7.13: Experimental and kinetics modelling results for the adsorptive PFOA removal by MIL-96-RHPAM2; [PFOA] = 1000 mg/L, [MOF] = 1 mg/mL.

To gain a further insight into the PFOA adsorption kinetics for MIL-96-RHPAM2, vapour phase adsorption experiments were conducted with a hydrocarbon analogue to PFOA; n-octane (C_8H_{18}). Figure 7.14 and Figure 7.15 show the n-octane vapour phase sorption results by MIL-96-RHPAM2. Even though a vapour phase adsorption time of 1000 mins is still insufficient to realize an equilibrium adsorption state, for a simplistic overview of its kinetics standing, only the first isotherm step range (0 – 1 mbar) was accounted in the PSO parameter estimations. The PSO model fitting yielded a PSO kinetics constant ($k_{PSO,n\text{-octane}}$) of 2×10^{-4} mg/g.min and a theoretical maximum equilibrium capacity (q_e) of 14 mg/g. The fundamental differences in liquid-phase adsorption and vapor adsorption are acknowledged, but in both cases, the kinetics rates are nonetheless similar (denoted by the proximity of $k_{PSO,n\text{-octane}}$ to the k_{PSO} in Table 7.4). Both sets of data confirm very slow adsorbate diffusion through the small micropores in the HPAM-modified MIL-96 (A1).

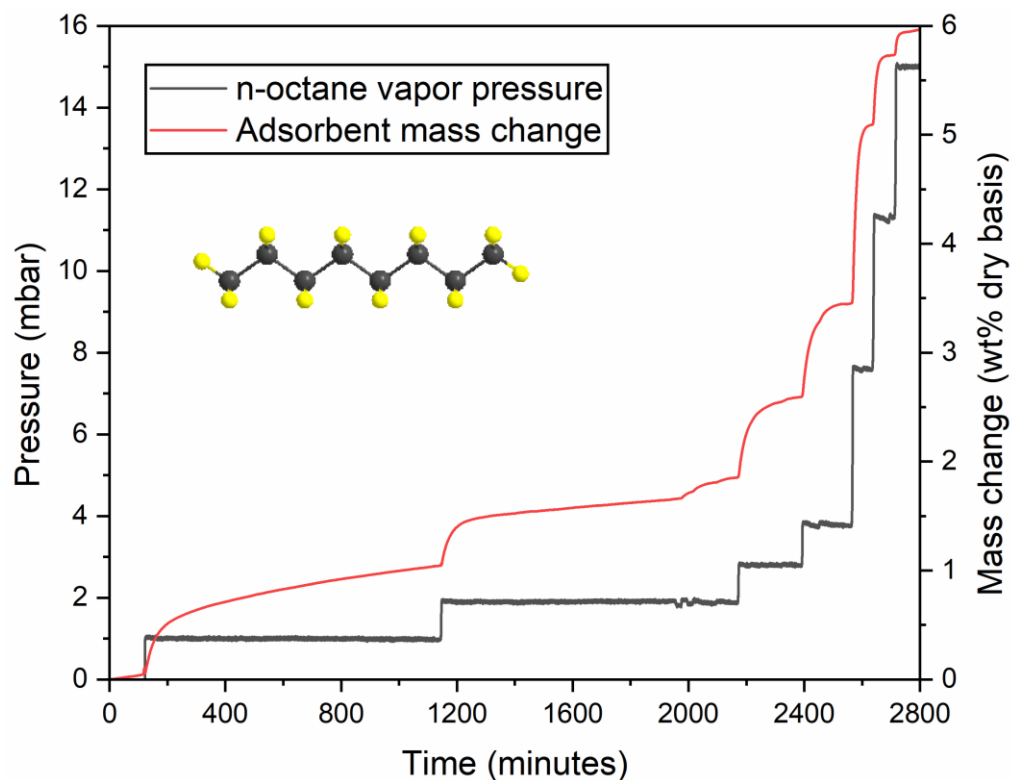


Figure 7.14: Kinetics plot of n-octane vapour sorption on MIL-96-RHPAM2.

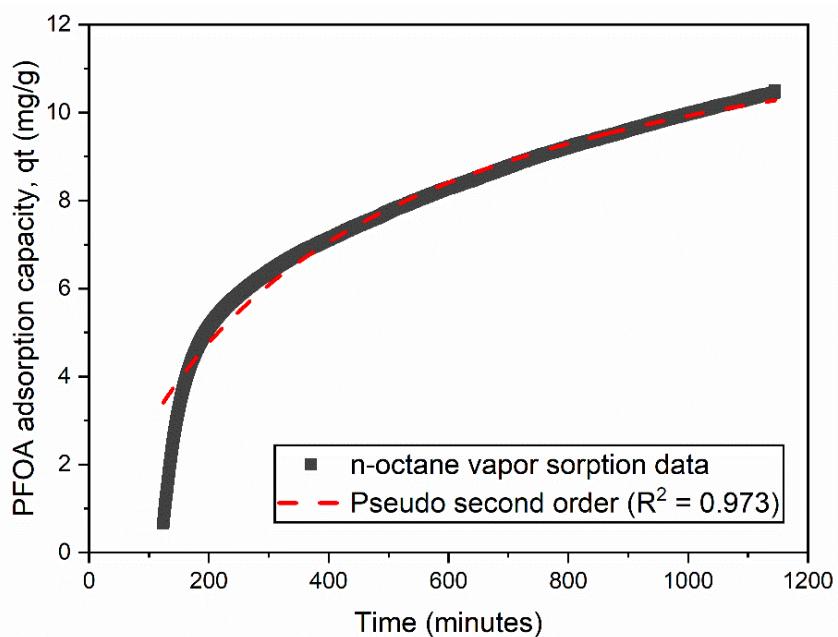


Figure 7.15: Pseudo second order kinetics model fitting of n-octane vapour adsorption on MIL-96-RHPAM2.

In comparison to the reported kinetics data for PFOA removal by several other adsorbents, MIL-96-RHPAM2 can adsorb PFOA at loading levels on a par with other adsorbents, but the extremely slow uptake would be a significant drawback for its practical use. Relative to other adsorption studies displayed in Table 7.4, the PFOA concentration used in this work is the highest. This concentration was chosen to allow the NMR spectrometer to detect the change in PFOA concentration before and after the adsorption processes.

Table 7.4: Comparison of the pseudo-second order kinetics parameters for PFOA adsorption by select MOFs and AC.

Sorbent used	Tested PFOA concentration (mg/L)	Pseudo-second order model parameter			Equilibrium time (hr)	Reference
		q_e (mg/g)	k_{psO} (g/mg.min)	R^2		
Bamboo-derived AC	120	393	2.7×10^{-5}	0.91	33.5	(Du <i>et al.</i> , 2015)
Fe ₃ O ₄ -modified AC	300	364	7.1×10^{-5}	0.998	29	(Xu <i>et al.</i> , 2020)
Perfluorinated UiO-66-(F4)	500	381	2.6×10^{-3}	0.993	1	(Sini <i>et al.</i> , 2018)
UiO-66		327	2.7×10^{-3}	0.996		
MIL-101 (Cr)	100	481	1.4×10^{-4}	0.967	1	(Liu <i>et al.</i> , 2015b)
Quaternized amine MIL-101 (Cr)-QDMEN		791	2.1×10^{-4}	0.985		
MIL-53 (Al)	1	100	7.3×10^{-2}	0.999	4	(Jun <i>et al.</i> , 2019)
ZIF-7	-	22	7.1×10^{-5}	0.994	1	(Chen <i>et al.</i> , 2016)
ZIF-8		177	2.0×10^{-5}	0.978		
ZIF-L		244	9.6×10^{-6}	0.985		
UiO-67	500	350	6.1×10^{-4}	0.999	1	(Sini <i>et al.</i> , 2019)
MIL-96-RHPAM2	1000	340*	1.7×10^{-4}	0.983	186	This work

*Shows the increase in adsorption capacity after the kinetics experiment was extended to 186 hrs, suggesting MIL-96-RHPAM2 has a very slow uptake rate.

7.2.10 Perfluorooctanoic acid adsorption and desorption processes

Knowing that perfluorinated compounds are hazardous chemicals, the safe regeneration of MOFs and economical reuse of the spent adsorbents is critically important. Although thermal regeneration is preferentially used for activated carbons, adsorbed perfluorinated compounds are not easily chemically decomposed as C-F is the strongest single bond in organic chemistry after B-F, Si-F and H-F. Therefore, wet based regeneration methods would be preferred.

To develop an efficient PFOA regeneration method from the spent MOF, the nature of the adsorption processes must first be understood. An earlier report on PFOA adsorption by Jun et al. (Jun *et al.*, 2019) using MIL-53 (Al) had confirmed the electrostatic interactions between the cationic MOF species (Al^{3+}) with the anionic carboxylate groups (COO^-) of PFOA as the main binding mechanism, supplemented by some H-bonding and hydrophobic interactions. So, with electrostatic interactions proposed as being the most prevalent, it was decided to trial saline solutions for regeneration, and to evaluate their ability to destabilize the electrostatic PFOA adsorption complex, thus facilitating adsorbent regeneration. Such aqueous based regeneration solutions would be highly compatible with the aqueous operational mode for these adsorbents.

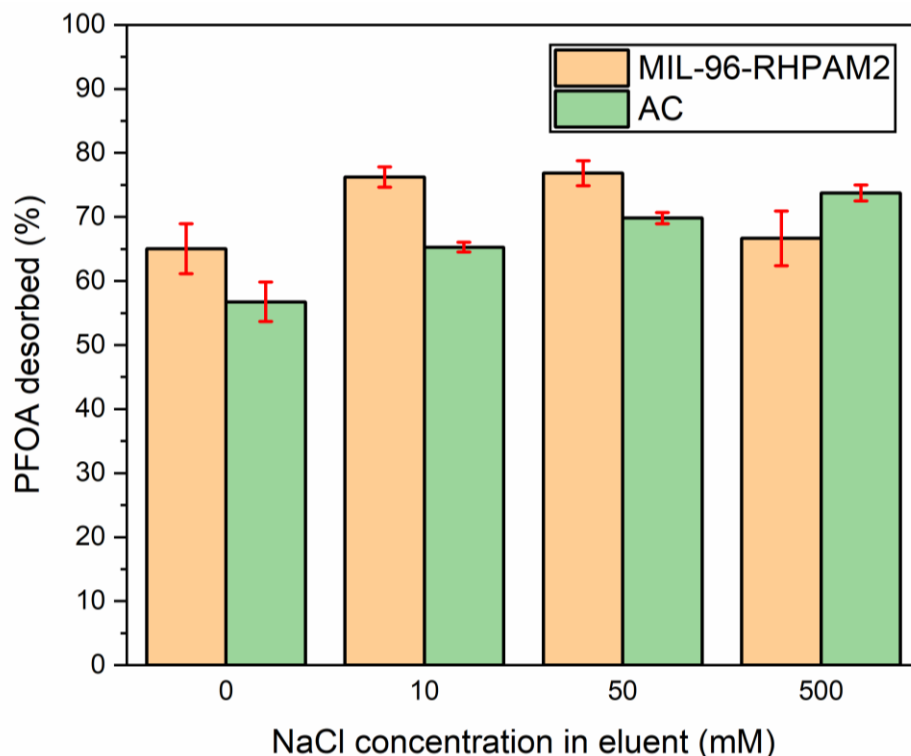


Figure 7.16: Percentage of PFOA desorbed from MIL-96-RHPAM2 and AC using NaCl solutions (temperature 25 °C, adsorbent dose = 2 mg/mL, [PFOA] = 1000 mg/L).

The positively charged Al^{3+} centre of MIL-96 is expected to have a strong interaction with the anionic carboxylate groups (COO^-) of PFOA. Previous studies have found that increasing the eluent ionic strength can result to weaker PFOA adsorption, thus, improving desorption efficiency due to compression of electrical double layer (Wang & Shih, 2011; Shih & Wang, 2013). However, contrary to these expectations, Figure 7.16 shows that increasing the eluent ionic strength has had limited effect on PFOA desorption by MIL-96-RHPAM2. An initial increased PFOA desorption quantity was observed going from 0 to 50 mM NaCl, but not at the highest tested salt concentration of 500 mM NaCl. The greater presence of Na^+ and Cl^- solution ions could have reduced the electrostatic forces between the Al^{3+} centre and the negatively charged, adsorbed PFOA molecules (Gao & Chorover, 2012). Nevertheless, the presence of Al^{3+} still provides a very strong electrostatic adsorption site for which simple screening by univalent Cl^- species from NaCl may not be strong enough to displace these strong intra-MOF interactions.

Apart from the Al^{3+} centre being a major MOF binding site, it is probable that the $-\text{NH}_2$ from the amide, which will also exist in a protonated form as a NH_3^+ contained in HPAM, also attaches to the anionic carboxylate of PFOA via strong electrostatic adsorption forces (Deng *et al.*, 2013; Liu *et al.*, 2015b; Ali *et al.*, 2020). In addition, the van der Waals interaction between the carbon chain of PFOA (8 carbons on the PFOA) and the main skeleton $(\text{CH}_2-\text{CH})_n$ of HPAM may also contribute to the adsorption process. Altogether, these strong PFOA adsorption mechanisms hinder the complete desorption of PFOA from aminated adsorbents such as MIL-96-RHPAM2. Figure 7.16 illustrates the subtle NaCl influence in the eluent to the PFOA desorption performance of MIL-96-RHPAM2.

Across the tested salinity window, the highest PFOA fraction desorbed reached a useful 77%, but not 100% recovery, providing future research scope to improve the best solvent/salt systems capable of complete PFOA desorption. Future work would be wise to consider di- and trivalent anions such as those found in Na_2SO_4 or Na_3PO_4 . Figure 7.17 presents the proposed mechanisms of PFOA adsorption onto MIL-96-RHPAM2. Note that a complete MIL-96-RHPAM2 structure contains the original MIL-96 and its attachment with the HPAM main chain. However, for visual clarity, only the grafted HPAM contribution on the MIL-96 (Al)'s surface to the PFOA adsorption is shown here. On the other hand, the role of the original MIL-96 (Al) backbone in the overall PFOA adsorption is illustrated separately in Figure 7.18.

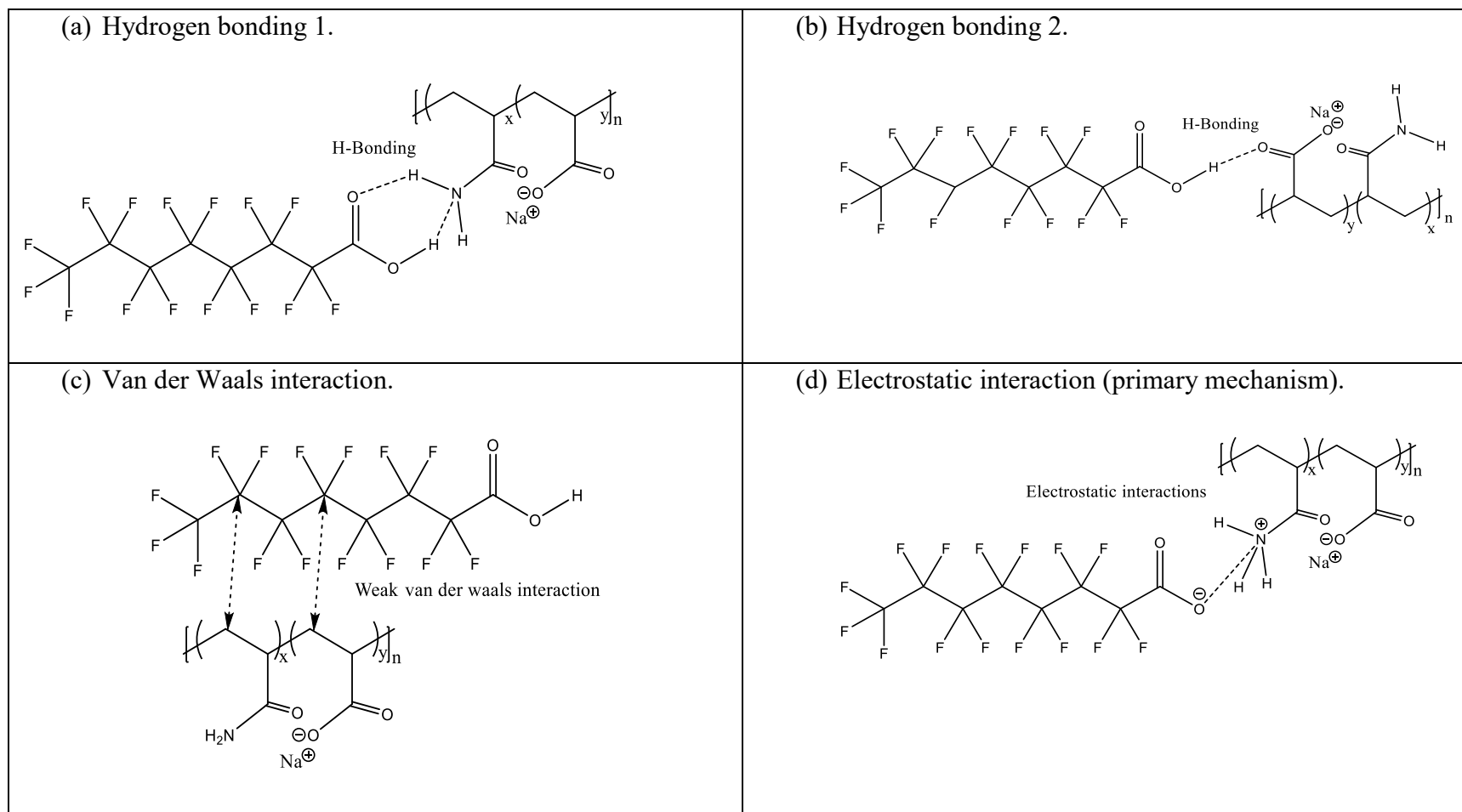


Figure 7.17: Proposed PFOA adsorption mechanisms by HPAM-treated MIL-96 (Al) used in this study; (a) hydrogen bonding between the -NH_2 of HPAM and PFOA, (b) hydrogen bonding between COO^- of HPAM and PFOA, (c) weak Van der Waals interaction established between the carbons of PFOA and the repeating HPAM monomer unit and (d) primary electrostatic interactions involving the COO^- groups of PFOA with the protonated amide (NH_3^+) on MIL-96-RHPAM2.

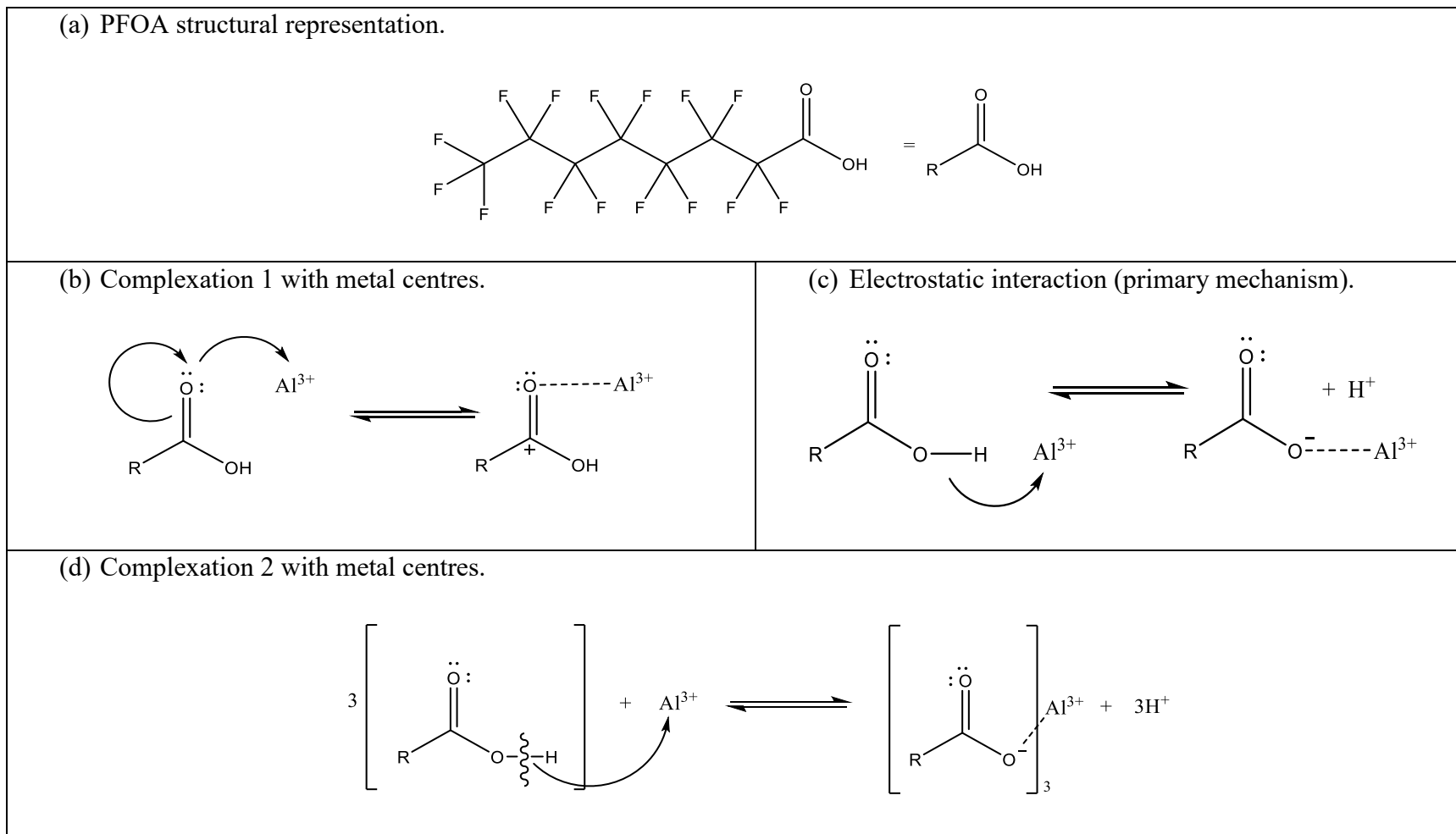


Figure 7.18: Proposed PFOA binding mechanisms with the MIL-96 (Al) original framework detailing (a) simplified PFOA structure, (b) formation of less prevalent 3° carbocation stable intermediate metal complex 1 between the PFOA and the Al metal centres (c) primary electrostatic interaction between the oppositely charged Al^{3+} of MIL-96 (Al) and COO^- groups on PFOA and (d) formation of more dominant metal complex 2.

Although PFOA desorption efficiency from AC is inferior to MIL-96-RHPAM2 at lower ionic strengths, AC's desorption efficiency is improved at the highest ionic strengths tested here. Similar to MOF, PFOA adsorption onto AC shares similar adsorption mechanisms (Wang & Shih, 2011; Wang *et al.*, 2019b) due to AC's diverse surface functional groups.

These results show that NaCl was a partially effective PFOA desorption facilitating agent for both adsorbents. Thus far, only ultrasonic-electrochemical oxidation system has offered the highest PFOA removal, up to 91% (Zhao *et al.*, 2013; Du *et al.*, 2014). However, the generation of numerous intermediate products and the involvement of electrical equipment make it a costly process option. For more cost-effective desorption options, it will be useful revisiting what Jun *et al.* reported (Jun *et al.*, 2019). They found that presence of divalent cations (Ca^{2+}) in the solution could serve as a bridge between neighbouring PFOA molecules, thereby promoting their MIL-53 (Al)'s adsorption capacity. On the contrary, presence of divalent anions (SO_4^{2-}) could induce extra adsorption competition between the original PFOA-MOF interactions. Resultantly, the MOF will show lower final PFOA adsorption capacity. Therefore, based on these findings, to improve MIL-96-RHPAM2's desorption efficiency, divalent (Ca^{2+} or Mg^{2+}) or trivalent cations (Al^{3+}) could be formulated into the regeneration liquids as these cations could destabilize the strong PFOA-MOF electrostatic interactions.

7.3 Conclusions

The addition of an anionic polymer (HPAM) to a cationic aluminium-based MOF, MIL-96 (Al) during the hydrothermal synthesis allowed the formation of larger MOF crystals with well-defined crystal habits, specifically into rod-shaped crystals for three of the HPAM formulations. Taking advantage of HPAM being a low cost and an environmentally friendly additive, a HPAM-modified MIL-96 (Al) (MIL-96-RHPAM2) showed promising particle size growth (225%) from 3.2 μm to 10.4 μm as well as the ability to control the crystal habit using this simple modification procedure. However, these new MIL-96 (Al)-HPAM materials lost significant amounts of their surface areas and pore volumes, a factor between 5 and 10, relative to MIL-96 (Al). Nevertheless, incorporating HPAM into the MIL-96 (Al) structure concurrently introduced a primary ammonium species from the grafted amide, which resulted in PFOA adsorption capacity of 340 mg/g. This uptake capacity is relatively similar to some other MOF and AC adsorbents, despite MIL-96-RHPAM2 having much lower surface area and pore volume.

However, these positive adsorption capacities were undermined by the very slow adsorption kinetics observed for MIL-96-RHPAM2, which may reflect the small micropores present in MIL-96 (Al) and other modified variants reported here. However, if improvements in the synthetic methods reported here could be implemented in a way which maintains the surface area and or pore volume of these new HPAM-modified adsorbents such as using lower initial HPAM concentrations, then the resulting modified adsorbents might offer class leading performance of over 1 g/g of PFOA adsorption.

Aqueous based regeneration of MIL-96-RHPAM2 and AC following PFOA adsorption was found to be 77% and 74% efficient, respectively. The desorption results indicate small improvements when saline regeneration solutions were used. Nevertheless, some scope still exists for further improvement and optimization in the salts selected for use in the regeneration solutions.

Chapter 8: Conclusions and Outlook

8.1 Conclusions

The contents in this thesis are divided into three central topics, which are:

- (1) Development of synthetically functionalized and chemically modified MOFs and their utility for adsorptive removal applications.
- (2) Removal of persistent organic molecules from water.
- (3) Removal of persistent organic molecules from humid atmospheric media.

In Chapter 4, two MOFs with high surface area and high water stability, MIL-101 (Cr) and its amino-functionalized version, MIL-101 (Cr)-NH₂ were used to adsorb 2-chlorophenol, a surrogate compound of the toxic and bio-resistant species phenol. The MOFs' performances were compared with an industrial-grade AC. It was concluded that:

1. The 3 times higher surface areas exhibited by MOFs compared to AC is not a guarantee of high adsorption capacity for solutes adsorbed from aqueous solutions.
2. Access of organic pollutants to an adsorbent's adsorption sites requires strong chemical interactions with the adsorbent. However, these may be compromised if there are strong solvent-adsorbent interactions as in the case of hydrophilic adsorbents when water is the solvent. Intrinsic adsorbent hydrophobicity as shown by AC appears to be the most important factor followed by contributions from its various surface functional groups. The introduced -NH₂ moiety in the parent MIL-101 (Cr) failed to show effective H-bonding to the 2-chlorophenol, rather the surrounding water molecules in the solutions strongly compete for adsorption sites in MIL-101 (Cr)-NH₂ driven by their very high local concentrations.
3. This study highlighted the importance of adsorbent hydrophobicity for capture of organic solutes and the less significance of adsorbent surface area.

Chapter 5 uses a vapour-based chemical deposition approach for successful transformation of hydrophilic MIL-101 (Cr) into a hydrophobic adsorbent. A hydrophobic, silicone-based polymer, polydimethylsiloxane (PDMS) was used as the surface coating agent. The effect of PDMS molecular weights and deposition times on the new adsorbents' surface area and pore volume were studied to produce a series of MIL-101-PDMS composites. The key findings are:

1. A MIL-PDMS composite that was developed from a 0.25 hr coating time using a low molecular weight-PDMS was able to retain the same surface area and the porosity of pristine MIL-101 (Cr).
2. This composite has higher molar hydrophobicity index (HI) values than pristine MIL-101 (Cr) for low RHs (< 10%) suggesting this material would be good for VOC capture in humid environments.
3. The PDMS coating within the composite's mesopores delayed the water mesopore condensation to higher than 40% RH, offering improved availability of the empty pore volume to adsorb a model VOC, toluene, at 40% RH.
4. At 40% RH and for both low and high, toluene concentrations, experimental co-adsorption studies showed that the new composite exhibited excellent VOC adsorption kinetics and uptake capacity. At 40% RH and for 0.5% P/P₀ toluene, the new material exhibited 44% and 59% higher values respectively than MIL-101 (Cr) and AC. AC lagged far behind both MOFs in terms of both uptake capacity and kinetics.
5. Nevertheless, the 90% RH exposure test revealed the limitations in the performance of this new composite due to the presence of some pore hydrophilicity inherited from the precursor MIL-101 (Cr). This facilitated significant moisture adsorption at 90% RH which compromised the concurrent toluene adsorption.

Chapter 6 evaluates the impact of engineering a MOF's hydrophobicity by means of solution-based surface treatments. Three surface treatments were evaluated including reactions with silanes, phosphorous oxy-acids and calixarenes were applied on hydrophilic MIL-100 (Fe). The treated materials' performances were then investigated for competitive toluene-water adsorption at 40% RH which represents average indoor humidity condition and two toluene concentrations at 0.5% P/P₀ (188 ppm, resembling a mid-level VOC exposure range) and 10% P/P₀ (3750 ppm, industrial solvent recovery concentration). The external and the internal material hydrophobicity

were defined from its water contact angle ($\theta_c > 90^\circ$) and water sorption isotherms, respectively.

The main conclusions are:

1. The silane-treated materials exhibited poor surface hydrophobicity and extreme surface area reduction. The silanes reacted with each other due to presence of residual moisture. Resultantly, the silanes did not graft onto the MOF surface. However, the reacted silane polymer is still present on the MOF surface, hence, the reason behind the pore blockage. Therefore, these materials were not studied further.
2. The phosphorous oxyacids-treated materials displayed high water contact angles ($> 120^\circ$), indicative of improved surface hydrophobicity, but there is a practical constraint because of the low phosphorous oxyacids' melting points ($\sim 100^\circ\text{C}$). For regeneration purposes, adsorbents are frequently thermally dried at temperatures higher than 100°C to ensure complete water/solvent evaporation, which could possibly compromise the grafted phosphorous oxyacids' stability. Besides, the high surface hydrophobicity did not contribute substantial improvements to the treated materials' uptake kinetics.
3. The surface functionalization MIL-100 (Fe)'s by calixarene molecules transformed it into a superhydrophobic material ($\theta_c > 150^\circ$). The best sample, MIL-Cx6-1 wt% displayed much faster toluene co-adsorption rate at both tested toluene concentrations compared to pristine MIL-100 (Fe). A high humidity test however diminished the Cx surface coating efficacy as it still adsorbed high water quantity after exposure to 90% RH. The sample's pore hydrophilicity is well supported by the material's water isotherm.
4. Water contact angle measurements can be used to evaluate a material's surface wettability, whilst water and toluene sorption isotherms-based hydrophobicity index values can provide better insights into the adsorption chemistry happening within the adsorbent's pores.
5. All vapour sorption experiments were benchmarked with AC which revealed mixed results. On the negative side, AC's high microporosity translated to slow toluene co-adsorption kinetics, but its intrinsic pore hydrophobicity afforded the material a significant advantage as it maintained high toluene co-adsorption uptake quantity post-exposure to 90% RH.
6. In summary, for effective removal of organic vapour from humid air, an ideal adsorbent would require these qualities: (1) it is originally hydrophobic to prevent excessive water

occupation in the pores, (2) it has high porosity, preferably micro and mesoporous to have good adsorption uptake and kinetics, (3) judicious surface treatments can be implemented like the grafting of calixarenes that improved the adsorbate-MOF chemical interactions. As a result, the grafted calixarene on the MIL-100 (Fe) surface led to nearly 2-times higher adsorption kinetics despite the treated MOF suffering from porosity than the pristine MOF due to slight pore blockage induced by the calixarenes.

7. While higher uptake capacity is a desirable adsorbent feature, adsorption kinetics is neglected in most studies. Although in industrial processes, a faster kinetics is preferred over a slow-diffusing adsorbent even if the final uptake capacity is superior.

Chapter 7 is dedicated on increasing a MOF's particle size for easier recovery and to minimize the pressure drop of a packed adsorbent bed. The theory of forming larger crystals during synthesis is centred on two conditions namely slow crystal growth and *in situ* pre-cluster formation. It has been explained that a MOF's scaffold is built from the connections of metal cation clusters and an organic bridging linker. By adding an anionic polymer, hydrolysed polyacrylamide (HPAM) into the synthesis solution, it had a dual function: primarily as a linker competitor that decelerated the crystal growth and secondly as an initiator for the MOF's nuclei clusters. An aluminium-based MOF MIL-96 (Al) was modified with different HPAM concentrations to produce adsorbents with increased particle sizes. These modified MIL-96 particles were then studied for adsorptive and desorptive removal of a persistent perfluorochemical, PFOA. A summary of the work is given below:

1. Controlled quantities of HPAM addition during MIL-96 (Al) synthesis facilitated particle size enlargement up to 225% diameter increase.
2. Addition of HPAM also induced morphological changes to MIL-96 (Al)'s crystals, from originally hexagonal bipyramid to elongated hexagonal rod shape.
3. The grafting of HPAM onto MIL-96 (Al) improved its PFOA uptake quantity due to the introduction of amide functionality, which can convert to primary ammonium species.
4. PFOA was mainly adsorbed by the HPAM-modified MIL-96 (Al) via strong electrostatic interactions while for AC, via acid-base interactions. As a result, the PFOA adsorbed by both materials could not be easily desorbed by eluents prepared with different ionic strengths.

8.2 Future work ideas

Below are future work recommendations on how to upgrade the experimental setup and improve the quality of the findings from this thesis.

8.2.1 To perform adsorption experiments based on industrially relevant conditions

8.2.1.1 Adsorptive purification of water contaminated with hazardous organics

A single-solute and batch mode experimental setup like in Chapter 4 and 7 only constitutes a small fraction of the contaminants' actual conditions in the environment. What was hoped from this kind of experiment is to first specify the adsorbent-adsorbate mechanisms in isolation before trialling a multi-solute experiment and ultimately, on field-collected water samples. If the individual adsorption mechanisms are not yet understood, the intra-molecular and competitive interactions between multiple solutes will bring another set of complexity. Setting realistic experimental parameters will inevitably require compacting the adsorbents into beds for the liquids to pass through.

The next task is to determine the contaminants' real-world concentrations (often very low), common co-existing pollutants, and surrounding environmental factors such as presence of humic acid, ionic species (e.g., Na^+ , Ca^{2+} , Mg^{2+} , Cl^- , NO_3^- , SO_4^{2-}) and lastly, solution pH. A neutral condition or pH 7 is mandatory as it reflects the general pH of river or rainwater. Moreover, the testing solutions should also be prepared according to the environment where the contaminants belong. For instance, although convenient, dissolution of organics in alcohols or ketones might be far from the reality.

8.2.1.2 Standardizing MOF evaluations on air purification experiments

Toluene is a commonly studied VOC pollutant, but real indoor air spaces or industrial gas streams would contain a wider spectrum of pollutants, which will also introduce the complication of multicomponent adsorption. A more comprehensive material assessment must be devised including (1) a wider range of relevant environmental pollutants, including multiple solutes in a single stream, combined with (2) breakthrough analysis, to understand their competitive adsorption mechanisms. Breakthrough analysis allows the possibility to run at much lower concentrations than the toluene P/P_0 of 0.5% achieved in the DVS system.

One major obstacle when comparing different adsorbents for air purification is the lack of consistent and unrealistic parameters used in the literature. For example, in Chapter 5 and 6, the use of two toluene concentrations (0.5% P/P_0 and 10% P/P_0) chosen here are partially arbitrary. The choices of specific vapour concentrations are predominantly dictated by the intended applications of the pursued work either on indoor air quality management or industrial separation context. Generally, these vapour concentrations should first be referred from OSHA/NIOSH guidelines for each, and every species being investigated.

While specifically for indoor air quality management, the VOC testing P/P_0 should be significantly below 0.1 Pa whereas for industrial gas streams, the working P/P_0 is significantly higher, at > 100 Pa (Kim *et al.*, 2019). So, to fulfil indoor air quality management requirements, it is recommended to study the adsorbent's behaviour up to 10 Pa (maximum 0.26% toluene P/P_0 at 25 °C) or known as the ambient, low-pressure region.

Additionally, it must be reminded that the maximum adsorption capacity obtained at P/P_0 greater than 100 Pa is not a direct predictor of its indoor air quality management suitability. Instead, the two designated indoor air quality management metrics are the material's 10% breakthrough volume and its low-pressure Henry's constant obtained from Langmuir isotherm analysis. Therefore, for clarity, the evaluations presented in this thesis are practically meant for removal of mid-range VOC concentrations (0.5% P/P_0) whereas the 10% P/P_0 results would be more appropriate to investigate the material's performance for a solvent-recovery scenario. It

is also in the latter case where MOF exudes as the clear winner given its significantly higher maximum capacity and adsorption kinetics than AC.

In conjunction with the above reasonings, it is important to clarify that very low P/P₀ detection especially for indoor air quality management is only currently achievable using a standard determination method for VOCs in air (United States Environmental Protection Agency, 1984). Basically, the method entails the VOCs to pass through a sorption tube filled with commercialized adsorbents such as Tenax TA[®], carbonized molecular sieves (Carbosive[™], Carboxen[™], Sulficarb[™]) or graphitized carbon (Carbopack[™], Carbograph[™]). Then, the collected VOCs are thermally desorbed and analysed using gas chromatography with mass-spectrometer for calculations of adsorption parameters. Therefore, for a rigorous indoor air quality management validation procedure, any adsorbent's performance should be compared to these conventional test methods.

8.2.2 To manipulate fine particulate MOF powders into more robust shapes and properties

The proof-of-concept study for the formation of larger MOF crystals was reported in Chapter 7. Since it uses a small-scale hydrothermal synthesis of MIL-96 (Al), it may not be upscalable. Moreover, the calculated BET surface area of this HPAM-treated MIL-96 (Al) was very low, implying an extreme pore blockage. Consequently, the adsorption experiments confirmed that the adsorbent possessed slow kinetics; only reaching equilibrium after 186 hrs of contact time. Even though the PFOA uptake quantity shown by MIL-96-RHPAM2 was higher than the pristine MIL-96 (Al), it needs to show superior removal performance kinetics for any potential industrial applications. Essentially, it was the attachment of -NH₂ from the amide in HPAM grafting that boosted the PFOA uptake via improved electrostatic and H-bonding interactions. Post-synthetic modification techniques like linker exchange may prove useful to insert pendant NH₂ or other functional groups (i.e., COOH, OH) into MOFs without compromising the final porosity.

The MOFs studied throughout Chapter 4 until 7 were all polydisperse and microcrystalline powders. The integration of these surface and functional chemistries into MOFs is crucial, but much work is needed on MOF particle engineering and its industrialization. Mechanical shaping technique could create specific MOF shapes and sizes. However, the associated high compacting pressures, usage of binders and wetting agents ultimately cause structural collapse and pore blockage. This concomitantly results in lower useable surface area for adsorption. On the other hand, there are brighter prospects on monolithic MOFs. The vast array of preparation strategies provides more opportunities to improve their shape, structure, composition, and performance. The ideal features of a MOF monolith are mainly dependent on the excellent performance of its powdered form. So, fundamental studies on powdered MOFs cannot be dismissed if this area wants to be developed.

8.2.3 Adsorbent reusability experiments using a thermal/pressure swing adsorption

The passive regeneration experiments in Chapter 5 and 6 were conducted at 40% RH and at 25 °C without any additional heating involved to desorb the adsorbed toluene molecules. The drawback is that the desorption process is incomplete. Although the industrially accepted method for adsorbent desorption/regeneration is attained through thermal or pressure swing adsorption, the tests shown here were meant to simulate the tolerance of the adsorbents against a sudden and repeated toluene concentration spike. For example, consider an adsorbent that is placed in a kitchen, thereby, exposed to fluctuating VOC levels depending on the household cooking frequency. Meanwhile, the natural desorption in between the adsorption cycles was used to probe the extent of water-toluene competition for the vacated pore sites. In other words, after the toluene molecules desorb from the adsorbent's pores, will there be possibilities of water to occupy the then empty pores? If yes, when toluene is introduced again into the system, the adsorbent would have shown lower uptake. However, the investigated MOFs still maintained the same toluene capacity even after undergoing 10 adsorption/desorption cycles, proving that they are very stable. Nevertheless, even after applying thermal and pressure swing adsorption treatment to a commercial AC, it was reported to have a greater likelihood to suffer from diminishing adsorption capacity because of its narrow pore blockage.

8.3 Perspectives on MOF advancements

Overall, this thesis has demonstrated that modified MOFs exhibited both positive and negative outcomes for environmental applications. When compared to AC, Chapter 4 and 7 indicate that MOFs have lower uptake capacity and adsorption rate while it is the opposite in Chapter 5 and 6. With more recursive improvements in the pipeline, MOFs can show great potentials as the next generation adsorbent. However, for the time being, MOFs are unlikely to be used in industrial separation processes due to their high synthesis costs and poor scalability. Although to some extent, these hurdles have been overcome by some companies which sell select MOFs for the commercial market, the prices are exorbitant. They are not as cost competitive as the easier and mass-produced AC. Besides, conventional adsorbents AC and zeolites have high water and thermal stability too. Hence, the reason for them being known as a one-size-fits all adsorbent type. With all due respect, it seems that MOF development efforts should better be directed for specific and small-scale applications where very minimal MOF quantities are required, yet able to generate the necessary performance (vide-supra in Section 1.3.3.4). To advance their progress via this route, these aspects must be considered which are: (1) reasonable costs, (2) superior performance and (3) facile regeneration.

8.3.1 Reasonable costs

The MOF syntheses need to be made more cost-effective in terms of their metal choices, linker sources and milder reaction conditions. Ecologically benign and low-cost metals such as Mg, Ca, Al, or Fe should be prioritized over other rare and toxic metals. Further cost reductions may be achieved by using cheaper ligand sources. Moreover, normal MOF hydrothermal and solvothermal synthesis procedures are conducted using harmful solvents, at high pressure and temperature. Instead, one can try to design a water-based, room temperature synthesis protocol.

8.3.2 Superior performance

Material hybridization involving MOFs with low-cost natural polymers (cellulose, β -cyclodextrin, chitosan) and functional carbons (graphene, carbon nanotubes) will moderate the final composite costs while also improving their physicochemical properties and performance. The cheaper substances function as a mechanically stable support to host the powdery MOFs. The composite's performance is enhanced through the diversity of functional groups that exist

in the MOFs and the additives. Furthermore, the fine particulate texture of MOFs is not the most convenient format to be used in many applications due to high pressure drop when packed in beds, difficult handling, and low mechanical strength. Studies dedicated to simplifying the densification of MOFs into either granule, pellets or preferably monoliths, will be highly valued to address these issues. Hitherto, in the making of these densified MOFs and composites alike, higher mechanical stability and higher porosity are the primary focus.

In addition, works should also be devoted towards enhancing the materials' hydrothermal, chemical stability and hydrophobicity which are important practical application requirements. This is so that the materials can perform excellently while also able to resist degradations in broader operating conditions: high humidity, high temperature and environments of ambient, mild, or harsh nature. In Chapter 5 and 6, both studied MOFs and AC showed poor toluene co-adsorption quantity at 80% RH. The question is, could the pore sizes be engineered to minimise this risk? Data in the literature suggests that to be feasible. In such pursuit, it would be highly encouraged to complement the laborious experimental refinements with computational calculations such as density functional theory models and Grand Canonical Monte Carlo simulations.

Additionally, research on flexible MOFs that can be triggered by external stimuli are very appealing. The rational regulation of their pore opening and closing responses will facilitate enhanced separation performances by these MOFs. These include materials such as MIL-53, MIL-88, and DUT-49.

8.3.3 Facile and safe regeneration

For MOFs that are used for aqueous phase applications, their regeneration procedures require extra safety precautions. For example, less toxic solvents for regeneration should be chosen. Then potential leaching of the MOF components into the waters (metals or linkers) must be considered thoroughly as they can cause serious secondary contamination. To circumvent these problems, a full life cycle assessment should be performed in advance to shortlist a few MOFs based on their least environmental impacts and to determine best practices for the MOF synthesis and disposal.

Chapter 9: References

- Abazari, R. & Mahjoub, A.R. (2018) Ultrasound-assisted synthesis of Zinc (II)-based metal organic framework nanoparticles in the presence of modulator for adsorption enhancement of 2, 4-dichlorophenol and amoxicillin. *Ultrasonics Sonochemistry*. 42, 577–584.
- Abazari, R., Salehi, G. & Mahjoub, A.R. (2018) Ultrasound-assisted preparation of a nanostructured zinc (II) amine pillar metal-organic framework as a potential sorbent for 2, 4-dichlorophenol adsorption from aqueous solution. *Ultrasonics Sonochemistry*. 46, 59–67.
- AbdulHalim, R.G., Bhatt, P.M., Belmabkhout, Y., Shkurenko, A., et al. (2017) A fine-tuned metal–organic framework for autonomous indoor moisture control. *Journal of the American Chemical Society*. 139 (31), 10715–10722.
- Abid, H.R., Rada, Z.H., Shang, J. & Wang, S. (2016) Synthesis, characterization, and CO₂ adsorption of three metal-organic frameworks (MOFs): MIL-53, MIL-96, and amino-MIL-53. *Polyhedron*. 120, 103–111.
- Agilent (2021) *An Introduction to the Fundamentals of FTIR Spectroscopy*. [Online]. 2021. Available from: <https://www.agilent.com/en/support/molecular-spectroscopy/ftir-spectroscopy/ftir-spectroscopy-basics-faqs> [Accessed: 21 September 2021].
- Agimelen, O.S., Mulholland, A.J. & Sefcik, J. (2017) Modelling of artefacts in estimations of particle size of needle-like particles from laser diffraction measurements. *Chemical Engineering Science*. 158, 445–452.
- Ahsan, M.A., Jabbari, V., Islam, M.T., Turley, R.S., et al. (2019) Sustainable synthesis and remarkable adsorption capacity of MOF/graphene oxide and MOF/CNT based hybrid nanocomposites for the removal of Bisphenol A from water. *Science of The Total Environment*. 673, 306–317.
- Ailijiang, N., Chang, J., Liang, P., Zhang, X., et al. (2020) Electrical stimulation on biodegradation of phenolics in a novel anaerobic–aerobic-coupled upflow bioelectrochemical reactor. *Chemical Engineering Journal*. 127840.
- Akiyama, G., Matsuda, R., Sato, H., Hori, A., et al. (2012) Effect of functional groups in

- MIL-101 on water sorption behavior. *Microporous and Mesoporous Materials*. [Online] 157, 89–93. Available from: doi:10.1016/j.micromeso.2012.01.015.
- Al-Degs, Y.S., El-Barghouthi, M.I., Khraisheh, M.A., Ahmad, M.N., et al. (2005) Effect of surface area, micropores, secondary micropores, and mesopores volumes of activated carbons on reactive dyes adsorption from solution. *Separation Science and Technology*. 39 (1), 97–111.
- Alderman, S.L. & Dellinger, B. (2005) FTIR investigation of 2-chlorophenol chemisorption on a silica surface from 200 to 500°C. *The Journal of Physical Chemistry A*. 109 (34), 7725–7731.
- Ali, M., Meaney, S.P., Giles, L.W., Holt, P., et al. (2020) Capture of Perfluorooctanoic Acid Using Oil-Filled Graphene Oxide–Silica Hybrid Capsules. *Environmental Science & Technology*. 54 (6), 3549–3558.
- Álvarez, J.R., Sánchez-González, E., Pérez, E., Schneider-Revueltas, E., et al. (2017) Structure stability of HKUST-1 towards water and ethanol and their effect on its CO₂ capture properties. *Dalton Transactions*. 46 (28), 9192–9200.
- Andersson, E.M., Scott, K., Xu, Y., Li, Y., et al. (2019) High exposure to perfluorinated compounds in drinking water and thyroid disease. A cohort study from Ronneby, Sweden. *Environmental Research*. 176, 108540.
- Andini, S., Cioffi, R., Montagnaro, F., Pisciotta, F., et al. (2006) Simultaneous adsorption of chlorophenol and heavy metal ions on organophilic bentonite. *Applied Clay Science*. 31 (1–2), 126–133.
- Arbaoui, A., Redshaw, C., Elsegood, M.R.J., Wright, V.E., et al. (2010) Iron (III) and Zinc (II) Calixarene Complexes: Synthesis, Structural Studies, and Use as Procatalysts for ϵ -Caprolactone Polymerization. *Chemistry–An Asian Journal*. 5 (3), 621–633.
- Arul, P. & John, S.A. (2018) Size controlled synthesis of Ni-MOF using polyvinylpyrrolidone: New electrode material for the trace level determination of nitrobenzene. *Journal of Electroanalytical Chemistry*. 829, 168–176.
- Ateia, M., Attia, M.F., Maroli, A., Tharayil, N., et al. (2018) Rapid removal of poly-and perfluorinated alkyl substances by poly (ethylenimine)-functionalized cellulose microcrystals at environmentally relevant conditions. *Environmental Science & Technology Letters*. 5 (12), 764–769.

- Ateia, M., Maroli, A., Tharayil, N. & Karanfil, T. (2019) The overlooked short-and ultrashort-chain poly-and perfluorinated substances: A review. *Chemosphere*. 220, 866–882.
- Avcı, C., Liu, Y., Pariente, J.A., Blanco, A., et al. (2019) Template-Free, Surfactant-Mediated Orientation of Self-Assembled Supercrystals of Metal–Organic Framework Particles. *Small*. 15 (31), 1902520.
- Azhar, M.R., Abid, H.R., Tade, M.O., Periasamy, V., et al. (2018) Cascade applications of robust MIL-96 metal organic frameworks in environmental remediation: Proof of concept. *Chemical Engineering Journal*. 341, 262–271.
- Azmi, L.H.M., Williams, D. & Ladewig, B.P. (2020) Can metal organic frameworks outperform adsorptive removal of harmful phenolic compound 2-chlorophenol by activated carbon? *Chemical Engineering Research and Design*. 158, 102–113.
- Badruddoza, A.Z.M., Bhattarai, B. & Suri, R.P.S. (2017) Environmentally friendly β -cyclodextrin–ionic liquid polyurethane-modified magnetic sorbent for the removal of PFOA, PFOS, and Cr (VI) from water. *ACS Sustainable Chemistry & Engineering*. 5 (10), 9223–9232.
- Bae, Y.-S., Liu, J., Wilmer, C.E., Sun, H., et al. (2014) The effect of pyridine modification of Ni–DOBDC on CO₂ capture under humid conditions. *Chemical Communications*. 50 (25), 3296–3298.
- Bahri, M., Haghghat, F., Kazemian, H. & Rohani, S. (2017) A comparative study on metal organic frameworks for indoor environment application: adsorption evaluation. *Chemical Engineering Journal*. 313, 711–723.
- Bao, Y., Niu, J., Xu, Z., Gao, D., et al. (2014) Removal of perfluorooctane sulfonate (PFOS) and perfluorooctanoate (PFOA) from water by coagulation: mechanisms and influencing factors. *Journal of Colloid and Interface Science*. 434, 59–64.
- Barbosa, M.O., Moreira, N.F.F., Ribeiro, A.R., Pereira, M.F.R., et al. (2016) Occurrence and removal of organic micropollutants: An overview of the watch list of EU Decision 2015/495. *Water Research*. 94, 257–279.
- Barpaga, D., Zheng, J., Han, K.S., Soltis, J.A., et al. (2019) Probing the Sorption of Perfluorooctanesulfonate Using Mesoporous Metal–Organic Frameworks from Aqueous Solutions. *Inorganic Chemistry*. 58 (13), 8339–8346.

- Barrett, E.P., Joyner, L.G. & Halenda, P.P. (1951) The determination of pore volume and area distributions in porous substances. I. Computations from nitrogen isotherms. *Journal of the American Chemical Society*. 73 (1), 373–380.
- Barton, S.S., Evans, M.J.B., Holland, J. & Koresh, J.E. (1984) Water and cyclohexane vapour adsorption on oxidized porous carbon. *Carbon*. 22 (3), 265–272.
- Batra, R., Chen, C., Evans, T.G., Walton, K.S., et al. (2020) Prediction of water stability of metal–organic frameworks using machine learning. *Nature Machine Intelligence*. 2 (11), 704–710.
- Bauer, J., Herrmann, R., Mittelbach, W. & Schwieger, W. (2009) Zeolite/aluminum composite adsorbents for application in adsorption refrigeration. *International Journal of Energy Research*. 33 (13), 1233–1249.
- Bavykina, A., Kolobov, N., Khan, I.S., Bau, J.A., et al. (2020) Metal–organic frameworks in heterogeneous catalysis: recent progress, new trends, and future perspectives. *Chemical Reviews*. 120 (16), 8468–8535.
- Bazan, A., Nowicki, P., Pórolniczak, P. & Pietrzak, R. (2016) Thermal analysis of activated carbon obtained from residue after supercritical extraction of hops. *Journal of Thermal Analysis and Calorimetry*. 125 (3), 1199–1204.
- Belkouteb, N., Franke, V., McCleaf, P., Köhler, S., et al. (2020) Removal of per- and polyfluoroalkyl substances (PFASs) in a full-scale drinking water treatment plant: Long-term performance of granular activated carbon (GAC) and influence of flow-rate. *Water Research*. 182, 115913.
- Benevelli, F., Khimyak, Y.Z. & Klinowski, J. (2004) ¹³C and 2D WISE NMR Studies of the Host Mobility in Two Aromatic Complexes of p-Tert-Butyl-Calixarene. *Journal of Inclusion Phenomena and Macrocyclic Chemistry*. 49 (3–4), 211–218.
- Benzaqui, M., Pillai, R.S., Sabetghadam, A., Benoit, V., et al. (2017) Revisiting the aluminum trimesate-based MOF (MIL-96): from structure determination to the processing of mixed matrix membranes for CO₂ capture. *Chemistry of Materials*. 29 (24), 10326–10338.
- Bernt, S., Guillerm, V., Serre, C. & Stock, N. (2011) Direct covalent post-synthetic chemical modification of Cr-MIL-101 using nitrating acid. *Chemical Communications*. [Online] 47 (10), 2838–2840. Available from: doi:10.1039/c0cc04526h.

- Bhadra, B.N., Cho, K.H., Khan, N.A., Hong, D.Y., et al. (2015) Liquid-Phase Adsorption of Aromatics over a Metal-Organic Framework and Activated Carbon: Effects of Hydrophobicity/Hydrophilicity of Adsorbents and Solvent Polarity. *Journal of Physical Chemistry C*. [Online] 119 (47), 26620–26627. Available from: doi:10.1021/acs.jpcc.5b09298.
- Bobbitt, N.S., Mendonca, M.L., Howarth, A.J., Islamoglu, T., et al. (2017) Metal–organic frameworks for the removal of toxic industrial chemicals and chemical warfare agents. *Chemical Society Reviews*.
- Brunauer, S., Emmett, P.H. & Teller, E. (1938) Adsorption of gases in multimolecular layers. *Journal of the American Chemical Society*. 60 (2), 309–319.
- Bueken, B., Van Velthoven, N., Willhammar, T., Stassin, T., et al. (2017) Gel-based morphological design of zirconium metal–organic frameworks. *Chemical science*. 8 (5), 3939–3948.
- Bullot, L., Vieira-Sellai, L., Chaplais, G., Simon-Masseron, A., et al. (2017) Adsorption of 1, 2-dichlorobenzene and 1, 2, 4-trichlorobenzene in nano- and micro-sized crystals of MIL-101 (Cr): static and dynamic gravimetric studies. *Environmental Science and Pollution Research*. 24 (34), 26562–26573.
- Burgaz, E., Erciyes, A., Andac, M. & Andac, O. (2019) Synthesis and characterization of nano-sized metal organic framework-5 (MOF-5) by using consecutive combination of ultrasound and microwave irradiation methods. *Inorganica Chimica Acta*. 485, 118–124.
- Burgher, F., Mathieu, L., Lati, E., Gasser, P., et al. (2011) Experimental 70% hydrofluoric acid burns: histological observations in an established human skin explants ex vivo model. *Cutaneous and Ocular Toxicology*. 30 (2), 100–107.
- Burtch, N.C., Jasuja, H. & Walton, K.S. (2014) Water stability and adsorption in metal-organic frameworks. *Chemical Reviews*. [Online] 114 (20), 10575–10612. Available from: doi:10.1021/cr5002589.
- Cabot (2016) Darco® BG 1 Activated Carbon - a High Performance and Cost Effective Solution for H₂S Removal. *Technical Brochure*. [Online]. Available from: www.cabotcorp.com/~/.../infosheet-darco-bg-1-biogas-purification-united-states.pdf.
- Canivet, J., Fateeva, A., Guo, Y., Coasne, B., et al. (2014) Water adsorption in MOFs: fundamentals and applications. *Chem. Soc. Rev.* [Online] 43 (16), 5594–5617. Available

from: doi:10.1039/C4CS00078A.

- Cheetham, A.K., Rao, C.N.R. & Feller, R.K. (2006) Structural diversity and chemical trends in hybrid inorganic–organic framework materials. *Chemical communications*. (46), 4780–4795.
- Chemviron Carbon (2013) *Filtrisorb*® 400 Agglomerated Coal Based Granular Activated Carbon. [Online]. pp.1–2. Available from: https://www.treitelonline.com/wp-content/uploads/2021/03/PDS_FILTRASORB-400.pdf.
- Chen, J., Shen, K. & Li, Y. (2017) Greening the Processes of Metal–Organic Framework Synthesis and their Use in Sustainable Catalysis. *ChemSusChem*. [Online] 10 (16), 3165–3187. Available from: doi:10.1002/cssc.201700748.
- Chen, M.-J., Yang, A.-C., Wang, N.-H., Chiu, H.-C., et al. (2016) Influence of crystal topology and interior surface functionality of metal-organic frameworks on PFOA sorption performance. *Microporous and Mesoporous Materials*. 236, 202–210.
- Chen, Z., Li, P., Anderson, R., Wang, X., et al. (2020) Balancing volumetric and gravimetric uptake in highly porous materials for clean energy. *Science*. 368 (6488), 297–303.
- Cheng, S., Zhang, J., Wang, Y., Zhang, D., et al. (2019) Global research trends in health effects of volatile organic compounds during the last 16 years: a bibliometric analysis. *Aerosol and Air Quality Research*. 19 (8), 1834–1843.
- Cheng, T., Li, J., Ma, X., Zhou, L., et al. (2021) The adsorption properties of microporous activated carbon prepared from pistachio nut shell for low-concentration VOCs under low-medium temperatures. *Environmental Science and Pollution Research*. 1–13.
- Chevalier, V., Martin, J., Peralta, D., Roussey, A., et al. (2019) Performance of HKUST-1 Metal-Organic Framework for a VOCs mixture adsorption at realistic concentrations ranging from 0.5 to 2.5 ppmv under different humidity conditions. *Journal of Environmental Chemical Engineering*. [Online] 7 (3), 103131. Available from: doi:10.1016/j.jece.2019.103131.
- Choe, J.H., Park, J.R., Chae, Y.S., Kim, D.W., et al. (2021) Shaping and silane coating of a diamine-grafted metal-organic framework for improved CO₂ capture. *Communications Materials*. 2 (1), 1–8.
- Choi, H.J., Dincă, M., Dailly, A. & Long, J.R. (2010) Hydrogen storage in water-stable metal–organic frameworks incorporating 1, 3-and 1, 4-benzenedipyrazolate. *Energy &*

- Environmental Science*. 3 (1), 117–123.
- Chu, F., Zheng, Y., Wen, B., Zhou, L., et al. (2018) Adsorption of toluene with water on zeolitic imidazolate framework-8/graphene oxide hybrid nanocomposites in a humid atmosphere. *RSC Advances*. 8 (5), 2426–2432.
- Chuang, Y.H., Tzou, Y.M., Wang, M.K., Liu, C.H., et al. (2008) Removal of 2-chlorophenol from aqueous solution by Mg/Al layered double hydroxide (LDH) and modified LDH. *Industrial & Engineering Chemistry Research*. 47 (11), 3813–3819.
- Chui, S.S.-Y., Lo, S.M.-F., Charmant, J.P.H., Orpen, A.G., et al. (1999) A chemically functionalizable nanoporous material [Cu₃ (TMA)₂ (H₂O)₃]_n. *Science*. 283 (5405), 1148–1150.
- Chun, J., Kang, S., Park, N., Park, E.J., et al. (2014) Metal–organic framework@microporous organic network: hydrophobic adsorbents with a crystalline inner porosity. *Journal of the American Chemical Society*. 136 (19), 6786–6789.
- Di Ciaula, A. & Portincasa, P. (2021) Relationships between emissions of toxic airborne molecules and type 1 diabetes incidence in children: An ecologic study. *World Journal of Diabetes*. 12 (5), 673.
- Clark, Christine M., Dutrow, B.L. (2021) *Single-crystal X-ray diffraction*. [Online]. 2021. Available from:
https://serc.carleton.edu/research_education/geochemsheets/techniques/SXD.html
[Accessed: 14 September 2021].
- Clark, C.A., Heck, K.N., Powell, C.D. & Wong, M.S. (2019) Highly defective UiO-66 materials for the adsorptive removal of perfluorooctanesulfonate. *ACS Sustainable Chemistry & Engineering*. 7 (7), 6619–6628.
- Clearco (2015) *Properties of Polydimethylsiloxane Fluids*. [Online]. Available from:
www.clearcoproducts.com.
- Clerici, M.G. & Kholdeeva, O.A. (2013) Syntheses. In: *Liquid Phase Oxidation via Heterogeneous Catalysis: Organic Synthesis and Industrial Applications*. [Online]. Wiley. p. Available from:
https://books.google.co.uk/books?id=7sQWdQCaB3IC&dq=solubility+of+Terephthalic+acid+in+hf&source=gbs_navlinks_s.
- de Clippel, F., Dusselier, M., Van de Vyver, S., Peng, L., et al. (2013) Tailoring nanohybrids

- and nanocomposites for catalytic applications. *Green Chemistry*. 15 (6), 1398–1430.
- Cordner, A., Vanessa, Y., Schaidler, L.A., Rudel, R.A., et al. (2019) Guideline levels for PFOA and PFOS in drinking water: the role of scientific uncertainty, risk assessment decisions, and social factors. *Journal of Exposure Science & Environmental Epidemiology*. 29 (2), 157.
- Dąbrowski, A., Podkościelny, P., Hubicki, Z. & Barczak, M. (2005) Adsorption of phenolic compounds by activated carbon—a critical review. *Chemosphere*. 58 (8), 1049–1070.
- David, R.O., Fahrni, J., Marcolli, C., Mahrt, F., et al. (2020) The role of contact angle and pore width on pore condensation and freezing. *Atmospheric Chemistry and Physics*. 20 (15), 9419–9440.
- DeCoste, J.B., Peterson, G.W., Schindler, B.J., Killops, K.L., et al. (2013) The effect of water adsorption on the structure of the carboxylate containing metal–organic frameworks Cu-BTC, Mg-MOF-74, and UiO-66. *Journal of Materials Chemistry A*. 1 (38), 11922–11932.
- Dedecker, K., Pillai, R.S., Nouar, F., Pires, J., et al. (2018) Metal-Organic Frameworks for Cultural Heritage preservation: the case of acetic acid removal. *ACS Applied Materials and Interfaces*. 10 (16), 13886–13894.
- Delville, M.H. & Taubert, A. (2018) *Hybrid Organic-Inorganic Interfaces: Towards Advanced Functional Materials*. [Online]. John Wiley & Sons. Available from: <https://books.google.co.uk/books?id=5D5FDwAAQBAJ>.
- Deng, S., Niu, L., Bei, Y., Wang, B., et al. (2013) Adsorption of perfluorinated compounds on aminated rice husk prepared by atom transfer radical polymerization. *Chemosphere*. [Online] 91 (2), 124–130. Available from: doi:10.1016/j.chemosphere.2012.11.015.
- Deria, P., Bury, W., Hod, I., Kung, C.-W., et al. (2015) MOF functionalization via solvent-assisted ligand incorporation: Phosphonates vs carboxylates. *Inorganic Chemistry*. 54 (5), 2185–2192.
- DesMarias, T.L. & Costa, M. (2019) Mechanisms of chromium-induced toxicity. *Current Opinion in Toxicology*. 14, 1–7.
- Devic, T. & Serre, C. (2014) High valence 3p and transition metal based MOFs. *Chem. Soc. Rev.* [Online] 43 (16), 6097–6115. Available from: doi:10.1039/C4CS00081A.
- Dias, E.M. & Petit, C. (2015) Towards the use of metal–organic frameworks for water reuse:

- a review of the recent advances in the field of organic pollutants removal and degradation and the next steps in the field. *J. Mater. Chem. A*. [Online] 3 (45), 22484–22506. Available from: doi:10.1039/C5TA05440K.
- Do, D.D., Junpirom, S. & Do, H.D. (2009) A new adsorption–desorption model for water adsorption in activated carbon. *Carbon*. 47 (6), 1466–1473.
- Dobaradaran, S., Nodehi, R.N., Yaghmaeian, K., Jaafari, J., et al. (2018) Catalytic decomposition of 2-chlorophenol using an ultrasonic-assisted Fe₃O₄–TiO₂@ MWCNT system: Influence factors, pathway and mechanism study. *Journal of Colloid and Interface Science*. 512, 172–189.
- Du, Z., Deng, S., Bei, Y., Huang, Q., et al. (2014) Adsorption behavior and mechanism of perfluorinated compounds on various adsorbents—a review. *Journal of Hazardous Materials*. 274, 443–454.
- Du, Z., Deng, S., Chen, Y., Wang, B., et al. (2015) Removal of perfluorinated carboxylates from washing wastewater of perfluorooctanesulfonyl fluoride using activated carbons and resins. *Journal of Hazardous Materials*. 286, 136–143.
- Duan, C., Yu, Y., Li, J., Li, L., et al. (2021) Recent advances in the synthesis of monolithic metal-organic frameworks. *Science China Materials*. 64, 1–15.
- Duan, C., Yu, Y., Yang, P., Zhang, X., et al. (2019) Engineering new defects in MIL-100 (Fe) via a mixed-ligand approach to effect enhanced volatile organic compounds adsorption capacity. *Industrial & Engineering Chemistry Research*.
- Edomwonyi-Otu, L.C. & Adedokun, D.O. (2018) Effect of heavy molecular weight polymer on quality of drinking water. *Materials Today Communications*. 15, 337–343.
- Ehhalt, D., Prather, M., Dentener, F., Derwent, R., et al. (2001) Chapter 4: Atmospheric Chemistry and Greenhouse Gases. In: *IPCC Third Assessment Report Climate Change 2001: The Scientific Basis*. [Online]. United States, Houghton, J. T. et al; Cambridge University Press, Cambridge, United Kingdom. pp. 241–287. Available from: <https://www.osti.gov/biblio/901482>.
- Eryılmaz, C. & Genç, A. (2021) Review of Treatment Technologies for the Removal of Phenol from Wastewaters. *Journal of Water Chemistry and Technology*. 43 (2), 145–154.
- European Communities (2001) Decision No. 2455/2001/EC of the European Parliament and

- of the Council of 20 November 2001 establishing the list of priority substances in the field of water policy and amending Directive 2000/60/EC. *Official Journal of the European Communities*. [Online] 44 (L 331), 1–5. Available from: doi:http://eur-lex.europa.eu/pri/en/oj/dat/2003/l_285/l_28520031101en00330037.pdf.
- Feng, D., Gu, Z.Y., Li, J.R., Jiang, H.L., et al. (2012) Zirconium-metalloporphyrin PCN-222: Mesoporous metal-organic frameworks with ultrahigh stability as biomimetic catalysts. *Angewandte Chemie - International Edition*. [Online] 51 (41), 10307–10310. Available from: doi:10.1002/anie.201204475.
- Feng, X., Qin, M., Cui, S. & Rode, C. (2018) Metal-organic framework MIL-100 (Fe) as a novel moisture buffer material for energy-efficient indoor humidity control. *Building and Environment*. 145, 234–242.
- Feng, X., Ye, M., Li, Y., Zhou, J., et al. (2020) Potential sources and sediment-pore water partitioning behaviors of emerging per/polyfluoroalkyl substances in the South Yellow Sea. *Journal of Hazardous Materials*. 389, 122124.
- Férey, G., Draznieks-Mellot, C., Serre, C., Millange, F., et al. (2005) A Chromium Terephthalate-Based Solid with Unusually Large Pore Volumes and Surface Area. *Science*. [Online] 309 (5743), 2040–2042. Available from: doi:10.1126/science.1116275.
- Férey, G., Serre, C., Mellot-Draznieks, C., Millange, F., et al. (2004) A hybrid solid with giant pores prepared by a combination of targeted chemistry, simulation, and powder diffraction. *Angewandte Chemie*. 116 (46), 6456–6461.
- Fernandez, C.A., Nune, S.K., Annapureddy, H. V, Dang, L.X., et al. (2015) Hydrophobic and moisture-stable metal–organic frameworks. *Dalton Transactions*. 44 (30), 13490–13497.
- Foo, K.Y. & Hameed, B.H. (2010) Insights into the modeling of adsorption isotherm systems. *Chemical Engineering Journal*. 156 (1), 2–10.
- Freundlich, H.M.F. (1906) Over the adsorption in solution. *Journal of Physical Chemistry*. 57 (385471), 1100–1107.
- Frilund, C., Hiltunen, I. & Simell, P. (2021) Activated Carbons for Syngas Desulfurization: Evaluating Approaches for Enhancing Low-Temperature H₂S Oxidation Rate. *ChemEngineering*. 5 (2), 23.
- Fu, J.H. & Schlup, J.R. (1993) Mid-and near-infrared spectroscopic investigations of

- reactions between phenyl glycidyl ether (PGE) and aromatic amines. *Journal of Applied Polymer Science*. 49 (2), 219–227.
- Gabbott, P. (2008) Introduction. In: Paul Gabbott (ed.). *Principles and Applications of Thermal Analysis*. [Online]. Wiley. pp. 88–89. Available from: https://books.google.co.uk/books?id=1u4v_tGUEQoC.
- Gan, L., Li, B., Guo, M., Weng, X., et al. (2018) Mechanism for removing 2, 4-dichlorophenol via adsorption and Fenton-like oxidation using iron-based nanoparticles. *Chemosphere*. 206, 168–174.
- Gao, L., Li, C.-Y.V., Yung, H. & Chan, K.-Y. (2013) A functionalized MIL-101 (Cr) metal-organic framework for enhanced hydrogen release from ammonia borane at low temperature. *Chemical Communications*. 49 (90), 10629–10631.
- Gao, X. & Chorover, J. (2012) Adsorption of perfluorooctanoic acid and perfluorooctanesulfonic acid to iron oxide surfaces as studied by flow-through ATR-FTIR spectroscopy. *Environmental Chemistry*. 9 (2), 148–157.
- Gao, Y., Yue, Q., Gao, B. & Li, A. (2020a) Insight into activated carbon from different kinds of chemical activating agents: A review. *Science of the Total Environment*. 746, 141094.
- Gao, Z., Song, G., Zhang, X., Li, Q., et al. (2020b) A facile PDMS coating approach to room-temperature gas sensors with high humidity resistance and long-term stability. *Sensors and Actuators B: Chemical*. 325, 128810.
- Garba, Z.N., Zhou, W., Lawan, I., Xiao, W., et al. (2019) An overview of chlorophenols as contaminants and their removal from wastewater by adsorption: A review. *Journal of Environmental Management*. 241, 59–75.
- Gebald, C., Repond, N., Ruesch, T. & Wurzbacher, J.A. (2019) *Low-pressure drop structure of particle adsorbent bed for adsorption gas separation process*.
- Giaya, A., Thompson, R.W. & Denkwicz Jr, R. (2000) Liquid and vapor phase adsorption of chlorinated volatile organic compounds on hydrophobic molecular sieves. *Microporous and Mesoporous Materials*. 40 (1–3), 205–218.
- Gokce, Y., Yaglikci, S., Yagmur, E., Banford, A., et al. (2021) Adsorption behaviour of high performance activated carbon from demineralised low rank coal (Rawdon) for methylene blue and phenol. *Journal of Environmental Chemical Engineering*. 9 (2), 104819.

- Goldstein, A.H., Nazaroff, W.W., Weschler, C.J. & Williams, J. (2020) How Do Indoor Environments Affect Air Pollution Exposure? *Environmental Science & Technology*.
- Gomes Silva, C., Luz, I., Llabrés i Xamena, F.X., Corma, A., et al. (2010) Water stable Zr–benzenedicarboxylate metal–organic frameworks as photocatalysts for hydrogen generation. *Chemistry-A European Journal*. 16 (36), 11133–11138.
- Guesh, K., Caiuby, C.A.D., Mayoral, A., Díaz-García, M., et al. (2017) Sustainable preparation of MIL-100 (Fe) and its photocatalytic behavior in the degradation of methyl orange in water. *Crystal Growth & Design*. 17 (4), 1806–1813.
- Guo, C., Zhang, Y., Guo, Y., Zhang, L., et al. (2018) A general and efficient approach for tuning the crystal morphology of classical MOFs. *Chemical Communications*. 54 (3), 252–255.
- Guo, H., Niu, B., Wu, X., Zhang, Y., et al. (2019) Effective removal of 2, 4, 6-trinitrophenol over hexagonal metal–organic framework NH₂-MIL-88B (Fe). *Applied Organometallic Chemistry*. 33 (1), e4580.
- Guo, X. & Wang, J. (2019) Comparison of linearization methods for modeling the Langmuir adsorption isotherm. *Journal of Molecular Liquids*. 296, 111850.
- Gupta, T. (2018) Historical Production and Use of Carbon Materials: The Activated Carbon. In: *Carbon*. Springer. pp. 47–70.
- Ha, J., Lee, J.H. & Moon, H.R. (2020) Alterations to secondary building units of metal–organic frameworks for the development of new functions. *Inorganic Chemistry Frontiers*. 7 (1), 12–27.
- Hadjltaief, H.B., Sdiri, A., Ltaief, W., Da Costa, P., et al. (2018) Efficient removal of cadmium and 2-chlorophenol in aqueous systems by natural clay: Adsorption and photo-Fenton degradation processes. *Comptes Rendus Chimie*. 21 (3–4), 253–262.
- Haghseresht, F. & Lu, G.Q. (1998) Adsorption characteristics of phenolic compounds onto coal-reject-derived adsorbents. *Energy & Fuels*. 12 (6), 1100–1107.
- Halasz, I., Agarwal, M., Marcus, B. & Cormier, W.E. (2005) Molecular spectra and polarity sieving of aluminum deficient hydrophobic HY zeolites. *Microporous and Mesoporous Materials*. 84 (1–3), 318–331.
- Hall, J.N. & Bollini, P. (2019) Structure, characterization, and catalytic properties of open-metal sites in metal organic frameworks. *Reaction Chemistry & Engineering*. 4 (2), 207–

- Hammer, A., Fedelich, N., Giani, S., Hempel, E., et al. (2021) *Thermal Analysis of Polymers Selected Applications*. [Online]. pp.1–8. Available from: <https://www.mt.com/gb/en/home/library/applications/lab-analytical-instruments/thermal-analysis-of-polymers.html>.
- Haouas, M., Volkringer, C., Loiseau, T., Férey, G., et al. (2009) The Extra-Framework Sub-Lattice of the Metal–Organic Framework MIL-110: A Solid-State NMR Investigation. *Chemistry–A European Journal*. 15 (13), 3139–3146.
- Haouas, M., Volkringer, C., Loiseau, T., Férey, G., et al. (2012) In situ NMR, ex situ XRD and SEM study of the hydrothermal crystallization of nanoporous aluminum trimesates MIL-96, MIL-100, and MIL-110. *Chemistry of Materials*. [Online] 24 (13), 2462–2471. Available from: doi:10.1021/cm300439e.
- Hara, Y., Kanamori, K. & Nakanishi, K. (2019) Self-Assembly of Metal–Organic Frameworks into Monolithic Materials with Highly Controlled Trimodal Pore Structures. *Angewandte Chemie*. 131 (52), 19223–19229.
- Hasan, Z., Choi, E.J. & Jung, S.H. (2013) Adsorption of naproxen and clofibrac acid over a metal–organic framework MIL-101 functionalized with acidic and basic groups. *Chemical Engineering Journal*. [Online] 219, 537–544. Available from: doi:10.1016/j.cej.2013.01.002.
- Hasan, Z. & Jung, S.H. (2015) Removal of hazardous organics from water using metal-organic frameworks (MOFs): Plausible mechanisms for selective adsorptions. *Journal of Hazardous Materials*. [Online] 283, 329–339. Available from: doi:10.1016/j.jhazmat.2014.09.046.
- He, S., Chen, L., Cui, J., Yuan, B., et al. (2020) General way to construct micro- and mesoporous metal–organic framework-based porous liquids. *Journal of the American Chemical Society*. [Online] 141 (50), 19708–19714. Available from: doi:10.1021/jacs.9b08458.
- Heinke, L., Gu, Z. & Wöll, C. (2014) The surface barrier phenomenon at the loading of metal-organic frameworks. *Nature Communications*. 5, 4562.
- Hidden Isochema (2021) *IGA Series - Gravimetric Gas and Vapor Sorption Analyzers*. [Online]. Available from: <https://hiddenisochema.com/content/uploads/2016/05/Hidden->

Isochema-IGA-Series-Brochure.pdf.

- Hinz, C. (2001) Description of sorption data with isotherm equations. *Geoderma*. 99 (3–4), 225–243.
- Ho, Y.-S. & McKay, G. (1999) Pseudo-second order model for sorption processes. *Process Biochemistry*. 34 (5), 451–465.
- Holder, C.F. & Schaak, R.E. (2019) Tutorial on powder X-ray diffraction for characterizing nanoscale materials. *ACS Nano*. [Online] 13 (7), 7359–7365. Available from: doi:10.1021/acsnano.9b05157.
- Homden, D.M. & Redshaw, C. (2008) The use of calixarenes in metal-based catalysis. *Chemical Reviews*. 108 (12), 5086–5130.
- Hong, D.Y., Hwang, Y.K., Serre, C., Férey, G., et al. (2009) Porous chromium terephthalate MIL-101 with coordinatively unsaturated sites: Surface functionalization, encapsulation, sorption and catalysis. *Advanced Functional Materials*. [Online] 19 (10), 1537–1552. Available from: doi:10.1002/adfm.200801130.
- Hönicke, I.M., Senkowska, I., Bon, V., Baburin, I.A., et al. (2018) Balancing mechanical stability and ultrahigh porosity in crystalline framework materials. *Angewandte Chemie International Edition*. 57 (42), 13780–13783.
- Horcajada, P., Salles, F., Wuttke, S., Devic, T., et al. (2011) How linker's modification controls swelling properties of highly flexible iron (III) dicarboxylates MIL-88. *Journal of the American Chemical Society*. 133 (44), 17839–17847.
- Horcajada, P., Serre, C., Vallet-Regí, M., Sebban, M., et al. (2006) Metal-organic frameworks as efficient materials for drug delivery. *Angewandte Chemie - International Edition*. [Online] 45 (36), 5974–5978. Available from: doi:10.1002/anie.200601878.
- Horcajada, P., Surblé, S., Serre, C., Hong, D.-Y., et al. (2007) Synthesis and catalytic properties of MIL-100 (Fe), an iron (III) carboxylate with large pores. *Chemical Communications*. (27), 2820–2822.
- Hou, J., Sapnik, A.F. & Bennett, T.D. (2020) Metal–organic framework gels and monoliths. *Chemical Science*. 11, 310–323.
- Hu, X.C., Andrews, D.Q., Lindstrom, A.B., Bruton, T.A., et al. (2016) Detection of poly-and perfluoroalkyl substances (PFASs) in US drinking water linked to industrial sites, military fire training areas, and wastewater treatment plants. *Environmental Science &*

Technology Letters. 3 (10), 344–350.

- Huang, C.Y., Song, M., Gu, Z.Y., Wang, H.F., et al. (2011) Probing the adsorption characteristic of metal-organic framework MIL-101 for volatile organic compounds by quartz crystal microbalance. *Environmental Science and Technology*. [Online] 45 (10), 4490–4496. Available from: doi:10.1021/es200256q.
- Huang, G., Yang, Q., Xu, Q., Yu, S., et al. (2016) Polydimethylsiloxane coating for a palladium/MOF composite: highly improved catalytic performance by surface hydrophobization. *Angewandte Chemie International Edition*. 55 (26), 7379–7383.
- Huang, M., Jiao, J., Zhuang, P., Chen, X., et al. (2018) Serum polyfluoroalkyl chemicals are associated with risk of cardiovascular diseases in national US population. *Environment International*. 119, 37–46.
- Hubbe, M.A., Azizian, S. & Douven, S. (2019) Implications of Apparent Pseudo-Second-Order Adsorption Kinetics onto Cellulosic Materials: A Review. *BioResources*. 14 (3), 1–45.
- Hunter-Sellars, E., Tee, J.J., Parkin, I.P. & Williams, D.R. (2020) Adsorption of volatile organic compounds by industrial porous materials: Impact of relative humidity. *Microporous and Mesoporous Materials*. 298, 110090.
- Hunter-Sellars, E., Saenz-Cavazos, P.A., Houghton, A.R., McIntyre, S.R., et al. (2021) Sol-Gel Synthesis of High-Density Zeolitic Imidazolate Framework Monoliths via Ligand Assisted Methods: Exceptional Porosity, Hydrophobicity, and Applications in Vapor Adsorption. *Advanced Functional Materials*. 31 (5), 2008357.
- Hynek, J., Ondrušová, S., Bůžek, D., Kovář, P., et al. (2017) Postsynthetic modification of a zirconium metal-organic framework at the inorganic secondary building unit with diphenylphosphinic acid for increased photosensitizing properties and stability. *Chemical Communications*. [Online] 53 (61), 8557–8560. Available from: doi:10.1039/c7cc05068b.
- Ibarra, I.A., Bayliss, P.A., Pérez, E., Yang, S., et al. (2012) Near-critical water, a cleaner solvent for the synthesis of a metal-organic framework. *Green Chemistry*. 14 (1), 117–122.
- Ismail, A.F., Khulbe, K.C. & Matsuura, T. (2015) *Gas Separation Membranes: Polymeric and Inorganic*. [Online]. Springer International Publishing. Available from:

<https://books.google.co.uk/books?id=n2u6CAAAQBAJ>.

- IUPAC (2014) Compendium of Chemical Terminology 2nd ed. (the ‘Gold Book’). *Blackwell Scientific Publications, Oxford*. [Online] 1670. Available from: doi:10.1351/goldbook.I03352.
- Jafari, S., Ghorbani-Shahna, F., Bahrami, A. & Kazemian, H. (2018) Effects of post-synthesis activation and relative humidity on adsorption performance of ZIF-8 for capturing toluene from a gas phase in a continuous mode. *Applied Sciences*. 8 (2), 310.
- Jang, H.M., Yoo, S., Choi, Y.-K., Park, S., et al. (2018) Adsorption isotherm, kinetic modeling and mechanism of tetracycline on Pinus taeda-derived activated biochar. *Bioresource Technology*. 259, 24–31.
- Jasuja, H., Burtch, N.C., Huang, Y.G., Cai, Y., et al. (2013) Kinetic water stability of an isostructural family of zinc-based pillared metal-organic frameworks. *Langmuir*. [Online] 29 (2), 633–642. Available from: doi:10.1021/la304204k.
- Jayaramulu, K., Geyer, F., Schneemann, A., Kment, Š., et al. (2019) Hydrophobic Metal–Organic Frameworks. *Advanced Materials*. [Online] 31 (32), 1–31. Available from: doi:10.1002/adma.201900820.
- Jeong, U., Dogan, N.A., Garai, M., Nguyen, T.S., et al. (2019) Inversion of Dispersion: Colloidal Stability of Calixarene-Modified Metal–Organic Framework Nanoparticles in Nonpolar Media. *Journal of the American Chemical Society*. [Online] 141 (31), 12182–12186. Available from: doi:10.1021/jacs.9b04198.
- Jhung, S.H., Lee, J.H., Yoon, J.W., Serre, C., et al. (2007) Microwave synthesis of chromium terephthalate MIL-101 and its benzene sorption ability. *Advanced Materials*. [Online] 19 (1), 121–124. Available from: doi:10.1002/adma.200601604.
- Joseph, L., Jun, B.-M., Jang, M., Park, C.M., et al. (2019) Removal of contaminants of emerging concern by metal-organic framework nanoadsorbents: A review. *Chemical Engineering Journal*. 369, 928–946.
- Jun, B.-M., Hwang, H.S., Heo, J., Han, J., et al. (2019) Removal of selected endocrine-disrupting compounds using Al-based metal organic framework: Performance and mechanism of competitive adsorption. *Journal of Industrial and Engineering Chemistry*. 79, 345–352.
- Jung, M.-W., Ahn, K.-H., Lee, Y., Kim, K.-P., et al. (2001) Adsorption characteristics of

- phenol and chlorophenols on granular activated carbons (GAC). *Microchemical Journal*. 70 (2), 123–131.
- Kajjumba, G.W., Emik, S., Öngen, A., Özcan, H.K., et al. (2019) Modelling of adsorption kinetic processes—errors, theory and application. In: Serpil Edebalı (ed.). *Advanced Sorption Process Applications*. [Online]. IntechOpen London, UK. pp. 187–206. Available from: doi:<http://dx.doi.org/10.5772/intechopen.80495>.
- Kalmutzki, M.J., Hanikel, N. & Yaghi, O.M. (2018) Secondary building units as the turning point in the development of the reticular chemistry of MOFs. *Science Advances*. 4 (10), eaat9180.
- Kang, I.J., Khan, N.A., Haque, E. & Jhung, S.H. (2011) Chemical and thermal stability of isotypic metal–organic frameworks: effect of metal ions. *Chemistry-A European Journal*. 17 (23), 6437–6442.
- Kang, M., Kim, J.E., Kang, D.W., Lee, H.Y., et al. (2019) A diamine-grafted metal-organic framework with outstanding CO₂ capture properties and a facile coating approach for imparting exceptional moisture stability. *Journal of Materials Chemistry A*. [Online] 7 (14), 8177–8183. Available from: doi:[10.1039/c8ta07965j](https://doi.org/10.1039/c8ta07965j).
- Karikkethu Prabhakaran, P. & Deschamps, J. (2015) Doping activated carbon incorporated composite MIL-101 using lithium: Impact on hydrogen uptake. *Journal of Materials Chemistry A*. [Online] 3 (13), 7014–7021. Available from: doi:[10.1039/c4ta07197b](https://doi.org/10.1039/c4ta07197b).
- Kaskel, S. (2016) *The Chemistry of Metal-Organic Frameworks, 2 Volume Set: Synthesis, Characterization, and Applications*. [Online]. Wiley. Available from: <https://books.google.co.uk/books?id=xJCbCgAAQBAJ>.
- Keshvardoostchokami, M., Majidi, M., Zamani, A. & Liu, B. (2021) Adsorption of phenol on environmentally friendly Fe₃O₄/chitosan/zeolitic imidazolate framework-8 nanocomposite: Optimization by experimental design methodology. *Journal of Molecular Liquids*. 323, 115064.
- Khoshakhlagh, A.H., Beygzadeh, M., Golbabaie, F., Saadati, Z., et al. (2020) Isotherm, kinetic, and thermodynamic studies for dynamic adsorption of toluene in gas phase onto porous Fe-MIL-101/OAC composite. *Environmental Science and Pollution Research*. 27 (35), 44022–44035.
- Kim, J.-H., Shin, W.S., Kim, Y.-H., Choi, S.-J., et al. (2005) Sorption and desorption kinetics

- of chlorophenols in hexadecyltrimethyl ammonium-montmorillonites and their model analysis. *Korean Journal of Chemical Engineering*. 22 (6), 857–864.
- Kim, K.-H., Szulejko, J.E., Raza, N., Kumar, V., et al. (2019) Identifying the best materials for the removal of airborne toluene. *Journal of Cleaner Production*. 241, 118408.
- Kim, M., Cahill, J.F., Fei, H., Prather, K.A., et al. (2012a) Postsynthetic ligand and cation exchange in robust metal–organic frameworks. *Journal of the American Chemical Society*. 134 (43), 18082–18088.
- Kim, M., Cahill, J.F., Su, Y., Prather, K.A., et al. (2012b) Postsynthetic ligand exchange as a route to functionalization of ‘inert’ metal–organic frameworks. *Chemical Science*. 3 (1), 126–130.
- Kitao, T., Zhang, Y., Kitagawa, S., Wang, B., et al. (2017) Hybridization of MOFs and polymers. *Chem. Soc. Rev.* [Online] 46 (11), 3108–3133. Available from: doi:10.1039/C7CS00041C.
- Kloda, M., Ondrušová, S., Lang, K. & Demel, J. (2021) Phosphinic acids as building units in materials chemistry. *Coordination Chemistry Reviews*. 433, 213748.
- Ko, N., Choi, P.G., Hong, J., Yeo, M., et al. (2015a) Tailoring the water adsorption properties of MIL-101 metal–organic frameworks by partial functionalization. *Journal of Materials Chemistry A*. 3 (5), 2057–2064.
- Ko, N., Hong, J., Sung, S., Cordova, K.E., et al. (2015b) A significant enhancement of water vapour uptake at low pressure by amine-functionalization of UiO-67. *Dalton Transactions*. 44 (5), 2047–2051.
- Krahnstöver, T., Plattner, J. & Wintgens, T. (2016) Quantitative detection of powdered activated carbon in wastewater treatment plant effluent by thermogravimetric analysis (TGA). *Water Research*. 101, 510–518.
- Krzeminski, P., Tomei, M.C., Karaolia, P., Langenhoff, A., et al. (2019) Performance of secondary wastewater treatment methods for the removal of contaminants of emerging concern implicated in crop uptake and antibiotic resistance spread: A review. *Science of the Total Environment*. 648, 1052–1081.

- Kumar, P., Anand, B., Tsang, Y.F., Kim, K.-H., et al. (2019a) Regeneration, degradation, and toxicity effect of MOFs: Opportunities and challenges. *Environmental Research*. 176, 108488.
- Kumar, P., Kim, K.H., Kwon, E.E. & Szulejko, J.E. (2015) Metal-organic frameworks for the control and management of air quality: Advances and future direction. *Journal of Materials Chemistry A*. [Online] 4 (2), 345–361. Available from: doi:10.1039/c5ta07068f.
- Kumar, P.S., Korving, L., Keesman, K.J., van Loosdrecht, M.C.M., et al. (2019b) Effect of pore size distribution and particle size of porous metal oxides on phosphate adsorption capacity and kinetics. *Chemical Engineering Journal*. 358, 160–169.
- Küsgens, P., Rose, M., Senkovska, I., Fröde, H., et al. (2009) Characterization of metal-organic frameworks by water adsorption. *Microporous and Mesoporous Materials*. [Online] 120 (3), 325–330. Available from: doi:10.1016/j.micromeso.2008.11.020.
- Kutsuna, S., Hori, H., Sonoda, T., Iwakami, T., et al. (2012) Preferential solvation of perfluorooctanoic acid (PFOA) by methanol in methanol–water mixtures: A potential overestimation of the dissociation constant of PFOA using a Yasuda–Shedlovsky plot. *Atmospheric Environment*. 49, 411–414.
- Lagergren, S. (1898) *Zur theorie der sogenannten adsorption geloster stoffe*.
- De Lange, M.F., Vlught, T.J.H., Gascon, J. & Kapteijn, F. (2014) Adsorptive characterization of porous solids: Error analysis guides the way. *Microporous and Mesoporous Materials*. 200, 199–215.
- Largitte, L. & Pasquier, R. (2016) A review of the kinetics adsorption models and their application to the adsorption of lead by an activated carbon. *Chemical Engineering Research and Design*. 109, 495–504.
- Launer, Phillip J.; Arkles, B. (2013) Infrared Analysis of Organosilicon Compounds: Spectra-Structure Correlations. In: Gerald L. Larson (ed.). *Silicon Compounds: Silanes & Silicones*. 3rd edition. [Online]. Morrisville, PA, Gelest Inc. pp. 175–178. Available from: gelest.com/wp-content/uploads/5000A_Section1_InfraredAnalysis.pdf.
- Lee, J. & Kwak, S.-Y. (2017) Tubular superstructures composed of α -Fe₂O₃ nanoparticles from pyrolysis of metal–organic frameworks in a confined space: effect on morphology, particle size, and magnetic properties. *Crystal Growth & Design*. 17 (9), 4496–4500.

- Li, A., Bueno-Perez, R., Wiggin, S. & Fairen-Jimenez, D. (2020a) Enabling efficient exploration of metal–organic frameworks in the Cambridge Structural Database. *CrystEngComm*. 22 (43), 7152–7161.
- Li, H., Eddaoudi, M., O’Keeffe, M. & Yaghi, O.M. (1999) Design and synthesis of an exceptionally stable and highly porous metal-organic framework. *Nature*. 402 (6759), 276–279.
- Li, H., Li, L., Lin, R.-B., Zhou, W., et al. (2019a) Porous metal-organic frameworks for gas storage and separation: Status and challenges. *EnergyChem*. 1 (1), 100006.
- Li, J., Chen, Y., Wu, Q., Wu, J., et al. (2019b) Synthesis of sea-urchin-like Fe₃O₄/SnO₂ heterostructures and its application for environmental remediation by removal of p-chlorophenol. *Journal of Materials Science*. 54 (2), 1341–1350.
- Li, J., Ren, H., Zou, X., Cai, K., et al. (2018a) Hard-template synthesis of micro-mesoporous organic frameworks with controlled hierarchicity. *Chemical Communications*. 54 (60), 8335–8338.
- Li, J., Ye, W. & Chen, C. (2019) Chapter 5 - Removal of toxic/radioactive metal ions by metal-organic framework-based materials. In: Changlun B T - Interface Science and Technology Chen (ed.). *Emerging Natural and Tailored Nanomaterials for Radioactive Waste Treatment and Environmental Remediation*. [Online]. Elsevier. pp. 217–279. Available from: doi:<https://doi.org/10.1016/B978-0-08-102727-1.00005-4>.
- Li, L., Li, B., Dong, J. & Zhang, J. (2016a) Roles of silanes and silicones in forming superhydrophobic and superoleophobic materials. *Journal of Materials Chemistry A*. 4 (36), 13677–13725.
- Li, L., Zheng, H., Wang, T., Cai, M., et al. (2018b) Perfluoroalkyl acids in surface seawater from the North Pacific to the Arctic Ocean: Contamination, distribution and transportation. *Environmental Pollution*. 238, 168–176.
- Li, M., Li, Y., Li, W., Liu, F., et al. (2020b) Synthesis and application of Cu-BTC@ ZSM-5 composites as effective adsorbents for removal of toluene gas under moist ambience: kinetics, thermodynamics, and mechanism studies. *Environmental Science and Pollution Research*. 27 (6), 6052–6065.
- Li, M., Liu, J., Xu, Y. & Qian, G. (2016b) Phosphate adsorption on metal oxides and metal hydroxides: A comparative review. *Environmental Reviews*. 24 (3), 319–332.

- Li, W., Zhao, H., Teasdale, P.R., John, R., et al. (2002) Synthesis and characterisation of a polyacrylamide–polyacrylic acid copolymer hydrogel for environmental analysis of Cu and Cd. *Reactive and Functional Polymers*. 52 (1), 31–41.
- Li, X., Zhang, L., Yang, Z., He, Z., et al. (2020c) Hydrophobic modified activated carbon using PDMS for the adsorption of VOCs in humid condition. *Separation and Purification Technology*. 239 (116517), 1–10.
- Li, X., Zhang, L., Yang, Z., Wang, P., et al. (2020d) Adsorption materials for volatile organic compounds (VOCs) and the key factors for VOCs adsorption process: A review. *Separation and Purification Technology*. 235, 116213.
- Li, Y.-Z., Wang, G.-D., Shi, W.-J., Hou, L., et al. (2020e) Efficient C₂H_n Hydrocarbons and VOC Adsorption and Separation in an MOF with Lewis Basic and Acidic Decorated Active Sites. *ACS Applied Materials & Interfaces*. 12 (37), 41785–41793.
- Li, Y., Yang, Z., Wang, Y., Bai, Z., et al. (2017) A mesoporous cationic thorium-organic framework that rapidly traps anionic persistent organic pollutants. *Nature Communications*. 8 (1), 1–11.
- Li, Y.H., Lee, C.W. & Gullett, B.K. (2001) *Characterization of Activated Carbons' Physical and Chemical Properties in Relation to Their Mercury Adsorption*. [Online]. Available from: https://cfpub.epa.gov/si/si_public_record_Report.cfm?Lab=NRMRL&dirEntryId=63671.
- Li, Z., Yuan, Y., Wu, H., Li, X., et al. (2021) Investigation of MOF-derived humidity-proof hierarchical porous carbon frameworks as highly-selective toluene absorbents and sensing materials. *Journal of Hazardous Materials*. 411, 125034.
- Liang, J., Fang, X., Lin, Y. & Wang, D. (2018) A new screened microbial consortium OEM2 for lignocellulosic biomass deconstruction and chlorophenols detoxification. *Journal of Hazardous Materials*. 347, 341–348.
- Lin, K.-Y.A. & Hsieh, Y.-T. (2015) Copper-based metal organic framework (MOF), HKUST-1, as an efficient adsorbent to remove p-nitrophenol from water. *Journal of the Taiwan Institute of Chemical Engineers*. 50, 223–228.
- Lin, Y., Kong, C. & Chen, L. (2013) Facile synthesis of aluminum-based metal-organic frameworks with different morphologies and structures through an OH⁻-assisted method.

Chemistry - An Asian Journal. [Online] 8 (8), 1873–1878. Available from:
doi:10.1002/asia.201300135.

- Linder, R., Seefeld, K., Vavra, A. & Kleinermanns, K. (2008) Gas phase infrared spectra of nonaromatic amino acids. *Chemical Physics Letters*. 453 (1–3), 1–6.
- Liu, B., Vikrant, K., Kim, K.-H., Kumar, V., et al. (2020) Critical role of water stability in metal–organic frameworks and advanced modification strategies for the extension of their applicability. *Environmental Science: Nano*. 7 (5), 1319–1347.
- Liu, B., Yang, F., Zou, Y. & Peng, Y. (2014) Adsorption of phenol and p-nitrophenol from aqueous solutions on metal–organic frameworks: effect of hydrogen bonding. *Journal of Chemical & Engineering Data*. 59 (5), 1476–1482.
- Liu, B., Younis, S.A. & Kim, K.-H. (2021) The dynamic competition in adsorption between gaseous benzene and moisture on metal-organic frameworks across their varying concentration levels. *Chemical Engineering Journal*. 421, 127813.
- Liu, D., Liu, Y., Dai, F., Zhao, J., et al. (2015a) Size-and morphology-controllable synthesis of MIL-96 (Al) by hydrolysis and coordination modulation of dual aluminium source and ligand systems. *Dalton Transactions*. 44 (37), 16421–16429.
- Liu, H.-B., Yang, B. & Xue, N.-D. (2016) Enhanced adsorption of benzene vapor on granular activated carbon under humid conditions due to shifts in hydrophobicity and total micropore volume. *Journal of Hazardous Materials*. 318, 425–432.
- Liu, K., Zhang, S., Hu, X., Zhang, K., et al. (2015b) Understanding the adsorption of PFOA on MIL-101 (Cr)-based anionic-exchange metal–organic frameworks: comparing DFT calculations with aqueous sorption experiments. *Environmental Science and Technology*. 49 (14), 8657–8665.
- Liu, S., Chen, J., Peng, Y., Hu, F., et al. (2018) Studies on toluene adsorption performance and hydrophobic property in phenyl functionalized KIT-6. *Chemical Engineering Journal*. 334, 191–197.
- Liu, X.-M., Xie, L.-H. & Wu, Y. (2020) Recent advances in the shaping of metal–organic frameworks. *Inorganic Chemistry Frontiers*. 7 (15), 2840–2866.
- Liu, X., Li, Y., Ban, Y., Peng, Y., et al. (2013) Improvement of hydrothermal stability of zeolitic imidazolate frameworks. *Chemical Communications*. 49 (80), 9140–9142.
- Liu, Z., Zhang, L. & Sun, D. (2020) Stimuli-responsive structural changes in metal–organic

- frameworks. *Chemical Communications*. 56 (66), 9416–9432.
- Lo, S.-H., Senthil Raja, D., Chen, C.-W., Kang, Y.-H., et al. (2016) Waste polyethylene terephthalate (PET) materials as sustainable precursors for the synthesis of nanoporous MOFs, MIL-47, MIL-53(Cr, Al, Ga) and MIL-101(Cr). *Dalton Trans.* [Online] 45 (23), 9565–9573. Available from: doi:10.1039/C6DT01282E.
- Loiseau, T., Lecroq, L., Volkringer, C., Marrot, J., et al. (2006) MIL-96, a porous aluminum trimesate 3D structure constructed from a hexagonal network of 18-membered rings and μ_3 -oxo-centered trinuclear units. *Journal of the American Chemical Society*. [Online] 128 (31), 10223–10230. Available from: doi:10.1021/ja0621086.
- Long, P., Wu, H., Zhao, Q., Wang, Y., et al. (2011) Solvent effect on the synthesis of MIL-96 (Cr) and MIL-100 (Cr). *Microporous and Mesoporous Materials*. 142 (2–3), 489–493.
- Lorenzo, M., Campo, J. & Picó, Y. (2018) Analytical challenges to determine emerging persistent organic pollutants in aquatic ecosystems. *TrAC Trends in Analytical Chemistry*. 103, 137–155.
- Lorenzo, M., Campo, J., Suárez-Varela, M.M. & Picó, Y. (2019) Occurrence, distribution and behavior of emerging persistent organic pollutants (POPs) in a Mediterranean wetland protected area. *Science of The Total Environment*. 646, 1009–1020.
- Lorignon, F., Gossard, A. & Carboni, M. (2020) Hierarchically porous monolithic MOFs: An ongoing challenge for industrial-scale effluent treatment. *Chemical Engineering Journal*. 393, 124765.
- Los Angeles County Sanitation Districts (2021) *Wastewater Treatment Process*. [Online]. 2021. Available from: <https://www.lacsd.org/services/wastewater-sewage/facilities/wastewater-treatment-process> [Accessed: 28 September 2021].
- Low, J.J., Benin, A.I., Jakubczak, P., Abrahamian, J.F., et al. (2009) Virtual High Throughput Screening Confirmed Experimentally: Porous Coordination Polymer Hydration. *Journal of the American Chemical Society*. [Online] 131 (43), 15834–15842. Available from: doi:10.1021/ja9061344.
- Lu, P., Wu, Y., Kang, H., Wei, H., et al. (2014) What can pK_a and NBO charges of the ligands tell us about the water and thermal stability of metal organic frameworks? *J. Mater. Chem. A*. [Online] 2 (38), 16250–16267. Available from: doi:10.1039/C4TA03154G.

- Lu, Q. & Sorial, G.A. (2007) The effect of functional groups on oligomerization of phenolics on activated carbon. *Journal of Hazardous Materials*. 148 (1–2), 436–445.
- Lu, X., Zhang, L., Wang, X., Gao, M., et al. (2020) Rapid increases in warm-season surface ozone and resulting health impact in China since 2013. *Environmental Science & Technology Letters*. 7 (4), 240–247.
- Lu, X.F., Fang, Y., Luan, D. & Lou, X.W.D. (2021) Metal–organic frameworks derived functional materials for electrochemical energy storage and conversion: a mini review. *Nano Letters*. 21 (4), 1555–1565.
- Luo, Z., Chen, H., Wu, S., Yang, C., et al. (2019) Enhanced removal of bisphenol A from aqueous solution by aluminum-based MOF/sodium alginate-chitosan composite beads. *Chemosphere*. 237, 124493.
- Lustig, W.P., Mukherjee, S., Rudd, N.D., Desai, A. V., et al. (2017) Metal–organic frameworks: functional luminescent and photonic materials for sensing applications. *Chem. Soc. Rev.* [Online] 46 (11), 3242–3285. Available from: doi:10.1039/C6CS00930A.
- Ma, X., Wang, W., Sun, C., Li, H., et al. (2021) Adsorption performance and kinetic study of hierarchical porous Fe-based MOFs for toluene removal. *Science of The Total Environment*. 793, 148622.
- Machado, L.M.M., Lütke, S.F., Perondi, D., Godinho, M., et al. (2020) Treatment of effluents containing 2-chlorophenol by adsorption onto chemically and physically activated biochars. *Journal of Environmental Chemical Engineering*. 8 (6), 104473.
- Mahalakshmi, G. & Balachandran, V. (2014) FT-IR and FT-Raman spectra, normal coordinate analysis and ab initio computations of Trimesic acid. *Spectrochimica Acta Part A: Molecular and Biomolecular Spectroscopy*. 124, 535–547.
- Mahdavi, H., Ahmadian-Alam, L. & Molavi, H. (2015) Grafting of sulfonated monomer onto an amino-silane functionalized 2-aminoterephthalate metal–organic framework via surface-initiated redox polymerization: proton-conducting solid electrolytes. *Polymer International*. 64 (11), 1578–1584.
- Mancini, F.R., Cano-Sancho, G., Gambaretti, J., Marchand, P., et al. (2020) Perfluorinated alkylated substances serum concentration and breast cancer risk: Evidence from a nested case-control study in the French E3N cohort. *International Journal of Cancer*. 146 (4),

917–928.

- Mandić, M., Todić, B., Živanić, L., Nikačević, N., et al. (2017) Effects of catalyst activity, particle size and shape, and process conditions on catalyst effectiveness and methane selectivity for Fischer–Tropsch reaction: a modeling study. *Industrial & Engineering Chemistry Research*. 56 (10), 2733–2745.
- Martínez-Jardines, M., Martínez-Hernández, S., Texier, A.-C. & Cuervo-López, F. (2018) 2-Chlorophenol consumption by cometabolism in nitrifying SBR reactors. *Chemosphere*. 212, 41–49.
- Mattiuzzi, A., Troian-Gautier, L., Mertens, J., Reniers, F., et al. (2020) Robust hydrophobic gold, glass and polypropylene surfaces obtained through a nanometric covalently bound organic layer. *RSC Advances*. 10 (23), 13553–13561.
- McDonald, B.C., de Gouw, J.A., Gilman, J.B., Jathar, S.H., et al. (2018) Volatile chemical products emerging as largest petrochemical source of urban organic emissions. *Science*. 359 (6377), 760–764.
- McNamara, J.D., Franco, R., Mimna, R. & Zappa, L. (2018) Comparison of activated carbons for removal of perfluorinated compounds from drinking water. *Journal-American Water Works Association*. 110 (1), E2–E14.
- Meng, P., Deng, S., Du, Z., Wang, B., et al. (2017) Effect of hydro-oleophobic perfluorocarbon chain on interfacial behavior and mechanism of perfluorooctane sulfonate in oil-water mixture. *Scientific Reports*. 7 (1), 1–11.
- Micromeritics (2020) *An introduction to non-local density functional theory models for porosity characterization*. [Online]. Available from: https://www.micromeritics.com/Repository/Files/WP_An_Introduction_to_Non-Local_Density_Functional_Theory.pdf.
- Miguel, G.S., Fowler, G.D. & Sollars, C.J. (1998) Pyrolysis of tire rubber: porosity and adsorption characteristics of the pyrolytic chars. *Industrial & Engineering Chemistry Research*. 37 (6), 2430–2435.
- Mon, M., Bruno, R., Ferrando-Soria, J., Armentano, D., et al. (2018) Metal-organic framework technologies for water remediation: Towards a sustainable ecosystem. *Journal of Materials Chemistry A*. [Online] 6 (12), 4912–4947. Available from: doi:10.1039/c8ta00264a.

- Montero-Montoya, R., López-Vargas, R. & Arellano-Aguilar, O. (2018) Volatile organic compounds in air: sources, distribution, exposure and associated illnesses in children. *Annals of Global Health*. 84 (2), 225.
- Moreno-Castilla, C. (2004) Adsorption of organic molecules from aqueous solutions on carbon materials. *Carbon*. 42 (1), 83–94.
- Morlay, C., Pilshofer, M., Quivet, E., Faure, R., et al. (2005) Adsorption isotherms of an imidazolinone herbicide on activated carbon. In: *Abstracts of Papers of the American Chemical Society*. 2005 p. U851.
- Morris, W., Wang, S., Cho, D., Auyeung, E., et al. (2017) Role of Modulators in Controlling the Colloidal Stability and Polydispersity of the UiO-66 Metal–Organic Framework. *ACS Applied Materials and Interfaces*. 9 (39), 33413–33418.
- Mukherjee, S., Sharma, S. & Ghosh, S.K. (2019) Hydrophobic metal-organic frameworks: Potential toward emerging applications. *APL Materials*. 7 (5), 50701.
- Munief, W.-M., Heib, F., Hempel, F., Lu, X., et al. (2018) Silane deposition via gas-phase evaporation and high-resolution surface characterization of the ultrathin siloxane coatings. *Langmuir*. 34 (35), 10217–10229.
- Namasivayam, C. & Kavitha, D. (2003) Adsorptive removal of 2-chlorophenol by low-cost coir pith carbon. *Journal of Hazardous Materials*. 98 (1–3), 257–274.
- Nandiyanto, A.B.D., He, X. & Wang, W.-N. (2019) Colloid-Assisted Growth of Metal-Organic Framework Nanoparticles. *CrystEngComm*. [Online] 1, 2268–2272. Available from: doi:10.1039/c9ce00033j.
- Netzsch (2021) *Thermogravimetric Analysis (TGA)*. [Online]. 2021. Available from: <https://www.netzsch-thermal-analysis.com/en/contract-testing/methods/thermogravimetric-analysis/> [Accessed: 14 September 2021].
- Ng, E.-P. & Mintova, S. (2008) Nanoporous materials with enhanced hydrophilicity and high water sorption capacity. *Microporous and Mesoporous Materials*. 114 (1–3), 1–26.
- Norris, C., Fang, L., Barkjohn, K.K., Carlson, D., et al. (2019) Sources of volatile organic compounds in suburban homes in Shanghai, China, and the impact of air filtration on compound concentrations. *Chemosphere*. 231, 256–268.
- Notestein, J.M., Katz, A. & Iglesia, E. (2006) Energetics of small molecule and water complexation in hydrophobic calixarene cavities. *Langmuir*. 22 (9), 4004–4014.

- Okolo, B., Park, C. & Keane, M.A. (2000) Interaction of phenol and chlorophenols with activated carbon and synthetic zeolites in aqueous media. *Journal of Colloid and Interface Science*. 226 (2), 308–317.
- Ortega-Méndez, J.A., Herrera-Melián, J.A., Araña, J., Espino-Estévez, M.R., et al. (2017) Performance and Economic Assessment of the Treatment of Phenol with TiO₂ Photocatalysis, Photo-Fenton, Biological Aerated Filter, and Wetland Reactors. *Chemical Engineering & Technology*. 40 (6), 1165–1175.
- Osmari, T.A., Gallon, R., Schwaab, M., Barbosa-Coutinho, E., et al. (2013) Statistical analysis of linear and non-linear regression for the estimation of adsorption isotherm parameters. *Adsorption Science & Technology*. 31 (5), 433–458.
- Padial, N.M., Quartapelle Procopio, E., Montoro, C., López, E., et al. (2013) Highly hydrophobic isorecticular porous metal–organic frameworks for the capture of harmful volatile organic compounds. *Angewandte Chemie International Edition*. 52 (32), 8290–8294.
- Pan, W., Fu, J. & Zhang, A. (2017) Theoretical study on the formation mechanism of pre-intermediates for PXDD/Fs from 2-Bromophenol and 2-Chlorophenol precursors via radical/molecule reactions. *Environmental Pollution*. 225, 439–449.
- Pan, Y., Li, Z., Zhang, Z., Tong, X.-S., et al. (2016) Adsorptive removal of phenol from aqueous solution with zeolitic imidazolate framework-67. *Journal of Environmental Management*. 169, 167–173.
- Paranychianakis, N. V, Salgot, M., Snyder, S.A. & Angelakis, A.N. (2015) Water reuse in EU states: necessity for uniform criteria to mitigate human and environmental risks. *Critical Reviews in Environmental Science and Technology*. 45 (13), 1409–1468.
- Park, J.M. & Jhung, S.H. (2020) A remarkable adsorbent for removal of bisphenol S from water: Aminated metal-organic framework, MIL-101-NH₂. *Chemical Engineering Journal*. 396, 125224.
- Pei, Y., Qin, J., Wang, J. & Hu, Y. (2021) Fe-based metal organic framework derivative with enhanced Lewis acidity and hierarchical pores for excellent adsorption of oxygenated volatile organic compounds. *Science of The Total Environment*. 148132.
- Perrich, J.R. (2018) *Activated Carbon Adsorption For Wastewater Treatment*. [Online]. CRC Press. Available from: <https://books.google.co.uk/books?id=oLpHDwAAQBAJ>.

- Pi, Y., Li, X., Xia, Q., Wu, J., et al. (2018) Adsorptive and photocatalytic removal of Persistent Organic Pollutants (POPs) in water by metal-organic frameworks (MOFs). *Chemical Engineering Journal*. [Online] 337 (December 2017), 351–371. Available from: doi:10.1016/j.cej.2017.12.092.
- Piekarski, D.J., Diaz, K.R. & McNERney, M.W. (2020) Perfluoroalkyl chemicals in neurological health and disease: Human concerns and animal models. *Neurotoxicology*. 77, 155–168.
- Pollack, A.Z., Mumford, S.L., Krall, J.R., Carmichael, A.E., et al. (2018) Exposure to bisphenol A, chlorophenols, benzophenones, and parabens in relation to reproductive hormones in healthy women: a chemical mixture approach. *Environment International*. 120, 137–144.
- Portilla, L. & Halik, M. (2014) Smoothly tunable surface properties of aluminum oxide core-shell nanoparticles by a mixed-ligand approach. *ACS Applied Materials & Interfaces*. 6 (8), 5977–5982.
- Pustovarenko, A., Goesten, M.G., Sachdeva, S., Shan, M., et al. (2018) Nanosheets of Nonlayered Aluminum Metal–Organic Frameworks through a Surfactant-Assisted Method. *Advanced Materials*. 30 (26), 1707234.
- Qin, C., Wen, G., Wang, X., Song, L., et al. (2011) Ultra-long Sialon nanobelts: large-scale synthesis via a pressure enhanced CVD process and photoluminescence characteristics. *Journal of Materials Chemistry*. 21 (16), 5985–5991.
- Rajabi, H., Mosleh, M.H., Mandal, P., Lea-Langton, A., et al. (2021) Sorption behaviour of xylene isomers on biochar from a range of feedstock. *Chemosphere*. 268, 129310.
- Rallapalli, P., Raj, M.C., Senthilkumar, S., Somani, R.S., et al. (2016) HF-free synthesis of MIL-101 (Cr) and its hydrogen adsorption studies. *Environmental Progress & Sustainable Energy*. 35 (2), 461–468.
- Rasheed, T., Bilal, M., Hassan, A.A., Nabeel, F., et al. (2020) Environmental threatening concern and efficient removal of pharmaceutically active compounds using metal-organic frameworks as adsorbents. *Environmental Research*. 185, 109436.
- Rashtian, J., Chavkin, D.E. & Merhi, Z. (2019) Water and soil pollution as determinant of water and food quality/contamination and its impact on female fertility. *Reproductive Biology and Endocrinology*. 17 (1), 5.

- Raza, W., Lee, J., Raza, N., Luo, Y., et al. (2019) Removal of phenolic compounds from industrial waste water based on membrane-based technologies. *Journal of Industrial and Engineering Chemistry*. 71, 1–18.
- Rellegadla, S., Prajapat, G. & Agrawal, A. (2017) Polymers for enhanced oil recovery: fundamentals and selection criteria. *Applied Microbiology and Biotechnology*. 101 (11), 4387–4402.
- Ren, J., Dyosiba, X., Musyoka, N.M., Langmi, H.W., et al. (2016) Green synthesis of chromium-based metal-organic framework (Cr-MOF) from waste polyethylene terephthalate (PET) bottles for hydrogen storage applications. *International Journal of Hydrogen Energy*. [Online] 41 (40), 18141–18146. Available from: doi:10.1016/j.ijhydene.2016.08.040.
- Riahi, K., Chaabane, S. & Thayer, B. Ben (2017) A kinetic modeling study of phosphate adsorption onto Phoenix dactylifera L. date palm fibers in batch mode. *Journal of Saudi Chemical Society*. 21, S143–S152.
- Richardson, S.D. (2008) Environmental Mass Spectrometry: Emerging Contaminants and Current Issues. *Analytical Chemistry*. [Online] 80 (12), 4373–4402. Available from: doi:10.1021/ac202903d.
- Rideh, L., Wehrer, A., Ronze, D. & Zoulalian, A. (1999) Modelling of the kinetic of 2-chlorophenol catalytic photooxidation. *Catalysis Today*. 48 (1–4), 357–362.
- Rieth, A.J. & Dincă, M. (2018) Tricking Inert Metals into Water-Absorbing MOFs. *Joule*. 2 (1), 18–20.
- Ritchie, H. & Roser, M. (2020) *CO2 and Greenhouse Gas Emissions*. [Online]. 2020. OurWorldInData.org. Available from: <https://ourworldindata.org/co2-and-other-greenhouse-gas-emissions> [Accessed: 28 July 2021].
- Rivera-Utrilla, J., Sánchez-Polo, M., Ferro-García, M.Á., Prados-Joya, G., et al. (2013) Pharmaceuticals as emerging contaminants and their removal from water. A review. *Chemosphere*. [Online] 93 (7), 1268–1287. Available from: doi:10.1016/j.chemosphere.2013.07.059.
- Roginsky, S. & Zeldovich, Y.B. (1934) The catalytic oxidation of carbon monoxide on manganese dioxide. *Acta Phys. Chem. USSR*. 1 (554), 2019.
- Rojas, S. & Horcajada, P. (2020) Metal–organic frameworks for the removal of emerging

- organic contaminants in water. *Chemical Reviews*. 120 (16), 8378–8415.
- Rout, P.R., Zhang, T.C., Bhunia, P. & Surampalli, R.Y. (2021) Treatment technologies for emerging contaminants in wastewater treatment plants: A review. *Science of The Total Environment*. 753, 141990.
- Safy, M.E.A., Amin, M., Haikal, R.R., Elshazly, B., et al. (2020) Probing the Water Stability Limits and Degradation Pathways of Metal-Organic Frameworks (MOFs). *Chemistry–A European Journal*. 26 (31), 7109–7117.
- Sah, A., Castricum, H.L., Blik, A., Blank, D.H.A., et al. (2004) Hydrophobic modification of γ -alumina membranes with organochlorosilanes. *Journal of Membrane Science*. 243 (1–2), 125–132.
- Saha, R., Nandi, R. & Saha, B. (2011) Sources and toxicity of hexavalent chromium. *Journal of Coordination Chemistry*. 64 (10), 1782–1806.
- Said, K.A.M., Ismail, A.F., Karim, Z.A., Abdullah, M.S., et al. (2021) A review of technologies for the phenolic compounds recovery and phenol removal from wastewater. *Process Safety and Environmental Protection*. 151, 257–289.
- Salari, M., Dehghani, M.H., Azari, A., Motevalli, M.D., et al. (2019) High performance removal of phenol from aqueous solution by magnetic chitosan based on response surface methodology and genetic algorithm. *Journal of Molecular Liquids*. 285, 146–157.
- Salthammer, T. (2016) Very volatile organic compounds: an understudied class of indoor air pollutants. *Indoor Air*. 26 (1), 25–38.
- Sanil, E.S., Cho, K.-H., Hong, D.-Y., Lee, J.S., et al. (2015) A polyhedral oligomeric silsesquioxane functionalized copper trimesate. *Chemical Communications*. 51 (40), 8418–8420.
- Saponar, A., Popovici, E.-J., Perhaita, I., Nemes, G., et al. (2012) Thermal behaviour of some ester derivatives of p-tert-butyl calix [n] arene. *Journal of Thermal Analysis and Calorimetry*. 110 (1), 349–356.
- Saputera, W.H., Putrie, A.S., Esmailpour, A.A., Sasongko, D., et al. (2021) Technology Advances in Phenol Removals: Current Progress and Future Perspectives. *Catalysts*. 11 (8), 998.
- Sauvé, S. & Desrosiers, M. (2014) A review of what is an emerging contaminant. *Chemistry*

Central Journal. 8 (1), 15.

- Scher, D.P., Kelly, J.E., Huset, C.A., Barry, K.M., et al. (2018) Occurrence of perfluoroalkyl substances (PFAS) in garden produce at homes with a history of PFAS-contaminated drinking water. *Chemosphere*. 196, 548–555.
- Schulz, M., Gehl, A., Schlenkrich, J., Schulze, H.A., et al. (2018) A Calixarene-Based Metal–Organic Framework for Highly Selective NO₂ Detection. *Angewandte Chemie International Edition*. 57 (39), 12961–12965.
- Selvaraj, M., Kim, B.H. & Lee, T.G. (2005) FTIR studies on selected mesoporous metallosilicate molecular sieves. *Chemistry Letters*. [Online] 34 (9), 1290–1291. Available from: doi:10.1246/cl.2005.1290.
- Seo, Y.-K., Yoon, J.W., Lee, J.S., Lee, U.-H., et al. (2012) Large scale fluorine-free synthesis of hierarchically porous iron (III) trimesate MIL-100 (Fe) with a zeolite MTN topology. *Microporous and Mesoporous Materials*. 157, 137–145.
- Seoane, B., Castellanos, S., Dikhtiarenko, A., Kapteijn, F., et al. (2016) Multi-scale crystal engineering of metal organic frameworks. *Coordination Chemistry Reviews*. 307, 147–187.
- Shah, A.I., Dar, M.U.D., Bhat, R.A., Singh, J.P., et al. (2020) Prospectives and challenges of wastewater treatment technologies to combat contaminants of emerging concerns. *Ecological Engineering*. 152, 105882.
- Shah, B.B., Kundu, T. & Zhao, D. (2019) Mechanical Properties of Shaped Metal–Organic Frameworks. *Topics in Current Chemistry*. [Online] 377 (5), 25. Available from: doi:10.1007/s41061-019-0250-7.
- Sharanyakanth, P.S. & Mahendran, R. (2020) Synthesis of metal-organic frameworks (MOFs) and its application in food packaging: A critical review. *Trends in Food Science & Technology*.
- Sharma, A. & Lee, B.-K. (2016) Rapid photo-degradation of 2-chlorophenol under visible light irradiation using cobalt oxide-loaded TiO₂/reduced graphene oxide nanocomposite from aqueous media. *Journal of Environmental Management*. 165, 1–10.
- Shen, K., Zhang, L., Chen, X., Liu, L., et al. (2018) Ordered macro-microporous metal-organic framework single crystals. *Science*. 359 (6372), 206–210.
- Shi, J., Han, R., Lu, S. & Liu, Q. (2021) A metal-OH group modification strategy to prepare

- highly-hydrophobic MIL-53-Al for efficient acetone capture under humid conditions. *Journal of Environmental Sciences*. 107, 111–123.
- Shi, X., Zhang, X., Bi, F., Zheng, Z., et al. (2020) Effective toluene adsorption over defective UiO-66-NH₂: An experimental and computational exploration. *Journal of Molecular Liquids*. 316, 113812.
- Shih, K. & Wang, F. (2013) Adsorption behavior of perfluorochemicals (PFCs) on boehmite: influence of solution chemistry. *Procedia Environmental Sciences*. 18, 106–113.
- Shimadzu (2012) Tips for practical HPLC analysis - Separation Know-how. *LC World Talk Special Issue*. 2.
- Shuai, J., Kim, S., Ryu, H., Park, J., et al. (2018) Health risk assessment of volatile organic compounds exposure near Daegu dyeing industrial complex in South Korea. *BMC Public Health*. 18 (1), 1–13.
- Sigma-Aldrich (2021a) *Basolite® A100*. [Online]. 2021. Available from: <https://www.sigmaaldrich.com/GB/en/product/aldrich/688738?context=product> [Accessed: 12 October 2021].
- Sigma-Aldrich (2021b) *Basolite® C300*. [Online]. 2021. Available from: <https://www.sigmaaldrich.com/GB/en/product/aldrich/688614> [Accessed: 12 October 2021].
- Sigma-Aldrich (2021c) *Basolite® F300*. [Online]. 2021. Available from: <https://www.sigmaaldrich.com/GB/en/product/aldrich/690872?context=product> [Accessed: 12 October 2021].
- Silva, P., Vilela, S.M.F., Tome, J.P.C. & Paz, F.A.A. (2015) Multifunctional metal–organic frameworks: from academia to industrial applications. *Chemical Society Reviews*. 44 (19), 6774–6803.
- Simonin, J.-P. (2016) On the comparison of pseudo-first order and pseudo-second order rate laws in the modeling of adsorption kinetics. *Chemical Engineering Journal*. 300, 254–263.
- Sindoro, M., Jee, A.Y. & Granick, S. (2013) Shape-selected colloidal MOF crystals for aqueous use. *Chemical Communications*. [Online] 49 (83), 9576–9578. Available from: doi:10.1039/c3cc45935g.
- Sini, K., Bourgeois, D., Idouhar, M., Carboni, M., et al. (2018) Metal-organic framework

- sorbents for the removal of perfluorinated compounds in an aqueous environment. *New Journal of Chemistry*. [Online] 42 (22), 17889–17894. Available from: doi:10.1039/c8nj03312a.
- Sini, K., Bourgeois, D., Idouhar, M., Carboni, M., et al. (2019) Metal-organic frameworks cavity size effect on the extraction of organic pollutants. *Materials Letters*. 250, 92–95.
- Smolin, S.K. (2018) Self-Regeneration of a Fixed Bed of Biologically Activated Carbon During Removal of 2-Chlorophenol from Water. *Journal of Water Chemistry and Technology*. 40 (5), 258–264.
- Song, X., Guo, L., Liao, X., Liu, J., et al. (2017) Hollow carbon nanopolyhedra for enhanced electrocatalysis via confined hierarchical porosity. *Small*. 13 (23), 1700238.
- Sophia A, C. & Lima, E.C. (2018) Removal of emerging contaminants from the environment by adsorption. *Ecotoxicology and Environmental Safety*. 150, 1–17.
- Sosa, J.D., Bennett, T.F., Nelms, K.J., Liu, B.M., et al. (2018) Metal–organic framework hybrid materials and their applications. *Crystals*. 8 (8), 325.
- Sousa, J.C.G., Ribeiro, A.R., Barbosa, M.O., Pereira, M.F.R., et al. (2017) A review on environmental monitoring of water organic pollutants identified by EU guidelines. *Journal of Hazardous Materials*. [Online] 344, 146–162. Available from: doi:10.1016/j.jhazmat.2017.09.058.
- Sparks, D.L. (2003) Sorption Phenomena on Soils. In: Charles R. Crumly (ed.). *Environmental Soil Chemistry*. 2nd edition. [Online]. Burlington, Academic Press. pp. 133–186. Available from: doi:https://doi.org/10.1016/B978-012656446-4/50005-0.
- Spycher, B.D., Lupatsch, J.E., Huss, A., Rischewski, J., et al. (2017) Parental occupational exposure to benzene and the risk of childhood cancer: A census-based cohort study. *Environment International*. 108, 84–91.
- Stockholm Convention Secretariat United Nations Environment (2017) The 16 New POPs. In: *Stockholm Convention on Persistent Organic Pollutants (POPs)*. 2017 UN Environment. pp. 1–25.
- Sudan, S., Gładysiak, A., Valizadeh, B., Lee, J.-H., et al. (2020) Sustainable Capture of Aromatic Volatile Organic Compounds by a Pyrene-Based Metal–Organic Framework under Humid Conditions. *Inorganic Chemistry*. 59 (13), 9029–9036.
- Sun, D., Adiyala, P.R., Yim, S. & Kim, D. (2019) Pore-Surface Engineering by Decorating

- Metal-Oxo Nodes with Phenylsilane to Give Versatile Super-Hydrophobic Metal–Organic Frameworks (MOFs). *Angewandte Chemie*. 131 (22), 7483–7487.
- Sun, Q., He, H., Gao, W.-Y., Aguila, B., et al. (2016) Imparting amphiphobicity on single-crystalline porous materials. *Nature Communications*. 7, 13300.
- Sun, Y., Sun, Q., Huang, H., Aguila, B., et al. (2017) A molecular-level superhydrophobic external surface to improve the stability of metal–organic frameworks. *Journal of Materials Chemistry A*. 5 (35), 18770–18776.
- Sun, Z., Zhang, J., Yang, J., Li, J., et al. (2018) Acclimation of 2-Chlorophenol-Biodegrading Activated Sludge and Microbial Community Analysis. *Water Environment Research*. 90 (12), 2083–2089.
- Sunderland, E.M., Hu, X.C., Dassuncao, C., Tokranov, A.K., et al. (2019) A review of the pathways of human exposure to poly-and perfluoroalkyl substances (PFASs) and present understanding of health effects. *Journal of Exposure Science & Environmental Epidemiology*. 29 (2), 131–147.
- Szulejko, J.E., Kim, K.-H. & Parise, J. (2019) Seeking the most powerful and practical real-world sorbents for gaseous benzene as a representative volatile organic compound based on performance metrics. *Separation and Purification Technology*. 212, 980–985.
- Szulejko, J.E. & Kim, K.H. (2019) Is the maximum adsorption capacity obtained at high VOC pressures (>1000 Pa) really meaningful in real-world applications for the sorptive removal of VOCs under ambient conditions (<1 Pa)? *Separation and Purification Technology*. [Online] 228 (September 2018), 115729. Available from: doi:10.1016/j.seppur.2019.115729.
- Taylor, J.M., Dawson, K.W. & Shimizu, G.K.H. (2013) A water-stable metal-organic framework with highly acidic pores for proton-conducting applications. *Journal of the American Chemical Society*. [Online] 135 (4), 1193–1196. Available from: doi:10.1021/ja310435e.
- Teodosiu, C., Gilca, A.-F., Barjoveanu, G. & Fiore, S. (2018) Emerging pollutants removal through advanced drinking water treatment: a review on processes and environmental performances assessment. *Journal of Cleaner Production*. 197, 1210–1221.
- The United Kingdom Parliamentary Office of Science and Technology (2018) *Persistent Chemical Pollutants*. (579).

- Thommes, M., Kaneko, K., Neimark, A. V., Olivier, J.P., et al. (2015) Physisorption of gases, with special reference to the evaluation of surface area and pore size distribution (IUPAC Technical Report). *Pure and Applied Chemistry*. [Online] 87 (9–10), 1051–1069. Available from: doi:10.1515/pac-2014-1117.
- Thurgood, P., Baratchi, S., Szydzik, C., Mitchell, A., et al. (2017) Porous PDMS structures for the storage and release of aqueous solutions into fluidic environments. *Lab on a Chip*. 17 (14), 2517–2527.
- Tian, N., Jia, Q., Su, H., Zhi, Y., et al. (2016) The synthesis of mesostructured NH₂-MIL-101 (Cr) and kinetic and thermodynamic study in tetracycline aqueous solutions. *Journal of Porous Materials*. 23 (5), 1269–1278.
- Tian, T., Zeng, Z., Vulpe, D., Casco, M.E., et al. (2018) A sol–gel monolithic metal–organic framework with enhanced methane uptake. *Nature Materials*. 17 (2), 174.
- Trung, T.K., Ramsahye, N.A., Trens, P., Tanchoux, N., et al. (2010) Adsorption of C₅–C₉ hydrocarbons in microporous MOFs MIL-100 (Cr) and MIL-101 (Cr): A manometric study. *Microporous and Mesoporous Materials*. 134 (1–3), 134–140.
- Tufail, A., Price, W.E., Mohseni, M., Pramanik, B.K., et al. (2021) A critical review of advanced oxidation processes for emerging trace organic contaminant degradation: Mechanisms, factors, degradation products, and effluent toxicity. *Journal of Water Process Engineering*. 40, 101778.
- UK DEFRA (2017) National Implementation Plan for the Stockholm Convention on Persistent Organic Pollutants. *United Kingdom of Great Britain and Northern Ireland*. [Online]. 1 (March). Available from: www.nationalarchives.gov.uk/doc/open-government-licence/version/3/ <https://consult.defra.gov.uk/eu-environment/uk-nip-for-stockholm-convention-on-pops-2017/> www.gov.uk/defra.
- United Nations World Water Assessment Programme (2018) The United Nations World Water Development Report 2018: Nature-Based Solutions for Water. *UN Water Report*. [Online]. Available from: doi:<https://unesdoc.unesco.org/ark:/48223/pf0000261424>.
- United States Department of Labor (2021a) *Substance Safety Data Sheet, Benzene*. [Online]. 2021. 1910.1028 App A Occupational Safety and Health Standards. Available from: [https://www.osha.gov/laws-regs/regulations/standardnumber/1910/1910.1028AppA#:~:text=1.,for any 15-minute period](https://www.osha.gov/laws-regs/regulations/standardnumber/1910/1910.1028AppA#:~:text=1.,for any 15-minute period.). [Accessed: 26 May 2021].

- United States Department of Labor (2021b) *Toluene Occupational Exposure Limits*. [Online]. 2021. Occupational Safety and Health Administration. Available from: <https://www.osha.gov/toluene/occupational-exposure-limits> [Accessed: 5 May 2021].
- United States Environmental Protection Agency (1984) Method for the determination of volatile organic compounds in ambient air using Tenax adsorption and gas chromatography/mass spectrometry (GC/MS). *U.S. EPA Technical Assistance Document*. [Online] 13 (3), 576. Available from: <https://www.epa.gov/sites/default/files/2019-11/documents/to-1.pdf>.
- United States Environmental Protection Agency (2014) Priority Pollutant List. *Effluent Guidelines*. [Online]. Available from: <https://www.epa.gov/eg/toxic-and-priority-pollutants-under-clean-water-act>.
- United States Environmental Protection Agency (2021) *Technical Overview of Volatile Organic Compounds*. [Online]. 2021. Indoor Air Quality. Available from: <https://www.epa.gov/indoor-air-quality-iaq/technical-overview-volatile-organic-compounds> [Accessed: 21 June 2021].
- Ursueguía, D., Díaz, E. & Ordóñez, S. (2020) Densification-Induced Structure Changes in Basolite MOFs: Effect on Low-Pressure CH₄ Adsorption. *Nanomaterials*. 10 (6), 1089.
- Valsecchi, S., Conti, D., Crebelli, R., Polesello, S., et al. (2017) Deriving environmental quality standards for perfluorooctanoic acid (PFOA) and related short chain perfluorinated alkyl acids. *Journal of Hazardous Materials*. 323, 84–98.
- Vashi, H., Iorhemen, O.T. & Tay, J.H. (2018) Aerobic granulation: A recent development on the biological treatment of pulp and paper wastewater. *Environmental Technology & Innovation*. 9, 265–274.
- Vecitis, C.D., Park, H., Cheng, J., Mader, B.T., et al. (2009) Treatment technologies for aqueous perfluorooctanesulfonate (PFOS) and perfluorooctanoate (PFOA). *Frontiers of Environmental Science & Engineering in China*. 3 (2), 129–151.
- Vellingiri, K., Kumar, P., Deep, A. & Kim, K.-H. (2017) Metal-organic frameworks for the adsorption of gaseous toluene under ambient temperature and pressure. *Chemical Engineering Journal*. 307, 1116–1126.
- Vikrant, K., Qu, Y., Szulejko, J.E., Kumar, V., et al. (2020) Utilization of metal–organic frameworks for the adsorptive removal of an aliphatic aldehyde mixture in the gas

- phase. *Nanoscale*. 12 (15), 8330–8343.
- Vilela, S.M.F., Salcedo-Abraira, P., Micheron, L., Solla, E.L., et al. (2018) A robust monolithic metal–organic framework with hierarchical porosity. *Chemical Communications*. 54 (93), 13088–13091.
- Van Vleet, M.J., Weng, T., Li, X. & Schmidt, J.R. (2018) In situ, time-resolved, and mechanistic studies of metal–organic framework nucleation and growth. *Chemical Reviews*. 118 (7), 3681–3721.
- Van de Voorde, B., Bueken, B., Denayer, J. & De Vos, D. (2014) Adsorptive separation on metal–organic frameworks in the liquid phase. *Chemical Society Reviews*. [Online] 43 (16), 5766–5788. Available from: doi:10.1039/C4CS00006D.
- Vundala, J. (2018) *Pre-oxidation and adsorption with powdered activated carbon for taste and odor control and optimizing coagulation for dissolved organic carbon removal*. [Online]. Colorado State University. Available from: https://mountainscholar.org/bitstream/handle/10217/193084/Vundala_colostate_0053N_14934.pdf?sequence=1.
- Wagner, M., Lin, K.-Y.A., Oh, W.-D. & Lisak, G. (2021) Metal-organic frameworks for pesticidal persistent organic pollutants detection and adsorption—A mini review. *Journal of Hazardous Materials*. 413, 125325.
- Wang, B., Wang, P., Xie, L.-H., Lin, R.-B., et al. (2019a) A stable zirconium based metal-organic framework for specific recognition of representative polychlorinated dibenzo-p-dioxin molecules. *Nature Communications*. 10 (1), 1–8.
- Wang, C., Liu, X., Keser Demir, N., Chen, J.P., et al. (2016) Applications of water stable metal–organic frameworks. *Chem. Soc. Rev.* [Online] 45 (18), 5107–5134. Available from: doi:10.1039/C6CS00362A.
- Wang, F. & Shih, K. (2011) Adsorption of perfluorooctanesulfonate (PFOS) and perfluorooctanoate (PFOA) on alumina: Influence of solution pH and cations. *Water Research*. 45 (9), 2925–2930.
- Wang, J. & Guo, X. (2020) Adsorption isotherm models: Classification, physical meaning, application and solving method. *Chemosphere*. 258, 127279.
- Wang, J., Muhammad, Y., Gao, Z., Shah, S.J., et al. (2021) Implanting polyethylene glycol into MIL-101 (Cr) as hydrophobic barrier for enhancing toluene adsorption under highly

- humid environment. *Chemical Engineering Journal*. 404, 126562.
- Wang, Q., Xu, H. & Li, X. (2005) Solubilities of terephthalic acid in dimethyl sulfoxide+ water and in N, N-dimethylformamide+ water from (301.4 to 373.7) K. *Journal of Chemical & Engineering Data*. 50 (2), 719–721.
- Wang, R., Dong, X.-Y., Xu, H., Pei, R.-B., et al. (2014) A super water-stable europium–organic framework: guests inducing low-humidity proton conduction and sensing of metal ions. *Chemical Communications*. 50 (65), 9153–9156.
- Wang, S., McGuirk, C.M., d’Aquino, A., Mason, J.A., et al. (2018a) Metal–organic framework nanoparticles. *Advanced Materials*. 30 (37), 1800202.
- Wang, W., Mi, X., Shi, H., Zhang, X., et al. (2019b) Adsorption behaviour and mechanism of the PFOS substitute OBS (sodium p-perfluorous nonenoxybenzene sulfonate) on activated carbon. *Royal Society Open Science*. 6 (9), 191069.
- Wang, X., Ma, C., Xiao, J., Xia, Q., et al. (2018b) Benzene/toluene/water vapor adsorption and selectivity of novel C-PDA adsorbents with high uptakes of benzene and toluene. *Chemical Engineering Journal*. 335, 970–978.
- Wang, Z., DeWitt, J.C., Higgins, C.P. & Cousins, I.T. (2017) A never-ending story of per- and polyfluoroalkyl substances (PFASs)? *Environmental Science & Technology*. 51 (5), 2508–2518.
- Watanabe, S., Ohsaki, S., Hanafusa, T., Takada, K., et al. (2017) Synthesis of zeolitic imidazolate framework-8 particles of controlled sizes, shapes, and gate adsorption characteristics using a central collision-type microreactor. *Chemical Engineering Journal*. 313, 724–733.
- Weber, T.W. & Chakravorti, R.K. (1974) Pore and solid diffusion models for fixed-bed adsorbers. *AIChE Journal*. 20 (2), 228–238.
- Whang, G.D., Cho, Y.M., Park, H. & Jang, J.G. (2004) The removal of residual organic matter from biologically treated swine wastewater using membrane bioreactor process with powdered activated carbon. *Water Science and Technology*. 49 (5–6), 451–457.
- Woellner, M., Hausdorf, S., Klein, N., Mueller, P., et al. (2018) Adsorption and detection of hazardous trace gases by metal–organic frameworks. *Advanced Materials*. 30 (37), 1704679.
- World Health Organization (2003) Chlorophenols in drinking-water. *Guidelines for Drinking*

- Water Quality*. [Online]. 2. Available from: doi:10.1016/j.kjms.2011.05.002.
- Wragg, D.S., Johnsen, R.E., Norby, P. & Fjellvåg, H. (2010) The adsorption of methanol and water on SAPO-34: in situ and ex situ X-ray diffraction studies. *Microporous and Mesoporous Materials*. 134 (1–3), 210–215.
- Wu, J., Liu, J. & Chung, T. (2018) Structural Tuning of Polymers of Intrinsic Microporosity via the Copolymerization with Macrocyclic 4-tert-butylcalix [4] arene for Enhanced Gas Separation Performance. *Advanced Sustainable Systems*. 2 (10), 1800044.
- Wu, Z., Yuan, X., Zhong, H., Wang, H., et al. (2016) Enhanced adsorptive removal of p-nitrophenol from water by aluminum metal–organic framework/reduced graphene oxide composite. *Scientific Reports*. 6 (1), 1–13.
- Xian, S., Yu, Y., Xiao, J., Zhang, Z., et al. (2015) Competitive adsorption of water vapor with VOCs dichloroethane, ethyl acetate and benzene on MIL-101 (Cr) in humid atmosphere. *RSC Advances*. 5 (3), 1827–1834.
- Xiao, L., Ling, Y., Alsbaiee, A., Li, C., et al. (2017) β -Cyclodextrin Polymer Network Sequesters Perfluorooctanoic Acid at Environmentally Relevant Concentrations. *Journal of the American Chemical Society*. [Online] 139 (23), 7689–7692. Available from: doi:10.1021/jacs.7b02381.
- Xie, L.-H., Liu, X.-M., He, T. & Li, J.-R. (2018) Metal-organic frameworks for the capture of trace aromatic volatile organic compounds. *Chem*. 4 (8), 1911–1927.
- Xie, L.H., Xu, M.M., Liu, X.M., Zhao, M.J., et al. (2020) Hydrophobic Metal–Organic Frameworks: Assessment, Construction, and Diverse Applications. *Advanced Science*. [Online] 7 (4). Available from: doi:10.1002/advs.201901758.
- Xu, J., Liu, Z., Zhao, D., Gao, N., et al. (2020) Enhanced adsorption of perfluorooctanoic acid (PFOA) from water by granular activated carbon supported magnetite nanoparticles. *Science of The Total Environment*. 137757.
- Xu, X.-Y. & Yan, B. (2016) Nanoscale LnMOF-functionalized nonwoven fibers protected by a polydimethylsiloxane coating layer as a highly sensitive ratiometric oxygen sensor. *Journal of Materials Chemistry C*. 4 (36), 8514–8521.
- Xue, N., Wang, L., Pei, M., He, Y., et al. (2016) Preparation and characterization of sodium polyacrylate-grafted bentonite and its performance removing Pb²⁺ from aqueous solutions. *RSC Advances*. 6 (101), 98945–98951.

- Xue, W., Zhang, Z., Huang, H., Zhong, C., et al. (2019) Theoretical Insights into the Initial Hydrolytic Breakdown of HKUST-1. *The Journal of Physical Chemistry C*. 124 (3), 1991–2001.
- Yadav, D., Rangabhashiyam, S., Verma, P., Singh, P., et al. (2021) Environmental and health impacts of contaminants of emerging concerns: recent treatment challenges and approaches. *Chemosphere*. 272, 129492.
- Yadav, M. & Xu, Q. (2013) Catalytic chromium reduction using formic acid and metal nanoparticles immobilized in a metal–organic framework. *Chemical Communications*. 49 (32), 3327–3329.
- Yaghi, O.M., Li, G. & Li, H. (1995) Selective binding and removal of guests in a microporous metal–organic framework. *Nature*. 378 (6558), 703.
- Yanagita, K., Hwang, J., Shamim, J.A., Hsu, W.L., et al. (2019) Kinetics of Water Vapor Adsorption and Desorption in MIL-101 Metal-Organic Frameworks. *Journal of Physical Chemistry C*. [Online] 123 (1), 387–398. Available from: doi:10.1021/acs.jpcc.8b08211.
- Yang, C., Kaipa, U., Mather, Q.Z., Wang, X., et al. (2011a) Fluorous metal-organic frameworks with superior adsorption and hydrophobic properties toward oil spill cleanup and hydrocarbon storage. *Journal of the American Chemical Society*. [Online] 133 (45), 18094–18097. Available from: doi:10.1021/ja208408n.
- Yang, J. & Yang, Y. (2020) Metal–organic frameworks for biomedical applications. *Small*. 16 (10), 1906846.
- Yang, J., Zhang, Y.-B., Liu, Q., Trickett, C.A., et al. (2017a) Principles of designing extra-large pore openings and cages in zeolitic imidazolate frameworks. *Journal of the American Chemical Society*. 139 (18), 6448–6455.
- Yang, K., Sun, Q., Xue, F. & Lin, D. (2011b) Adsorption of volatile organic compounds by metal–organic frameworks MIL-101: Influence of molecular size and shape. *Journal of Hazardous Materials*. 195, 124–131.
- Yang, K., Xue, F., Sun, Q., Yue, R., et al. (2013) Adsorption of volatile organic compounds by metal-organic frameworks MOF-177. *Journal of Environmental Chemical Engineering*. [Online] 1 (4), 713–718. Available from: doi:10.1016/j.jece.2013.07.005.
- Yang, Q., Zhao, Q., Ren, S., Chen, Z., et al. (2017b) Assembly of Zr-MOF crystals onto magnetic beads as a highly adsorbent for recycling nitrophenol. *Chemical Engineering*

Journal. 323, 74–83.

- Yang, Y., Ding, Q., Yang, M., Wang, Y., et al. (2018) Magnetic ion exchange resin for effective removal of perfluorooctanoate from water: study of a response surface methodology and adsorption performances. *Environmental Science and Pollution Research*. 25 (29), 29267–29278.
- Yang, Y., Zheng, Z., Ji, W., Xu, J., et al. (2020) Insights to perfluorooctanoic acid adsorption micro-mechanism over Fe-based metal organic frameworks: Combining computational calculation with response surface methodology. *Journal of Hazardous Materials*. 395, 122686.
- Yoonus, H. & Al-Ghamdi, S.G. (2020) Environmental performance of building integrated grey water reuse systems based on Life-Cycle Assessment: A systematic and bibliographic analysis. *Science of The Total Environment*. 712, 136535.
- Yu, C., Liao, R., Cai, X. & Yu, X. (2019) Sodium polyacrylate modification method to improve the permeant performance of bentonite in chemical resistance. *Journal of Cleaner Production*. 213, 242–250.
- Yuan, J., Liu, X., Akbulut, O., Hu, J., et al. (2008) Superwetting nanowire membranes for selective absorption. *Nature Nanotechnology*. [Online] 3 (6), 332–336. Available from: doi:10.1038/nnano.2008.136.
- Zhang, B., Li, F., Wu, T., Sun, D., et al. (2015) Adsorption of p-nitrophenol from aqueous solutions using nanographite oxide. *Colloids and Surfaces A: Physicochemical and Engineering Aspects*. 464, 78–88.
- Zhang, F., Sang, X., Tan, X., Liu, C., et al. (2017) Converting Metal-Organic Framework Particles from Hydrophilic to Hydrophobic by an Interfacial Assembling Route. *Langmuir*. [Online] 33 (43), 12427–12433. Available from: doi:10.1021/acs.langmuir.7b02365.
- Zhang, J., Tian, B., Wang, L., Xing, M., et al. (2018) Heterogeneous Photo-Fenton Technology. *Photocatalysis*. 100, 241–258.
- Zhang, N., Yang, X., Yu, X., Jia, Y., et al. (2014a) Al-1, 3, 5-benzenetricarboxylic metal-organic frameworks: A promising adsorbent for defluoridation of water with pH insensitivity and low aluminum residual. *Chemical Engineering Journal*. 252, 220–229.
- Zhang, Q., Singh, S. & Stuckey, D.C. (2017) Fouling reduction using adsorbents/flocculants

- in a submerged anaerobic membrane bioreactor. *Bioresource technology*. 239, 226–235.
- Zhang, W., Hu, Y., Ge, J., Jiang, H.L., et al. (2014b) A facile and general coating approach to moisture/water-resistant metal-organic frameworks with intact porosity. *Journal of the American Chemical Society*. [Online] 136 (49), 16978–16981. Available from: doi:10.1021/ja509960n.
- Zhang, X., Chen, Z., Liu, X., Hanna, S.L., et al. (2020) A historical overview of the activation and porosity of metal–organic frameworks. *Chemical Society Reviews*. 49 (20), 7406–7427.
- Zhang, X., Lv, X., Shi, X., Yang, Y., et al. (2019a) Enhanced hydrophobic UiO-66 (University of Oslo 66) metal-organic framework with high capacity and selectivity for toluene capture from high humid air. *Journal of Colloid and Interface Science*. 539, 152–160.
- Zhang, X., Shi, X., Chen, J., Yang, Y., et al. (2019b) The preparation of defective UiO-66 metal organic framework using MOF-5 as structural modifier with high sorption capacity for gaseous toluene. *Journal of Environmental Chemical Engineering*. 7 (5), 103405.
- Zhang, X., Yang, Y., Lv, X., Wang, Y., et al. (2019c) Adsorption/desorption kinetics and breakthrough of gaseous toluene for modified microporous-mesoporous UiO-66 metal organic framework. *Journal of Hazardous Materials*. 366, 140–150.
- Zhang, X., Yang, Y., Song, L., Chen, J., et al. (2019d) Enhanced adsorption performance of gaseous toluene on defective UiO-66 metal organic framework: equilibrium and kinetic studies. *Journal of Hazardous Materials*. 365, 597–605.
- Zhao, C., Xu, Y., Xiao, F., Ma, J., et al. (2021) Perfluorooctane sulfonate removal by metal-organic frameworks (MOFs): Insights into the effect and mechanism of metal nodes and organic ligands. *Chemical Engineering Journal*. 406, 126852.
- Zhao, H., Gao, J., Zhao, G., Fan, J., et al. (2013) Fabrication of novel SnO₂-Sb/carbon aerogel electrode for ultrasonic electrochemical oxidation of perfluorooctanoate with high catalytic efficiency. *Applied Catalysis B: Environmental*. [Online] 136–137, 278–286. Available from: doi:10.1016/j.apcatb.2013.02.013.
- Zhao, T., Jeremias, F., Boldog, I., Nguyen, B., et al. (2015) High-yield, fluoride-free and large-scale synthesis of MIL-101(Cr). *Dalton Transactions*. [Online] 44 (38), 16791–

16801. Available from: doi:10.1039/C5DT02625C.

Zhao, T., Yang, L., Feng, P., Gruber, I., et al. (2017) Facile synthesis of nano-sized MIL-101 (Cr) with the addition of acetic acid. *Inorganica Chimica Acta*. 471, 440–445.

Zhao, Z., Li, X. & Li, Z. (2011) Adsorption equilibrium and kinetics of p-xylene on chromium-based metal organic framework MIL-101. *Chemical Engineering Journal*. 173 (1), 150–157.

Zheng, X., He, W., Rehman, S. & Zhang, P. (2020a) Facile Synthesis of Hydrophobic Metal–Organic Gels for Volatile Organic Compound Capture. *ACS Applied Materials & Interfaces*. 12 (37), 41359–41367.

Zheng, X., Liu, S., Rehman, S., Li, Z., et al. (2020b) Highly improved adsorption performance of metal-organic frameworks CAU-1 for trace toluene in humid air via sequential internal and external surface modification. *Chemical Engineering Journal*. [Online] 389 (August 2019), 123424. Available from: doi:10.1016/j.cej.2019.123424.

Zhu, M., Hu, P., Tong, Z., Zhao, Z., et al. (2017) Enhanced hydrophobic MIL(Cr) metal-organic framework with high capacity and selectivity for benzene VOCs capture from high humid air. *Chemical Engineering Journal*. [Online] 313, 1122–1131. Available from: doi:10.1016/j.cej.2016.11.008.

Zorainy, M.Y., Alkalla, M.I.G., Kaliaguine, S. & Boffito, D.C.C. (2021) Revisiting the MIL-101 metal-organic framework: design, synthesis, modifications, advances, and recent applications. *Journal of Materials Chemistry A*. (39), 22159–22217.

Chapter 10: Appendices

10.1 Appendix for Chapter 3

10.1.1 Differences between DSC and DTA

Table A10.1 shows the differences between DSC and DTA techniques.

Table A10.1: Comparison between DSC and DTA techniques.

Technique	DSC	DTA
Description	The difference in heat flow to the sample and a reference sample at the same temperature, is recorded as a function of temperature. As they are heated at a constant rate, the sample will undergo changes. So, it may require less or more heat energy to maintain at the same temperature with the reference sample.	Measures the temperature difference between a reference (non-reactive, generally alumina) and a test sample while the two samples are subjected to identical and controlled thermal cycles (heating or cooling). The sample will undergo changes that can increase or decrease its temperature than the reference material temperature.
Plot (y-axis vs x-axis)	Heat flow versus temperature of reference material.	Temperature difference versus temperature of reference material.
Expected trend on the plot	<p>In an endothermic reaction, heat is absorbed by the sample and therefore, heat flow to the sample is higher than that to the reference. This produces an upward peak.</p> <p>If the sample undergoes an exothermic reaction, so, the material releases heat. It requires less heat flow from the DSC to maintain at the reference temperature. This produces a downward peak.</p>	<p>Exothermic is an upward peak due to the occurrence of a chemical change.</p> <p>Endothermic is a downward peak due to the occurrence of a physical change.</p> <p>Area under the peak will give the material's heat capacity.</p>

10.1.2 Data from AC's water sorption validation experiment on IGA

The percentage of standard deviation is calculated by multiplying the average adsorption capacity with 100 and dividing it with the standard deviation. Table A10.2 shows the water adsorption data while Table A10.3 shows the water desorption data by AC in the IGA validation experiment.

Table A10.2: Water adsorption data at 25 °C by AC on IGA.

Water P/P ₀ (%)	Average adsorption capacity (g/g)	Standard deviation	Standard deviation (%)
0	0	0	0
3.2	0.0023	0.0005	21.9
5.1	0.0033	0.0005	14.1
7.9	0.0049	0.0006	11.5
9.5	0.0060	0.0008	12.6
18.9	0.0145	0.0022	15.0
28.4	0.0340	0.0063	18.5
34.7	0.0597	0.0074	12.5
41.0	0.1013	0.0131	13.0
45.7	0.1419	0.0111	7.8
50.5	0.1847	0.0102	5.5
55.2	0.2396	0.0121	5.0
59.9	0.2721	0.0174	6.4
78.9	0.3754	0.0166	4.4

Table A10.3: Water desorption data at 25 °C by AC on IGA.

Water P/P ₀ (%)	Average desorption capacity (g/g)	Standard deviation	Standard deviation (%)
78.9	0.3772	0.0140	3.7
59.9	0.3481	0.0136	3.9
55.2	0.3359	0.0136	4.0
50.5	0.3175	0.0122	3.9
45.7	0.2346	0.0113	4.8
41.0	0.1514	0.0064	4.2
34.7	0.0755	0.0103	13.7
28.4	0.0421	0.0061	14.5
18.9	0.0203	0.0028	13.7
9.5	0.0104	0.0012	12.0
7.9	0.0092	0.0010	10.5
5.0	0.0072	0.0008	10.7
3.2	0.0058	0.0007	11.2
0.3	0.0028	0.0004	14.8

10.1.3 Steps to setting up a competitive adsorption experiment on a DVS machine

Figure A10.1 shows the method stage interface on the DVS software for pre-drying step before introducing 40% RH into the system. In Figure A10.2, after the sample reaches an equilibrium at 40% RH condition, the step is continued with a 40% RH/0.5% toluene P/P₀ condition.

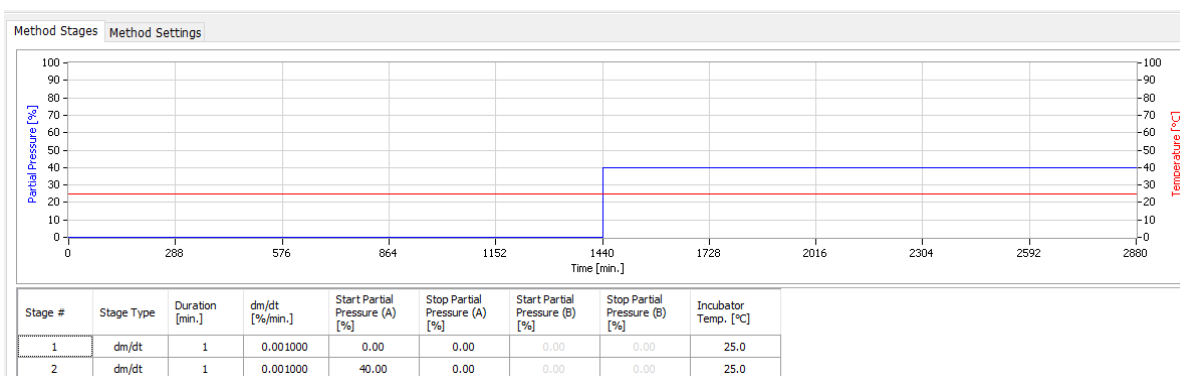


Figure A10.1: DVS method stage. Step 1: sample drying and 40% RH adsorption step.

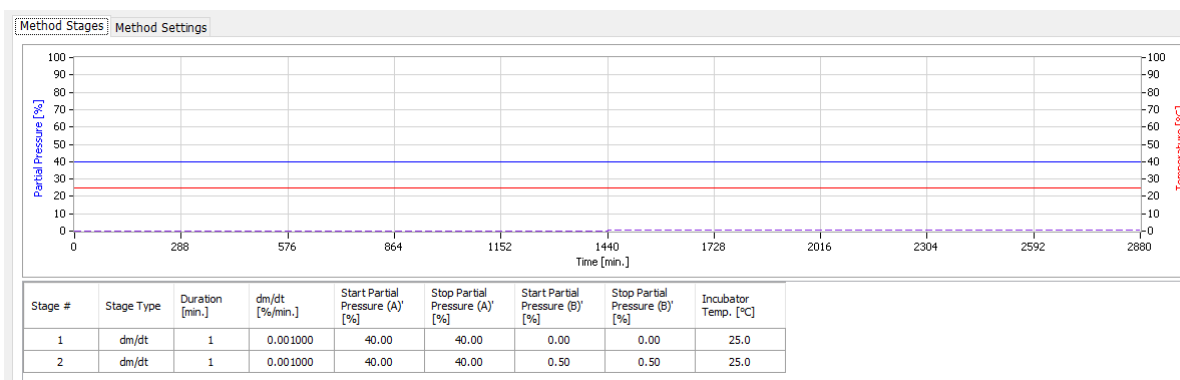


Figure A10.2: DVS method stage. Step 2: competitive adsorption experiment at 40% RH with 0.5% toluene P/P₀.

Figure A10.3 shows the DVS method settings for the pre-drying and 40% RH adsorption step. Notice that only Reservoir A (water) is used in this condition. The loop control mode for Reservoir A is best set to “Closed” compared to an “Open” as it will activate the mass flow controller to rely on a continuous feedback loop of the solvent flow rate, thus, keeping the target P/P₀ at a consistent level. Figure A10.4 shows the DVS method settings for the competitive adsorption condition (40% RH and 0.5% toluene P/P₀). The only difference is in the active reservoir specification, now inclusive of both Reservoir A (water) and B (toluene).

Method Stages | Method Settings

General Settings

Name: 2 component drying and 40%RH

Description:

Save Data Interval: 10 seconds

Active Reservoir: Reservoir A

Total Gas Flow (A) [sccm]: 200

Total Gas Flow (B) [sccm]: 200

Loop Control Mode (A): Closed

Loop Control Mode (B): Open

Update Sample Mass:

Run Dry Calibration:

DMDT Settings

Minimum Stage Time [Minutes]: 10

Maximum Stage Time [Minutes]: 1440

Stability Duration [Minutes]: 20

Figure A10.3: DVS method settings for Step 1, pre-drying and 40% RH equilibration.

Method Stages | Method Settings

General Settings

Name: 2 component 40% RH and 0.5% VOC

Description:

Save Data Interval: 10 seconds

Active Reservoir: Reservoir A+B

Total Gas Flow (A) [sccm]: 200

Total Gas Flow (B) [sccm]: 200

Loop Control Mode (A): Closed

Loop Control Mode (B): Closed

Update Sample Mass:

Run Dry Calibration:

DMDT Settings

Minimum Stage Time [Minutes]: 10

Maximum Stage Time [Minutes]: 1440

Stability Duration [Minutes]: 20

Figure A10.4: DVS method settings for Step 2, at 40% RH with 0.5% toluene P/P₀ adsorption.

10.2 Appendix for Chapter 4

10.2.1 MIL-101 (Cr) structural integrity using PXRD analysis

Figure A10.5 shows the additional PXRD analysis for MIL-101 (Cr) after 3-day immersion in pH = 1 and pH = 11 solutions. All peaks remained intact at the same position with the simulated MIL-101 (Cr).

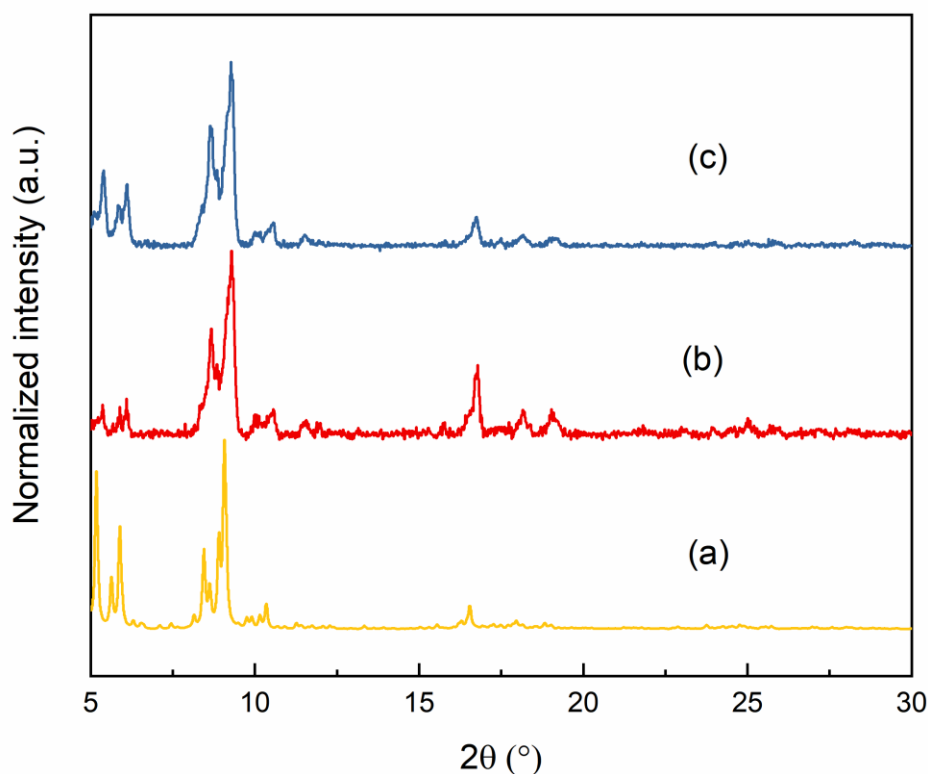


Figure A10.5: PXRD patterns of (a) simulated MIL-101 (Cr) and after 3-day immersion in (b) pH = 1 and (c) pH = 11 solutions.

10.2.2 N₂ adsorption and desorption isotherms

Figure A10.6 shows the complete N₂ adsorption and desorption isotherm plots of all studied adsorbents including pre-soaked MIL-101 (Cr) in acidic (pH 1) and alkaline (pH 11) solutions that lasted for 3 days.

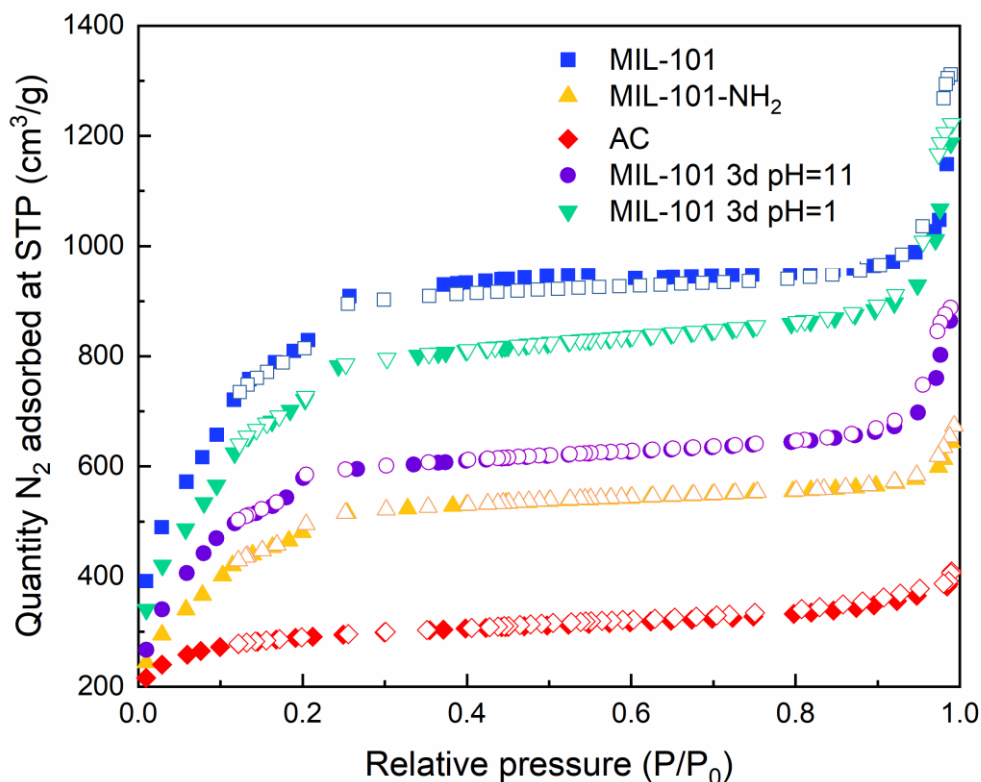


Figure A10.6: N₂ adsorption and desorption isotherms of all tested adsorbents where full symbols denote adsorption while empty symbols are for desorption.

10.2.3 FTIR and elemental analysis

Figure A10.7 shows the measured FTIR spectra for 2-CP saturated MIL-101 (Cr) and its pristine form. Based on the FTIR spectra, none of the peaks on the pristine MOF shifted, meaning there is no new bond formation. An initial assumption is that adsorption of 2-CP takes place via physical sorption. It was reported that presence of physi-sorbed 2-CP on the surface can be confirmed when an absorption band each at 1338 cm⁻¹ and 3570 cm⁻¹ appears (Alderman & Dellinger, 2005). These bands correspond to 2-CP's O-H bending and stretching, respectively. However, none of them was observed on the spectra. So, it is unclear to conclude the type of adsorption occurred with the adsorbents whether it was through physical or chemical sorption. Besides, the van der Waals interaction between the MOF and 2-CP albeit weak, can lead to tight packing of 2-CP within the pores such that the vibrational motion of the adsorbed species is strongly hindered (Andini *et al.*, 2006) and not easily detected via FTIR measurement. Moreover, by using the equilibrium maximum adsorption capacity of MIL-101

(Cr) (125 m/g), it is understood that only about 0.6 mg 2-CP can be adsorbed by 5 mg of MOF. This adsorbed quantity is scarcely available on the MOF surface (constitutes only 12 wt% of the MOF amount) to be detected by the FTIR instrument. Plus, the in vacuo drying process could have evaporated the molecule even though theoretically, the activation temperature is lower than 2-CP's boiling point (175 °C).

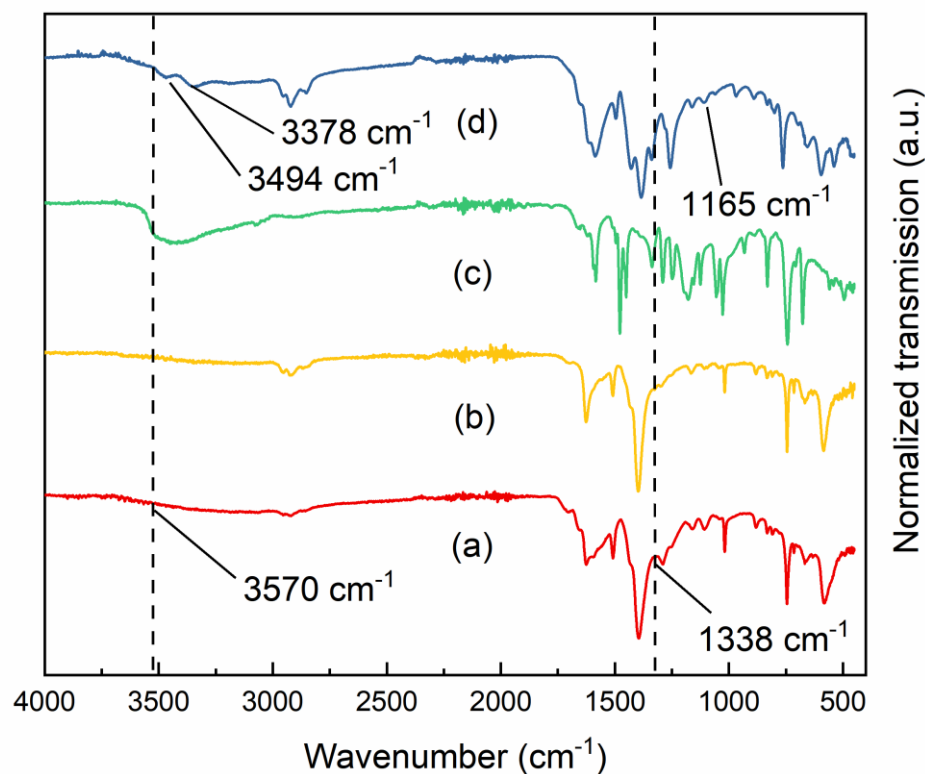


Figure A10.7: Comparison of the measured FTIR spectra between (a) fresh MIL-101 (Cr), (b) 2-CP loaded MIL-101 (Cr), (c) 2-CP and (d) MIL-101 (Cr)-NH₂.

The FTIR spectra for 2-CP loaded AC and fresh AC samples were not able to be measured as the instrument is not suitable to detect dark-coloured material. An Attenuated Total Reflection tip made from Germanium (Ge) must be used instead of diamond. Since carbon-based materials are highly absorbing, the high refractive index of the Ge crystal will limit the sample's depth of penetration. A diamond crystal is more widely used due to its high chemical and physical robustness as well as its broad measurable spectral range.

The characteristic signals for amino-functionalized MIL-101 (Cr)-NH₂ can be observed at 1165, 3378 and 3494 cm⁻¹. The last two vibrations happen due to the asymmetric and symmetric N-H stretching of the amino group whereas the lower end band is caused by C-N stretching vibration. All signals are in accordance with values reported in literature (Bernt *et al.*, 2011; Tian *et al.*, 2016). The elemental analysis in Table A10.4 also verifies successful -NH₂ grafting as could be judged from the MIL-101 (Cr)-NH₂'s higher N and H wt% than the original MIL-101 (Cr).

Table A10.4: Elemental analysis of sorbents used in Chapter 4.

Sample	N wt%	C wt%	H wt%	S wt%
AC	1.2 ± 0.03	88.3 ± 0.5	0.6 ± 0.04	1.0 ± 0.07
MIL-101 (Cr)	2.8 ± 0.2	42.6 ± 1.8	4.4 ± 0.3	0
MIL-101 (Cr)-NH ₂	5.1 ± 0.07	38.6 ± 0.8	4.6 ± 0.05	0

10.2.4 Linear Langmuir-1 isotherm plots

The linear Langmuir-1 equations for each adsorbent can be taken from Table A10.5. The maximum Langmuir adsorption capacity (q_m) could only be calculated for MIL-101 (Cr) and AC because the linear fitting for MIL-101 (Cr)-NH₂ gave a negative y-intercept as seen in Figure A10.8.

Table A10.5: Details about the linear Langmuir isotherm plots.

Sample	Linear fit relation	R ²
MIL-101 (Cr)	$y = 0.0083x + 0.253$	0.9942
MIL-101 (Cr)-NH ₂	$y = 0.0119x - 0.293$	0.9764
AC	$y = 0.0029x + 0.0039$	0.9990

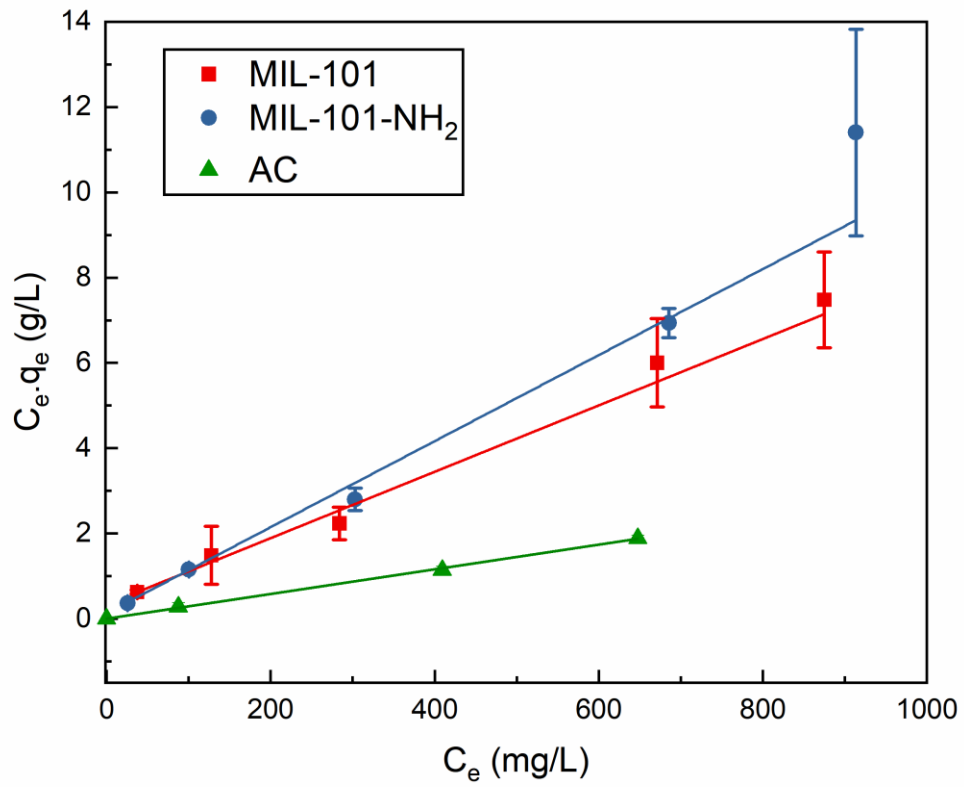
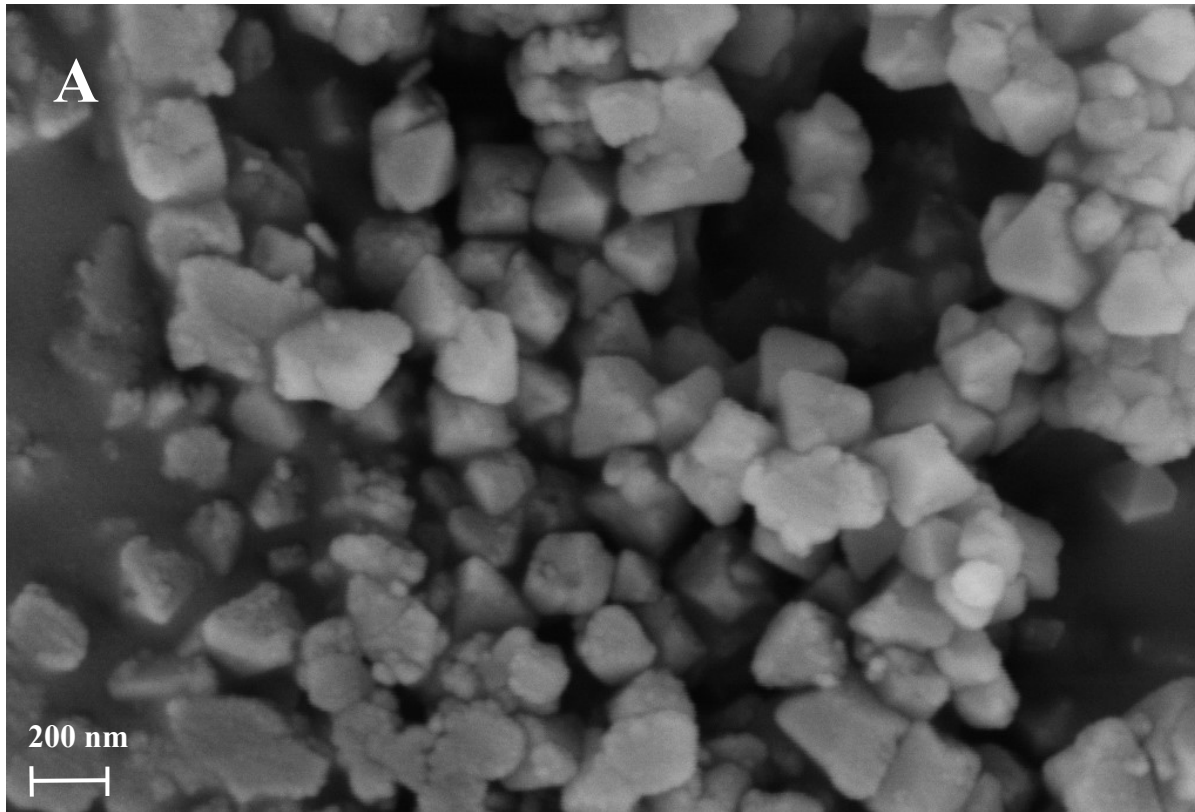


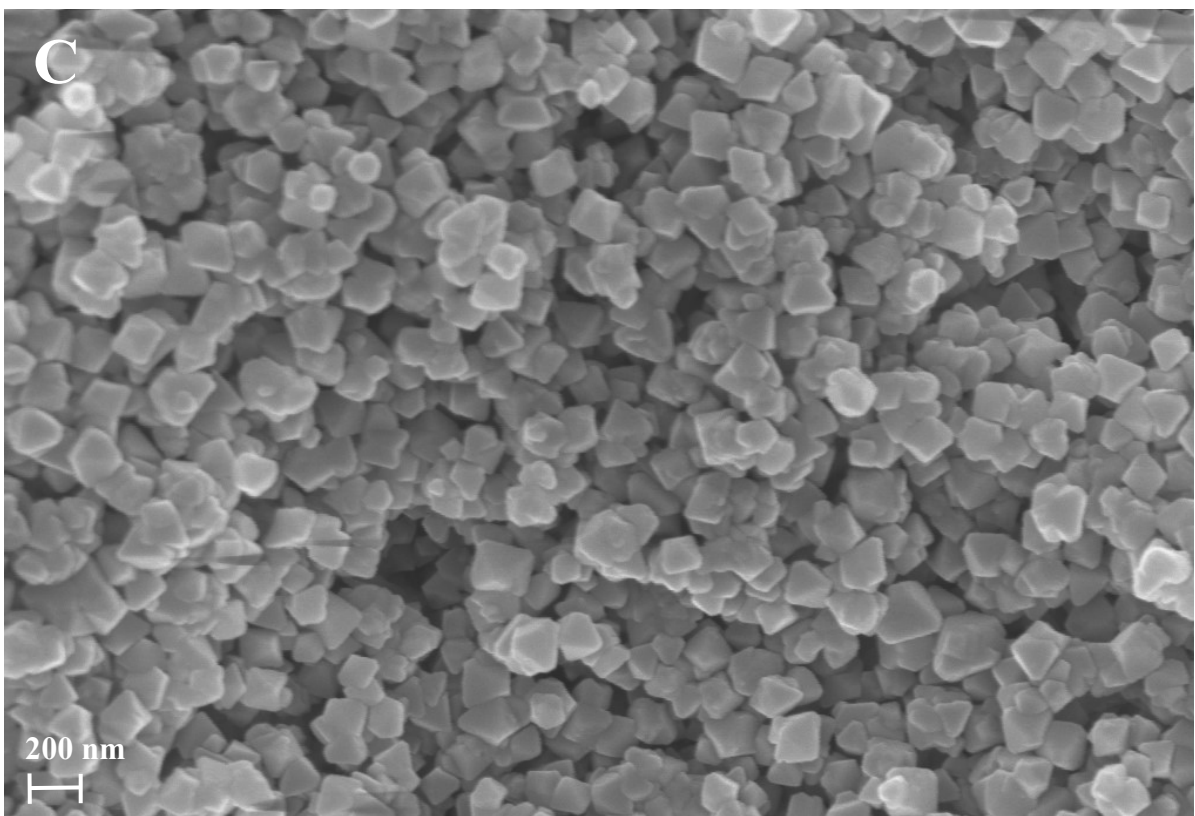
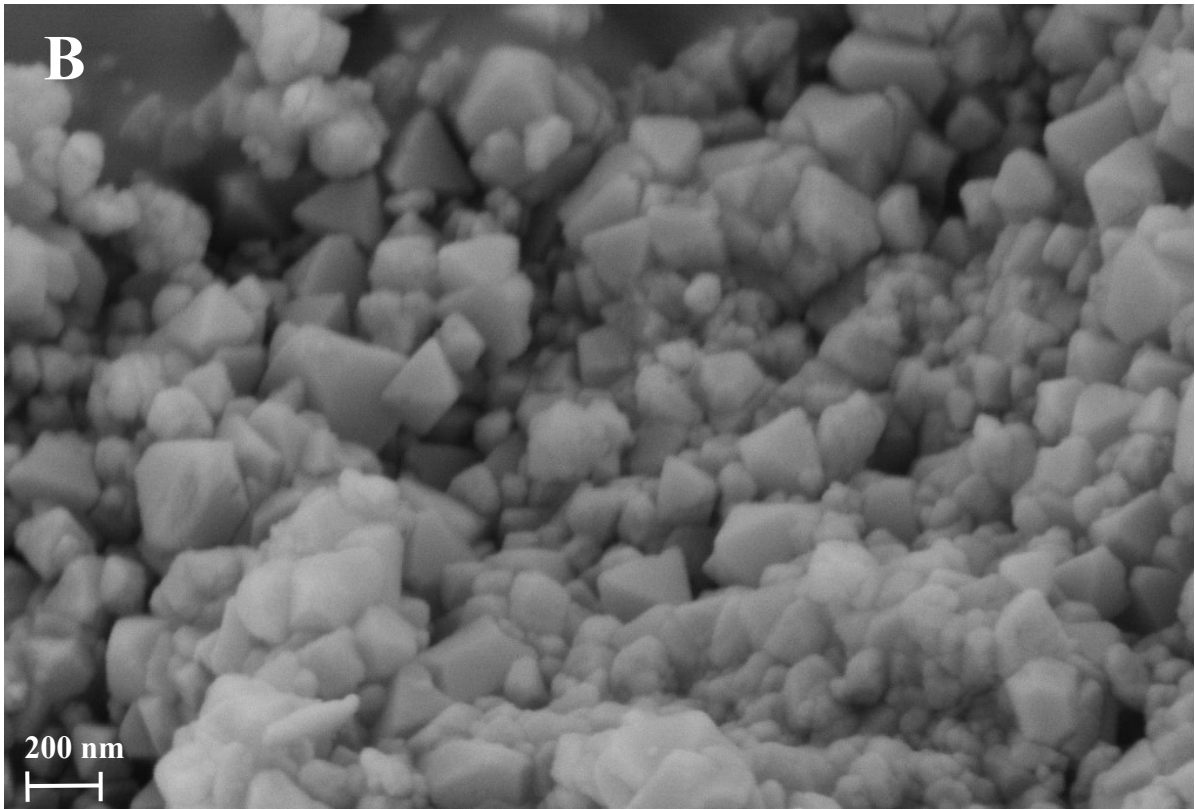
Figure A10.8: Linear isotherm plots of Langmuir-1 type for all studied adsorbents.

10.3 Appendix for Chapter 5

10.3.1 SEM images of MIL-101-PDMS composites

Figure A10.9 shows the SEM images of the pristine MIL-101 (Cr) and other investigated MIL-101-PDMS composites.





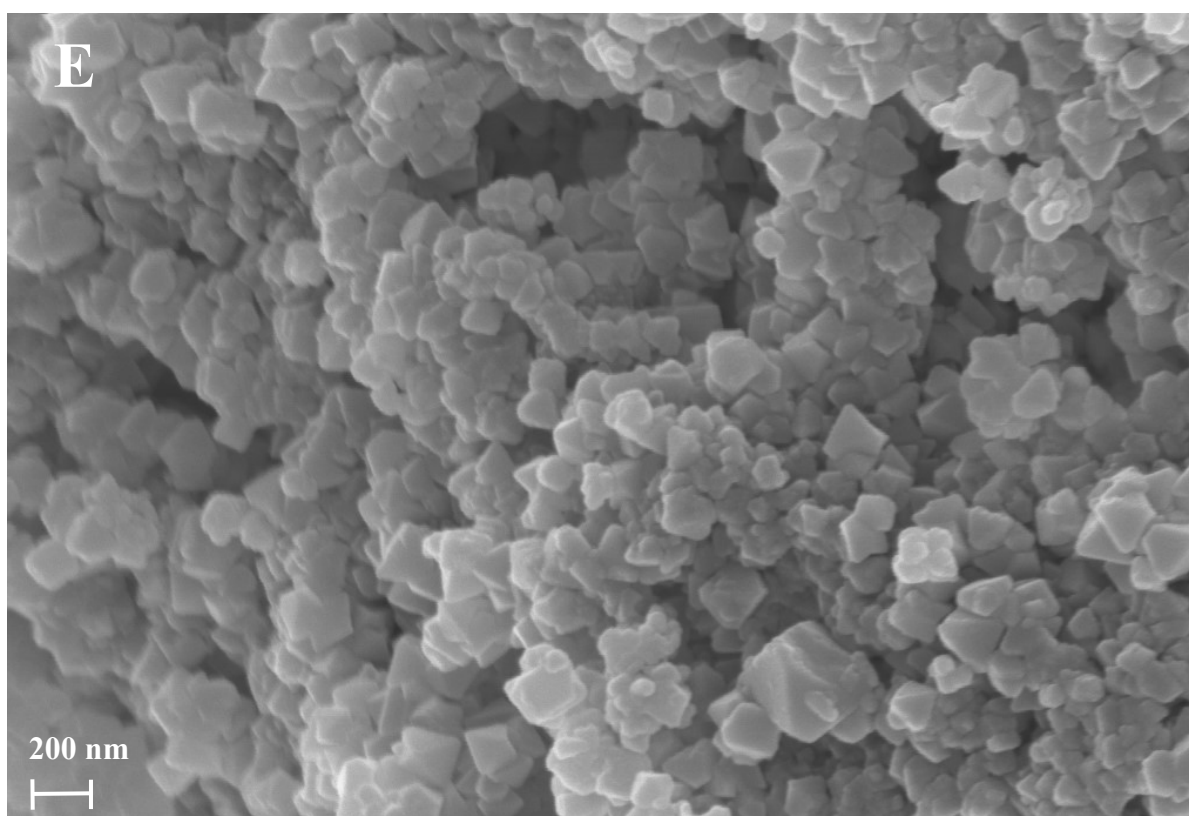
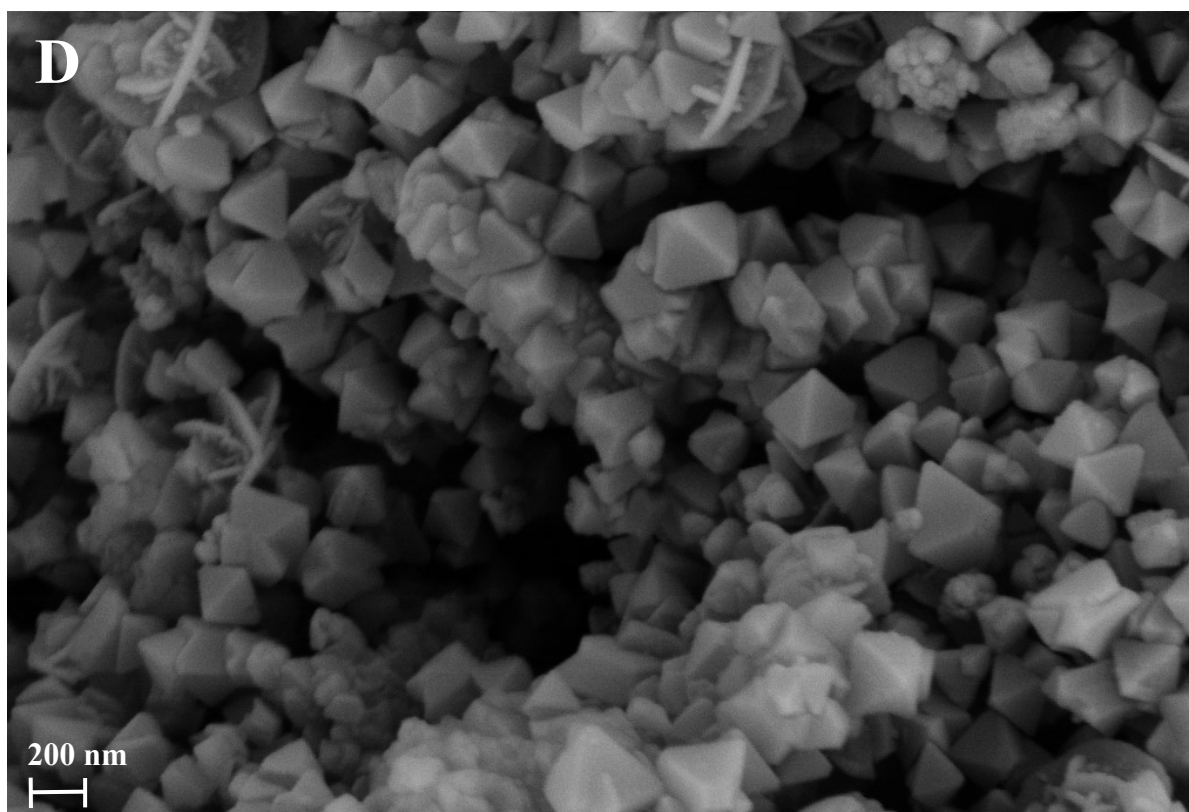


Figure A10.9: SEM images of (A) pristine MIL-101 (Cr), (B) MIL-PDMS-Sigma-0.25, (C) MIL-PDMS-Sigma-6, (D) MIL-PDMS-Dow-0.25 and (E) MIL-PDMS-Dow-6.

10.4 Appendix for Chapter 6

10.4.1 Hydrophobic chemical agent structural properties

Table A10.6 compares phosphonic and phosphinic acids in several criteria. They each belong to a different acid category, but since they commonly have one P=O bond, both will be referred as phosphorous oxyacids (PA) from now on. However, if necessary, the specific suffixes -onic and -inic acids will be used accordingly. Their key difference is that phosphinic acids are monoprotic whereas phosphonic acids are diprotic which can be identified from their one and two replaceable protons (H^+) in their molecular structures respectively. The H^+ may also be substituted with another functionality (R) either from an alkyl or aryl group.

Table A10.6: Differences between phosphonic and phosphinic acids.

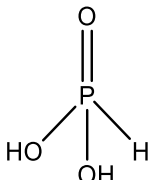
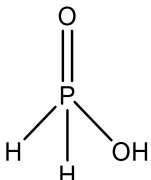
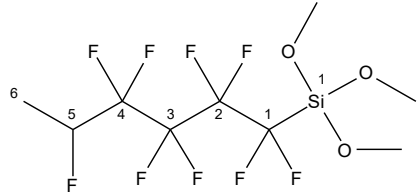
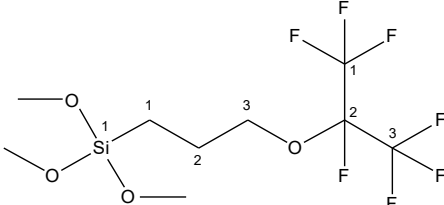
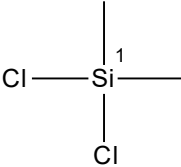
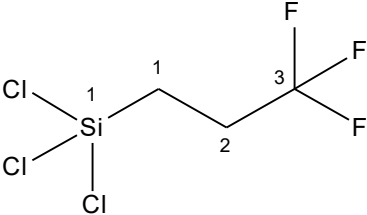
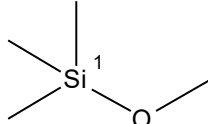
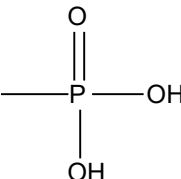
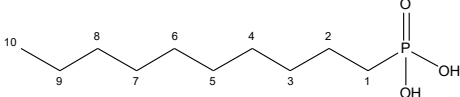
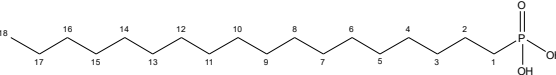
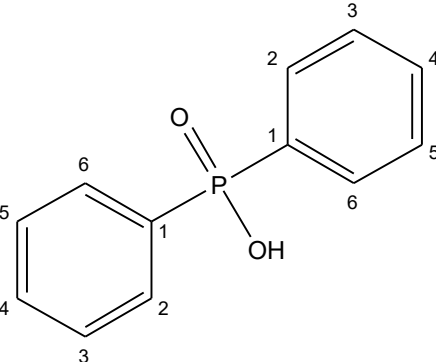
Name	Phosphonic acids	Phosphinic acids
Alternate name	Organic derivatives of phosphorous acids or phosphonates	Hypophosphorous acid
Property	Colourless, low melting point solids that are soluble in water and common alcohols but dissolve poorly in organic solvents	
Molecular formula	$R-P(O)(OH)_2$	$R-P(H)(O)(OH)$
Acid category	Diprotic	Monoprotic
Primary uses	Bioactive purposes (herbicides, medical drugs), surface functionalization, chelating agent	Industrial electrodeless nickel plating, salt, flame retardant, reducing agent
General chemical structure		

Table A10.7 lists the properties of the hydrophobic chemicals used in this work. The molecular diameter was approximated from Connolly solvent excluded volume by assuming the molecule bearing a spherical shape. It was not possible to compute the diameter of ODPA as the long linearity may exceed the limit of a spherical-shaped molecule.

Table A10.7: The chemical structures of the hydrophobic agents.

Chemical	Chemical structure	Size (Å)
Nonafluorohexyltrimethoxysilane (NS)		7.6
3-(heptafluoroisopropoxy)propyltrimethoxysilane (HS)		7.6
Dimethyldichlorosilane (DMDCS)		5.7
Trichloro (3,3,3-trifluoropropyl) silane (TCTFPS)		6.5
Methoxytrimethylsilane (MTMS)		6.0
Methyl phosphonic acid (MPA)		5.0
1-decylphosphonic acid (DPA)		7.5
n-octadecyl phosphonic acid (ODPA)		N/A
Diphenylphosphinic acid (DiPPA)		6.9

10.4.2 Silane surface modification

Figure A10.10 shows the reaction mechanisms of silane hydrolysis and condensation reaction on the MOF surface. The silanes can rapidly form covalent bonds with the MOF's metal atoms (Kloda *et al.*, 2021). Research has shown that silanes with longer carbon chain length can increase the treated surface's static water contact angle (θ_c) (Choe *et al.*, 2021). However, in this work, only MIL-NS-7.5 vol% and MIL-TCTFPS-7.5 vol% became hydrophobic while other substrates stayed unchanged; hydrophilic. See Figure A10.11 for the samples' static water contact angle images. Table A10.8 compares the pore properties and the static water contact angles of the MIL-100-HT samples before and after silanisation. It is apparent that not only does the higher substrate concentration led to lower porosity in the coated materials, but the different silane molecular structures also contributed towards the porosity reduction.

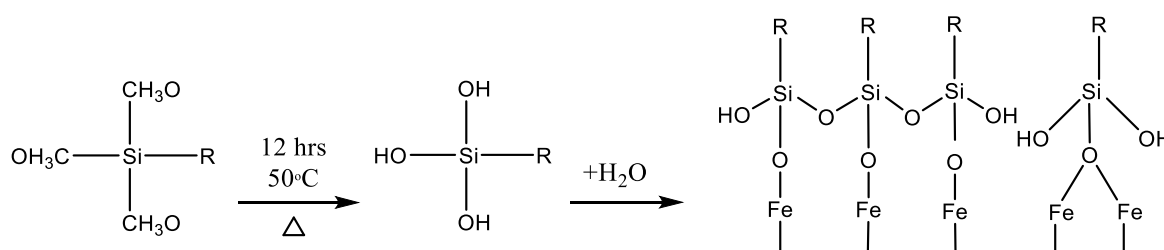


Figure A10.10: Silanisation reaction on the surface of the MOF MIL-100 (Fe). The silane model shown has R as a fluoroalkyl pendant group.

MIL-MTMS-7.5 vol% has a volumetric loading quantity (7.5 vol%) similar to the two hydrophobic samples. However, its surface area did not decrease as much due to the smaller MTMS diameter. The only exception is that it did not become hydrophobic. Between the two hydrophobic samples, MIL-TCTFPS-7.5 vol% at least has some residual surface area. So, for a preliminary performance review, it was assessed for 95% P/P₀ toluene adsorption. As expected, it showed minimal uptake (73 mg/g) in line with the considerable loss of porosity. See Figure A10.12 for the adsorption data. From these shortfalls, it can be deduced that the use of silanes could not accomplish the hydrophobic objective without compromising the surface area. Therefore, this technique was discontinued in favour of a more practical chemical coating method.

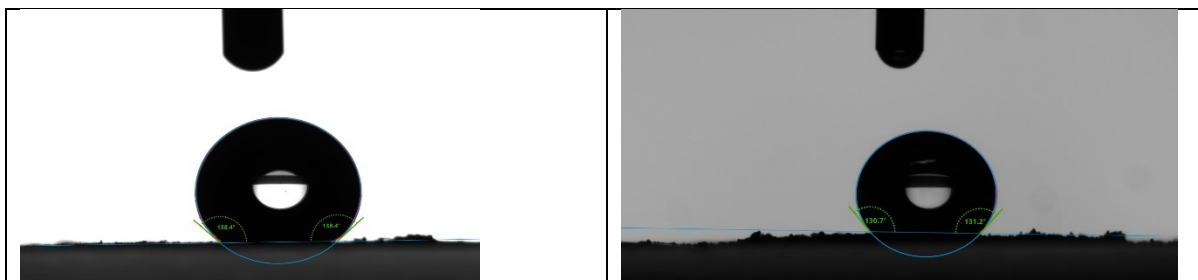


Figure A10.11: Static water contact angle at $t = 0$ s for (left) MIL-NS-7.5 vol% and (right) MIL-TCTFPS-7.5 vol%.

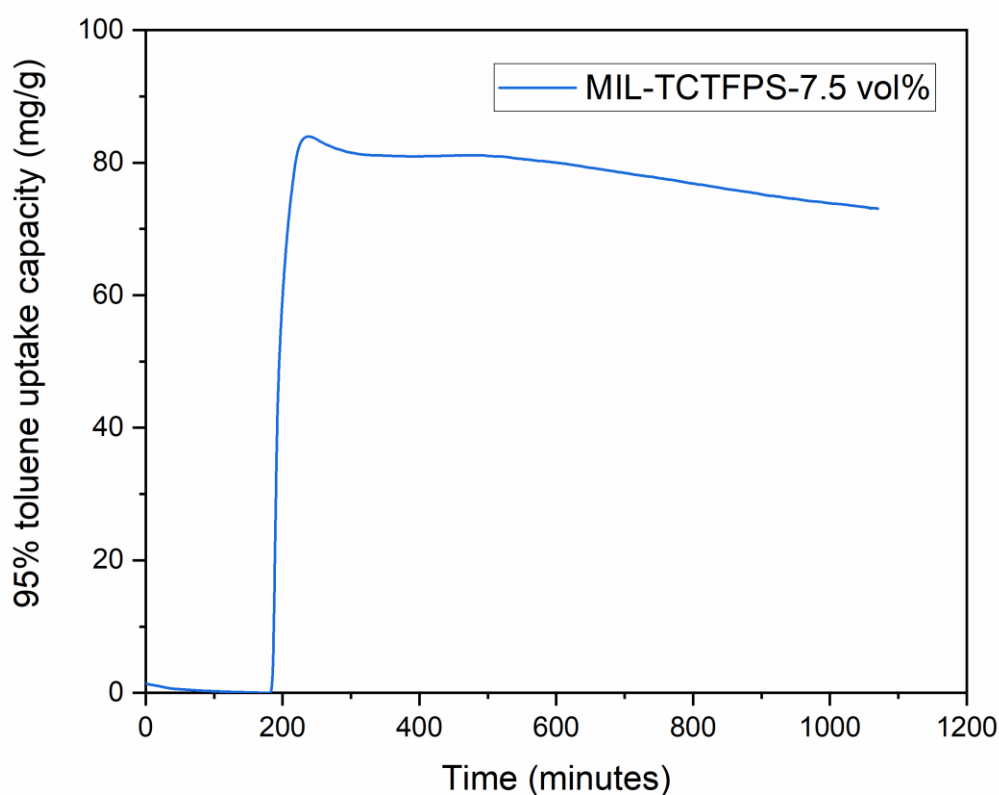


Figure A10.12: 95% toluene P/P_0 uptake capacity of MIL-TCTFPS-7.5 vol%.

Chemical coatings like silanes can be introduced onto a surface via two approaches namely wet and vapor-phase. Wet chemical coating protocols seem to be less preferred over vapor-phase deposition as it is more difficult to precisely control the homogeneity and the monolayer formation, and wet methods require solvent removal. Furthermore, scaling up a wet coating technique would consume a substantial amount of solvent that eventually produces high waste volumes. A wet approach's effectiveness may also be constrained by low method

reproducibility and potential side reactions like polymerization (Mattiuzzi *et al.*, 2020). It is therefore not surprising that most reports that employed wet silane polymerization experienced dramatic surface area reductions which limited the treated materials' maximum uptake quantity (Sah *et al.*, 2004; Mahdavi, Ahmadian-Alam & Molavi, 2015; Choe *et al.*, 2021). In contrast, for silane vapor-phase the risks from their reactivity with atmospheric gases can be minimized provided that the chemicals are handled under an enclosed, inert atmosphere (Munief *et al.*, 2018).

Table A10.8: Pore properties and static water contact angles of MIL-100 (Fe) and its silane-modified variants.

Sample	BET surface area (m ² /g)	Total pore volume (cm ³ /g)	Static water contact angle (°)
MIL-100-HT	1702	0.935	34.2 ± 2.0
MIL-NS-1 vol%	1125	0.635	0
MIL-NS-2.5 vol%	588	0.328	0
MIL-NS-7.5 vol%	1	0 (not measurable)	132.9 ± 2.6
MIL-HS-1 vol%	1020	0.574	0
MIL-DMDCS-1 vol%	744	0.443	0
MIL-TCTFPS-7.5 vol%	23	0.0715	125.1 ± 3.1
MIL-MTMS-7.5 vol%	1430	0.771	0

10.4.3 PXRD patterns of PA-treated MIL-100 (Fe)

Figure A10.13 shows the PXRD patterns for all PA-treated samples. They all present identical PXRD peaks compared to the untreated MIL-100 (Fe), implying retained material crystallinity. No structural changes were observed due to the low quantities of PA used in the treatment. However, an unexpected peak at 7.5° appeared in MIL-DiPPA-50 mM's patterns possibly due to ODPa carry-over impurity. The minor misalignment compared to ODPa powder patterns at 7.9° to a lower 2θ value may be caused by background noise elimination.

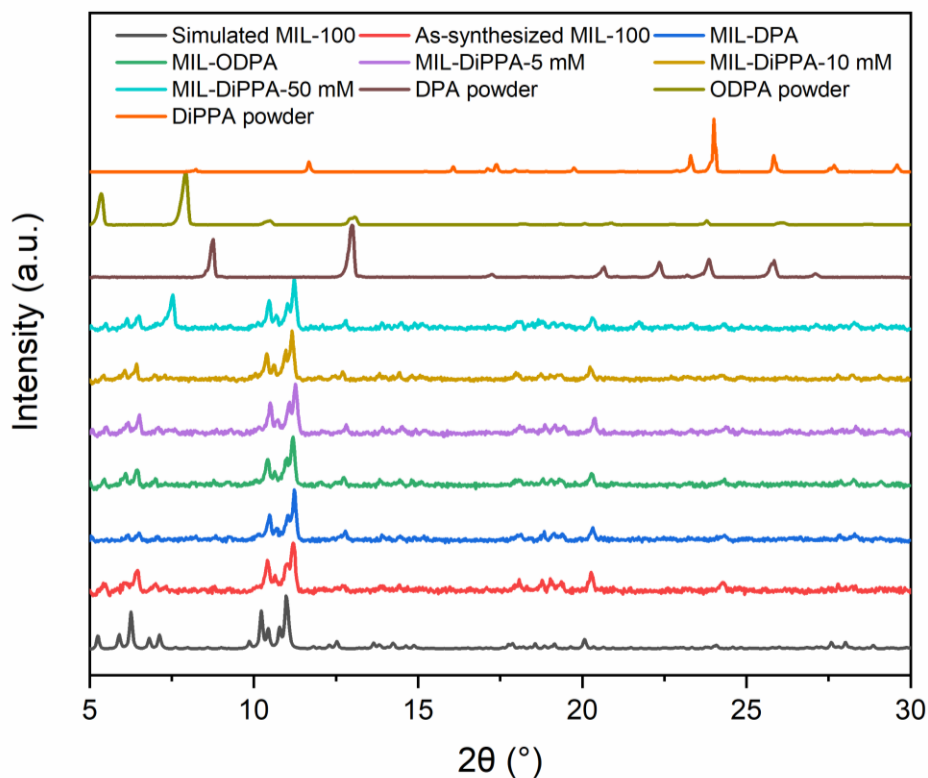


Figure A10.13: PXR D patterns of PA-treated MIL-100 (Fe).

10.4.4 Sample colour changes after calixarene coating treatment

Figure A10.14 shows the varying degrees of colour change observed on MIL-Cx samples after coated with calixarene molecules.

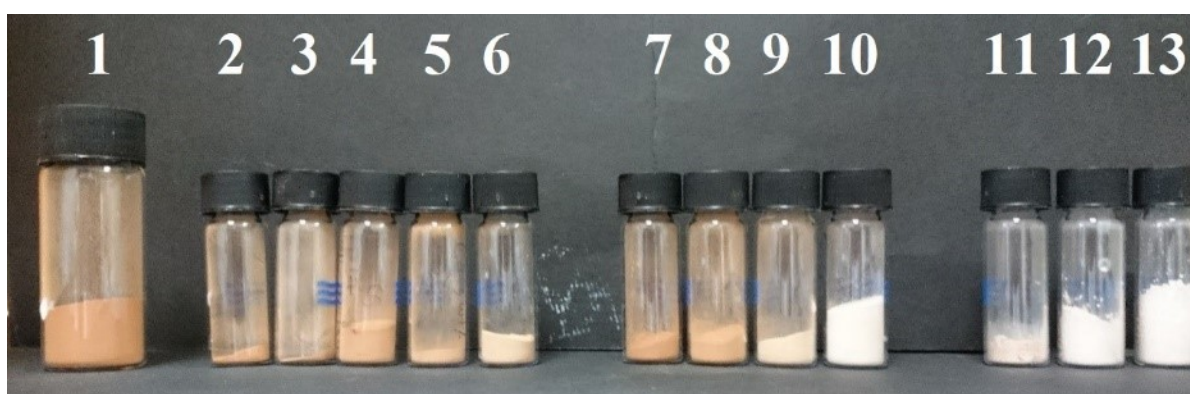
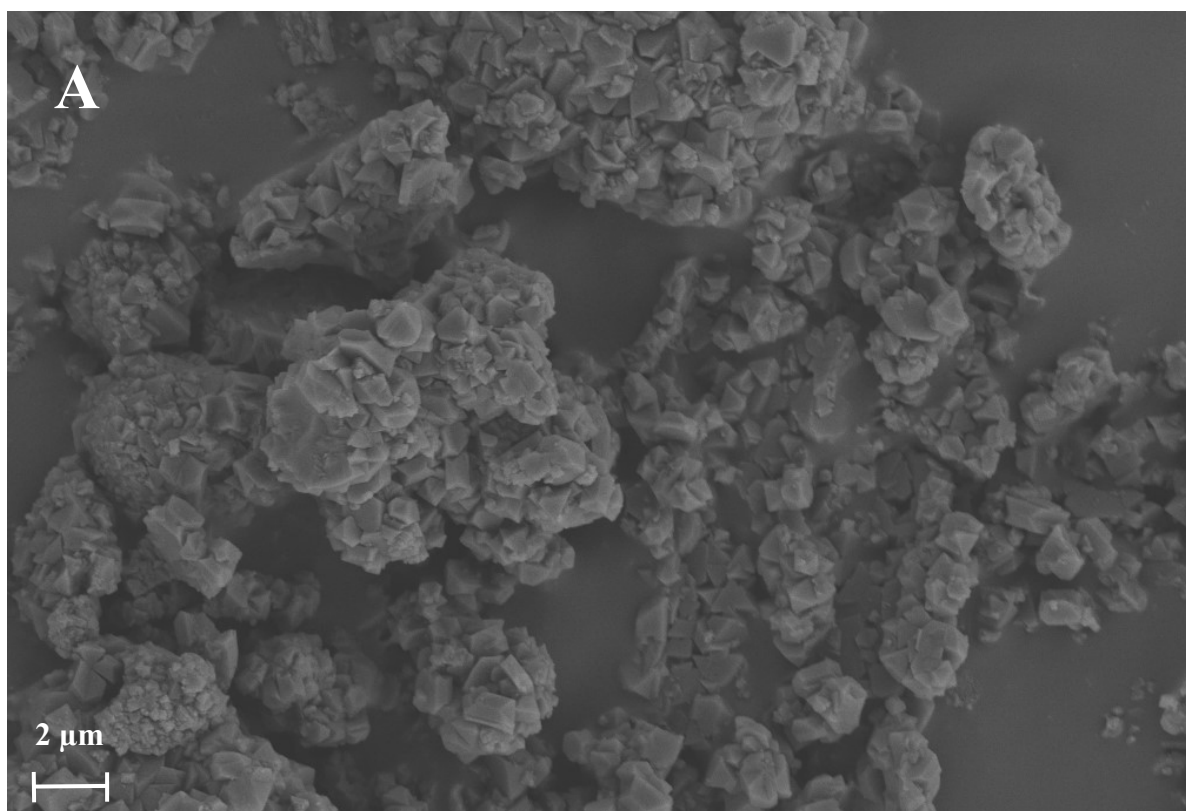
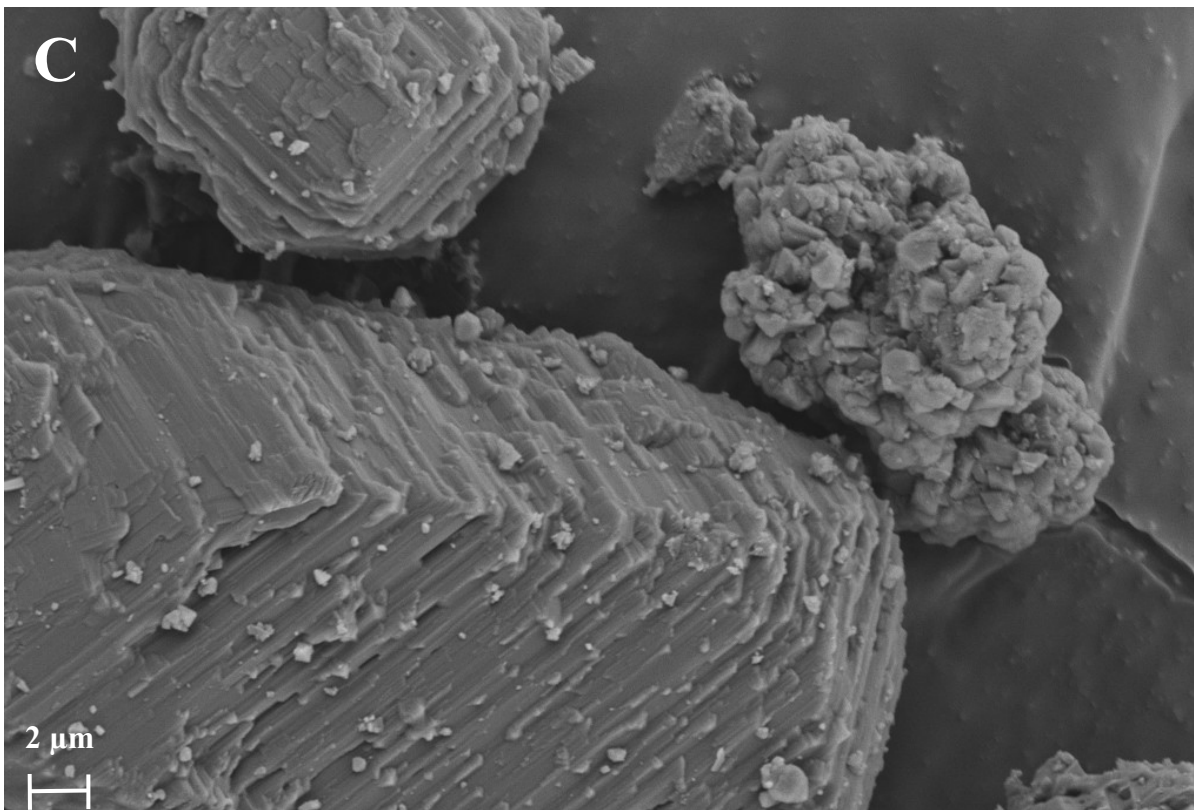
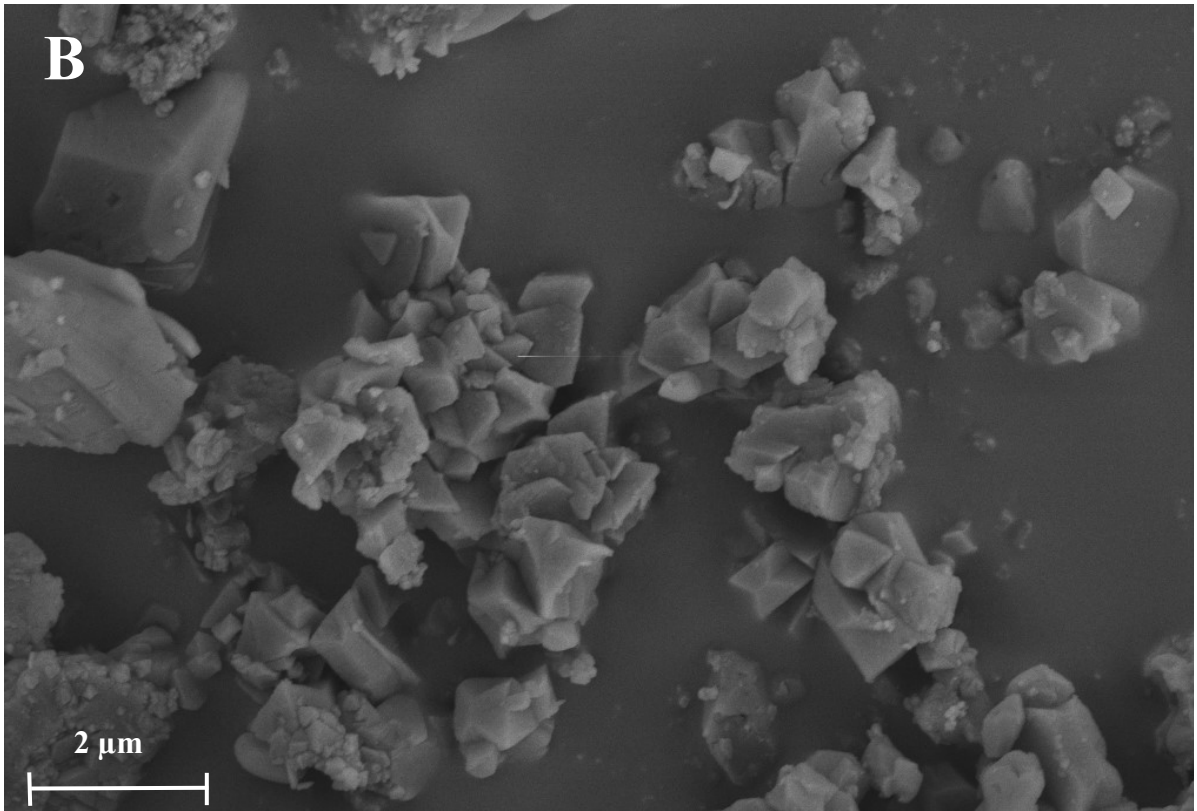


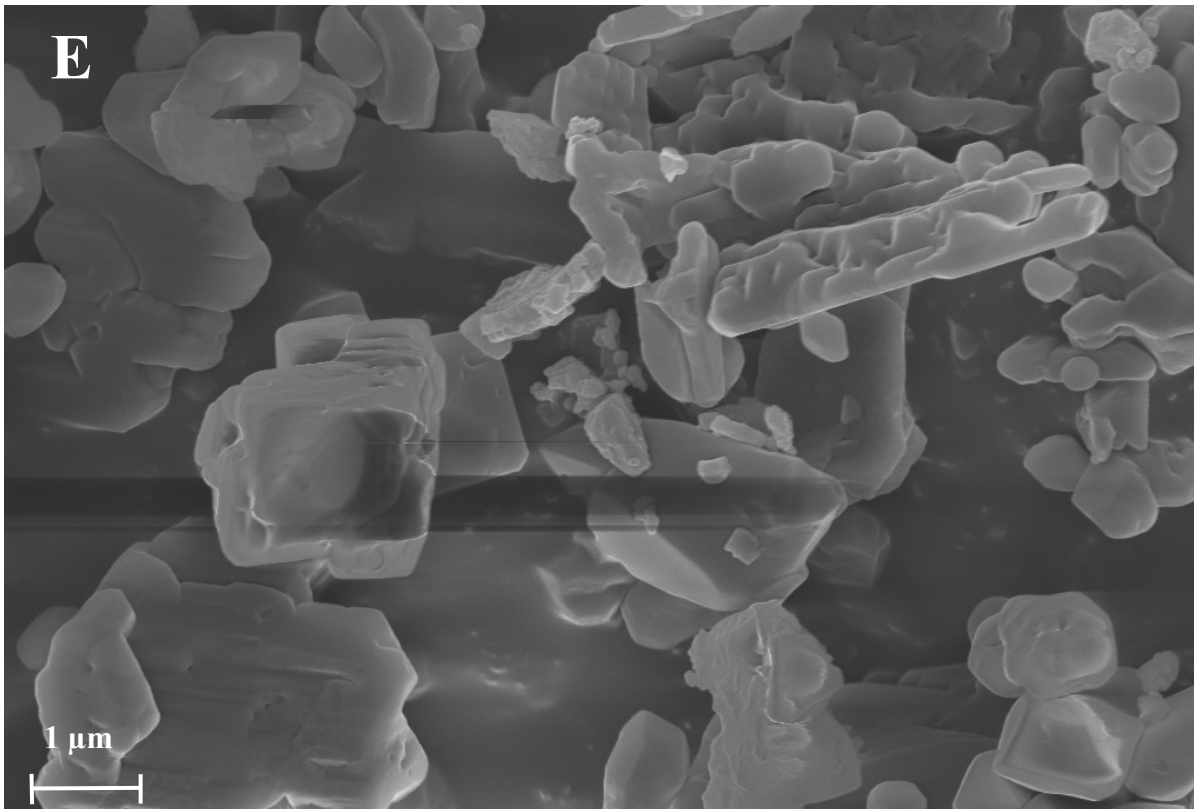
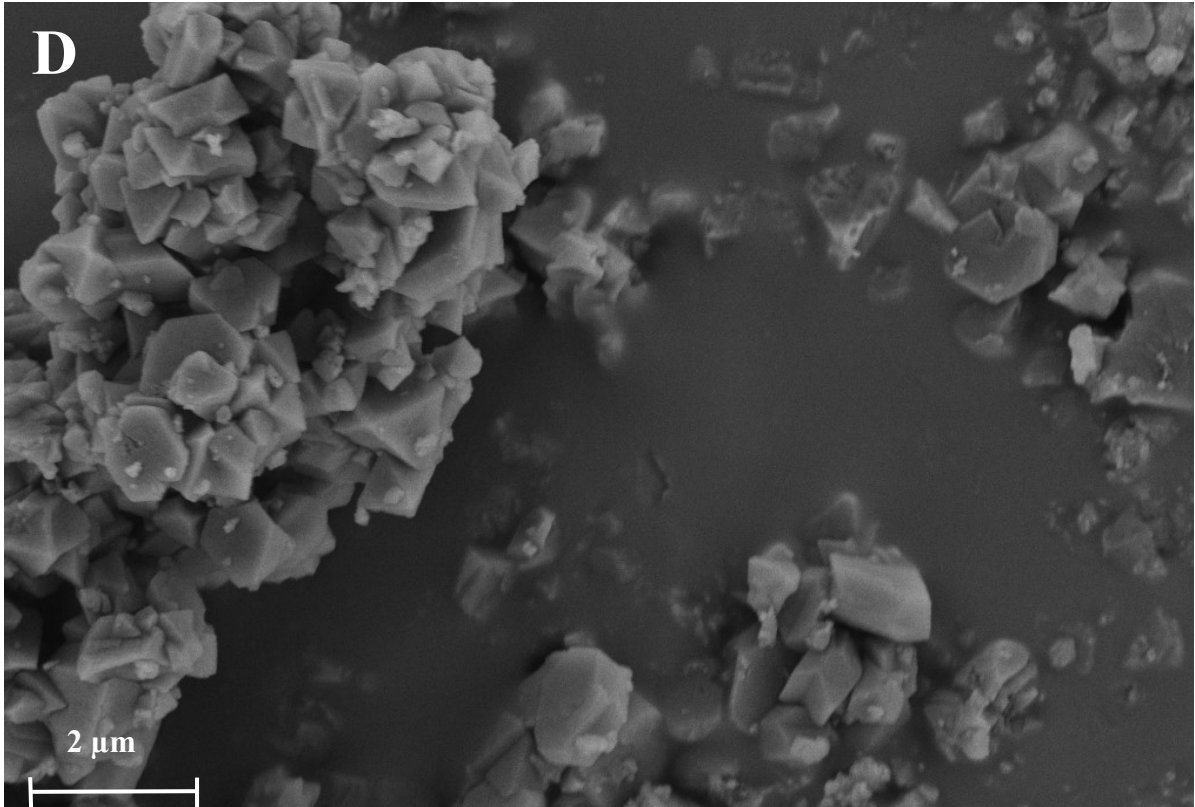
Figure A10.14: Numbered from the left are vials containing the pristine (1) MIL-100 (Fe), (2 – 6) MIL-Cx4-0.3, 0.5, 1, 3, 5 wt%, (7 – 10) MIL-Cx6-0.5, 1, 3, 5 wt% and (11 – 13) MIL-Cx8-1, 3, 5 wt%.

10.4.5 SEM images of calixarene-treated MIL-100 (Fe)

Figure A10.15 shows the SEM images of the calixarene-treated samples compared to the pristine MIL-100 (Fe). Low Cx4 and Cx6 loading (1 wt%) does not bring any crystallographic changes to the coated samples, except for MIL-Cx8-1 wt% where the crystals started displaying some degree of latitudinal transformation from the original shapes. At 5 wt% Cx loading, greater differences were observed; development of layer-like structures in MIL-Cx4-5 wt% while MIL-Cx6-5 wt% and MIL-Cx8-5 wt% show their extended latitudinal versions. Detailed crystallographic analyses must be done to inspect these structural discrepancies. However, studies have shown that the ability of the Cx frame to attach to the cationic metal atoms during the complexation will result in conformational and co-ordinational changes which might possibly be the factor for the visual nuances (Homden & Redshaw, 2008; Arbaoui *et al.*, 2010).







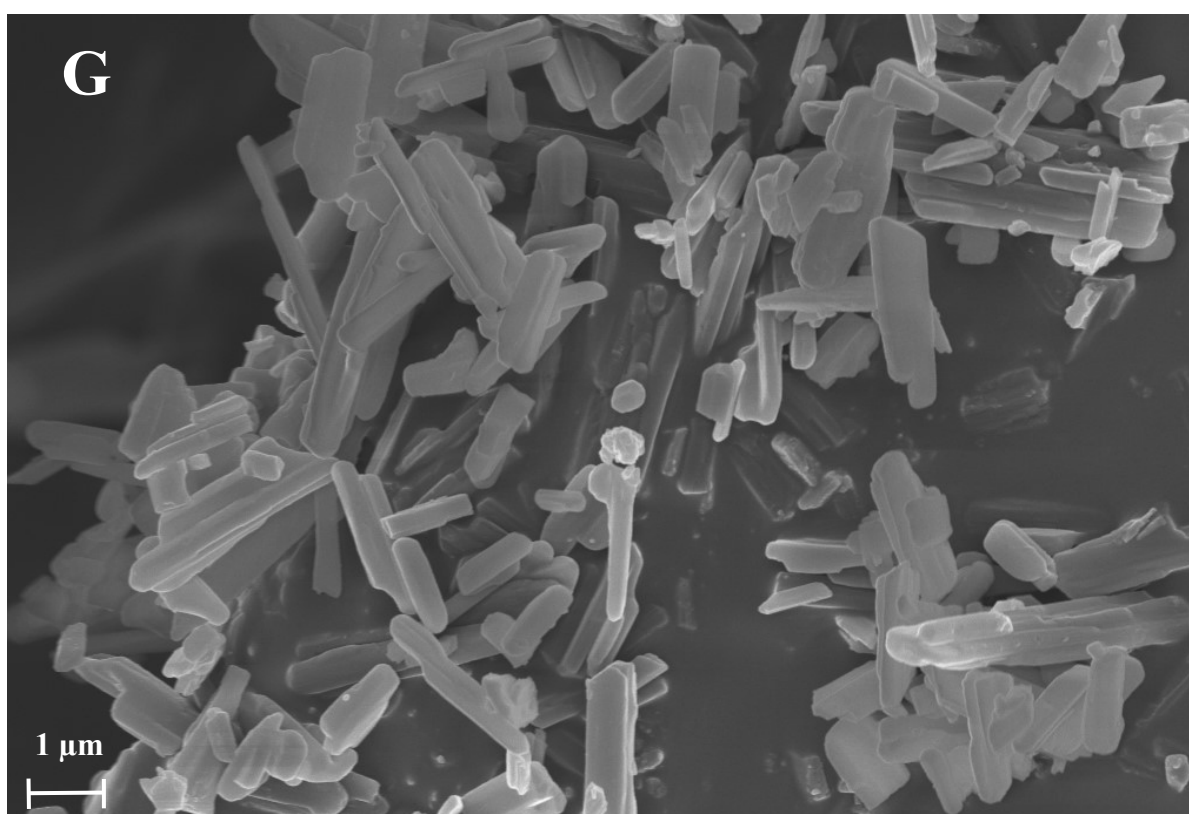
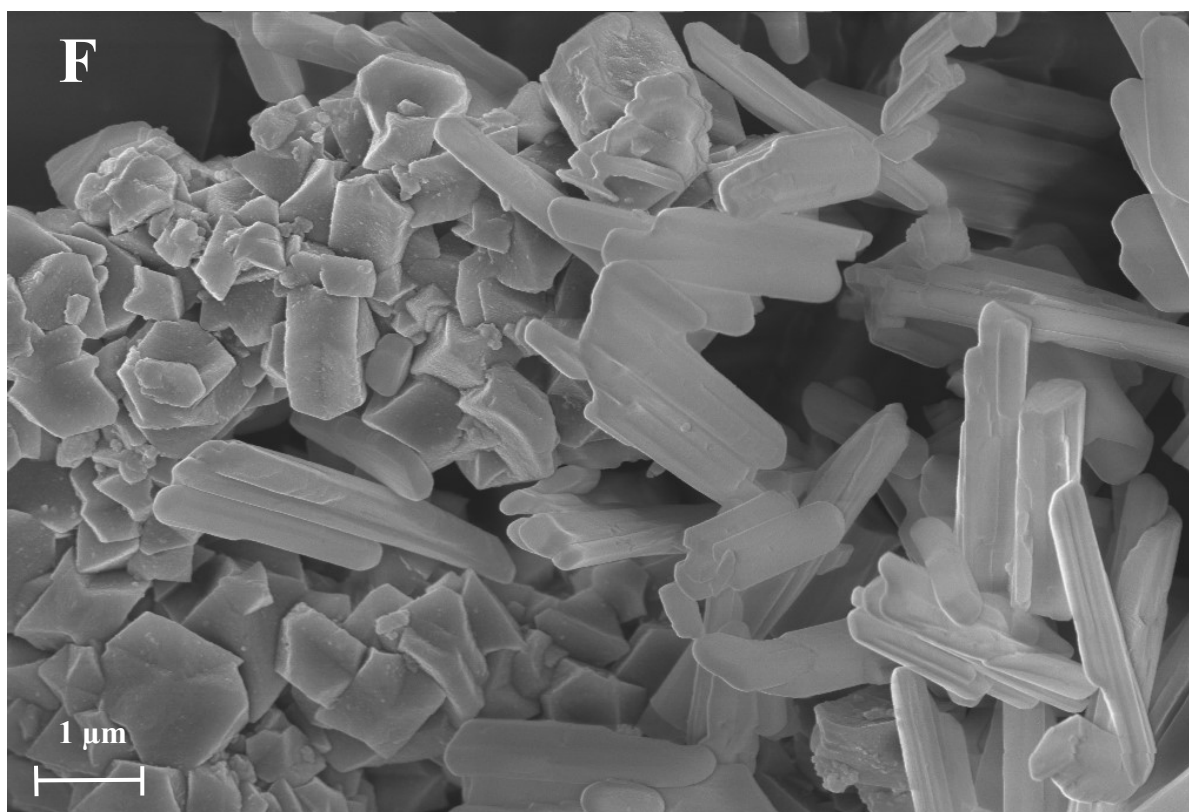


Figure A10.15: SEM images of (A) pristine MIL-100 (Fe), (B) MIL-Cx4-1 wt%, (C) MIL-Cx4-5 wt% (D) MIL-Cx6-1 wt%, (E) MIL-Cx6-5 wt%, (F) MIL-Cx8-1 wt% and (G) MIL-Cx8-5 wt%.

10.4.6 FTIR spectra of PA-treated MIL-100 (Fe)

The FTIR spectra in Figure A10.16 of the dry PA-functionalised powder indicate the presence of the PA molecules. Compared to the spectrum of the pristine MIL-100 (Fe), three regions were identified from the newly PA-imposed features (Portilla & Halik, 2014). Both MIL-DPA and MIL-ODPA exhibit a broad signal between 1000 cm^{-1} to 1200 cm^{-1} that is attributed to the overlap of the P-O and the P=O vibrations of the PA anchor groups covalently bonded to the MOF surface. The presence of DiPPA is confirmed by the growing appearance of the characteristic P=O vibrations at 1063 and 1136 cm^{-1} along with DiPPA's incremental concentrations (Hynek *et al.*, 2017). The two peaks emerging in MIL-DPA and MIL-ODPA's spectra at around 2850 cm^{-1} and 2920 cm^{-1} correspond to the methylene (CH_2) group's vibrations of the PA aliphatic carbon chain, followed by a small shoulder at 2945 cm^{-1} of the methyl (CH_3) groups at the end of the alkyl chain. These CH absorption bands were only visible on MIL-DPA, but faintly on MIL-ODPA's FTIR spectra possibly due to MIL-DPA's higher grafting density. Therefore, only MIL-DPA was tested for TGA analysis.

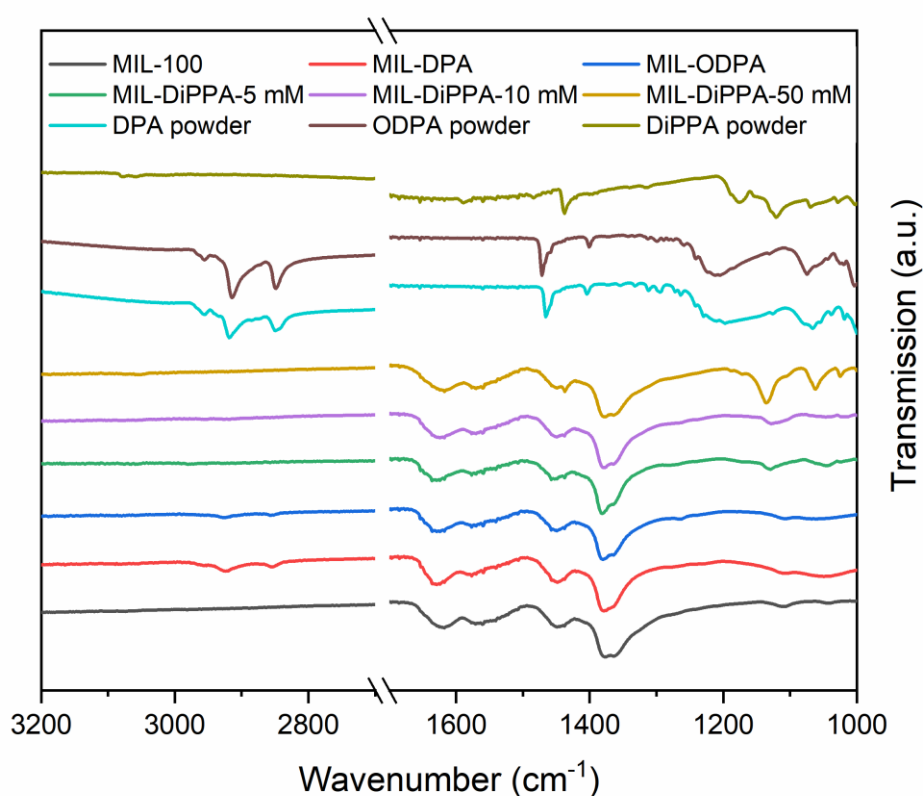


Figure A10.16: FTIR spectra of PA-treated MIL-100 (Fe).

Phosphonic acids have been previously shown to form strong bonds with the metal centre but if used in excess, they could substitute the carboxylic acid linker of the MOF (Deria et al., 2015). However, the 5 mM PA concentration used in this work may be too dilute to see any appreciable changes in the carboxylic acid spectra of the original MIL-100 (Fe). Such a feature would appear as a broad peak between 2500 and 3300 cm^{-1} . Normally, a linker displacement can be directly verified from a significant deviation from the theoretical PXRD patterns, but previous PXRD scans for all PA-coated MIL-100 (Fe) did not show this behaviour. On the other hand, the advantage of coating with phosphinic acid such as DiPPA is its stronger covalent bonding ability (Kloda et al., 2021) with the MOF's inorganic metal centres, but it does not impose the same linker displacement effect (Hynek et al., 2017).

10.4.7 Porosity analysis for PA-treated MIL-100 (Fe)

Table A10.9 shows the BET surface area and the total pore volume of the PA-treated samples. These coated samples presented minimal surface area and total pore volume reductions. Almost intact resemblance was observed in the pore size distribution plots of MIL-PA samples as shown in Figure A10.17. It confirms that the coatings are residing along the outer pore periphery or on the crystal surface instead of situated inside the pores.

Table A10.9: Porosity analysis for select PA-treated MIL-100 (Fe).

Sample	BET surface area (m^2/g)	External surface area (m^2/g)	V_{total} (cm^3/g)	V_{micro} (cm^3/g)	$V_{\text{micro}}/V_{\text{total}}$
MIL-100 (Fe)	1805	65	0.810	0.735	0.907
MIL-DPA	1578	63	0.682	0.609	0.893
MIL-ODPA	1430	60	0.634	0.563	0.888
MIL-DiPPA-5 mM	1401	100	0.693	0.537	0.775
AC	1179	242	0.805	0.470	0.584

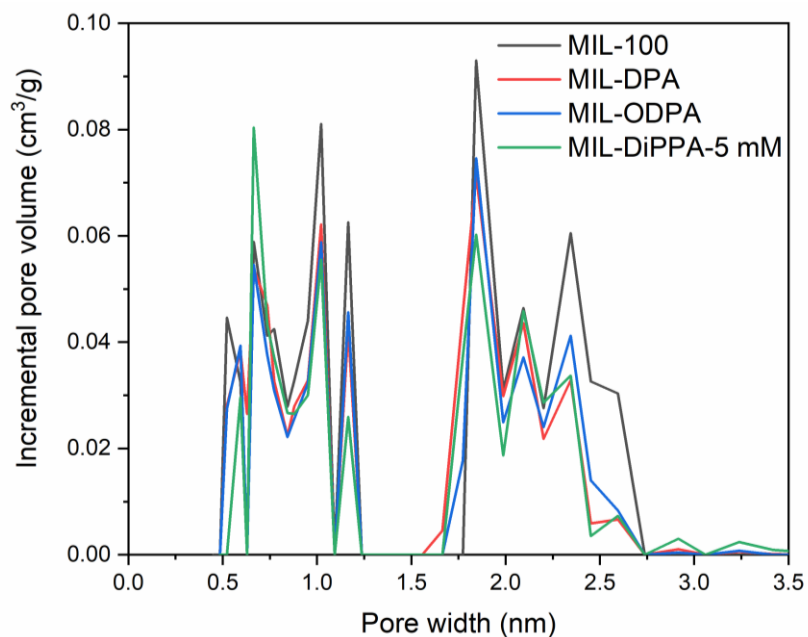


Figure A10.17: Pore size distribution plots for MIL-PA samples.

10.4.8 Porosity analysis for Cx-treated MIL-100 (Fe) samples

Figure A10.18 shows the pore size distribution plots for the calixarene-treated MIL-100 (Fe) samples. The similarity observed in the overlay plots means these calixarene coatings can keep their materials' porosities intact.

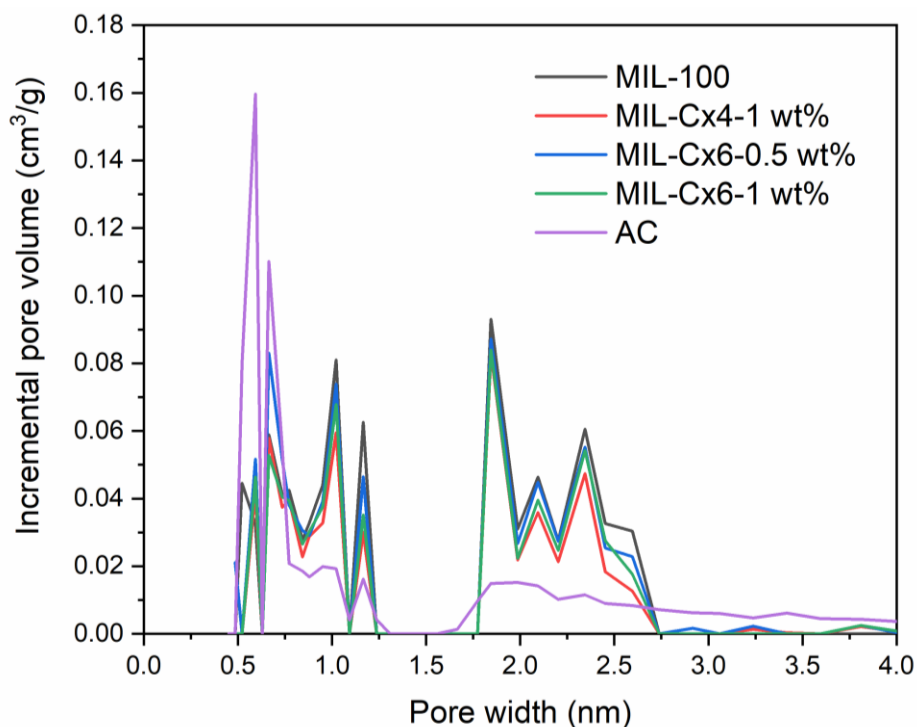


Figure A10.18: Pore size distribution plots for calixarene-treated MIL-100 (Fe) samples.

10.4.9 N₂ adsorption and desorption isotherms

Figure A10.19 shows the N₂ adsorption and desorption isotherm plots for all studied MIL-100 (Fe) samples.

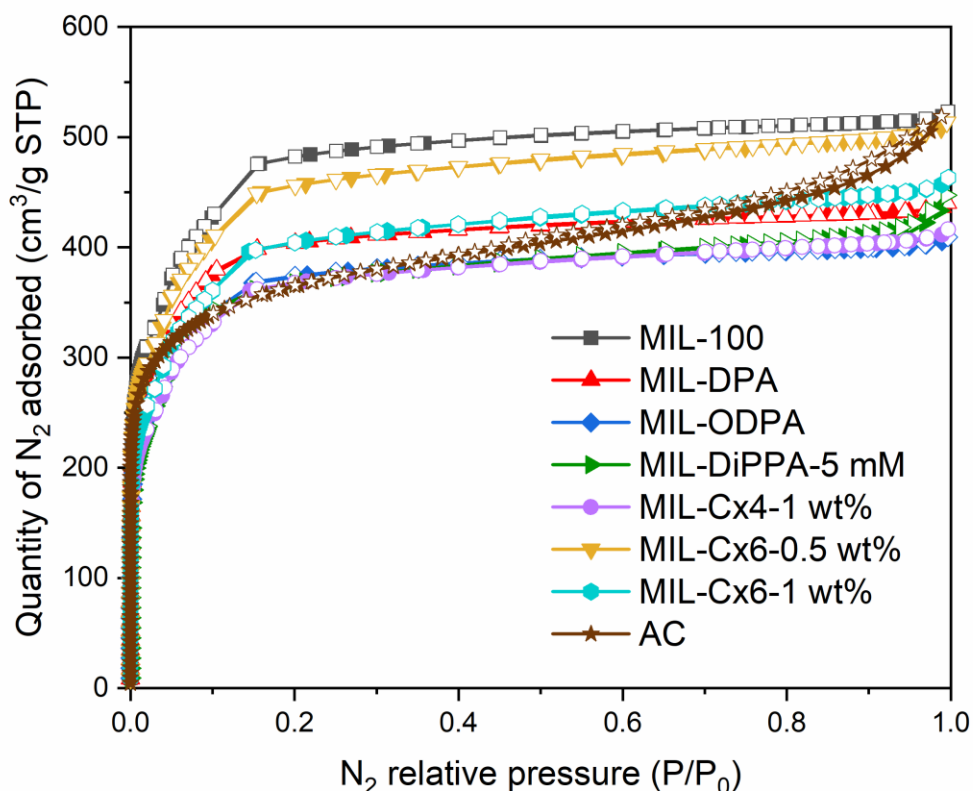


Figure A10.19: N₂ adsorption and desorption isotherm plots for all studied samples. Filled shapes refer to adsorption while empty shapes are for desorption.

10.4.10 Water contact angles of PA-treated MIL-100 (Fe)

Table A10.10 compiles the water contact angles measured on all PA-treated MIL-100 (Fe). The PA-treated MIL-100 (Fe) samples exhibit a major improvement in their advancing water contact angles, becoming hydrophobic ($> 120^\circ$). There is a minimal difference in the advancing water contact angles of MIL-ODPA compared to MIL-DPA despite the difference in PA chain length. Moreover, considering that MIL-DPA has a higher surface area, this is a more suitable material to be used in further detailed studies.

Table A10.10: Advancing water contact angles of all PA and Cx-treated MIL-100 (Fe) samples.

Sample	Advancing water contact angle (°)
MIL-100 (Fe)	34.2 ± 2.0
MIL-DPA	132.4 ± 5.3
MIL-ODPA	138.6 ± 2.0
MIL-DiPPA-5 mM	123.4 ± 2.0

10.4.11 Water contact angle images of Cx-treated MIL-100 (Fe)

Figure A10.20 shows the effect of water contact on MIL-Cx4-1 wt% and MIL-Cx6-1 wt%.

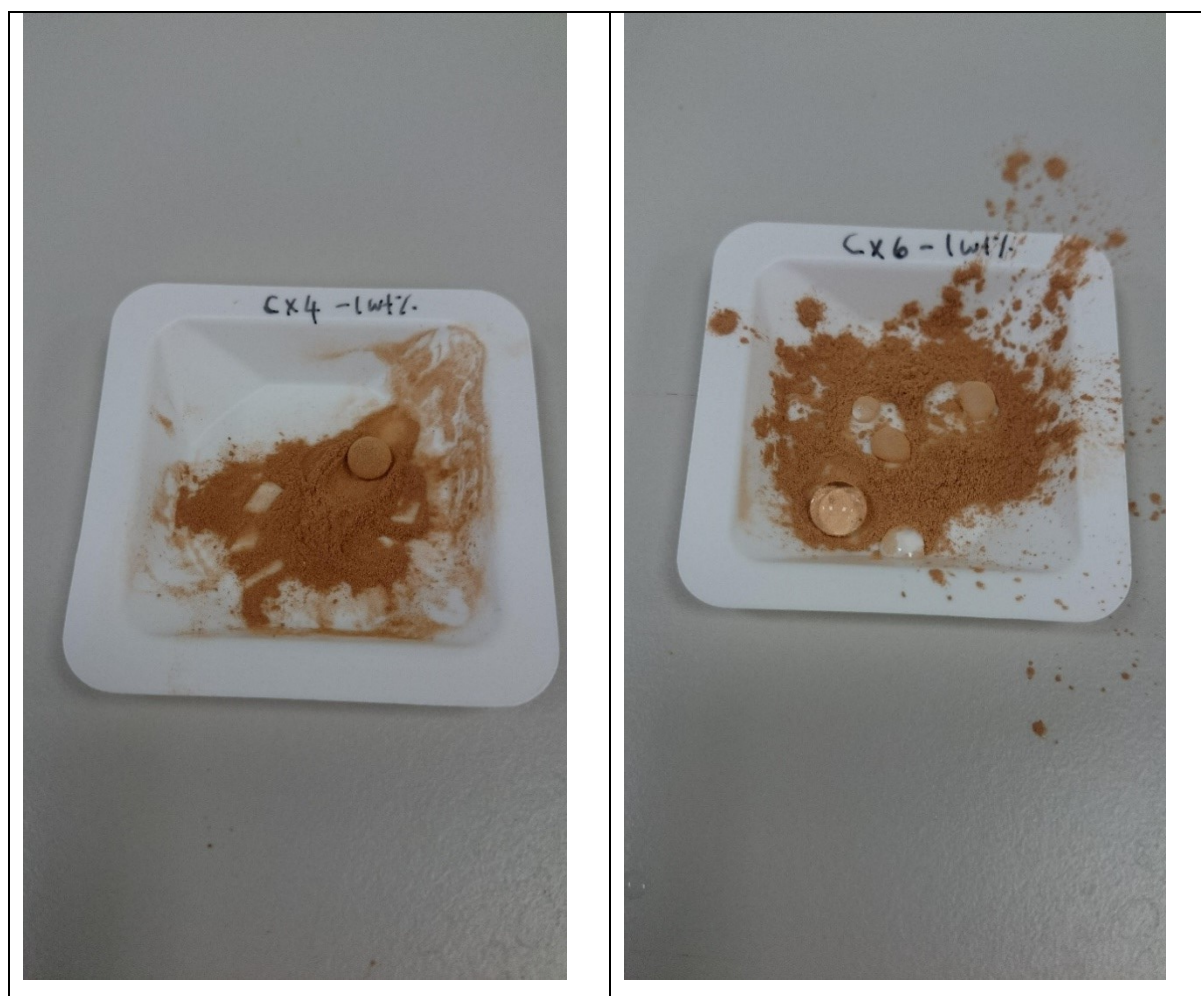


Figure A10.20: Images showing formation of a liquid marble when (left) MIL-Cx4-1 wt% and (right) MIL-Cx6-1 wt% powder is in contact with water droplets.

10.4.12 Water sorption isotherms of PA-treated MIL-100 (Fe)

Figure A10.21 shows the water adsorption and desorption isotherms of selected PA-treated MIL-100 (Fe). The order of maximum water adsorption uptake at 80% RH for the PA-MIL-100 samples is: MIL-DPA < MIL-DiPPA-5 mM < MIL-100 (Fe). The 80% RH capacity for MIL-DiPPA-5 mM is higher than MIL-DPA although the former has a lower surface area. It is difficult to infer any explanation for this, but the inconsistency is perhaps caused by variation among the synthesized material batches. More importantly, among these samples, only MIL-DPA prolonged MIL-100 (Fe)'s first inflection point, originally located at 20% water P/P₀ to 40% water P/P₀. This nominally higher P/P₀ shift could result from its improved hydrophobicity, with the coating present around the MIL-DPA's mesopores.

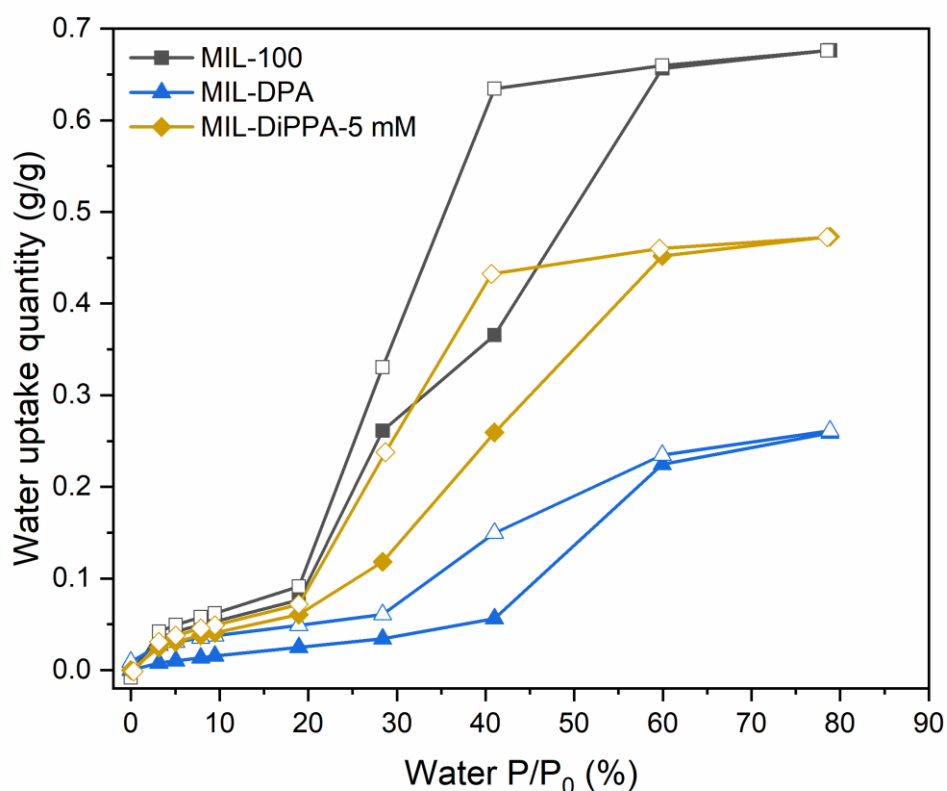


Figure A10.21: Water adsorption and desorption isotherms of PA-treated MIL-100 (Fe). Filled symbols denote adsorption while empty symbols refer to desorption.

10.4.13 Toluene sorption isotherms of PA-treated MIL-100 (Fe)

Figure A10.22 shows the dry toluene adsorption and desorption isotherms of selected PA-treated samples. It shows a clear difference between the toluene uptake quantity of the PA-coated samples and of the pristine MIL-100 (Fe). The order of 80% P/P₀ toluene uptake agrees with their previous 80% RH water adsorption capacity order: MIL-DPA < MIL-DiPPA-5 mM < MIL-100 (Fe), where MIL-DiPPA-5 mM (1401 m²/g) with lower surface area shows higher uptake than the higher surface area MIL-DPA (1578 m²/g). This confirms that the disproportionate material's surface area with the order of 80% water or 80% toluene P/P₀ uptake is due to some subtle variations between batches despite rigorous adherence to the synthesis, handling protocols and identical storage conditions. These precautions are expected to eliminate any major variations due to different sample properties post-synthesis.

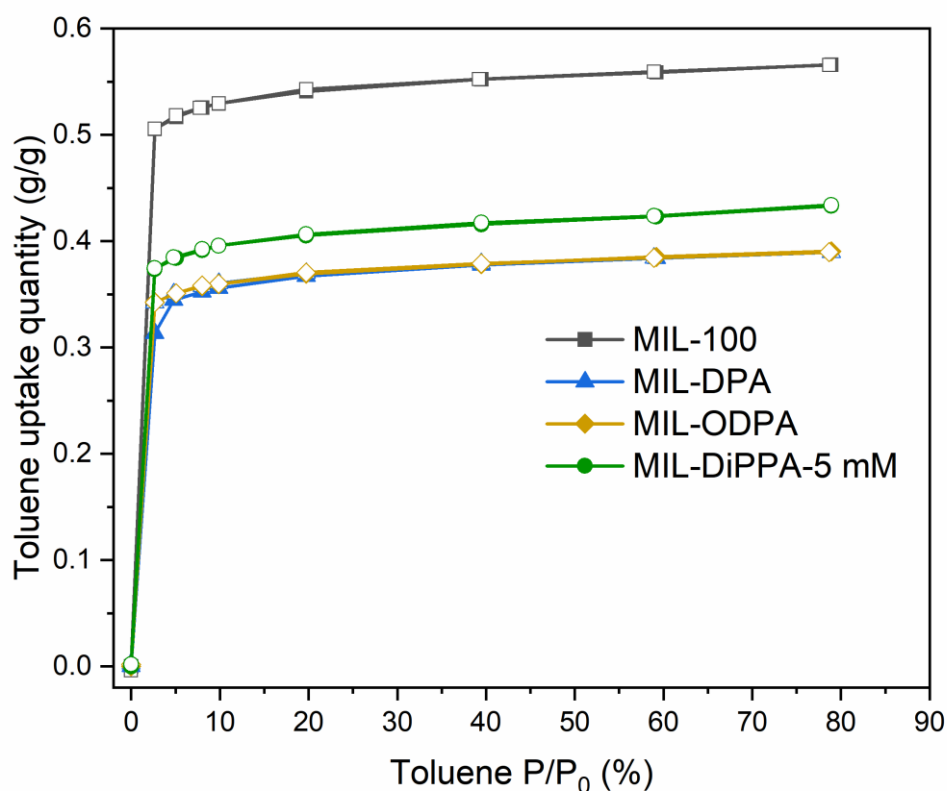


Figure A10.22: Dry toluene adsorption and desorption isotherms of PA-treated MIL-100 (Fe). Full shapes refer to adsorption whereas empty shapes are for desorption.

Since MIL-100 (Fe) has the highest surface area relative to its PA-treated counterparts, when only toluene is present for adsorption at a given time, high surface area becomes the primary factor to obtain maximum adsorption quantity. In terms of the adsorption mechanism, even though MIL-100 (Fe) contains Fe metal centres that may function as strong Lewis acid sites (electron-pair acceptors), the toluene molecules were found to have a distribution preference around the ligand proximity. The absence of hysteresis in the toluene isotherms also suggests the formation of a strong π - π conjugate stacking interaction between the toluene and the trimesic acid ligand (Duan *et al.*, 2019).

10.4.14 Hydrophobicity index of PA-treated MIL-100 (Fe)

Figure A10.23 shows the calculated hydrophobicity index for the studied PA-treated MIL-100 (Fe). Among the family of PA coatings investigated, only MIL-DPA showed a comparable HI improvement. As for MIL-DiPPA-5 mM, this preliminary finding may signal its susceptibility towards water adsorption and its lower prevalence in co-adsorption situation.

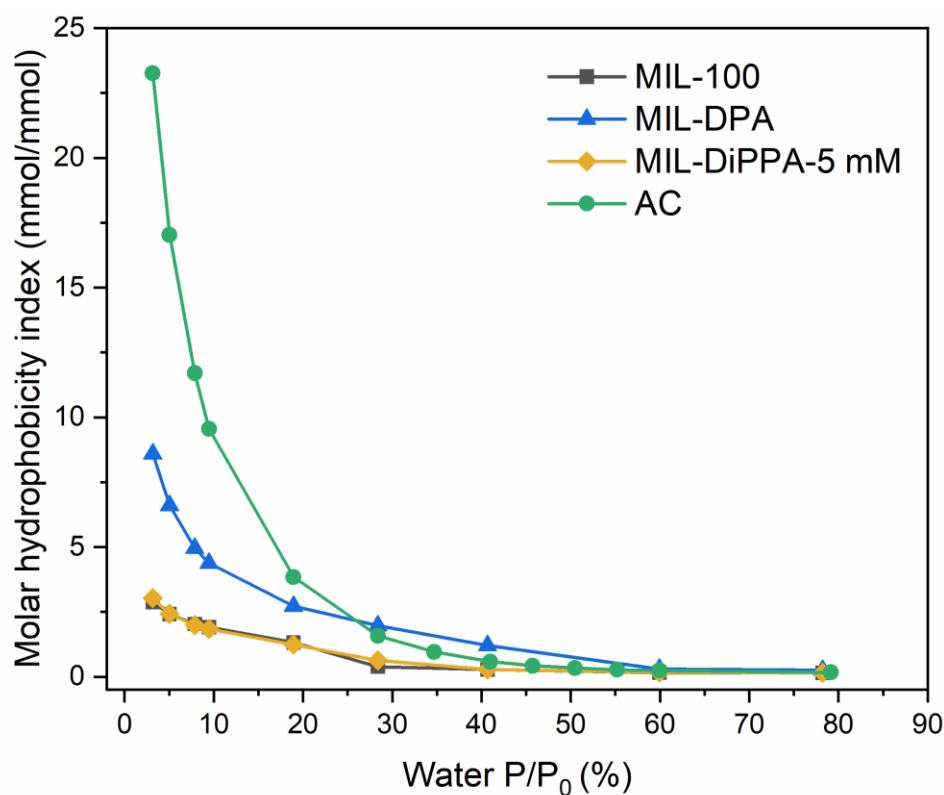


Figure A10.23: Molar hydrophobicity index of PA-treated MIL-100 (Fe).

10.4.15 Uptake capacity of PA-treated MIL-100 at 40% RH and 0% toluene

The figures presented in Section 10.4.15 and 10.4.16 summarise the measured equilibrium toluene adsorption quantity and kinetics by all PA coated samples at 0%, 0.5% and 10% toluene P/P_0 concentrations in parallel with 40% RH background. Figure A10.24 shows the 40% RH and 0% toluene P/P_0 uptake capacity by all studied MIL-PA samples. After coating different types of PA on the MIL-100 precursor, their 40% water P/P_0 uptake capacities reduced proportionally with their degree of pore blockage. In other words, these coatings were not too protective against water adsorption unlike AC that showed very low uptake capacity. Since the MIL-DiPPA group's uptake capacity is inversely related to the DiPPA concentration increment, so, it is reasonable to focus only on the lowest concentration sample, namely MIL-DiPPA-5 mM for further analysis.

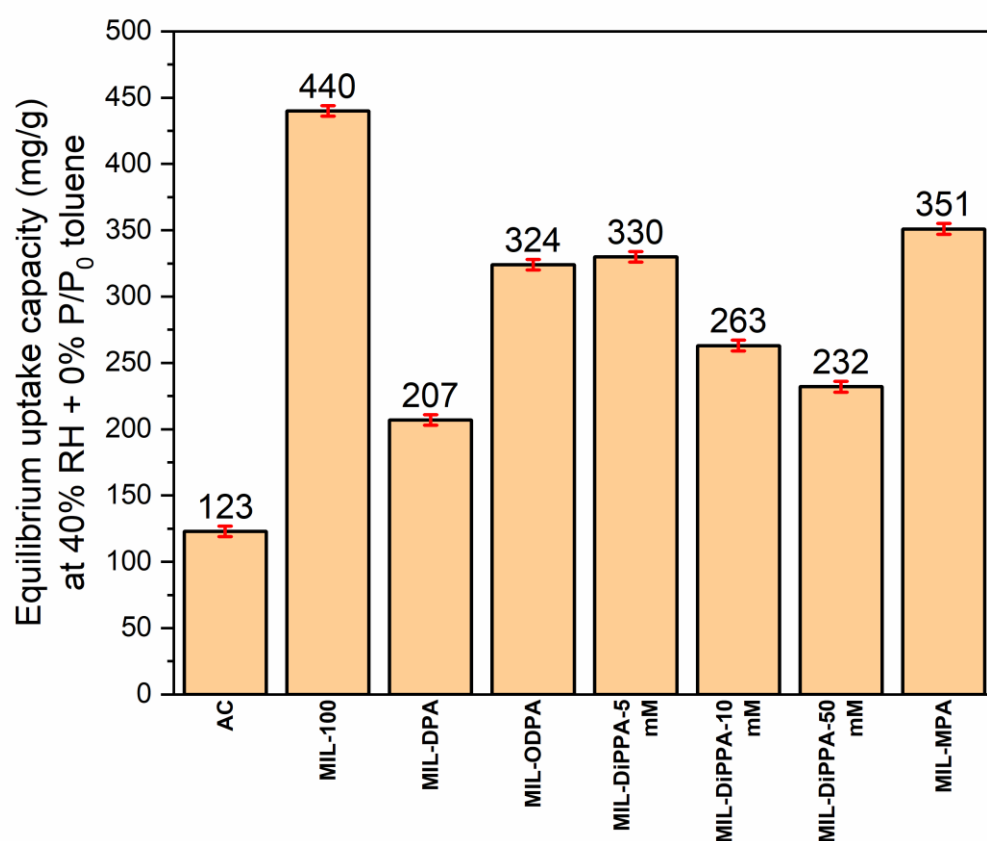


Figure A10.24: 40% RH and 0% toluene P/P_0 adsorption capacity of PA-treated MIL-100 (Fe).

10.4.16 Uptake capacity of PA-treated MIL-100 (Fe) at 40% RH and 0.5% toluene

Figure A10.25 shows the 40% RH and 0.5% toluene P/P_0 adsorption capacity exhibited by MIL-100 (Fe) and selected PA-treated samples. They are relatively similar between one another. Even after implementing the PA treatment, the MIL-PA samples still have higher surface areas compared to AC based on the data from Table 6.3. However, their uptake is significantly lower than AC. This implies that the order of competitive 0.5% toluene P/P_0 uptake by the adsorbents cannot be simply ascribed to their differences in surface area and is most likely influenced by other dominant property effects such as hydrophobicity. Plus, MIL-MPA also did not show any higher uptake than MIL-100 (Fe). It is interpreted that although the CH_3 group in the MPA has a hydrophobic nature, it might form hydrogen bonding with water while in the process of adsorbing toluene. This water preference and occupation could be the reason for its lower co-toluene uptake.

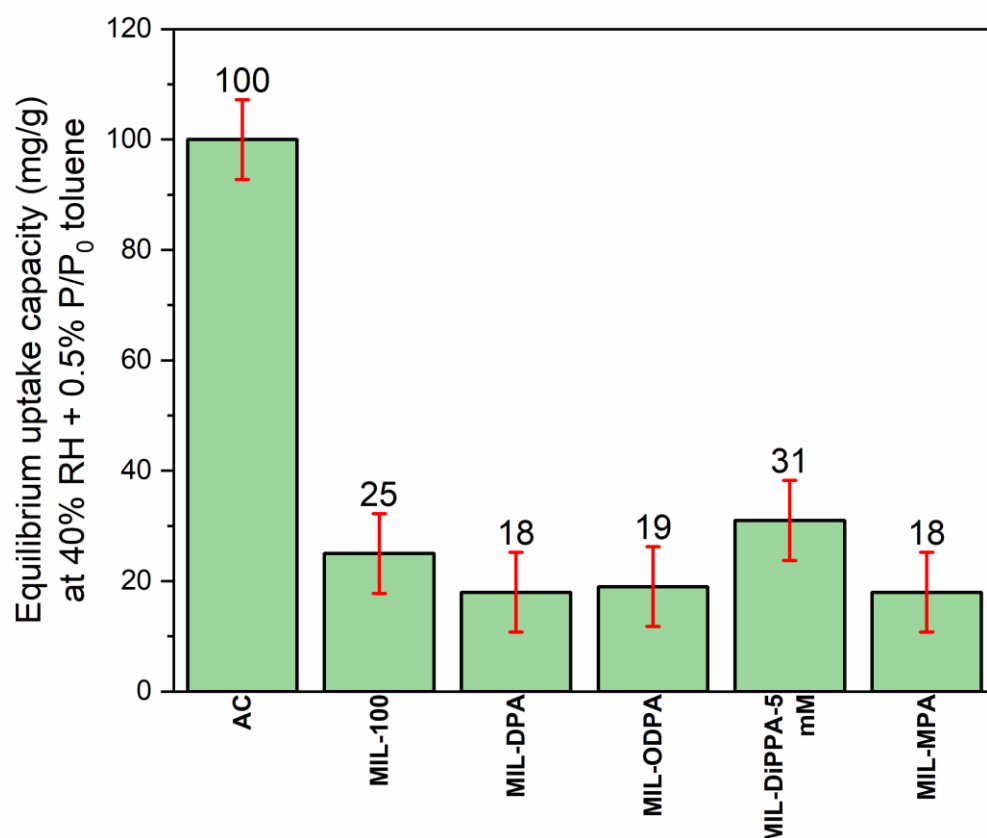


Figure A10.25: 40% RH and 0.5% toluene P/P_0 adsorption capacity of PA-treated MIL-100 (Fe).

10.4.17 Uptake capacity of PA-treated MIL-100 (Fe) at 40% RH and 10% toluene

Figure A10.26 shows the 40% RH and 10% toluene P/P₀ uptake capacity by all MIL-PA samples. Here, AC once again showed the highest toluene adsorption uptake at 40% RH and 10% toluene P/P₀ compared to the MOFs because of its intrinsic hydrophobicity. All PA-treated MIL-100 (Fe) exhibited lower uptake than the pristine MIL-100 (Fe) due to their reduced surface area. When tested at low toluene concentration or 0.5% toluene P/P₀, the PA coatings seem to function well as observed from the relatively unchanged uptake capacity compared to MIL-100 (Fe). However, as the toluene concentration increases to 10% P/P₀, the limited coating quantity is no longer effective to provide the same water protection, hence, the vast difference obtained here between the MIL-100 (Fe)'s uptake quantity and these samples. Earlier discussions have alerted that there could be some chances of the introduced PA slightly altering the ligand framework. Capacity-wise, it appears that the untreated hydrophobic ligand contained in the MIL-100 (Fe) framework could have helped it to attain a moderately higher capacity compared to the rest MIL-PA samples.

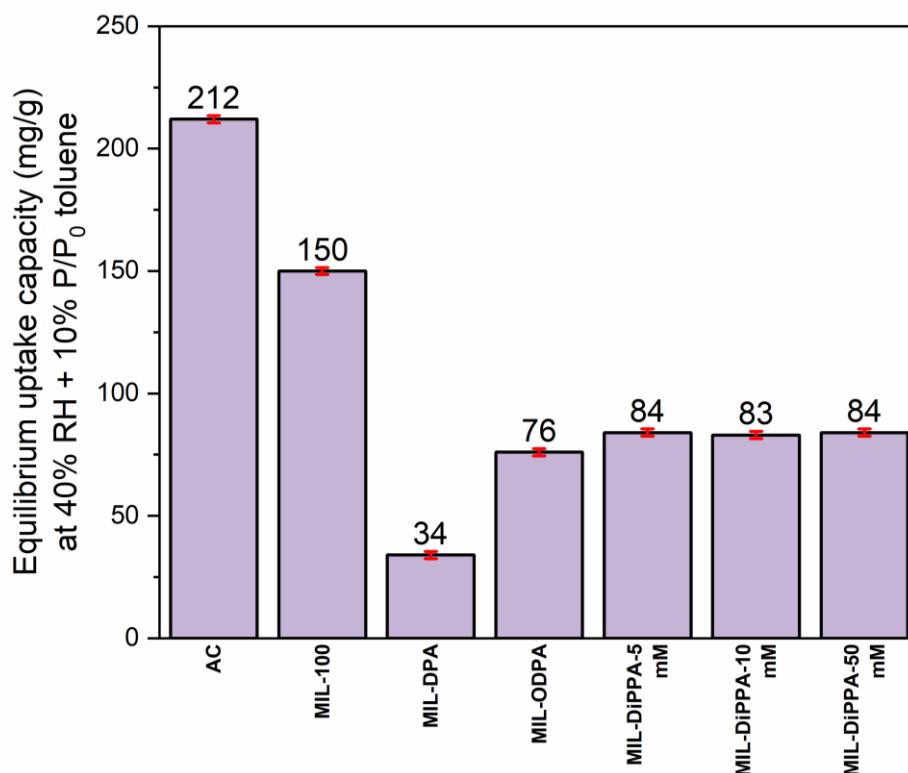


Figure A10.26: 40% RH and 10% toluene P/P₀ adsorption capacity of PA-treated MIL-100 (Fe).

10.4.18 Adsorption kinetics of PA-treated MIL-100 (Fe) at 40% RH and 0.5% toluene

Figure A10.27 shows the toluene adsorption kinetics of selected PA-treated samples at 40% RH and 0.5% toluene P/P₀. AC was not included in the complete kinetics plot Figure A10.27 (left) due to the excessive time taken to reach equilibrium within the DVS' stipulated steady state mass set point ($dm/dt = 0.001$ or 1440 mins, whichever is achieved first). Additionally, the inferior capacity of all MIL-100 (Fe) materials compared to AC will diminish the MIL-100 (Fe) plots. MIL-DiPPA-5 mM has nominally higher final uptake than the pristine MIL-100 (Fe) despite its lower surface area. This is an excellent indicator of the DiPPA's surface coating advantage in enhancing the toluene-sorbate interaction.

To check this, a downscaled adsorption plot within the first 120 minutes of adsorption time is shown in Figure A10.27 (right). In line with the initial expectation, MIL-DiPPA-5 mM's linear initial kinetics *slope* is at par with the pristine MIL-100 (Fe). The remaining PA-treated samples demonstrated slower adsorption rate than the pristine MIL-100 (Fe). Despite the definite loss of surface area after the PA treatment, an optimized concentration and minimized steric hindrance of phosphinic acids could be potentially useful to enhance the toluene-sorbate interaction at low toluene concentration compared to when using phosphonic acids. So, the increasing order of 40% RH/0.5% toluene P/P₀ by MIL-PA samples is as follows (values in bracket are the linear initial *slopes*):

MIL-100 (Fe) (0.104) > MIL-DiPPA-5 mM (0.101) > AC (0.081) > MIL-ODPA (0.075) > MIL-DPA (0.065).

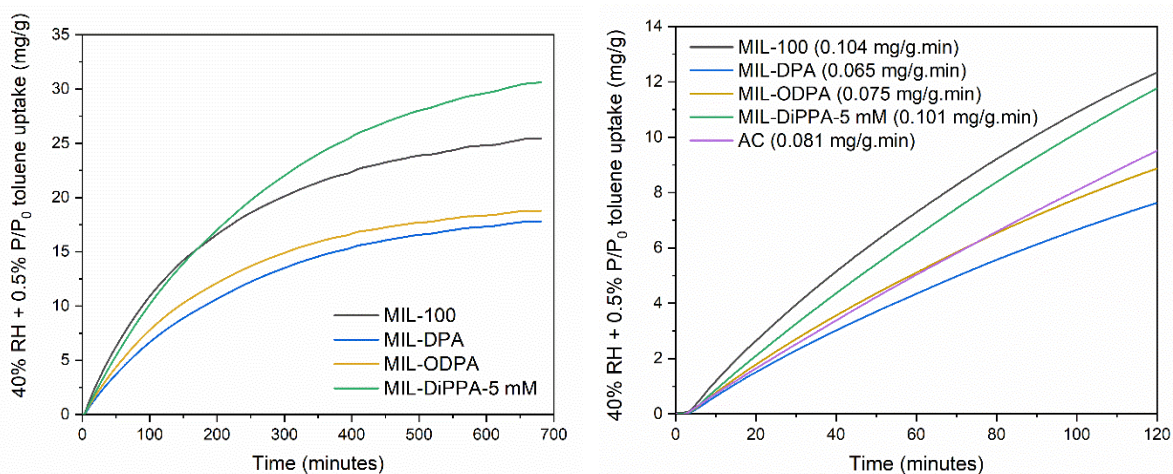


Figure A10.27: (Left) 40% RH and 0.5% toluene P/P₀ full range adsorption kinetics of PA-treated MIL-100 (Fe). (Right) The first 120-minute adsorption rate is shown on the right inclusive of the linear-fitted slope values given in the legend brackets.

10.4.19 Adsorption kinetics of PA-treated MIL-100 (Fe) at 40% RH and 10% toluene

Figure A10.28 (left) shows the adsorption kinetics performance of all PA-treated samples when assessed at 40% RH and 10% toluene P/P₀ concentration. It is observed that all PA-treated MOFs showed a decrease in their equilibrium uptake capacities because of their capped surface areas. Although AC's micro porosity and lower surface area caused slower uptake and lower adsorption quantity until the 110th minute, it eventually gained trajectory as soon as the toluene build-up able to penetrate its pores. The lapse of toluene uptake in the initial adsorption phase may as well be because of the proximity between the toluene molecular diameter (5.5 Å) and AC's pore size. By and large, the inherent hydrophobicity of AC gives it a prominent quality to protect the pores from being inundated with water whilst simultaneously capable of adsorbing toluene molecules.

Within the first 30 minutes adsorption at 40% RH and 10% toluene P/P₀ as shown in Figure A10.28 (right), MIL-100 (Fe) is still the sample with the highest kinetics compared to other studied PA-treated samples. AC displays the lowest *slope*. At a higher toluene P/P₀ concentration, it has indeed undermined the coating effectiveness which indirectly implies high surface area as a more important factor amongst MOFs. This is proven by the higher capacity and kinetics shown by the untreated MIL-100 (Fe).

Until this juncture, it is obvious that there is a difficult trade-off between maintaining the treated material's surface area post-modification and yielding the desired hydrophobic effect for an effective humid toluene capture. So, the increasing order of 40% RH/10% toluene P/P_0 by MIL-PA samples is as follows (values in bracket are the linear initial *slopes*):

MIL-100 (Fe) (3.227) > MIL-DiPPA-10 mM (2.621) > MIL-DiPPA-50 mM (2.572) > MIL-DiPPA-5 mM (2.298) > MIL-ODPA (1.976) > AC (1.864) > MIL-DPA (1.577).

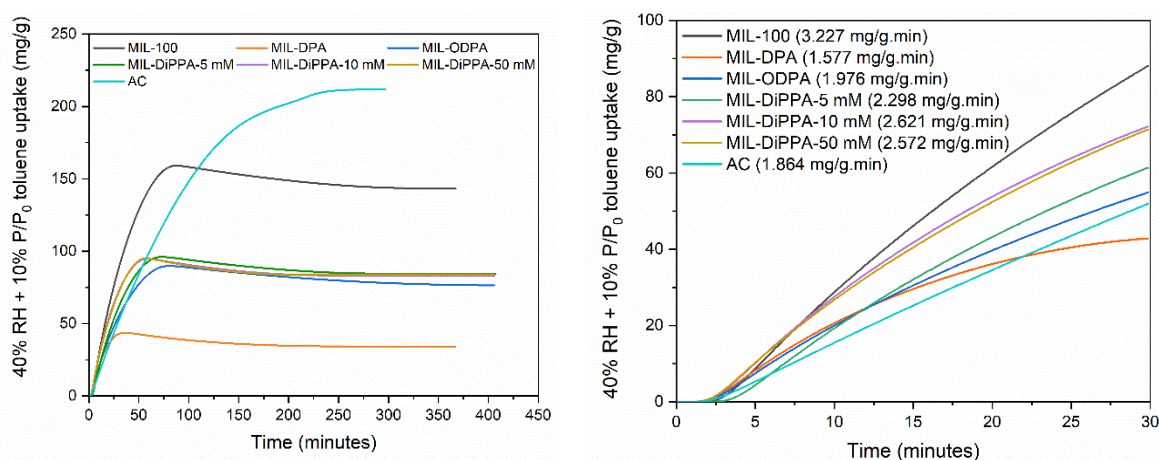


Figure A10.28: (Left) 40% RH and 10% toluene P/P_0 full range adsorption kinetics of PA-treated MIL-100 (Fe). (Right) The first 30-minute adsorption rate is shown on the right inclusive of the linear-fitted slope values given in the legend brackets.

10.4.20 Overall kinetics analysis of PA-treated MIL-100 (Fe) using a linear initial slope fit

Table A10.11 shows the estimated linear initial *slope* values for all PA-treated MIL-100 (Fe). The unit of the *slope* is equivalent to the uptake rate of each sample. At 40% RH and 0.5% toluene P/P_0 , the PA-treated samples did not show much improvement compared to the pristine MIL-100 (Fe). Similarly, at 40% RH and 10% toluene P/P_0 , the PA-treated samples failed to achieve a better kinetics performance than the original MIL-100 (Fe).

Table A10.11: Linear-fitted parameters of all PA-treated MIL-100 (Fe) samples.

Sample	Experimental q_e values and their linear-fitted parameters					
	40% RH/0.5% toluene P/P ₀			40% RH/10% toluene P/P ₀		
	q_e (mg/g)	<i>slope</i> (mg/g.min)	R ²	q_e (mg/g)	<i>slope</i> (mg/g.min)	R ²
MIL-100 (Fe)	26	0.104	0.989	150	3.227	0.995
MIL-DPA	19	0.065	0.993	36	1.577	0.952
MIL-ODPA	19	0.075	0.992	82	1.976	0.992
MIL-DiPPA-5 mM	34	0.101	0.996	88	2.298	0.993
MIL-DiPPA-10 mM	-	-	-	86	2.621	0.987
MIL-DiPPA-50 mM	-	-	-	86	2.572	0.990
AC	100*	0.081	0.998	212	1.864	0.999

* The value may not represent AC's equilibrium uptake due to its slow adsorption rate.

10.4.21 Overall kinetics analysis of PA-treated MIL-100 (Fe) using a nonlinear pseudo first order kinetics model

Table A10.12 shows the calculated PFO kinetics parameters of all PA-treated samples at 0.5% and 10% toluene P/P₀ concentrations. At 0.5% toluene P/P₀, the PA-treated MIL-100 (Fe) samples exhibit roughly similar $q_e.k_1$ values compared to the pristine version, indicating little to no improvement on the PA-treated samples' kinetics. Similar poor performance was noticed at 10% toluene P/P₀. However, the data at higher toluene concentration could be potentially overestimated, inferring from the poor fitting values ($R^2 < 0.98$) obtained from the PFO model.

Table A10.12: Fitted values of the PA-treated MIL-100 (Fe) samples' adsorption kinetics profiles using nonlinear pseudo-first order equation.

Sample	Experimental q_e and pseudo first order-fitted model parameters							
	40% RH/0.5% toluene P/P ₀				40% RH/10% toluene P/P ₀			
	q_e (mg/g)	$k_1 \times 10^3$ (min ⁻¹)	$q_e \cdot k_1$ (mg/g.min)	R ²	q_e (mg/g)	$k_1 \times 10^3$ (min ⁻¹)	$q_e \cdot k_1$ (mg/g.min)	R ²
MIL-100 (Fe)	26	5.2	0.135	0.999	150	35.7	5.36	0.932
MIL-DPA	19	4.2	0.080	0.999	36	113.5	4.09	0.678
MIL-ODPA	19	5.0	0.095	0.999	82	43.5	3.57	0.987
MIL-DiPPA-5 mM	34	3.5	0.119	0.999	88	45.1	0.397	0.895
MIL-DiPPA-10 mM	-	-	-	-	86	59.3	5.10	0.889
MIL-DiPPA-50 mM	-	-	-	-	86	57.8	4.97	0.898
AC	100*	-	-	-	212	9.98	2.32	0.994

* The value may not represent AC's equilibrium uptake due to its slow adsorption rate.

10.5 Appendix for Chapter 7

10.5.1 SEM images of MIL-101-HPAM

Figure A10.29a – c shows SEM images of HPAM-modified MIL-101 (Cr) (maximum tested $R_{\text{HPAM}} = 0.6$). Even though larger sized cluster formation was observed at higher HPAM loadings, the primary crystal size and morphology are similar across all MIL-101 (Cr) samples. The linker that was used, terephthalic acid (TPA) has lower water solubility compared to HPAM (Wang, Xu & Li, 2005). Pre-mixing of these two species appears counter effective since the ready miscibility of HPAM and the partial dissolution of TPA molecules in water ($\text{pK}_{\text{a}1} = 3.51$ at $25\text{ }^{\circ}\text{C}$) led to no observable change of the morphology. Besides, due to the small change in hydrated particle size (still within nanometre range) and no trace of HPAM detected in the FTIR spectra, agglomeration is possibly just a side product of unwashed HPAM adhering on the surface when being in contact with water. Although the powders were studied under dry conditions for SEM visualization, even an elevated temperature activation ($120\text{ }^{\circ}\text{C}$) appears insufficient to remove the already penetrated HPAM located within the pores of MIL-101 (Cr), hence, the reason to observation of more clusters with higher HPAM quantities.

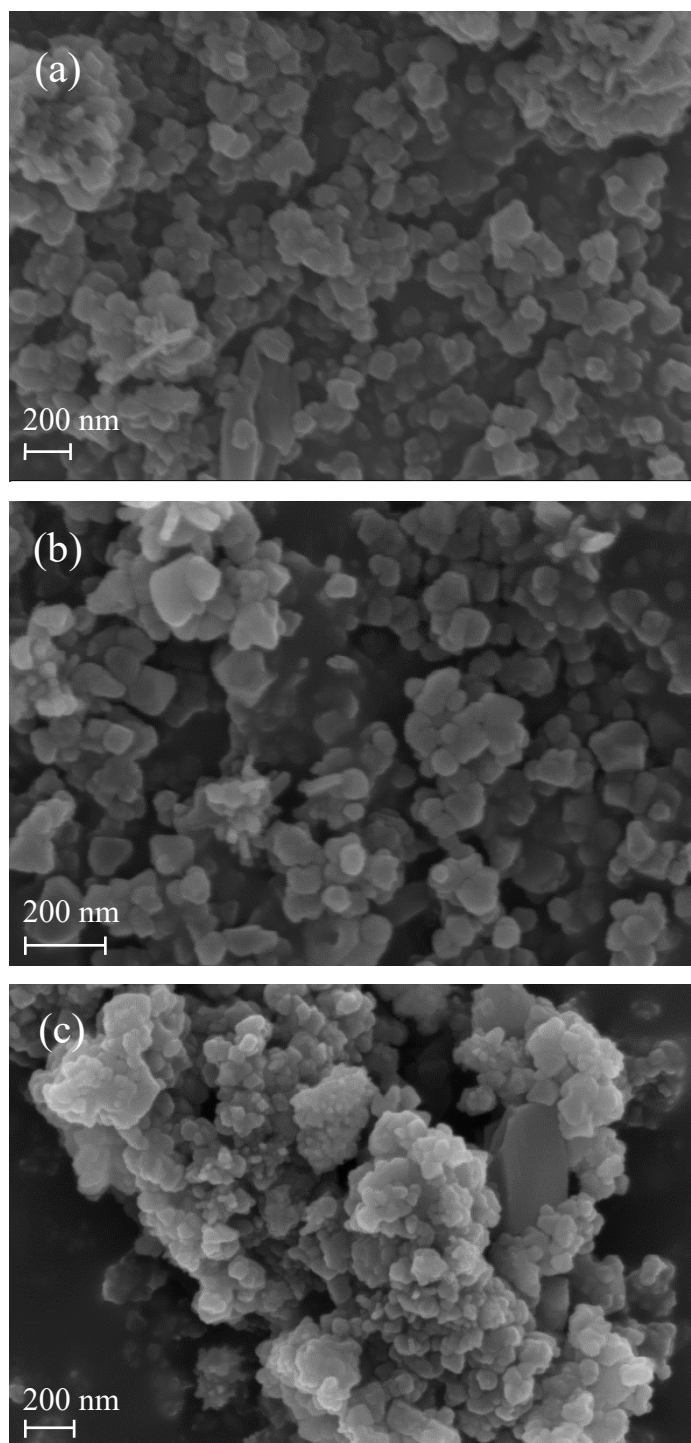


Figure A10.29: SEM images of HPAM-modified MIL-101 (Cr) where (a) MIL-101 (RHPAM = 0), (b) MIL-101 with 1 mL HPAM (RHPAM = 0.2) and (c) MIL-101 with 3mL HPAM (RHPAM = 0.6).

10.5.2 FTIR analysis of HPAM-treated trimesic acid ligand

To identify the ligand-polymer interaction during the pre-mixing step in the synthesis, only the ligand was hydrothermally treated with HPAM. The analysis of interactions between the treated-TMA and HPAM can be seen in Figure A10.30. It can be observed that the HPAM-treated TMA ligand's spectra matched with the original ligand spectra (Mahalakshmi & Balachandran, 2014) except for the bands between 1000 and 1500 cm^{-1} which became more intense and broader in the presence of HPAM. The broadening suggests formation of inter and intra molecular hydrogen bonding between the ligand and the polymer during the hydrothermal process (Nandiyanto, He & Wang, 2019).

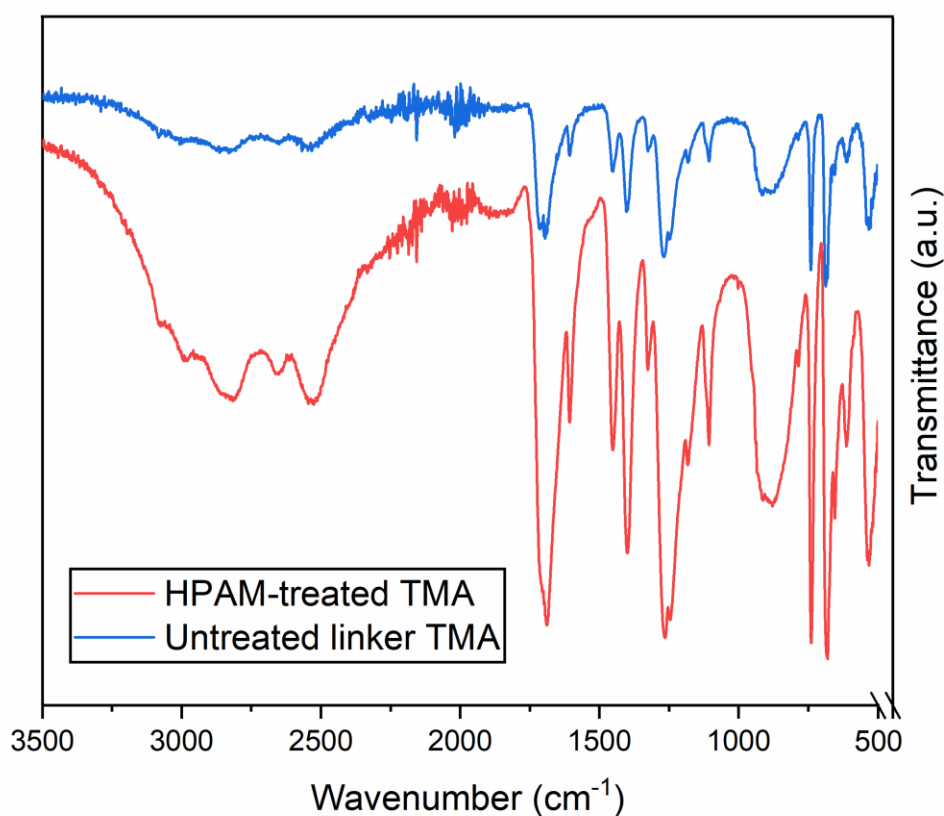


Figure A10.30: FTIR spectra of the linker trimesic acid (TMA) before and after the hydrothermal heating process with HPAM.

10.6 Granted permission for copyrighted materials

All licences were requested on 26th October 2021 and were approved on the same day. All articles published by the American Chemical Society can be redistributed without prior permission. Other sources that are used in this thesis, but not listed here have the Creative Commons Attribution 4.0 International (CC BY 4.0) license, hence, making them open access materials.

Figure	Granted licence number
1.1	5176530644090
1.3	1157142-1
1.5	1157148-1
2.2	5176560876580
2.3	5176560965454
2.4	5176561061159
2.6	5176561452602
2.7	5176570389911
2.11	5176570697777
2.12	5176600994898
2.13	5176601097458
2.15	1157175
2.16	5176601488738
3.6	5176610407298
3.12	5176610504856

Table	Granted licence number
1.2	1157182-1
2.5	5176621242257, 5177030226149
3.3	5176660024645